Diagenetic Controls on the Phyllosilicate Fabric of Mudstones

By

Ruarri J. Day-Stirrat

A thesis submitted to the University of Newcastle Upon Tyne in partial fulfilment of the requirements for the degree of Doctor of Philosophy in the Faculty of Science

School of Civil Engineering and Geosciences
University of Newcastle Upon Tyne
Newcastle Upon Tyne, UK.
May 2006

Declaration

I, hereby, certify that the work described in this thesis is my own, except where otherwise acknowledged and has not been submitted previously for a degree at this, or any other University

Ruarri J. Day-Stirrat

Dedication:

This thesis is dedicated to my Mum,

Susan Day,

and my Grandparents,

Patrick and Naomi Day.

Who laid the foundations for who I am today.

Acknowledgements:

I would like to thank Professor Andrew Aplin for giving me the opportunity to complete this thesis. I would also like to extend my thanks for his advice, guidance, support and enthusiasm throughout my Ph.D. I, also, gratefully acknowledge the advice and friendship of Dr. Kuncho Kurtev.

I would like to extend my gratitude to Professor Ben van der Pluijm, Dr. John Solum and Dr. Anja Schleicher (University of Michigan, Ann Arbor) for the opportunity to use their HRXTG setup and their help with interpretation of the data. Additionally, Dr. Andy Brown and Dr. Catherine Love (Leeds University) are thanked for their help in using the SEM and TEM. Access to Steve Hillier's XRD setup (Macaulay Institute, Aberdeen) is also greatly appreciated, as were the time and discussions with James Illife (BP Exploration, UK). Thanks are extended to Jan Środoń (Polish Academy of Sciences, Krakow) for supplying the samples from the Podhale Basin and BP Exploration for releasing samples and logs for the Northern North Sea.

The best technicians a Ph.D student could wish for are also acknowledged, Phil Green, Trevor Whitfield, Rob Hunter and Ian Harrison. A special thanks to Yvonne Hall for fixing everything related to administration, her speed, knowledge and can do attitude made everything move so smoothly.

Finally, Charlie Stalvies, Omar Baki, Jon Allinson, Maggie White and Julian Moore are thanked for their help support and perseverance during my years in Newcastle and Sasha Abrajevitch and Sergei Ziabrev while in Michigan. The volleyball boys and girls (assorted locals and foreigners) are thanked for the good times, the useless advice (jump higher re Roris!) and the opportunity to gain a degree in patience, tolerance and fortitude!

Abstract:

Changes to the orientation of phyllosilicates in mudstones in the Podhale Basin and the Northern North Sea have been quantified using High Resolution X-ray Texture Goniometry (HRXTG). Samples were studied from four wells: Chochołów PIG-1 and Bukowina Tatrzańska PIG-1 from the Podhale Basin, and Magnus 211/12-2 and Rhum 3/29a4 from the Northern North Sea. The samples cover a temperature range of ~60 to 170°C. Porosity and pore size distributions were quantified by mercury intrusion porosimetry. Changes in mineralogy with depth have been addressed by Quantitative X-ray Diffraction (XRD). Analytical Transmission Electron Microscopy (ATEM) was performed on illite-smectite from selected samples from the Podhale Basin. All wells were subjected to 1-D maturity modelling using Genesis 4.8®.

Maximum burial temperatures of the Podhale samples range from ~60 to ~170°C (3 and 8 km). XRD reveals that the sample sets straddle part of the smectite to illite R0 to R1 ordering transition zone and that illitization terminates at ~80% illite layers. An increase in chlorite and a decrease in both kaolinite and K-feldspar occur over the same depth/temperature interval. Quartz contents increase with increasing temperature. At the top of the sequence, porosities are close to 10%, indicating very substantial compaction. However, HRXTG shows that there is only a modestly preferred alignment of both illite-smectite and chlorite-kaolinite. A strongly aligned fabric is developed through the smectite to illite transition in Chochołów, with a less marked but readily measurable increase beyond the transition in Bukowina Tatrzańska. Samples from Chochołów document a strong relationship between millimetre-scale fabric and clay mineral transformations, but the relationship is more complex in Bukowina Tatrzańska. The trend in %I in illite-smectite shows a gradual increase with depth from ~37% layers to ~75% layers in Chochołów, with a fabric change from ~3.4 m.r.d. to 5.2 m.r.d. The trend in the %I in illite-smectite is constant at ~75% of layers in Bukowina Tatrzańska, but with a fabric increase from ~4.8 m.r.d. to ~6.2 m.r.d. ATEM has been performed on end member samples to determine chemical variation in illite-smectite. ATEM reveals significant differences in the octahedral sheet Fe concentrations of samples from Bukowina Tatrzańska with increasing temperature, pointing to continued crystallite change beyond the termination of smectite illitization. A relationship between SADP and structural formulae has been found. Single crystal patterns dominate where structural formulae reveal little or no substitution in the octahedral sheet.

Samples from Magnus (~3200m; ~120°C) and Rhum (~4800m; ~150°C) consist of Tertiary, Cretaceous and Jurassic sediments of varying thicknesses and maturity. Porosity reduction in both wells is from relatively uncompacted sediments (~45%) to tight muds (~5%). Preferred alignment of phyllosilicates is weak in shallow samples from both wells (m.r.d. ~ 2.3) and only shows a modest increase in Magnus as compaction and burial diagenesis (smectite illitization) proceed. Stronger phyllosilicate alignments are developed at the base of Rhum (6.1 m.r.d.). Generally, a high correlation between the two mineral peaks exists, the exception being the Jurassic of Rhum where low kaolinite and chlorite abundance as measured by XRD explains the low fabric development by HRXTG. XRD also reveals an increase in the %I in illite-smectite, 60% in Magnus and 65% in Rhum, with increasing depth and temperature. XRD reveals differences in mineralogy between the Jurassic, Cretaceous and Tertiary reflecting differences in depositional environment and sediment input.

1-D maturity modelling has established a correlation between, vitrinite reflectance, %I in illite-smectite and the development of preferred alignment of phyllosilicates. Little change in preferred alignment at porosities >15% has been noted, with the major changes occurring between ~15% and 5% porosity; this coincides with the change between R0 and R1 ordering in I-S and sits in a temperature range between 75°C and 125°C. The mechanism for preferred orientation change is therefore postulated to be dependent on the dissolution-precipitation reaction mechanism in smectite to illite formation in a high effective stress environment.

Contents:

List of Figures:

List of Tables:

Chapter 1: Introduction to the Diagenetic Controls on the Phyllosilicate Fabric of Mudstones:

1.0: Introduction:

This thesis is concerned with the quantification of preferred alignment of phyllosilicates in mudstones from the Podhale Basin, Southern Poland, and the Northern North Sea, UK, and how preferred alignments develop with increasing burial depth, porosity reduction and diagenetic mineral change.

1.1: The Controls on the Phyllosilicate Fabric of Mudstones:

1.1.1: Depositional Controls:

Fine-grained siliciclastic sediments dominate sedimentary systems around the world (O'Brien & Slatt, 1990; Schieber & Zimmerle, 1998; Aplin et al., 1999). The processes by which these sediments are deposited have long been the subject of investigation (e.g. Hjulstrøm, 1955; McCave, 1971, 1972; Rieke & Chilingarian, 1974; Potter et al., 1980; Chamley, 1989; Schieber, 1998). Fine-grained siliciclastic sediments probably have a random preferred alignment of phyllosilicates at deposition (e.g. Oertel, 1970; Oertel & Curtis, 1972; Page & Wenk, 1979; Curtis, 1980; O'Brien & Slatt, 1990; Sintubin, 1994; Ho et al., 1995, 1999; van der Pluijm et al., 1998; Merriman & Peacor, 1999; Jacob et al 2000; Matenaar, 2002; Worden et al., 2005) resulting from flocculation (e.g. Chamley, 1989; O'Brien & Slatt, 1990; Kranck, 1991) in estuaries, aggregation (e.g. McCave, 1971; Chamley, 1989) in deeper water settings and bioturbation (e.g. Bennett et al., 1991) at oxic sediment water interfaces. In exceptional circumstances depositionally aided preferred alignments of phyllosilicates may develop. Matenaar (2002) has recorded high alignments in sediments with low depositional rates in deep marine settings. In addition, the depositional environment has selected phyllosilicates at the expense of quartz, feldspar and other non-phyllosilicates pointing to particle make up being a significant factor in preferred alignment of phyllosilicates in mudstones. A decrease in fabric intensity with increasing quartz content during cleavage development was noted by Sintubin (1994). This suggests that the shape of the grains is significant both at deposition and beyond, additionally; the importance of

grain size has been noted by Matenaar (2002) and tacitly implied by Ho et al. (1999). Grain size, grain shape and grain content of a mudstone will affect alignment however mudstones tend to have a random preferred alignment of phyllosilicates at deposition.

As burial of these sediments in subsiding basins proceeds they are subjected to changes in compaction state and mineralogy. These changes act on sediments to rotate the platy phyllosilicates they contain into a preferred alignment until eventually beyond the diagenetic realm slatey cleavage is developed. Two processes act alone or in unison to alter the preferred alignment of phyllosilicates in mudstones; the first is mechanical rotation or kinking of discrete phyllosilicate grains; the second is chemical alternation either as phyllosilicate neo-crystallisation or dissolution-precipitation. Grain kinking and rotation prevails in low-energy environments (Sintubin, 1994; Ho et al., 1995, 1996) as mechanical processes are the most energetically favourable (van der Pluijm et al., 1998). At later stages of burial diagenesis and cleavage development (in the low-grade metamorphic zone) and in the necessarily higher stress environments grain dissolution and neocrystallisation (MacEwan et al., 1961; Nadeau et al., 1984; Ahn & Peacor, 1986a; Inoue et al, 1987; Altaner & Ylagan, 1997) become prevalent in the formation of phyllosilicate preferred orientations either parallel to bedding (e.g. Ho et al., 1999) or parallel to cleavage (Ho et al., 1995. 1996, 1999; van der Pluijm et al., 1998).

1.1.2: Mechanical Compaction and Rotation of Grains:

Mechanical compaction is the dominant process in the first few kilometres of burial for siliciclastic sediments (e.g. Athy, 1930; Hedberg, 1936; Giles et al., 1998) and is essentially the stress driven rearrangement of grains which causes porosity reduction and the expulsion of pore fluids (e.g Hedberg, 1936). Burial is associated with massive changes in physical properties. Initially high surface porosities of ~70% are reduced to <5% at ~4km (e.g. Athy, 1930; Hedberg, 1936; Sclater & Christie, 1980; Dzevanshir et al., 1986;

Giles et al., 1998) and this is associated with permeability variability (e.g. Olsen, 1962; Scheidegger, 1974; Neuzil, 1994; Schlomer & Krooss, 1997; Yang & Aplin, 1998; Dewhurst et al., 1999) of as much as 3 orders of magnitude at any given porosity and is related to lithology of the mudstone and therefore grain size (Yang & Aplin, 1998). The flocs or aggregates of phyllosilicates with edge-to-face morphologies (e.g. O'Brien & Slatt, 1990), which give rise to this initially high surface porosity are suggested to be short lived (Sintubin, 1994) as the reduction of porosity by increased effective stress (Terzaghi, 1921; Skempton, 1970; Burland, 1990; Dewhurst et al., 1998) causes mechanical rotation of grains in response to loading (Aplin et al., 1995; Dewhurst et al., 1998; 1999; Yang & Aplin, 1998) into face-to-face (O'Brien & Slatt, 1990) morphologies and therefore the development of a preferred alignment of phyllosilicates.

1.1.3: Diagenesis and Rotation of Grains:

Burial induces temperature increases in the sediment pile due to geothermal gradients and conditions for diagenetic mineral reactions become more prevalent. Smectite illitization is one of the most significant change and has been recorded in many basins around the world (e.g. Burst, 1959; Powers, 1967; Artru & Gauthier, 1968; Perry & Hower, 1970; Hower et al., 1976; Boles & Franks, 1979; Środoń & Eberl, 1984; Pollastro, 1985; Bell, 1986; Land et al., 1987; Inoue et al., 1987; Buryakovsky et al., 1995; Huggett, 1995; Schegg & Leu, 1996; Wang et al., 1996; Lynch, 1997; Land et al., 1997; Rask et al., 1997; Son et al., 2001; Thyne et al., 2001; Nadeau et al., 2002). Illitization is instigated at low temperatures, ~60°C (Perry & Hower, 1970; Hower et al., 1976; Kisch, 1983; Freed and Peacor, 1989) and proceeds to eventual slate formation at temperatures above ~200°C (e.g. Knipe, 1981; Ho et al., 1996; van der Pluijm et al., 1998; Jacob et al., 2000). The literature is full of reference to the effects of diagenesis on the physical properties of sandstones and carbonates (e.g. Galloway, 1974; Bathurst, 1975; Bjørkum, 1996; Fabricius, 2000), in which temperature increase drives dissolution and/or cementation that affect porosity. Little is known, however, about the

effects of mineral diagenesis on physical properties of mudstones (e.g. porosity reduction and increased alignment of phyllosilicates).

Where in sandstones the effects of mineral diagenesis can easily be seen as phyllosilicates filling the pore space between large rounded quartz grains visualising the effects of mineralogical change in mudstones is much harder due to their grain sizes. Mudstones have grain sizes that are often not more than a few micrometers in diameter so the only recourse to corroborate diagenetic change on their physical properties is to observe and quantify their phyllosilicate alignment into a preferred fabric orientation (e.g. Oertel, 1970; Oertel & Curtis, 1972; Page & Wenk, 1979; Curtis, 1980; Ho et al., 1995, 1999; van der Pluijm et al., 1998; Merriman & Peacor, 1999; Jacob et al 2000; Matenaar, 2002; Worden et al., 2005). Where mineralogical change can be viewed is as pyrite replacement in detrital grains and in authigenic mineral precipitation in microfossil tests.

The nature of the mechanism of smectite illitization becomes significant when porosities are low and the space for grain rotation becomes reduced. The mechanism of smectite illitization may be a solid-state transformation (e.g. Hower et al., 1976) or a dissolution-precipitation reaction mechanism (e.g. Boles & Franks, 1979) or a combination of the two (Ahn & Peacor, 1986a; Inoue et al., 1987). A solid-state transformation points to mechanical processes driving realignment by rotating grains, whereas dissolution-precipitation allows new minerals to form perpendicular to loading, implying the vertical component of effective stress governs the orientation into which new minerals grow. It follows that should diagenetic mineral reactions such as smectite illitization be important in fabric reorientation the kinetics of the transformation becomes potentially significant (e.g. Pytte & Reynolds, 1989; Elliott et al., 1991; Velde & Vasseur, 1992; Huang et al., 1993; Hillier et al., 1995; Elliott & Matisoff, 1996; Elliott et al., 1999) and the availability of reactants e.g. K-feldspar (e.g. Hower et al., 1976; Boles & Franks, 1979) results in fabric change being partly governed by K-feldspar availability and its dissolution kinetics (Altaner, 1989).

1.2: Aims of this Study:

The overall rationale for this work is to investigate the factors that influence the alignment of phyllosilicates in mudstones by:

- Attempting to separate the effects of clay mineral change (illitization of smectite) and mechanical compaction (porosity reduction) as the major controls on the phyllosilicate fabric of mudstones.
- Testing the mechanism of illitization through quantifying the change in preferred alignment of phyllosilicates.

1.2.1: Principle Techniques:

Previous studies have used X-ray texture goniometry (XTG) to quantify the orientation of phyllosilicates (e.g. Oertel, 1970; 1983; Sintubin, 1994). However, to improve upon this original method High Resolution X-ray Texture Goniometry (HRXTG) was developed (van der Pluijm et al., 1994) and is able to record variations in the 'strain states' of compacted rocks on the mm-scale. Two studies have used this technique to assess mineral alignment, diagenesis and porosity reduction. They have partially shown the correlation between smectite to illite diagenesis with increased preferred fabric alignment of phyllosilicates in mudstones from the Gulf of Mexico (Ho et al., 1999; Matenaar, 2002). Where Ho et al. (1999) did not provide any systematic description of the lithologies studied; Matenaar (2002) provided ample sediment descriptions (porosity and grain size distributions). Each study, however, suffered from complex geology; varying grain sizes which had an effect on the preferred fabric alignment (Ho et al., 1999) and overpressure and/or rapid burial (Matenaar, 2002) which resulted in a complex relationship between mineral diagenesis and fabric development whose results are difficult to interpret.

Transmission Electron Microscopy (TEM) is used to assess mineral change in illite-smectite in the context of mineralogical change. It has been used previously in a variety of studies to assess mudstone chemistries (e.g. Ahn &

Peacor, 1986a; Bell, 1986; Klimentidis & Mackinnon, 1986; Jiang et al., 1994), diagenesis (e.g. Ahn & Peacor, 1986a & 1986b; Inoue et al., 1987; Hover et al., 1999; Masuda et al., 2001; Nadeau et al., 2002; Kim et al., 2004), eventual metamorphism (e.g. Merriman & Peacor, 1998; Merriman, 2002) and mineral structures (e.g. Nadeau, 1998; Peacor, 1998), as well as the morphology of crystallites (e.g. Ahn & Peacor, 1986a; Inoue et al., 1987) and the disorder created in Selected Area Diffraction Patterns by variable cation substitution (McCarty & Reynolds, 1995). Analytical Transmission Electron Microscopy allows the construction of accurate structural formulae and the detailed changes in the octahedral and tetrahedral cation ratios have been noted between smectite, mixed-layer illite-smectite with varying percentages of illite in the mixed layer and end-member illite (e.g. Ramseyer & Boles, 1986; Ahn & Peacor, 1986a; Jiang et al., 1990; Li et al., 1997; Hover et al., 1999; Masuda et al., 2001). Analytical Transmission Electron Microscopy has been included in this fabric study to assess the detailed chemistries of samples where there is no change in illitization of smectite with increased burial depth and therefore temperature but an increase in preferred phyllosilicate alignment.

1.3: Thesis Outline:

This thesis is divided into four stand alone data chapters with their own discussions and one extended discussion chapter that deals with the thesis data as a whole and places it in the context of other HRXTG studies related to diagenesis and compaction in mudstones. Additionally, recommendations for future work and research directions are made. The format puts emphasis on the fact that the studies stand alone as pieces of work with unique and subtle discussions to each piece and may be readily converted into papers that further express this subtly.

Chapter 2 deals with the mineralogy, physical characteristics and phyllosilicate fabric of deeply buried, thermally and mineralogically mature

mudstones from two wells in the Podhale Basin of southern Poland. The study will combine mineralogical and diagenetic maturity with quantified preferred alignments of phyllosilicates. The deep burial of the sample set will allow the assessment of the mechanism of phyllosilicate rotation and the role of effective stress. **Chapter 3** discusses the illite-smectite mineral variation from selected samples from the Podhale Basin and utilises Analytical Transmission Electron Microscopy to give a detailed understanding of the structural formulae of I/S material and how these relate to the nature of the Selected Area Diffraction Patterns produced. The chapter will test whether there are differences in structural formulae between samples over the depth range of the Podhale Basin and especially beyond the termination of the illitization of smectite. Similar to **Chapter 2**, **Chapter 4,** reports the mineralogy, physical characteristics and preferred orientation of phyllosilicates in mudstones from two wells in the Northern North Sea. The samples cover the entire depth profile of the two wells, where no uplift or erosion has taken place. Consequently, deposition fabrics and the role of mechanical compaction in the early stages of burial may be assessed. **Chapter 5** focuses on 1-D maturity modelling to assess maximum burial depths and the way in which development of phyllosilicate fabric is related to maturity in the Podhale Basin and Northern North Sea. The modelling will allow the data in **Chapters 2** and **4** to be integrated with HRXTG results gathered by Ho et al., (1999) and Matenaar (2002) in **Chapter 6,** where recommendations for future work and research directions are made.

Chapter 2: Preferred Fabric Orientation in Deeply Buried Mudstones from the Podhale Basin, Southern Poland: Relationship to the Illitization of Smectite

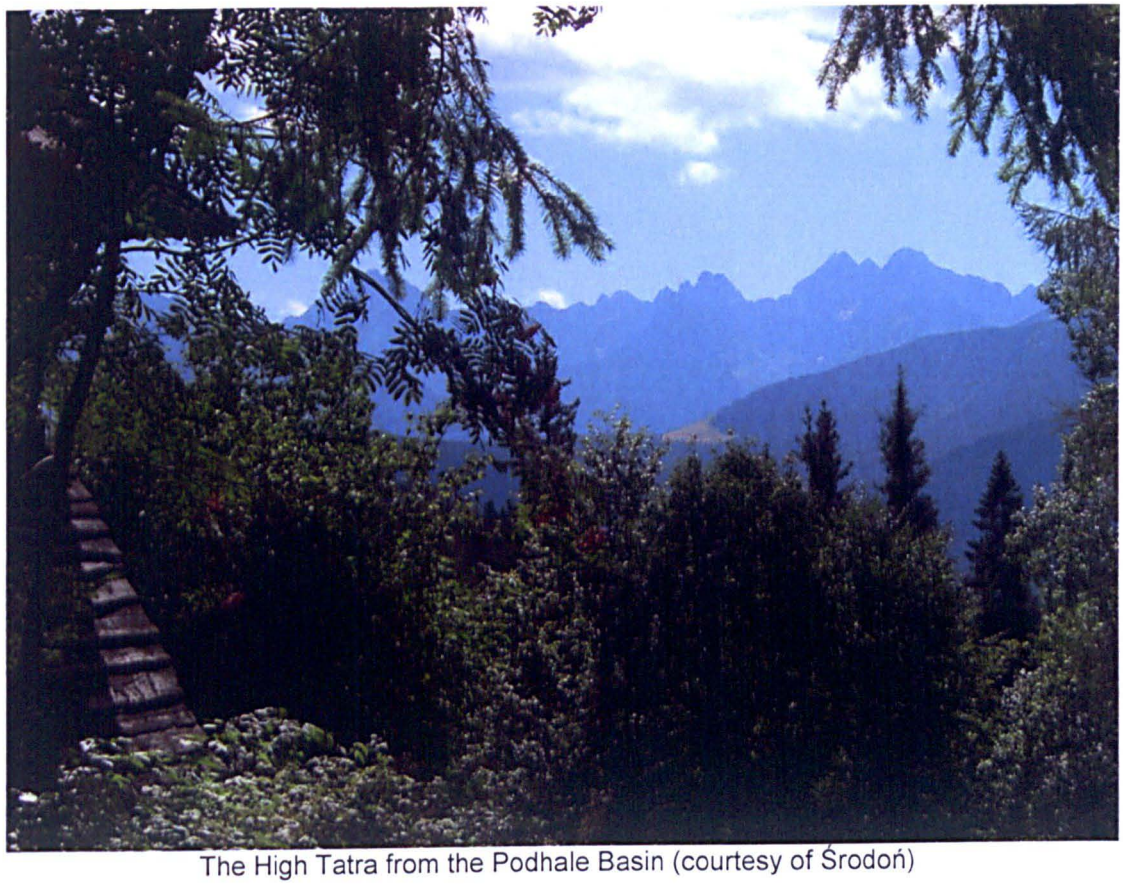

The High Tatra from the Podhale Basin (courtesy of Środoń)

2.0: Introduction:

The Podhale Basin in southern Poland has been described in terms of its mineralogy (Środoń et al., in press), stratigraphy (Olszewska & Wieczorek, 1998; Westwalewicz-Magilska, 1986) and depositional characteristics (Wieczorek, 1989). No study has combined mineralogy and diagenetic maturity with a study of the preferred orientation of phyllosilicate minerals in the Podhale Basin.

The Cainozoic of the Gulf Coast was recognised by early workers (e.g. Burst, 1959) as an accessible area to study the mineralogical changes associated with the smectite to illite transition at depth. The diagenesis of illite (also referred to as illitization) has been recognised in other areas and in other geological Era, the Jurassic of South-eastern France (e.g. Artru and Gauthier, 1968), Carboniferous of Central Poland (Środoń & Eberl, 1984) and the Cainozoic and Mesozoic of the Rocky Mountains (Pollastro, 1985).

The above studies all describe a change in mineralogy with depth, with the Gulf of Mexico (Perry & Hower, 1970; Hower et al., 1976; Boles & Franks, 1979; Ahn & Peacor, 1986) providing the bulk of the studies on the illitization of smectite which is the most prominent phyllosilicate diagenetic reaction. The classic work of Hower et al (1976) described a reaction where;

$$\text{Smectite} + \text{K-feldspar} = \text{illite} + \text{quartz}$$

Essentially, this reaction occurs as a solid-state transformation. Boles and Franks (1979) described a reaction that formed illite from the selective cannibalisation of smectite, with significant dissolution of phyllosilicates:

$$\text{Smectite} + \text{K-feldspar} = \text{illite} + \text{chlorite} + \text{quartz} + H^+$$

In contrast, Ahn and Peacor (1986) and Inoue et al. (1987) have described through Transmission Electron Microscopy studies mechanisms for transformation that may well be intermediate between solid-state

transformation and dissolution-precipitation, with mineral growth dependent on illite/smectite morphology as described in Transmission Electron Microscopy studies (e.g. Ahn & Peacor, 1986; Bell, 1986).

The nature of the reaction mechanism (Hower et al., 1976; Boles & Franks, 1979; Ahn & Peacor, 1986; Inoue et al, 1987) as well as the compaction of the sediment in response to loading (e.g. Athy, 1930; Hedberg, 1936; Sclater & Christrie, 1980) will have a significant impact of the preferred alignment of mudstones. Although separating the effects of both is not entirely possible as they are occurring coincidently.

The preferred orientation of phyllosilicate minerals in mudstones may be viewed on a variety of scales under the scanning electron microscope (O'Brien, 1970; O'Brien & Slatt, 1990), however, quantifying the degree of preferred orientation of phyllosilicates between samples has proven difficult (Worden et al., 2005; Charpentier et al., 2003).

X-ray Texture Goniometry has been used to quantify the orientation of phyllosilicate minerals in various studies (Oertel, 1970; Oertel & Curtis, 1972; Wenk, 1985; Sintubin, 1994). Van der Pluijm et al (1994) developed High Resolution X-ray Texture Goniometry to improve upon the traditional technique as their method measures orientations over mm-scale distances. It has been used in several studies (Aplin et al., 2003; Charpentier et al., 2003; Ho, et al., 1995; 1996; 1999; 2001; Jacob, et al., 2000; Van der Pluijm, et al., 1998) to quantify mineral alignment in both mudstones and low grade metamorphic pelites.

The aims of this study are to:

- Assess phyllosilicate preferred alignment using HRXTG in mineralogically well characterised mudstones from the Podhale Basin.
- Discuss the formation of the virtual profile well constructed for the Podhale Basin by Środoń et al (in press) and describe the maximum

burial depths and temperatures which are important for an understanding of fabric development and the illitization of smectite.

2.1: Geology and Samples:

2.1.1: Geological setting:

The Podhale Palaeogene Basin, Southern Poland (Figure 2.1a) belongs to the much larger, Central Carpathian Palaeogene Basin, and is situated between the Pieniny Klippen Belt to the north and the Tatra Mountains to the south (Figure 2.1b). The Podhale Basin is suggested to be a fore-arc basin at the north-east border of the North-Pannonian unit (Kazmer et al., 2003, Tari et al., 1993). Subsidence rates within the basin were controlled by collapse structures resulting from subcrustal tectonic erosion at the base of the Tatra (Baráth et al., 1997) and is presently filled with a 3000m thick sequence of deposits (Olszewska & Wieczorek 1998), consisting of upwards coarsening (Westwalewicz-Magilska, 1986) sandstones, mudstones and siltstones termed the Podhale Flysch, covering a Mesozoic Basement that is exhumed in the Tatra Mountains.

According to Środoń (pers. Comms. 2003) Chochołów PIG-1 comprises the Chochołów, Zakopane and Szaflary beds, whereas Bukowina Tatrzańska consists of only the Chochołów and Zakopane beds. Olszewska and Wieczorek (1998) describe the Szaflary beds as Eocene age clastic deposits rare in foraminifera and consider them to have been deposited along a tectonically controlled submarine ramp (after Wieczorek, 1989) and comprise mudstones and siltstones. The Zakopane beds are richer in foraminifera and have the appearance of dark shaley mudstone material that consists of a generally upwards coarsening sequence related to submarine fan sedimentation, with minor intercalations of thin bedded sandstones and local intercalations of ferruginous dolomites. The Chochołów beds are psammitic deposits, very poor in foraminifera with a similar depositional characteristic to the Zakopane beds; thin bedded claystones, mudstones and sandstones

dominate a generally mudstone rich lithofacies, with local intercalations of thick bedded sandstones.

The depositional mechanisms at play in the Palaeogene are the subject of some controversy. Westwalewicz-Mogilska (1986) suggests three S-SW fed submarine fans, whereas Wieczorek (1989) counters this argument with the suggestion of just one fan migrating E to W based on transport directions of the deposits.

The profile of Wieczorek and Olszewska (1999) through the Podhale Basin suggests that it is an asymmetric structure which is deeper in its northern limb and that the Palaeogene part of the basin was developed on an uneven topography of the Mesozoic basement thought to result from karstification of the carbonate basement and general extensional faulting. Márton et al (1999) describe the basin structure as an asymmetrical synclinorium, which is disturbed by E-W trending reverse faults and folding close to the basin margins.

Within the centre of the basin there are numerous NW and NE striking strike-slip faults. It is usual in fore-arc basins for regionally based tectonism to be a controlling factor in stratigraphy, often folding, faulting and tilting along with tectonic subsidence and/or uplift occur. Márton et al (1999) conclude from their palaeomagnetic study that the flysch in the Podhale Basin must have travelled a few hundred kilometres from its depositional location, some time after the Miocene. This displacement was also accompanied by a 60° counter-clockwise rotation relative a Stable Europe.

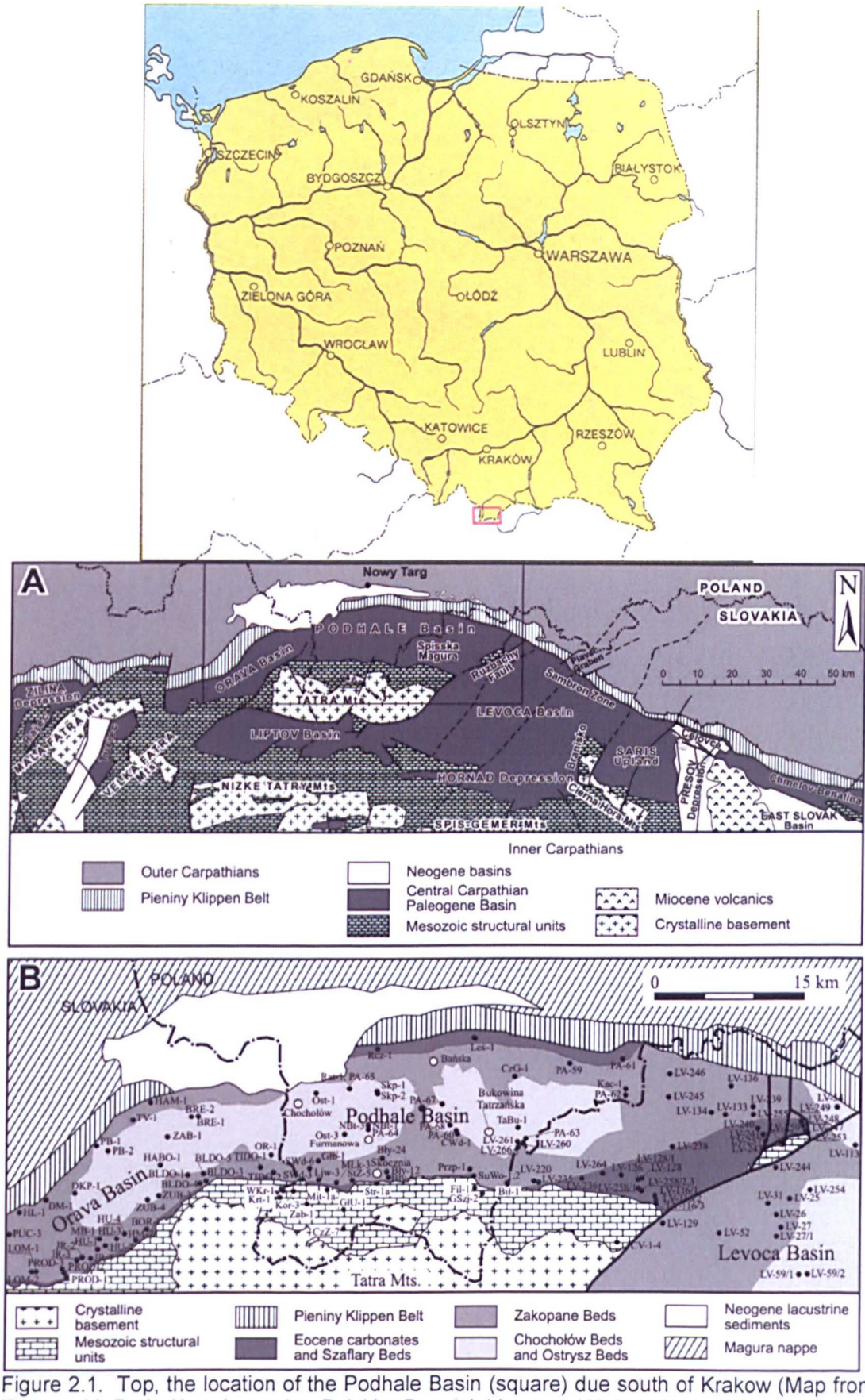

Figure 2.1. Top, the location of the Podhale Basin (square) due south of Krakow (Map from Tatrzanski Park Narodowy, by Polskie Przedsiebiorstwo Wydawnictw Kartograficznych, Warszawa-Wroclaw).The Podhale Basin, middle, with its surrounding sub-basins and major structural faults. The Podhale Basin lithologies, bottom, and the well locations, Chochołów in the west and Bukowina Tatrzańska in the east (Środoń, 2005. pers. comms).

2.1.2: Samples:

The sample set consists of core fragments from two boreholes in the Podhale Basin, Chochołów PIG-1 (Chi) in the west and Bukowina Tatrzańska PIG-1 (BkT) in the east. The suite comprises 19 samples in total, 8 from the Bukowina Tatrzańska borehole and 11 from the Chochołów PIG-1 borehole. Samples were chosen based on similarity in terms of colour, apparent grain size and bedding characteristics at the hand specimen scale, to represent the entire lengths of the two profiles.

Present day burial depths for Bukowina Tatrzańska PIG-1 range from 102m to 2200m and from 193m to 2967m for Chochołów PIG-1. These depths do not equate to maximum burial depths, as a significant amount of uplift and erosion has occurred (Środoń et al, in press).

As a consequence of modelling the Podhale Basin, Środoń et al (in press) have demonstrated a 20°C/km to 25°C/km palaeogeothermal gradient (present day geothermal gradient is 21°C/km +/- 2°C, Cebulak et al., 2004), deduced from I/S palaeothermometry, which has been used in various studies to estimate temperature (Hoffman & Hower, 1979; Pollastro, 1993; Środoń, 1995). The maximum palaeotemperatures quoted by Środoń et al (in press) are 135°C for the Chochołów PIG-1 well and 174°C for the Bukowina Tatrzańska PIG-1 well, which are adequate temperatures for the illitization of smectite to proceed (Weaver, 1989), the important phyllosilicate diagenetic marker in the basin. The timing of maximum palaeotemperatures estimated through K-Ar dating methods at ~15.8Ma Środoń et al (in press).

2.2: Analytical methods:

2.2.1: High Resolution X-ray Texture Goniometry:

A thin section perpendicular to the main fabric direction of the sample was prepared for SEM observations and another for the High Resolution X-ray Texture Goniometry measurements which consisted of a section about

200μm in thickness, cut perpendicular to bedding and polished. The section for the SEM observations was prepared with a surface oriented parallel to that of the section for High Resolution X-ray Texture Goniometry, allowing direct observation.

The technique seeks to quantify maximum preferred orientation and in a compacting sequence of sedimentary rocks bedding is assumed to be perpendicular to maximum effective stress. This is not necessarily the case for slates (van der Pluijm et al, 1998) where mineral growth associated with cleavage formation may develop preferred alignments in other orientations. Bedding is parallel to the surface of deposition and may describe layers more than 1cm thick (on the hand specimen or outcrop scale). Laminae in the context of mudstones may be viewed in the same way as bedding, where each laminae represents a small scale bedding plane, as a consequence the thin section was cut perpendicular to the lamination/bedding seen in the hand specimen.

A portion of the polished section was then glued to an aluminium sample holder (12mm diameter, 100mm^2 area) for X-ray analysis. The area of interest was aligned manually with the X-ray beam on the diffractometer.

High Resolution X-ray Texture Goniometry was performed on a modified Enraf-Nonius CAD4 single crystal diffractometer (Figure 2.2) with a MoKα source rather than the standard CuKα source, as intensities and hence mineral peaks are higher and allow greater accuracy of measurement.

Phyllosilicate 001/002 peaks are measured in transmission mode as X-rays pass through the sample and the detector is positioned at a preset 2-Θ angle to receive X-rays diffracted by a specific set of planes of a specific phase. Rotation allows different orientations to be measured and in full scan mode 1296 measurements are performed per mineral peak. Diffraction intensity data are collected every 2.5φ (0-360) for angles of 0-40ω (in 9 steps).

Mineral peaks (Figure 2.3) are identified by an initial 2-Θ scan over a narrow range of 2-Θ angles (0.5-6.0° 2-Θ Mo, corresponding to 1-13°2-Θ Cu).

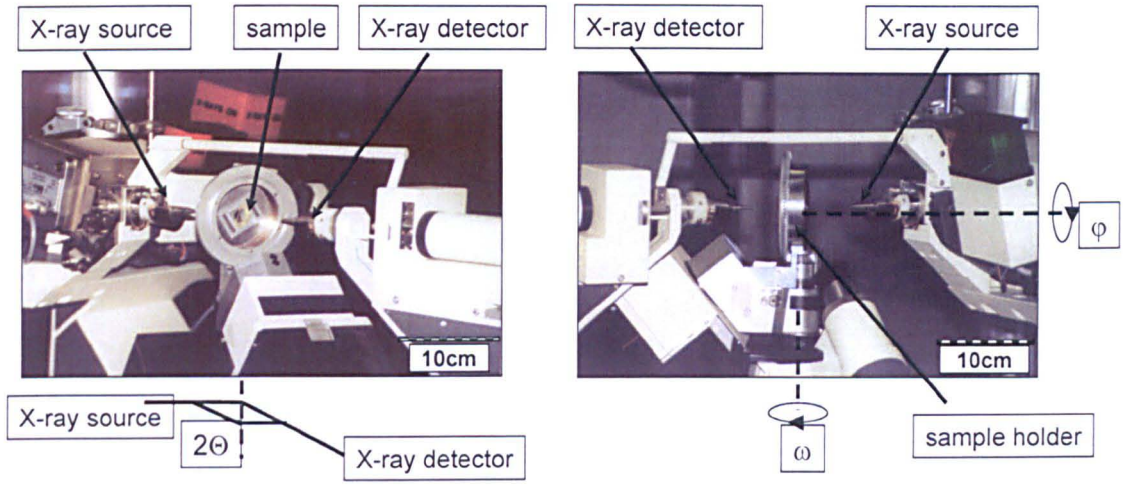

Figure 2.2.The Enraf-Nonius CAD4 single-crystal diffractometer, x-ray source, x-ray detector and sample are noted along with the rotation and rotation angles of the machine.

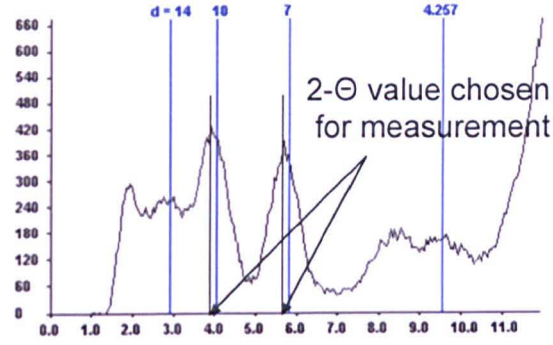

Figure 2.3. Diffractogram resulting from a 2-Θ scan using a Mo source, showing the 2-Θ angles used for preferred orientation quantification.

The results of the full scan are relative pole densities (a pole figure), expressed in terms of multiples of a random distribution (m.r.d.), conveyed as a contoured projection showing orientations of a given pole of a given set of planes (Wenk, 1985).

The samples are corrected for background and absorption effects (sample thickness) and are then normalised so that the results are concentration-independent. When a sample rotates around the incident beam there is no change in X-ray path length or irradiation volume. Tilting of the sample

relative to the beam increases both path length and the irradiated sample volume (van der Pluijm et al., 1994). The diffracted intensity decreases with increasing path length because of absorption but increases with irradiated volume, therefore the change in intensity is a function of both of these effects. Only angles 0-40°2-Θ of the whole area of a complete pole figure is measured. This results in the blank areas on the lower hemisphere projection, however, intensities are still normalised against the whole area of a complete pole figure as the intensity contribution from the non-measured area is small (Ho et al., 1996). Intensity distributions expressed as multiples of a random distribution (m.r.d.) show the degree of alignment of phyllosilicate minerals. Multiples of a random distribution is the density of a given pole and is calculated relative to the average pole density, which is determined by distributing the integrated total pole density uniformly over the full sphere (Wenk, 1985; Ho et al., 1999).

Intensity is a measure of the concentration of crystals aligned parallel to each other. A value for the multiple of a random distribution is produced even when the sample has not been prepared perpendicular to maximum fabric alignment, so a stereographic projection showing centred contour lines validates the multiple of a random distribution value, by assessing whether the initial thin-section cut for the sample was perpendicular to maximum preferred fabric orientation. Investigations by various workers (Ho et al., 1995; 1996; 1999; 2001; Jacob et al., 2000; Matenaar, 2002; van der Pluijm et al., 1998) as well as measurements from this study reveal that typical maximum pole densities for sedimentary rocks are:

<1.8 mrd = no/ very weak fabric

2-3 = weak fabric

3-4 = moderate fabric

4-5 = strong fabric

>5 = very strong fabric

2.2.2: Back Scattered Electron Microscopy (BSEM):

Backscattered Scanning Electron Microscopy (BSEM) was performed on two machines: A Hitachi S3200N Scanning Electron Microscope, with a tungsten filament, fitted with an Imaging - Everhart-Thornley & Robinson BSE Detector and an XEDS - Noran UTW SiLi detector was used at the Electron Microbeam Analysis Laboratory at the University of Michigan. The machine was operated at 20kV and 2nA, with a spot size of 2μm and a working distance of ~16mm, magnification varied between 400 and 800X.

At the University of Newcastle-Upon-Tyne BSEM was performed on a Hitachi S2400 Scanning Electron Microscope fitted with an Oxford Instruments Isis 200 Ultra Thin Window X-ray detector. The machine was operated at 20kV and 2nA, with a spot size of 2μm and a working distance of ~10mm, magnifications varied between 100 and 5000X.

2.2.3: Mercury Porosimetry:

Porosities and pore size distributions were determined on a one gram block of sample that was freeze dried (Delage & Lefebvre, 1984) for 24 hours, then dried in an oven at 105°C for a further 24 hours. Samples remained in the oven until they were loaded for analysis. Porosities were calculated from bulk volume and grain density.

A further three grams of sample was taken and ground to a fine powder and used for grain density determinations (British Standard 733, 1987), these values were used in calculations of porosity rather than an arbitrary value of 2.65g/cm^3. Grain densities were measured using the small pycnometer method at 20°C, with a quartz standard (2.65g/cm^3) in each sample batch. Repeat analyses were made; the quartz standard was repeatable to within 0.02g/cm^3.

Analysis took place on a *Micromeritics*© Autopore II 9220 machine and yielded a figure for porosity, and a pore size distribution. Pore diameters were calculated from the mercury intrusion data. The analysis used the assumption that the surface tension of mercury was 0.48 N/m and the contact angle between mercury and the particle surface was 141°. The pore radius, r, is given by:

$$r = 746{,}000/p$$

Where r is the pore throat radius (nm) and p is the pressure in kPa.

2.3: Results:

2.3.1: High resolution X-ray Texture Goniometry:

Initial 2-Θ scans on the sample set produced strong, easily identifiable peaks. 2-Θ scans are shown in Appendix 2.1. The scans have peaks at an approximate d-spacing of 14Å, 10Å, 7Å and 4.257Å. These correspond to peaks for chlorite (001), mica, chlorite+kaolinite (002) and quartz, respectively. Pole-figure scans (full-scans) were obtained at two values of 2-Θ for each sample. One was obtained at the maximum intensity of the broad peak in the range d~12-10Å, corresponding to the mixed layer phase illite-smectite. It is stressed that d~10Å corresponds to pure mica, usually detrital in origin, so a peak measurement was not taken at this value. A peak at a d-spacing of 12.5Å corresponds to pure smectite at an intermediate relative humidity, if it is in the Na form (one water layer). Ca smectite is characterised by a 15Å d-spacing under these conditions (Moore & Reynolds, 1997). No result for the natural exchange cation in these clays is offered, so the peak measured between 14Å (chlorite) and 10Å (mica) represents the mixed layer phase illite smectite and is migrating towards 10Å with increasing depth (and therefore illitization of smectite), d-spacing values ranged from 11.13Å to 10.12Å from the initial 2-Θ scan (see Table 2.1). The other full-scans were obtained from the peak at a d-spacing close to 7Å, chlorite+kaolinite (002).

Operationally, a value of 2-Θ for each peak was obtained in the initial 2-Θ scan. Then the value for Θ was entered into the settings for the full-scan. Consequently, quoted d-spacing (Table 2.1) values are calculated using the Bragg equation [1];

$$2d\sin\theta = n\lambda \qquad [1]$$

Re-arranged so that d is the subject

$$\mathrm{d} = \mathrm{n}\lambda/2\sin\theta$$

where λ is the wavelength for Molybdenum Kα radiation (0.710730Å). This value is a customary weighted average of $K\alpha_1$ and $K\alpha_2$, where $K\alpha_1$ is taken to have twice the weight of $K\alpha_2$ (Brindley & Brown, 1980). The results suggest

that the samples are more illitic than smectitic as they are closer to 10Å than 12Å and there is a slight migration from 12Å to 10Å as the deeper samples are encountered, but the 2-Θ scan cannot quantify this.

The maximum pole densities, expressed as multiples of a random distribution, of all poles for both mineral peaks are recorded in Table 2.1. Using the presentation standard of Ho et al (1999), all pole figures were processed through two smoothing cycles and rotated so that the maxima are positioned at the centre of the plot, which allows all plots to refer to the same orientation (Appendix 2.1).

Typical maximum pole densities expressed as multiples of random distributions (m.r.d.) defined in previous studies (Ho et al., 1995; 1996; 1999; 2001; Jacob et al., 2000; Matenaar, 2002; van der Pluijm et al., 1998) suggest that a multiple of random distribution between 3 and 4 (m.r.d.) represent a sample with a moderate fabric, 4 and 5 (m.r.d.) represents a strong fabric and values greater than 5 (m.r.d.) represent a very strong fabric. At the lowest depth (current well depth) for samples from the Chochołów PIG-1 borehole there is always a fabric present but with a low alignment of phyllosilicate minerals. It ranges between 3.38 m.r.d. at the top of the section and 6.99 m.r.d. at the base for the illite-smectite peak and between 2.84 m.r.d. and 7.44 m.r.d. for the chlorite+kaolinite peak (Table 2.1; Figure 2.4).

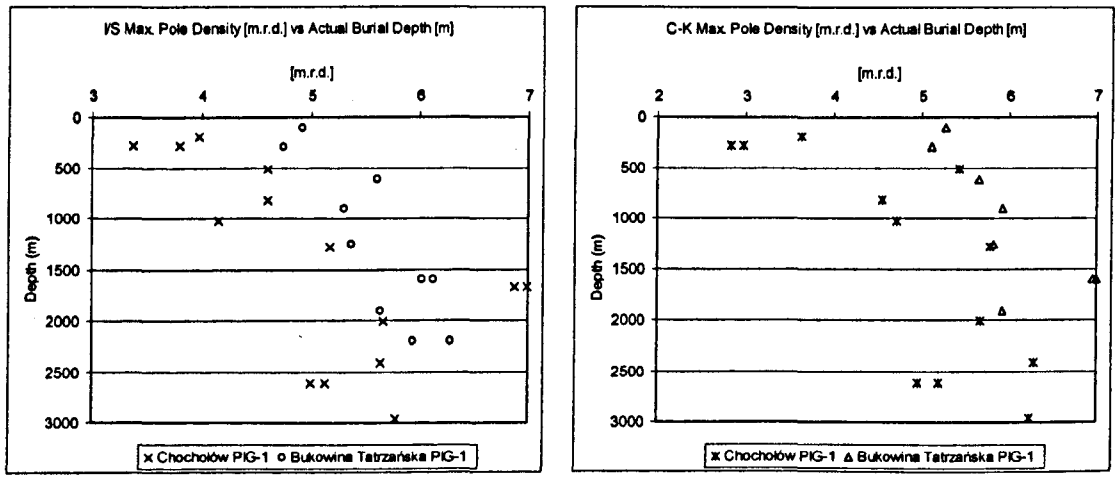

Figure 2.4. Increase of I/S Maximum Pole Density [m.r.d.] with Actual Burial Depth [m] for Chochołów PIG-1 and Bukowina Tatrzańska PIG-1, left, and increase of C-K Maximum Pole

Density [m.r.d.] with Actual Burial Depth [m] for Chochołów PIG-1 and Bukowina Tatrzańska PIG-1, right. It should be noted that where two points plot at the same depth these represent a second analysis in order to verify the result.

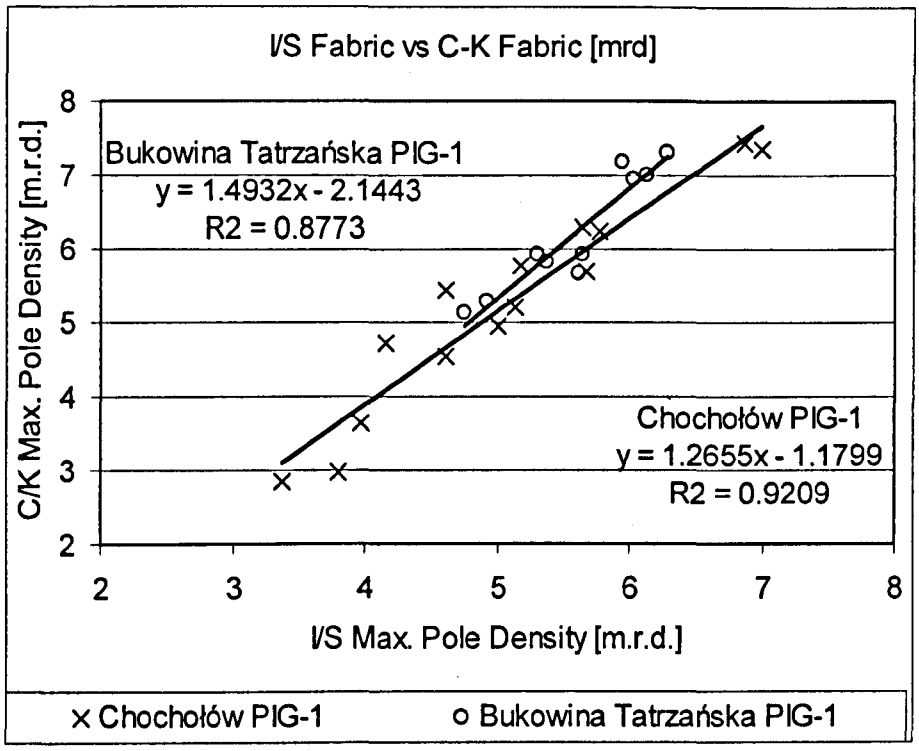

Figure 2.5. Correlations between I/S and C-K fabric [mrd] for both Chochołów PIG-1 and Bukowina Tatrzańska PIG-1

In Bukowina Tatrzańska PIG-1 the results are less spread, they range between 4.75 and 6.29 m.r.d. for the illite-smectite peak and 5.12 and 7.32 m.r.d. for the chlorite+kaolinite peak.

The maximum pole densities (m.r.d.) increase with depth for both mineral peaks with illite-smectite and chlorite+kaolinite giving complementary results, for shallower depths the fabric in the chlorite+kaolinite peak is fractionally weaker than in illite-smectite (Figures 2.4 & 2.5). This reverses at depth and the fabric as depicted in the chlorite+kaolinite pole figures is stronger than that in illite-smectite pole figures but not by more than half a unit of measurement. Where two results exist for the same sample this represents a re-cut of the sample material and a re-analysis for fabric alignment. The re-analyses produced results that were no more than 0.42 m.r.d. different to the original analyses. This validates the machine and the operator as the results of the second sampling concur with the first and show that any variability from the obtained general trend is a result of the sample rather

than an error. There is a high correlation coefficient between I/S and chlorite + kaolinite fabrics for both Chochołów PIG-1 and Bukowina Tatrzańska PIG-1, R^2 of 0.9209 and 0.8773 respectively (Figure 2.5).

Table 2.1. HRXTG data for Podhale Mudstones.
Sample number (Chi=Chochołów PIG-1, BkT= Bukowina Tatrzańska), Actual Burial Depth (m), Maximum Pole Density [m.r.d.] for the I/S and C-K peaks, Contour interval, degrees 2-Θ for I/S peak andC-K peak, d-spacing values for I/S peak and C-K peak.

Well and sample	Actual Burial Depth [m]	I-S' Max. Pole Density [m.r.d.]	C-K' Max. Pole Density [m.r.d.]	Contour interval [m.r.d.]	'I-S' Peak. Degrees 2-Θ	'C-K ' Peak Degrees 2-Θ	I-S' Kα ave. d-spacing	C-K' Kα ave. d-spacing
Chi-04	193	3.97	3.63	0.25	3.73	5.63	10.90	7.23
Chi-06	280	3.38	2.84	0.25	3.89	5.76	10.40	7.03
Chi-06	280	3.80	2.98	0.25	3.99	5.82	10.15	6.97
Chi-12	513	4.61	5.43	0.50	3.70	5.53	10.87	7.22
Chi-20	820	4.61	4.55	0.25	3.99	5.69	10.12	7.09
Chi-23	1031	4.16	4.72	0.25	3.61	5.63	11.13	7.11
Chi-28	1283	5.18	5.78	0.50	3.80	5.60	10.61	7.17
Chi-38	1671	6.99	7.36	0.50	3.99	5.69	10.12	7.09
Chi-38	1671	6.87	7.44	0.50	3.95	5.76	10.22	7.01
Chi-44	2011	5.67	5.68	0.50	3.95	5.53	10.24	7.26
Chi-56	2410	5.65	6.29	0.50	3.89	5.69	10.38	7.09
Chi-60	2611	5.00	4.96	0.50	3.89	5.69	10.38	7.09
Chi-60	2611	5.14	5.20	0.50	3.89	5.69	10.36	7.07
Chi-66	2967	5.78	6.23	0.50	3.86	5.66	10.46	7.11
BkT-01	102	4.92	5.27	0.50	3.83	5.63	10.56	7.18
BkT-06	293	4.75	5.12	0.50	3.95	5.69	10.15	7.02
BkT-12	610	5.61	5.66	0.50	3.99	5.69	10.10	7.07
BkT-17	902	5.31	5.93	0.50	3.89	5.76	10.41	7.04
BkT-23	1261	5.38	5.82	0.50	3.92	5.60	10.28	7.17
BkT-28	1594	6.13	7.00	0.50	3.99	5.76	10.15	7.04
BkT-28	1594	6.03	6.96	0.50	3.95	5.69	10.22	7.09
BkT-35	1904	5.65	5.93	0.50	3.92	5.63	10.31	7.15
BkT-41	2200	5.94	7.18	0.50	3.89	5.63	10.36	7.15
BkT-41	2200	6.29	7.32	0.50	4.02	5.69	10.10	7.12

2.3.2: Backscattered Scanning Electron Microscopy (BSEM):

Selected images for Chochołów PIG-1 and Bukowina Tatrzańska PIG-1 are presented in Figures 2.6-2.28. Magnifications range from x100 to x2500. The images reflect the whole of the depth profile in the Podhale Basin. The BSEM micrographs were taken in a consistent way to make comparisons between the textural and mineralogical make up of each sample. Figures 2.6

to 2.15 show the textures of the samples at x100 and x250 magnifications. The development of phyllosilicate preferred orientations increase with depth. The shallow samples (Chochołów-06; Figures 2.6 & 2.7 and Chochołów-20; Figures 2.8 & 2.9) have less well developed visual phyllosilicate preferred orientations than the deeper samples (e.g. Chochołów-38; Figures 2.10 & 2.11). The difference between the preferred orientations in Bukowina Tatrzańska-23 (Figures 2.12 & 2.13) and Bukowina Tatrzańska-35 (Figures 2.14 & 2.15) are more difficult to observe in terms of their visual appearance, however, they are as well aligned as the deeper samples from the Chochołów PIG-1 well.

The effect of silt sized material on the preferred orientation of phyllosilicates is dependent on the nature of the grain. Rounded or angular quartz grains will disrupt preferred orientations in matrix sized phyllosilicates but silt size phyllosilicates will promote preferred orientations. The effects of silt size quartz on the preferred fabric orientation can be seen in samples Chochołów-06 (Figure 2.7) and Chochołów-20 (Figure 2.9). The effects are more noticeable at higher magnifications. Chochołów-20 (Figures 2.16 and 2.17) and Chochołów-38 (Figure 2.18) demonstrate quartz breaking up the alignment of phyllosilicates, with <4μm long matrix phyllosilicates bending and wrapping around angular quartz grains.

Large elongate grains in Chochołów-20 (Figure 2.16) (~3-20 μm in thickness) are comprised of stacks of phyllosilicates and subangular grains of other minerals (~5-40 μm) and are probably detrital in origin. EDX analysis showed the subangular grains to be predominantly quartz and the large phyllosilicates to be micaeous or chloritic. The matrix material surrounding the large grains consists of smaller subangular grains having a size range ~0.5-3μm that were barely resolvable by BSEM and a fine-grained elongate material that has phyllosilicate characteristics. The silt size phyllosilicates in Chochołów-20 (Figure 2.16) are supporting finer grained minerals and are therefore promoting preferred alignment.

Where pyrite replacement has occurred in large phyllosilicate minerals (Figures 2.19 and 2.20) it represents the only direct evidence for these large phyllosilicates being detrital inputs rather than the result of in situ growth. The effect they have on phyllosilicate preferred orientation is to promote alignment (Figures 2.21 and 2.22). They act as tables onto which other mineral grains align themselves (Figure 2.22).

The matrix material is heavily influenced by their adjacent grains (Figures 2.17, 2.18 & 2.24), where they bend and wrap around larger grains. In regions of the sample where they are free from the influence of quartz they align themselves in random orientations (Figure 2.23 Chochołów-06) or in preferred orientations (Figure 2.25, Chochołów-56) and this behaviour is related to depth in samples from the Podhale Basin.

Unlike in sandstones where diagenetic mineral growth can be seen as overgrowths or phyllosilicates filling pore spaces, diagenesis is much harder to view in BSEM micrographs of mudstones. The main diagenetic process visible is pyrite replacement in detrital grains where iron from chlorite or biotite has been scavenged by pyrite, resulting in individual pyrite cubes or larger framoid formations. The round phyllosilicate structure at the centre of Figures 2.26 and 2.27 is a diagenetic chlorite grain, which probably replaced a detrital kaolinite grain and was initially deposited as a faecal pellet. The grain is relatively euhedral and its internal structure is fibrous and complex in its texture and it appears to exhibit more of a mineral replacement morphology due to various greyscales visible in this image.

Maximum pole densities for Bukowina Tatrzańska-28 (1595m, Figure 2.28) are 6.13 mrd (I/S peak) and 7.00 mrd (chlorite + kaolinite peak). HRXTG thus indicates a strongly aligned phyllosilicate fabric, somewhat inconsistent with observations made through BSEM. This highlights the different scales of observation of the two techniques: 1mm^2 for HRXTG, seventy times more than the image in Figure 2.28.

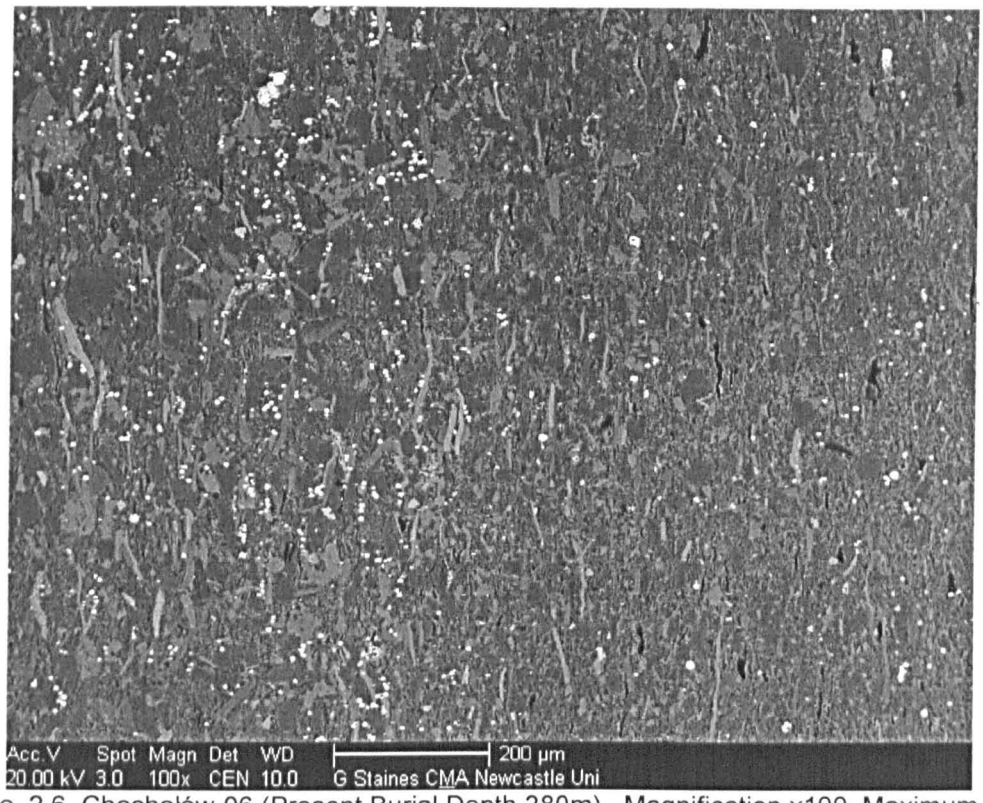

Figure 2.6. Chocholów-06 (Present Burial Depth 280m). Magnification x100, Maximum Pole Densities are 3.38/3.8 m.r.d. (I/S peak) and 2.84/2.96 m.r.d. (chlorite + kaolinite peak). Preferred phyllosilicate orientation is aligned vertically. Chlorite is a mixture of large (<10µm) detrital material and neoformed small (>2 µm) packets, chlorite composes less than 10% of the whole rock (see Table 2.3). Kaolinite comprises less than 3% of the whole rock and is consumed in diagenetic mineral reactions. The phyllosilicate fraction of the whole rock is dominated by mixed-layer I/S with additional detrital mica, free illite and smectite.

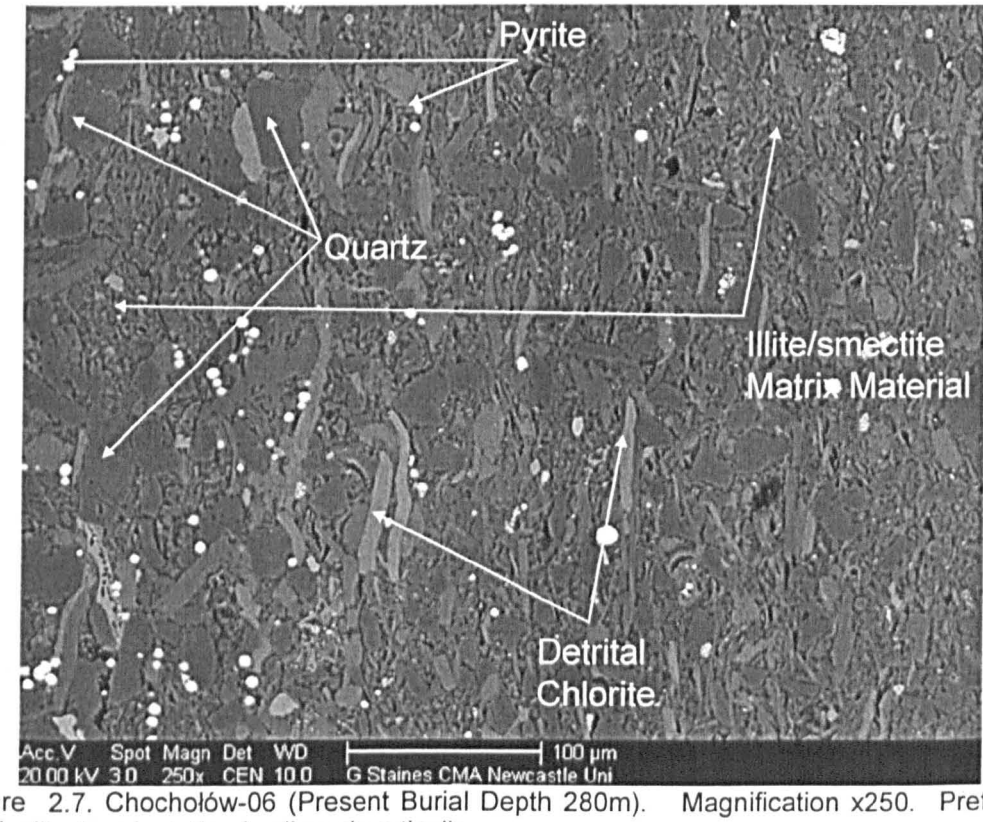

Figure 2.7. Chocholów-06 (Present Burial Depth 280m). Magnification x250. Preferred phyllosilicate orientation is aligned vertically.

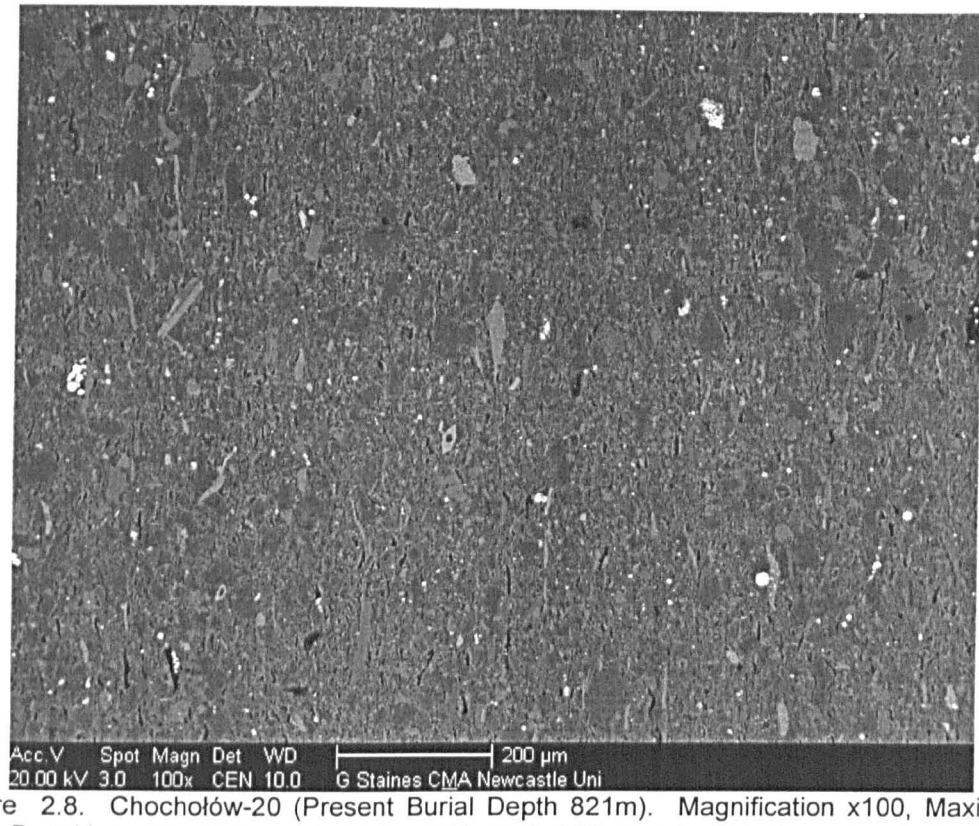

Figure 2.8. Chocholów-20 (Present Burial Depth 821m). Magnification x100, Maximum Pole Densities are 4.61 m.r.d. (I/S peak) and 4.55 m.r.d. (chlorite + kaolinite peak). Preferred phyllosilicate orientation is aligned vertically.

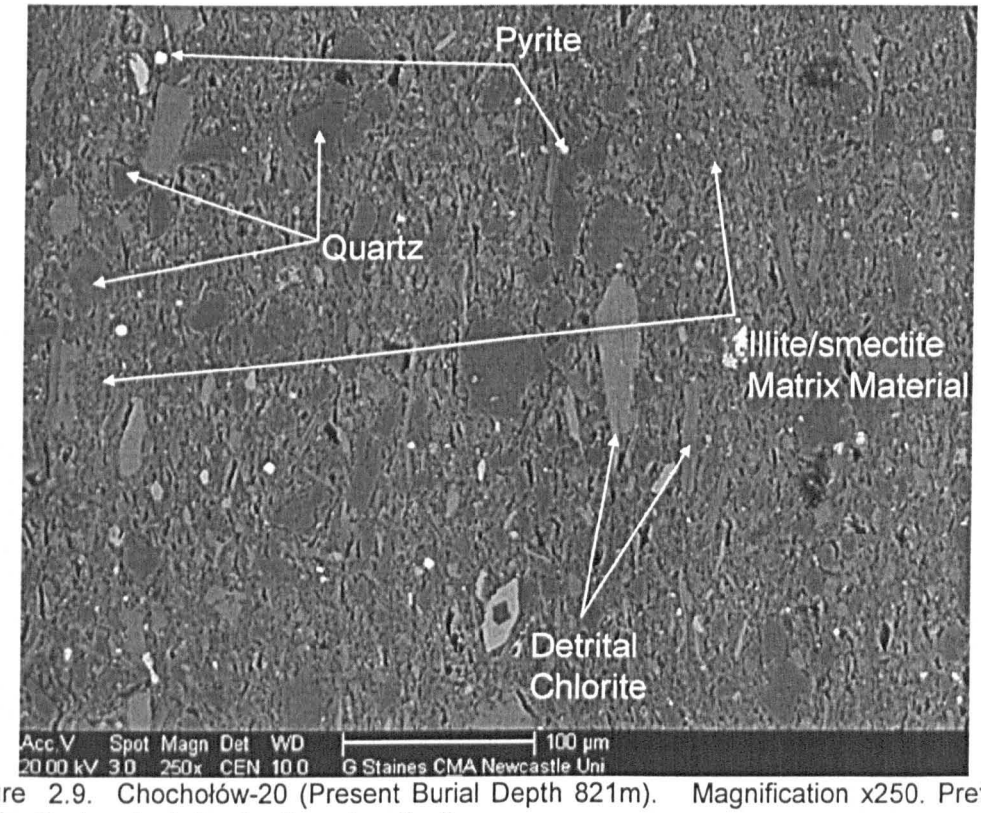

Figure 2.9. Chocholów-20 (Present Burial Depth 821m). Magnification x250. Preferred phyllosilicate orientation is aligned vertically.

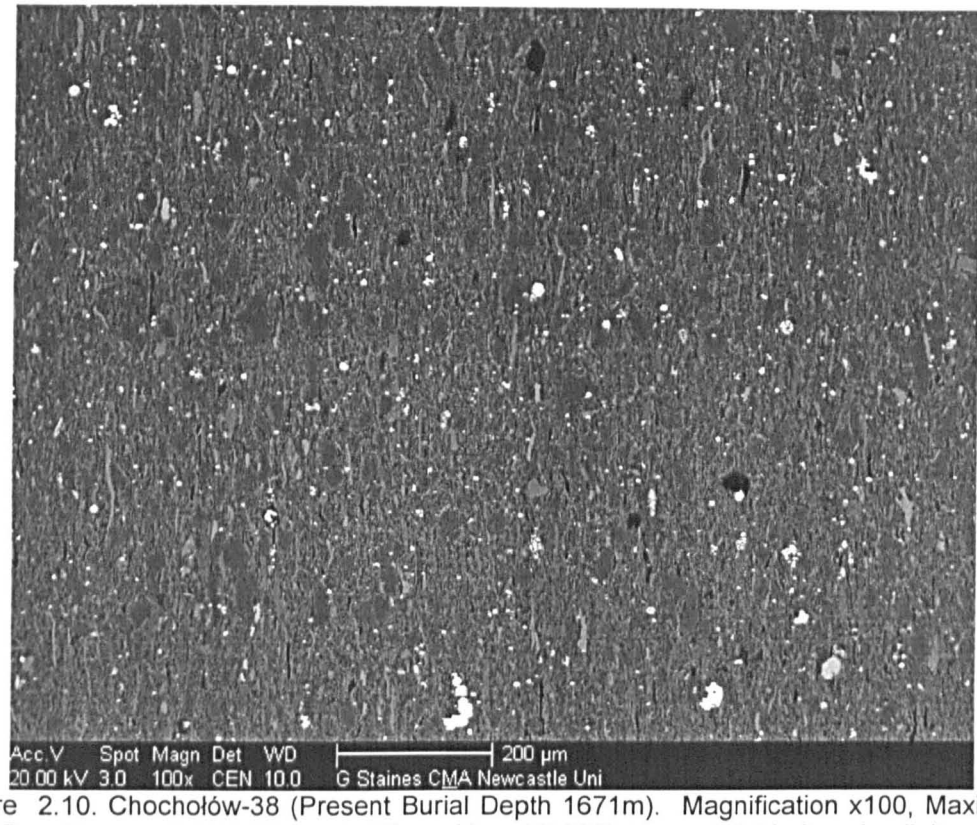

Figure 2.10. Chochołów-38 (Present Burial Depth 1671m). Magnification x100, Maximum Pole Densities are 6.99/6.87 m.r.d. (I/S peak) and 7.36/7.44 m.r.d. (chlorite + kaolinite peak). Preferred phyllosilicate orientation is aligned vertically.

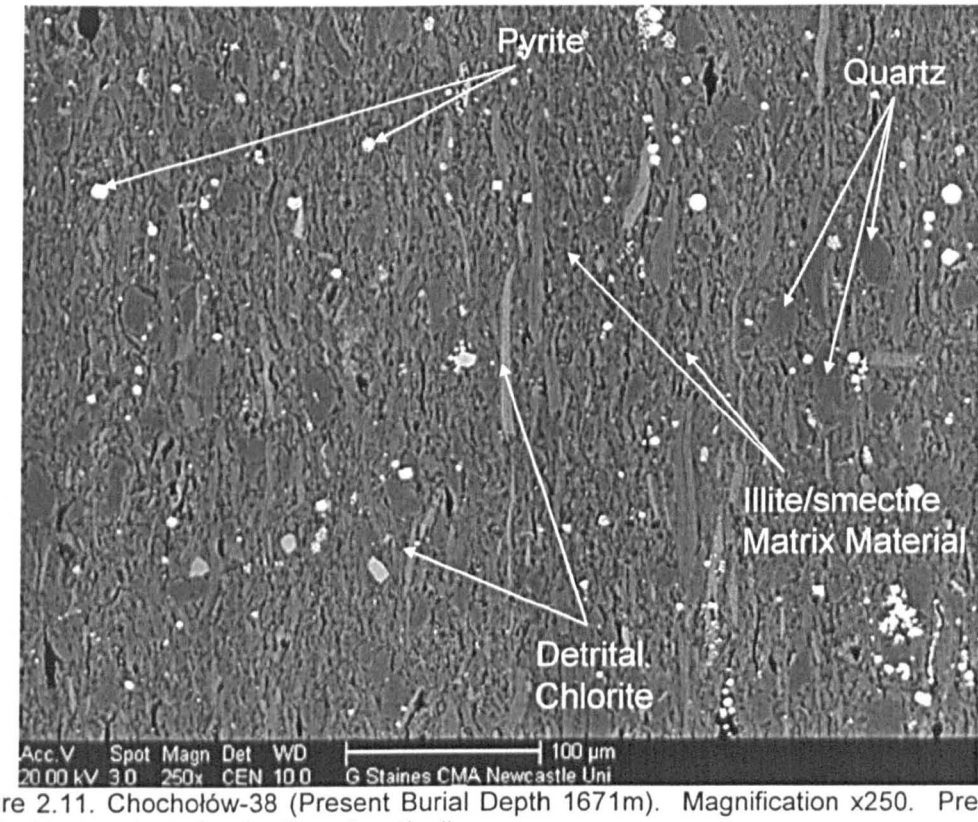

Figure 2.11. Chochołów-38 (Present Burial Depth 1671m). Magnification x250. Preferred phyllosilicate orientation is aligned vertically.

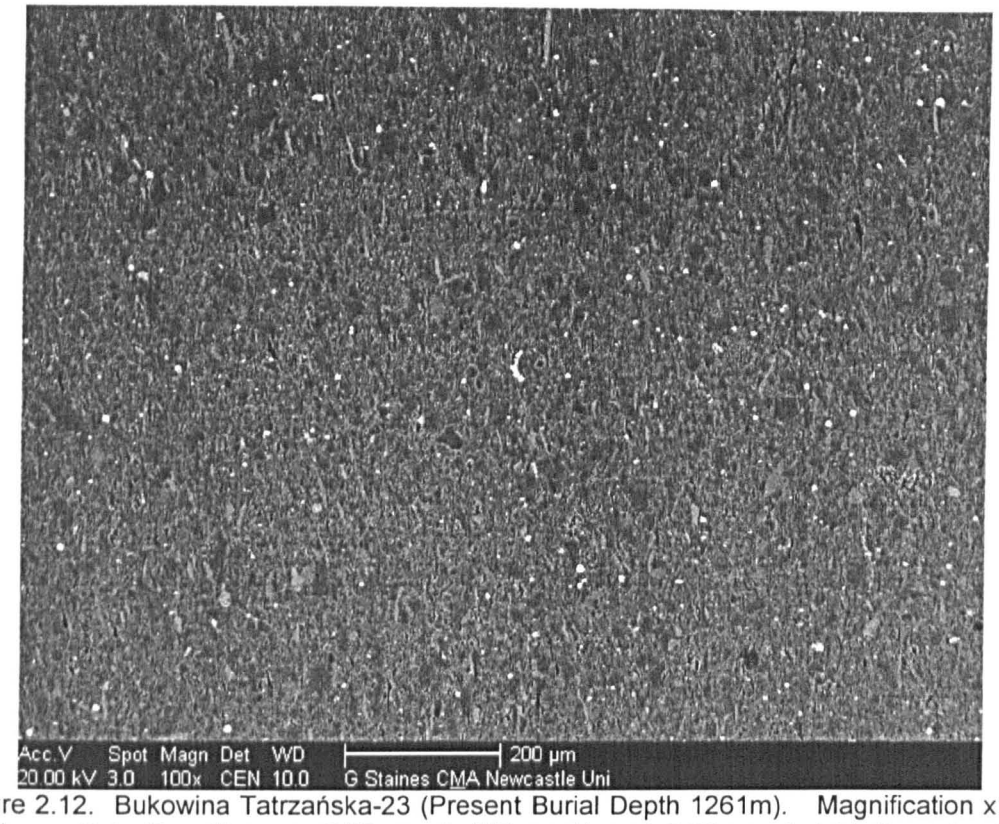

Figure 2.12. Bukowina Tatrzańska-23 (Present Burial Depth 1261m). Magnification x100, Maximum Pole Densities are 5.38 m.r.d. (I/S peak) and 5.82 m.r.d. (chlorite + kaolinite peak). Preferred phyllosilicate orientation is aligned vertically.

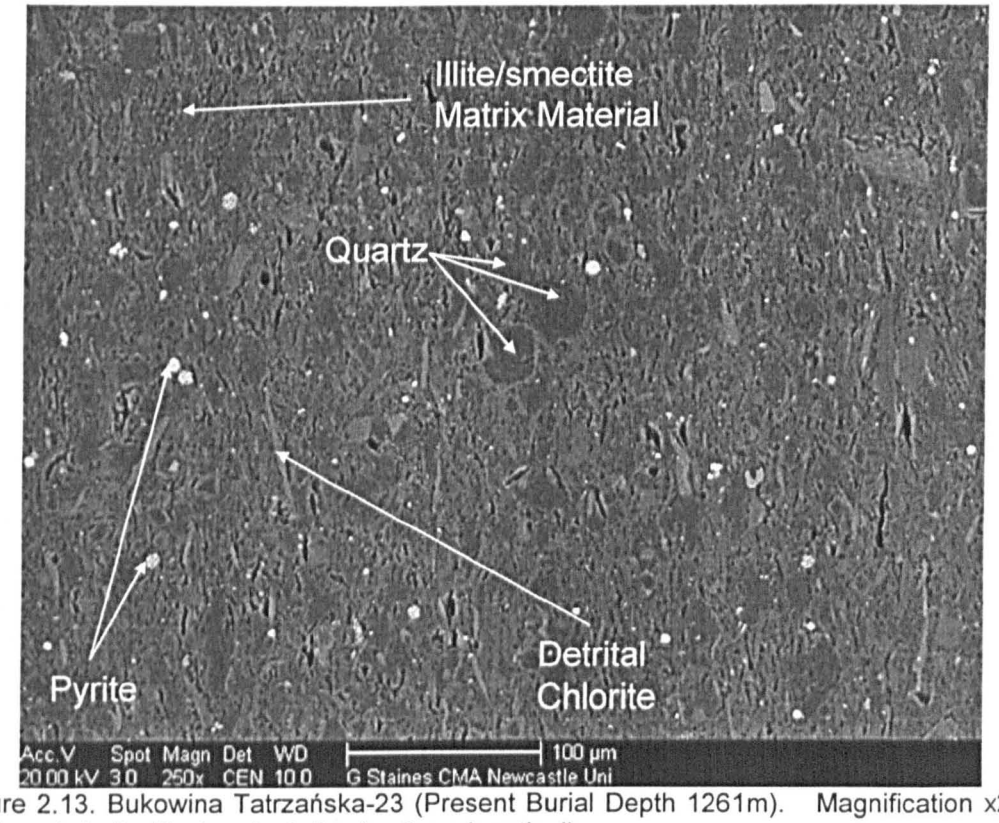

Figure 2.13. Bukowina Tatrzańska-23 (Present Burial Depth 1261m). Magnification x250. Preferred phyllosilicate orientation is aligned vertically.

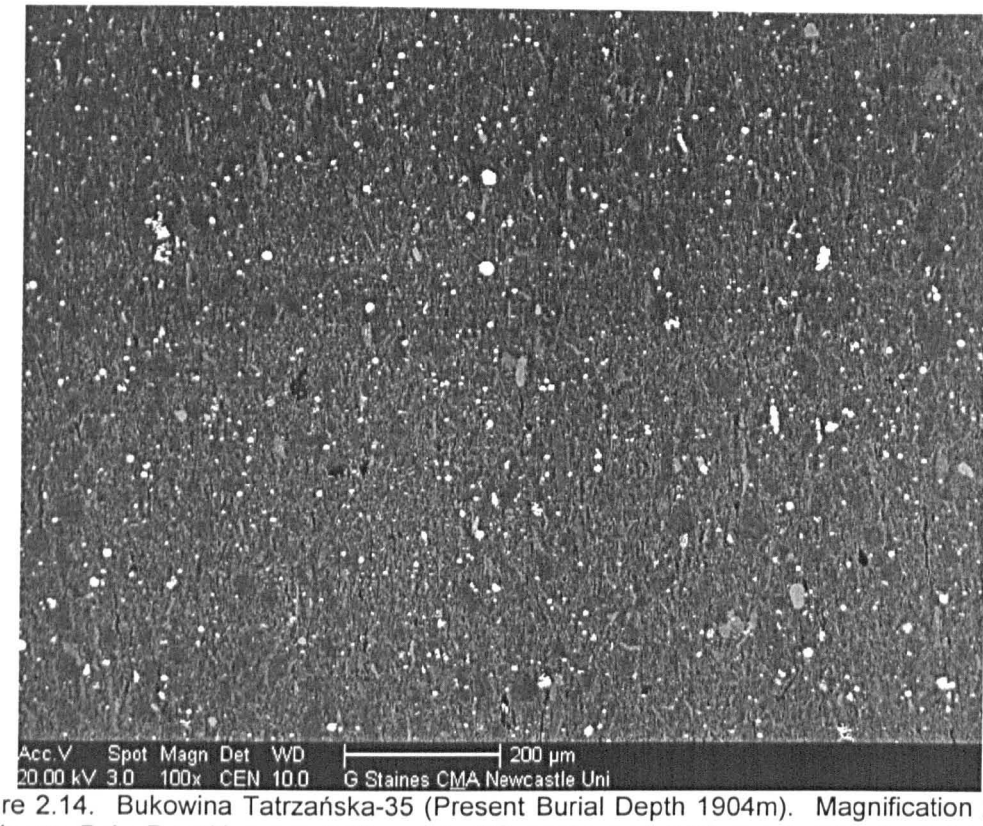

Figure 2.14. Bukowina Tatrzańska-35 (Present Burial Depth 1904m). Magnification x100, Maximum Pole Densities are 5.65 m.r.d. (I/S peak) and 5.93 m.r.d. (chlorite + kaolinite peak). Preferred phyllosilicate orientation is aligned vertically.

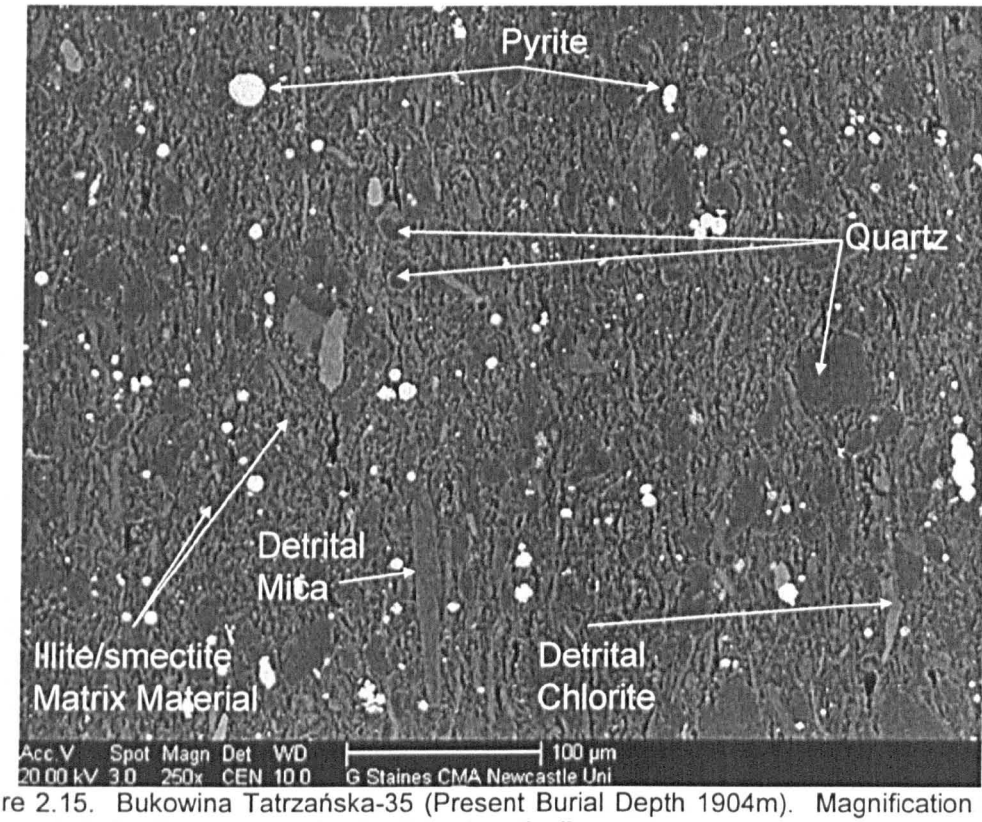

Figure 2.15. Bukowina Tatrzańska-35 (Present Burial Depth 1904m). Magnification x250. Preferred phyllosilicate orientation is aligned vertically.

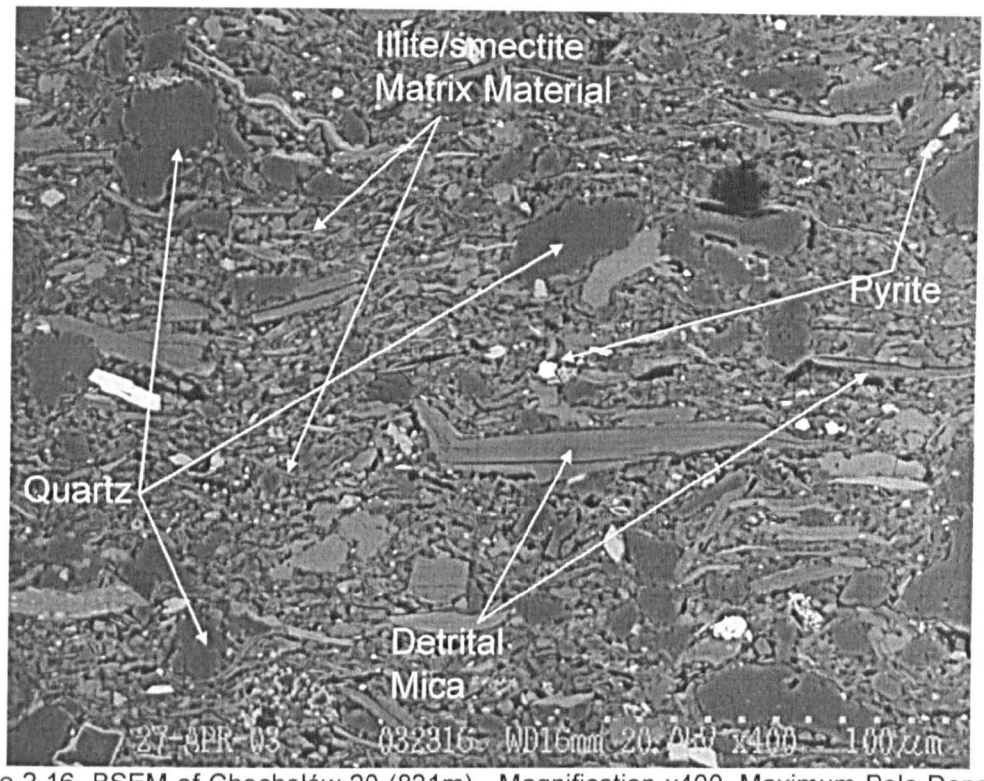

Figure 2.16. BSEM of Chocholów-20 (821m). Magnification x400, Maximum Pole Densities are 4.61 m.r.d. (I/S peak) and 4.55 m.r.d. (chlorite + kaolinite peak). Silt size quartz is matrix supported.

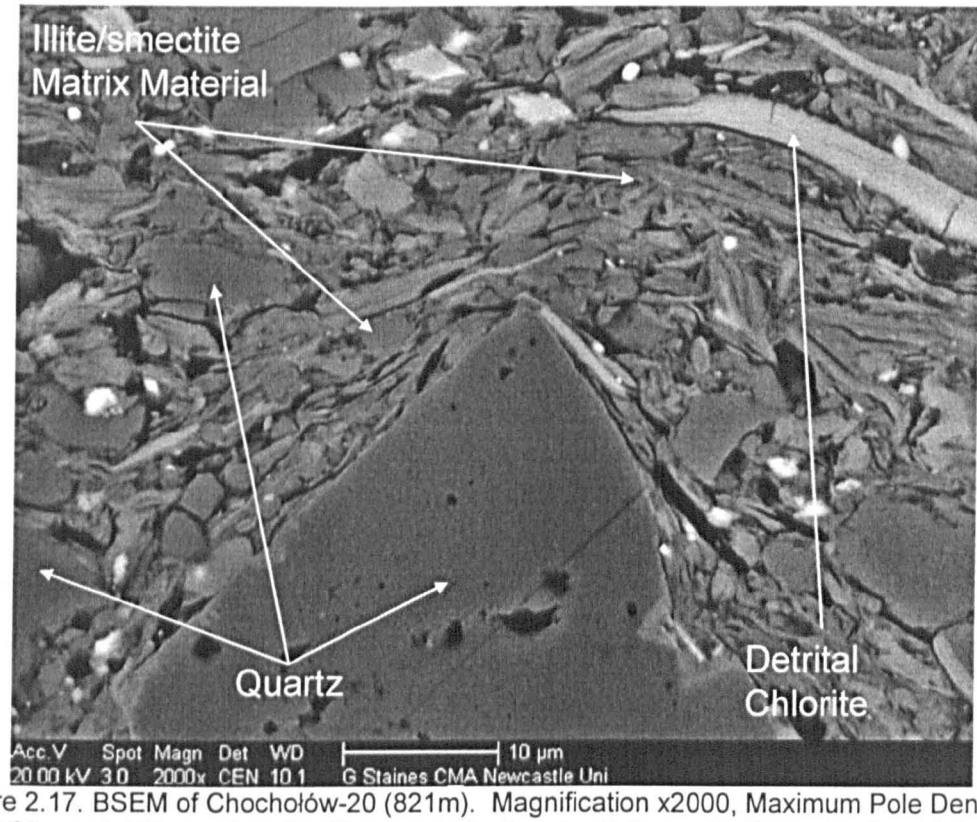

Figure 2.17. BSEM of Chocholów-20 (821m). Magnification x2000, Maximum Pole Densities are 4.61 m.r.d. (I/S peak) and 4.55 m.r.d. (chlorite + kaolinite peak). Illustrates local influence of angular quartz grains on phyllosilicate alignment.

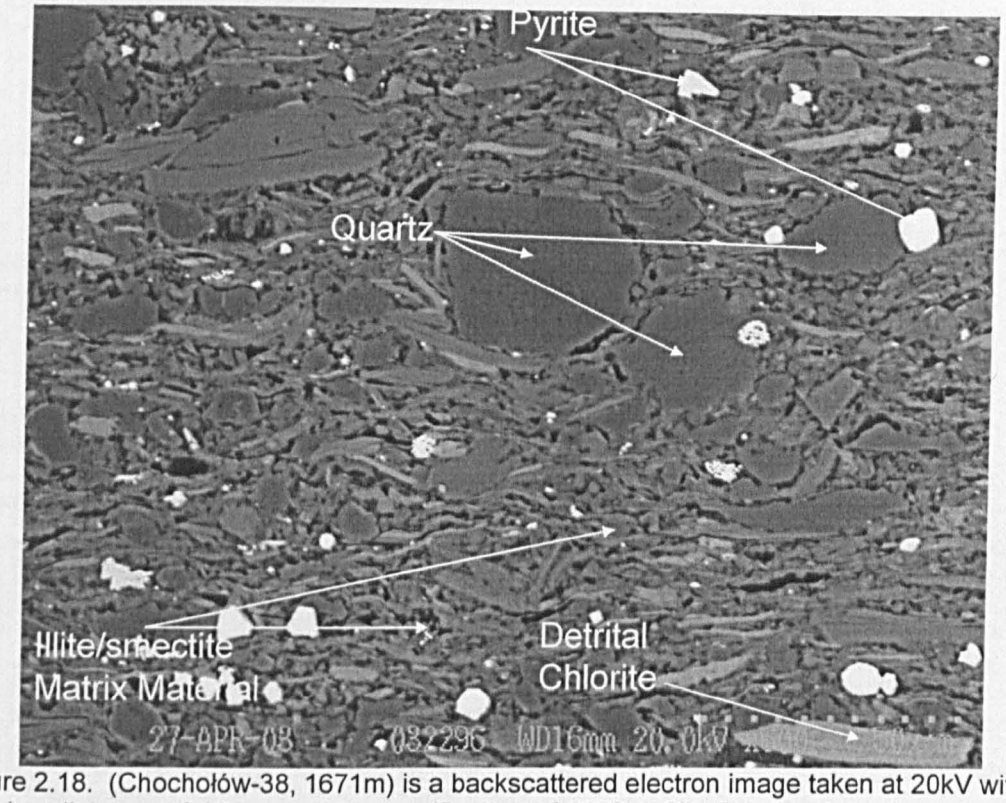

Figure 2.18. (Chochołów-38, 1671m) is a backscattered electron image taken at 20kV with a working distance of 16mm and a magnification of 600X. Silt size quartz is disrupting the alignment of platy-phyllosilicates.

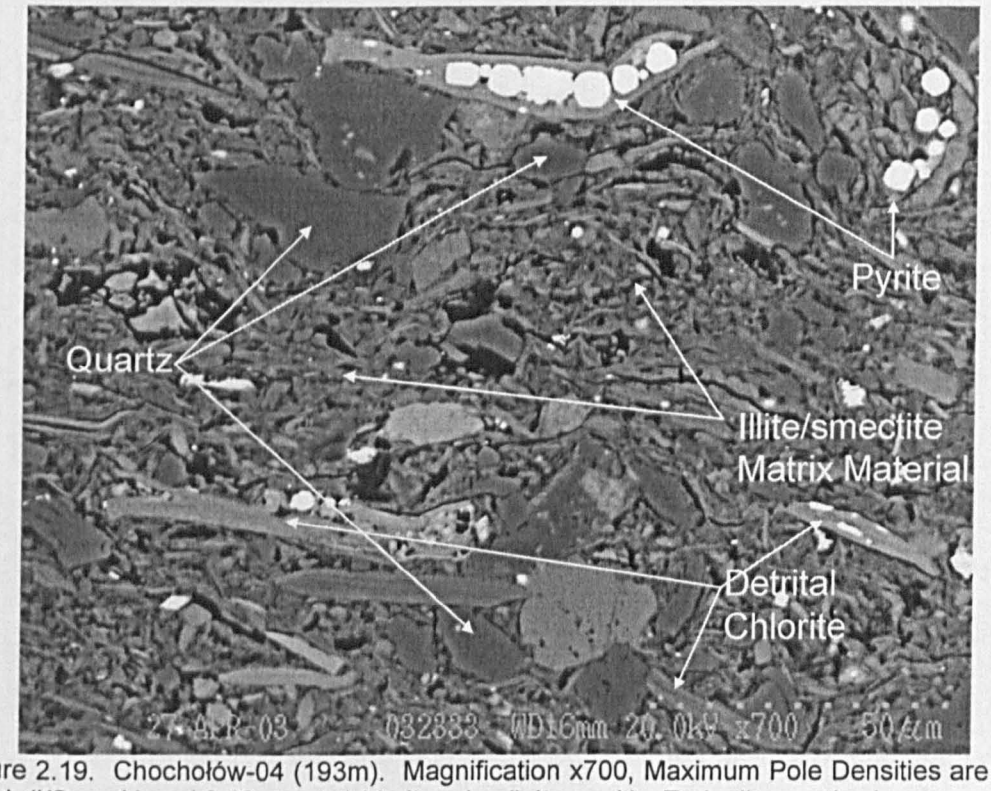

Figure 2.19. Chochołów-04 (193m). Magnification x700, Maximum Pole Densities are 3.97 m.r.d. (I/S peak) and 3.63 m.r.d. (chlorite + kaolinite peak). Early diagenetic changes can be seen in the pyrite crystals scavenging iron from a large grain, top of image.

Figure 2.20. (Chocholów-06, 280m) is a backscattered electron image taken at 20Kv with a working distance of 16mm and a magnification of 600X. Pyrite replacement in a detrital chlorite.

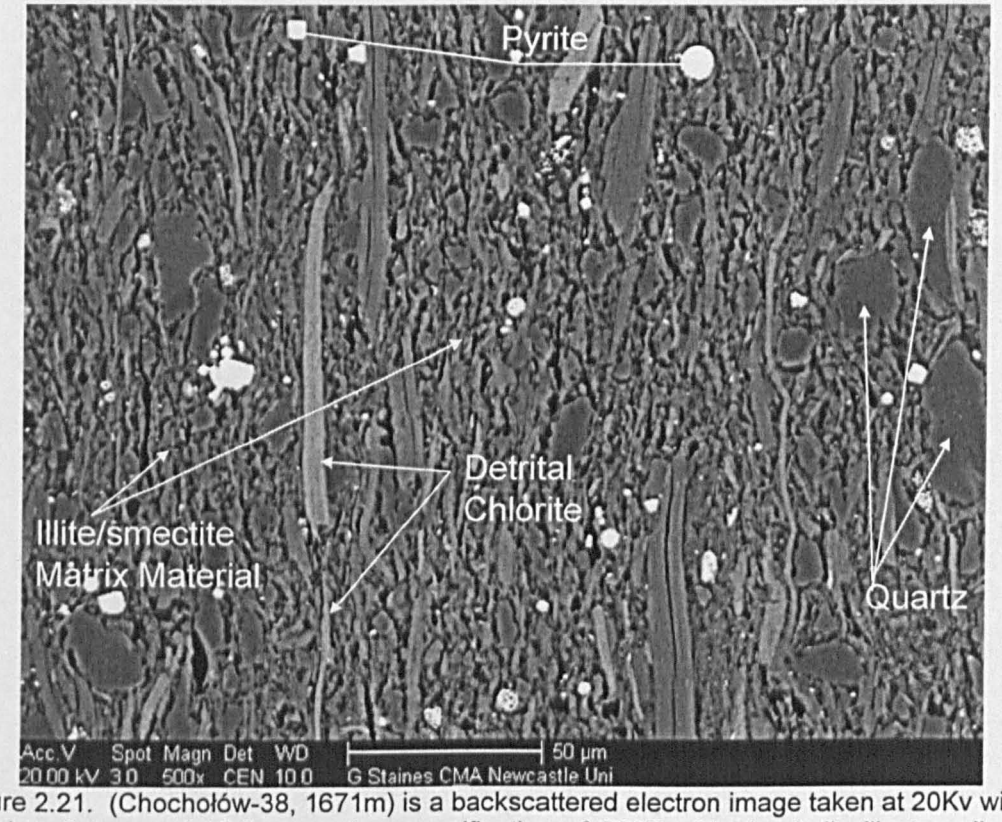

Figure 2.21. (Chocholów-38, 1671m) is a backscattered electron image taken at 20Kv with a working distance of 10.0mm and a magnification of 500X. Matrix phyllosilicates aligning themselves parallel to large silt sized phyllosilicates.

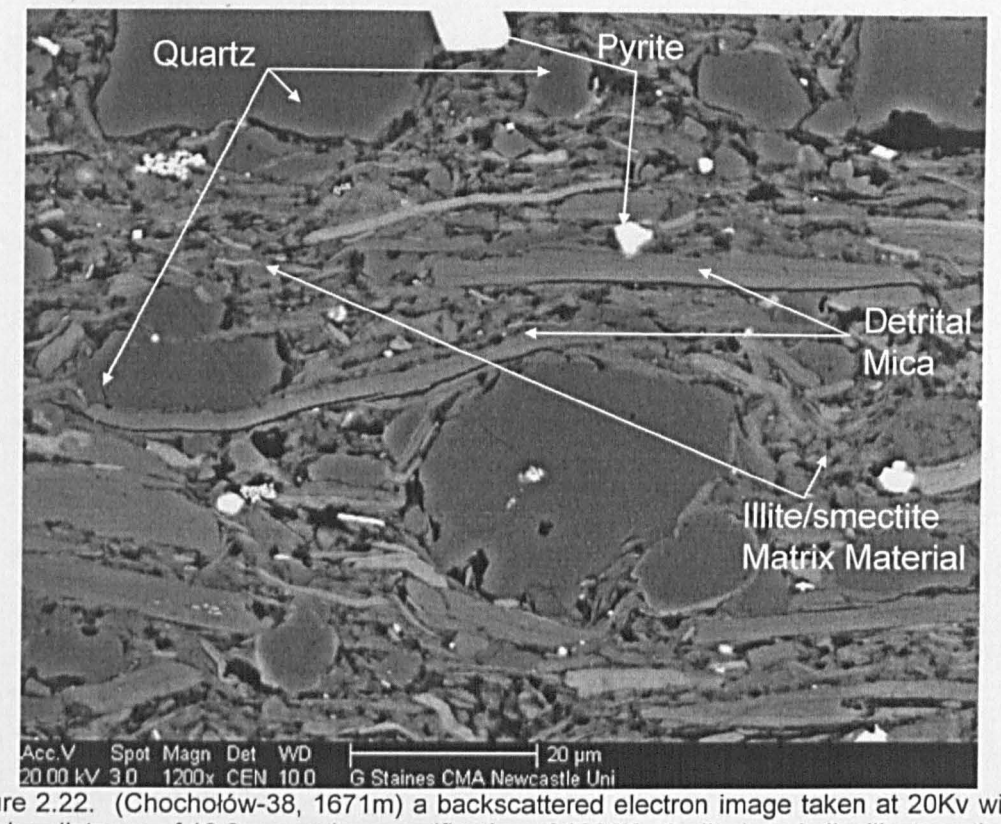

Figure 2.22. (Chochołów-38, 1671m) a backscattered electron image taken at 20Kv with a working distance of 10.0mm and a magnification of 1200X. A silt size phyllosilicate acting as a 'table' between two quartz grains to support phyllosilicate alignment above it. Area to the left of the rounded quartz grain in the centre of the micrograph shows more porosity (black areas) relative to the rest of the micrograph. But porosity and organic matter have not been separated in this image.

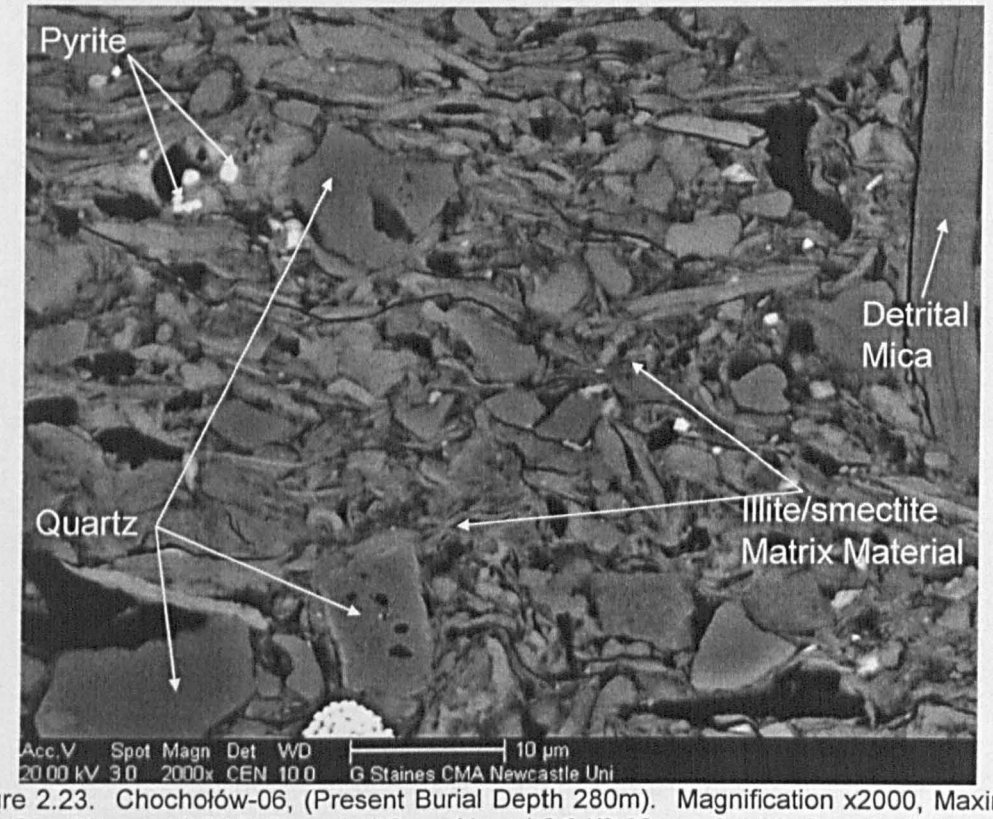

Figure 2.23. Chochołów-06, (Present Burial Depth 280m). Magnification x2000, Maximum Pole Densities are 3.38/3.8 m.r.d. (I/S peak) and 2.84/2.96 m.r.d. (chlorite + kaolinite peak). The <2µm phyllosilicate matrix shows low preferred orientation alignment.

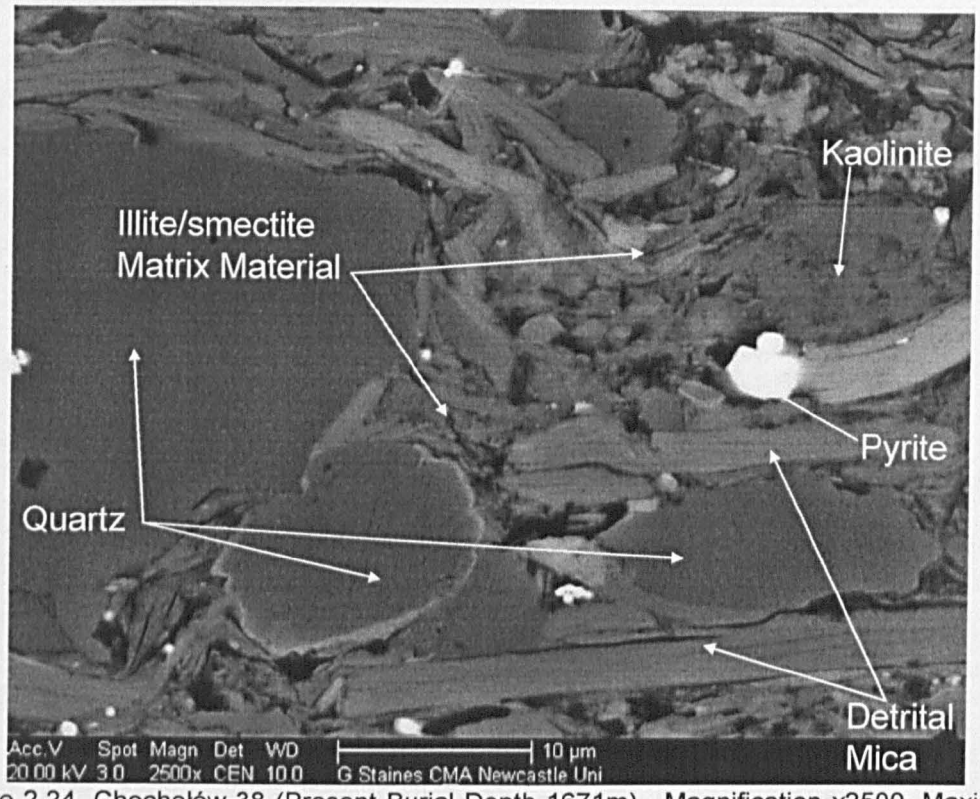

Figure 2.24. Chocholów-38 (Present Burial Depth 1671m). Magnification x2500, Maximum Pole Densities are 6.99/6.87 m.r.d. (I/S peak) and 7.36/7.44 m.r.d. (chlorite + kaolinite peak). The matrix alignment is disrupted by quartz grains, with <2µm phyllosilicates wrapping around angular quartz grains. Authigenic kaolinite is also visible.

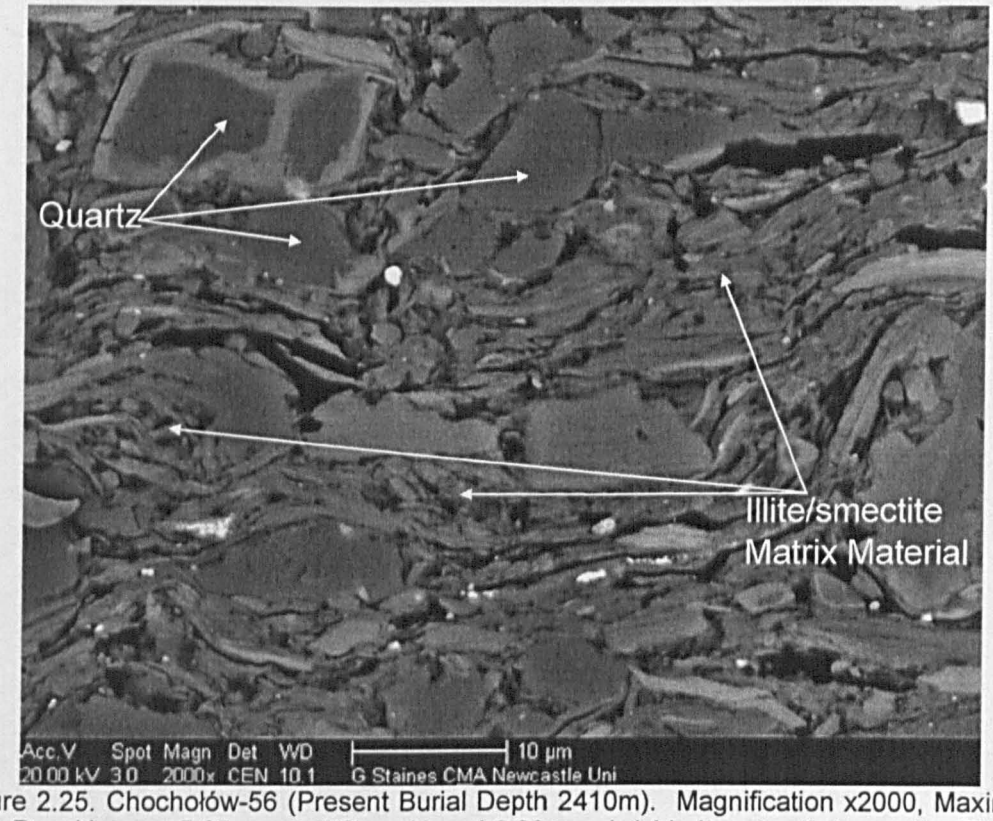

Figure 2.25. Chocholów-56 (Present Burial Depth 2410m). Magnification x2000, Maximum Pole Densities are 5.65 m.r.d. (I/S peak) and 6.29 m.r.d. (chlorite + kaolinite peak). Silt size quartz free area, centre of micrograph. Matrix phyllosilicates have developed a preferred orientation.

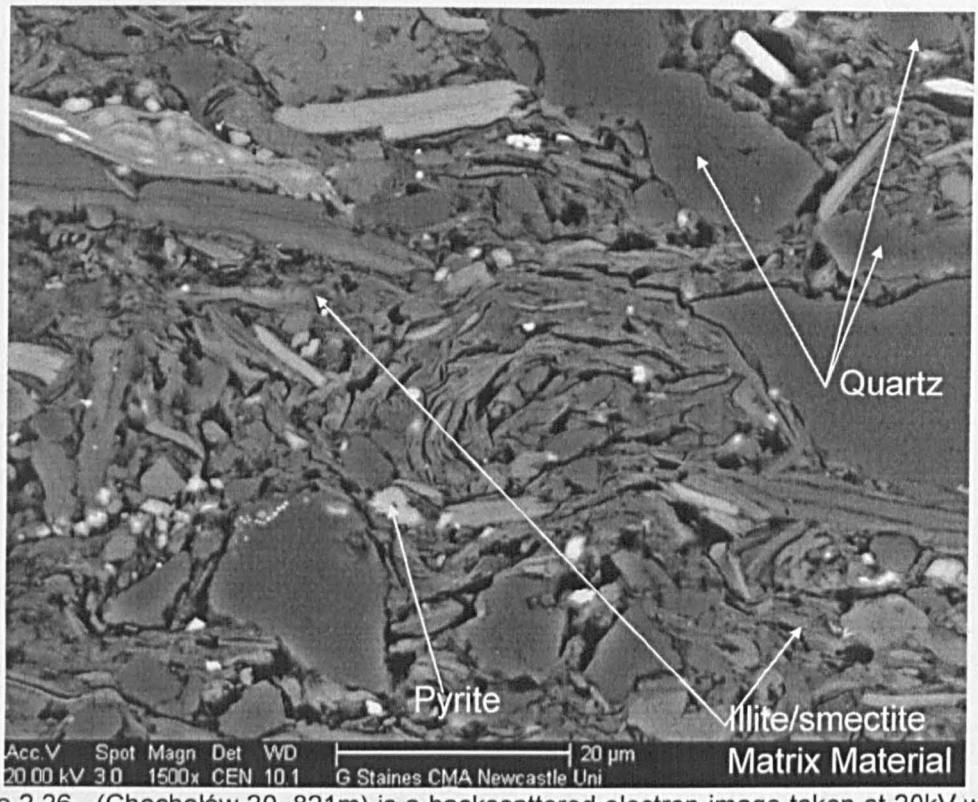

Figure 2.26. (Chocholów-20, 821m) is a backscattered electron image taken at 20kV with a working distance of 10.1mm and a magnification of 1500X. Centre of micrograph, a phyllosilicate faecal pellet, the pellet structure decreases phyllosilicate alignment. Contrasts in the BSEM micrograph suggest variably mineralogy which may have been inherited or diagenetic in origin.

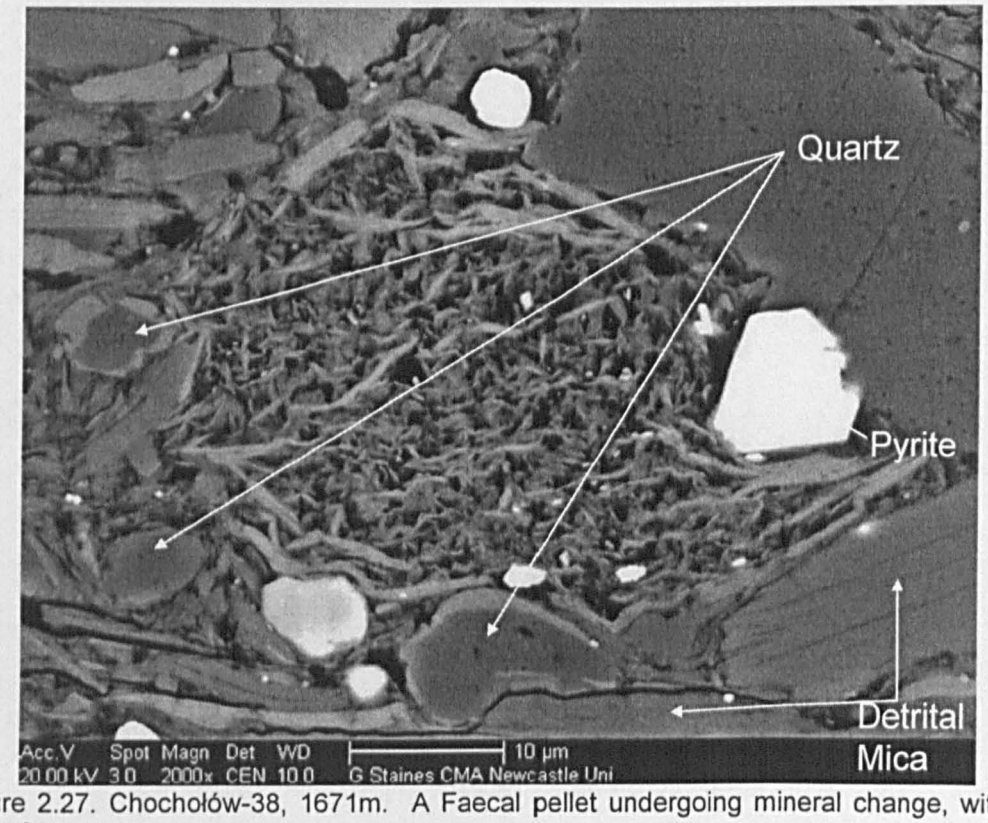

Figure 2.27. Chocholów-38, 1671m. A Faecal pellet undergoing mineral change, with no loss of structure.

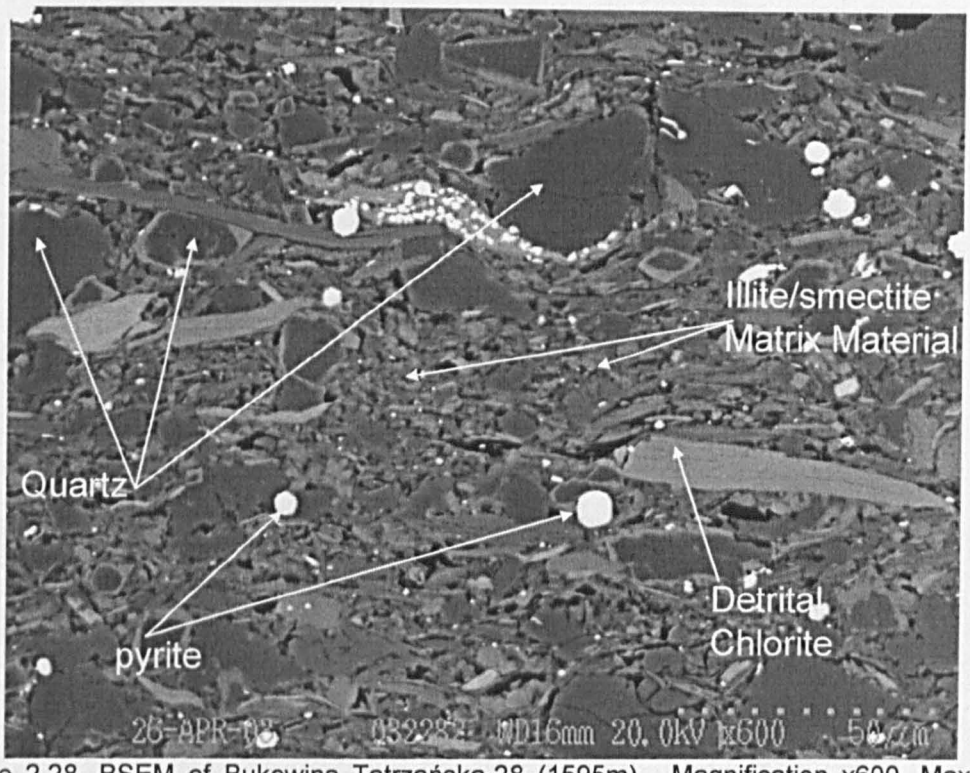

Figure 2.28. BSEM of Bukowina Tatrzańska-28 (1595m). Magnification x600, Maximum Pole Densities are 6.13 m.r.d. (I/S peak) and 7.00 m.r.d. (chlorite + kaolinite peak). HRXTG thus indicates a strongly aligned phylosilicate fabric, somewhat inconsistent with this image. This highlights the different scales of observation of the two techniques: 1mm2 for HRXTG, seventy times more than this image.

2.3.3: Porosity:

Porosity values for both Chochołów PIG-1 and Bukowina Tatrzańska PIG-1 were low ranging from 10% at the top of Chochołów PIG-1 to 2% at the base of Bukowina Tatrzańska PIG-1 (Figure 2.29), these values represent very tight mudstones which have been subjected to a great deal of compaction. The porosity data suggest that current borehole depths are too shallow as at 100m burial depth fresh sediments have around 60% porosity (Athy, 1930; Hedberg, 1936; Sclater & Christrie, 1980). The porosity of these samples are more in keeping with burial to greater than 4km. The nature of the burial of these samples has been discussed by Środoń et al (in press) and their maximum burial depths will be addressed later in this chapter. As would be expected from samples with such low porosities the pore throat radii were small, ranging from 20nm to 5nm (Figure 3.30). These values represent very

tight mudstones whose pores are small and poorly connected (Yang & Aplin, 1998; Schlömer & Krooss, 1998).

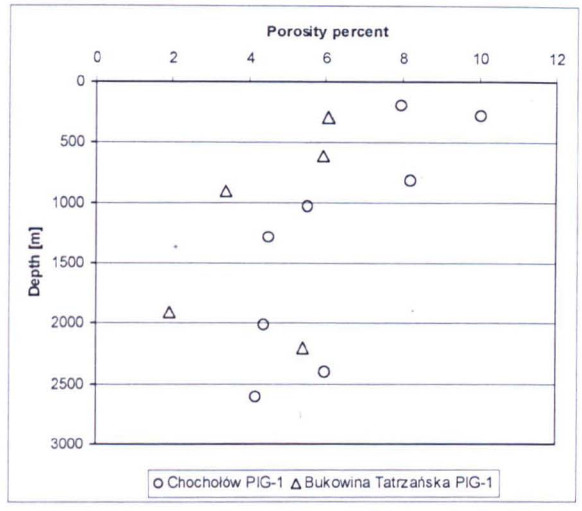

Figure 2.29. Porosity percent against actual well depth [m] for Chochołów PIG-1and Bukowina Tatrzańska PIG-1.

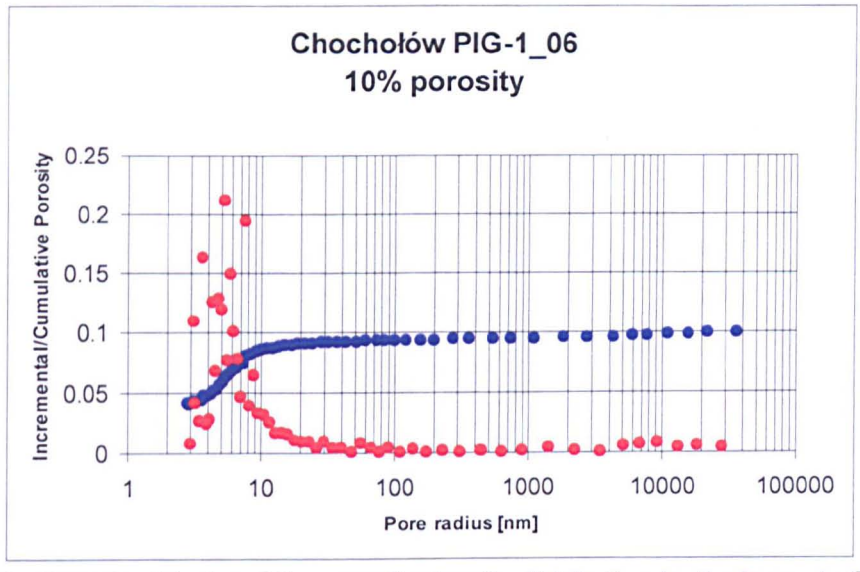

Figure 2.30. Porosity (blue) and the porosity density distribution (red) of sample Chochołów PIG-1_06. Porosity is 10% and the pore size distribution is from 3 nm to 20nm.

2.3.4: Mineralogy and Geochemistry:

The mineralogy and geochemistry (Tables 2.2 and 2.3) of these samples are presented by Środoń et al (in press).

The %S in I/S decreases down Chochołów PIG-1 from ~63% of layers to ~24% of layers (Figure 2.31) and consequently there is a change in the ordering of these smectite layers with illite in I/S from randomly interstratified (R0) to ordered layering (R1). However, Bukowina Tatrzańska PIG-1 shows no decrease in %S in I/S with increasing depth and remains constant at ~24%S (Figure 2.31).

Table 2.2. Percentage smectite in I/S, ordering and K_2O% in the whole rock as determined by Środoń et al, (in press).

Sample	Actual Burial Depth (m)	%S in I/S	Ordering	K20 (%)
Chł-4	193.4	52	0	3.62
Chł-6	280.1	50	0	3.56
Chł-12	513.5	63	0	3.21
Chł-20	820.5	47	0	2.95
Chł-23	1031.2	45	0/1	2.9
Chł-28	1283.1	44	0/1	3
Chł-38	1671.1	24	1	4.7
Chł-44	2011.5	32	1	3.4
Chł-56	2410.4	27	1	4.24
Chł-60	2611.3	24	1	2.9
Chł-66	2967.5	31	1	2.9
BkT-1	102.2	25	1	3.5
BkT-6	293.7	24	1	3.55
BkT-12	610.5	26	1	3.1
BkT-17	902.7	25	1	3.3
BkT-23	1261.2	20	1	3.3
BkT-28	1594.6	30	1	3.1
BkT-35	1904.3	18	1	3.4
BkT-41	2200.6	24	1	3.3

Table 2.3. QXRD analysis of Środoń et al, (in press)

Sample	Actual Burial Depth (m)	Quartz	K-Feldspar	Plagioclase	Calcite	Dolomite	Halite	Pyrite	Siderite	Anatase	Kaolinite	Illite + Mica + Fe-Smectite	Chlorite	Total clay	Total
Chł-4	193	19.0	2.2	3.0	7.7	3.8	0	1.5	0	0	3.2	45.8	0.7	49.7	86.9
Chł-6	280	24.3	2.3	5.9	10.2	5.4	0	1.5	0.4	0	1.5	46.8	4.0	52.3	102.3
Chł-12	514	18.5	2.2	3.7	11.9	3.5	0	1.2	0.3	0	3.2	50.2	2.6	56.0	97.3
Chł-20	821	22.9	1.5	4.7	10.5	4.1	0	0.7	0.7	0	3.6	49.2	2.1	54.9	100.0
Chł-23	1031	21.7	1.3	3.6	10.0	4.5	0	0.9	0.8	0.2	2.9	43.9	2.6	49.4	92.4
Chł-28	1283	20.4	0.5	5.7	10.4	4.7	0	2.3	0	0	2.6	49.1	3.6	55.3	99.3
Chł-38	1671	16.3	1.5	5.0	0.9	4.5	0.6	2.3	0	0.6	1.0	60.8	7.4	69.2	100.9
Chł-44	2012	26.0	1.0	7.0	3.7	6.2	0.5	2.5	0.2	0.4	1.0	53.9	5.2	60.1	107.6
Chł-56	2410	20.5	0.5	6.5	3.6	5.2	1.2	1.8	0	0.5	0.8	60.1	4.8	65.7	105.5
Chł-60	2611	27.5	0.4	9.0	13.2	4.6	0	1.2	0.2	0.7	0	41.1	4.7	45.8	102.6
Chł-66	2968	22.4	0.5	6.0	17.0	6.7	0	1.5	0.2	0.5	0	41.8	4.2	46.0	100.8
BkT-1	102	26.6	0.8	7.1	9.5	7.5	0	0.9	0	0.5	0.8	53.6	5.6	60.0	112.9
BkT-6	294	25.2	0.5	6.8	7.3	6.5	0	0.9	0.5	0.5	0.5	54.3	5.6	60.4	108.6
BkT-12	611	27.0	1.0	6.6	5.4	7.6	0	1.2	0	0.5	0	52.0	6.1	58.1	107.4
BkT-17	903	24.1	0.5	5.3	6.9	6.9	0.5	1.3	0	0.5	0	48.1	3.1	51.2	97.2
BkT-23	1261	23.3	1.0	4.5	6.1	7.8	0	1.0	0	0.4	0	50.7	4.2	54.9	99.0
BkT-28	1595	27.0	0	6.2	11.2	5.5	0	1.5	0	0.4	0	46.8	4.4	51.2	103.0
BkT-35	1904	29.4	0.5	6.3	0.8	6.2	0.5	2.4	0	0.5	0	50.1	3.6	53.7	100.3
BkT-41	2201	26.4	0	5.7	8.8	4.2	1.0	3.0	0	0.3	0	51.5	4.0	55.5	104.9

Bukowina Tatrzańska PIG-1 shows little change in mineralogy with increasing depth. Chochołów PIG-1 on the other hand shows consistent trends with increasing depth; kaolinite decreases (Figure 2.32), chlorite increases (Figure 2.33), quartz increases (Figure 2.34), and K-feldspar decreases (Figure 2.35) to ~0.5% and this decrease is coincident with smectite illitization termination. K_2O in the whole rock (Figure 2.36) remains constant with depth for both wells.

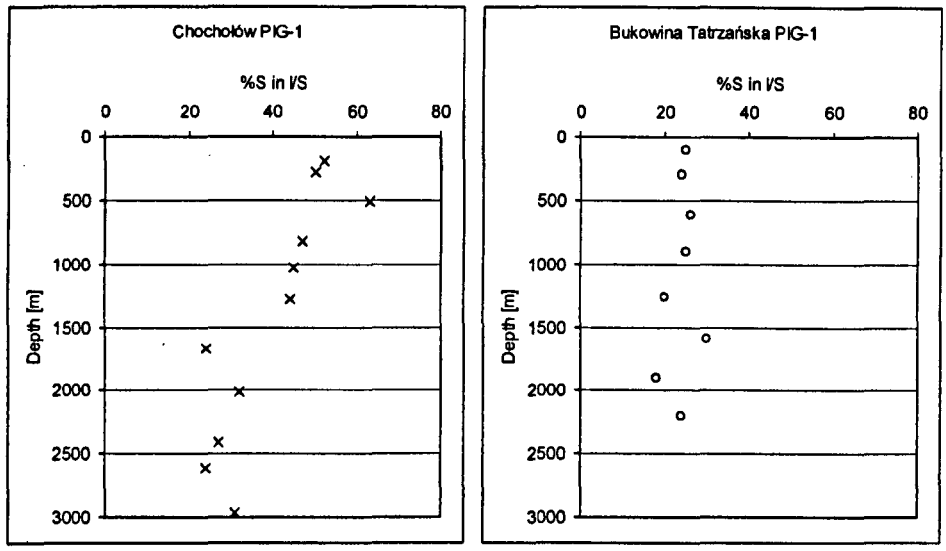

Figure 2.31. % Smectite in illite/smectite for Chochołów PIG-1, left, and Bukowina Tatrzańska PIG-1, right against actual burial depth.

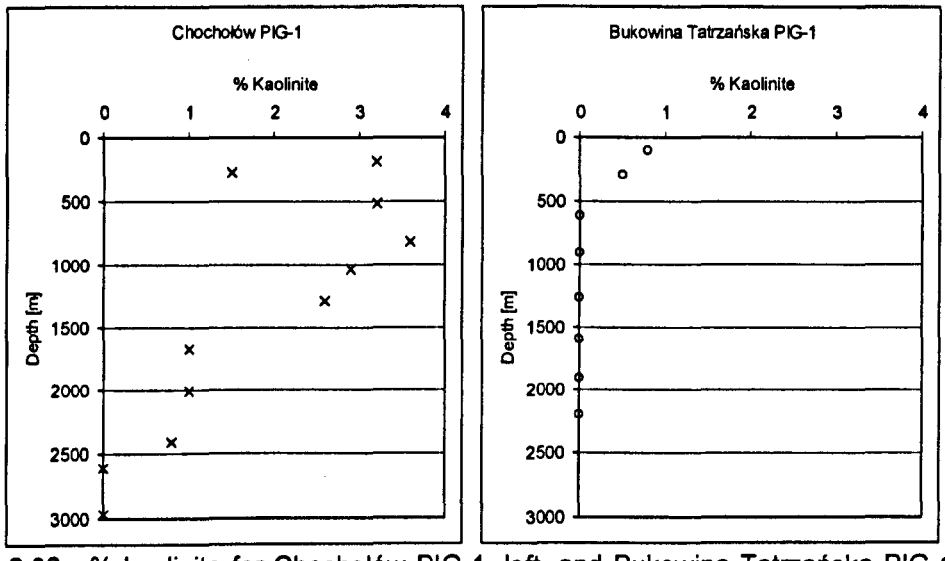

Figure 2.32. % kaolinite for Chochołów PIG-1, left, and Bukowina Tatrzańska PIG-1, right against actual burial depth.

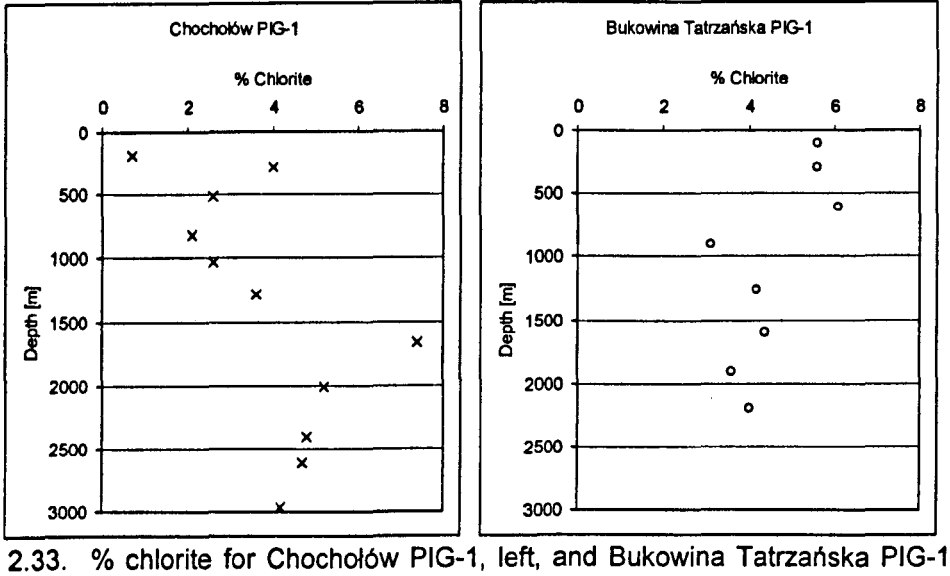

Figure 2.33. % chlorite for Chochołów PIG-1, left, and Bukowina Tatrzańska PIG-1, right against actual burial depth.

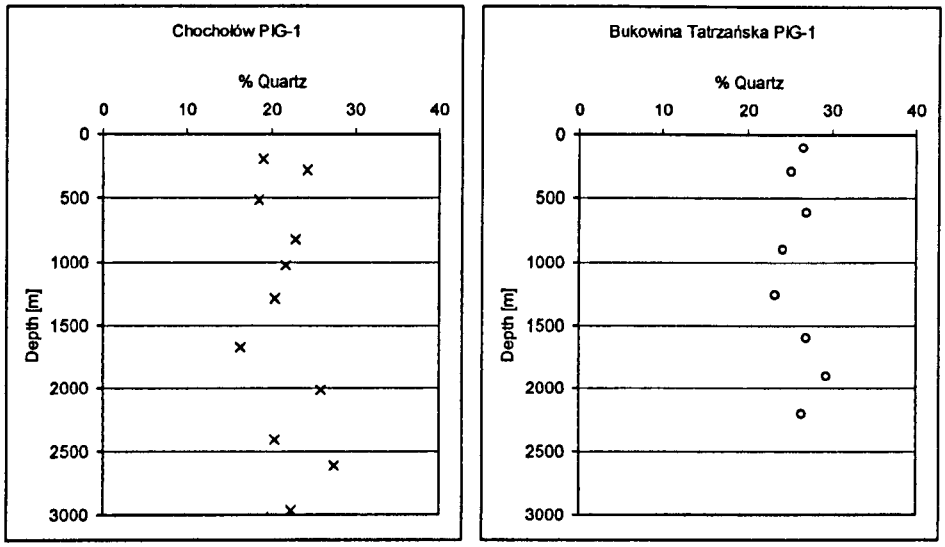

Figure 2.34. % quartz for Chochołów PIG-1, left, and Bukowina Tatrzańska PIG-1, right against actual burial depth.

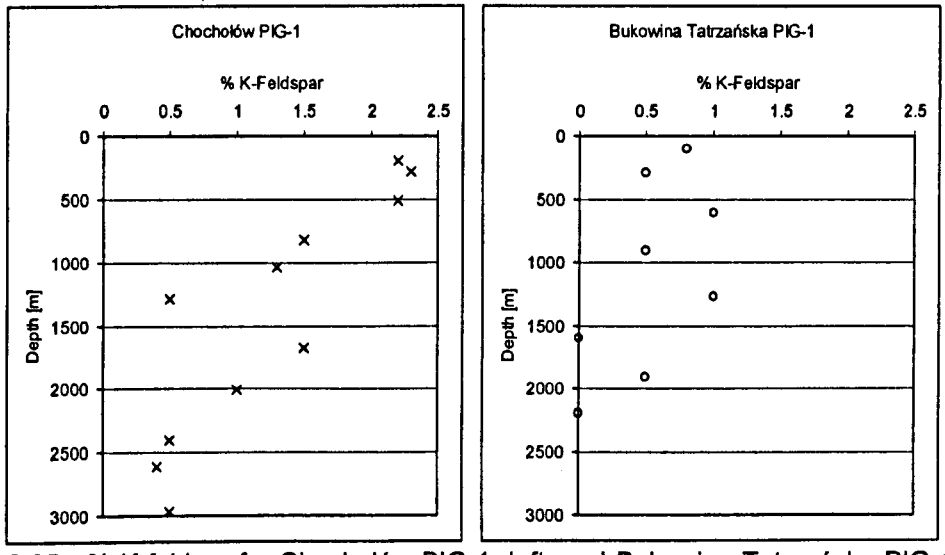

Figure 2.35. % K-feldpar for Chochołów PIG-1, left, and Bukowina Tatrzańska PIG-1, right against actual burial depth.

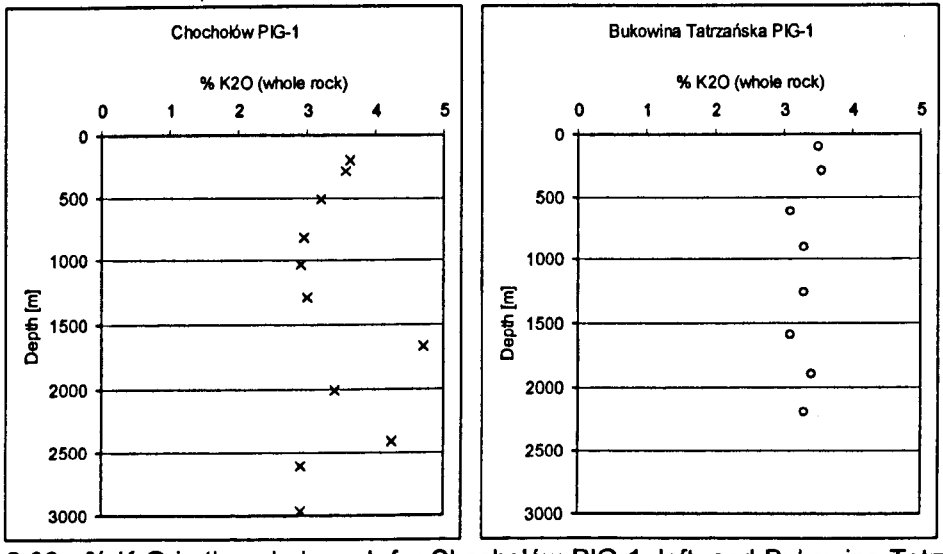

Figure 2.36. % K_2O in the whole rock for Chochołów PIG-1, left, and Bukowina Tatrzańska PIG-1, right against actual burial depth.

2.4: Discussion:

2.4.1: Maximum Burial Depth and Well Relationship:

The present day relationship between Bukowina Tatrzańska PIG-1 and Chochołów PIG-1 does not represent the maximum burial depths for these two wells.

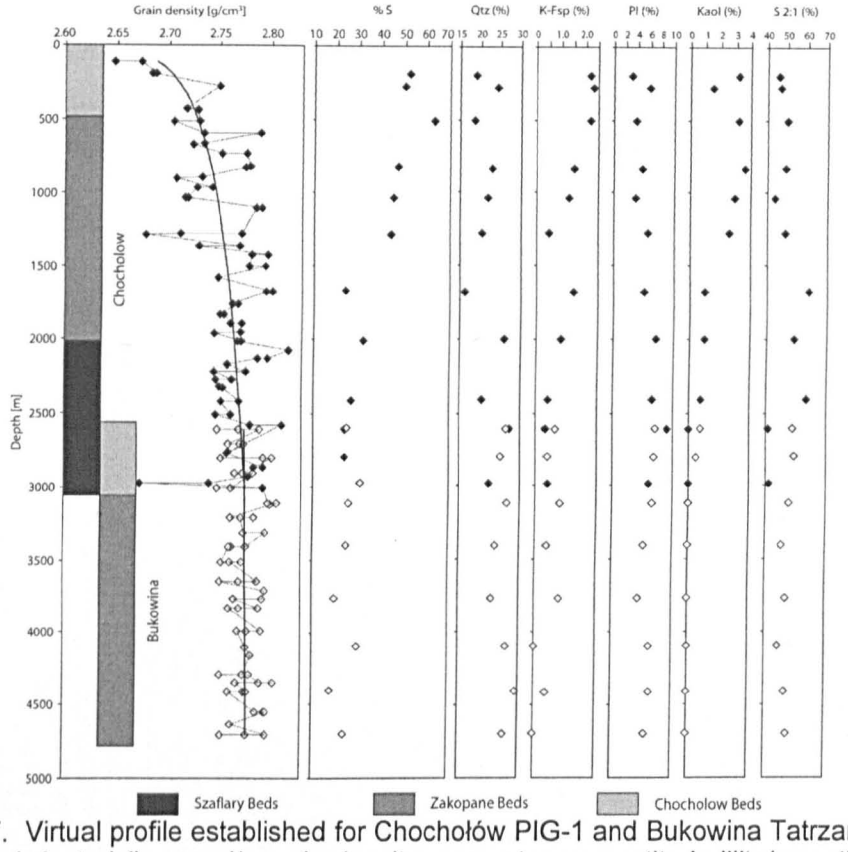

Figure 3.37. Virtual profile established for Chochołów PIG-1 and Bukowina Tatrzańska PIG-1 (After Środoń et al (in press)), grain density, percentage smectite in illite/smectite, quartz percent, K-feldspar percent, plagioclase percent, kaolinite percent and the percentage of 2:1 clay material against actual burial depth for Chochołów PIG-1 and the addition of 2606m to Bukowina Tatrzańska PIG-1.

Środoń et al (in press) have applied a variety of physical (grain density) and chemical techniques (QXRD) to unravel the basin complexities in the Podhale region. Their key findings are presented in Figure 3.37. Essentially, a range of data types have been integrated to demonstrate and overlap in the two wells with Bukowina Tatrzańska PIG-1 receiving an additional 2606m to its actual burial depth.

Applying the same methodology to the porosity data gathered in this study (Figure 2.38) suggests that this approach is valid as the Bukowina

Tatrzańska PIG-1 borehole plots below Chochołów PIG-1 in a continuous trend.

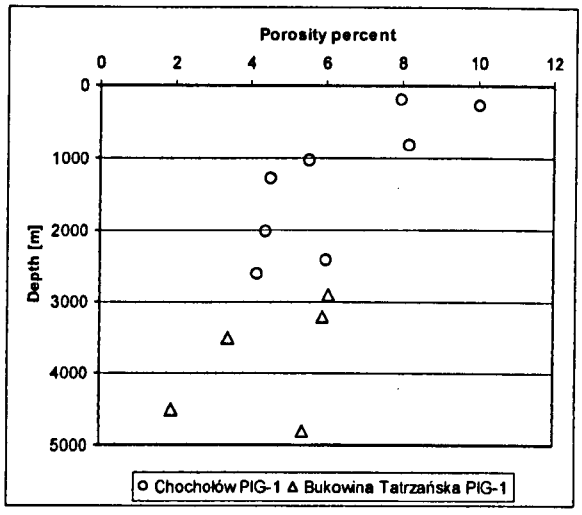

Figure 2.38. Virtual profile for the percent porosity for Chochołów PIG-1 and Bukowina Tatrzańska PIG-1 applying an addition of 2606m to Bukowina Tatrzańska PIG-1 following the methodology of Środoń et al (in press).

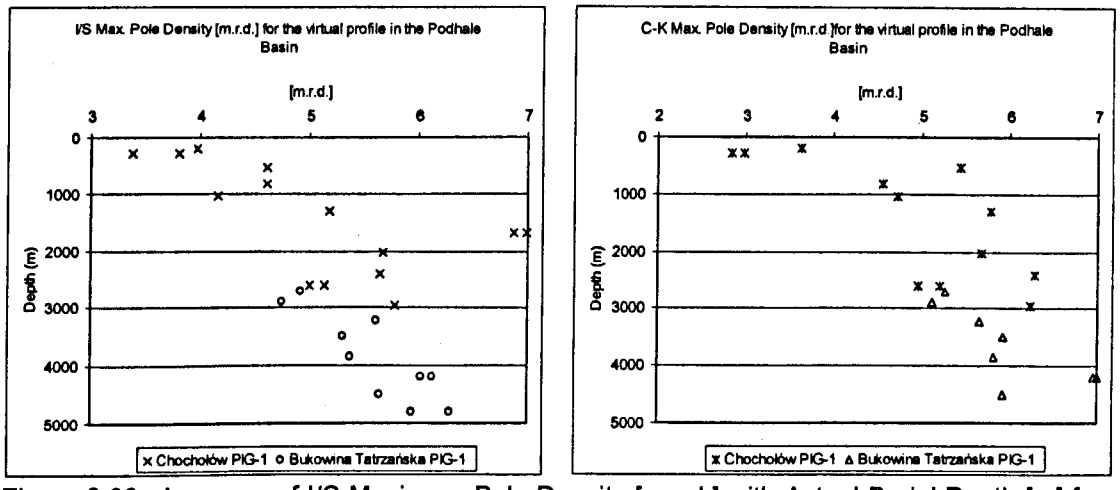

Figure 2.39. Increase of I/S Maximum Pole Density [m.r.d.] with Actual Burial Depth [m] for Chochołów PIG-1 and applying an addition of 2606m to Bukowina Tatrzańska PIG-1 following the methodology of Środoń et al (in press), left, and the increase of C-K Maximum Pole Density [m.r.d.] with Actual Burial Depth [m] for Chochołów PIG-1 and applying an addition of 2606m to Bukowina Tatrzańska PIG-1 following the methodology of Środoń et al (in press), right.

With the addition of 2606m to the actual depths of Bukowina Tatrzańska PIG-1 actual burial depth the virtual profile validity is established further with the appreciation of the HRXTG data presented previously. Bukowina Tatrzańska PIG-1 establishes a continuous profile with Chochołów PIG-1 and shows a change in preferred phyllosilicate alignment from ~3 m.r.d. to ~ 6 m.r.d. over a ~5000m depth profile for both peaks (2.39).

Środoń et al (in press) have noted that there has been erosion and uplift in the Chochołów PIG-1 well. The porosity data presented previously suggest that current borehole depths are too shallow as at 100m burial depth fresh sediments have around 60% porosity (Athy, 1930; Hedberg, 1936; Sclater & Christrie, 1980). The porosities of these samples, shallowest at 10%, are more in keeping with porosities at ~4km.

The Methylphenanthrene Index (MPI) is a maturity parameter based on aromatic hydrocarbons that may be used in the absence of reliable vitrinite reflectance data to give a quantifiable measure of maturity. The MPI was devised, by Radke and Welte (1981) from the distribution of phenanthrene and methylphenanthrene isomers. The Radke and Welte (1981) study showed good correlation between MPI and mean vitrinite reflectance (R_m) allowing a calculated mean reflectance (R_c) to be calculated from MPI data.

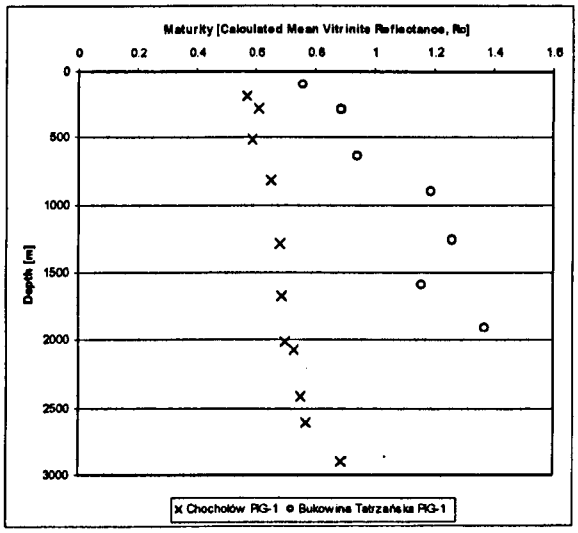

Figure 2.40. Maturity [Calculated Mean Vitrinite Reflectance] against actual burial depth for Chochołów PIG-1 (Rospondek and Marynowski 2004) and Bukowina Tatrzańska PIG-1 (Marynowski, 2005; pers comms).

Kotarba and Środoń (pers comms) demonstrated that the vitrinite reflectance data for Chochołów PIG-1 and Bukowina Tatrzańska PIG-1 are compromised by the occurrence of reworked vitrinite, resulting in wholly unreliable maturity assumptions from this index. Rospondek and Marynowski (2004) published

MPI data for the Chochołów PIG-1 well and Marynowski (pers comms) holds data for Bukowina Tatrzańska, the results can be seen in Figure 2.40.

The data have been joined into a synthetic profile based on the overlap of the R_c data and checked against grain density and mineralogical trends following the methodology of Środoń et al (in press) (Figure 2.41).

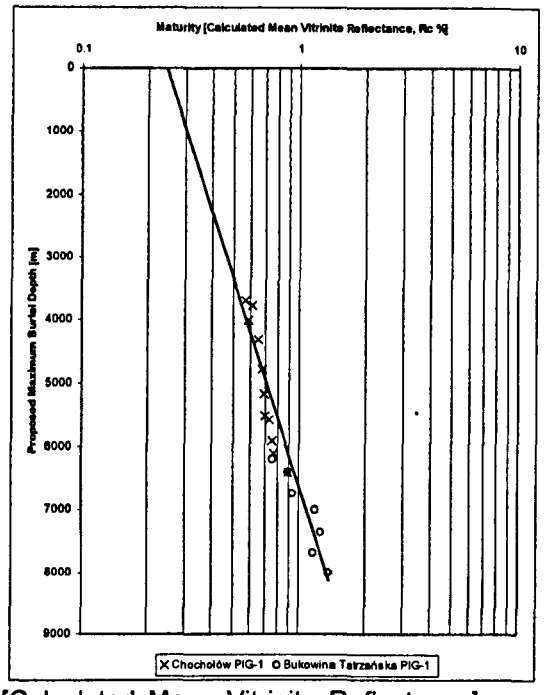

Figure 2.41. Maturity [Calculated Mean Vitrinite Reflectance] versus proposed maximum burial depth. Maturity calculated from methylphenanthrene data. See text for more detail of how maximum burial depth was estimated. X=Chochołów PIG-1; o=Bukowina Tatrzańska PIG-1. Figure shows regression line back to a surface maturity of 0.25Rc. The trend line is logarithmic, y = 4759.5Ln(x) + 6768.

The addition of 3500m to the profile is based on Figure 2.41 and has placed the data on a log scale and a line has been used to extrapolate the data back to the surface and an R_c value of 0.25, a typical maturity for surface sediments (Sweeney & Burnham, 1990; Teichmueller, 1970 for references and profiles). Consequently, 3500m of eroded sediment are required to bring the data into line with this point of the surface (Table 2.4).

This result is in keeping with the ~4km of sediment Środoń et al (in press) have proposed to have been eroded from the western part of the Podhale Basin and ~7km in the eastern part. Consequently, the wells are now in proposed maximum burial situations, which allows a better appreciation of

the fabric development, compaction in general and the diagenetic reactions at play in the basin.

Table 2.4. Maturity [Calculated Mean Vitrinite Reflectance] data for Chochołów PIG-1 (Rospondek & Marynowski, 2004) and Bukowina Tatrzańska PIG-1 (Marynowski, 2005. pers comms) after Radke and Welte (1981), along with actual well depth [m] and proposed maximum burial depth [m].

Chochołów PIG-1		
Depth [m]	Proposed Maximum Burial Depth [m]	Mean Calculated Vitrinite Reflectance, Rc
193	3693	0.57
280	3780	0.61
513	4013	0.59
593	4093	0.65
820	4320	0.68
1283	4783	0.69
1671	5171	0.69
2011	5511	0.7
2075	5575	0.73
2410	5910	0.75
2511	6011	0.77
2900	6400	0.89
Bukowina Tatrzańska PIG-1		
Depth [m]	Maximum Burial Depth [m]	Mean Calculated Vitrinite Reflectance, Rc
102	6208	0.76
293	6399	0.89
640	6746	0.94
902	7008	1.19
1261	7367	1.26
1594	7700	1.16
1904	8010	1.37
2201	8307	~

In modelling the Podhale Basin, Środoń et al (in press) have demonstrated a 20°C/km to 25°C/km palaeogeothermal gradient (present day geothermal gradient is 21°C/km +/- 2°C, Cebulak et al., 2004), deduced from I/S palaeothermometry, which has been used in various studies to estimate temperature (Hoffman & Hower, 1979; Pollastro, 1993; Środoń, 1995) and fixing the calculated vitrinite reflectance data from MPI analysis to the to the plot of Suggate (1998).

Table 2.5. Maximum Burial Temperatures experienced by the for Chochołów PIG-1 and Bukowina Tatrzańska PIG-1 wells based on present day geothermal gradient (after Cebulak et al., 2004) and maximum and minimum palaeogeothermal gradients [after Środoń et al., (in press)].

Well and Sample	Maximum Palaeotemperature [°C] based on; 21°C/km, geothermal gradient (after Cebulak et al, 2004)	Maximum Palaeotemperature [°C] based on; Środoń et al (in press) minimum geothermal gradient 20°C/km	Maximum Palaeotemperature [°C] based on; Środoń et al (in press) minimum geothermal gradient 25°C/km	Proposed Maximum Burial Depth [m]
Chochołów-04	77.6	73.9	92.3	3693
Chochołów-66	135.8	129.3	161.7	6467
Bukowina Tatrzańska-01	130.4	124.2	155.2	6208
Bukowina Tatrzańska-41	174.3	166.0	207.5	8307

The maximum palaeotemperatures quoted by Środoń et al (in press) are in Table 2.5. These are adequate temperatures for the illitization of smectite to proceed (Weaver, 1989), the important phyllosilicate diagenetic marker in the basin.

Środoń et al (in press) have used the inflection point of the maturity curve, taken to be at 0.7% R_o (Rc in this study) and proposed to be characteristic of sedimentary basins (Suggate, 1998), with depth to be the key marker in their modelling reconstruction of the Podhale Basin, having joined the Chochołów PIG-1 and Bukowina Tatrzańska PIG-1 wells into a virtual profile. This method requires a stable heat flow through time in the basin. Additionally, this inflection point becomes the only marker point. Środoń et al. (in press), therefore, conclude that ~4km of erosion from Chochołów PIG-1 has taken place and ~7km from Bukowina Tatrzańska PIG-1.

The methodology in this study uses an extrapolation of a log plot back to a surface value of 0.25%R_o and estimates ~3.5km of erosion in Chochołów PIG-1 and ~6.5km in Bukowina Tatrzańska PIG-1.

The amounts of erosion estimated by both methods are similar but have uncertainties. One requires an inflection point at 0.7% R_o fitted to modelled geothermal gradients. This 0.7% R_o has been noted by Suggate (1998) and additionally by Honty et al, (2004) from the East Slovak Basin to the south of the Podhale. The other erosion estimate requires extrapolation. The effect of this 500m difference described by the two estimations will result in a

~10°C difference. If maturity is the sole parameter taken as a marker this will have implications for geothermal gradient and/or heat flow. Therefore, extrapolation back to a surface value of 0.25% R_o is more robust. In terms of loading 500m will not have a great deal of effect on the porosity as the results suggest overpressuring in the Basin as a whole, the porosity measurements alone suggest that there has been up lift and erosion.

Yang and Aplin (2004) have published a relationship between mudstone porosity and effective stress, as a function of clay fraction. Using this relationship and assuming average clay contents of 55% (Table 2.3), a porosity of 10% for the shallowest Chochołów PIG-1 samples (Figure 2.38) suggests that the maximum effective stress that these samples have been subjected to is around 27 MPa. At a burial depth of 3.6 km, the lithostatic stress is around 80MPa and the estimated pore pressure (lithostatic stress minus effective stress) is then around 53 MPa. Since the hydrostatic stress at 3.6 km is around 35 MPa, it appears that the Chochołów PIG-1 samples were substantially overpressured at maximum burial.

2.4.2: Chemical Changes Related to Diagenesis:

Although potassium from K-feldspar is decreasing in abundance with depth (Figure 2.35) and is suspected of being used in the smectite to illite conversion the plot of percent K_2O against depth (Figure 2.36) exhibits a constant trend. This suggests that potassium is being conserved within a closed system and the majority of potassium is from K-feldspar and is driving the illitization of smectite. Since, the amount of 2:1 clays in the Podhale Basin does not change significantly with depth, more evidence that the mudstones in the basin are acting as a closed system, thereby following the reactions of Hower et al (1976) rather than those of Boles and Franks (1979). The QXRD presented earlier does not unfortunately distinguish between 2:1 illite, mica and Fe-smectite so it is not possible to apply a methodology of looking at the ratio of illite:chlorite (Land et al, 1987) to see if the system is truly closed with respect to potassium or whether the basin diagenetic

reactions are following a mechanism closer Al conservation (Boles & Franks, 1979).

The illitization of smectite terminates at ~80% illite layers in the Podhale Basin (Figure 2.31) and the reaction is dependent on time, temperature and a supply of potassium ions. There is abundantly enough time and temperature for these sediments to achieve diagenetic maturity (e.g. Elliott et al, 1999; Elliott & Matisoff, 1996; Hillier et al, 1995; Huang et al, 1993; Velde & Vasseur, 1992; Elliott et al, 1991; Pytte & Reynolds, 1989; Freed & Peacor, 1989) as they are Palaeogene in age and have reached 170°C+ maximum burial temperatures (Środoń et al., in press). The fact that the reaction has terminated at ~20% smectite layers suggests that there are not enough sources of potassium to facilitate the reaction beyond ~20% of layers, as commonly observed in basins around the world (Hower et al, 1976; Pearson et al, 1982; Środoń & Eberl, 1984; Eberl, 1993;). K-feldspar has been depleted to around half of one percent and the point in the system where it has changed is at ~6000m (maximum burial depth) in the Chocholow PIG-1 borehole which is coincident with the termination of the smectite to Illite reaction. This suggests that in this basin K-feldspar is the driving force behind the illitization of smectite and its consequent termination. K-feldspar is almost entirely depleted in Bukowina Tatrzanska PIG-1 hence in this borehole the illitization of smectite has terminated. The illitization of smectite as perceived by Hower et al (1976) and Boles and Franks (1979) are not the only diagenetic reactions using K-feldspar. Potassium feldspar and kaolinite are converted to illite and water (after Giles et al 1998; K-feldspar + 2Kaolinite= illite + water). As a result K-feldspar and kaolinite may be depleted by this reaction as well as illitization of smectite in the mixed layer phase I/S. BSEM images presented early suggest kaolinite change, although whether illite or chlorite is the end product is not entirely clear and little evidence for diagenetic phyllosilicate mineral change in mudstones was observed in BSEM, because it occurs in the less than 2μm fraction that is often below the resolution of the technique. The K-feldspar dissolution that is occurring in the basin has not been observed in BSEM images.

The depth of ~6000m (maximum burial depth) appears to be critical as it is the termination point for many mineral and chemical reactions; however organic maturity is continuing to increase beyond illitization of smectite termination (Figure 2.42). Kaolinite depletion (Figure 2.32), chlorite increase (Figure 2.33) and illite growth all terminate at this depth. Quartz percent (Figure 2.34) is continuing to increase after ~6000m (maximum burial depth) when the illitization reaction is seen to terminate, this can be attributed to three factors 1; a change of depositional environment over time and/or a change in sediment type and flow into the basin, 2; diagenetic quartz growth associated with the illitization of smectite (e.g. Hower et al, 1976; Boles & Franks, 1979), silica being a product of the reaction, 3; flow of silica rich pore waters through the system (e.g. Land et al, 1987; Land et al, 1997), which is unlikely as K_2O demonstrates that the system is closed or from diagenetic quartz formation out of pre-existing pore waters. The most likely explanation is that quartz continues to increase when the other reactions have terminated as a result of silica released during much earlier illitization of smectite, placing higher concentrations of silica into the closed system, which then precipitates as diagenetic quartz as a steady process unaffected by the termination of the diagenetic reactions in the basin.

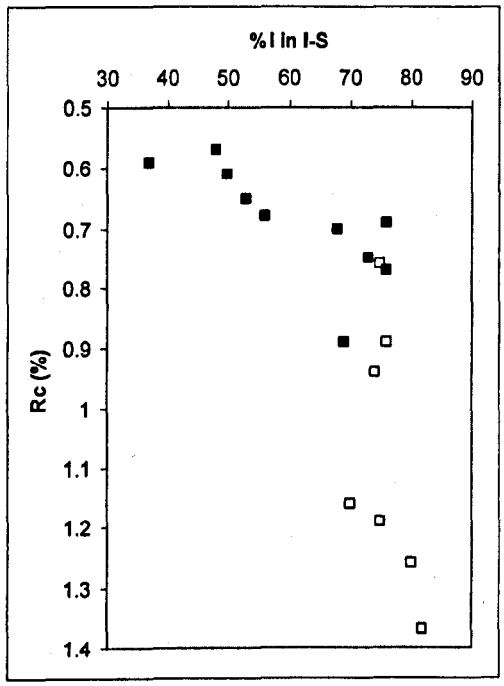

Figure 2.42. % illite in mixed layer illite-smectite as a function of theoretical vitrinite reflectance R_c. Solid squares: Chochołów PIG-1; open squares: Bukowina Tatrzańska PIG-1.

If the complete quantitative mineral composition (Table 2.3) from Środoń et al. (in press) is used to calculate water-free grain density, based on structural formulae of the component minerals and their average chemical composition, the value of 2.81-2.82 g/cm^3 is obtained. Measured grain densities always involve some water, which is very difficult to remove, hence the trend observed by Środoń et al (in press) (Figure 2.37). The 2.65 g/cm^3 value measured for the top of Chocholow PIG-1 implies 9.3% water (if dry density of 2.82 is assumed) and 2.78 g/cm^3, characteristic for the bottom of Bukowina implies 2.2% water. These values are of the same order as the measured porosities of these samples (Figure 2.38). It is possible that these amounts of water were released by the rock in the course of diagenesis may be related to the conversion of smectite into illite occurring at the same depth range.

Making the assumption that illitization of smectite is driven by the dissolution of K-feldspar and the evidence presented above does seem to suggest that it is, then the dissolution of 2.2% K-feldspar (typical value of the shallow Chocholow samples) provides ~0.32% K_2O for illitization. Alteration from 40%I to 80%I in illite-smectite clay material is a ~1.7 to ~5.0% K_2O (Środoń et al., 1986) alteration, thus the clay is gaining 3.3% K_2O. It follows that the mass of illite-smectite accounts for ~10% of the bulk rock. The mass of interlayer water in such illite-smectite is not more than a few percent, less than 1% of the whole rock. This calculation makes it clear that the water responsible for the measured grain density changes does not correspond to the interlayer water lost by illite-smectite. Consequently, there remains some pore fluid water in the system.

Additionally, the presented calculation indicates that the reactive clays (illite, smectite, kaolinite, chlorite) account only for about 15% of the rock, while 40% corresponds to non-reactive fine-grained detrital illite and mica. These volumetric relations suggest that the grains of detrital illite and mica should dominate the process of realignment of clay particles in the course of

diagenesis of the studied rocks and have important implications for the mechanically or chemically induced preferred orientation enhancement.

2.4.3: Fabric Changes:

Fabric alignment, as quantified by HRXTG, is a parameter that is strongly influenced first by depositional processes (McCave, 1970; McCave, 1971; Kranck et al, 1996a,b; O'Brien & Slatt, 1990), then, at least in the early stages of diagenesis, by sedimentary loading (Maltman, 1981) and finally the vertical component of effective stress at greater depths (Matenaar, 2002). This study has shown that Bukowina Tatrzańska PIG-1 has a much stronger fabric alignment than Chochołów PIG-1.

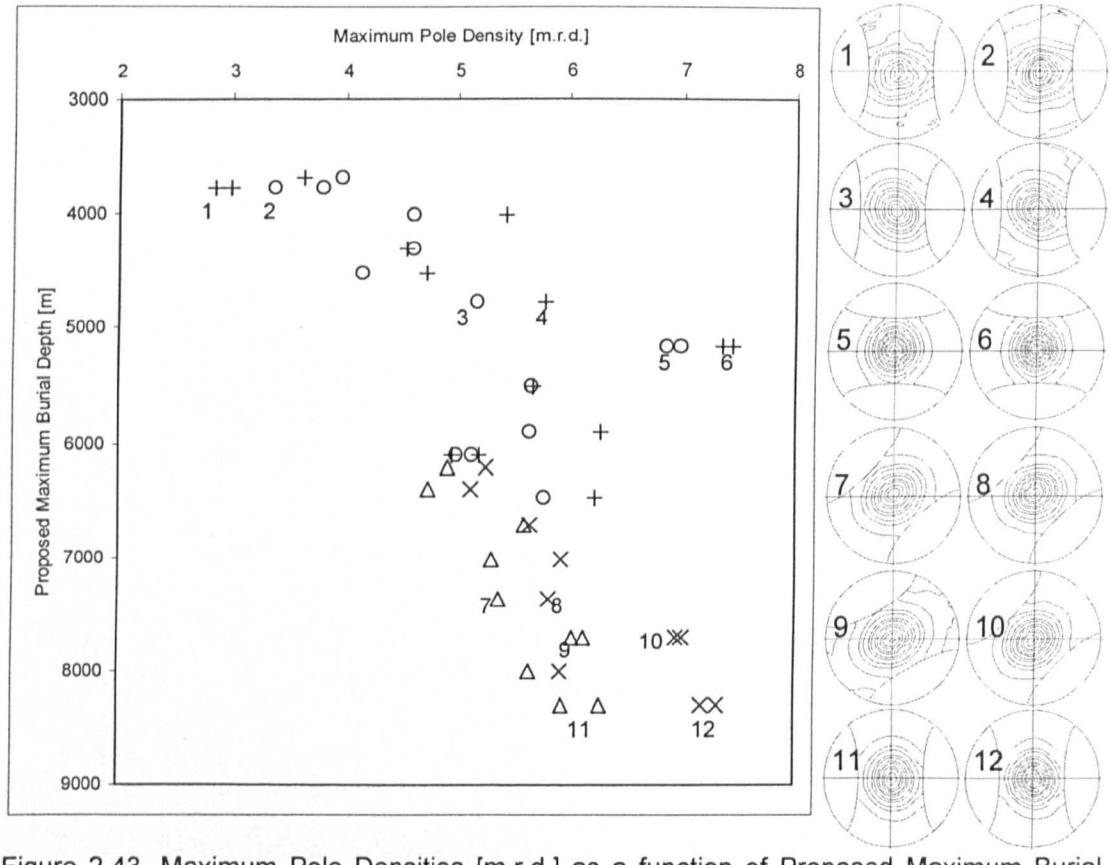

Figure 2.43. Maximum Pole Densities [m.r.d.] as a function of Proposed Maximum Burial Depth [m]. Circles: pole densities of I-S in Chochołów PIG-1 samples; triangles: pole densities of I-S in Bukowina Tatrzańska PIG-1 samples; +: pole densities of C-K in Chochołów PIG-1; x: pole densities of C-K in Bukowina Tatrzańska PIG-1. To the right, representative illite-smectite and chlorite/kaolinite pole figures are also displayed for 6 depth intervals. The numbers of these samples are shown on the main figure.

The data in Appendix 2.1 and the Figure 2.43 show that maximum pole densities range from weak (2-3 m.r.d.) to very strong (>7 m.r.d.). The samples have gone though a large part of the smectite to illite transition (Środoń et al., in press) and from random to ordered stratification. These results are qualitatively consistent with observations made using BSEM which show evidence of aligned fabrics even in areas where silt sized quartz is abundant and intuitively would be thought to disrupt and deplete alignment.

Squeezing clay or compacting sediment tends to rotate phyllosilicates to a position normal to compression and such preferred orientations were produced experimentally by Sorby (1853, 1856). There is a bulk of literature which shows that mechanical compaction (e.g. Athy, 1930; Hedberg, 1936; Sclater & Christrie, 1980) and clay mineral recrystallisation (e.g. Bowles et al., 1969; Vasseur et al., 1995; Ho et al., 1999; Aplin et al., 2005 in press) are taking place on a variety of scales. It should be held in mind that sedimentary processes (Kranck et al, 1996a,b; Bennet et al, 1991; McCave, 1970;) and bioturbation (O'Brien, 1987) strongly influence initial depositional and near surface fabrics.

Interestingly and notwithstanding the above caveat, Ho et al. (1999) presented evidence for a major reorganisation of phyllosilicate fabric as a direct result of the smectite to illite transition. In the samples described by Ho et al. (1999) as fine-grained, maximum pole densities jump dramatically from approximately 3 m.r.d. to between 6 m.r.d. and 7 m.r.d. and this abrupt change occurred coincident with the S to I transition zone, but appears influenced by grain size as lower fabric alignments are recorded in 'sandy' samples. In the samples presented here, which are also fine-grained, there is no such jump in the change in fabric intensity through the I/S transition zone (Środoń et al., in press) which occurs roughly between 5000 and 5500m (maximum burial depth). Instead, the trend in fabric intensity, after an initial rapid increase with depth, is a continuous increase and this trend is marked by both of the mineral peaks measured, illite-smectite and chlorite+kaolinite (Figure 2.43). As is suggested by the starting values for

the percentage of smectite in illite-smectite and by the ordering present in the uppermost samples, there is some portion of the curve missing and this erosion has been established. Consequently, it is not possible to know whether there was some fabric developed at the time of sedimentation or what the starting percentages of smectite were, however Bennett et al. (1991) have shown that modern muds from the Mississippi Delta possess a primary depositional texture of edge-to-face grain contacts which highlights the importance of flocculation in the deposition of phyllosilicates, similarly O'Brien and Slatt (1990) note flocculation at deposition, which lends itself to low preferred orientation development.

The X-ray diffraction data show that the smectite has largely been converted to illite and that this reaction has effectively terminated at close to 80% illite layers. Additionally, Środoń et al (in press) have described a basinal history (thermal gradient) that would allow for the reaction to run to completion in the presence of more K-feldspar or an open system, so it appears that some fabric alignment may be caused by diagenetic mineral reactions. Fabric is continuing to increase in a steady way, beyond the termination of the smectite to illite transition, this is entirely in keeping with the few previous studies of shales and metamorphic pelites that show recrystallisation continuing with increasing thermal stress (e.g. Peacor, 1992; Merriman and Peacor, 1998) into the early stages of metamorphism (the epizone). Figure 2.44 shows that although the I/S transition has effectively terminated, I/S fabric alignment continues to develop.

Therefore, it appears that the samples are, predominantly, documenting mechanically controlled chemical compaction processes and the later phase of recrystallisation in terms of the I/S trend, both of which have led to a realignment of phyllosilicates on the square millimetre scale as measurable through High Resolution X-ray Texture Goniometry and observable on the BSEM scale. By mechanically controlled, the suggestion is that the orientation of maximum stress is dictating the orientation into which new fabric is developed. It should be noted that perhaps only 15% of the clay in the system is reactive clay, meaning out of equilibrium with the environment,

but it is this phyllosilicate percentage that is facilitating change. Consequently, reactions in the mudstones of the Podhale Basin are not wholesale dissolution and then re-precipitation.

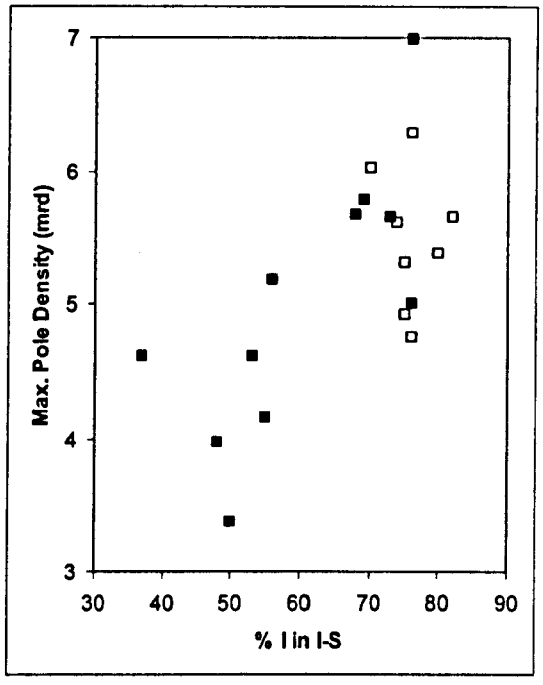

Figure 2.44. Maximum pole density as a function of % illite in mixed layer illite-smectite. Solid squares: Chochołów PIG-1; open squares: Bukowina Tatrzańska PIG-1.

Historically two mechanisms for I/S change have been proposed, the MacEwan Crystallite Model and the Fundamental Particle Model. The MacEwan Crystallite Model (MacEwan et al., 1961) is in essence a solid-state transformation model, where layers of illite and smectite are pictured as intimately interlayered, stacked either randomly or regularly into fixed sequences. The sequence acts as a coherent unit and scatters x-rays. In this model, the transition from smectite to illite is made by remodelling the chemistry and structure in place without disrupting the stack of layers. A reaction that occurs in this way involves local bond breaking, diffusion and bond formation in which reactant and product 2:1 layers are virtually identical structurally, the only differences are in composition. An indication for this type of reaction are maintenance of morphology and polytype as the proportion of illite increases, thus there is an implied memory for orientation of structure of individual layers (Dong & Peacor, 1996). The MacEwan

Crystallite Model (Figure 2.45.) assumes that the division of unit cells occurs in the middle of each octahedral sheet (Altaner and Ylagan, 1997).

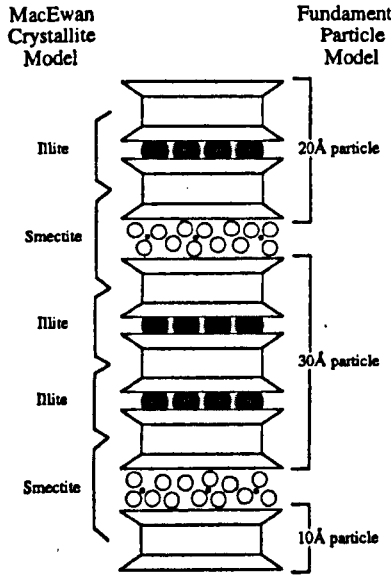

Figure 2.45. Divisions made between unit cells in the MacEwan Crystallite Model and the Fundamental Particle Model (after Altaner and Ylagan. 1997).

Where, in the MacEwan Crystallite Model the division between layers is made through the middle of each octahedral sheet, the Fundamental Particle Model divides them at the interlayer space (Figure 2.45).

The tenets of the Fundamental Particle Model (after Nadeau et al 1984) are:

1. Smectitic separates consist of primary aggregates of single 2:1 layer, 10 Å thick particles, called elementary smectite layers.
2. Regularly interstatified *R*1 I/S separates consist of primarily of 20 Å thick particles defined by two 2:1 layers called elementary illite particles.
3. Illite separates consist of 20 Å to 160 Å thick particles with a mean thickness of 70 Å.

The formation of fundamental particles by direct precipitation, rather than rearrangement of the structure of precursor minerals, is the basis for this model, a dissolution-crystallisation (DC) model. The DC model involves the complete dissolution of the precursor mineral followed by nucleation and growth of a new mineral as a separate or epitaxic grain. During dissolution, the structural memory of the precursor mineral is lost and, therefore, indications of a DC mechanism are changes in polytype and loss of morphological characteristics of the precursor (Altaner and Ylagan. 1997).

Pollastro (1985) concluded that smectitic I/S dissolves and reprecipitates as both illitic I/S and discrete illite, resulting in decreasing abundance of I/S as illitization proceeds.

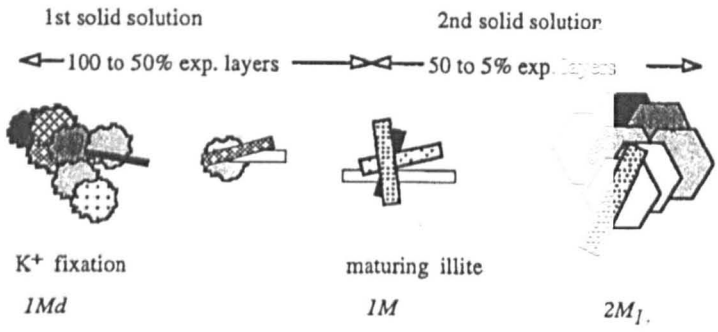

Figure 2.46. Shows the three phases envisaged for the Two-Solid-Solution Model (after Inoue et al., 1987).

Inoue et al (1987) proposed a model in which anhedral smectite crystallites (10 Å thick) become unstable, a Two-Solid-Solution Model, dissolve and recrystallise forming thin (20 Å thick) euhedral illite laths. Some of which in turn dissolve and grow into larger (> 40 Å thick) euhedral illite laths (discussed further in next section). The Two-Solid-Solution Model (Figure 2.46), after Inoue et al. (1987), is neither a continuous transformation process by solid-state reaction nor a neoformation process associated with stepwise dissolution-precipitation as laid down in the Fundamental Particle Model. The Two-Solid-Solution Model is a complex neoformation process consisting of two elementary transformation reactions and a dissolution-precipitation reaction in the intermediate stage. During the two transformation reactions (100-50% expandable and 50-0% expandable), unstable smectite dissolves and reprecipitates as elementary illite particles.

What is presented here is an idea of localised dissolution and re-precipitation around regions of grain defects or at the edge of grains that are in stress contact with other grains either quartz or other clay materials. This is due to the fact that only around 15% of the phyllosilicates in the mudstones are reactive and sites of change are attributed to localised stress areas or areas of defect.

The mechanism presented would allow the necessary rotation of grains by mechanical processes and the associated diagenetic reactions to occur penecontemporaneously. As porosity and the ease of rotation decreases this mechanically controlled chemical compaction and development of phyllosilicate preferred orientation allows for diagenetic changes in the reactive clay fraction to facilitate fabric reorientation but the driver behind the continued change is the vertical component of maximum stress. The view presented is that porosities of less than 6% and pore size distributions in the range of 3 to 20nm are too small to account for continued wholesale mechanical rotation of platy phyllosilicates.

Figure 3.38 shows the slight decrease in porosities with depth. The starting values for porosity are low, 10% and decrease to 2% with small pore radii (20 to 3nm) at the base of Bukowina Tatrzańska PIG-1, which suggest that these samples have undergone a high degree of mechanical rotation and grain packing long before the S to I transition zone was reached and therefore any reorientation as a result of mineral recrystallisation is not going to be as stark as that noted by Ho et al. (1999). Partial evidence for this has been observed in BSEM micrograph (Figure 2.23 Chochołów-06) where matrix phyllosilicates have aligned themselves in random orientations and this has been replaced by preferred orientations (Figure 2.25, Chochołów-56) as diagenesis has proceeded. BSEM has been used extensively in the past to assess fabric alignment in a qualitative way (O'Brien, 1970; O'Brien, 1987; O'Brien & Slatt, 1990). Latterly, image analysis techniques using captured BSEM images have been used to try to quantify phyllosilicate alignment (Worden et al, 2005; Charpentier et al, 2003) in matrix material. The technique is selective and does not take into consideration the effects of quartz and other non-platy phyllosilicates that have been shown to disrupt fabric alignment (Figures 2.17, 2.18 & 2.22).

It is possible that the increase in fabric intensity, beyond that which can easily be attributed to mechanical processes, is as a result of the chemically controlled dissolution-reprecipitation mechanism outlined above. However, the importance of the vertical component of stress in this scenario cannot be

overlooked in response to an acceptance of an idea of dissolution/recrystallisation. As, clearly, without this vertical component of stress the platy phyllosilicate minerals would not have aligned themselves in a preferred orientation, as flocculation does not lend itself to phyllosilicate alignment (Bennet et al., 1991; O'Brien & Slatt, 1990).

To attribute this fabric increase at such low porosities and pore size distributions, and high rates of thermal stress to purely mechanical processes is somewhat difficult to resolve, as there is simply no space within the sample matrix to accommodate the necessary rotation of phyllosilicate grains on a variety of scales. It should be noted if a purely chemical process is envisaged in the Bukowina Tatrzańska PIG-1 well one would have to imagine continuous recrystallisation of both chlorite and illite-smectite (without any change in %S), potentially hard to imagine. The hypothesis of the control of reactive clay minerals over the clay particle realignment does not resolve why kaolinite and chlorite have the same amount of preferred orientation as I/S. The diagenetic evolution of kaolinite and chlorite in this work suggests that they are passive in reorientation into a preferred fabric and that they rely on diagenetic change to facilitate the initial reorientation and then allow vertical stress to govern their reorientation. Figure 2.43 suggests that the reorientation of I/S occurs prior to chlorite + kaolinite.

X-ray diffraction data demonstrates that the percentage of quartz is increasing, some of which will undoubtedly go towards reducing the porosities on the scales observed. This quartz increase can only be related to diagenesis as there is a general upwards coarsening in the Podhale flysch (Westwalewicz-Mogilska, 1986) and as the sample suite has shown a remarkable homogeneity and consistency in chemical and physical trends. Consequently, the observed trend in the quartz percentage with depth is related to diagenesis as silica is released into the system (Hower et al,. 1976; Boles and Franks, 1979).

2.5: Conclusions:

Chochołów PIG-1 and Bukowina Tatrzańska PIG-1 are documenting the alignment of illite-smectite and chlorite+kaolinite in a high temperature (~170°C at the base of Bukowina Tatrzańska PIG-1, Środoń et al, in press), mature (~25%S) basin with a high component of vertical stress (10 to 2% porosity and 20 to 5 nm pore radii). The view of this alignment under such conditions is as a function of both mechanical compaction initially and then chemical compaction as mechanical rotation becomes less energetically viable, but is governed overall by effective stress. The control on the illitization of smectite, the main diagenetic phyllosilicate mineral reaction in the basin, in turn is the availability of potassium through K-feldspar dissolution to facilitate change.

Chapter 3: Analytical Electron Microscopy of illite-smectite in samples from the Podhale Basin

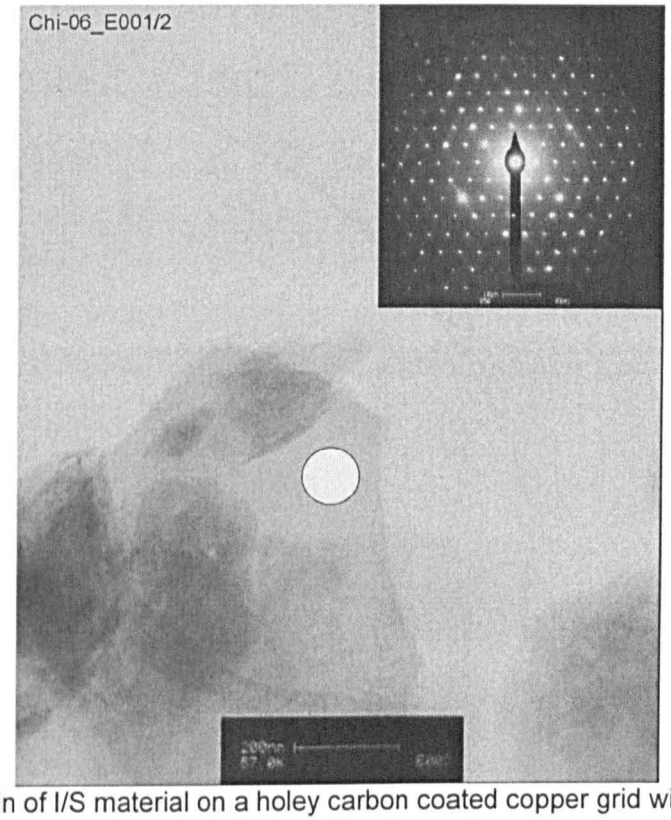

A dispersed grain of I/S material on a holey carbon coated copper grid with its associated selected area diffraction pattern.

3.0: Introduction:

The illitization of smectite has been used by many workers from Gulf Coast sediments (e.g. Burst, 1959; Powers, 1967; Perry & Hower, 1970; Hower et al., 1976; Boles & Franks, 1979) and from other basins around the world the Jurassic of South-eastern France (e.g. Artru & Gauthier, 1968), Carboniferous of Central Poland (e.g. Środoń & Eberl, 1984) and the Cainozoic and Mesozoic of the Rocky Mountains (e.g. Pollastro, 1985). These studies describe an increase in the proportion of illite in mixed-layer (interstratified) illite/smectite (I/S) with increasing temperature. Ordered I/S is described in the later stages of the reaction (e.g. Perry & Hower, 1970) in terms of Reichweite Ordering (after Jadgozinski, 1949).

The classic work by Hower et al. (1976), on the Gulf Coast sediments, envisages a solid-state illitization mechanism for this change, where the basic reaction is:

$$\text{Smectite} + Al^{3+} + K^{+} = \text{illite} + Si^{4+}.$$

This reaction implies that smectite transforms to illite by fixing K in interlayer sites with a penecontemporaneous substitution of Al for Si in the tetrahedral sheet. The source of the Al and K reactants is the local dissolution of K-feldspar and/or mica in a closed system (Hower et al., 1976). The excess Si produced in the reaction forms quartz either as cement or grain coatings. Hower et al. (1976) noted that the K_2O and Al_2O_3 content in the <0.1μm fraction increased and SiO_2 decreased, whereas it remained constant in the whole rock chemistry.

Boles and Franks (1979) prefer a dissolution-precipitation reaction, with the following reactants and products:

$3.93K^{+}$ +

$1.57KNaCa_2Mg_4Fe_4Al_{14}Si_{38}O_{100}(OH)_{20}\cdot 10H_2O$ =

$K_{5.5}Mg_2Fe_{1.5}Al_{22}Si_{35}O_{100}(OH)_{20}$

$+1.57Na^{+} + 3.14Ca^{2+} + 4.28Mg^{2+} + 4.78Fe^{2+} + 24.66Si^{4+}$

$+ 57O^{2-} + 11.40\ OH^{-} + 15.70H_2O$

The reaction describes the supply of Al to be from the smectite itself and not from an external source; therefore smectite is consumed in this reaction rather than conserved. The reaction of Boles and Franks (1979) describes a dissolution-precipitation reaction whereas Hower et al (1976) describes a solid-state transformation.

Largely these results have been gained through XRD analysis on separated clay fractions and therefore related average changes to a polymineralic mix, even within interstratified I/S. Analytical Transmission Electron Microscopy (ATEM) using an ion beam thinning technique has demonstrated differences in TEM and XRD data (Ahn & Peacor, 1986a,b), where at the TEM scale, packets of crystallites maybe observed as end-member phases, XRD views the same sample as having variable amounts of smectite in the mixed-layer phase illite-smectite. This difference reflects the difference in resolution between the two techniques; XRD on the 'bulk' scale, ATEM on crystallite packets. This therefore has lead to differences in the mechanisms for the smectite to illite conversion being postulated(e.g. MacEwan et al., 1961; Nadeau et al., 1984a,b; Ahn & Peacor, 1986a; Inoue et al, 1987; Altaner & Ylagan, 1997). ATEM has been shown to be able to clearly distinguish end-member illite from end-member smectite chemistries both in terms of Energy Dispersive X-ray Spectroscopy (EDS) (e.g. Kim et al., 2004; Severin, 2004) as well as Selected Area Diffraction Patterns (SADP) (e.g. Bell, 1986; Ahn & Peacor, 1986; Środoń et al., 1992; Dong & Peacor, 1996; Kim et al., 2004).

Ion beam thinning is not the only technique available for ATEM. Grain dispersal on a holey carbon substrate has been successfully used to distringuish between illite and smectite (e.g. Klimentidis & Mackinnon, 1986; Hover et al., 1999). What this latter technique cannot do is use lattice fringe imaging to quantify the %I in I/S (e.g. Ahn & Peacor, 1986a). Both ion beam thinning and dispersion techniques are subject to the same problems of light elements (Na, K) being mobile under the electron beam (van der Pluijm et al., 1988).

This study applies an Analytical Transmission Electron Microscopy (ATEM) technique on a dispersed clay size fraction with a view to being able to construct structural formulae for individual analyses for each sample measured backed up by a selected area diffraction pattern (SADP), which allows semi-independent confirmation of the phase measured and the nature of the crystal stacking.

The main aim of this chapter is to assess the detailed chemistries of I/S material from 5 samples in the Podhale Basin using Analytical Transmission Electron Microscopy (ATEM). The first part of the study deals with the applicability of BSEM to the determination of phyllosilicate chemistries. The primary aim, which may only be exploited by ATEM, is to explore why there is no change in the percentage of illite in illite/smectite, as quantified by XRD, over ~2000m in the deepest (6000m to 8300m maximum burial depth) and hottest (~125°C to 174°C, according to Środoń et al, in press) parts of the well profile discussed in Chapter 2 and to see if there are any significant structural formulae differences in I/S even though by XRD the expandability of I/S is identical. Additionally, the HRXTG made in Chapter 2 suggested continued fabric formation beyond I/S termination. Various diagenetic studies have shown phyllosilicate preferred orientation to be partly linked to I/S change (e.g. Ho et al., 1999; Matenaar, 2002; Worden et al., 2005).

3.1: Transmission Electron Microscopy:

3.1.1: Samples and Methods:

Five samples were selected for analysis by Transmission Electron Microscopy. Chochołów-06, Chochołów-28, Chochołów-60, Bukowina Tatrzańska-06 and Bukowina Tatrzańska-41 were taken to represent the whole of the depth range for boreholes Chochołów PIG-1 and Bukowina Tatrzańska PIG-1 from the Podhale Basin. Bukowina Tatrzańska-06 and Bukowina Tatrzańska-41 were selected because in a well with little variation in the percentage of smectite in I/S these two samples had exactly the same percentage of illite in I/S (76%) but are separated by nearly 2000m depth difference. Chochołów-06, Chochołów-28 and Chochołów-60 represent the full conversion of smectite to illite seen in the Podhale Basin. In addition an illite and smectite standard were used in initial BSEM EDS analysis and this samė illite standard was used in the TEM analysis.

Table 3.1 states the key physical and mineralogical differences between the 5 samples chosen for ATEM analysis. They have a large overall change in preferred orientation development in the entire basin but little change beyond ~6000m, which coincides with the termination of I/S change and a relatively constant porosity with depth increase.

Table 3.1 Present day depth [m], maximum burial depth [m], %I in I/S, Maximum Pole density [m.r.d.] I/S, Maximum Pole Density [m.r.d.] C/K and porosity percent as measured by mercury intrusion porosimetry for the 5 samples selected for TEM analysis.

	Depth [m]	Maximum Burial Depth [m]	%I in I/S	Maximum Intensity [mrd] I/S	Maximum Intensity [mrd] C/K	Porosity [%]
Chochołów-06	280	3780	50	3.38/3.30	2.84/2.98	10
Chochołów-28	1283	4783	56	5.18	5.78	5
Chochołów-60	2511	6011	76	5.00/5.14	4.96/5.20	ND
Bukowina Tatrzańska-06	293	6394	76	4.75	5.12	6
Bukowina Tatrzańska-41	2200	8301	76	5.94/6.29	7.18/7.32	5

3.1.2: Chemical Analysis by SEM-EDS:

Backscattered Scanning Electron Microscopy (BSEM) was initially performed to test the general method devised for calculating mineral formulae from compositional data generated using the SEM's Energy Dispersive X-ray System (EDS). This step was included prior to TEM analysis as more data could be generated in a shorter time than through TEM. Although the resolutions and the interaction volumes of the two techniques differ, standard materials should not be overly affected by the different interaction volumes and will therefore allow an appreciation of the method before time consuming and difficult ATEM is undertaken.

EDS analysis was performed on a CamScan series 3 SEM with a tungsten filament and operating at 20 kV in backscattered mode, with a working distance of 10mm. The SEM was fitted with an Oxford Instruments ISIS UTW (ultra thin window) EDS (energy dispersive X-ray) detector.

Montmorillonite-smectite (hereafter referred to only as smectite) from Ward's Natural Science (item:46V0435) (http://www.wardsci.com) and illite shale (hereafter referred to as illite, item:46V0315) were used as two internal standards for initial BSEM observation and later TEM observation. The standard materials used were not pure minerals, rather they were commercially available rock materials exceptionally rich in either illite or smectite.

Samples Chochołów-06 and Bukowina Tatrzańska-41 were selected for initial EDS analysis in BSEM mode representing the %I extremes of the sample set's mixed layer phase I/S. The sample preparation technique involved embedding the samples in a resin block (Epo-Thin®, a low viscosity resin from Buehler) and then polishing the samples to produce a flat surface for the electron beam. Samples Chochołów-06 and Bukowina Tatrzańska-41 were simply embedded with the 'up-face' perpendicular to bedding/maximum fabric intensity. This way the samples were measured on an adjacent surface to that used for High Resolution X-ray Texture

Goniometry. The BSEM images presented in Chapter 2 are directly applicable to the samples analysed by TEM here.

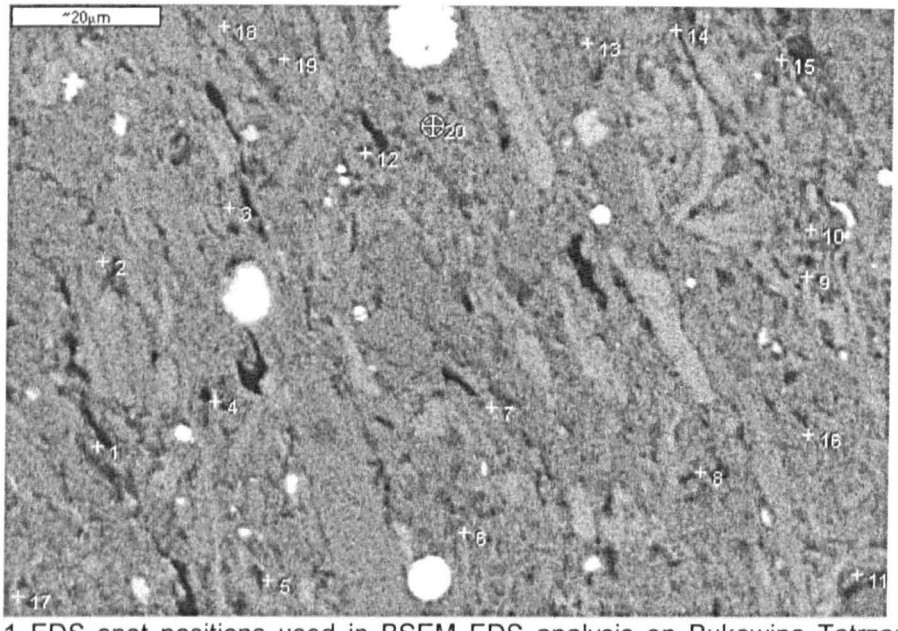

Figure 3.1 EDS spot positions used in BSEM EDS analysis on Bukowina Tatrzańska-41. Magnification is 500X. Spot positions are on matrix material not large phyllosilicates.

The illite and smectite standards were prepared slightly differently, as they were essentially ground material that were set in resin and then polished to the surface for interaction with the electron beam. For both the samples and the standards an area under the beam was selected for EDS analysis (Figure 3.1) and 20 spot positions were selected manually and auto-saved for each selected area on the sample surface.

The spot selection criterion was that the area measured should be the fine-grained, phyllosilicate matrix material; all the large, detrital, phyllosilicate material and non-phyllosilicate material was ignored. The number of measurements taken varied from between 160 to 260 spot positions from 8 to 13 different areas on the sample block (2cm by 2cm block), for each sample.

Figure 3.2 shows a typical EDS trace for the illite standard, with a strong K peak and the presence of smaller Fe peaks. The Si and Al peaks are in

proportion to those published by Severin (2004) and Kim et al (2004) for illite. The raw EDS data were converted into structural formulae units and elemental concentrations expressed as wt% oxides using the conversion methods detailed by Weaver (1989) and Moore & Reynolds (1997).

Spreadsheets for each sample were produced in which the intent was to interpret chemical composition in terms of atomic ratios in the octahedral, tetrahedral and interlayer sheet. Two basic assumptions are made; (1) the cation charge is equal to the anion charge; (2) the anion charge is known from the structural studies of coarse grained phyllosilicates (Weaver, 1989) and is equal to 22 anions ($O_{10}[OH]_2$). An additional assumption is that the tetrahedral cations add up to 4.0. The calculation method first involves the atomic percentages being converted to atomic proportions. Next a K factor is calculated from cation valancy by which the atomic proportions are multiplied by to produce the structural formulae (See Weaver, 1989; Moore & Reynolds, 1997). Tetrahedral sheet compositions are determined first with all available Si attributed to this sheet, plus whatever additional Al is required to make the tetrahedral sheet contain 4.0 cations. The rest of the Al is attributed to the octahedral sheet along with all the Fe, Mg and Ti. The interlayer contains K^+, Ca^{2+} and Na^+ (although Na^+ was not measured in this study due to mobility under the electron beam).

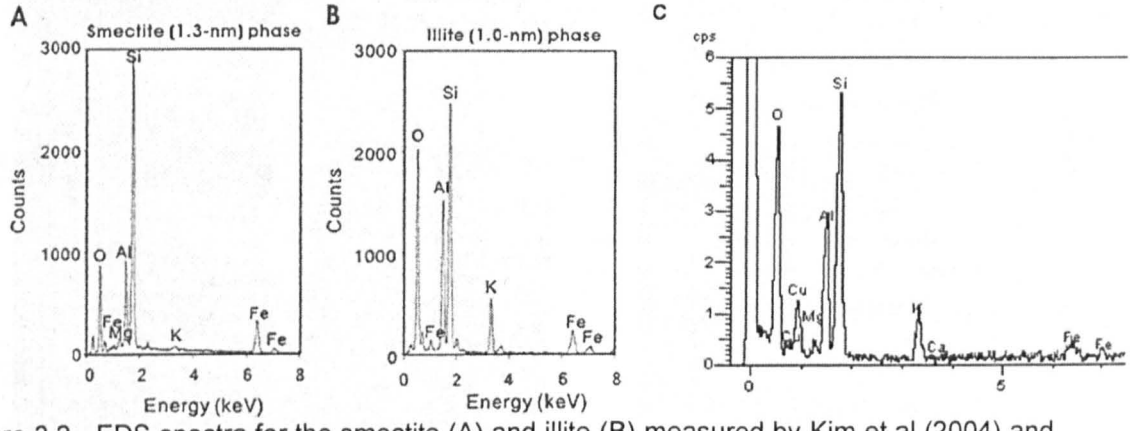

Figure 3.2. EDS spectra for the smectite (A) and illite (B) measured by Kim et al (2004) and the illite standard (C) measured from BSEM EDS analysis in this study.

3.1.3: TEM technical settings:

Transmission Electron Microscopy (TEM) has been used in a variety of ways to assess mudstone and shale chemistries (e.g. Bell, 1986; Klimentidis & Mackinnon, 1986; Jiang et al., 1994), diagenesis (e.g. Ahn & Peacor, 1986a & 1986b; Inoue et al., 1987; Hover et al., 1999; Masuda et al., 2001; Nadeau et al., 2002; Kim et al., 2004), eventual metamorphism (e.g. Merriman & Peacor, 1998; Merriman, 2002) and mineral structures (e.g. Nadeau, 1998; Peacor, 1998). TEM in this study was primarily employed to describe the detailed chemistry of individual minerals using Analytical Transmission Electron Microscopy (ATEM) as well as obtaining images and selected area diffraction patterns (SADP) in order to relate the chemical analysis to known minerals. Samples were examined using a Philips/FEI CM200 electron microscope equipped with a Field Emission Gun (FEG), and a Gatan Imaging Filter (GIF). The extinction voltage was set at 3.21 kV, giving a typical energy resolution of 0.8eV. All analyses were undertaken at the University of Leeds in the Material Science Department.

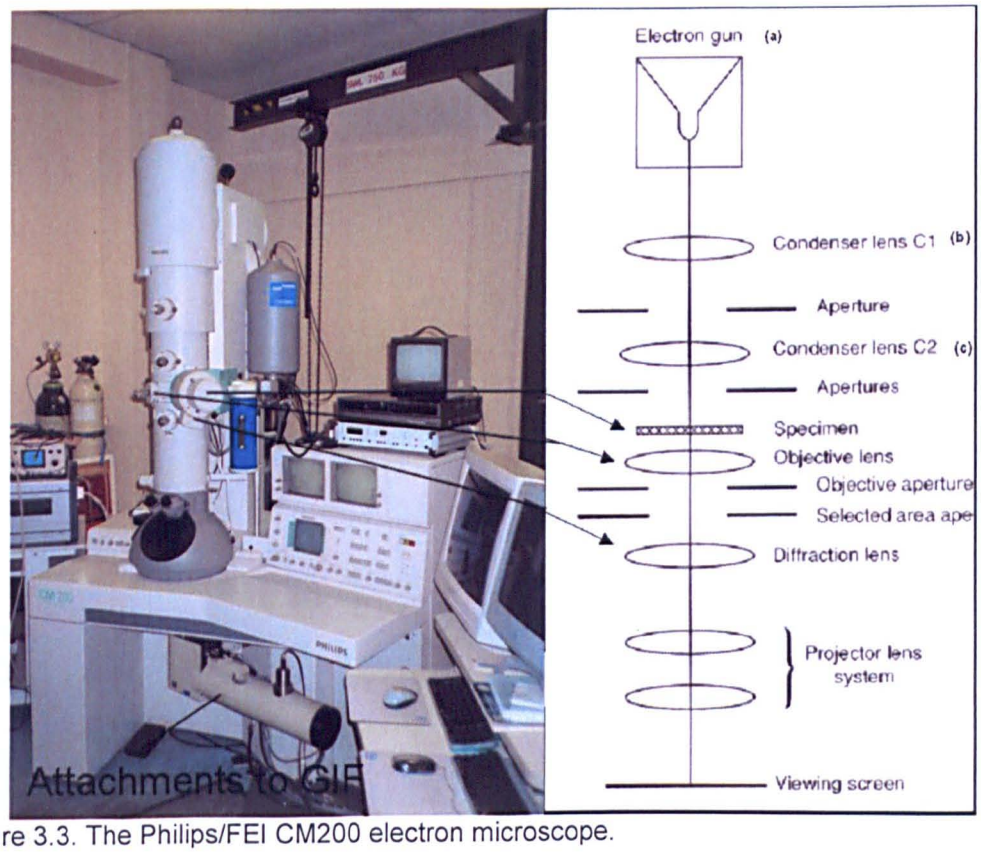

Figure 3.3. The Philips/FEI CM200 electron microscope.

The selected samples were initially separated using a freeze-thaw method which disaggregates the samples without destroying the grain size (Yang and Aplin, 1997). The less than 2μm fraction of the sample was then separated by centrifugation applying Stokes' Law (4 minutes 22 seconds at 800rpm). Selected samples were prepared specifically for the TEM by grinding the less than 2μm samples with ethanol in a pestle and mortar. 0.5g of sample was used in an excess of ethanol as a dilute solution of sample was required. A small droplet of sample (~10μl) was then placed on a carbon coated 200-mesh copper grid and allowed to evaporate to dryness, with well dispersed grains of importance. This dispersion method was used in preference to other sample preparation techniques, such as ion-milling and diamond microtoming (Merriman & Peacor, 1998), as it is significantly faster to prepare the sample and because no layer sequence information was sought, in the form of lattice fringe imaging.

3.1.4: Analytical Transmission Electron Microscopy (ATEM):

Energy Dispersive Spectroscopic (EDS) techniques allow quantitative chemical data to be obtained from discrete mineral phases (e.g. Kim et al., 2004). Typically this technique has a resolution of 75Å. Analyses were carried out by focusing the electron beam into a 0.2μm probe and moving it onto discrete isolated grains. Magnification was at 50,000 times and data were acquired at between 1000 and 3000 counts per second with a live time of 50 seconds. EDS data were gathered for each selected sample spot and then manipulated using Oxford Instruments ISIS EDS. The exposure of the sample to the beam was kept to a minimum, as was beam diameter, to avoid electron beam damage to the sample and to negate the fact that some elements (Na, K) are mobile under the beam (van der Pluijm et al, 1988). A significant advantage of ATEM relative to conventional electron microprobe analysis is that ATEM data are obtained over extremely thin areas, and hence no matrix correction factor (ZAF) is required (Merriman & Peacor, 1998), resulting from the fact that the X-ray intensity measured is directly proportional to the concentration of the element measured. A significant

disadvantage is that the thickness of the sample area measured is not known, and hence the exact volume that is being excited, however, should sample thickness become an issue special mounts of Pt shadowed separates may be utilised to determine sample thickness (e.g. Nadeau, 1985). This was not an issue in this study as ample grains were available for analysis so grains that appeared too thick were ignored. The selection of thick or thin grains is slightly subjective in that thick grains appear darker than thin grains on the TEM stage.

The elemental composition of individual phases can be calculated by correcting the characteristic element X-ray intensities by using the 'K-value' procedure described by Cliff and Lorimer (1975). A fundamental requirement of this correction procedure requires specimens to be sufficiently thin so as X-ray fluorescence and X-ray absorption are negligible, and specimens are said to adhere to the thin-film criterion (Cliff & Lorimer, 1975). If this criterion is satisfied the characteristic X-ray intensity ratio for any two elements is directly proportional to their concentration (Cliff & Lorimer, 1975), as described in the equation (a):

$$I_1/I_2=K*C_1/C_2 \qquad (a)$$

where I_1 and I_2 are the observed X-ray intensities, C_1 and C_2 are the weight fractions of the two elements and K is the proportionality constant or K-value, determined experimentally by analysis of standards of known composition (Cliff & Lorimer, 1975). For the analysis of silicates, K-values are always determined relative to silica, as shown in equation (b) below:

$$K_{ASi}=(C_{Astd}*I_{Sistd})/(C_{Sisd}*I_{Sistd}) \qquad (b)$$

Where, K_{ASi} is the K-value of element A relative to Si, C_{Astd} and C_{Sistd} are the weight fractions of A and Si respectively within the standard, I_{Sistd} and I_{Sistd} are the observed characteristic X-ray intensities of Si and element A produced during analysis of a standard (Cliff & Lorimer, 1975).

Rock (2003) had previously determined K-values for biotite and paragonite standards using the Philips/FEI CM200 used in this study, these K-values were evoked in this study, as ATEM advantageously only requires these K-values to be determined once. Once determined, no additional standard data need be obtained at the times of analysis of an unknown (Merriman & Peacor, 1998) as K-values do not change.

Table 3.2. Biotite and paragonite standards used for ATEM.

Standard	Element	K-values
Biotite	Mg	2.35
	Al	1.25
	Si	1.00
	K	1.09
	Ti	1.18
	Fe	1.33
Paragonite	Na	5.83
	Al	1.21

The chemical composition of an unknown grain may then be determined by placing the measured characteristic X-ray intensity of each element into equation (c):

$$C_A/C_{Si}=K_{ASi}*I_A/I_{Si} \quad (c)$$

Where C_A and C_{Si} are the weight fractions of A and Si respectively within the unknown silicate and I_A and I_{Si} are the observed X-ray intensities of Si and A produced during the analysis of the sample.

3.1.5: Diffraction Pattern Imaging:

A selected area diffraction pattern (SADP) was taken prior to EDS analysis in order to verify the mineral phase being analysed. The method of analysis employed was to produce a SADP of a single thin phyllosilicate grain, capture the image of the grain the SADP was taken from and then to collect the EDS data. An image was only collected if a clear single phase was present. Figure 3.4 shows the difference between a polycrystalline phyllosilicate of either rotated layers (turbostratic layering) of the same phase or the interlayering of different phases. This contrasts with single crystal

patterns that show clearly defined single points and it is these patterns that have been collected and analysed.

Electrons (at a given kV) have a specific wavelength so that the planes of atoms in a crystal will diffract them in a specific way. Powder diffraction files (PDF) (International Centre for Diffraction Data) allow the relationship between the various points in a diffraction pattern to be analysed and identified.

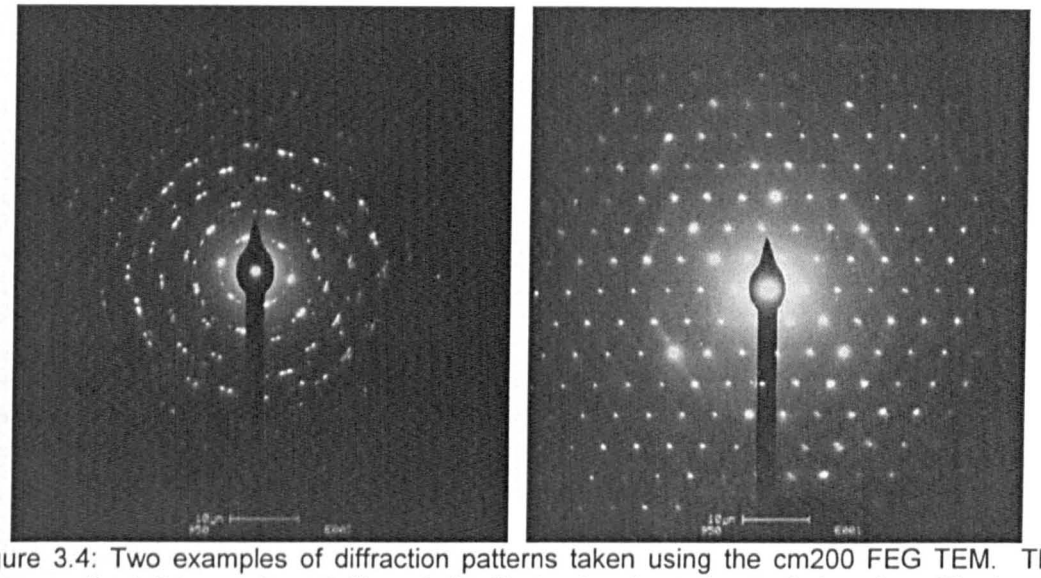

Figure 3.4: Two examples of diffraction patterns taken using the cm200 FEG TEM. The image on the left is a polycrystalline phyllosilicate showing turbostratic layering. The image on the right is a single crystal with a more visibly coherent relationship between layers as evidenced by the hexanets. The large irregularly spaced diffraction bright spots allude to defects in the crystal lattice.

Due to the platy nature of phyllosilicates, the dispersion method utilised in this study will present (001) crystal layers normal to the electron beam. The dispersion method assumes that the c* axis of a phyllosilicate is parallel to the electron beam and as a result will only exhibit (*hk0*) diffraction data also the method yields no information on the nature of layer sequences from lattice fringe imaging. Lattice fringe imaging is where in mixed layer I/S the interlayering between wavy smectite packets of crystallites and more coherent and larger packets of illite can be seen (e.g. Ahn & Peacor, 1986a), and which may show a variety of interfaces between the two (Bell, 1986). Additonally, using the %I in I/S can be measured by counting layer sequences. Turbostratic stacking is a type of crystalline structure where the

basal planes have rotated sideways relative to each other causing the spacing between the planes to be slightly greater than the ideal for a particular mineral. This causes the collective pattern of all the layers to be circles which are each equivalent to a single reflection from a single crystal pattern (Moore & Reynolds, 1997; Nadeau et al., 2002).

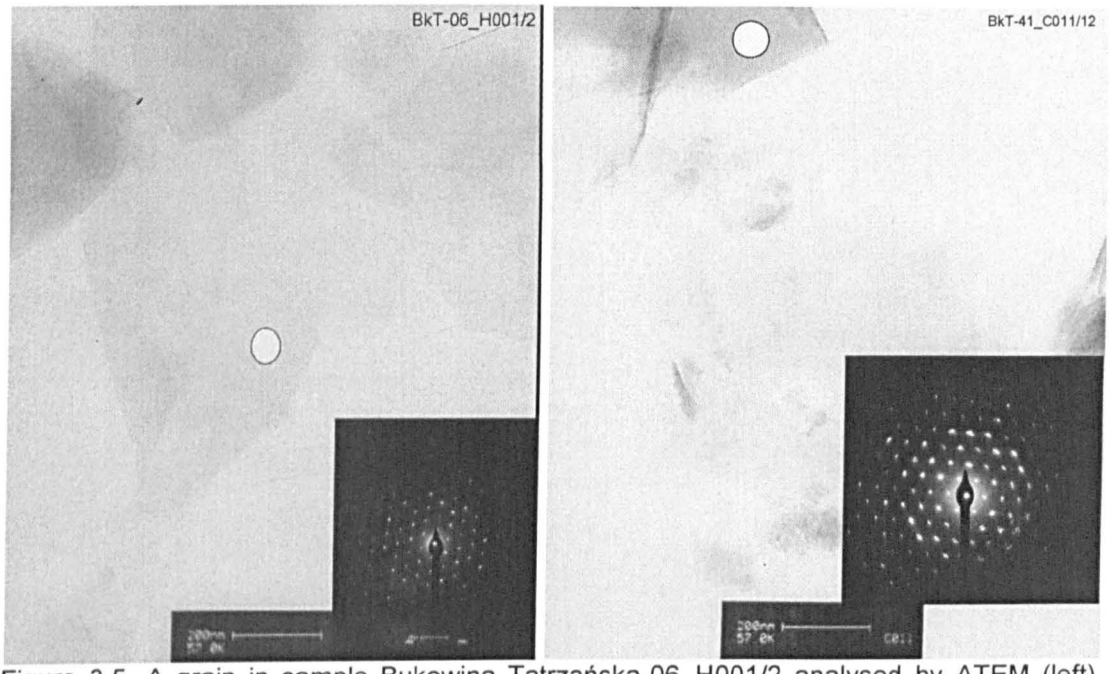

Figure 3.5. A grain in sample Bukowina Tatrzańska-06_H001/2 analysed by ATEM (left). The grain is thin and consequently produces single crystal SADP, the circle shows the area of the electron beam position. A grain in sample Bukowina Tatrzańska-41_C011/12 analysed by ATEM (right), the grain is thicker and consequently produces some turbostratic SADP.

Figures 3.5 and 3.6 show the spot on the grain analysed and the associated SADP collected from samples Bukowina Tatrzańska-06, Bukowina Tatrzańska-41 and Chochołów-06. Bukowina Tatrzańska-06 shows a thin grain and consequently produces a single crystal SADP that appears to be well ordered and free of any defects. Chochołów-06 on the other hand is slightly thicker and the SADP reveals a single crystal but with some slight crystal defects evidenced by the increased brightness of some of the diffraction spots.

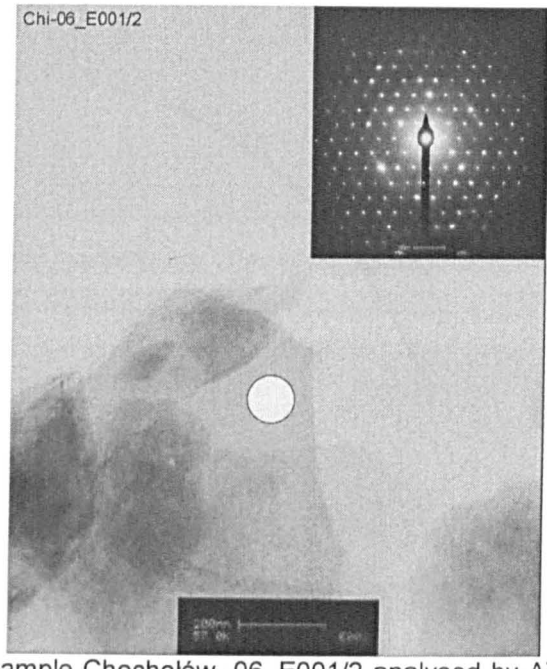

Figure 3.6. A grain in sample Chochołów -06_E001/2 analysed by ATEM. The grain is thin and consequently produces single crystal SADP, the circle shows the area of the electron beam position.

3.1.6: Indexing Selected Area Diffraction Patterns:

Indexing is the measurement of SADPs relative to characterised examples. The indexing has been undertaken to marry the chemical data gained by ATEM with diffraction data and consequently a better understanding of the phase measured will be gained. It is essentially the calculation of the d-spacings that have produced the 'spots' on the diffraction pattern and then assigning these spots to the correct diffraction peaks on the PDF associated with the characterised example by way of Miller Indices.

What follows is a worked example of a method used to index a SADP of the illite standard. The SADP pattern in question is R007 and the indexing of this pattern is presented as a series of steps. The method follows that outlined in Goodhew and Humphreys (1988) and the data for the *h,k,l* reflections (d-spacings [Å]) comes from the powder diffraction files (PDF) (International Centre for Diffraction Data, 1996).

Step 1 was to define *r* values (distances between spots) for 2,3 or 4 spots close to the centre of the pattern (Figure 3.7, line1). Because the measurement of *r* is of critical importance to the indexing process it is done directly from the negative rather than from a digital copy. As the *r* values are on the millimetre scale an average of several points was taken.

Step 2 was to tabulate (Table 3.3) these *r* values and to calculate the d-spacing [Å] from equation [D]

$$\lambda l = rd \qquad [D]$$

where: λl = 24.1Å, the camera constant in the machine used in the this study (Goodhew and Humphreys, 1988).

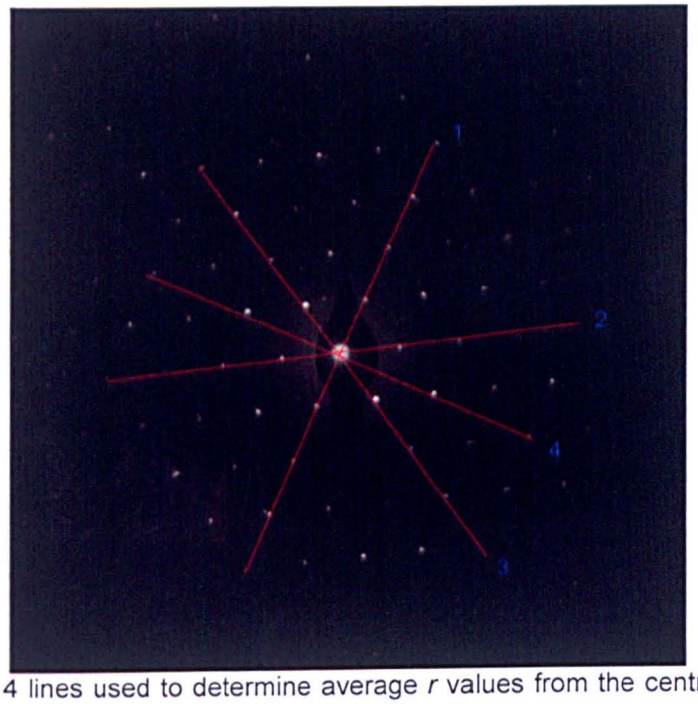

Figure 3.7. The 4 lines used to determine average *r* values from the centre of the pattern, for the illite standard SADP R007.

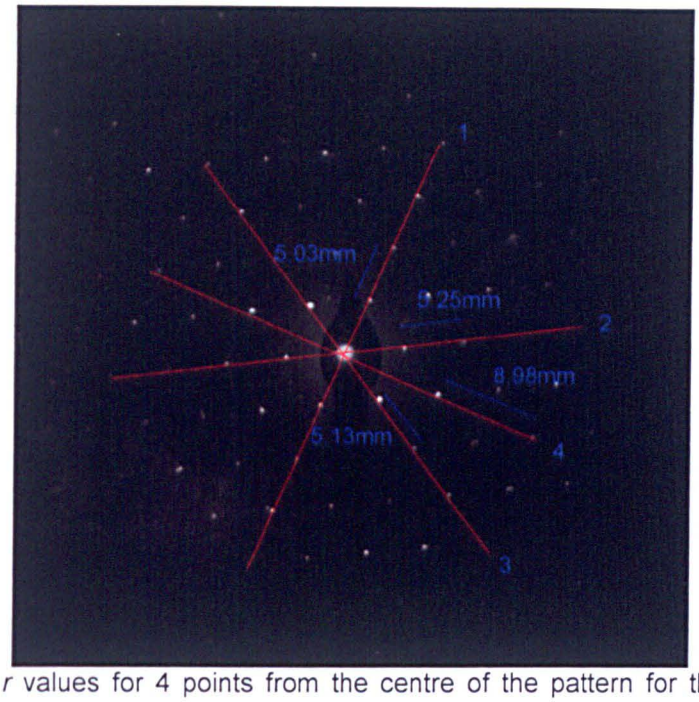

Figure 3.8. The *r* values for 4 points from the centre of the pattern for the illite standard R007.

Table 3.3. d-spacings for R007 from *r* values (Step 2).

Point Line	*r* (mm)	d-spacing [Å] at 24.1Å camera constant
1	5.03	4.79
2	5.25	4.59
3	5.13	4.69

Step 3 is to refer to PDF tables and look for, in this case, three appropriate d-spacings with a 'long-short-long sequence' in the ~4.5Å d-spacing region. The 'long-short-long sequence' refers to the d-spacing calculated from equation [D] and a comparison with the d-spacings quoted in the PDF. PDF Reference Code 00-040-0020, a Potassium Magnesium Aluminium Silicate Hydroxide with a chemical formula similar to that of the illite standard was the only PDF looked at that revealed the correct criteria for indexing this SADP. Principally the other PDFs did not have enough diffraction spots in the ~4.5Å d-spacing region to create a match with the measured results. Therefore they were inappropriate. The other possible PDFs were:

00-021-0993, a Potassium Magnesium Aluminium Silicate Hydroxide, (Magnesium 1M Muscovite Mica)

00-013-0135, a Calcium Magnesium Aluminium Silicate Hydroxide Hydrate, (Montmorillonite-15A)

00-013-0305, a Calcium Magnesium Iron Aluminium Silicate Hydroxide Hydrate, (Ferroan Saponite-15A)

00-040-0021, a Potassium Magnesium Aluminium Silicate Hydroxide.

Table 3.4. Peak number as defined in PDF 00-040-0020 used to index the illite standard R007, *h,k,l* reflection (miller indices) and d-spacing [Å] are shown.

Peak number	*h,k,l* reflection (miller indices)	d-spacing [Å]
3	0,2,0	4.51277
4	1,1,0	4.48902
5	-1,1,1	4.46776
6	0,2,1	4.40193
7	1,1,1	4.30267
8	0,2,2	4.11154

The three d-spacings [Å] in Tables 3.3 and 3.4 do not match and could be the result of; a) inaccurate measurement of the '*r*' value or b) the use of an incorrect camera constant, which in this work was not been measured and can vary each time a new sample is introduced to the electron beam (Goodhew & Humphreys, 1988). Consequently, if the camera constant is varied Table 3.4 suggests that there are ample *h,k,l* reflections to find the necessary three appropriate d-spacings with a 'long-short-long sequence'. This is critical as the method requires the definition of three *h,k,l* reflections (a d-spacing value) that fit with the specified mineral.

Step 4 is to alter the camera constant to achieve d-spacings (Table 3.5) in agreement with PDF 00-040-0020. This is done, in this case, by fixing 4.51[Å] (*h,k,l* reflection 0,2,0) as the base value and re-calculating the camera constant based on equation [1].

Table 3.5. d-spacing [Å] resulting from re-calculation of the camera constant and associated *h,k,l* reflections in PDF 00-040-0020.

Point line	*r* (mm)	d-spacing at 24.1[Å] camera constant	d-spacing at re-calculated camera constant 22.69[Å]	*h,k,l* reflections
1	5.03	4.79	4.51	0,2,0
2	5.25	4.59	4.32	1,1,1
3	5.13	4.69	4.42	0,2,1

The re-calculation of the camera constant has resulted in d-spacings that remain consistent with PDF 00-040-0020. The next stage of this step in the SADP indexing is to add the Miller Indices of the *h,k,l* reflections. The *h,k,l* reflections do not match those measured in R007 as the vectors do not allow

addition as 1,1,1 cannot be achieved by the vector addition of 0,2,1 and 0,2,0.

Step 5 is to alter the camera constant again and fix it to 4.49[Å] (*h,k,l* reflection 1,1,0) (Table 3.6)

Table 3.6. d-spacing [Å] resulting from the second re-calculation of the camera constant and associated *h,k,l* reflections in PDF 00-040-0020.

Point line	*r* (mm)	d-spacing at 24.1[Å] camera constant	d-spacing at re-calculated camera constant 22.59[Å]	*h,k,l* reflections
1	5.03	4.79	4.49	1,1,0
2	5.25	4.59	4.30	1,1,1
3	5.13	4.69	4.40	0,2,1

The second re-calculation of the camera constant has resulted in d-spacings consistent with PDF 00-040-0020. The *h,k,l* reflections now match those measured in R007. There is freedom to determine specific indices as so far only the general indices (Goodhew & Humphreys, 1988) have been determined. So, if this freedom is invoked and 1,1,0 becomes 1,-1,0, then the vector addition of 1,-1,0 and 0,2,1 will result in 1,1,1 as $(1,-1,0)+(0,2,1)=(1,1,1)$ (Figure 3.9).

Step 6 is to again change the camera constant, to check that no more than one solution within a camera constant range of ~21Å and 26Å (lower and upper limits of acceptable camera constants, Brown, 2005 Pers. Comms.) is possible. This time the camera constant is fixed to 4.47[Å] (*h,k,l* reflection -1,1,1) the results are given in Table 3.7.

Table 3.7. d-spacing [Å] resulting from the second re-calculation of the camera constant and associated *h,k,l* reflections in PDF 00-040-0020.

Point line	*r* (mm)	d-spacing at 24.1[Å] camera constant	d-spacing at re-calculated camera constant 22.49[Å]	*h,k,l* reflections
1	5.03	4.79	4.47	-1,1,1
2	5.25	4.59	4.30	1,1,1
3	5.13	4.69	4.40	0,2,1

Once again applying vector additions this result does not explain the diffraction pattern for R007 as: $(-1,1,1)+(0,2,1)\neq 1,1,1$

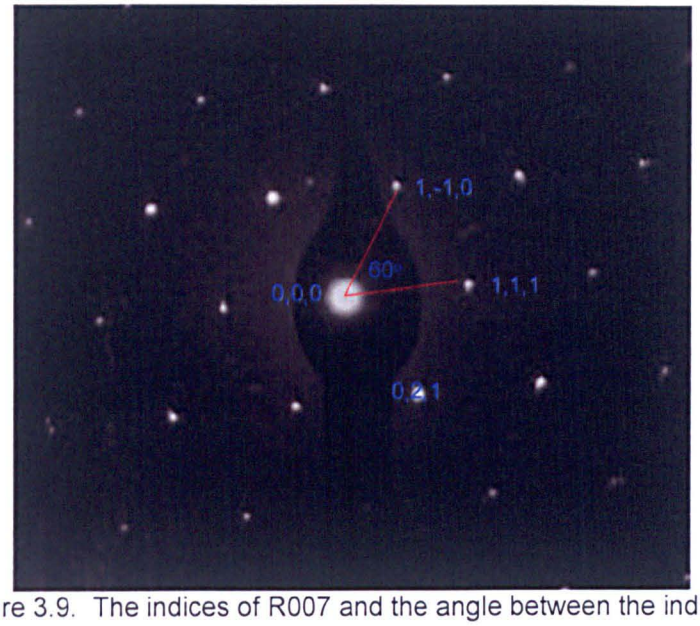

Figure 3.9. The indices of R007 and the angle between the indices.

Step 7 is to use the other data in the PDF table to test whether the angle between the diffraction points is valid. This is done by applying equation [E] (Andrews et al., 1971):

Equation [E]:

$$\text{Cos}\theta = (1/a^2.h1.h2)+(1/b^2.k_1.k_2.\sin^2\beta)+(1/c^2.l_1.l_2)-(1/ac.(l_1h_2+l_2h_1).\cos\beta)/$$
$$\sqrt{}\,[((1/a^2.h_1^2)+(1/b^2.k_1^2.\sin^2\beta)+(1/c^2.l_1^2)-$$
$$(2h_1l_1/ac.\cos\beta))x((1/a^2.h_2^2)+(1/b^2.k_2^2.\sin^2\beta)+(1/c^2.l_2^2)-(2h_2l_2/ac.\cos\beta))]$$

Equation [E] calculates the angle θ between $(h_1k_1l_1)$ and $(h_2k_2l_2)$ for monoclinic crystal systems, where; $a \neq b \neq c$ and $a = \gamma = 90 \neq \beta$ and β=95.7300. This data are from the crystallographic parameters listed on the PDF for 00-040-0020. $(h_1k_1l_1)$ and $(h_2k_2l_2)$ are equal to (1,-1,0) and (1,1,1) respectively.

When the equation of Andrews et al. (1971) is applied to the *h,k,l* reflections as shown in Figure 3.9 the resultant angle of 59.86014° for θ is achieved which satisfies the crystallographic requirement as the crystal system is monoclinic therefore the angle between spots must be ~60°.

3.1.7: Indexing Uses and Uncertainties:

The basic difficulty in indexing samples correctly is a); measuring the distance between points on the SADP (*r* values) correctly and b); having to change the camera constant to fit the d-spacing taken from a PDF. Indexing in this study cannot stand alone as a piece of work. It was undertaking in order to confirm or not confirm the phase analysed by EDS. That is to say the structural formulae calculated from the atomic ratios are the primary identification tool, with indexing confirming the structural formula to a known mineral. As a result of the above uncertainties not every sample was indexed directly. The approach was to match the indexed sample to the other samples by overlaying the negatives. Such an approach yielded exact matches, a close match and no match (see later sections).

There is no difficulty in separating chlorite and mixed layer I/S as it is easy to differentiate between the two in the SADP because the *r*-values in chlorite are much larger than in I/S. Additionally, the greater concentrations of Fe in chlorites create very different initial EDS spectra. Consequently, a SADP and the EDS spectra may screen out any chlorites from the analyses. What indexing does not directly allow is an appreciation of exact mineralogy (i.e. the %S in I/S).

3.2: Results:

3.2.1: SEM EDS on illite and smectite standards:

The rationale for gaining chemical information by BSEM was to test the EDS software, which is the same for both the CamScan series 3 (SEM) and the Phillips/FEI CM200 Electron Microscope (TEM). Additionally, the spreadsheets designed to calculate structural formulae from atomic weights were to be tested.

The results of the structural formulae determined for the illite and smectite standards are in Figure 3.10 as a plot of tetrahedral and octahedral Al against tetrahedral Si following the convention of Ahn & Peacor (1986a). The data plot into two distinct regions, the smectite has low Al and high Si with the illite standard having less Si but more Al. Additionally, ATEM and SEM data may be compared as data for (a) standards and (b) samples was collected. Structural formulae for the illite and smectite standards are listed in Appendix 3.1.

The two other octahedral cations may be plotted in the same way (Figure 3.11). The Fe cation concentrations are broadly similar between standards with the separation of the data coming from the illite standard having less Si. Both standards have a mean Fe cation concentration of ~0.2 cations. The Mg cation concentrations for the illite standard are ~0.2 cations in the octahedral sheet; the smectite standard shows much more variation with two clusters at around ~0.2 and 0.3 cations (Figure 3.12). The cation make up of the interlayer sheet (Figure 3.13) also describes a difference between the standards with the illite having high K concentrations (~0.6 cations) and the smectite standard having very low K concentrations (~0.02 cations). The interlayer Ca (Figure 3.14) shows the smectite standard rich in Ca relative to the illite and overall has a low concentration of interlayer cations relative to illite.

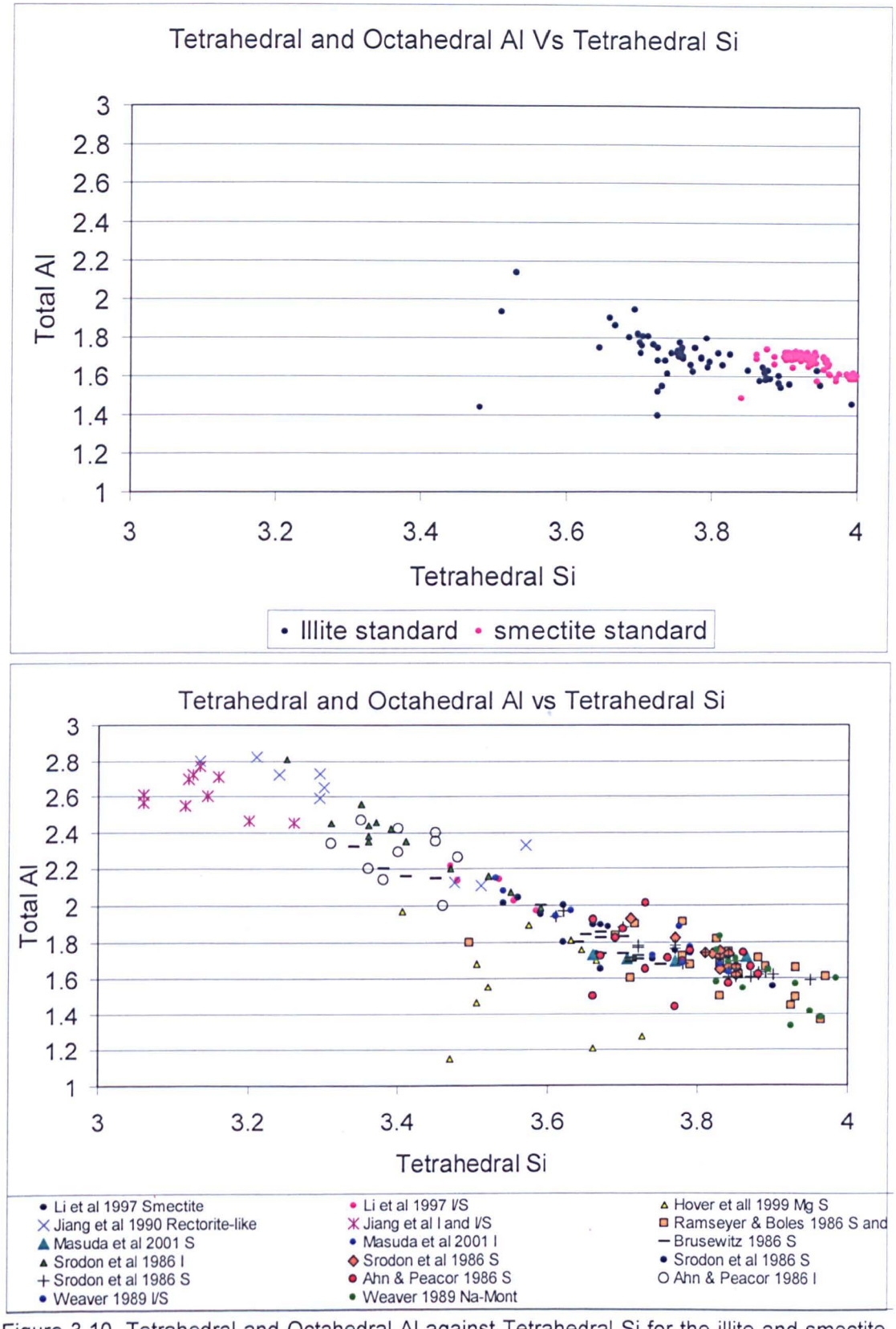

Figure 3.10. Tetrahedral and Octahedral Al against Tetrahedral Si for the illite and smectite standards, (top) and (bottom) global data plotted using the convention of Ahn & Peacor (1986a). Data are from a variety of techniques; Atomic absorption Spectroscopy, DC Plasma-Emission Spectroscopy, Ignited weights, X-ray fluorescence and not Analytical Electron Microscopy alone. The division of the data into illite and smectite is based on the individual author's descriptions.

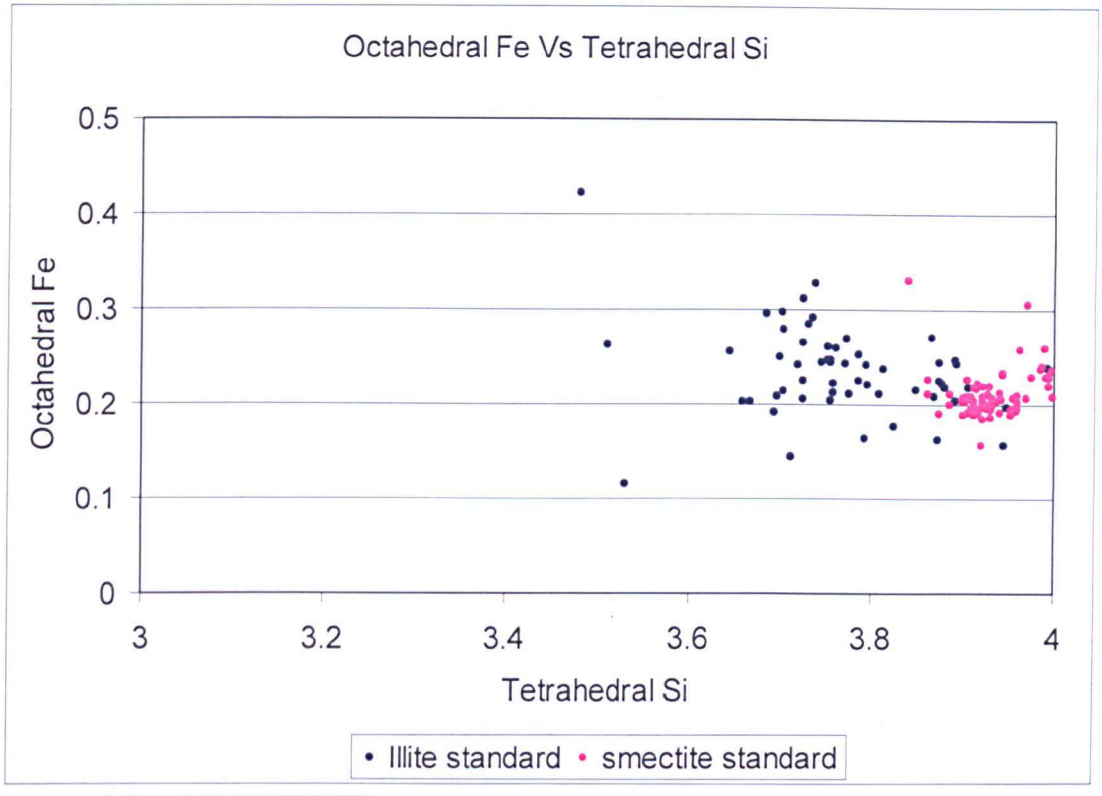

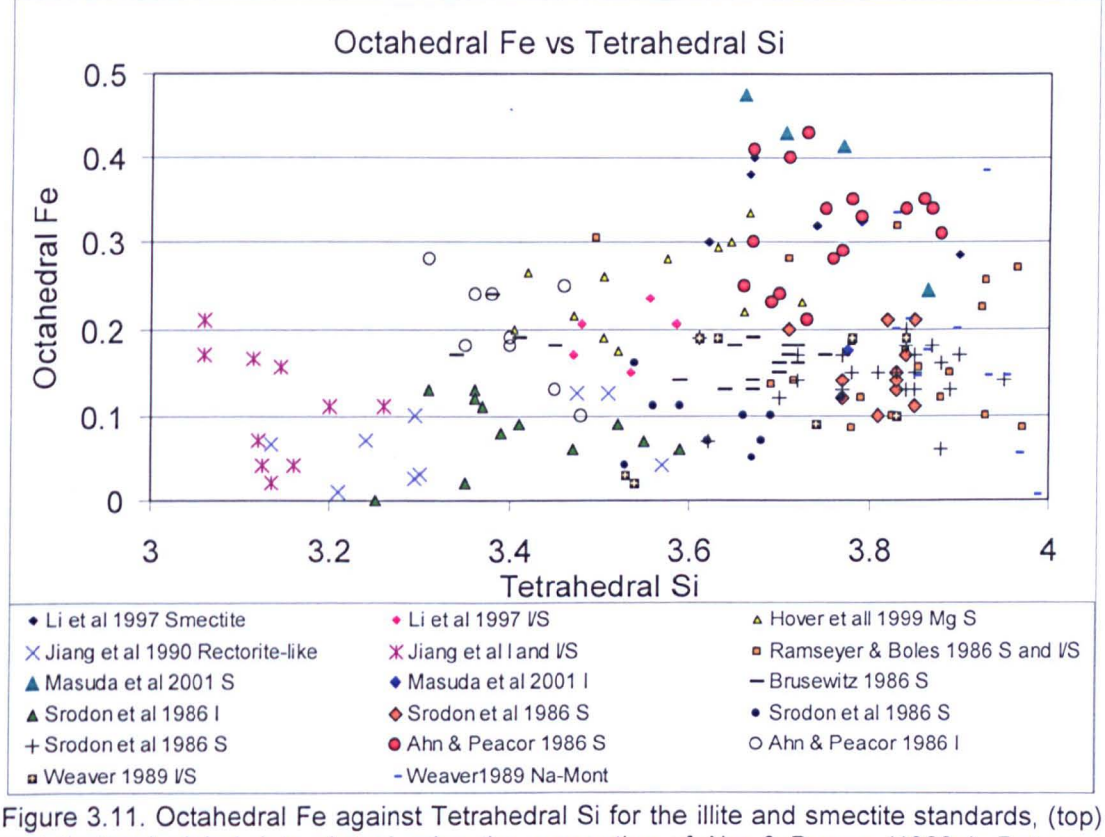

Figure 3.11. Octahedral Fe against Tetrahedral Si for the illite and smectite standards, (top) and (bottom) global data plotted using the convention of Ahn & Peacor (1986a). Data are from a variety of techniques; Atomic absorption Spectroscopy, DC Plasma-Emission Spectroscopy, Ignited weights, X-ray fluorescence and not Analytical Electron Microscopy alone. The division of the data into illite and smectite is based on the individual author's descriptions.

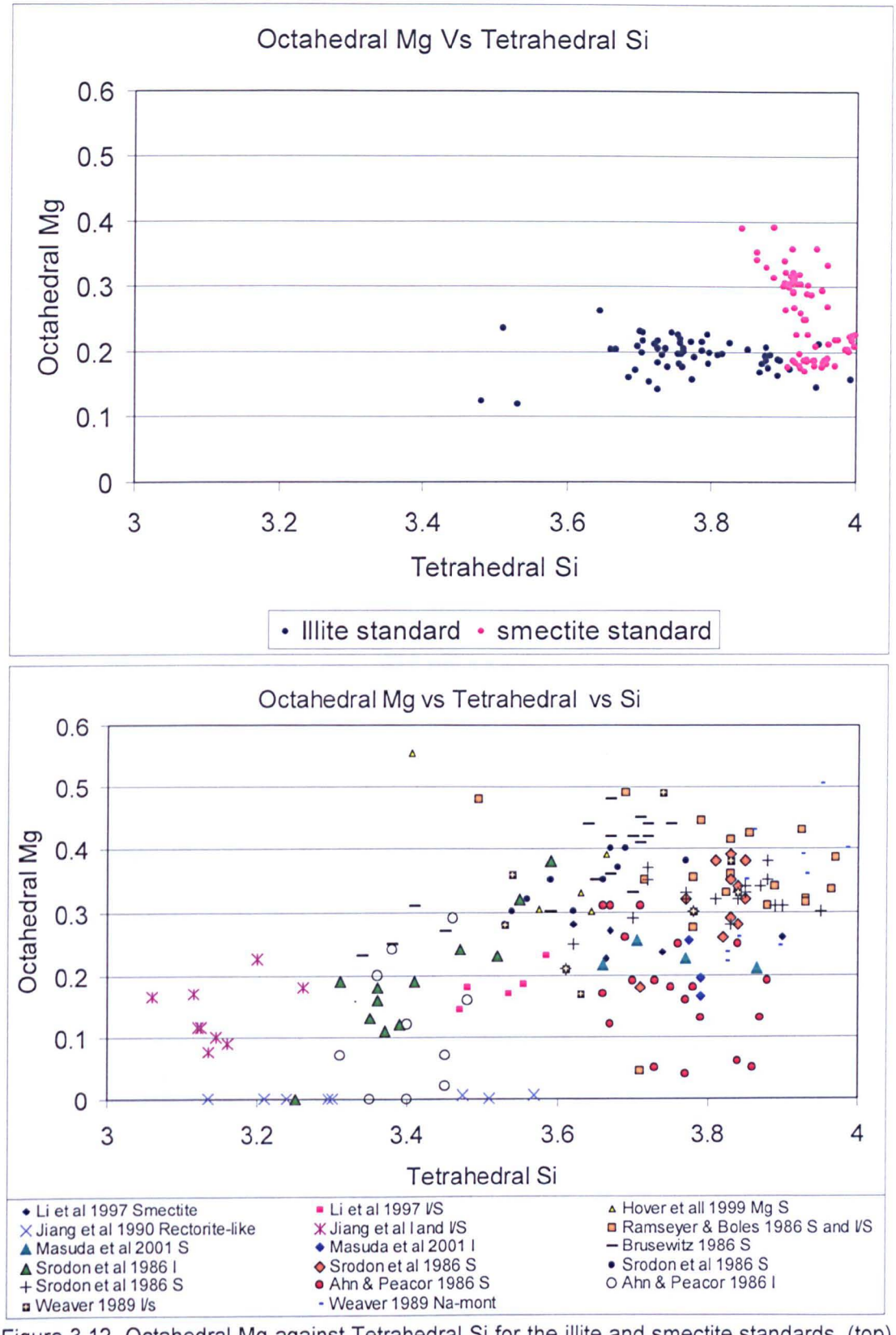

Figure 3.12. Octahedral Mg against Tetrahedral Si for the illite and smectite standards, (top) and (bottom) global data plotted using the convention of Ahn & Peacor (1986a). Data are from a variety of techniques; Atomic absorption Spectroscopy, DC Plasma-Emission Spectroscopy, Ignited weights, X-ray fluorescence and not Analytical Electron Microscopy alone. The division of the data into illite and smectite is based on the individual author's descriptions.

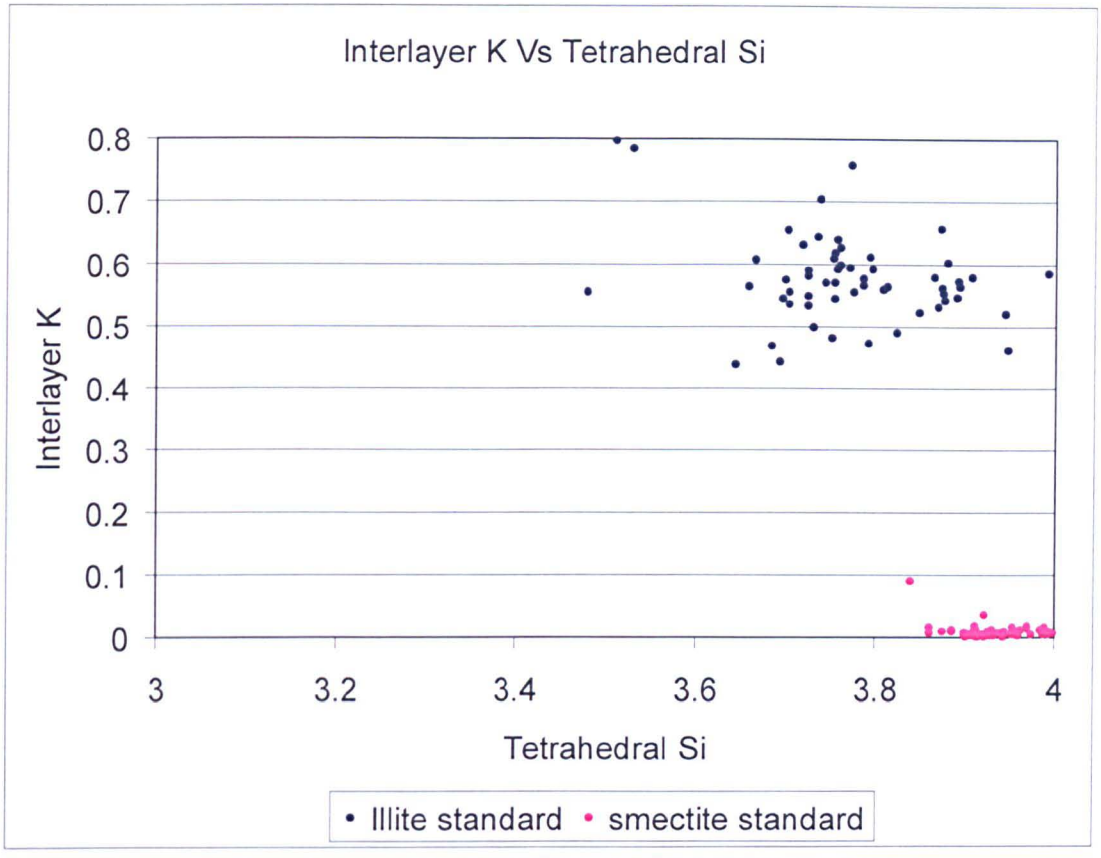

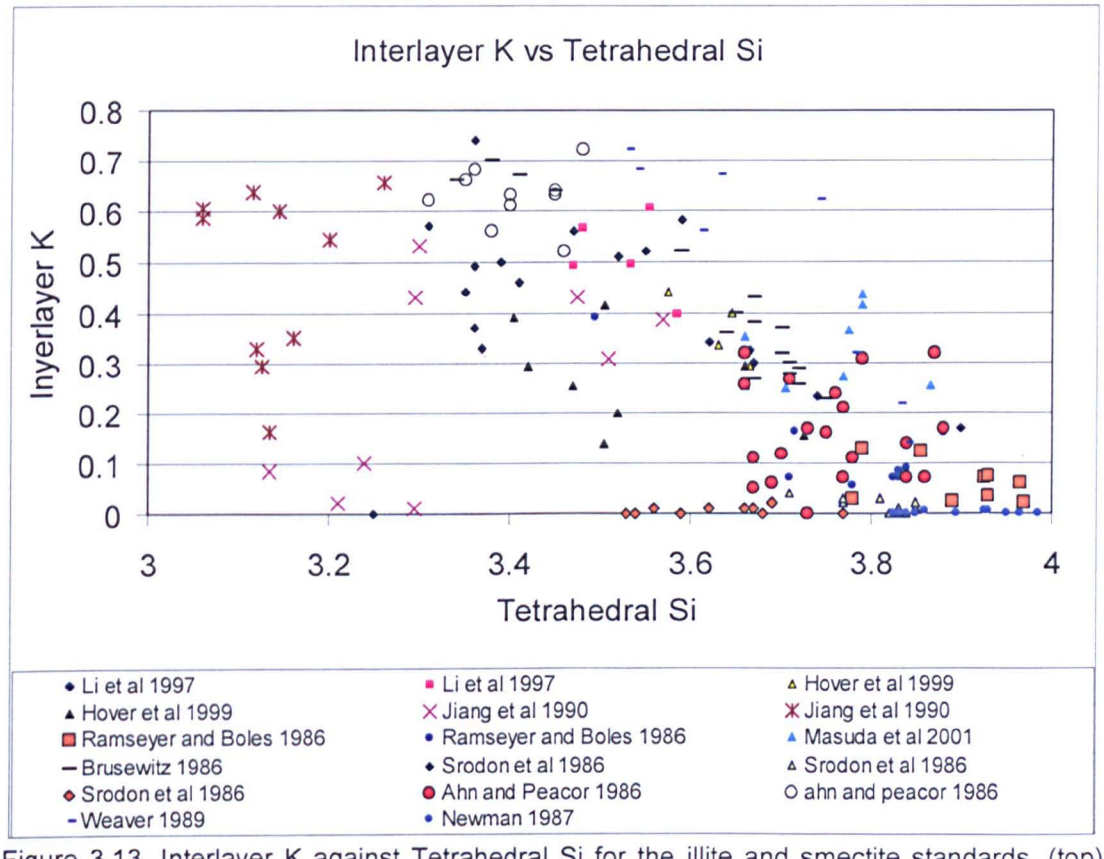

Figure 3.13. Interlayer K against Tetrahedral Si for the illite and smectite standards, (top) and (bottom) global data plotted using the convention of Ahn & Peacor (1986a). Data are from a variety of techniques; Atomic absorption Spectroscopy, DC Plasma-Emission Spectroscopy, Ignited weights, X-ray fluorescence and not Analytical Electron Microscopy alone. The division of the data into illite and smectite is based on the individual author's descriptions.

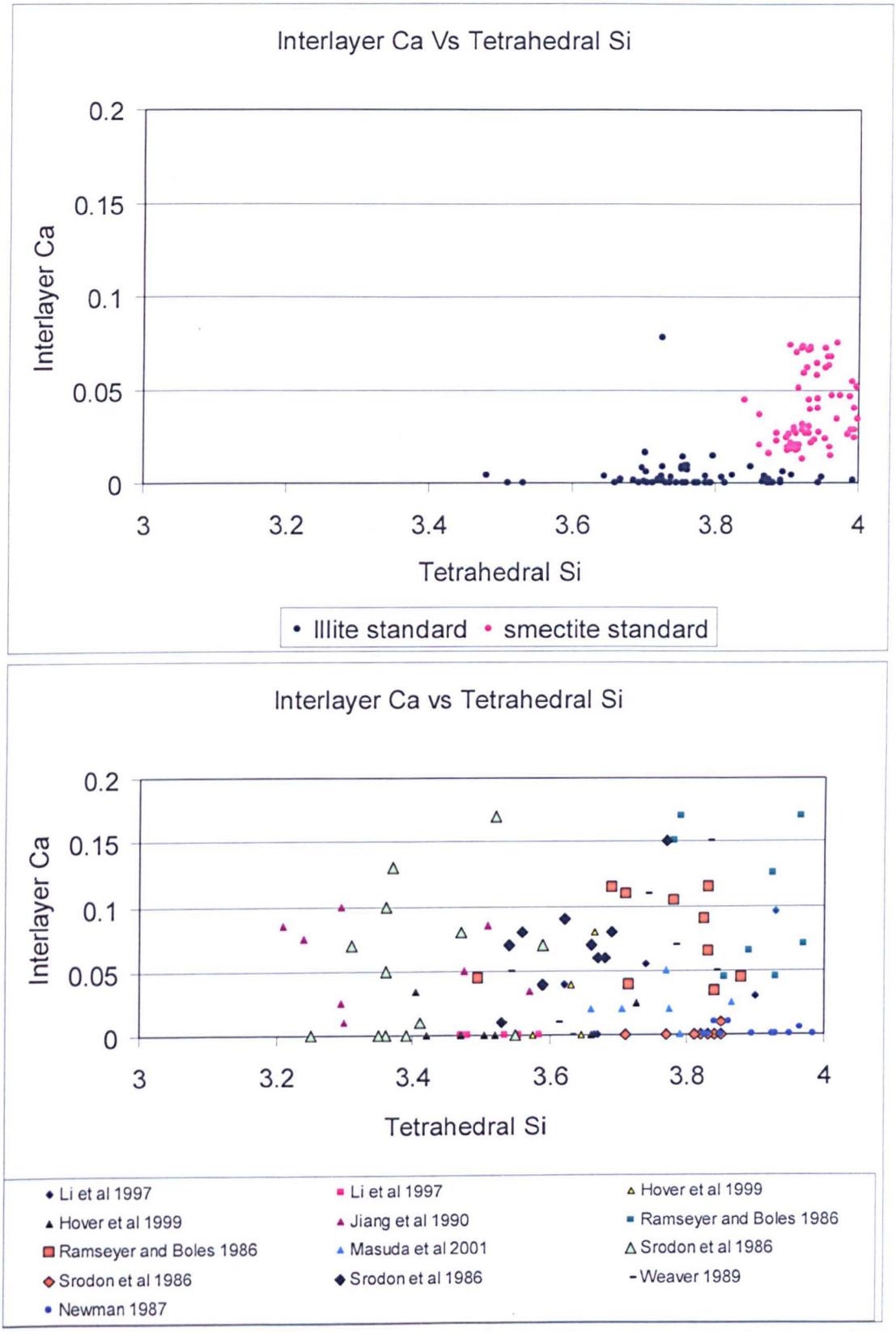

Figure 3.14. Interlayer Ca against Tetrahedral Si for the illite and smectite standards, (top) and (bottom) global data plotted using the convention of Ahn & Peacor (1986a). Data are from a variety of techniques; Atomic absorption Spectroscopy, DC Plasma-Emission Spectroscopy, Ignited weights, X-ray fluorescence and not Analytical Electron Microscopy alone. The division of the data into illite and smectite is based on the individual author's descriptions.

The average chemistries of 58 results from the illite standard and 99 results from the smectite standard are:

Illite standard: $(Al_{1.46}Fe_{0.23}Mg_{0.19}Ti_{0.04})(Si_{3.77}Al_{0.23})O_{10}(OH)_2Ca_{0.004}Na_{0.00}K_{0.58}$

Standard deviation: $(Al_{0.11}Fe_{0.05}Mg_{0.03}Ti_{0.07})(Si_{0.10}Al_{0.10})O_{10}(OH)_2Ca_{0.01}Na_{0.00}K_{0.08}$

Smectite standard: $(Al_{1.60}Fe_{0.21}Mg_{0.24}Ti_{0.01})(Si_{3.97}Al_{0.03})O_{10}(OH)_2Ca_{0.04}Na_{0.00}K_{0.02}$

Standard deviation: $(Al_{0.04}Fe_{0.03}Mg_{0.06}Ti_{0.07})(Si_{0.07}Al_{0.07})O_{10}(OH)_2Ca_{0.017}Na_{0.00}K_{0.08}$

A test of the accuracy of the data is through summation of the cations in the octahedral sheet, the total should equal 2.00 cations (Weaver, 1989). The smectite has an average of 2.06 (± 0.05) cations and the illite 1.92 (± 0.04) cations.

There are two possibilities as to why the octahedral cations do not total two; (1) there is some impurity in the standard material changing the chemistries; or (2) the detection through the EDS software is not working correctly. The EDS has an error of 5% (Brown, 2005 pers. comm.), which equates to an error margin of ± 0.1 cations. The average results are within the machine error. Additionally, in the plot of total Al against tetrahedral Si (Figure 3.10) the difference between the standards is only ~ 0.2 Si cations. Ahn & Peacor (1986a) recorded twice that, but from single crystal analysis, with the illite plotting at 3.4 Si cations and 2.4 Al cations. The standards do not have significantly different Fe cation concentrations (Figure 3.11) whereas the global trend describes a broad decrease between smectite and illite. The smectite standard has more Mg (0.05 cations) than the illite standard, with the global trend describing a decrease in octahedral Mg concentrations from smectite to illite (Figure 3.12). The illite standard has significantly more interlayer K than the smectite standard. The global trend has significant scatter but a general increase in K from smectite to illite (Figure 3.13). Interlayer Ca is much higher in the smectite standard then in the illite but the spread of the data is marked by the high standard deviation.

The accuracy of the octahedral totals and the ability to separate standard materials (Figures 3.10 to 3.14) based on published plotting conventions of

structural formulae (Ahn & Peacor, 1986a) suggests that the methodology used construct structural formulae from EDS data is robust.

3.2.2: XRD on the illite and smectite standards:

X-ray diffraction was run on the illite and smectite standards with a view to trying to explain why the illite and smectite standards had plotted so close together in Figure 3.10, as end members in the global trend should not.

X-ray Powder diffraction was run at Newcastle University. The sample preparation was aimed at simple random orientation, with sample powder being placed in the sample holder and prepared with a minimum of pressing, however, alignment cannot be ruled out by this method. The samples were air-dried on running.

The machine used was a PANalytical X'Pert Pro diffractometer, fitted with an X'Celerator and a secondary monochromator. The X'Celerator an attachment to the X'Pert and has the effect of giving a good quality pattern in a fraction of the time of the traditional diffractometer. The secondary monochromator eliminates fluorescent scattering from the specimen, and so results in a better peak: background ratio for samples containing transition metals and rare earth elements.

Scans covered the range 2.5 - 70 degrees, programmed to a nominal step size of 0.033 degrees 2-theta and time per step of 2 seconds. Scans are carried out in "continuous" mode, rather than "step scan" and take about 54 minutes per run. Radiation is Cu K-alpha: lambda = 1.54180 angstroms.

Phase identification is carried out by means of the X'Pert accompanying software program High Score and the ICDD database, Sets 1-49 (1999). It should be noted that the machine and software are not set up for clay mineral analysis, the software database is particularly poor in characterised

clay minerals and no glycolation is offered to discuss any mixed layering. The scans were purely done to assess purity of the two standards.

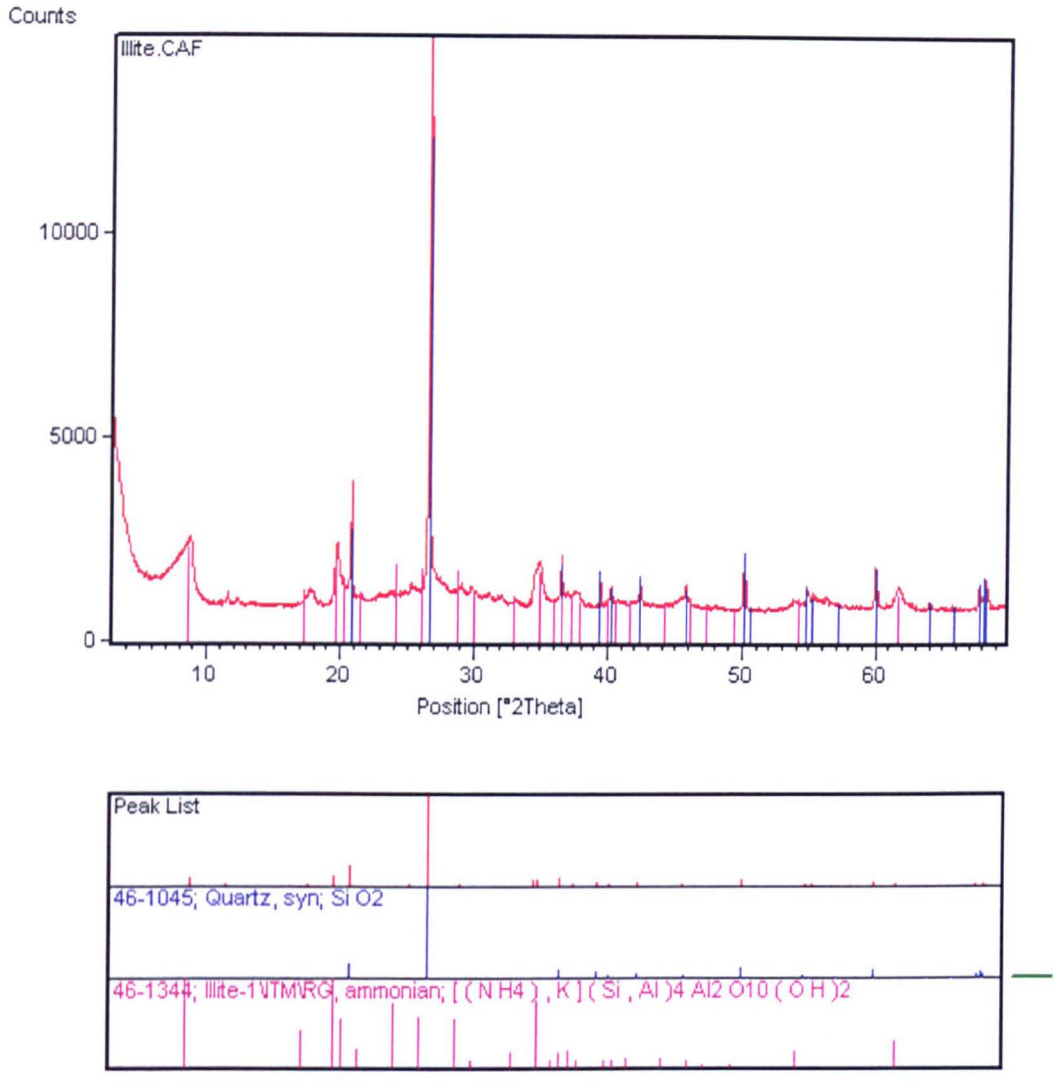

Figure 3.15. Illite standard with phase identification carried out by means of the X'Pert software program High Score and the ICDD database, Sets 1-49 (1999). A strong quartz peak is evident. The illites in the database were minimal.

The illite standard shows a strong quartz peak (Figure 3.15). This was not observed in the BSEM when the EDS data was collected mainly due to the fine grained nature of the standard, so much of the sample 'matrix' was below the resolution of that technique. This would go some way to explaining why the average structural formulae are not as distinct in their

tetrahedral Si/Al ratios as the literature suggests they might be (e.g. Ahn & Peacor, 1986a; Weaver, 1989; Masuda et al., 2001).

However, the accuracy of the octahedral totals does not suggest quartz interference with the electron beam, thereby artificially increasing Si concentrations. The illite trace also has signs of mixed layering due to the peak in the less than 10 degrees 2-theta region. The degree of mixed layering has not been assessed.

The smectite trace is a lot cleaner (Figure 3.16), with no quartz peak at 26.5 degrees 2-theta. The trace has been matched to a montmorillonite by the ICDD database but possibly not the right one due to it only having a few clay minerals characterised, but peaks characteristic of smectite are present in the spectrum.

Consequently, the low degree of separation between illite and smectite standards in terms of the octahedral and tetrahedral cations reflects the fact that the differences in structural formulae may be small, the exception being the interlayer K and Ca concentrations that are indicative illite and smectite.

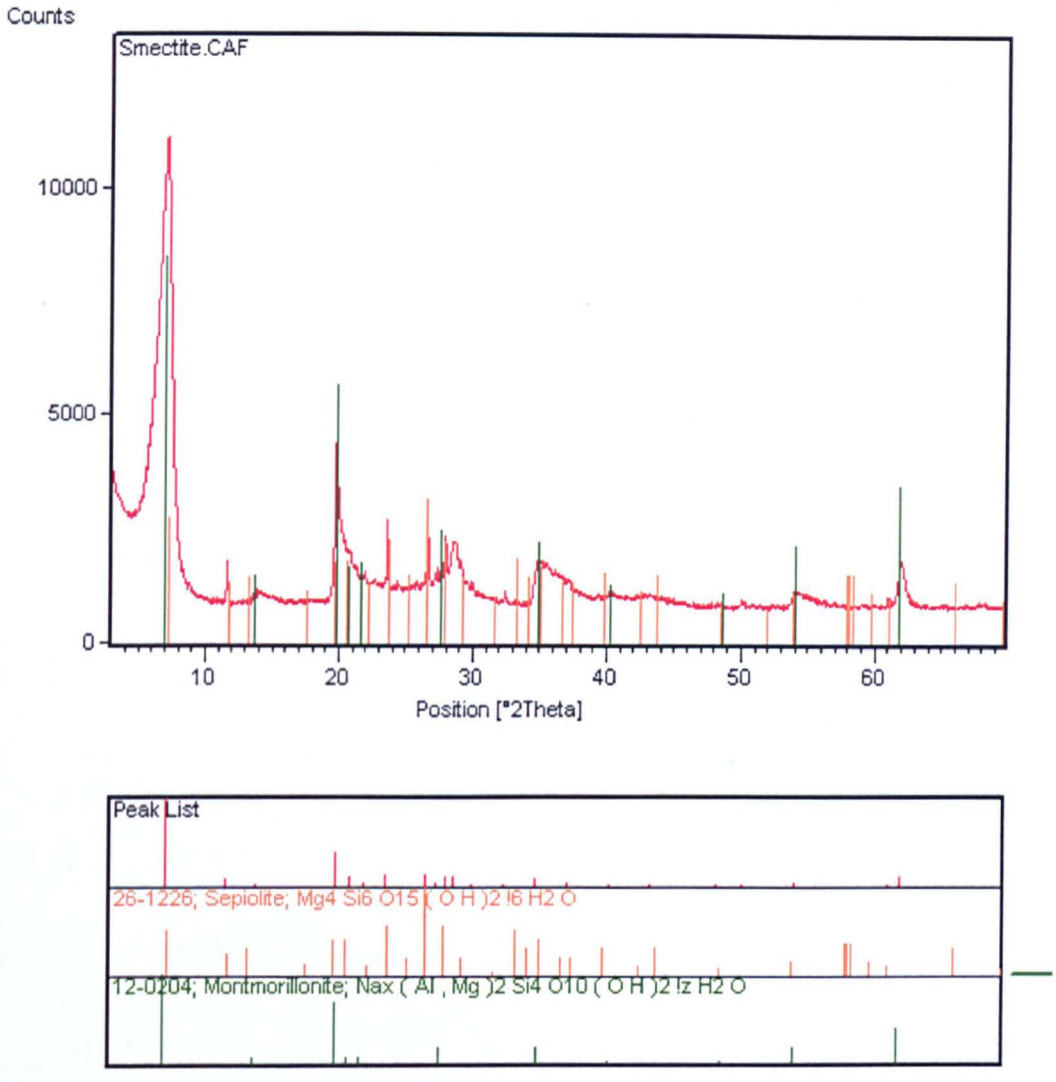

Figure 3.16. Smectite standard with phase identification carried out by means of the X'Pert software program High Score and the ICDD database, Sets 1-49 (1999). There is a good fit by the software for a montmorillonite, sepiolite is there as a comparison.

3.2.3: SEM EDS on Chochołów-06 and Bukowina Tatrzańska-41:

When two samples in this study Chochołów-06 and Bukowina Tatrzańska-41, representing extreme end members of the I/S transition (see chapter 2 for details) are presented to the electron beam (Figure 3.17, 3.18, 3.19, 3.20 & 3.21) under BSEM conditions, using the same method as for the illite and smectite standards, the results do not fit well with the global trend. Quite simply there is a large spread of the data for all cations. With the multiple substitutions possible in the octahedral sheet, the Mg and Fe cation variability could be explained by substitution of Al for either Mg or Fe or both. The structural formulae may be seen in Appendix 3.2. The key test of accuracy is the total of the octahedral cations for Chochołów-06 (average octahedral total 1.88 with a standard deviation of 0.35 cations) and Bukowina Tatrzańska-41 (average octahedral total 1.84 with a standard deviation of 0.37 cations).

These results suggest that the method devised for calculating structural formulae from atomic ratios is robust but that the interaction volume of the technique is too large for heterogeneous samples such as mudstones. Even a standard material that is comprised of some quartz may significantly contaminate the result. The results for Chochołów-06 and Bukowina Tatrzańska-41 show that the beam has interacted with the chlorite, kaolinite, K-feldspar, pyrite, calcite and so on that these samples contain (see chapter 2) and has therefore produced results that reflect this. So the calculation of structural formulae is valid but SEM interacts on a crystal aggregate scale (Velde, 1992) whereas a higher resolution technique would act on a single crystal scale.

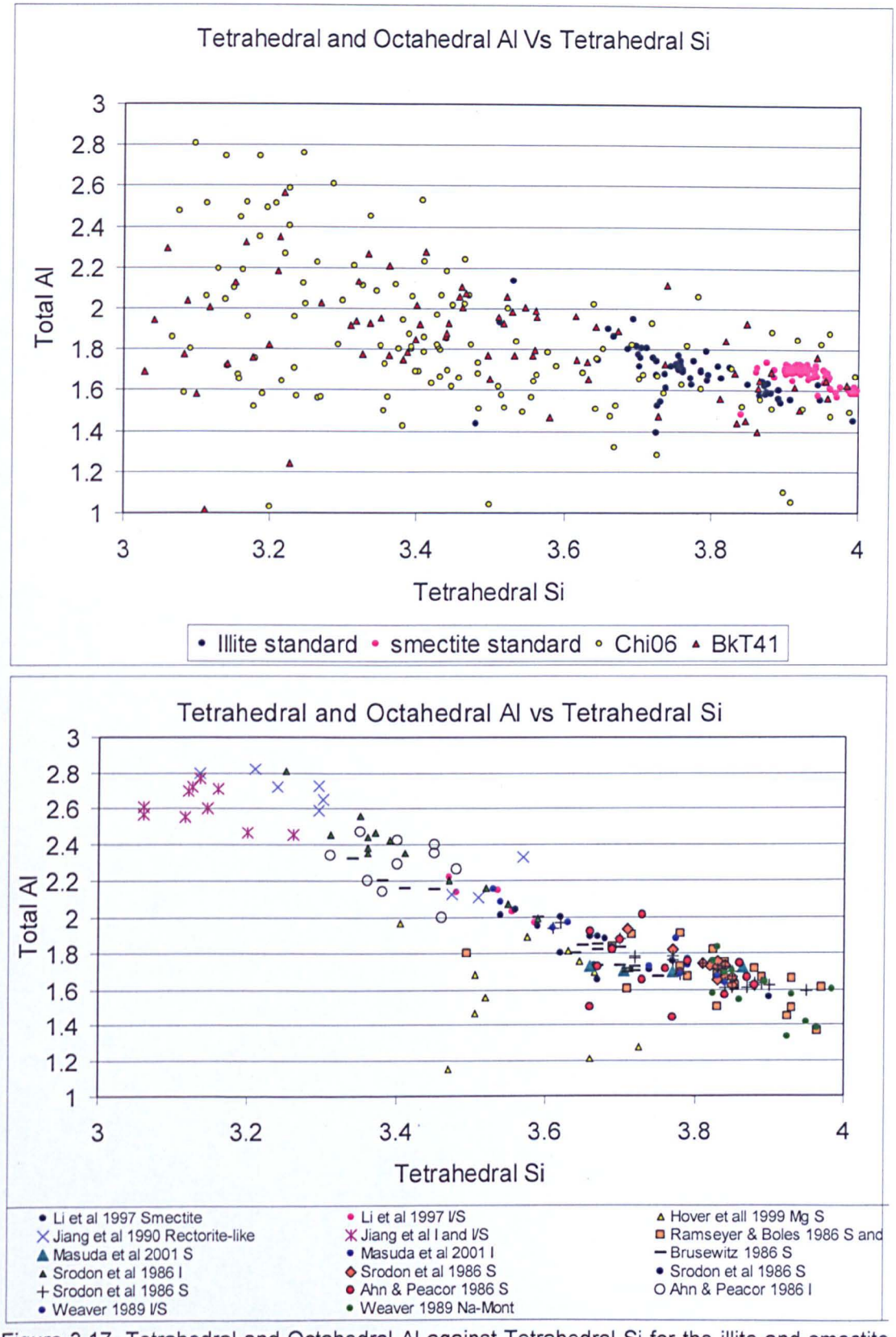

Figure 3.17. Tetrahedral and Octahedral Al against Tetrahedral Si for the illite and smectite standards and samples Chochołów-06 and Bukowina Tatrzańska-41, (top) and (bottom) global data plotted using the convention of Ahn & Peacor (1986a). Data are from a variety of techniques; Atomic absorption Spectroscopy, DC Plasma-Emission Spectroscopy, Ignited weights, X-ray fluorescence and not Analytical Electron Microscopy alone. The division of the data into illite and smectite is based on the individual author's descriptions.

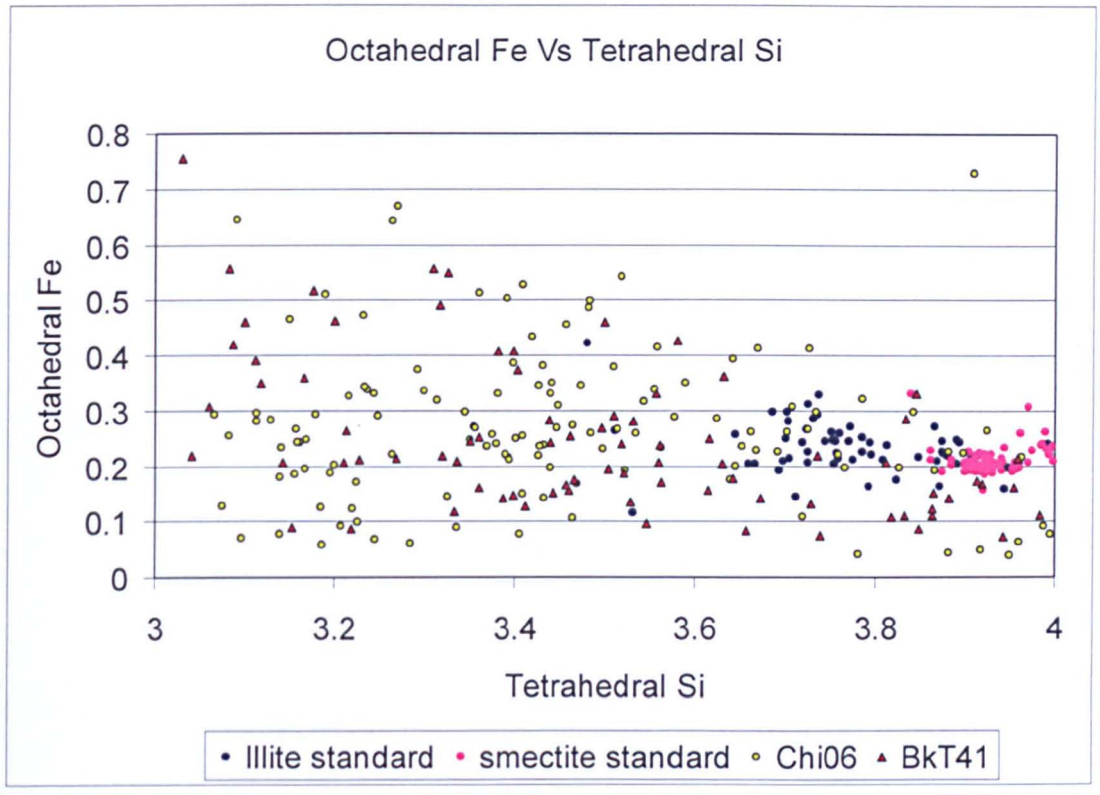

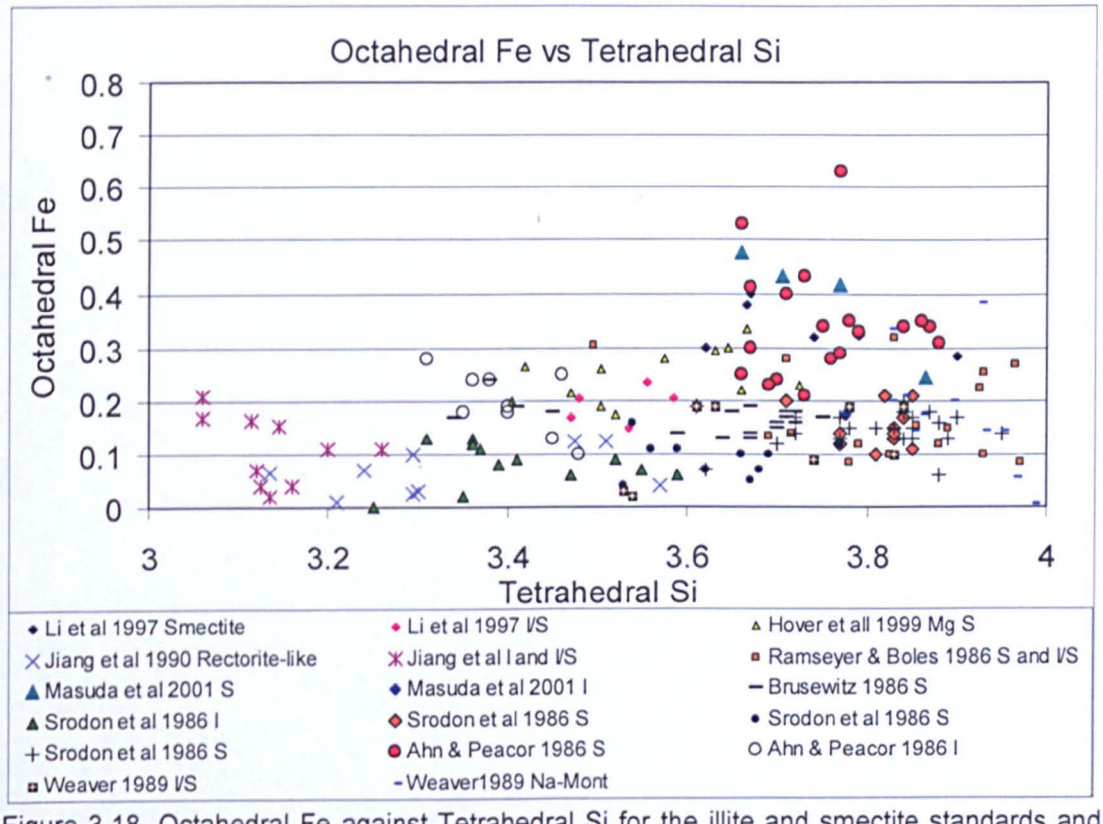

Figure 3.18. Octahedral Fe against Tetrahedral Si for the illite and smectite standards and samples Chochołów-06 and Bukowina Tatrzańska-41, (top) and (bottom) global data plotted using the convention of Ahn & Peacor (1986a). Data are from a variety of techniques; Atomic absorption Spectroscopy, DC Plasma-Emission Spectroscopy, Ignited weights, X-ray fluorescence and not Analytical Electron Microscopy alone. The division of the data into illite and smectite is based on the individual author's descriptions.

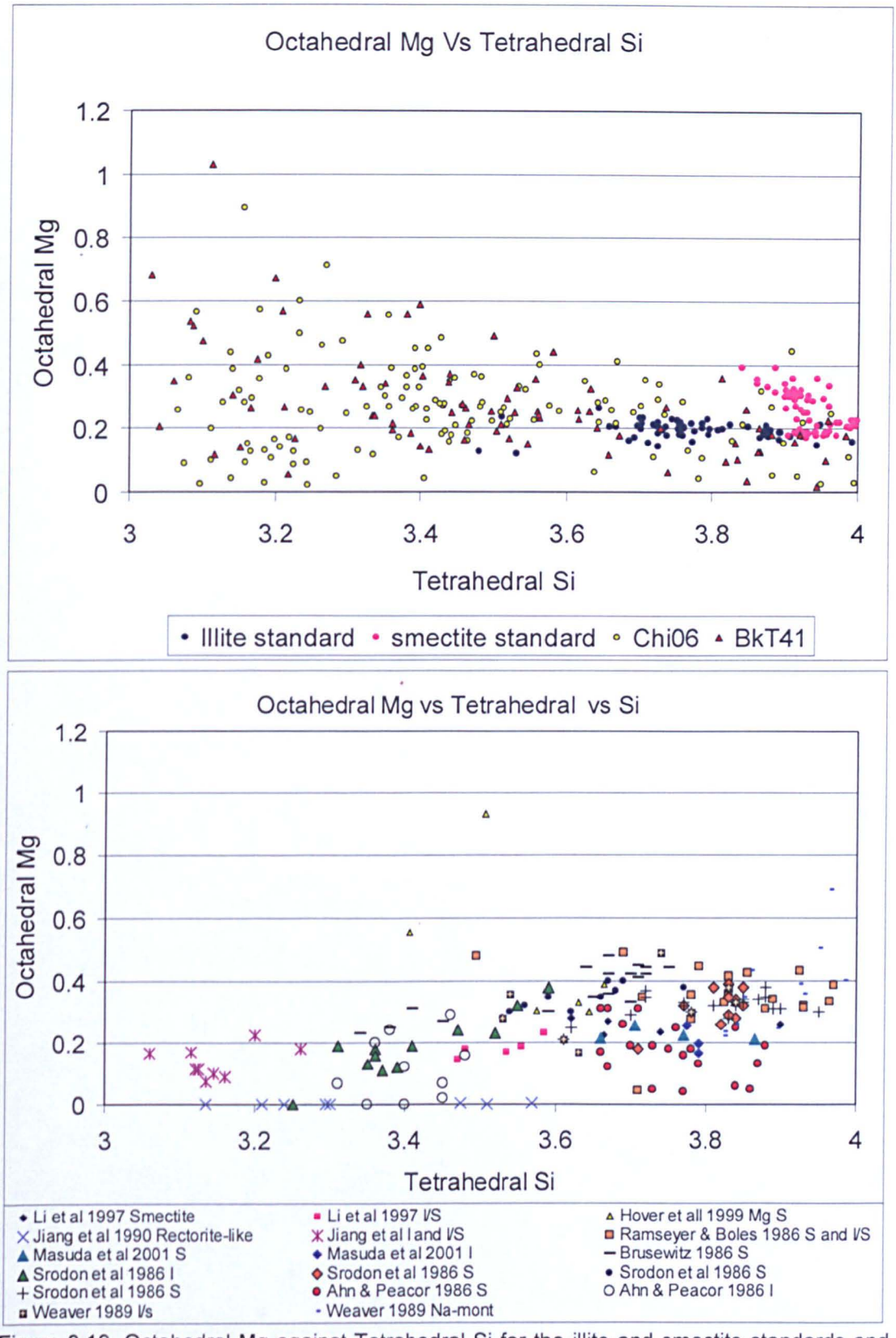

Figure 3.19. Octahedral Mg against Tetrahedral Si for the illite and smectite standards and samples Chochołów-06 and Bukowina Tatrzańska-41, (top) and (bottom) global data plotted using the convention of Ahn & Peacor (1986a). Data are from a variety of techniques; Atomic absorption Spectroscopy, DC Plasma-Emission Spectroscopy, Ignited weights, X-ray fluorescence and not Analytical Electron Microscopy alone. The division of the data into illite and smectite is based on the individual author's descriptions.

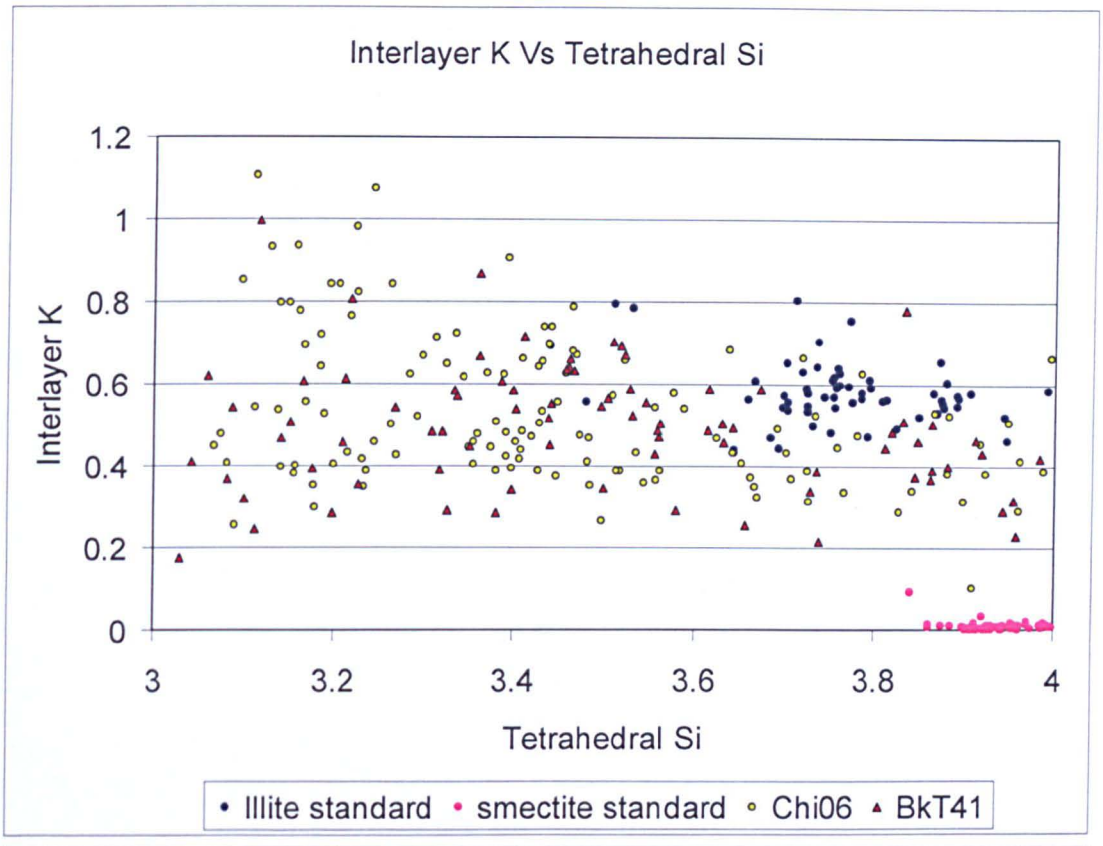

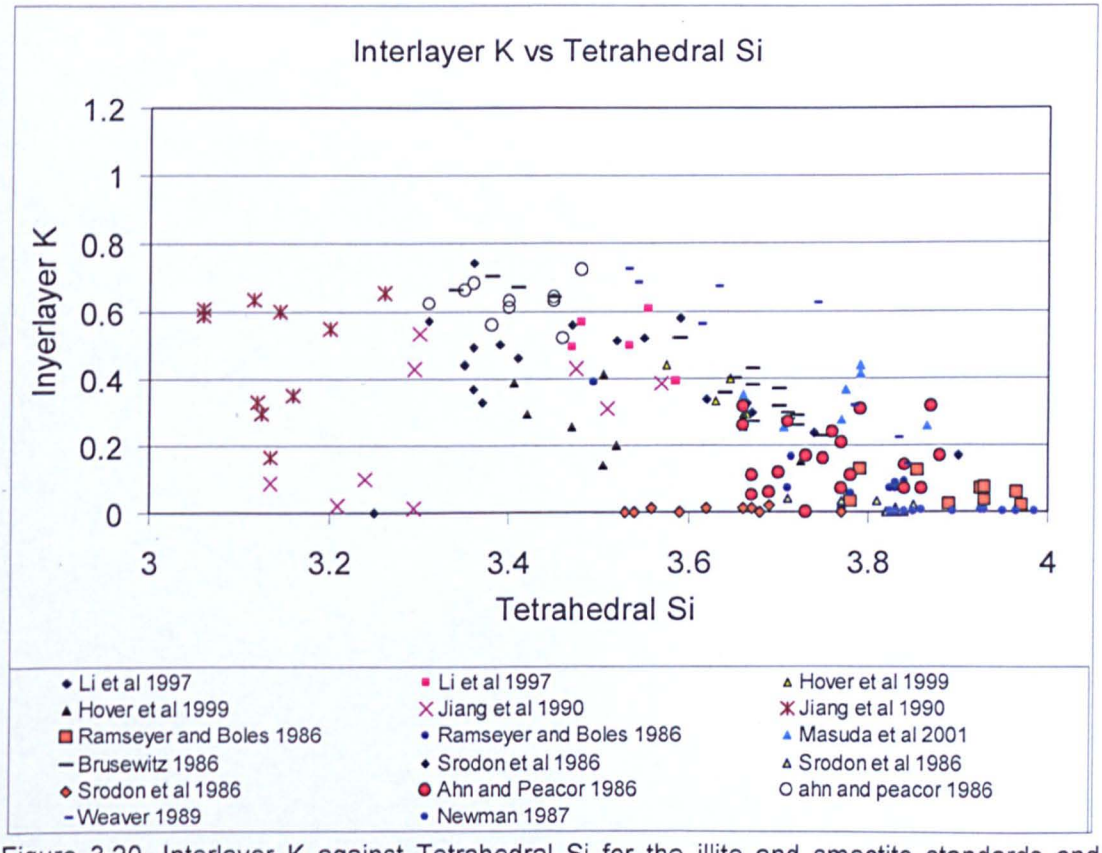

Figure 3.20. Interlayer K against Tetrahedral Si for the illite and smectite standards and samples Chochołów-06 and Bukowina Tatrzańska-41, (top) and (bottom) global data plotted using the convention of Ahn & Peacor (1986a). Data are from a variety of techniques; Atomic absorption Spectroscopy, DC Plasma-Emission Spectroscopy, Ignited weights, X-ray fluorescence and not Analytical Electron Microscopy alone. The division of the data into illite and smectite is based on the individual author's descriptions.

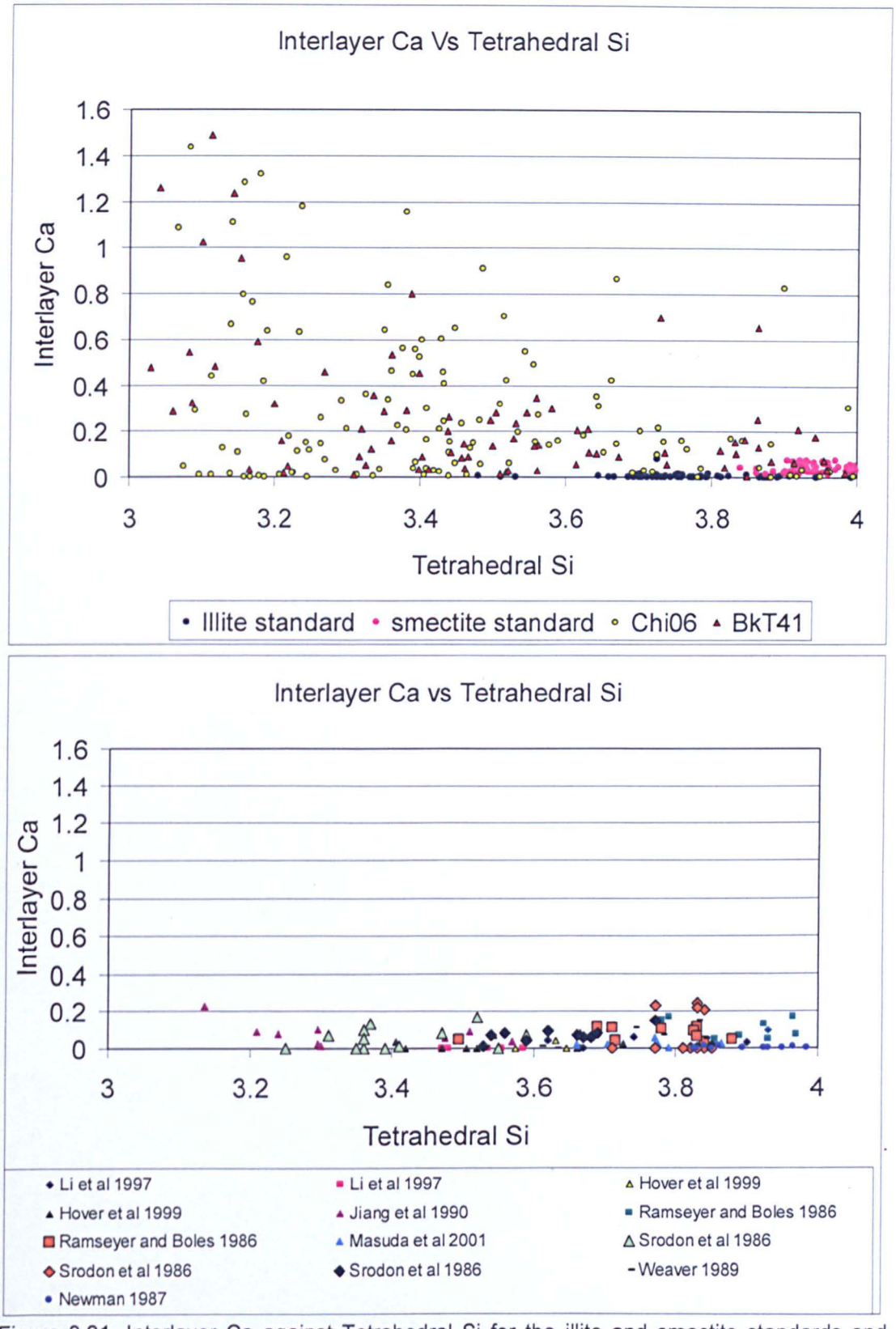

Figure 3.21. Interlayer Ca against Tetrahedral Si for the illite and smectite standards and samples Chochołów-06 and Bukowina Tatrzańska-41, (top) and (bottom) global data plotted using the convention of Ahn & Peacor (1986a). Data are from a variety of techniques; Atomic absorption Spectroscopy, DC Plasma-Emission Spectroscopy, Ignited weights, X-ray fluorescence and not Analytical Electron Microscopy alone. The division of the data into illite and smectite is based on the individual author's descriptions.

3.2.4: Analytical Transmission Electron Microscopy:

The sampling criteria for the samples analysed consisted of selecting a grain under the TEM that was thin (see earlier sections for images of analysed areas). Next a SADP was taken to assess whether it was a single crystal; if it was a single crystal an image of this SADP was captured, then the EDS data were collected for the same live time for each sample.

Standard structural formulae for a half cell and associated elemental concentrations expressed as weight percent oxides are presented below in Tables 3.8 to 3.13 for the illite standard, Bukowina Tatrzańska-06, Bukowina Tatrzańska-41, Chochołów-06, Chochołów-28, and Chochołów-60, respectively. The I/S oxide weight percents are obtained by normalising the atomic ratios to 95 wt% following the convention of Merriman et al., (1995). The structural formula units are presented after applying the conversion methods detailed by Weaver (1989) and Moore & Reynolds (1997) to the atomic ratios as measured by EDS.

The average structural formulae for the illite standard calculated from measurements gathered from ATEM-EDS based on 11 results is:

Illite standard: $(Al_{1.40}Fe_{0.31}Mg_{0.28}Ti_{0.02})(Si_{3.51}Al_{0.49})O_{10}(OH)_2Ca_{0.02}Na_{0.00}K_{0.70}$
Standard Deviation: $(Al_{0.15}Fe_{0.14}Mg_{0.04}Ti_{0.01})(Si_{0.10}Al_{0.10})O_{10}(OH)_2Ca_{0.02}Na_{0.00}K_{0.24}$

The composition of tetrahedral Si and total Al is midway between end-member illites and smectites based on previous studies (e.g. Li et al., 1997; Hover et al., 1999; Jiang et al., 1990; Ramseyer & Boles, 1986; Masuda et al., 2001; Ahn & Peacor, 1986a; Brusewitz, 1986; Środoń et al., 1986; Weaver, 1989). The average total cation summation is 2.00 cations with a standard deviation of 0.08 (Table 3.14).

The illite standard (Table 3.8) has octahedral sheet cation totals within the 5% error margin of analysis (2.00 cations $\pm$ 0.1 cations). There is interlayer variability obvious in analyses RT and R013 with low values being insufficient for charge balance between the interlayer sheet and the charge set up

between substitution in the octahedral and tetrahedral sheets, this is due to potassium mobility. The Si/Al ratios are consistent with the global dataset (e.g. Figure 3.10). Sample illite-R009 has a lot of Fe and Mg substitution for Al. In fact the illite standard is a poor standard as it has a lot of variability in crystal composition compared to the other five measured samples.

The average structural formulae for the illite standard calculated from measurements gathered from SEM-EDS based on 58 results is:

Illite standard: $(Al_{1.46}Fe_{0.23}Mg_{0.19}Ti_{0.04})(Si_{3.77}Al_{0.23})O_{10}(OH)_2Ca_{0.004}Na_{0.00}K_{0.58}$

Standard deviation: $(Al_{0.11}Fe_{0.05}Mg_{0.03}Ti_{0.07})(Si_{0.10}Al_{0.10})O_{10}(OH)_2Ca_{0.01}Na_{0.00}K_{0.08}$

When comparing the averages by ATEM and SEM-EDS, the significant differences lie in the tetrahedral Si to Al ratio and that octahedral Fe and Mg concentrations are higher. Additionally the ATEM has measured more interlayer K than was recorded by SEM.

The average structural formulae below are based on samples that comprise I/S material. The selection criterion was based on the structural formulae conforming to published data for smectite, I/S or illite material. The differentiation of chlorite from illite from the structural formulae unit is straight forward as the Si/Al ratios are hugely different. End-member smectite and illite range from 4.00 Si to 3.00 Si in the tetrahedral sheet. Chlorite has much lower Si and higher Fe. Additionally, the EDS spectra give a good first approximation of whether illite, smectite or chlorite is being sampled (Severin, 2004). Also, kaolinite has roughly equal Si and Al abundances (Weaver, 1989) so attributing I/S material to kaolinite is unlikely.

The average structural formulae of samples that comprise illitic material are:

Bukowina Tatrzańska-06: $(Al_{1.63}Fe_{0.18}Mg_{0.16}Ti_{0.02})(Si_{3.33}Al_{0.67})O_{10}(OH)_2Ca_{0.07}Na_{0.00}K_{0.73}$

Standard Deviation: $(Al_{0.17}Fe_{0.05}Mg_{0.09}Ti_{0.02})(Si_{0.12}Al_{0.12})O_{10}(OH)_2Ca_{0.10}Na_{0.00}K_{0.29}$

Bukowina Tatrzańska-41: $(Al_{1.75}Fe_{0.10}Mg_{0.18}Ti_{0.02})(Si_{3.39}Al_{0.61})O_{10}(OH)_2Ca_{0.04}Na_{0.00}K_{0.57}$

Standard Deviation: $(Al_{0.14}Fe_{0.03}Mg_{0.12}Ti_{0.02})(Si_{0.13}Al_{0.13})O_{10}(OH)_2Ca_{0.05}Na_{0.00}K_{0.27}$

Chochołów-06: $(Al_{1.74}Fe_{0.13}Mg_{0.13}Ti_{0.02})(Si_{3.39}Al_{0.61})O_{10}(OH)_2Ca_{0.06}Na_{0.00}K_{0.51}$

Standard Deviation: $(Al_{0.19}Fe_{0.06}Mg_{0.09}Ti_{0.01})(Si_{0.17}Al_{0.17})O_{10}(OH)_2Ca_{0.08}Na_{0.00}K_{0.23}$

Chochołów-28: $(Al_{1.66}Fe_{0.13}Mg_{0.15}Ti_{0.02})(Si_{3.17}Al_{0.83})O_{10}(OH)_2Ca_{0.05}Na_{0.00}K_{0.95}$
Standard Deviation: $(Al_{0.19}Fe_{0.10}Mg_{0.12}Ti_{0.01})(Si_{0.11}Al_{0.11})O_{10}(OH)_2Ca_{0.13}Na_{0.00}K_{0.22}$

Chochołów-60: $(Al_{1.66}Fe_{0.15}Mg_{0.14}Ti_{0.02})(Si_{3.29}Al_{0.71})O_{10}(OH)_2Ca_{0.10}Na_{0.00}K_{0.73}$
Standard Deviation: $(Al_{0.21}Fe_{0.05}Mg_{0.12}Ti_{0.01})(Si_{0.11}Al_{0.11})O_{10}(OH)_2Ca_{0.11}Na_{0.00}K_{0.21}$

Bukowina Tatrzańska-06 (average of 16 results), Bukowina Tatrzańska-60 (average of 11 results), Chochołów-06 (average of 14 results), Chochołów-28 (average of 11 results) and Chochołów-60 (average of 10 results).

The standard deviations of the tetrahedral sheet cations are very consistent for the 5 samples, with little variation within a sample. Equally the standard deviation of the Al cation in the octahedral sheet is consistent but standard deviations within the sample are quite large, but partly reflect the multiple substitutions possible in the octahedral sheet. The standard deviation of the Fe cation is similar for four of the samples with only Chochołów-28 being much different, essentially there is not a great deal of Fe cation variation within the sample. The five samples have quite consistent Mg cation concentrations in their octahedral sheet and are more variable than the Fe concentrations. The standard deviations in the interlayer are large showing the variable interlayer charges between individual crystals. Also, part of the large standard deviation may result from the fact that K and to some extent Ca are mobile under an electron beam so some of the interlayer may be lost. The interlayer should therefore be treated with caution.

The measured crystallites in Bukowina Tatrzańska-06 (Table 3.9) have consistent octahedral cation totals but with sample HT being too low and H015 and H020 too high. H015 is too high because the analysis has attributed too much Al to the sample whereas H020 has too much Fe and Mg substitution and HT not enough of either Al or its possible substitutes. It is accepted that I/S has an interlayer of ~0.55-1.00 K^+ cations (Środoń et al, 1986), several crystals from this sample have too little K to meet the charge needs for substitution, interlayer cation mobility under the X-ray beam could explain this (van der Pluijm et al., 1988). H026 and H032 are very close to mica based on their Si/Al tetrahedral ratios (Weaver, 1989).

Original work by Hower and Mowatt (1966) established the interlayer charge value of $0.75/O_{10}(OH)_2$ for illite and illite rich I/S. Subsequently, this was updated to $\sim 0.55/O_{10}(OH)_2$ for mixed-layer I/S with less than 50%I and $\sim 1.0/O_{10}(OH)_2$ for more ordered I/S (Środoń et al, 1986) but as has been latterly demonstrated, illite is a mixture of high and low charges (Inoue et al, 1978; Eslinger et al, 1979; Brusewitz, 1986). The concentration of K in the interlayer space should range from ~0.55 cations in illite layers in randomly interstratified I/S (R=0;>50% smectite layers) to ~1.0 cations for illite layers in ordered I/S, where R>0 (Środoń et al., 1986). As a consequence the distributions presented in Tables 3.9 and 3.10 shows that for both Bukowina Tatrzańska-06 and Bukowina Tatrzańska-41 there are structural formulae calculated from ATEM data that do not allow charge balancing as the interlayer cation concentration is too low.

The crystals analysed from Bukowina Tatrzańska-41 (Table 3.10) are similar to Bukowina Tatrzańska-06. Where octahedral totals do not total 2.00 cations these crystals also have low potassium in their interlayers. The main difference between Bukowina Tatrzańska-06 and Bukowina Tatrzańska-41 is that Bukowina Tatrzańska-41 has less Fe in the octahedral sheet and this Fe has been replaced by Al.

The octahedral totals for crystals from Chochołów-06 (Table 3.11) are close to 2.00 cations except for E013 and E017 which have an Si/Al ratio that is comparable to a mica. Additional crystals, E005, E011 and E030 are also very like end-member illite (Weaver, 1989 for a discussion of illite structural formulae). Generally the interlayer charge is either higher or lower than the 0.55-1.0 layer charge window.

Only K029 has an octahedral total that is too low for crystals in Chochołów-28 (Table 3.12). All the Si/Al ratios are very consistent and with much lower Si than the other samples in this study and are more characteristic of end-member illite-smectite material. There is more Fe substitution in these crystals than in Chochołów-06 or Chochołów-60 but the Mg substitution is

similar. The variation in the interlayer K is notable and may be explained by the Si/Al ratios producing more layer charge in the tetrahedral sheet that needs to be offset by the interlayer.

Crystals from Chochołów-60 (Table 3.13) have generally good octahedral totals except for J005 and J007 which are too low. The Si/Al ratio is more like end-member illite than Chochołów-06, but less so than Chochołów-28. In general the average structural formulae are comparable to Chochołów-06.

The difference between Chochołów-06 and Chochołów-60 is expected based on the fact that they have 50% and 76% I in I/S, respectively (Środoń et al., in press). More illitic material will have lower Si cation concentrations (Ahn and Peacor, 1986a). Chochołów-28 is anomalous as it has 56% I in I/S, yet its Si cation distribution lower than Chochołów-60.

Table 3.8: Illite standard structural formulae for a half cell and associated elemental concentrations expressed as wt% oxides normalised to 95% (after Merriman 2002).

	R001	*R003*	*R005*	*R007*	*R009*	*R013*
Si	3.56	3.61	3.67	3.53	3.39	3.43
Al	0.44	0.39	0.33	0.47	0.61	0.57
Tet. Sum	4.00	4.00	4.00	4.00	4.00	4.00
Al	1.43	1.55	1.45	1.45	0.99	1.46
Fe	0.35	0.25	0.31	0.2	0.68	0.3
Mg	0.27	0.26	0.21	0.27	0.22	0.3
Ti	0	0	0.03	0.01	0.02	0.04
Oct. Sum	2.05	2.06	2.00	1.93	1.91	2.10
Ca	0.03	0	0	0	0.04	0.03
K	0.51	0.47	0.5	0.95	0.98	0.47
Inter. Sum	0.54	0.47	0.50	0.95	1.02	0.50
SiO_2	54.32	55.88	56.33	52.23	48.49	52.6
Al_2O_3	24.13	25.37	23.15	24.11	19.46	26.29
TiO_2	0.21	0.02	0.55	0.19	0.39	0.76
Fe_2O_3	7.08	5.12	6.33	3.95	12.92	6.13
MgO	2.77	2.75	2.18	2.63	2.14	3.11
CaO	0.38	0.14	0.42	0.84	0.56	0.44
K_20	6.11	5.73	6.05	11.06	11.04	5.68
Total	95	95	95	95	95	95

	R015	*R017*	*R019*	*R021*	*RT*
Si	3.58	3.37	3.52	3.42	3.56
Al	0.42	0.63	0.48	0.58	0.44
Tet. Sum	4.00	4.00	4.00	4.00	4.00
Al	1.43	1.45	1.44	1.25	1.47
Fe	0.24	0.2	0.18	0.39	0.35
Mg	0.24	0.28	0.36	0.32	0.29
Ti	0	0.03	0.03	0.03	0.01
Oct. Sum	1.91	1.96	2.01	1.99	2.12
Ca	0.01	0.05	0.02	0.03	0
K	0.92	0.93	0.69	0.85	0.35
Inter. Sum	0.93	0.98	0.71	0.88	0.35
SiO_2	53.19	50.07	53.5	50.51	55.11
Al_2O_3	23.38	26.26	24.85	22.93	25.03
TiO_2	0.47	0.5	0.7	0.55	0.22
Fe_2O_3	4.77	3.88	3.7	7.56	7.26
MgO	2.37	2.8	3.69	3.19	2.96
CaO	0.11	0.64	0.27	0.4	0.18
K_20	10.7	10.86	8.28	9.86	4.24
Total	95	95	95	95	95

Table 3.9: Bukowina Tatrzańska-06 structural formulae for a half cell and associated elemental concentrations expressed as wt% oxides normalised to 95% (after Merriman 2002)., 76% illite in I/S.

	HT	*H003*	*H007*	*H009*	*H011*	*H013*	*H015*	*H018*
Si	3.29	3.36	3.22	3.38	3.52	3.32	3.22	3.42
Al	0.71	0.64	0.78	0.62	0.48	0.68	0.78	0.58
Tet. Sum	4.00	4.00	4.00	4.00	4.00	4.00	4.00	4.00
Al	1.37	1.66	1.32	1.68	1.66	1.76	2.02	1.76
Fe	0.23	0.20	0.34	0.18	0.12	0.14	0.17	0.07
Mg	0.25	0.22	0.28	0.03	0.16	0.07	0.00	0.17
Ti	0.00	0.00	0.02	0.01	0.00	0.01	0.02	0.01
Oct. Sum	1.85	2.08	1.96	1.90	1.94	1.98	2.21	2.01
Ca	0.34	0.19	0.00	0.03	0.04	0.00	0.04	0.01
K	0.75	0.22	1.18	0.91	0.73	0.80	0.05	0.71
Inter. Sum	1.09	0.41	1.18	0.94	0.77	0.80	0.09	0.72
SiO_2	48.67	52.40	46.43	50.66	53.39	50.30	51.46	52.61
Al_2O_3	26.03	30.52	25.62	29.21	27.60	31.49	37.93	30.38
TiO_2	0.06	0.03	0.32	0.16	0.53	0.21	0.33	0.25
Fe_2O_3	4.44	4.19	6.50	3.54	2.50	2.76	3.59	1.34
MgO	2.46	2.31	2.70	0.30	1.61	0.71	0.40	1.73
CaO	4.70	2.81	0.04	0.41	0.63	0.01	0.61	0.14
K_2O	8.64	2.75	13.39	10.71	8.75	9.51	0.69	8.55
Total	95	95	95	95	95	95	95	95
	H020	*H022*	*H024*	*H026*	*H028*	*H030*	*H032*	*H034*
Si	3.13	3.26	3.17	3.39	3.07	3.39	3.10	3.46
Al	0.87	0.74	0.83	0.61	0.93	0.61	0.90	0.54
Tet. Sum	4.00	4.00	4.00	4.00	4.00	4.00	4.00	4.00
Al	1.21	1.72	1.49	1.54	1.04	1.58	1.44	1.53
Fe	0.31	0.14	0.22	0.26	0.56	0.19	0.22	0.15
Mg	0.67	0.05	0.24	0.15	0.29	0.16	0.31	0.23
Ti	0.02	0.01	0.00	0.05	0.06	0.02	0.05	0.02
Oct. Sum	2.21	1.92	1.95	2.00	1.95	1.95	2.02	1.93
Ca	0.12	0.06	0.10	0.07	0.22	0.01	0.04	0.00
K	0.67	0.89	1.01	0.55	0.89	0.90	1.02	0.94
Inter. Sum	0.79	0.95	1.11	0.62	1.11	0.91	1.06	0.94
SiO_2	46.46	48.84	46.54	51.70	43.80	50.73	45.44	51.93
Al_2O_3	26.13	31.35	28.87	27.72	23.78	27.82	28.98	26.28
TiO_2	0.40	0.28	0.00	1.08	1.05	0.36	0.97	0.43
Fe_2O_3	6.03	2.84	4.28	5.36	10.67	3.88	4.34	2.94
MgO	6.63	0.49	2.38	1.55	2.77	1.56	3.01	2.36
CaO	1.61	0.78	1.30	0.96	2.95	0.14	0.53	0.07
K_2O	7.74	10.423	11.63	6.63	9.98	10.52	11.72	10.99
Total	95	95	95	95	95	95	95	95

Table 3.10: Bukowina Tatrzańska-41 structural formulae for a half cell and associated elemental concentrations expressed as wt% oxides normalised to 95% (after Merriman 2002). 76% illite in I/S.

	C001	*C003*	*C005*	*C007*	*C010*	*C012*
Si	3.41	3.28	3.24	3.22	3.52	3.38
Al	0.59	0.72	0.76	0.78	0.48	0.62
Tet. Sum	4.00	4.00	4.00	4.00	4.00	4.00
Al	1.85	1.77	1.88	1.94	1.50	1.76
Fe	0.09	0.11	0.04	0.07	0.07	0.10
Mg	0.24	0.19	0.00	0.10	0.35	0.18
Ti	0.00	0.01	0.01	0.00	0.07	0.02
Oct. Sum	2.18	2.08	1.93	2.11	1.99	2.06
Ca	0.06	0.00	0.10	0.03	0.16	0.00
K	0.17	0.67	0.75	0.47	0.45	0.58
Inter. Sum	0.23	0.67	0.85	0.50	0.61	0.58
SiO_2	54.47	49.83	49.19	50.14	54.44	52.31
Al_2O_3	33.02	32.18	34.07	35.93	26.10	31.27
TiO_2	0.09	0.19	0.26	0.11	1.41	0.35
Fe_2O_3	1.93	2.27	0.81	1.52	1.52	2.13
MgO	2.55	1.94	0.27	1.00	3.64	1.90
CaO	0.83	0.63	1.43	0.50	2.38	0.05
K_2O	2.11	7.96	8.97	5.79	5.52	6.99
Total	95	95	95	95	95	95

	C014	*C016*	*C018*	*C020*	*CT*
Si	3.28	3.47	3.40	3.67	3.41
Al	0.72	0.53	0.60	0.33	0.59
Tet. Sum	4.00	4.00	4.00	4.00	4.00
Al	1.79	1.58	1.62	1.65	1.85
Fe	0.09	0.17	0.14	0.10	0.09
Mg	0.02	0.13	0.19	0.38	0.24
Ti	0.01	0.03	0.03	0.00	0.00
Oct. Sum	1.91	1.91	1.98	2.13	2.18
Ca	0.00	0.02	0.00	0.00	0.06
K	0.97	0.86	0.82	0.34	0.17
Inter. Sum	0.97	0.88	0.82	0.34	0.23
SiO_2	49.30	52.21	51.39	57.86	54.47
Al_2O_3	31.95	27.07	28.55	26.44	33.02
TiO_2	0.23	0.66	0.69	0.40	0.09
Fe_2O_3	1.88	3.40	2.75	2.00	1.93
MgO	0.16	1.27	1.91	4.00	2.55
CaO	0.02	0.23	0.01	0.14	0.83
K_2O	11.45	10.17	9.69	4.16	2.11
Total	95	95	95	95	95

Table 3.11: Chocholów-06 structural formulae for a half cell and associated elemental concentrations expressed as wt% oxides normalised to 95% (after Merriman 2002)., 50% illite in I/S.

	E001	*E003*	*E005*	*E007*	*E009*	*E011*	*E013*
Si	3.31	3.65	3.12	3.30	3.56	3.12	3.08
Al	0.69	0.35	0.88	0.70	0.44	0.88	0.92
Tet. Sum	4.00	4.00	4.00	4.00	4.00	4.00	4.00
Al	1.93	1.77	1.47	2.00	1.59	1.73	1.03
Fe	0.07	0.07	0.20	0.09	0.14	0.07	0.74
Mg	0.00	0.10	0.23	0.06	0.28	0.19	0.63
Ti	0.01	0.02	0.02	0.01	0.00	0.03	0.00
Oct. Sum	2.01	1.96	1.92	2.16	2.01	2.02	2.40
Ca	0.00	0.02	0.00	0.00	0.02	0.01	0.07
K	0.68	0.52	1.34	0.24	0.66	0.95	0.19
Inter. Sum	0.68	0.54	1.34	0.24	0.68	0.96	0.26
SiO_2	50.24	57.21	44.78	52.55	54.52	46.67	45.97
Al_2O_3	33.77	28.18	28.50	36.38	26.23	33.08	24.62
TiO_2	0.17	0.47	0.41	0.28	0.35	0.69	0.19
Fe_2O_3	1.37	1.46	3.72	2.00	2.88	1.37	14.71
MgO	1.24	1.01	2.24	0.60	2.88	1.88	6.31
CaO	0.16	0.24	0.33	0.14	0.28	0.15	0.97
K_2O	8.05	6.43	15.04	3.05	7.86	11.15	2.23
Total	95	95	95	95	95	95	95
	E017	*E019*	*E021*	*E024*	*E026*	*E028*	*E030*
Si	3.25	3.59	3.50	3.44	3.32	3.26	3.04
Al	0.75	0.41	0.50	0.56	0.68	0.74	0.96
Tet. Sum	4.00	4.00	4.00	4.00	4.00	4.00	4.00
Al	2.10	1.61	1.48	1.63	1.62	1.69	1.55
Fe	0.04	0.15	0.24	0.18	0.15	0.19	0.20
Mg	0.00	0.20	0.25	0.16	0.14	0.09	0.33
Ti	0.04	0.00	0.03	0.02	0.01	0.03	0.02
Oct. Sum	2.18	1.96	2.00	1.99	1.92	2.00	2.10
Ca	0.06	0.03	0.19	0.02	0.25	0.01	0.09
K	0.04	0.67	0.34	0.66	0.55	0.76	0.82
Inter. Sum	0.10	0.70	0.53	0.68	0.80	0.77	0.91
SiO_2	51.95	0.69	54.05	52.54	50.58	49.26	45.07
Al_2O_3	38.62	33.08	25.88	28.45	29.69	31.16	31.59
TiO_2	0.83	0.15	0.63	0.49	0.15	0.59	0.36
Fe_2O_3	0.80	11.15	5.02	3.64	3.12	3.89	3.85
MgO	1.34	46.67	2.57	1.62	1.39	0.92	3.27
CaO	0.94	1.88	2.72	0.34	3.54	0.16	1.31
K_2O	0.52	1.37	4.14	7.91	6.53	9.02	9.56
Total	95	95	95	95	95	95	95

Table 3.12: Chocholów-28 structural formulae for a half cell and associated elemental concentrations expressed as wt% oxides normalised to 95% (after Merriman 2002)., 56% illite in I/S.

	K009	*K011*	*K013*	*K015*	*K017*	*K021*
Si	3.17	3.18	3.37	3.30	3.26	3.14
Al	0.83	0.82	0.63	0.70	0.74	0.86
Tet. Sum	4.00	4.00	4.00	4.00	4.00	4.00
Al	1.99	1.57	1.65	1.65	1.77	1.68
Fe	0.03	0.06	0.06	0.23	0.23	0.04
Mg	0.00	0.35	0.27	0.01	0.05	0.23
Ti	0.02	0.02	0.03	0.03	0.01	0.02
Oct. Sum	2.04	2.00	2.01	1.92	2.06	1.97
Ca	0.00	0.00	0.01	0.02	0.01	0.01
K	0.68	1.13	0.82	0.90	0.60	1.15
Inter. Sum	0.68	1.13	0.83	0.92	0.61	1.16
SiO_2	48.83	46.95	51.09	49.26	49.85	46.35
Al_2O_3	36.85	29.78	29.38	29.82	32.52	31.87
TiO_2	0.43	0.44	0.69	0.57	0.20	0.35
Fe_2O_3	0.55	1.25	1.27	4.47	4.61	0.73
MgO	0.05	3.45	2.73	0.09	0.56	2.26
CaO	0.04	0.06	0.09	0.30	0.09	0.19
K_2O	8.26	13.07	9.75	10.49	7.18	13.25
Total	95	95	95	95	95	95
	K025	*K027*	*K029*	*K031*	*K033*	
Si	3.10	3.06	3.17	3.09	3.26	
Al	0.90	0.94	0.83	0.91	0.74	
Tet. Sum	4.00	4.00	4.00	4.00	4.00	
Al	1.77	1.75	1.45	1.58	1.26	
Fe	0.07	0.11	0.20	0.18	0.35	
Mg	0.15	0.13	0.10	0.15	0.34	
Ti	0.01	0.00	0.02	0.01	0.02	
Oct. Sum	2.00	1.99	1.77	1.92	1.97	
Ca	0.01	0.02	0.47	0.00	0.01	
K	1.05	1.03	0.67	1.27	1.13	
Inter. Sum	1.06	1.05	1.14	1.27	1.14	
SiO_2	46.00	45.37	46.96	44.83	47.06	
Al_2O_3	33.67	33.87	28.53	30.64	24.52	
TiO_2	0.17	0.08	0.33	0.27	0.39	
Fe_2O_3	1.33	2.20	3.88	3.42	6.78	
MgO	1.46	1.27	1.04	1.44	3.33	
CaO	0.18	0.29	6.55	0.01	0.13	
K_2O	12.19	11.92	7.72	14.39	12.78	
Total	95	95	95	95	95	

Table 3.13:. Chocholów-60 structural formulae for a half cell and associated elemental concentrations expressed as wt% oxides normalised to 95% (after Merriman 2002)., 76% illite in I/S.

	J001	*J005*	*J007*	*J009*	*J011*
Si	3.32	3.26	3.20	3.28	3.47
Al	0.68	0.74	0.80	0.72	0.53
Tet. Sum	4.00	4.00	4.00	4.00	4.00
Al	1.81	1.46	1.27	1.78	1.53
Fe	0.10	0.14	0.23	0.14	0.17
Mg	0.14	0.07	0.32	0.07	0.21
Ti	0.02	0.00	0.01	0.01	0.03
Oct. Sum	2.07	1.67	1.83	2.00	1.94
Ca	0.05	0.49	0.38	0.07	0.11
K	0.49	0.79	0.85	0.62	0.65
Inter. Sum	0.54	1.28	1.23	0.69	0.76
SiO_2	51.62	48.03	46.59	50.26	52.81
Al_2O_3	32.71	27.54	25.70	32.45	26.64
TiO_2	0.48	0.03	0.17	0.23	0.62
Fe_2O_3	2.00	2.82	4.54	2.94	3.42
MgO	1.48	0.72	3.10	0.76	2.19
CaO	0.77	6.75	5.14	0.95	1.54
K_2O	5.94	9.10	9.76	7.42	7.79
Total	95	95	95	95	95
	J013	*J015*	*J017*	*J019*	*J021*
Si	3.37	3.25	3.12	3.19	3.37
Al	0.63	0.75	0.88	0.81	0.63
Tet. Sum	4.00	4.00	4.00	4.00	4.00
Al	1.80	1.67	1.45	1.72	1.93
Fe	0.08	0.16	0.21	0.17	0.10
Mg	0.05	0.10	0.31	0.01	0.01
Ti	0.01	0.05	0.02	0.02	0.01
Oct. Sum	1.94	1.98	1.99	1.92	2.05
Ca	0.07	0.06	0.05	0.09	0.04
K	0.70	0.76	1.13	0.89	0.45
Inter. Sum	0.77	0.82	1.18	0.98	0.49
SiO_2	51.63	49.02	45.41	47.59	52.78
Al_2O_3	31.63	31.04	28.69	32.11	33.99
TiO_2	0.26	0.92	0.33	0.32	0.12
Fe_2O_3	1.59	3.16	3.99	3.28	2.05
MgO	0.53	1.00	3.07	0.08	0.06
CaO	0.96	0.84	0.67	1.20	0.52
K_2O	8.41	9.02	12.84	10.42	5.48
Total	95	95	95	95	95

Table 3.14: The average octahedral total and standard deviation for the illite standard, Bukowina Tatrzańska-06, Bukowina Tatrzańska-41, Chochołów-06, Chochołów-28, and Chochołów-60 from ATEM measurement. The octahedral totals are within the 5% error margin (0.10 cations) of the EDS software.

Sample	Average Octahedral Total	Octahedral Total Standard Deviation
Illite standard	2.00	0.08
Bukowina Tatrzańska-06	1.98	0.09
Bukowina Tatrzańska-41	2.04	0.10
Chochołów-06	2.02	0.08
Chochołów-28	1.97	0.07
Chochołów-60	1.97	0.08

Figures 3.22, 3.23 and 3.24 plot the data from Tables 3.9, 3.10, 3.11, 3.12 and 3.13 using the convention of Ahn and Peacor (1986) and may be compared to the global dataset.

The octahedral and tetrahedral Al against Si (Figure 3.22) for the Podhale Basin as a whole is directly comparable to other published data. The caveat being that at low Si cation concentrations, Al cation concentration is slightly decreased from levels that would be predicted based on the global trend (Figure 3.22). The Fe cation concentrations will plot comparably with the global dataset. The Mg cation concentrations are more spread than in the global data set for crystals with low tetrahedral Si cation concentrations, with as much as twice the Mg cation concentration at a given Si cation concentration. This will account for the slightly decreased levels of Al cation concentration at low Si. This additional Mg cation concentration is a source phenomena rather than a measurement error as the illite standard has Mg cation concentrations of ~0.2 cations. Elevated Mg cation concentrations have been recorded by Hover et al. (1999) in which Mg has substituted for Al in high Mg environments.

Using the plotting convention of Ahn & Peacor (1986a) the Si/Al concentrations in the Chochołów well do not show a great deal of separation between samples. Chochołów-06 has higher Si concentrations than Chochołów-60, making it more 'smectitic' but the intermediate sample Chochołów-28 plots beyond Chochołów-60 making it the most like and end-

member illite sample (Figure 3.25). There is no trend in the Fe and Mg concentrations (Figures 3.26 and 3.27).

The amount of octahedral Fe and Mg is slightly above those of the global trend for the portion of the plot between 3.0 and 3.6 Si cations (Figures 3.23 and 3.24) and explains the low Al concentrations relative to the global trend. The low Al cation concentrations have been offset by Fe and Mg substitutions, where Hover et al. (1999) sampled a very Mg rich, albeit smectite, sample they noted similar trends in the Mg and Fe substitution of Al in the octahedral sheet. Additionally, the (Fe + Mg) contents and the Al/Si ratios are very similar to those published by Garrels (1984) and Nadeau & Bain (1986).

Overall, the ATEM data presented here as structural formulae are very similar to previously published data. Where there is divergence it is due to the cation make up of the phase analysed being dependent on the cation make of the initial smectite material that it started from during the smectite to illite transition, assuming the phase analysed is interstratified I/S, and from the initial composition of the input material into the basin should smectite have evolved form another phase prior to illitization (Środoń, 1975).

The Bukowina Tatrzańska-06 well shows no separation in the Si/Al concentrations (Figure 3.28), however, there appears to be half as much Fe cation concentration in Bukowina Tatrzańska-41 as in Bukowina Tatrzańska-06 (Figure 3.29), with ~0.2 cations in Bukowina Tatrzańska-06 and ~0.1 cations in Bukowina Tatrzańska-41. This is confirmed by the average structural formula units presented above. The Mg cation concentrations show a large spread from between 0.0 cations to ~0.4 cations, but with no particular trends evident (Figure 3.30).

The global dataset may be split into data that have been derived from ATEM analysis and is therefore directly comparable to this study (Li et al., 1997; Hover et al., 1999; Jiang et al., 1990; Ramseyer & Boles, 1986; Masuda et al., 2001; Ahn & Peacor, 1986a) and what may be described as bulk data

from techniques such as Atomic absorption Spectroscopy, DC Plasma-Emission Spectroscopy, Ignited weights, X-ray fluorescence (Brusewitz, 1986; Środoń et al., 1986; Weaver, 1989). The Si/Al ratios are also around those noted by Środoń et al. (1986) measured from bulk analyses. The majority of the results from Tatrzańska-06, Bukowina Tatrzańska-41, Chochołów-06, Chochołów-28 and Chochołów-60 are most in keeping with those published by Jiang et al. (1990), with Si cation concentrations of around 3.2.

The percentage of illite in I/S for the samples measured vary between 50 and 76%; Chochołów-06 (50%), Chochołów-28 (56%), Chochołów-60 (76%), Tatrzańska-06 (76%), Bukowina Tatrzańska-41 (76%). The percentage illite in I/S for the illite material of Ahn and Peacor (1986) is 80%, whereas their smectite samples are 40%I and are associated with 3.7 Si cations in their tetrahedral sheet (Figure 3.22). Chochołów-06 (50%I) has a spread of Si cations in the tetrahedral sheet and would make a connection with the data published by Ahn and Peacor (1986a). Jiang et al. (1990) do not offer a percentage of illite in I/S but ordering of R2 (but according to Środoń and Eberl, (1984) R2 ordering does not exist) and locally R3 in their interpretations of the XRD traces points to high percentages of illite in I/S (more than 80%), however, the ordering in the Podhale Basin does not go beyond R1 (Środoń et al. in press).

The ATEM analyses using microprobe techniques on thin-sections are sometimes viewed as end-member phases rather than mixed-layer I/S, as the textural characterisation identified the analysed 'crystallite packets' as end-member phases on the scale of the electron beam (Ahn & Peacor, 1986a). How much the analyses in this study were end-member 'crystallite packets' cannot be assessed in the same way as no lattice fringe imaging was produced. Consequently, the samples in this study must be viewed as averages of mixed layer I/S, as in the study by Hover et al. (1999) where the same dispersion technique as used here was utilised. Chochołów-60 (76%I), Tatrzańska-06 (76%I), Bukowina Tatrzańska-41 (76%I) are mixed-layer phases but have the same Si/Al characteristics as end-member crystallite

packets. Chochołów-28 (56%I) has very low Si cation concentrations in the tetrahedral sheet and does not fit with the idea of analysing an average of mixed layer I/S as this would produced a higher Si cation concentration. The analysis of this sample may show the results of end-member illite that was inherited into the system as a sample with 56% illite in I/S does not have the necessary ordering of illite and smectite layers in a mixed phase to allow the analysis of end-member 'crystallite packets' within a mixed-layer phase (Ahn & Peacor, 1986a). It is known that I/S tends to have a higher (Mg + Fe) content and a lower Al/Si ratio than coexisting illite, regardless of the environment of formation prior to diagenesis (Frey, 1970; Foscolos & Kodama, 1974; Hower et al., 1976; Boles & Franks, 1979). So, it appears that coexisting illite has been analysed in this sample.

Chochołów-06 (50%I) has a variable Si/Al ratio, the high Si analyses are more comparable to the 40%I samples of Ahn & Peacor (1986a), albeit with a 10% difference in I/S. This demonstrates that there is a trend in Si/Al ratio as illitization proceeds and that there is not a jump in the ratio as is inferred by Ahn and Peacor (1986a).

There appears to be a relationship between %I in I/S and the Si/Al; ratio in the tetrahedral sheet, with illite rich I/S having less Si in the tetrahedral sheet than the smectite rich I/S, with the associated structural formulae being a function of the relative number of illite and smectite layers. It is possible to have relatively low Si cation concentrations in mixed-layer I/S (~3.4 cations) but with more than 90%I in I/S (R3 ordering). This therefore points to the composition of the starting material in a smectite to illite transition as being important in the context of the end-member structural formulae.

The quality of the structural formulae produced from the ATEM data has already been assessed, with octahedral totals within the 5% error of the EDS software (Brown, 2005, Pers. Comms.) and comparable to the published octahedral totals (e.g. Środoń et al., 1986) except where stated. It is important to note that the interlayer K (varying between 0.04 and 1.34) is in doubt due to beam mobilisation of light phases (van der Pluijm et al, 1988).

As a consequence, techniques such as Atomic Absorption Spectroscopy, DC Plasma-Emission Spectroscopy, Ignited weights, X-ray fluorescence give a better analysis of the interlayer but at the loss of the crystallite scale. Where K is low (less than 0.5 cations in the interlayer) it is insufficient to meet the charge needs of a mixed-layer I/S set up through substitution of Fe and Mg for Al in the octahedral sheet. As a result this study treats the interlayer with caution.

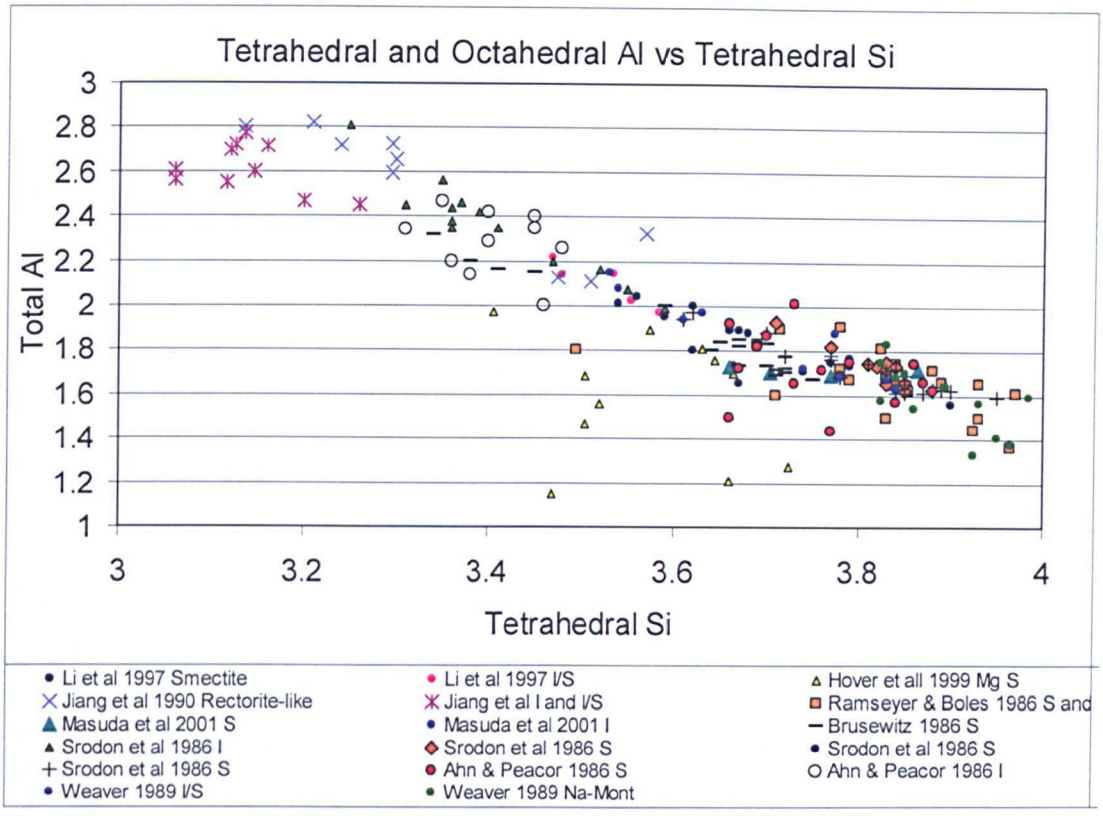

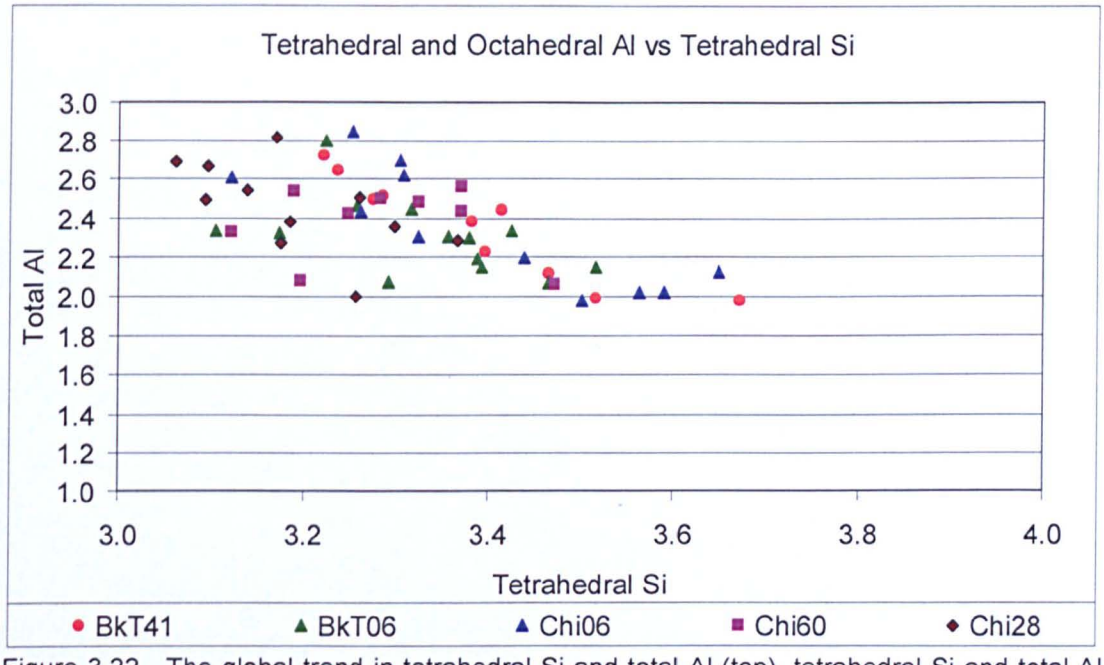

Figure 3.22. The global trend in tetrahedral Si and total Al (top), tetrahedral Si and total Al for Bukowina Tatrzańska-41, Bukowina Tatrzańska-06, Chochołów-06, Chochołów-28 and Chochołów-60, (bottom).

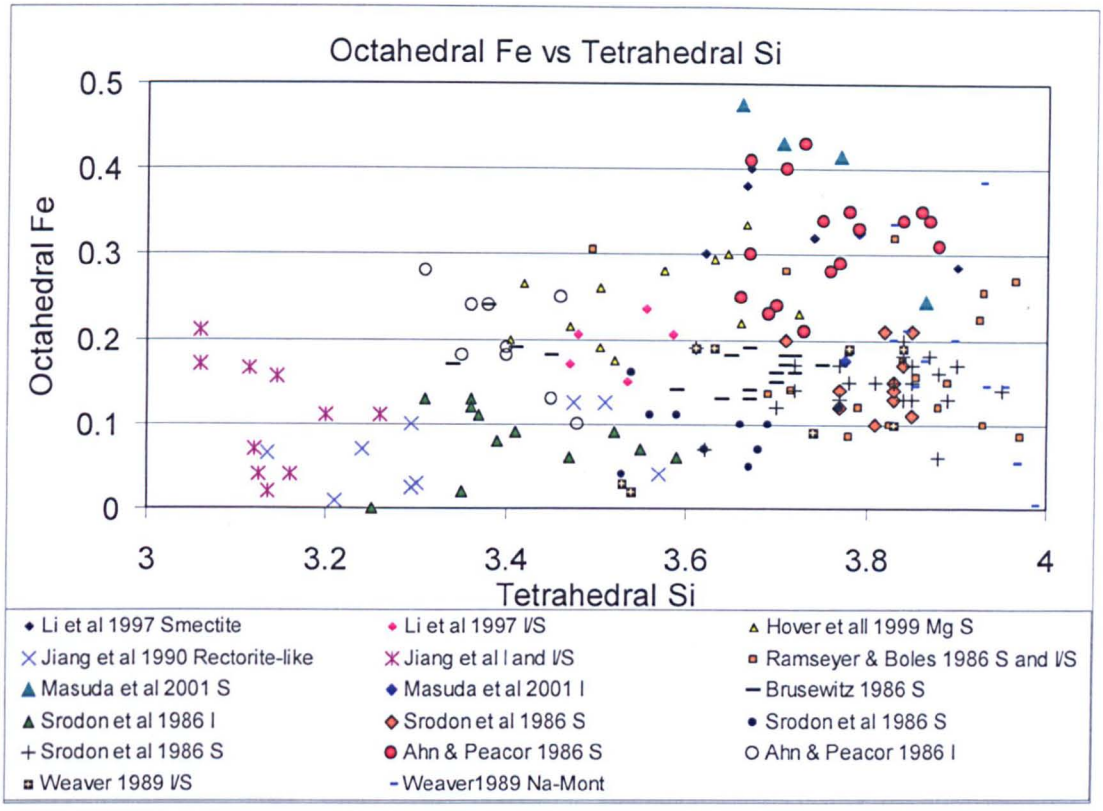

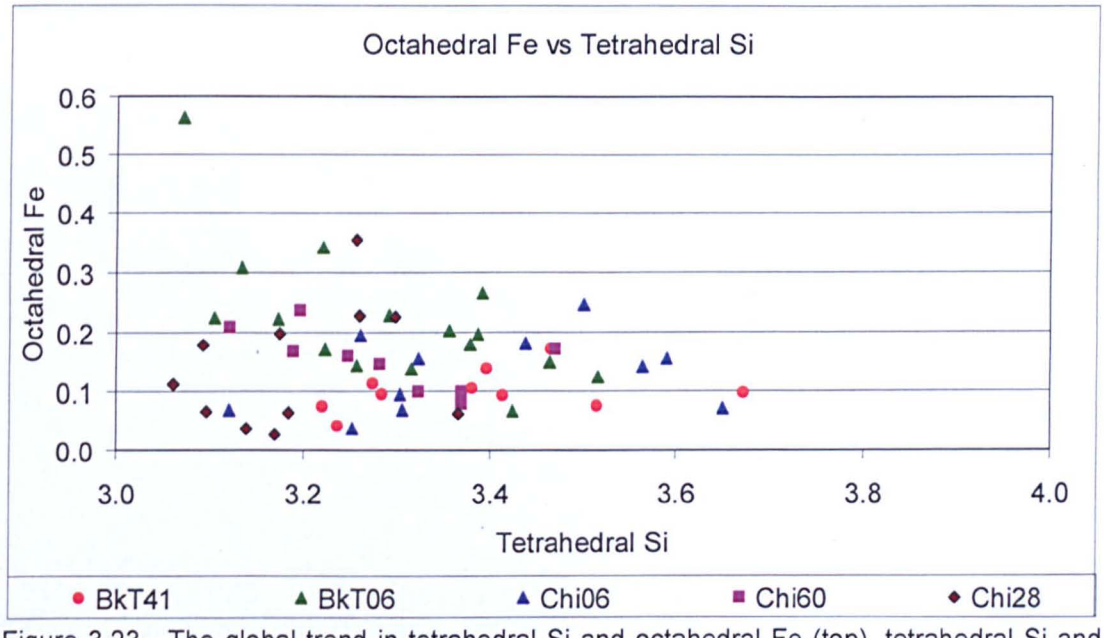

Figure 3.23. The global trend in tetrahedral Si and octahedral Fe (top), tetrahedral Si and octahedral Fe for Bukowina Tatrzańska-41, Bukowina Tatrzańska-06, Chochołów-06, Chochołów-28 and Chochołów-60, (bottom).

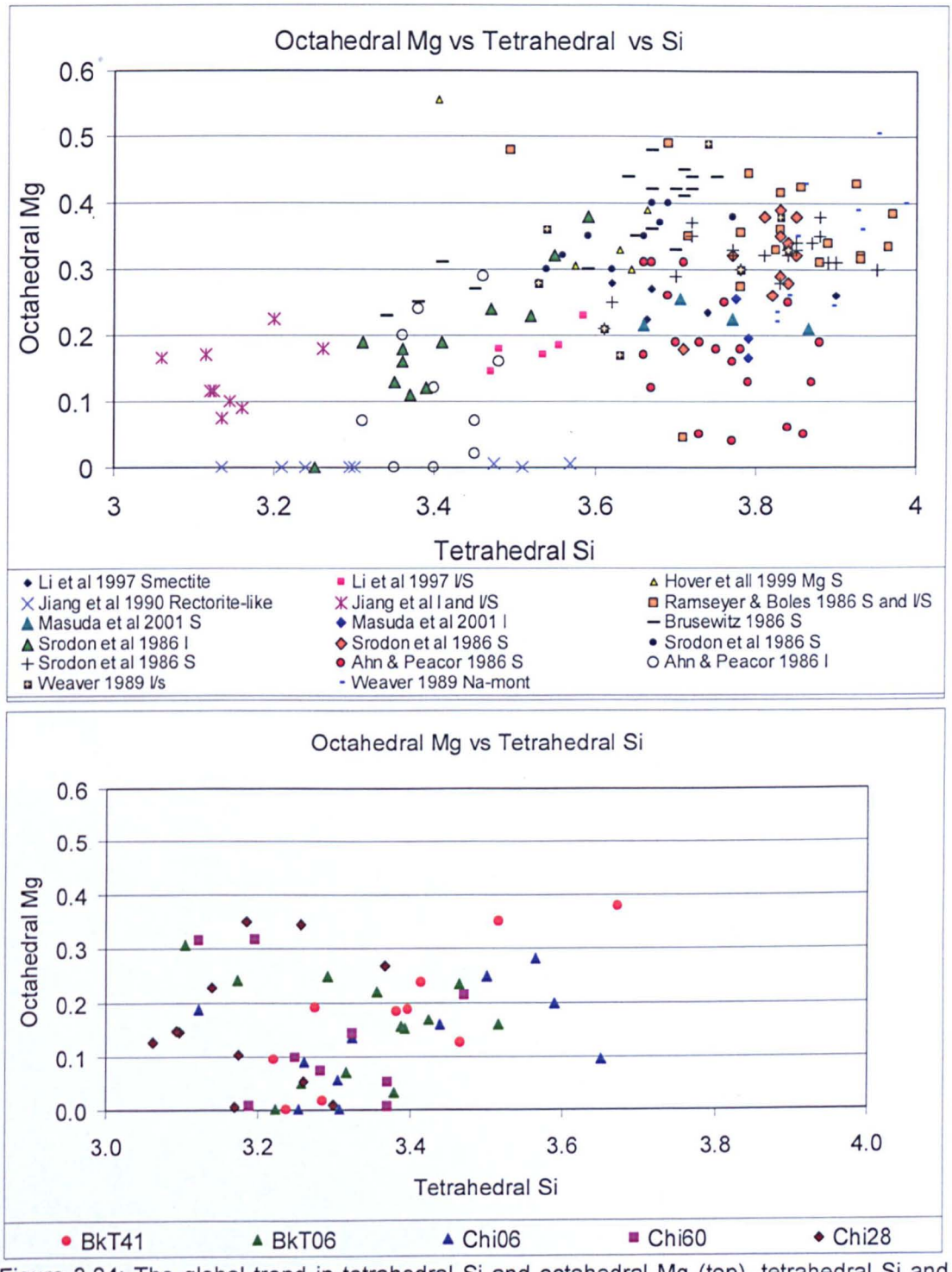

Figure 3.24: The global trend in tetrahedral Si and octahedral Mg (top), tetrahedral Si and octahedral Fe for Bukowina Tatrzańska-41, Bukowina Tatrzańska-06, Chochołów-06, Chochołów-28 and Chochołów-60, (bottom).

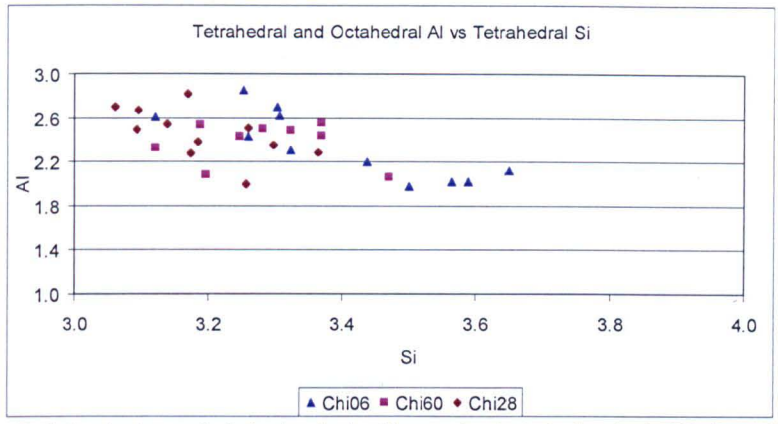

Figure 3.25: Octahedral and tetrahedral Al against tetrahedral Si for Chochołów-06, Chochołów-28, Chochołów-60

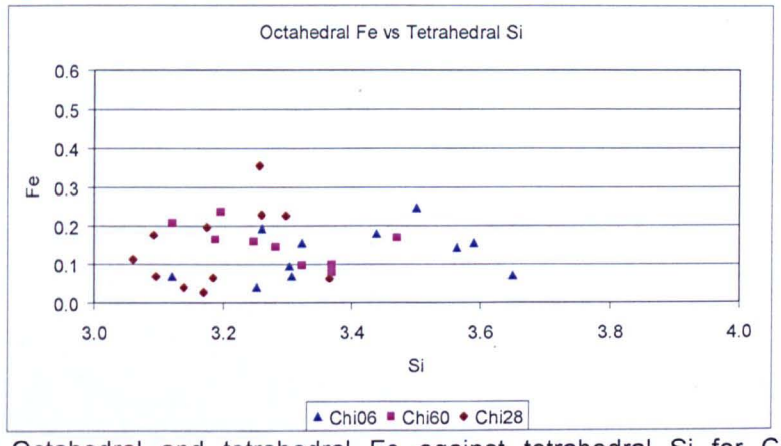

Figure 3.26: Octahedral and tetrahedral Fe against tetrahedral Si for Chochołów-06, Chochołów-28 and Chochołów-60

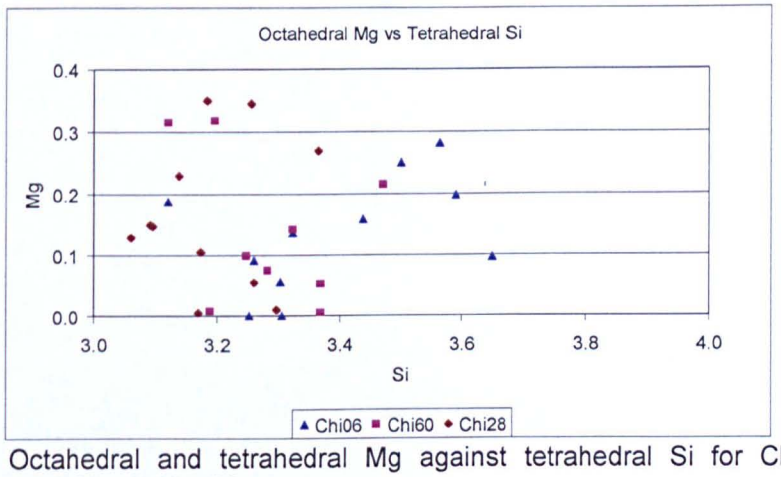

Figure 3.27: Octahedral and tetrahedral Mg against tetrahedral Si for Chochołów-06, Chochołów-28 and Chochołów-60

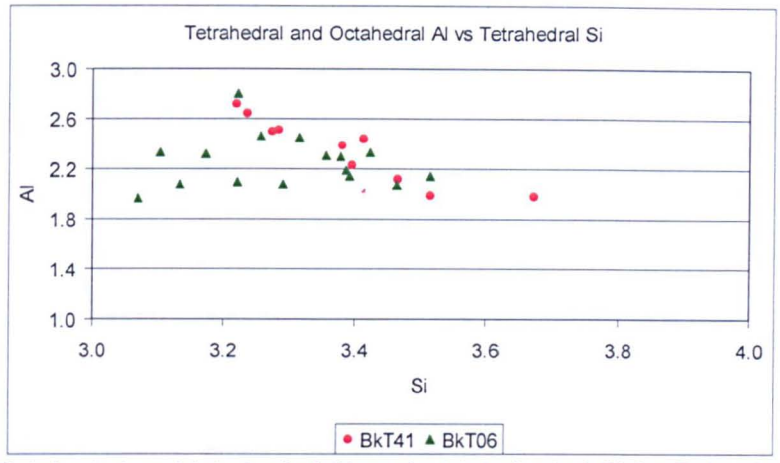

Figure 3.28: Octahedral and tetrahedral Al against tetrahedral Si for Bukowina Tatrzańska-06 and Bukowina Tatrzańska-41.

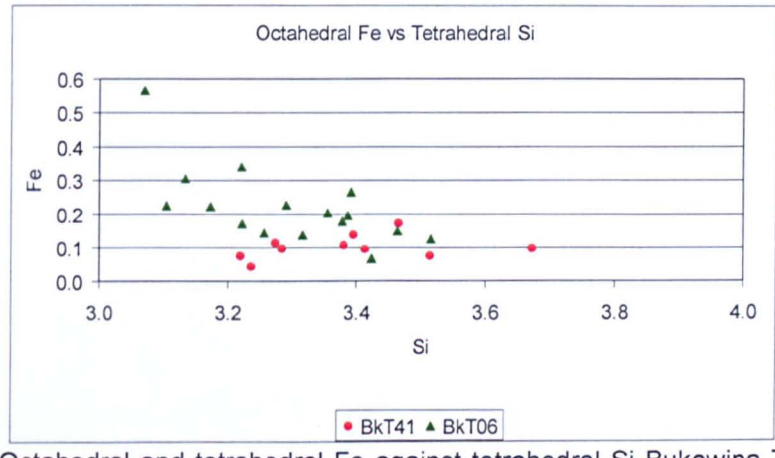

Figure 3.29: Octahedral and tetrahedral Fe against tetrahedral Si Bukowina Tatrzańska-06 and Bukowina Tatrzańska-41.

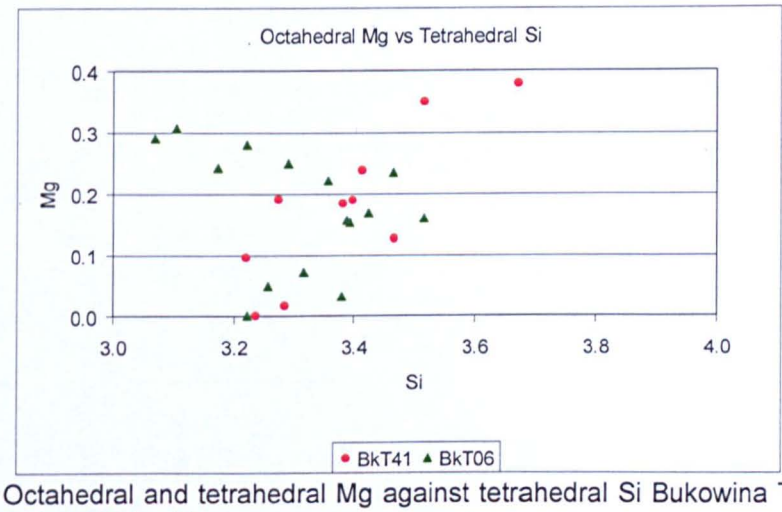

Figure 3.30: Octahedral and tetrahedral Mg against tetrahedral Si Bukowina Tatrzańska-06 and Bukowina Tatrzańska-41.

3.2.5: Tests of normality and distribution of the Structural Formulae: Kolmogorov-Smirnov Test:

Figure 3.26 and the average structural formulae quoted previously for Bukowina Tatrzańska-06 and Bukowina Tatrzańska-41 highlight an apparent difference between these two samples in terms of their octahedral Fe cation concentrations. These two samples, however, have the same percentage of illite in the mixed layer phase illite-smectite as recorded by XRD (76%). They are separated by ~2000m, which by taking the 21°C/km palaeogeothermal gradient quoted by Środoń et al. (in press) equates to a maximum temperature difference of ~40°C.

In this section the samples from the Podhale Basin will be statistically tested to see if Bukowina Tatrzańska-06 and Bukowina Tatrzańska-41 are different and how they compare to the other measured results from Chochołów-06, Chochołów-28 and Chochołów-60.

The Kolmogorov-Smirnov test (Chakravarti et al., 1967 and references within) is designed to determine if two datasets differ significantly. The Kolmogorov-Smirnov Test makes no assumption about the distribution of data. It is a distribution free test and is non-parametric. The Student's t-test only gives a reliable result if the data are normally distributed. The divergences from the expected normal concentrations calculated in the Kolmogorov-Smirnov test for the cumulative fractions (Whittaker & Robinson, 1967) test the normality of the distributed.

The Kolmogorov-Smirnov test is based on the empirical distribution function (ECDF). Given *N ordered* data points $Y_1, Y_2, ..., Y_N$, the ECDF is defined as

$$E_N = n(i)/N$$

where $n(i)$ is the number of points less than Y_i and the Y_i are ordered from smallest to largest value. This is a step function that increases by 1/N at the value of each ordered data point (Chakravarti et al., 1967).

The Kolmogorov-Smirnov Test is a robust test that cares only about the relative distribution of the data (Whittaker & Robinson, 1967) not its

adherence to normality or not, so it can deal with small datasets and does not make type I and type II errors, typical in the Student's t-test. If the t-test is applied to non-normal data, this increases the risk of error.

When comparing like data, for example the distribution of Fe cation concentration in the octahedral sheet, the Kolmogorov-Smirnov Test uses the maximum vertical deviation between the two curves as the D-statistic and describes the difference between these two datasets. The Kolmogorov-Smirnov Test does not care about the relative distribution no confidence interval need be applied. Since, cumulative fraction is plotted, a cumulative fraction total of 1.0 or 100%, the D-statistic is quoted as a percentage and the larger this percentage the more degree of difference there is between comparable compared data. In other words the D-statistic is a measure of separation.

3.2.5.1: Kolmogorov-Smirnov Test results, divergence from normality:

The divergence or adherence to normality for cations from Bukowina Tatrzańska-06, Bukowina Tatrzańska-41, Chochołów-06, Chochołów-28 and Chochołów-60 can be seen in Figures 3.31, 3.32, 3.33, 3.34, 3.35 & 3.36 and a summary of results may be seen in Table 3.15. The distribution of Si cation concentrations in Bukowina Tatrzańska-06 is nearly normal as it adheres closely to a straight line relationship as laid down by the Kolmogorov-Smirnov Test (Figure 3.31). The more 'bow-shaped' distribution of the Si cation concentration in Bukowina Tatrzańska-41 demonstrates a lack of normality. The method of plotting makes the x-axis comparable to that in Figure 3.22 and shows the spread of the data. Bukowina Tatrzańska-41, although not normally distributed has a more homogeneous distribution than Bukowina Tatrzańska-06.

The Fe cation concentration distributions in the octahedral sheet for Chochołów-06, Chochołów-28 and Chochołów-60 do not have a normal

distribution (Figure 3.35). Chochołów-60 is the closest to being normally distributed. Chochołów-06 is skewed by one data point that has caused the tail at the top of the distribution to form. ATEM analysis E013 has produced this tail. The same sample has high Mg and an octahedral total that is outside of 5% of 2.00, so this point is somewhat erroneous, however, by ranking the data in the Kolmogorov-Smirnov test the effect of this outlier on the distribution when compared to other data is negated. Consequently, no data points have been removed and this will have no effect on the D-statistic calculated in the next section.

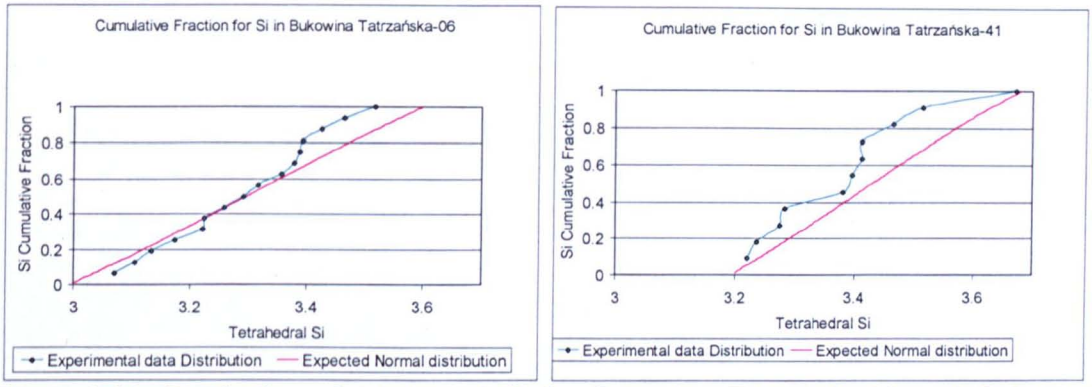

Figure 3.31. Distribution of tetrahedral Si for Bukowina Tatrzańska-06 and Bukowina Tatrzańska-41, relative to the expected normal distribution, both calculated in the Kolmagorov-Smirnov Test. Bukowina Tatrzańska-06 is nearly normal as it adheres closely to a straight line relationship, whereas Bukowina Tatrzańska-41 shows a divergence from normality.

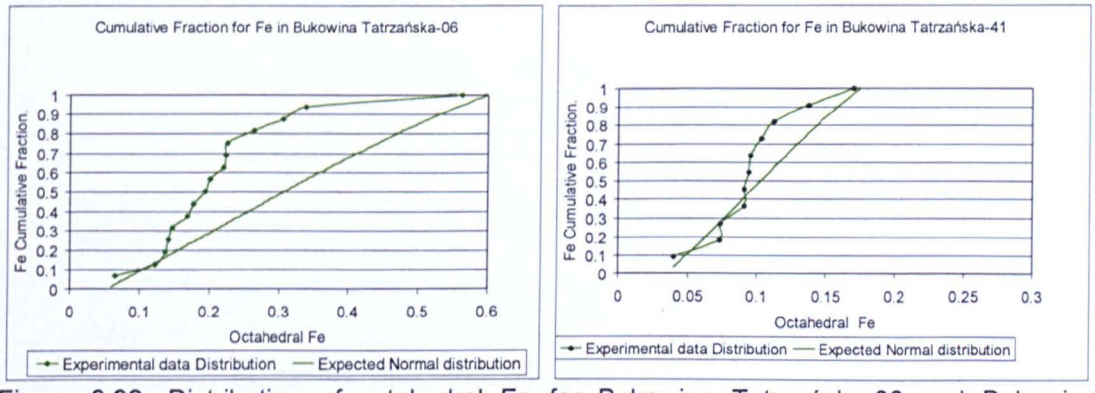

Figure 3.32. Distribution of octahedral Fe for Bukowina Tatrzańska-06 and Bukowina Tatrzańska-41, relative to the expected normal distribution, both calculated in the Kolmagorov-Smirnov Test. Bukowina Tatrzańska-06 and Bukowina Tatrzańska-41 shows a divergence from normality.

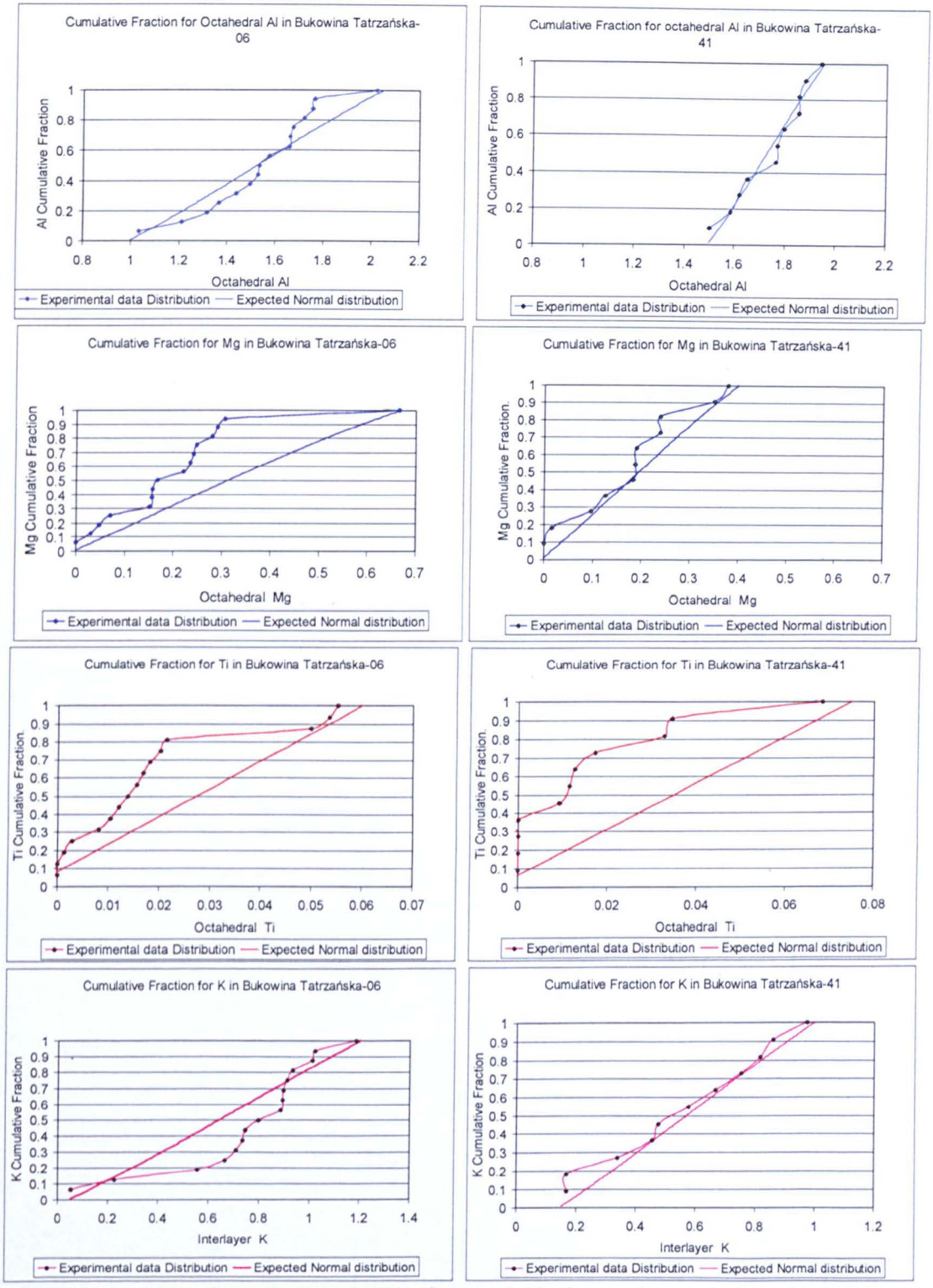

Figure 3.33. Distribution of octahedral Al (first row) Mg (second row) and the Ti (third row) and interlayer K (fourth row), for Bukowina Tatrzańska-06, left-hand column and Bukowina Tatrzańska-41, right-hand column, relative to the expected normal distribution, both calculated in the Kolmagorov-Smirnov Test. Only the Mg and Ti cation concentrations in Bukowina Tatrzańska-41 show a close to normal distribution.

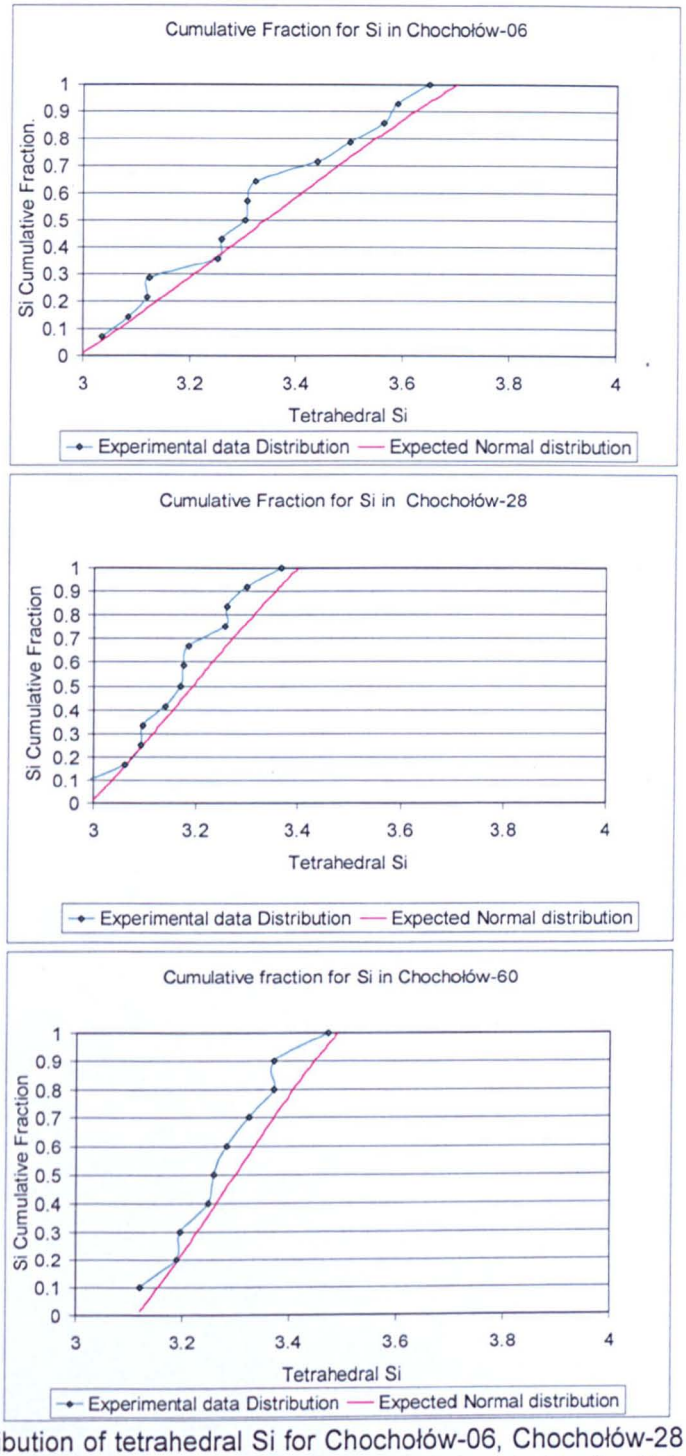

Figure 3.34. Distribution of tetrahedral Si for Chochołów-06, Chochołów-28 and Chochołów-60, relative to the expected normal distribution, both calculated in the Kolmagorov-Smirnov Test. Chochołów-06, Chochołów-28 and Chochołów-60 are nearly normal as the distributions adhere nearly to a straight line relationship.

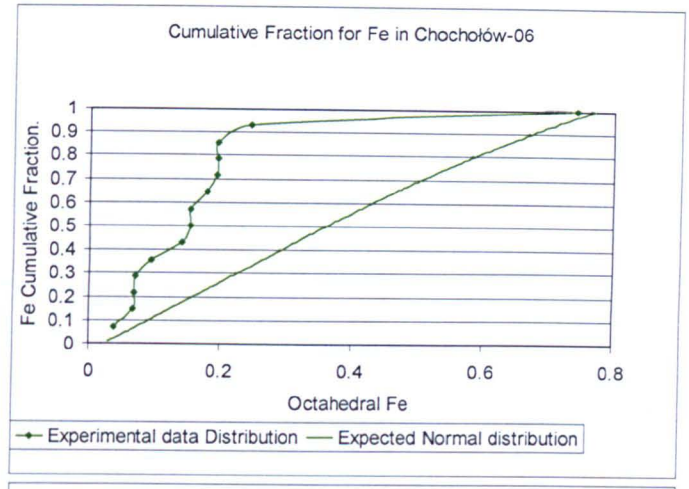

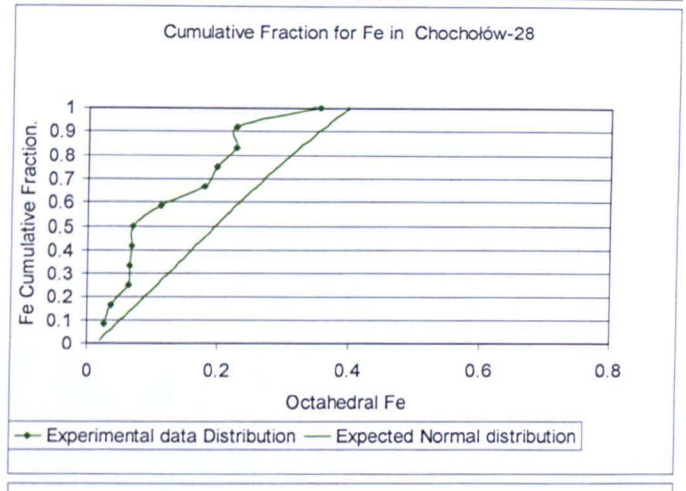

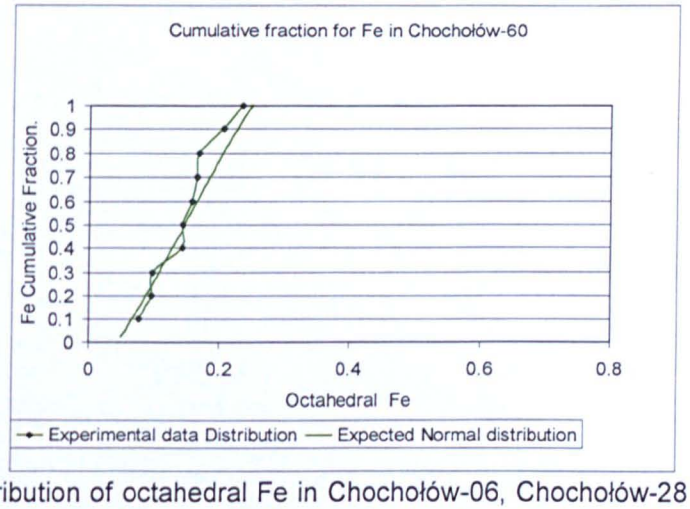

Figure 3.35. Distribution of octahedral Fe in Chochołów-06, Chochołów-28 and Chochołów-60, relative to the expected normal distribution, both calculated in the Kolmagorov-Smirnov Test. Chochołów-06, Chochołów-28 are not normally distributed as they do not adhere to a straight line relationship. Chochołów-60 is the closest to being normally distributed.

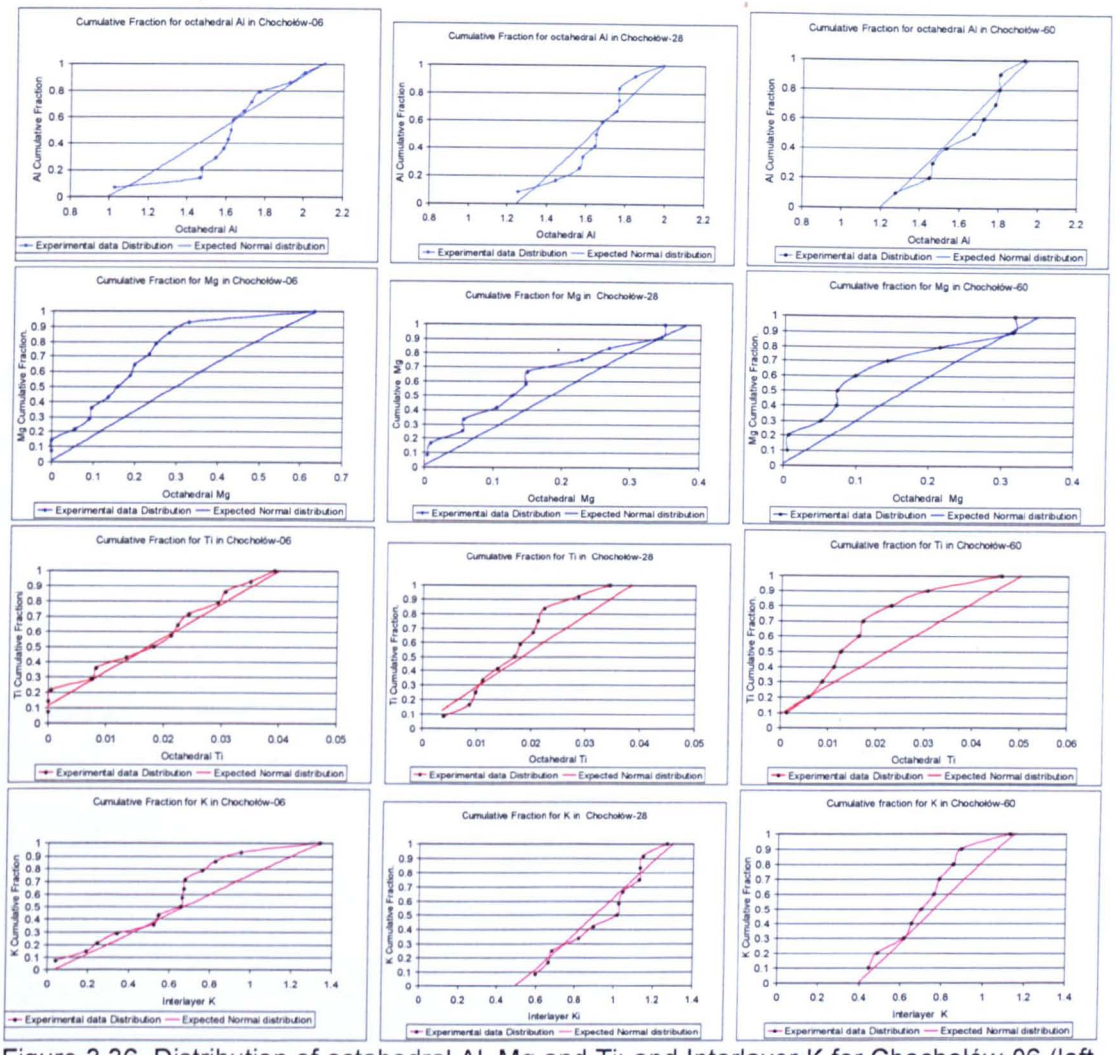

Figure 3.36. Distribution of octahedral Al, Mg and Ti; and Interlayer K for Chochołów-06 (left-hand column), Chochołów-28 (centre column), and Chochołów-60 (right-hand column), relative to the expected normal distribution, both calculated in the Kolmagorov-Smirnov Test. Only octahedral Ti cation concentration in Chochołów-06 and K interlayer cation concentration in Chochołów-28 have a near normal distribution.

Table 3.15. Adherence or divergence of the cation distributions in samples from the Podhale Basin. N=not normally distributed, (Y) is nearly normally distributed.

	Octahedral					
Sample	Si	Fe	Mg	Al	Ti	K
Bukowina Tatrzańska-06	(Y)	N	N	N	N	N
Bukowina Tatrzańska-41	N	N	N	(Y)	N	(Y)
Chochołów-06	(Y)	N	N	N	(Y)	N
Chochołów-28	(Y)	N	N	N	N	N
Chochołów-60	(Y)	Y	N	N	N	N

3.2.5.2: Kolmogorov-Smirnov Test results, divergence between samples:

All divergence between samples (D-statistic) may be viewed in Table 3.16 to 3.20, with the method for calculating the D-statistic demonstrated in Figures 3.37, 3.38 and 3.39.

Table 3.16. D Statistic difference between Bukowina Tatrzańska-06 and Bukowina Tatrzańska-41, Chochołów-06, Chochołów-28 and Chochołów-60.

	Bukowina Tatrzańska-06			
	Bukowina Tatrzańska-41	Chochołów-06	Chochołów-28	Chochołów-60
Element	D Statistic	D Statistic	D Statistic	D Statistic
Si	23	19	41	21
Fe	74	30	45	43
Mg	11	12	39	40
Al	46	19	31	11
Ti	15	20	15	12

Table 3.17. D Statistic difference between Bukowina Tatrzańska-41 and Bukowina Tatrzańska-06, Chochołów-06, Chochołów-28 and Chochołów-60.

	Bukowina Tatrzańska-41			
	Bukowina Tatrzańska-06	Chochołów-06	Chochołów-28	Chochołów-60
Element	D Statistic	D Statistic	D Statistic	D Statistic
Si	23	26	62	45
Fe	74	48	36	52
Mg	11	8	27	32
Al	46	33	40	44
Ti	15	23	32	26

Table 3.18. D Statistic difference between Chochołów-06 and Bukowina Tatrzańska-06, Bukowina Tatrzańska-41, Chochołów-28 and Chochołów-60.

	Chochołów-06			
	Bukowina Tatrzańska-06	Bukowina Tatrzańska-41	Chochołów-28	Chochołów-60
Element	D Statistic	D Statistic	D Statistic	D Statistic
Si	19	26	36	24
Fe	30	48	18	18
Mg	12	8	18	27
Al	19	33	10	14
Ti	20	23	18	22

Table 3.19. D Statistic difference between Chochołów-28 and Bukowina Tatrzańska-06, Bukowina Tatrzańska-41, Chochołów-06 and Chochołów-60.

	Chochołów-28			
	Bukowina Tatrzańska-06	Bukowina Tatrzańska-41	Chochołów-06	Chochołów-60
Element	D Statistic	D Statistic	D Statistic	D Statistic
Si	41	62	36	36
Fe	45	36	18	40
Mg	39	27	18	20
Al	31	40	10	18
Ti	15	32	18	20

Table 3.20. D Statistic difference between Chochołów-60 and Bukowina Tatrzańska-06, Bukowina Tatrzańska-41, Chochołów-06 and Chochołów-28.

	Chochołów-60			
	Bukowina Tatrzańska-06	Bukowina Tatrzańska-41	Chochołów-06	Chochołów-28
Element	D Statistic	D Statistic	D Statistic	D Statistic
Si	21	45	24	36
Fe	43	52	18	40
Mg	40	32	27	20
Al	11	44	14	18
Ti	12	26	22	20

The difference in the Si octahedral cation distribution between Bukowina Tatrzańska-06 and Bukowina Tatrzańska-41 is calculated to be 23% and is not significant (Figure 3.37). The D-statistic calculated for the Fe cation distributions in the octahedral sheet is statistically different (D=74%). This confirms the difference noted in the average structural formulae and in Figure 3.29. The D-statistics for the Mg (D=11%) and Ti (D=15%) cation distributions confirms no significant difference between Bukowina Tatrzańska-06 and Bukowina Tatrzańska-41. The difference in the Fe cation distribution is counter acted by the octahedral Al cation distribution (D=46%) and Figure 3.37 succinctly demonstrates this. The tetrahedral Al cation distribution is not plotted as it will have exactly the same D-statistic as the Si cation distribution. This is due to the fact that in assigning all the available Si to the tetrahedral sheet then completing the tetrahedral sheet cation occupancy with Al to a total of 4.00 cations, the tetrahedral Al will vary by the same factor as the Si cation concentration.

The D-statistic for the Si cation concentration in the Chochołów well does not show a significant difference between samples (Figure 3.38). Chochołów-28 has less Si than either Chochołów-06 or Chochołów-60, which in turn are similar to each other. Chochołów-28 differs from both Chochołów-06 and Chochołów-60, but Chochołów-06 is intermediate between Chochołów-28 and Chochołów-60. The Mg, Ti and Al cation concentrations do not differ significantly between samples.

The deep sample from the Chochołów well (Chochołów-60) has been compared to the Bukowina Tatrzańska well (samples Bukowina Tatrzańska-06 and 41 in Figure 3.39). Sample Bukowina Tatrzańska-06 overlaps with Chochołów-60 in terms of their depth ranges (Chapter 2; Środoń et al., in press). The Si cation concentrations do not differ significantly and both have characteristics of end-member illite (following the convention of Ahn and Peacor, 1986a). The Fe and Mg cation distributions differ by the same amount (~40%) with Bukowina Tatrzańska-06 having more octahedral substitution than Chochołów-60. Chochołów-60 represents an intermediate position between Bukowina Tatrzańska-06 and Bukowina Tatrzańska-41 in terms of their Si and Fe cation distributions. Figure 3.39 suggests that Chochołów-60 differs in the amount of Mg substitution in the octahedral sheet.

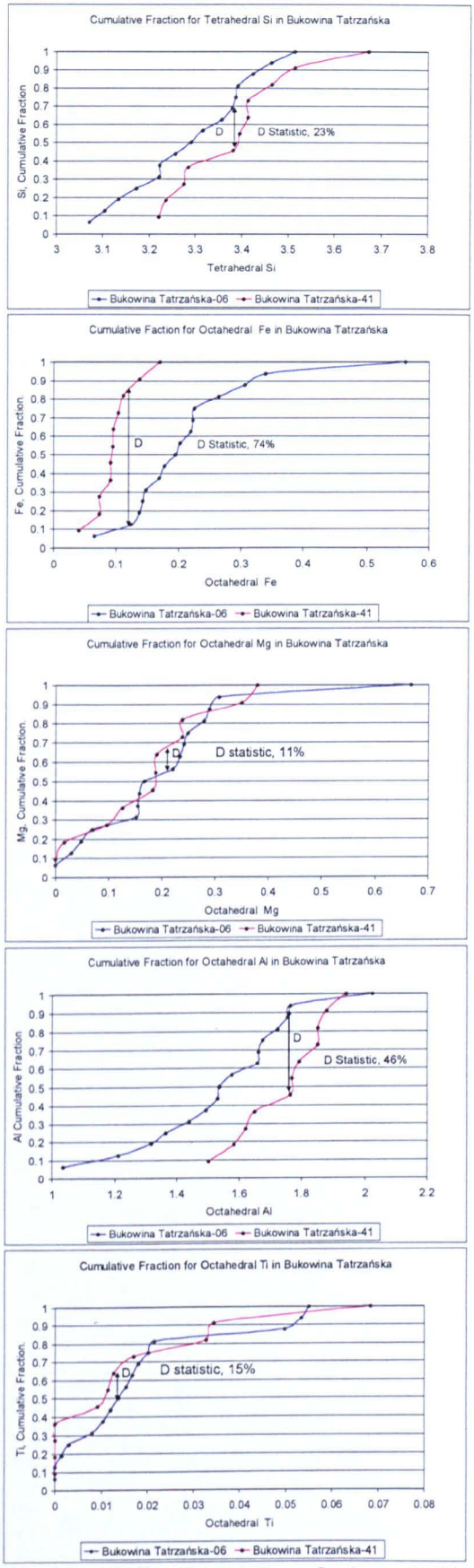

Figure 3.37. D-statistic calculated in the Kolmogorov-Smirnov test highlighting the difference between samples in the Bukowina Tatrzańska well. A high D-statistic in the Fe and Al concentrations shows a significant difference, low D-statistic in the other cation concentrations shows no significant difference.

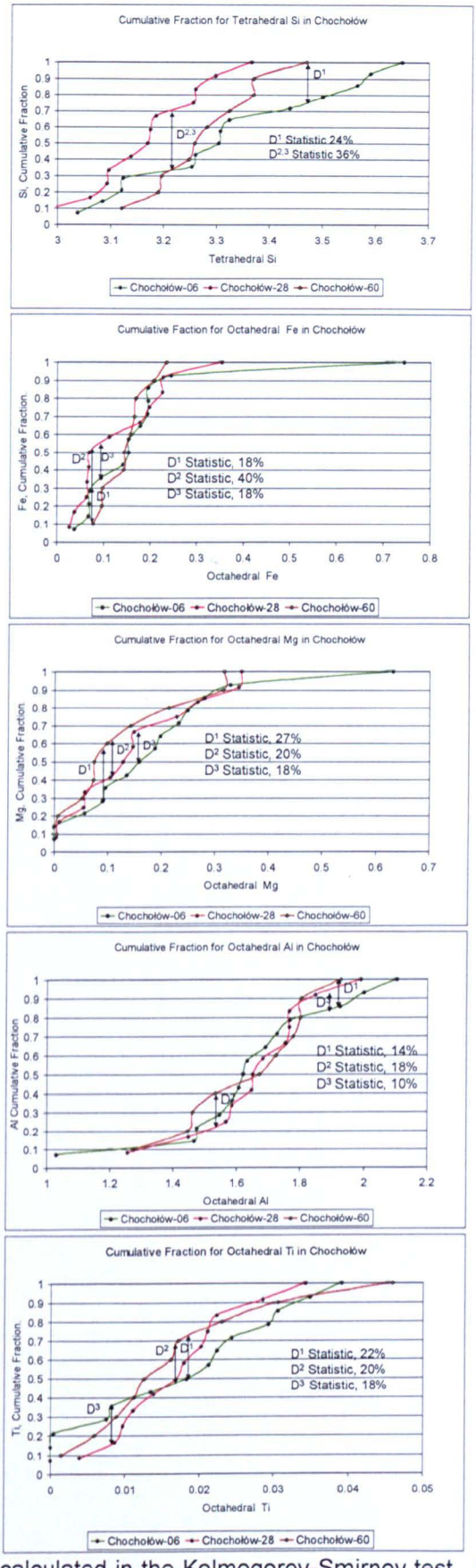

Figure 3.38. D-statistic calculated in the Kolmogorov-Smirnov test. D^1= difference between Chochołów-06 and Chochołów-60, D^2= difference between Chochołów-28 and Chochołów-60, D^3= difference between Chochołów-28 and Chochołów-06.

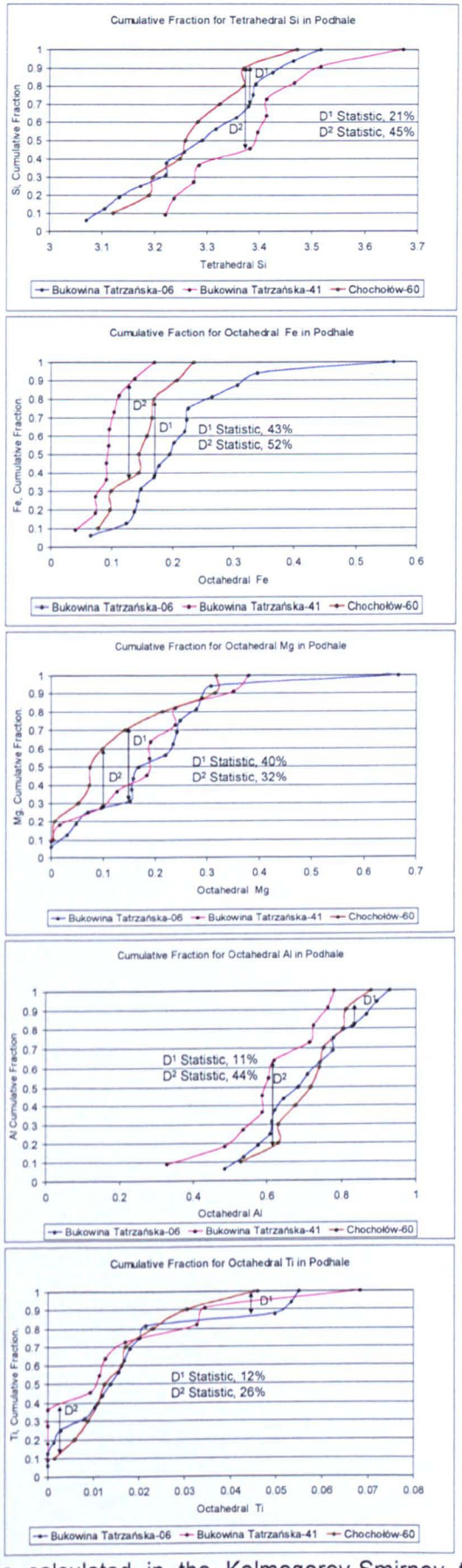

Figure 3.39. D-statistic calculated in the Kolmogorov-Smirnov test for how Bukowina Tatrzańska-06 compares with Chochołów-60 (D^1) and Bukowina Tatrzańska-41 with Chochołów-60 (D^2).

3.2.6: Selected Area Diffraction Patterns (SADP):

The SADPs presented in Figures 3.40 and 3.41 represent the end member samples of the illitization of smectite in the Podhale Basin. Presented are four SADPs for Bukowina Tatrzańska-41 (Figure 3.40) and four SADPs for Chochołów-06 (Figure 3.41) and these diffraction patterns may be cross referenced with the ATEM data for these samples presented in Table 3.10 and Table 3.11 respectively. Bukowina Tatrzańska-41_C005 shows a good single crystal pattern with clear hexanets, there is some evidence for lattice defects seen in the irregular brighter diffraction spots. Bukowina Tatrzańska-41_C010 shows a dominant crystal pattern but the less bright diffuse spots and small ring structures hint at a slight polycrystalline stacking. The polycrystalline turbostratic layering may be observed in Bukowina Tatrzańska-41_C012, the diffuseness of the spots is clear however as they are centred on the same spot it is the same phase diffracting the electron beam and that what is seen are stacking effects in a thick crystal, although no crystal thickness measurements are offered in this study. Bukowina Tatrzańska-41_C014 is similar to Bukowina Tatrzańska-41_C005 in that a single crystal has been selected and that there are irregular, brighter spots indicating crystal defects. The two samples do not have the same defects. When these four SADPs are cross referenced with the ATEM data what becomes evident is that Tatrzańska-41_C005 and Tatrzańska-41_C014 have very low amounts of substitution of Fe and Mg for Al in the octahedral sheet and low tetrahedral Si concentrations (below 3.25 cations). The other two samples have a lot of substitution, so producing a single crystal pattern appears related to substitution, which enhances the turbostratic arrangement in these crystals.

Chochołów-06_E007 is a single crystal diffraction pattern with some turbostratic stacking, however the irregular bright spots in the diffraction spot arrangement points to crystal defects. Chochołów-06_E017 has crystal defects but is a good single crystal with little turbostratic stacking. Chochołów-06_E026 and Chochołów-06_E030 exhibit turbostratic stacking and the interaction of two discrete phases. One phase is dominant and has

some crystal defects that have diffracted the electron beam irregularly. The ATEM data for Chochołów-06_E007 and Chochołów-06_E017 show low substitution of Fe and Mg for Al in the octahedral sheet and a low concentration of Si in the tetrahedral sheet. Conversely, Chochołów-06_E026 and Chochołów-06_E030 have significantly higher amounts of octahedral substitution and relatively higher Si concentrations.

On the other hand the variability in chemistry associated here could be due to the beam interacting with a thick grain that is comprised of more than one phase or two grains overlying each other in the dispersion under the beam, thereby creating an artificial 'mixed-phase'.

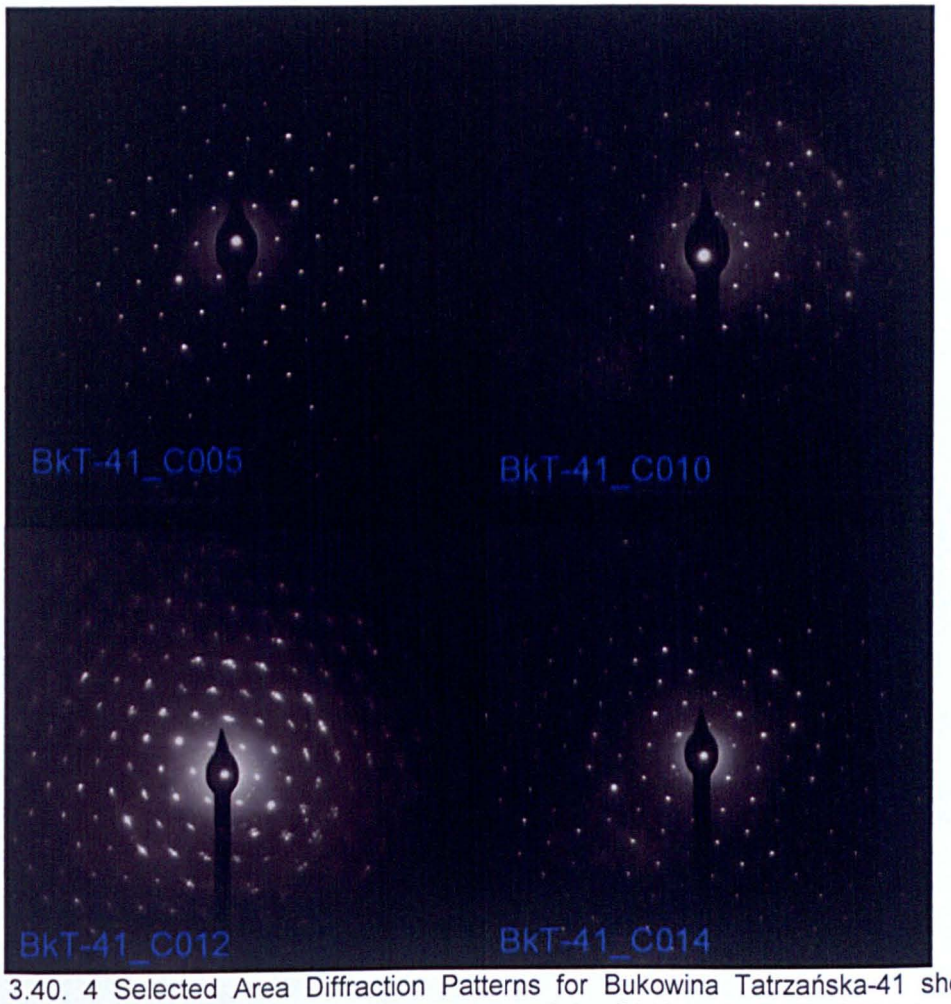

Figure 3.40. 4 Selected Area Diffraction Patterns for Bukowina Tatrzańska-41 showing variable crystal structures. C005, top left, C010, top right, C012, bottom left, C014, top right. Structural formulae and wt% oxides for each can be seen in Table 3.10. Coo5 and C014 are single crystal patterns. A slight ring pattern in C010 is from polycrystalline stacking.

In comparing SADP (Figures 3.40 and 3.41) with their associated structural formulae what may be noted is that there is a relationship between Si:Al ratio

and diffraction pattern. Where the ratio is close to 3:1, single crystal patterns are more evident (Bukowina Tatrzańska-41 C005 and C014). Additionally, the cleanliness of the octahedral sheet has an effect on the nature of the SADP produced. Where few Fe and Mg cations have substituted for Al cations in the octahedral sheet the diffraction patterns are more developed into single crystal arrangements (e.g. Bukowina Tatrzańska-41 C005, Chochołów-06 E017). Diffraction pattern E030 (Chochołów-06) demonstrates that the Si:Al ratio in the tetrahedral sheet appears to be the more dominant factor in single crystal diffraction pattern formation as it has a ratio of 3.04:0.96 but 0.55 Fe, Mg and Ti substitutions for Al in the octahedral sheet yet has produced a clear single crystal pattern.

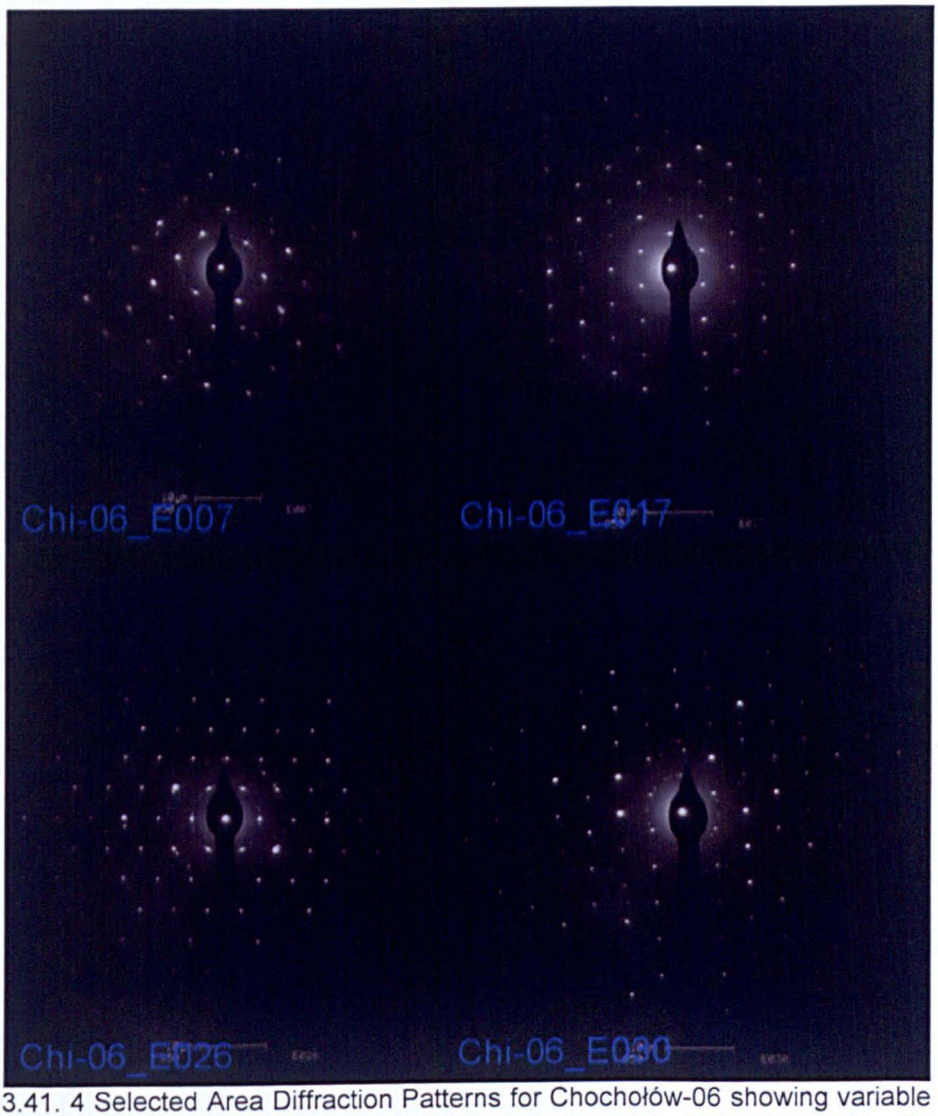

Figure 3.41. 4 Selected Area Diffraction Patterns for Chochołów-06 showing variable crystal structures. E007, top left, E017, top right, E026, bottom left, E030, top right. Structural formulae and wt% oxides for each can be seen in Table 3.11. Single crystal patterns show some crystal deflects noticeable from large irregular spaced diffraction spots.

Similar patterns have been noted by various workers (e.g. Dong & Peacor, 1996; Kim et al., 2004; Hover et al., 1999), in which smectite has produced ring patterns whereas pure illite has produced single crystal patterns, but most of this work has been done using ion beam thinning to produce the working surface rather than dispersion and identification was through lattice fringe imaging rather than a chemical identification. All SADPs may be viewed in Appendix 3.3.

3.2.7: Indexing Selected Area Diffraction Patterns:

The SADP for the illite standard crystal R007 has been previously indexed to a characterised sample from the PDF database.

The other SADPs in this study have not been indexed in the same way. This is because they are numerous and the benefits of indexing are small due to the inherent inaccuracies of the technique as already noted. The two significant sources of error in the indexing are the initial measurements of the distances between diffraction spots and the camera length used in the analysis. Therefore, with these inaccuracies in mind the approach taken to indexing the other SADPs is to use a comparison approach between them and R007. The comparison was done by overlaying the negatives of R007 and each diffraction patterns in turn. The overlaying of negatives can actually be done with more accuracy than measuring the distance between diffraction spots. Three types of diffraction patterns were then defined relative to R007. An exact match was recorded where all the diffraction spots overlaid exactly with those of R007. A close match was recorded where the diffraction pattern did not exactly match R007 but the pattern was within ~0.2mm, either because of ring formation or because defining the exact 'centre' spot was not possible due to over exposure of the negative producing a very large 'centre' spot and general diffraction spots. No match was recorded when the diffraction pattern clearly did not match R007 and was not close to being recorded as a close match. Clearly, there is some

subjectivity involved in deciding what is a close match and what is not, but it is no more inaccurate than deciding whether the distance between spots is 5.90mm or 5.92mm using a standard ruler.

Chlorite produced a diffraction pattern with much increased 'r' values (see previous section for definition), so confusing a chlorite with an 'illite' did not occur.

Single crystal patterns or stacked crystal patterns were also noted and as previously stated these appear to have a relationship to the Si:Al ratios in the tetrahedral sheet and to the amount of octahedral substitution in the structural formulae.

Where single crystals have a SADP that yields an exact match with R007, it is noticeable that the structural formulae are not identical (Table 3.21). R007 has a Si:Al ratio of 3.53:0.47 and Fe, Mg and Ti substitution for Al of 0.48. The matched pattern often have different ratios such as H003 and H013 (Bukowina Tatrzańska-06) that are ~3.35:0.64, Si:Al. Also, H013 has much less octahedral substitution (0.22 cations).

This relationship is not true for Bukowina Tatrzańska-41 and Chochołów-06 where the samples that match have very similar Si:Al ratios to R007. Mismatches or matches in structural formulae between samples that have exact SADP matches with R007 also occur for Chochołów-28 and Chochołów-60. Consequently the relationship between the indexed sample and those with exact matches are not clear in terms of their structural formulae and could be the effects of polytypes (Moore & Reynolds, 1997) or complex 'double diffraction' (Moore & Reynolds, 1997; Goodhew & Humphrey, 1988).

Table 3.21: SADP for the 5 samples from the Podhale Basin compared to the indexed illite standard sample R007. (n/a – no available information)

Sample	Match relative to illite standard R007	Single Crystal or Stacked
Bukowina Tatrzanska-06		
H003	Exact Match	Turbostratic
H007	Close Match	Single Crystal Pattern
H009	No Match	Single Crystal Pattern
H011	No Match	Single Crystal Pattern
H013	Exact Match	Single Crystal Pattern
H015	No Match	Single Crystal Pattern
H018	Close Match	Single Crystal Pattern
H020	Close Match	Single Crystal Pattern
H024	No match	Turbostratic
H026	No SADP	n/a
H028	No SADP	n/a
H030	No SADP	n/a
H032	No SADP	n/a
H034	No SADP	n/a
Bukowina Tatrzanska-41		
C001	No Match	Turbostratic
C003	Close Match	Single Crystal Pattern
C005	Close Match	Single Crystal Pattern
C007	Close Match	Turbostratic
C010	Exact Match	Single Crystal Pattern
C012	No Match	Turbostratic
C014	Close Match	Single Crystal Pattern
C016	Close match	Turbostratic
C018	Close Match	Single Crystal Pattern
C020	Close Match	Turbostratic
CT	No SADP	n/a
Chocholow-06		
E001	No Match	Turbostratic
E003	No Match	Turbostratic
E005	Close Match	Single Crystal Pattern
E007	No Match	Turbostratic
E009	No Match	Single Crystal Pattern
E011	No Match	Single Crystal Pattern
E013	No Match	Turbostratic
E017	Close Match	Single Crystal Pattern
E019	Exact Match	Single Crystal Pattern
E021	Close Match	Turbostratic
E024	No Match	Turbostratic
E026	Close Match	Turbostratic
E028	Close Match	Single Crystal Pattern
E030	No Match	Single Crystal Pattern
Chocholow-28		
K009	No Match	Single Crystal Pattern
K011	No Match	Single Crystal Pattern
K013	Exact Match	Single Crystal Pattern
K015	Exact Match	Single Crystal Pattern
K017	Exact Match	Single Crystal Pattern
K021	No Match	Single Crystal Pattern
K025	Exact Match	Single Crystal Pattern
K027	Close Match	Single Crystal Pattern
K029	Close Match	Single Crystal Pattern
K031	Close Match	Single Crystal Pattern
K033	Exact Match	Single Crystal Pattern
Chocholow-60		
J001	Close Match	Single Crystal Pattern
J005	Exact Match	Single Crystal Pattern
J007	Close Match	Single Crystal Pattern
J009	Exact Match	Single Crystal Pattern
J011	Close Match	Single Crystal Pattern
J013	Exact Match	Single Crystal Pattern
J015	Close Match	Single Crystal Pattern
J017	Close Match	Turbostratic
J019	Close Match	Single Crystal Pattern
J021	No Match	Turbostratic

3.3: Discussion:

3.3.1: Statistical differences between samples in the Podhale Basin and the relation to I/S change:

XRD has revealed a difference in the %I in I/S between the 5 samples analysed by ATEM to produce the structural formulae already stated. Chapter 2 has demonstrated that maximum burial depths differ greatly from present day burial depths (Table 3.22).

Table 3.22. Sample, present day depth[m] and maximum burial depth[m] for the 5 samples analysed by ATEM

Sample	Present day depth [m]	Maximum Burial depth [m]
Chochołów-06	280	3780
Chochołów-28	1283	4783
Chochołów-60	2611	6111
Bukowina Tatrzańska-06	293	6400
Bukowina Tatrzańska-41	2200	8307

The Kolmogorov-Smirnov Test has demonstrated that most of the cations in the structural formulae of the 5 analysed samples are not normally distributed and as a consequence an appreciation of the D-statistic from the Kolmogorov-Smirnov Test allows the differences between the samples to be judged.

The D-statistic from the Kolmogorov-Smirnov Test reveals that there is only a small difference between Chochołów-06 and Chochołów-60 in terms of their structural formulae, (D-statistics are: Si 24%, Fe 18%, Mg 27%, Al 14%, Ti 22%) for an increase in the %I in I/S from 50% to 76% (R0 to R1 ordering) yet there are consistent diagenetic increases and decreases in other minerals (Table 3.23, see Chapter 2).

There is less Si cation concentration in Chochołów-60 than in Chochołów-06 (24%) decrease is offset by the Al cation concentrations (14%), which also balances the substitutions of Fe (18%) and Mg (27%) to give a structural formulae total of 6.00 cations.

Table 3.23. The mineralogy of Bukowina Tatrzanska PIG-1 by QXRD (From Środoń et al, in press), where Qtz=Quartz, K-Fsp=K-feldspar, Pl=Plagioclase, Cal=Calcite, Dol=Dolomite, Hal=Halite, Py=Pyrite, Ant=Antase, Kln=Kaolinite, 2:1(I+M+Fe-S)= undifferentiated Illite, Mica, Iron-smectite, Chl=Chlorite.

Sample	Present day Depth [m]	Maximum Burial depth [m]	Qtz	K-Fsp	Pl	Cal	Dol	Hal	Py	Ant	Kln	2:1 (I+M+Fe-S)	Chl	Total clay	Total	K_2O (%)
Chł-4	193.4	3693.4	19	2.2	3	7.7	3.8	0	1.5	0	3.2	45.8	0.7	49.7	86.9	3.62
Chł-6	280.1	3780.1	24.3	2.3	5.9	10.2	5.4	0	1.5	0	1.5	46.8	4	52.3	102.3	3.56
Chł-12	513.5	4013.5	18.5	2.2	3.7	11.9	3.5	0	1.2	0	3.2	50.2	2.6	56	97.3	3.21
Chł-20	820.5	4320.5	22.9	1.5	4.7	10.5	4.1	0	0.7	0	3.6	49.2	2.1	54.9	100	2.95
Chł-23	1031.2	4531.2	21.7	1.3	3.6	10	4.5	0	0.9	0.2	2.9	43.9	2.6	49.4	92.4	2.9
Chł-28	1283.1	4783.1	20.4	0.5	5.7	10.4	4.7	0	2.3	0	2.6	49.1	3.6	55.3	99.3	3
Chł-38	1671.1	5171.1	16.3	1.5	5	0.9	4.5	0.6	2.3	0.6	1	60.8	7.4	69.2	100.9	4.7
Chł-44	2011.5	5511.5	26	1	7	3.7	6.2	0.5	2.5	0.4	1	53.9	5.2	60.1	107.6	3.4
Chł-56	2410.4	5910.4	20.5	0.5	6.5	3.6	5.2	1.2	1.8	0.5	0.8	60.1	4.8	65.7	105.5	4.24
Chł-60	2611.3	6111.3	27.5	0.4	9	13.2	4.6	0	1.2	0.7	0	41.1	4.7	45.8	102.6	2.9
Chł-66	2967.5	6467.5	22.4	0.5	6	17	6.7	0	1.5	0.5	0	41.8	4.2	46	100.8	2.9

The equations of Boles and Franks (1979) and Hower et al. (1976) attribute I/S change to smectite converting to illite with Fe and Mg released, this Fe and Mg release from the octahedral sheet of a smectite or mixed layer phase is seen clearly in the global data set (Figures 3.23 and 3.24). So if the ATEM technique as used here has taken an average of the interstratified I/S 'crystallite packet' the 26% difference in I/S between Chochołów-06 and Chochołów-60 in terms of the %I in I/S by XRD has been represented as a 24% difference in the Si cation concentration in the tetrahedral sheet of the structural formulae. Chochołów-06 and Chochołów-60 are distinct in that they show a decrease in tetrahedral Si consistent with increasing illite character and implies a release of silica into the system (Hower et al, 1976) or as quartz (Boles & Franks, 1979).

As has already been discussed Chochołów-28 does not fit with this trend as the 'crystallite packets' analysed have different characteristics to those of Chochołów-06 and Chochołów-60. With the implication that the 'crystallite packets' analysed from Chochołów-28 represent a localised phenomena of illite-rich packets that are not reflective of the sample as a whole as the bulk

analysis by XRD suggests a much higher %I in I/S that is inferred from the structural formulae calculations alone.

3.3.2: Iron ratios in Bukowina Tatrzanska-06 and Bukowina Tatrzanska-41; Relation to QXRD and Rc:

There is no significant difference between the Si cation concentration in samples from Bukowina Tatrzanska-06 and Bukowina Tatrzanska-41 (Figure 3.37). There is a significant difference in Fe cation concentrations (Figures 3.29 and 3.37). This difference is not marked by the Mg cation concentration, consequently it is the octahedral Al concentration that is higher in compensation. XRD (Chapter 2) indicates these samples have the exact same percentage of illite in I/S (76%), further they are separated by some 2000m and this according to Środoń et al (in press) corresponds to a temperature difference of nearly 40°C [their calculated geothermal gradient is 21°C/km and is close to the present day recorded geothermal gradient of 19-23°C Cebulak et al, (2004)]. At 76% illite in I/S the palaeo-temperature in the Podhale Basin is around 130°C and this smectite in I/S at this temperature is in keeping with studies from the North Sea (Lanson et al., 2002). Consequently, the base of Bukowina Tatrzanska is at ~170°C plus with apparently no change in I/S from that which was present at 130°C.

While no change in the percentage of illite in I/S has been recorded the Theoretical Vitrinite Reflectance (R_c) as tabulated in chapter 2 (after Rospondek & Marynowski, 2004 and Marynowski 2005 pers. comms), which is directly comparable to Vitrinite Reflectance (Vr) and has been calculated from the Methylphenanthrene Index (MPI) (Radke & Welte 1981), has been shown to increase from 0.89 to 1.37 (from sample Bukowina Tatrzańska-06 to sample Bukowina Tatrzańska-35, no result from Bukowina Tatrzańska-41 has been recorded). So where by XRD no mineralogical change has been seen to occur considerable organic maturation has occurred and is a function of the increased temperature down the borehole.

The average mineral formulae and the D-statistic from the Kolmogorov-Smirnov Test suggest that the only significant differences in terms of mineral chemistry between these two samples are the loss of iron which is replaced in the octahedral sheet by aluminium and the decrease in interlayer potassium as the effects of layer substitution decreases (change in valency, as some Fe is Fe^{2+} and not all Fe^{3+}) the need for charge compensation in the interlayer.

The differences between Bukowina Tatrzańska-06 and Bukowina Tatrzańska-41 may result from diagenetic change assuming homogeneous starting materials or inherited from heterogeneous input into the basin at the time of sedimentation that has lead to different chemical characteristics as recorded by the structural formulae.

Table 3.24. The chemistry of Bukowina Tatrzanska PIG-1 by QXRD (From Środoń et al, in press), where Qtz=Quartz, K-Fsp=K-feldspar, Pl=Plagioclase, Cal=Calcite, Dol=Dolomite, Hal=Halite, Py=Pyrite, Ant=Antase, Kln=Kaolinite, 2:1(I+M+Fe-S)= undifferentiated Illite, Mica, Iron-smectite, Chl=Chlorite.

Sample	Present day Depth [m]	Maximum Burial Depth [m]	Qtz	K-Fsp	Pl	Cal	Dol	Hal	Py	Ant	Kln	2:1 (I+M+Fe-S)	Chl	Total clay	Total	K_2O (%)
BkT-1	102.2	6208.5	26.6	0.8	7.1	9.5	7.5	0	0.9	0.5	0.8	53.6	5.6	60	112.9	3.5
BkT-6	293.7	6400	25.2	0.5	6.8	7.3	6.5	0	0.9	0.5	0.5	54.3	5.6	60.4	108.6	3.55
BkT-12	610.5	6716.8	27	1	6.6	5.4	7.6	0	1.2	0.5	0	52	6.1	58.1	107.4	3.1
BkT-17	902.7	7009	24.1	0.5	5.3	6.9	6.9	0.5	1.3	0.5	0	48.1	3.1	51.2	97.2	3.3
BkT-23	1261.2	7367.5	23.3	1	4.5	6.1	7.8	0	1	0.4	0	50.7	4.2	54.9	99	3.3
BkT-28	1594.6	7700.9	27	0	6.2	11.2	5.5	0	1.5	0.4	0	46.8	4.4	51.2	103	3.1
BkT-35	1904.3	8010.6	29.4	0.5	6.3	0.8	6.2	0.5	2.4	0.5	0	50.1	3.6	53.7	100.3	3.4
BkT-41	2200.6	8306.9	26.4	0	5.7	8.8	4.2	1	3	0.3	0	51.5	4	55.5	104.9	3.3

Supposing the input material is the same for both samples and given the consistent trends in mineralogy in Table 3.24 (After Środoń et al., in press) for the Bukowina Tatrzańska well this might be possible. Then following the smectite to illite reaction of Boles and Franks (1979) the sink for the Fe released is chlorite, although Table 3.24 does not lend any solid evidence for this. No chlorite analyses were performed to assess the possible iron uptake in these phases.

The source of the aluminium in the change in structural formulae between Bukowina Tatrzańska-06 and Bukowina Tatrzańska-41 is a little harder to attribute as K-feldspar and kaolinite as reactants in the illitization of smectite

in a closed system (after Hower et al, 1976) have essentially been depleted, the consistent K_2O concentrations in the rock point to a closed system. The source for the aluminium may simply be from the basinal pore fluids, implying fluid flow within the closed system where mineral sources such as kaolinite, K-feldspar and plagioclase have been consumed in diagenetic reactions (e.g. Hower et al, 1976; Boles and Franks, 1979) or from biotite that has been altered in early stage reactions releasing Al into the system (pyrite formation and replacement in biotite grains has been seen in BSEM in chapter 2 highlighting biotite degradation) and is now being used by the illitic material to become more pure, because this reaction is now the most energetically favourable given a depleted supply of K to carry illitization further.

3.3.3: Mineralogical change relative to structural formulae change in the Podhale as a whole:

Chochołów-60 and Bukowina Tatrzańska-06 are separated by ~300m in maximum burial in a continuous burial profile. Figure 3.39 and Table 3.20 demonstrate that there are some differences between these samples in terms of their octahedral cation make up, with Chochołów-60 having less Fe and Mg than Bukowina Tatrzańska-06. When Bukowina Tatrzańska-41 is added to Figure 3.39 it appears that Chochołów-60 is intermediate between Bukowina Tatrzańska-06 and Bukowina Tatrzańska-41.

Given the differences highlighted between Chochołów-06 and Chochołów-60 (Figure 3.38), Bukowina Tatrzańska-06 and Bukowina Tatrzańska-41 (Figure 3.37) and with an overlap in the cation distributions between Bukowina Tatrzańska-06 and Chochołów-60 (Figure 3.39). There appears to be a gradation in the structural formulae and specifically ratio of Si to Al in the tetrahedral sheet and Fe and Mg occupancy in the octahedral sheet (the exception being Chochołów-28). First with the decrease in the percentage of smectite layers in the mixed-layer I/S, matched with a decrease in the ratio of Si to Al in the tetrahedral sheet (e.g. Jiang et al, 1990; Środoń et al, 1986; Ahn & Peacor, 1986a) and then from the cleaning of the octahedral sheet of

Fe and Mg without further change in interstratification of smectite and illite by XRD. The fact that there has been no more smectite conversion in the mixed-layer phase is a function of K availability, which is known to be a key reaction driver (e.g. Hower et al., 1976; Boles & Franks, 1979). Yet it is envisioned that the 'crystallite packets' maintain the same interfaces between smectite and illite layers in the stacking sequence (Bell, 1986; Ahn & Peacor, 1986a) and the same interlayer chemistry, keeping the character of smectite, as smectite has more Ca and less K than illite, relative to the neoformed interstratified illite layers or larger more coherent illite crystallite packets (e.g. Nadeau et al, 1984a,b; Nadeau, 1985; Nadeau & Bain, 1986; Nadeau 1998). Further the chemical change is facilitated by the flux of Al to illite and Si, Fe and Mg to other mineral phases such as quartz and chlorite implicit in the equations of Hower et al. (1976) and Boles and Franks, (1979). The Al is sourced from K-feldspar even though it has been depleted by this stage. Work by Altaner (1989) has demonstrated that the rate of illitization of smectite is slower than K-feldspar dissolution. Consequently, Al may be present in the system from and reside in pore fluids. So it would appear that 'crystallite packets' are changing in terms of their cation distribution but not their mineralogical characteristics in XRD.

3.3.4: Octahedral cation substitution and Selected Area Diffraction Pattern (SADP):

It is well known that smectite material produces concentric ring patterns in SADPs associated with turbostratic disorder (Moore & Reynolds, 1997) and such ring structures have been noted in diagenetic studies by various workers using ion beam thinning techniques in ATEM (Ahn & Peacor, 1986a; Li et al, 1997) and in dispersion techniques (Hover et al, 1999; Nadeau et al, 2002). The reason smectite produces turbostratic disorder results from a low concentration of hydrated cations in the interlayer space and the weak mutual attraction between them and adjacent 2:1 layers leads to relatively large distances across the interlayer. This results in no 'keying' effects

between layers and the relative position of layers becomes random (Moore & Reynolds, 1997).

This study did not find such advanced ring patterns in SADPs. Rather more coherent patterns were produced with some turbostratic disorder principally because the XRD data pointed to more illite material or higher grade I/S material with R1 or R3 ordering with little smectite present either as discrete packets or as interstratified layers in I/S to diffuse the SADP.

These results are in keeping with previous studies of high grade I/S, with ~80% I in I/S (Jiang et al, 1990; Ahn & Peacor, 1986a). The coherency of a 'crystallite packet' also has an effect on the SADP, with larger packets producing more clearly identified single crystal patterns (Ahn & Peacor 1986a; Li et al., 1997). The nature of the smectite and illite interfaces in interstratified 'crystallite packets' will have an effect on the SADP (Bell, 1986), as the boundary between smectite and illite layers might be layer terminating, which will change the crystal lattice planes under the scale of the electron beam and will produce what appears to be small amounts of turbostratic disorder (see Figures 3.40 & 3.41). Chochołów-28 is quite distinct from the other four samples analysed and may represent an original I/S interlayering where there was no change in the boundary between smectite and illite layers (Bell, 1986). Consequently, the SADPs produced are the most coherent and with the least turbostratic stacking disorder, however, with no lattice fringe imaging this cannot be tested and the sample is still anomalous as it has 56%I in I/S but with 'crystallite packets' with a structural formulae characterisitic closer to end-member illite (e.g. Jiang et al., 1990; Środoń et al, 1986).

This study has noted a link between octahedral substitution of Fe and Mg for Al and the apparent increase in disorder in the SADP. This is due to $n60^\circ$ or $n120^\circ$ rotation in a regular way (Weaver, 1989; Moore and Reynolds, 1997) in which the interlayer cations (usually K) sit in the hexagonal or trigonal holes in the surface planes of tetrahedral sheets. Due to the regular spacing of these holes arbitary rotation is impossible and only sets of $n60^\circ$ or $n120^\circ$

rotations are allowed (distinct from smectite). These regular rotations give rise to polytypes (Moore & Reynolds, 1997). McCarty and Reynolds (1995) found *n*60° disorder in K-bentonites (I/S) and a correlation between Fe and Mg substitution in the octahedral sheet and increased disorder. The effects of *n*60° rotations on the SADPs are complicated because 60°, 180° and 300° rotations do not produce the same results (Moore & Reynolds, 1997).

The link between substitution and the effect on SADP is most obvious in Chochołów-28 where the low amounts of octahedral substitution of Mg and Fe for Al has produced the most ordered diffraction patterns, for example analysis K009 (Figure 3.42 and Table 3.12). This is contrasted by Chochołów-06, analysis E026 (Figure 3.41 and Table 3.11).

It has been statistically demonstrated that sample Bukowina Tatrzańska-06 has twice as much Fe in its octahedral sheets than Bukowina Tatrzańska-41, with Al making up this difference with all other parameters the roughly equal. The relationship between SADP and structural formulae is not as clear as was demonstrated by McCarty and Reynolds (1995), as Bukowina Tatrzańska-41 appears to have more turbostratic disorder than Bukowina Tatrzańska-06. This disorder in the SADP may therefore result from polytypism in Bukowina Tatrzańska-41 whereas the analyses from Bukowina Tatrzańska-06 were unwittingly produced from the same polytype.

Chochołów-06 has fewer single crystal patterns than Chochołów-60. The D-statistic for the all cations in the tetrahedral and octahedral sheets for the two samples differs by ~20%. So it appears that a 20% difference in cation concentration is enough to markedly change the amount of disorder in the SADP. However, this conclusion must be held in the context of the %I in I/S between these samples, which as so increased, by 26%.

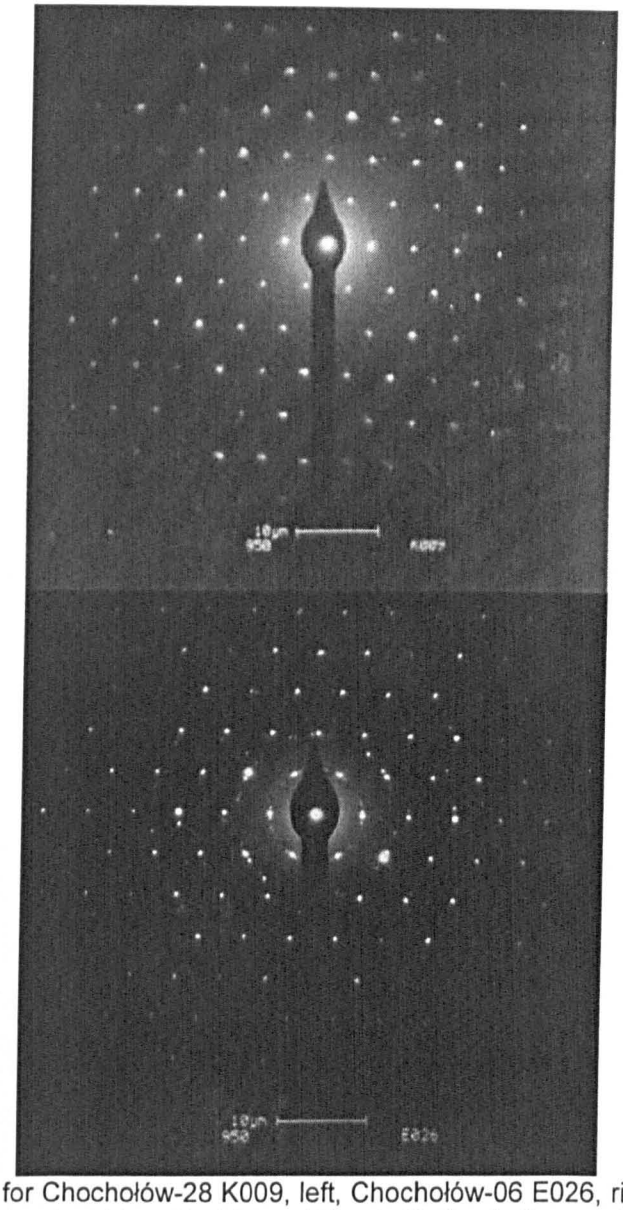

Figure 3.42. SADPs for Chochołów-28 K009, left, Chochołów-06 E026, right. K009 has less Si in the tetrahedral sheet and less Fe, Mg and Ti substitution in the octahedral sheet.

The perfect crystal with every atom in exactly the correct position does not exist as substitution and the effects of impurities will break up the perfect crystal system. Crystal defects in this study have been noted as irregularly spaced diffraction spots. The defects can result from cation vacancy in an irregular way or through the incorporation of interstitial cations. Additionally, the imposition into the octahedral sheet of cations of the incorrect size or valancy can produce defects (e.g. Ti).

The SADPs that show crystal defects may give a hint as to why the cation totals do not always equal 2.00 cations in the octahedral sheet. Low totals

may show an irregular vacancy in the sheet where in the more mature samples (80% I in I/S) have lost Mg and Fe and the necessary Al has not filled these vacant sites. Additionally, high totals may result from Fe and Mg released and replaced by Al being taken into the crystal structure as interstitial cations.

3.4: Conclusions:

The dispersion method employed in this study, over other techniques such as ion-milling and diamond microtoming (e.g. used by Ahn & Peacor, 1986a; Nadeau et al, 1984a), has been proven to be a good technique for preparing and sampling accurately the chemistries of clay minerals in terms of the tetrahedral and octahedral cation contents. The interlayer represents more of an issue due to beam mobilisation of light elements such as K.

The ATEM results coupled with the single crystal SADPs show that the technique may extract data from single crystals in a consistent way and that many different grains be sampled quickly and effectively using absolutely repeatable procedures. Since no information on the coherency of clay packages from lattice fringe imaging were sought in this study, the very fast sample preparation and data collection times were the main advantages of the technique employed. Where the dispersion technique is somewhat weak in the indexing of SADPs as one is never sure what axis the sample will be orientated in and relies on the phyllosilicate lying with its c* axis parallel to the electron beam. The indexing offered in this chapter should not stand alone as a dataset rather it should be viewed as an additional piece of evidence for the phase analysed after consideration of whether a single crystal has been sampled and hence the quality of the ATEM data. The principle weaknesses to indexing are the fact that the camera constant is not measured and is therefore fixed in applying the technique outlined here and that the initial measurement of the distance between spots has to be done to the millimetre on a negative photograph, allowing tiny yet unavoidable errors

to creep in. This study, therefore, recommends that grain dispersion be used only for ATEM as the quality has proven to be high and the exact same method may be applied on samples many weeks apart with no need to re-calibrate standards after the initial measurement; the additional information of SADPs is a requisite as it proves the analysis of a single phase.

Where ion beam thinning would have improved this work is in the nature of the I/S interlayers as this techniques would have given more of an insight through lattice fringe imaging into the make up of the 'crystallite packets' in terms of size and the coherency as diagenetic grade proceeds. The issue of beam danger increases with this technique as the sample needs to be subjected to the beam in order to collect another piece of information increasing the likelihood of elemental loss.

The ATEM results on the five samples from the Podhale Basin show uniform compositions of analyses within a sample. The octahedral totals are close to the optimum values and demonstrate that the technique is robust.

In the Chochołów well composition has been shown to change with decreasing %S in I/S. Tetrahedral Si decreases along with octahedral Fe and Mg and is co-incident with total Al increase. In the Bukowina Tatrzańska well, for no change in %S in I/S, there is a ~40°C temperature increase. Octahedral Fe is substantially decreased with increasing temperature and this is offset by Al increase.

The Kolmogorov-Smirnov Test has allowed comparison between samples and has demonstrated significant differences in samples from the Bukowina Tatrzańska well and more subtle differences between samples in the Chochołów well. Additionally, the deepest sample from the Chochołów well is intermediate between samples from Bukowina Tatrzańska.

A relationship between SADP and structural formulae has been found. Single crystal patterns dominate where the structural formulae reveal little or no substitution in the octahedral sheet.

Chapter 4: Diagenesis and Fabric Reorientation of Phyllosilicates from; Rhum and Magnus in the Northern North Sea

The Rhum Rig

4.0: Northern North Sea; Rhum 3/29a4 and Magnus 211/12-2:

The overall aim of this Chapter is to describe and understand changes to phyllosilicate composition and fabric in two wells from the Northern North Sea: Rhum 3/29a4 and Magnus 211/12-2.

Specific aims are to:

- Describe the key fabric changes in relation to compaction and mineralogical change.
- Discuss the mineralogy and fabric development in the context of the different depositional environments and ages encountered.
- Assess the effects of compaction on fabric development.

Fabric orientation studies have previously predominantly concentrated on studies of metamorphic cleavage development in a structural geology context (Oertel, 1970; Oertel et al., 1989; Ho et al., 1995, 1996, 2001; van der Pluijm et al., 1998; Jacob et al., 2000). Additionally similar principles have been applied to the investigation of mineralogical changes during burial diagenesis and low-grade metamorphism (Ahn & Peacor, 1986; Freed & Peacor, 1989; Merriman et al., 1990; Merriman & Peacor, 1998), although these studies did not quantify fabric orientation. In studies that are strictly sedimentalogical in approach there is a common paradigm that phyllosilicates are deposited in a random orientation or as flocs and these studies have presented SEM images to show this (O'Brien, 1970; O'Brien & Slatt, 1990). The premise then follows that any increase in preferred orientation must be caused by compaction effects, the increase in maximum effective stress (Oertel & Curtis, 1972; Curtis et al., 1980; Sintubin, 1994; Ho et al.,1999; Jacob et al., 2000). As mineralogical changes take place as a function of increasing temperature and stresses increased levels of preferred orientations may be observed (Ho et al., 1995, 1996, 1999, 2001: van der Pluijm et al., 1998; Jacob et al., 2000).

The North Sea has been described recently in the context of diagenesis; illitization (e.g. Thyne et al., 2001, Nadeau et al, 2002), rock properties (e.g. Bjørlykke, 1998), mineralogy and geochemistry (e.g. Thyberg et al., 2000; Pearson et al., 1982), High Resolution Scanning Electron Microscopy (e.g. Huggett, 1995) and extensively in overview by Glennie (1990). There has only been one previous fabric study (Matenaar 2002) on samples from the North Sea using High Resolution X-ray Texture Goniometry (HRXTG). The North Viking Graben was analysed using 8 samples from several wells at variable depths and ages. Additionally, an image analysis technique has been used to quantify preferred orientation (Worden et al., 2005) in mudstones from the Upper Cretaceous Shetland Group, Northern North Sea.

The North Sea was selected because it is has been the basis for many previous studies related to diagenesis but has yet to receive a fully quantified fabric assessment. The fabric study presented here takes many more samples than have ever been studied before in the North Sea from two wells, Rhum 3/29a4 (950m to 4830m) and Magnus 211/12-2 (1449m to 3220m). The samples represent the full, or close to full, depth range of the boreholes and consequently full chemical and physical profiles, with maximum burial temperatures of ~150°C in Rhum 3/29a4 and ~120°C in Magnus 211/12-2. The samples have been analysed for mineralogy, porosity as well as fabric alignment using HRXTG, and have been visually recorded using Back Scattered Electron Microscopy (BSEM). This is a new departure for the North Sea as previously such in depth analysis has only been done for the Gulf of Mexico (Ho et al., 1999; Matenaar, 2002) and the Podhale Basin (Chapter 2).

4.1: Samples and Locations:

4.1.1: Field Locations and well data:

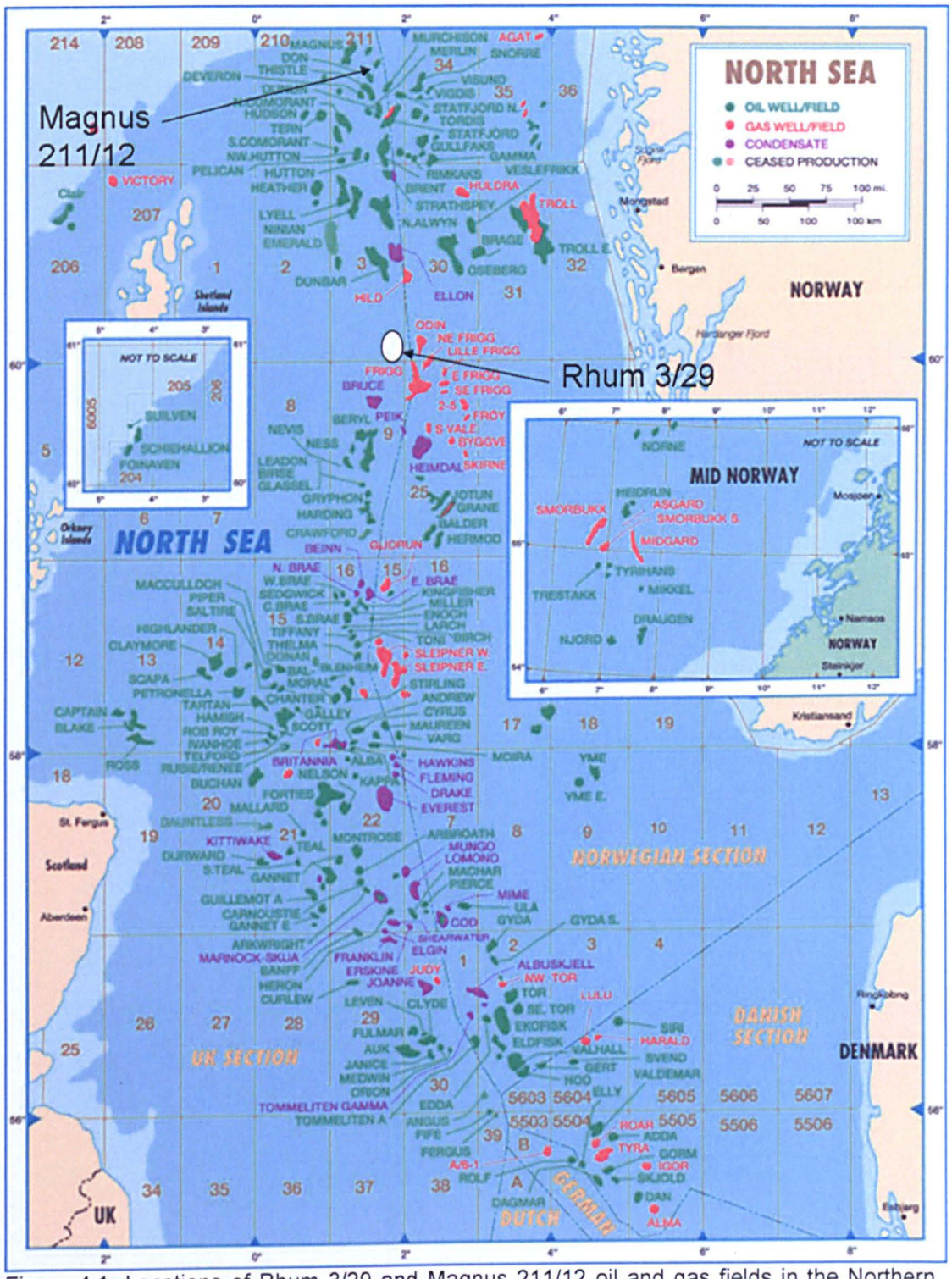

Figure 4.1: Locations of Rhum 3/29 and Magnus 211/12 oil and gas fields in the Northern North Sea modified from nns_map_ worldoil.com inc.

The wells sampled are Rhum 3/29a4 and Magnus 211/12-2. Their locations can be viewed in Figure 4.1 and in detail in Figures 4.2 & 4.3.

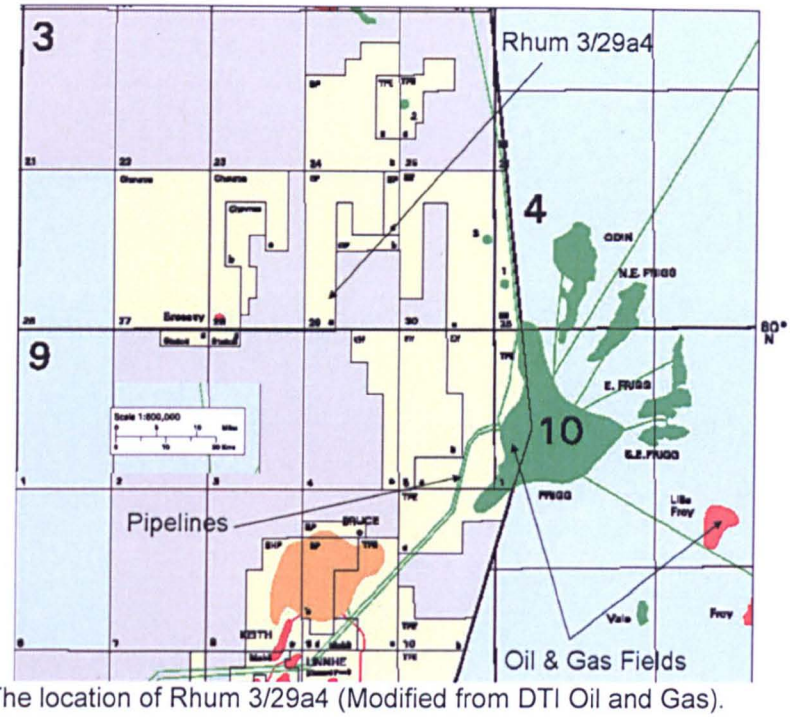

Figure 4.2: The location of Rhum 3/29a4 (Modified from DTI Oil and Gas).

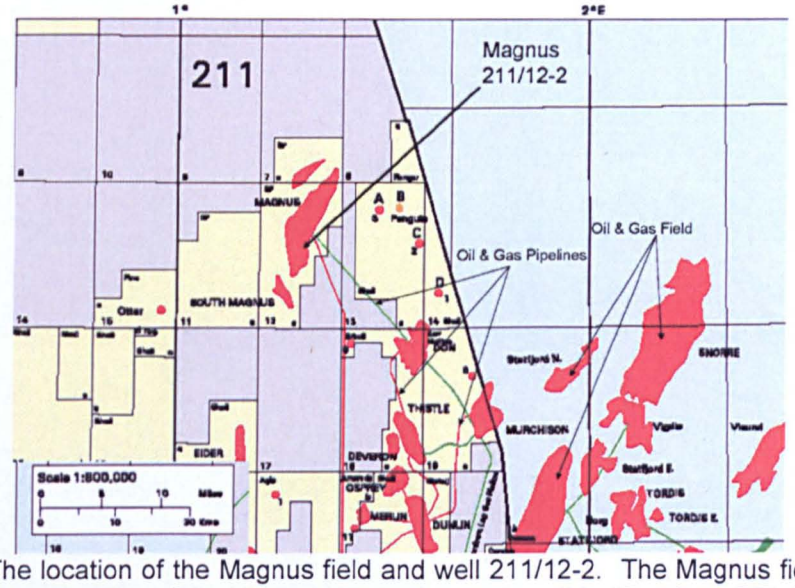

Figure 4.3: The location of the Magnus field and well 211/12-2. The Magnus field is east of Shetland and at the edge of the UK and Norwegian sectors (Modified from DTI Oil and Gas).

These wells were selected as they represent continuous profiles with no apparent uplift or erosion previously characterised by XRD. The base of Rhum 3/29a4 is at 150°C and the base of Magnus 211/12-2 is at ~120°C. Rhum 3/29a4 has been sampled down to 4800m whereas Magnus 211/12-2

is only sampled to 3200m this is as a result of Rhum 3/29a4 being located on a deeper section of graben, the ages are nonetheless the same however maximum burial temperatures will be higher for Rhum 3/29a4 than Magnus 211/12-2, therefore they may be viewed as related wells, with age ranges of Tertiary to Jurassic in Rhum 3/29a4 and Tertiary to Late Cretaceous in Magnus 211/12-2 Both wells have associated completion log information, although Rhum 3/29a4 is of much higher quality than Magnus 211/12-2 and allows a good understanding of lithology and associated logging information, (pressures and bottom hole temperatures). The significant downside to these samples in terms of using them for a diagenetic study is that they are of variable ages (Jurassic to Tertiary) with attendant variation in depositional environments.

Rhum 3/29a4 and Magnus 211/12-2 are treated in this study as a single study area but two distinct wells.

4.1.2: Sample descriptions:

Tables 4.1 & 4.2 give descriptions of the samples analysed for fabric alignment and mineral composition for Rhum 3/29a4 and Magnus 211/12-2 respectively. Figures 4.4 and 4.5 give a lithological column and information on sampled horizons for Rhum 3/29a4 and Magnus 211/12-2 respectively. The data are visual observation of the core material and information synthesised from the completion logs for the cuttings material, the cuttings were general very small so little information or visual descriptions could be described. The names of formations are those that appear on the completion logs.

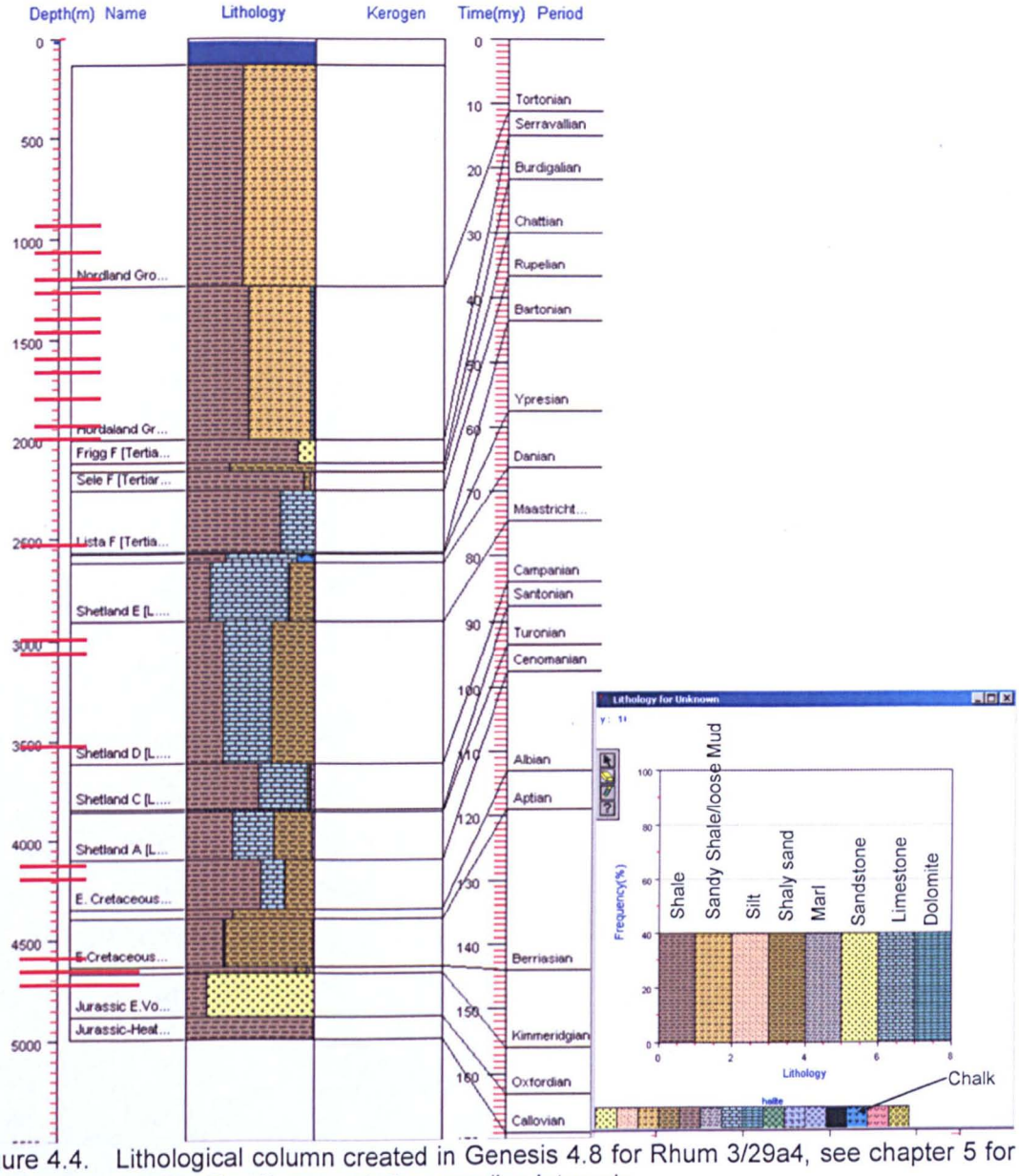

Figure 4.4. Lithological column created in Genesis 4.8 for Rhum 3/29a4, see chapter 5 for construction details. Red lines mark the sampling intervals.

4.1.2.1: Rhum 3/29a4 sample description:

Table 4.1: Sample descriptions and ages of samples from Rhum 3/29a4

Depth [m]	Description	Ct/Cr	Age
950	Mudstone: medium grey to moderate brown grey, firm to moderately hard, silty, trace mica.	Cutting	Tertiary to Recent, Nordland Group, Undifferentiated Formation.
1050	Siltstone: dark grey brown to dusky yellow brown, firm to moderately hard, crumbly, slightly dolomitic, mica, disseminated pyrit	Cutting	Tertiary to Recent, Nordland Group, Undifferentiated Formation.
1150	Mudstone: medium grey to moderate brown grey, firm to moderately hard, silty, trace mica.	Cutting	Tertiary to Recent, Hordaland Group, Undifferentiated Formation.
1250	Mudstone: medium dark to dark grey, firm to moderately hard, subblocky, non to local slightly calcareous, trace disseminated pyrite and glauconite.	Cutting	Tertiary to Recent, Hordaland Group, Undifferentiated Formation.
1350	Mudstone: dark grey to dark brownish grey, moderately hard, blocky to subfissile, silty, slightly dolomitic, trace disseminated pyrite, rare trace very fine glauconitic nodules.	Cutting	Tertiary to Recent, Hordaland Group, Undifferentiated Formation.
1450	Mudstone: dark grey to dark brownish grey, moderate hard, blocky to subfissile, slightly dolomitic, silty, disseminated pyrite, trace mica& carbonaceous specks, are glauconite.	Cutting	Tertiary to Recent, Hordaland Group, Undifferentiated Formation.
1550	Mudstone: medium to dark grey, grey black to brown black, moderately hard, blocky to subfissile, silty, variable traces of mica, pyrite&carbonaceous specks, rare glauconite.	Cutting	Tertiary to Recent, Hordaland Group, Undifferentiated Formation.
1650	Mudstone: moderate to dark brown grey, medium to dark grey, moderate hard, silty, occasional limestone intercalations, variable silty, traces of mica, pyrite&carbonaceous specks	Cutting	Tertiary to Recent, Hordaland Group, Undifferentiated Formation.
1750	Mudstone: moderate to dark brown grey, medium to dark grey, moderate hard, silty, occasional limestone intercalations, variable silty, traces of mica, pyrite&carbonaceous specks	Cutting	Tertiary to Recent, Hordaland Group, Undifferentiated Formation.
1850	Mudstone: moderate to dark brown grey, medium to dark grey, moderate hard, silty, occasional limestone intercalations, variable silty, traces of mica, pyrite&carbonaceous specks	Cutting	Tertiary to Recent, Hordaland Group, Undifferentiated Formation.
1950	Mudstone: medium to dark grey, moderate to dark brown grey, firm to moderately hard, blocky, silty, very slightly dolomitic, trace disseminated pyrite&carbonaceous specks	Cutting	Tertiary to Recent, Hordaland Group, Undifferentiated Formation.
2550	Mudstone: greenish black, brownish black, becoming locally greyish brown to greyish black, firm to moderately hard, crumbly to blocky, locally micropyritic and microcarbonaceous	Cutting	Tertiary to Recent, Rogaland Group, Lista Fm
3060	Mudstone: medium grey, occasionally light grey, firm, blocky to crumbly, locally subblocky, slightly to moderately calcareous, occasionally slightly micromicaceous and microcarbonaceous.	Cutting	Late Cretaceous, Shetland Group, Shetland 'D' Fm
3140	Mudstone: medium grey, occasionally light grey, firm, blocky to crumbly, locally subblocky, hygroturgid, slightly to moderately calcareous, occasionally	Cutting	Late Cretaceous, Shetland Group, Shetland 'D' Fm

	slightly micromicaceous and microcarbonaceous.		
3550	Mudstone: light grey, becoming medium to dark grey and occasionally olive grey, firm to moderately hard, subblocky to blocky, moderately calcareous, slighty silty, micromicaceous and microcarbonaceous, in part micropyritic	Cutting	Late Cretaceous, Shetland Group, Shetland 'D' Fm
4300	Mudstone: greyish red to dark reddish brown interbedded with dark grey and occasionally medium to light bluish grey, firm to moderately hard, locally soft and hygoturgid, micromicaeous, non to slightly calcareous	Cutting	Cretaceous, Early-Late Albian, Cromer Knoll Group, Rodby Fm.
4330	Mudstone: greyish red to dark reddish brown interbedded with dark grey and occasionally medium to light bluish grey, firm to moderately hard, locally soft and hygoturgid, micromicaeous, non to slightly calcareous	Cutting	Cretaceous, Early-Late Albian, Cromer Knoll Group, Rodby Fm.
4632	Mudstone: medium to medium dark grey, locally light to medium grey and olive grey, firm to moderate hard, blocky calcareous, micromicaceous,	Cutting	Early Cretaceous, Valanginian, Cromer Knoll Group, Lower Valhall Fm
4650	Mudstone: brownish to greyish black and dusky yellow brown, firm to moderately hard, crumbly to blocky, micropyritic and microcarbonaceous, slightly calcareous, with occasional calcite mottling.	Cutting	Early Cretaceous, Late Ryazanian, Humber Group, Kimmeridge Clay, Upper Reservoir.
4707 .64	Mudstone: dark to brownish black, hard, fissile, occasionally sandy laminations, very silty	Core	Late Jurassic, Early Middle Volgian, Humber Group Kimmeridge Clay, Upper Main Reservoir
4712 .40	Mudstone: dark to brownish black, hard, fissile, occasionally sandy laminations, very silty	Core	Late Jurassic, Early Middle Volgian, Humber Group Kimmeridge Clay, Upper Main Reservoir
4759 .50	Mudstone: dark grey to brownish black, moderately hard to hard, angular, subfissile, micropyritic, traces of mica, with common laminations and thin interbeds of sandstone	Core	Late Jurassic, Early Middle Volgian, Humber Group Kimmeridge Clay, Upper Main Reservoir
4771 .51	Mudstone: dark grey to brownish black, moderately hard to hard, angular, subfissile, micropyritic, traces of mica, with common laminations and thin interbeds of sandstone	Core	Late Jurassic, Early Middle Volgian, Humber Group Kimmeridge Clay, Upper Main Reservoir
4830 .51	Mudstone: dark grey, hard, fissile, pyretic non calcareous, and minor olive grey, sandy sitstone	Core	Middle Jurassic, Early Volgian-Kimmeridgian, Humber Group Kimmeridge Clay, Lower Reservoir

Samples of mudstones were selected for Rhum 3/29a4 using the following criteria. The Tertiary samples were selected at 100m intervals from 950m to 1950m. This was done as the cuttings samples were of poor quality so finding suitable material for HRXTG was potentially problematic, also these were the sampling intervals used for initial XRD by BP. Sample R2450 (2450m) was chosen as representative of the Lower Tertiary mudstones in the absence of other suitable samples in the Lower Tertiary.

The Cretaceous of the Shetland group was very difficult to sample as there were no good samples (1cm^2 pieces of mudstones). The cuttings bags

contained mostly dry dust or material that effervesced under HCl, as a consequence only 3 samples from the Shetland 'D' formation were selected, as they did not effervesce and where of a suitable size to be potentially cut into thin sections for BSEM and HRXTG. Similarly, the cuttings from the Lower Cretaceous were of equally low quality but 4 samples were selected from 4300m to 4650m.

Five samples from the Jurassic were sampled. These were taken from thin shale/mudstone horizons interbedded within the sandstone units of the Upper Main Reservoir, Lower Main Reservoir and Lower Reservoir (Completion Log nomenclature). These Jurassic samples were selected from high quality core material; laminations were obvious so the samples were marked with their correct orientations to bedding.

4.1.1.2: Magnus well 211/12-2 sample description:

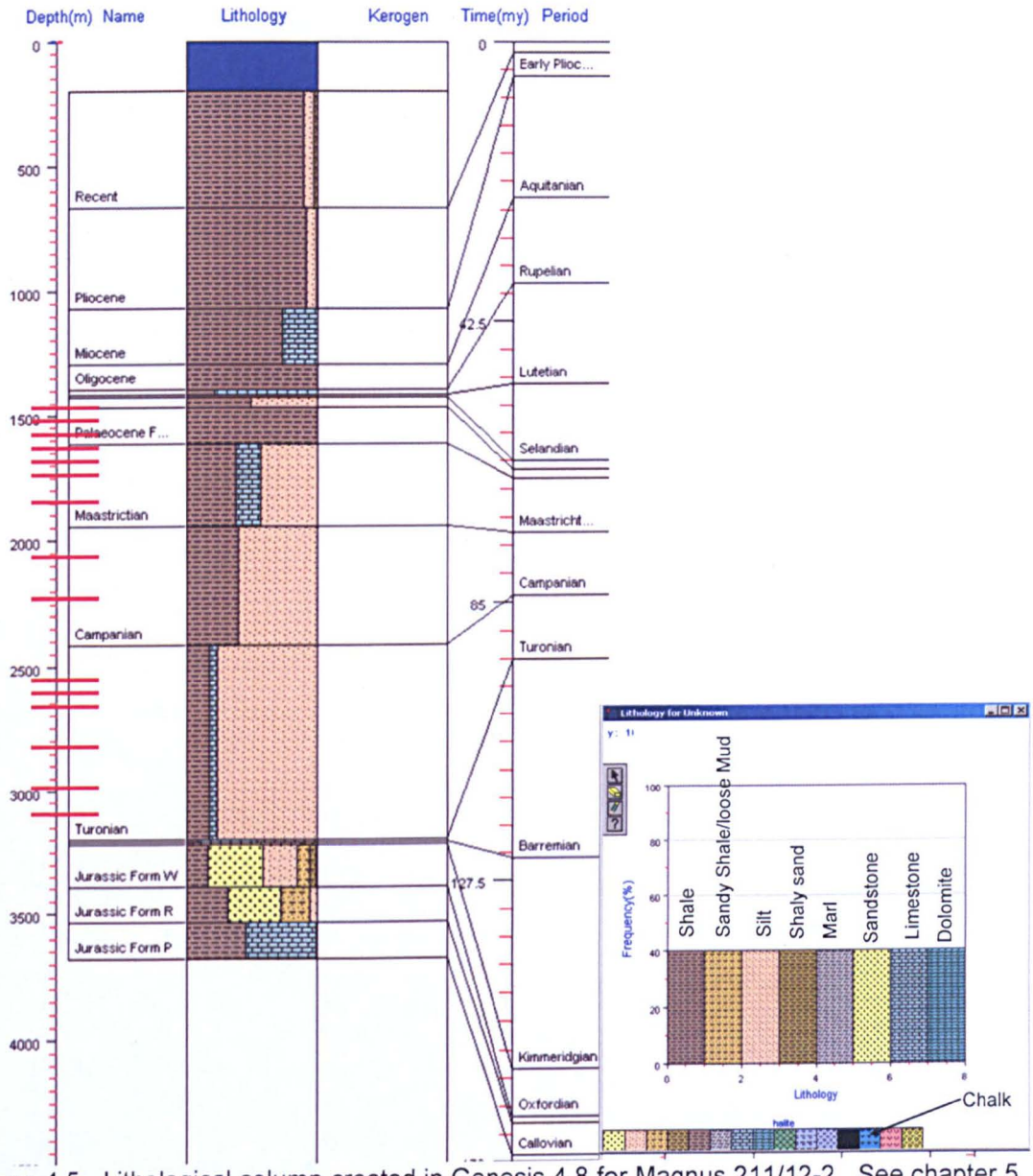

Figure 4.5. Lithological column created in Genesis 4.8 for Magnus 211/12-2. See chapter 5 for details of construction. Red lines mark the sampling intervals.

Table 4.2: Sample descriptions and ages of samples from Magnus 211/12-2.

SWC no.	Depth [m]	Description	Age
54	1449.0	Siltstone, clayey, Packstone texture, grey blue, Calcareous, Shells.	Tertiary, Palaeogene, Palaeocene, "Formation IV"
48	1532.0	Mudstone, Silty, Medium grey, Micaceous.	Tertiary, No Formation Information
40	1567.0	Siltstone, clayey, Wackestone texture, grey green, calcareous, Mica.	Tertiary, No Formation Information
34	1580.0	Siltstone, clayey, Wackestone texture, Grey brown, calcareous, Mica, mottled.	Tertiary, No Formation Information
21	1610.0	Mudstone, Silty, Mudstone texture, Medium grey, Calcareous, Pyritic.	Tertiary, No Formation Information
03	1700.0	Mudstone, Mudstone texture, Medium grey, Calcareous, Pyritic.	Upper Cretaceous, Maastrichtian
101	1802.5	Mudstone, Silty, Dark grey, Calcareous, Micaceous, Well consolidated.	Upper Cretaceous, Maastrichtian
82	2098.0	Siltstone, clayey, Packstone texture, Medium grey, Micaceous, Mottled, Well consolidated.	Upper Cretaceous, (Turonian)-Campanian
77	2399.5	Mudstone, Silty, Wackestone texture, Medium grey, Calcareous, Micaceous, Glauconitic, Laminated, Poorly consolidated.	Upper Cretaceous, (Turonian)-Campanian
73	2602.0	Mudstone, Medium grey, Micaceous, Well consolidated.	Upper Cretaceous, Campanian
89	2706.0	Siltstone, clayey, Wackestone texture, Medium grey, Calcareous, Micaceous, Glauconitic, Well consolidated.	Cretaceous,
69	2775.5	Mudstone, Silty, Medium grey, Calcareous, Micaceous, Well consolidated.	Cretaceous,
87	2880.5	Mudstone, Silty, Medium grey, Micaceous, Poorly consolidated.	Cretaceous,
190	3035.0	Shale, Mudstone texture, Medium grey, Micaceous, Calcareous, Well consolidated.	Cretaceous
175	3220.0	Shale, Mudstone texture, Dark grey, Micaceous, Well consolidated.	Upper Jurassic, Late Kimmeridgian, "Formation S"

The sampling criterion for Magnus 211/12-2 was quite simple all the available sample material was taken and entirely consisted of side wall core, which was taken from mudstone horizons; in turn these points had been marked on the completion log.

4.1.3: Depositional environments:

The sample sets in this study have ages that range from the Late Tertiary to Middle Jurassic. This represents a considerable time interval, in the range of 150Ma, and as a result the depositional character and material inputs into the Northern North Sea and specifically Rhum 3/29a4 and Magnus 211/12-2 have been quite variable.

It has been demonstrated by Matenaar (2002) that there must be an appreciation of sedimentation regime in a fabric study as depositional environment has been shown to have an effect on fabric alignment. Maltman (1981) has acknowledged the importance of phyllosilicate grain shape on depositional fabric development but due to their small size and charged character (Weaver, 1989) other mechanisms of deposition are prevalent. Flocculation causing a house of cards structure (O'Brien & Slatt, 1990) will break up this natural alignment of phyllosilicates. Sintubin (1994 and references therein) has impressed the point that original depositional structures such as laminations are dependent on low level of bioturbation, which are usually associated with anoxia.

Below is a short description of the various depositional and tectonic settings of the Northern North Sea for the Jurassic to the Late-Tertiary as sedimentation regime and source area changed significantly throughout the depositional time period.

4.1.3.1: Jurassic depositional environments:

The detailed analysis of onshore and offshore areas has demonstrated that marine mudstones were both numerous and distinctive throughout the Late Jurassic of the North Sea. Very slow sedimentation rates associated with mudstone and siltstone deposition has promoted the growth of authigenic minerals (e.g. pyrite) (Underhill, 1998; MacQuaker et al, 1997) and has

preserved high amounts of total organic carbon (Schmitz, 1994) in the Upper Jurassic Kimmeridge Clay sampled here. The onshore and offshore diagenesis has been described by MacQuaker et al. (1997). The Jurassic samples presented here are from the Kimmeridge Clay Formation which is characterised by slow sedimentation rates and anoxia.

4.1.3.2: Cretaceous depositional environments:

Cretaceous sediments were deposited over the entire continental shelf of Western Europe, these sediments have been divided into the Cromer Knoll Group, broadly siliciclastic, and the Shetland Group, in the Northern North Sea, which is a more argillaceous version of the Upper Cretaceous Chalk Group found in other areas (Worden et al., 2005; Oakman & Partington, 1998). The depositional style of the late Jurassic continued into the Early Cretaceous, the global sea level rise of the Cretaceous (Haq et al, 1988) flooded previously exposed landmasses resulting in initial shallow marine deposition followed by deeper depositional regimes, evidenced by carbonate production and the interlaying of mudstone horizons. This in turn had an effect on the depositional characteristics of the mudstones sampled in this study from the Cretaceous to those of the Jurassic Kimmeridge Clay Formation. The Cretaceous mudstones are distal/shelf deposits representing normal marine deposition with higher energy environments, in oxic and possibly bioturbated regimes.

4.1.3.3: Tertiary depositional environments:

The Tertiary sequences are thick deposits, 2500m in Rhum 3/29a4 and 1600m in Magnus 211/12-2. The dominant depositional environments were fans and fan deltas (Bowman, 1998), with the Lista and Sele (encountered in Rhum 3/29a4 but not sampled due to grain size) formations describing a

wide spread progradation of small submarine fan complexes controlled by localised accommodation space loss or creation.

The bulk of the mudstone input in the Tertiary was from normal terrestrial sedimentation from various source areas. There is a strong imprint of Tertiary Volcanism on the samples in this study associated with the opening of the Atlantic (Thyberg et al, 2000; Ziegler, 1999; Hinz et al, 1992) which produced volcaniclastic inputs (England et al, 1992) to the whole of North West Europe, and specifically to the North Sea Basin. Consequently, the samples analysed from the Tertiary are the most complex, in terms of their mineralogical assemblages.

4.2: Analytical Methods:

4.2.1: Quantitative X-ray Diffraction (QXRD):

X-ray Diffraction (QXRD) was used to quantify the mineral species present in wells Rhum 3/29a4 and Magnus 211/12-2. The analysis was undertaken at the Macaulay Land Use Research Institute (MLURI), Aberdeen. The quantification method utilised a full-pattern fitting method using corundum as the internal standard. The patterns are then scaled to fit intensity and any small shifts (less than the step size) are accommodated using a cubic spline interpolation, using the least squares routines of an Excel Solver. Essentially, the method involves fitting the whole of the observed diffraction pattern with a synthetic pattern. This synthetic pattern is in turn the sum of patterns calculated for each phase in the sample (Snyder & Bish, 1989; Bish, 1994; Mumme et al., 1996). The full-pattern fitting method is predicated on the fact that the diffraction pattern is the sum total of all of the effects, both instrumental and specimen related. As a consequence, the method requires phase identification and then allowing the computer program (Excel Solver) to fit the data until the best fit between the synthetic pattern and the experimental pattern is obtained. The key to this method is the pattern fits only what the user asks the Excel Solver to find, if a phase is missed no

fitting occurs. Therefore, the technique requires the characterisation of numerous pure samples in a database used by the Excel Solver to calculate a synthetic pattern. The minerals in the database are constantly updated and re-analysed (Hillier, 2005, Pers. Comms).

The accuracy of the procedure is +/- 3wt% (Hillier, 2003), with a lower limit detection (LLD) of less than 0.5 wt% for all minerals except mica (LLD=1wt%). This is due to the non-basal peaks from mica in a random powder being stronger diffractors than the basal peak.

4.2.1.1: Spray drying sample preparation:

The samples were spray dried to produce truly random powders for X-ray powder diffraction. The method is described by Hillier (2002a, b and 1999) and essentially consists of preparing the samples as aqueous slurries and spray drying in a heated chamber. The spherical spray droplets produced by spraying dry in the chamber form spherical granules, which due to their shape and the way spheres pack together allows a truly random arrangement of particles (Hillier, 2002a; b; 1999). Random arrangements are required as all the *hkl* reflections of the minerals present with their correct relative intensities of their reflections are required in a quantitative analysis (Hillier, 2003; Moore & Reynolds, 1997).

4.2.1.2: Machine settings:

Samples were run on a Siemens D5000 X-ray diffractometer, using cobalt K-alpha radiation (K-alpha = 1.790260 (Brindley & Brown, 1984)) selected with a diffracted beam monochromator. Patterns were obtained by step scanning from 2-75° 2-theta with a step size of 0.02 degrees and counting for 2 seconds per step.

4.2.1.3: Clay mineralogy and percentage of illite in Illite/smectite:

The <2μm clay size fraction of samples from Rhum 3/29a4 and Magnus 211/12-2 were separated and analysed by XRD. The analysis required orientated clay mineral aggregates so specimens were prepared using a technique similar to the "Millipore® Filter Transfer Method" outlined in Moore and Reynolds (1997).

The relative percentage of clay minerals in the <2μm clay size fraction were previously determined for these samples by MLURI for BP Exploration with a view to assessing the percentage of illite in illite/smectite. The <2μm clay size fraction was extracted by centrifuging the sample material and using Stokes' Law .

Stokes' Law is an equation relating the terminal settling velocity of a smooth, rigid sphere in a viscous fluid of known density and viscosity to the diameter of the sphere when subjected to a known force field. It is used in the particle-size analysis of soils and disaggregated mudstones by the pipette, hydrometer, or centrifuge methods, here the centrifuge method was employed. The equation is:

$V = (2gr^2)(d1-d2)/9\mu$

Where;

V = velocity of fall (cm sec),

g = acceleration of gravity (cm sec),

r = "equivalent" radius of particle (cm),

d1 = density of particle (g cm),

d2 = density of medium (g cm), and

μ = viscosity of medium (dyne sec cm).

The timings used to extract the <2μm clay size fraction by centrifuging were:

2 minutes 48 seconds at 1000rpm

4 minutes 22 seconds at 800rpm

7 minutes 47 seconds at 600rpm

These analyses are not repeated in this study BP has kindly supplied that data, however, an appreciation of the sample preparation is important. In preparation the <2μm clay size fraction of the samples were vacuum filtered onto a filter paper and then peeled onto a glass slide. The slides were then analysed on a Siemens D5000, using cobalt K-alpha radiation with a diffracted beam monochromator under air-dried, ethylene glycol solvated (60°C for 24 hours) and heat treatment to 375°C (for a detailed discussion of these procedures see Moore & Reynolds, 1997). The percentages of illite in illite/smectite were determined using the methodology of Moore and Reynolds (1997):

1- The diffraction patterns of air-dried, ethylene glycol solvated and heat treated to 375°C give provisional identification of I/S.

2-The Reichweite or ordering type (Jagorzinski, 1947) is determined by the position of reflections between 5 and 8.5° 2Θ for ethylene glycol solvated samples.

3- The percent illite can be determined using a value of °Δ2Θ from Table 8.3 of Moore and Reynolds (1997), which varies between 9.01 and 10.31 °Δ2Θ for 001/002 reflections and 15.80 and 17.39 °Δ2Θ for 002/003 reflections.

4.2.2: High Resolution X-ray Texture Goniometry (HRXTG):

The analytical methods employed in these analyses were entirely the same as those employed for the Podhale samples (Chapter 2). As there was a significant delay between blocks of analyses, two Podhale samples were re-run to check reproducibility. The original run gave I/S peak maximum intensities of 6.99 m.r.d. and 6.87 m.r.d. for sample Chochołów-38 and 4.61 m.r.d. for Chochołów-12. The re-measurement gave values of 6.77 m.r.d. and 4.38 m.r.d. for Chochołów-38 and Chochołów-12 respectively. Variance of within +/- 0.5 m.r.d. was deemed an acceptable repeat result providing the pole figures were complete (Figure 4.6) based on analyses made during the setting up of the machine in 1994 (van der Pluijm, 2005, Pers. Comms.).

Repeat analysis was on the same thin section as the original measurement. No record of the exact millimetre of beam interaction with the sample was kept from the original run, so the re-analysis took place on the same available surface as the original measurement is ($1cm^2$). Therefore, variance between the original and the re-analysis was the result of slight sample heterogeneity on a square millimetre scale over an available analysis surface of a square centimetre.

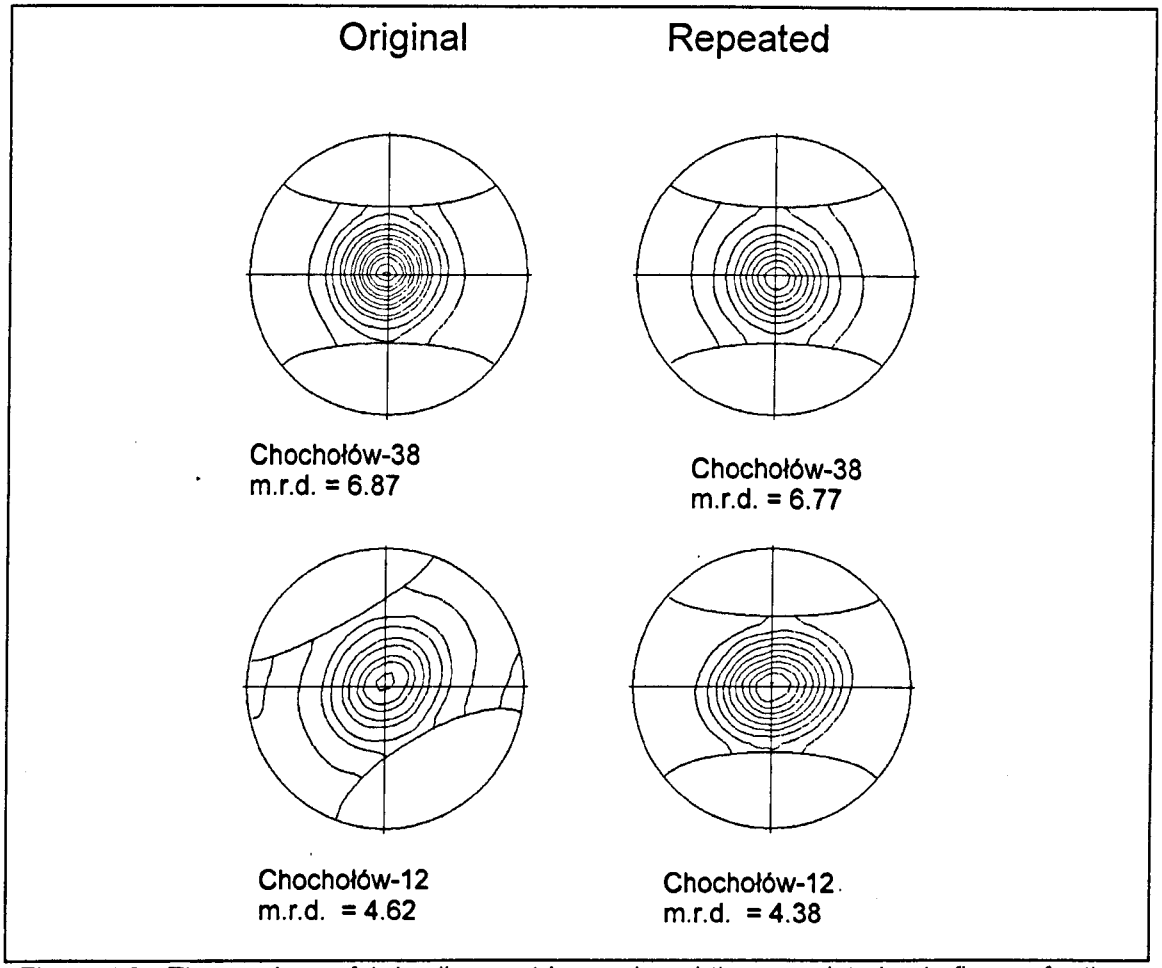

Figure 4.6. The maximum fabric alignment in m.r.d. and the associated pole figures for the repeated measurements of Chochołów-38 and Chochołów-12 from different blocks of analysis. Rotation of the pole figure in Chochołów-12 is not significant.

Despite similar pole figures, 2-theta scans of the re-run samples differed from the originals. Figure 4.7 demonstrates that intensity in the d-10Å to d-7Å region of the trace (3.5 to 7.0° 2-theta) is not as high in the repeated runs for both samples as it was in the original run. Also, any characteristic peaks for the various phases present are drastically reduced. The quartz peak, in the repeated run, at a d-spacing of 4.257Å appears much more intense than in

the original run in its relative intensity in comparison to the 3.5 to 7.0° 2-theta region of the trace.

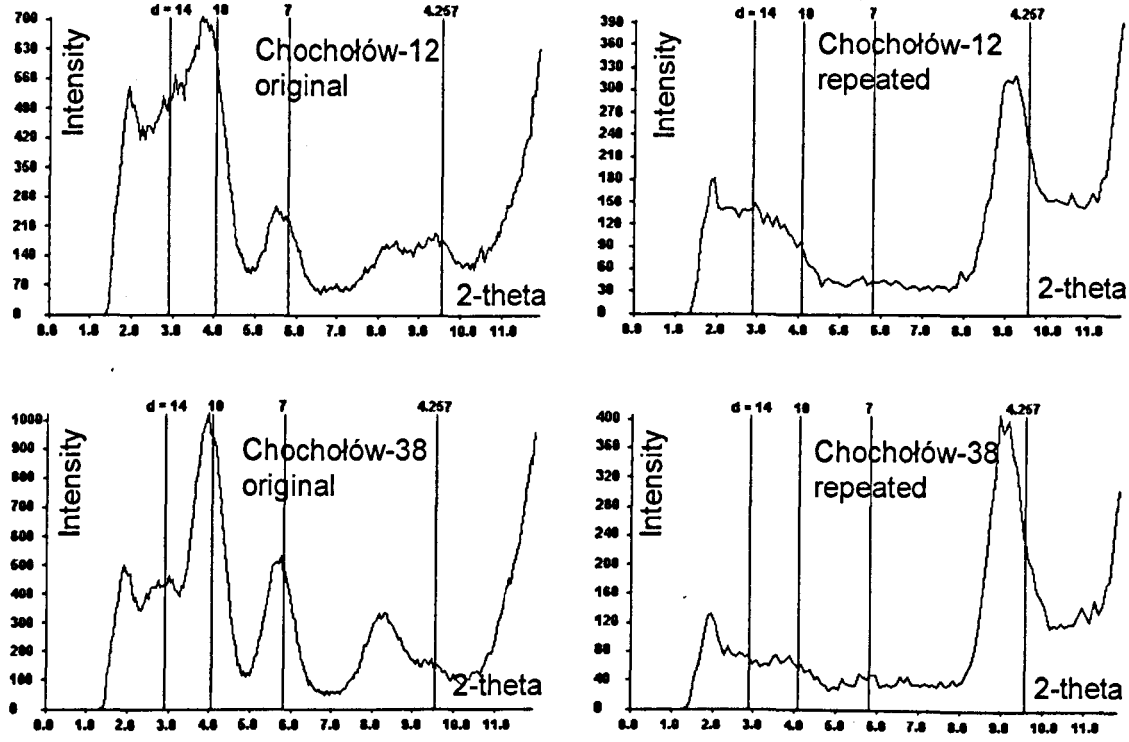

Figure 4.7. The "2-theta scans" for Chocholow-12 and Chocholow-38, on the left the original traces from chapter 2, on the right the repeated traces.

The data as collected by the Enraf-Nonius CAD4 Single Crystal diffractometer are plotted (Figure 4.7) and analysed using a program called XPFG2 written by Ho (1995). In order to assess whether this program is performing the same function from run to run, the raw data (gathered as a .VAX file) may be imported to an Excel file and re-plotted (Figure 4.8). In comparing the original and repeated runs of Chocholow-38 and the two methods of graphical data description, it is clear that the original and repeated runs have not produced the same "2-theta scan" but this is not a function of the XPFG2 program incorrectly presenting the data, rather the problem lies elsewhere.

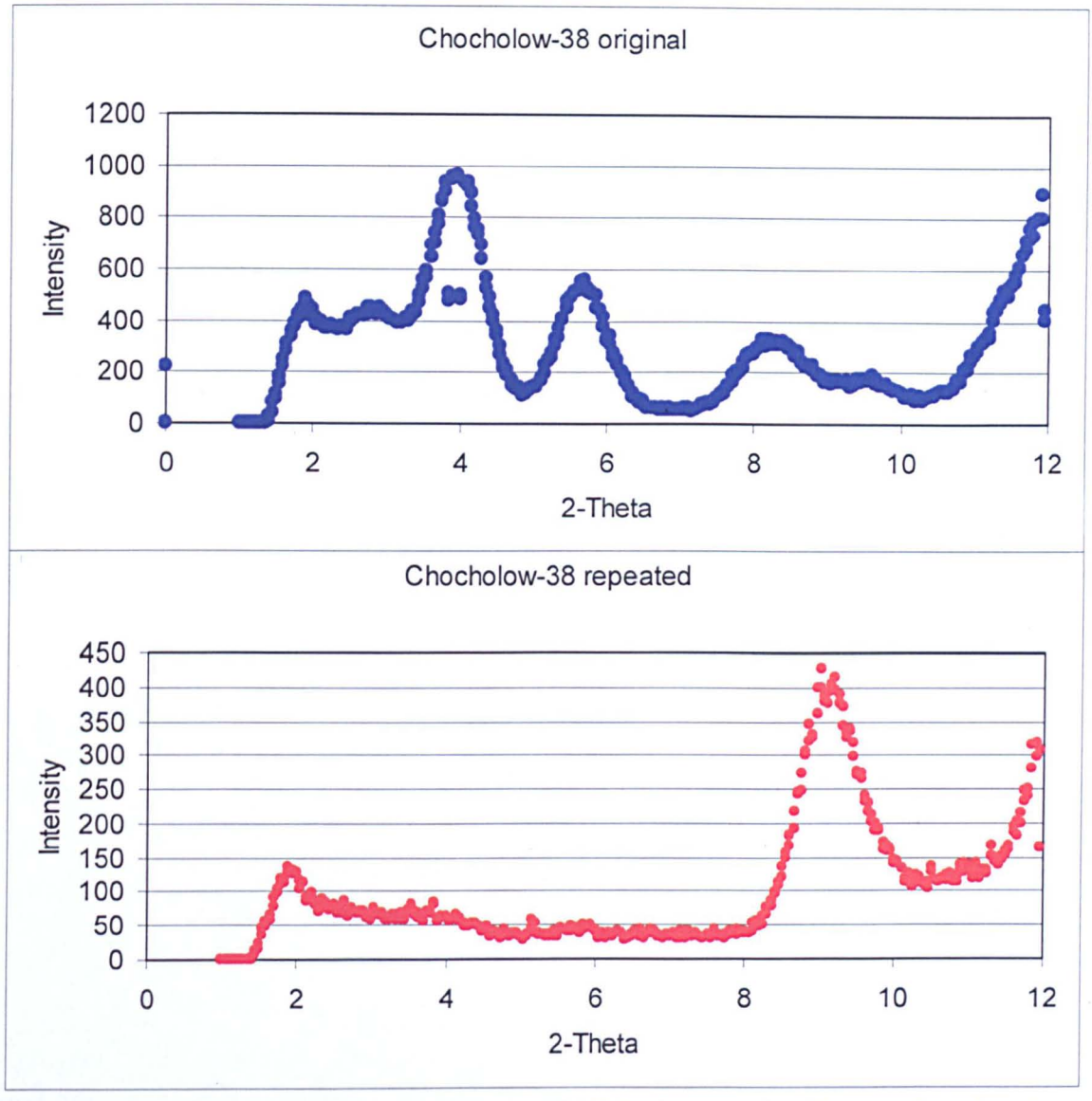

Figure 4.8. The "2-theta scan" raw data from the .VAX file imported into Excel and re-plotted for sample Chocholow-38 for both the original and repeated runs.

A "2-theta scan" was performed on a blank, i.e. with just the sample holder. This was done to assess whether there was something blocking the source or detector on the goniometer head. The 'blank' "2-theta trace may be seen in Figure 4.9. The background best fit curve is also plotted and shows clearly that the trace produced is that of the background with no false reading due source or detector contamination. Overlaying the original and repeated run for sample of Chocholow-38 with the background best fit curve clearly demonstrates the loss of intensity from run to run.

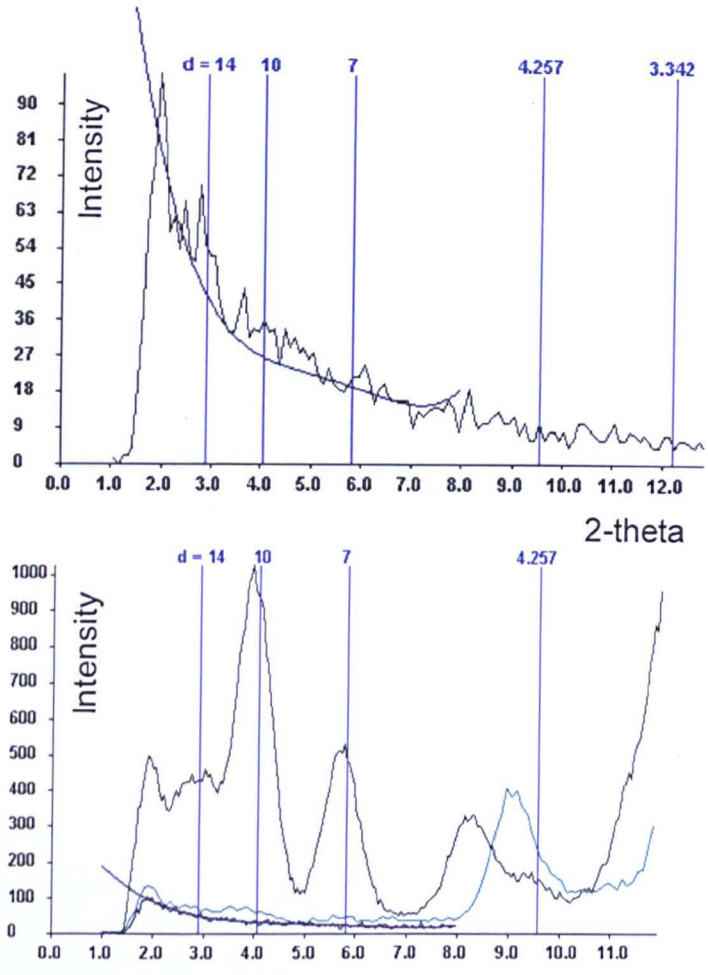

Figure 4.9. The top trace produced by the goniometer with no sample in the holder. The smooth line represents background best fit curve. The bottom trace is sample Chocholow-38 for both the original run (strong peaks) the repeated run (low intensity line) overlain by no sample curve and the background best fit curve.

The final test of the machine involved running another sample over a longer "2-theta scan" and for a longer step time. Sample M1610 from this analysis was run over 0.5 to 40° 2-theta and for a step time of 4 seconds (Figure 4.10). Overlain on this trace is the standard trace for the same spot on the sample run over 0.5 to 12° 2-theta. The intensities are increased by the longer step time and no shift in the data is observed. The trace for no sample and the background best fit curve are also shown.

The strenuous assessment of the nature of the "2-theta scan" between the original and repeated runs has been done as the qualitative assessment of the diagenetic grade of illite-smectite has been inferred by this method in chapter 2, here in this chapter no qualitative assessment may be offered as peak identification is hampered by the loss of intensity. The "full scan" pole figures and quantification of fabric alignment assigned by maximum intensity

is not affected by this loss of intensity in the "2-theta scan". The full scan is normalised so it is independent of concentration of sample parameters such as mineral content by summing all data points over the whole pole figure and weighting them with respect to their areal distributions (van der Pluijm et al., 1994).

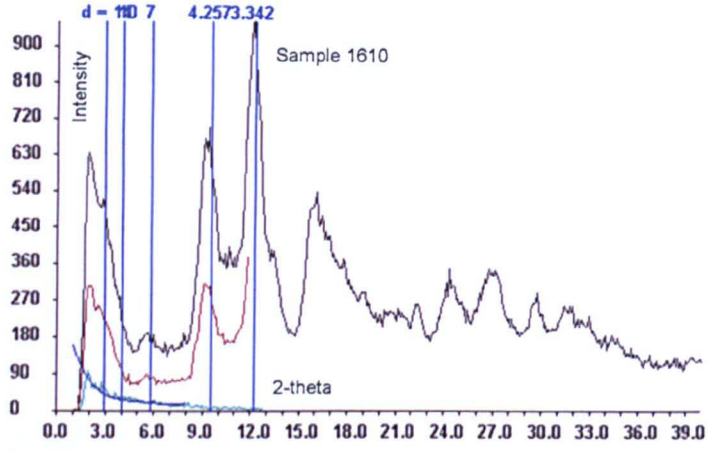

Figure 4.10. Sample M1610 from this analysis was run over 0.5 to 40° 2-theta and for a step time of 4 seconds. Overlain on this trace is the standard trace for the same spot on the sample run over 0.5 to 12° 2-theta. The intensities are increased by the longer step time. The trace for no sample and the background best fit curve are also shown.

4.2.3: Backscattered Scanning Electron Microscopy (BSEM):

At the University of Newcastle-Upon-Tyne BSEM was performed on a Hitachi S2400 Scanning Electron Microscope fitted with an Oxford Instruments Isis 200 Ultra Thin Window X-ray detector. Images were captured at an accelerating voltage of 20kV using a working distance between 10.0 and 10.1mm.

4.2.4: Mercury Intrusion Porosimetry (MICP):

Porosities and pore size distributions were determined on a one gram block of sample freeze dried (Delage & Lefebvre 1984) for 24 hours, then oven dried at 105°C for a further 24 hours. Samples remained in the oven until they were loaded for analysis. A further three grams of sample was taken

and ground to a fine powder and used for grain density determinations. Porosity is determined from bulk volume (from MICP prior to injection of mercury) and measured grain density. Grain densities (Gs) were measured using the small pycnometer method at 20°C (British Standard, 733, 1987), with a quartz standard (2.65g/cm^3) in each sample batch, using the equation:

Gs (gcm^{-3}) = [mass bottle & sample – mass bottle] / [mass bottle & water + mass bottle & sample – mass bottle – mass bottle & sample & water]. Repeat analyses were made; the quartz standard was repeatable to within 0.02g/cm^3.

Analysis took place on a *Micromeritics*© Autopore 9220 machine and yielded a figure for porosity, and a pore size distribution. The analysis used the assumption that the surface tension of mercury was 0.48 N/m and the contact angle between mercury and the particle surface was 141°. The pore radius, r, then is given by:

$$r = 746{,}000 / p$$

where r is the pore throat radius (nm) and p is the pressure in kPa.

4.3: Results:

4.3.1: Quantitative X-ray Diffraction (QXRD):

The results of the full pattern fitting method can be seen graphically in Figures 4.11 and 4.12. Figure 4.11 demonstrates that the full-pattern fitting for the whole trace has fitted the raw data for both peak position and intensity. Generally there is an excellent fit between the experimental data and the synthetic trace.

Figure 4.12 is an enlarged section of the trace between 20° and 45° 2-theta of the raw data and the full-pattern fitted data. The full-pattern fitted lines are smoother than the raw data and this has resulted in some slight mismatches e.g. between 26° and 27° 2-theta (anorthite, a calcium variety of plagioclase feldspar) and around 32° (clinoptilolite) but the exact nature of the effects these small mismatches have on the quantification is unclear (Hillier, 2005, Pers. Comms). Additionally, due to the varying expandability of these samples slight mismatches occur in the region of 7° and 10° 2-theta. This is due to the synthetic trace matching the phase but not its percentage expandability but is within the error margin of the technique (Hillier 2003; Hillier, 2005 Pers. Comms.). Nevertheless the raw data has been full-pattern fitted for both intensity and peak position. Getting a good fit is to some extent dependant on asking the least squares routine of the Excel Solver to look for a specific phase as the synthetic pattern is the sum of patterns calculated for each phase in the sample (Snyder & Bish, 1989; Bish, 1994; Mumme et al., 1996), if this is not done no good fit will be achieved (Hillier, 2003). In the case of Rhum 4830 the pattern has been resolved as the correct phases were searched for.

The initial phase selection was simply to select the most commonly associated minerals in mudstones and shales (e.g. from Weaver, 1989) and run the trace through the Excel Solver. If a poorly fitted pattern was produced, comparing the trace with 2-theta angles in the PDF of minerals (from the international centre for diffraction data, 1996) would yield a likely

new mineral to add to the least squares routine (providing it has been characterised in house). Mixed-layer minerals present a problem in that peak positions shift depending on diagenetic maturity. In this case three mixed-layer illite-smectites were used in the Excel Solver to calculate phases with R0, R1 and R3 ordering. Two saponite minerals previously analysed at MLURI were used to calculate tri-octahedral smectite abundance. Four 'smectite' minerals (strictly nontronite and montmorillonite) were used to calculate di-octahedral smectite abundance. Pure 'illite' was resolved using three illite varieties characterised previously at MLURI. The full-pattern fitting method, therefore, represents the synthesis of various known and locally characterised minerals that have been selected based on iteration with the traces and the solution yielded by the Excel Solver. All traces for Rhum 3/29a4 and Magnus 211/12-2 are in Appendix 4.1.

The percentages of all the mineral species present in Rhum 3/29a4 and Magnus 211/12-2 have been normalised so that they are free from the barite assumed to be present in the non-normalised data as drilling mud contamination. Quartz exhibits a general background level between 20 and 40%, representing a large variation but is marked by a low zone between 1350m and 1950m, which is co-incident with inflated levels of tri-octahedral smectite in the Tertiary samples and may be attributed to the Tertiary volcanism that was prevalent in the region as the Atlantic opened (Thyberg et al, 2000; Ziegler, 1999; Hinz et al., 1992). Smectite is not a volcanic mineral however smectite may form from the transformation of volcanic glass (e.g. de la Fuente et al, 2002; Tomita et al, 1993 and preferences therein) and specifically tri-octahredral smectite may form from andesitic pyroclastic rocks (Son et al., 2001). Di-octahedral smectite (Figure 4.13) is also high in the same zone, (see Table 4.3 & 4.4) however there is a general decrease in this phase and the tri-octahedral smectite down the well, consistent with diagenetic reactions (e.g. Hower et al., 1976, Boles & Franks, 1979).

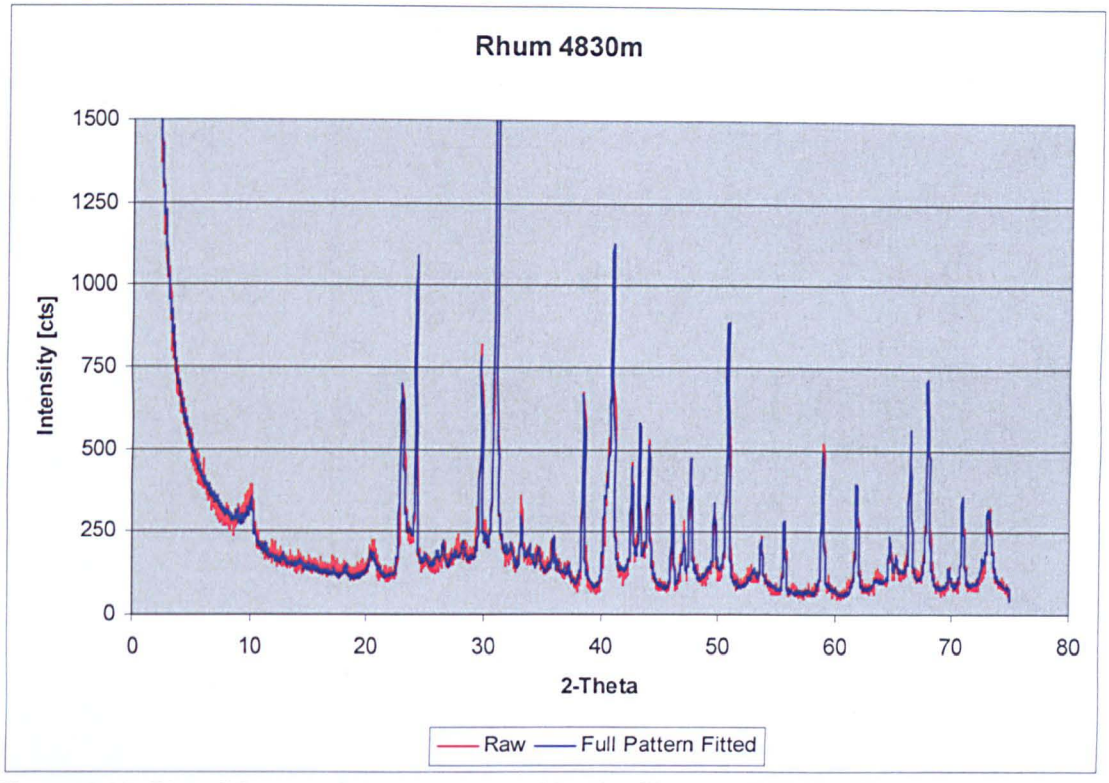

Figure 4.11: Plot of the raw data as measured by the Siemens D5000 diffractometer and the Full Pattern Fitted results used to quantify mineralogy for characteristic sample Rhum 4830m from Rhum 3/29a4.

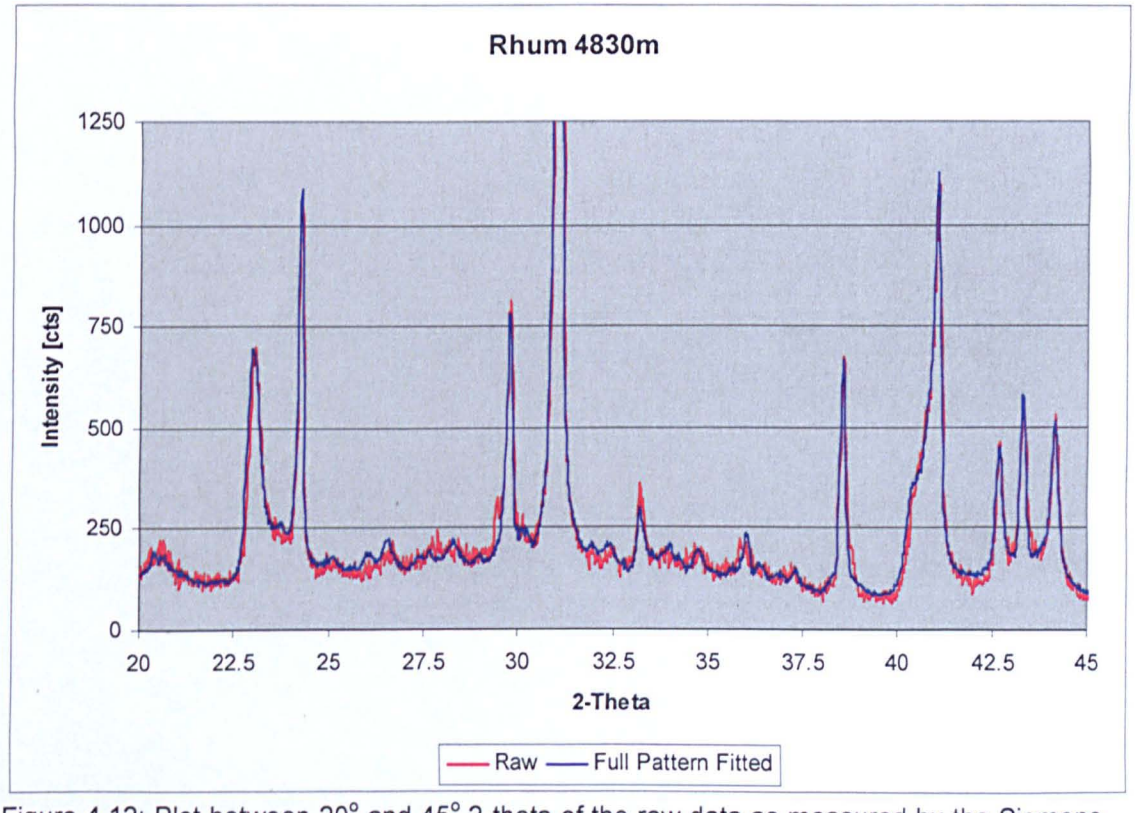

Figure 4.12: Plot between 20° and 45° 2-theta of the raw data as measured by the Siemens D5000 diffractometer and the Full Pattern Fitted results used to quantify mineralogy for the characteristic sample Rhum4830m Rhum 3/29a4.

Table 4.3. Whole Rock Quantitative X-ray Diffraction analysis on samples from Rhum 3/29a4, using the full-pattern fitting method. The label I/S refers to the mixed layer phase illite/smectite.

Depth [m]	Sample	Quartz	Plagioclase	K-Feldspar	Calcite	Dolomite	Pyrite	Clinoptilolite	Halite	Period/Sub-Period
950	R0950-B	40.59	5.85	6.59	3.84	0.37	2.36	4.61	0.43	Tertiary
1050	R1050-B	30.46	5.54	5.40	3.61	0.39	2.10	4.25	0.59	Tertiary
1130	R1130-B	18.83	6.05	4.63	1.79	0.47	1.22	2.16	0.54	Tertiary
1250	R1250-B	55.88	3.84	6.18	4.95	0.35	1.06	2.95	0.64	Tertiary
1350	R1350-B	9.95	7.71	4.43	0.66	0.49	1.60	8.29	0.53	Tertiary
1450	R1450-B	8.48	6.67	3.18	0.84	0.53	2.19	7.83	0.78	Tertiary
1550	R1550-B	7.54	7.34	3.67	1.23	0.54	2.39	9.49	0.57	Tertiary
1650	R1650-B	6.52	7.19	3.69	0.49	0.50	2.61	7.58	1.03	Tertiary
1750	R1750-B	7.94	7.57	3.41	1.13	0.40	2.83	5.64	0.68	Tertiary
1850	R1850-B	8.53	8.19	3.23	0.71	0.24	2.59	8.14	0.75	Tertiary
1950	R1950-B	11.84	6.09	2.82	0.78	0.16	1.68	1.93	0.38	Tertiary
2450	R2450-B	23.87	9.25	3.85	1.28	0.47	1.52	2.29	0.61	Tertiary
2550	R2550-B	28.46	7.10	3.55	0.92	0.28	1.99	1.97	0.01	Tertiary
3060	R3060-B	29.01	7.61	1.15	6.19	0.07	0.61	0.56	0.07	Cretaceous
3140	R3140-B	32.56	7.06	1.83	4.73	0.41	1.19	2.23	0.56	Cretaceous
4300	R4300-B	30.39	6.65	1.01	0.63	0.29	0.74	1.00	0.08	Cretaceous
4330	R4330-B	24.19	4.34	1.26	0.72	0.14	0.45	0.56	0.17	Cretaceous
4632	R4632-B	29.18	3.58	1.47	2.20	2.07	4.69	2.69	0.55	Cretaceous
4650	R4650-B	32.15	2.65	2.16	0.41	1.01	7.00	2.20	0.22	Cretaceous
4707	R4707-B	85.44	1.36	0.00	0.14	0.49	3.79	0.50	0.05	Jurassic
4712	R4712-B	17.33	1.08	0.33	0.21	0.00	10.33	1.51	0.00	Jurassic
4771	R4771-B	36.28	0.52	0.52	0.21	0.07	6.20	1.62	0.00	Jurassic
4830	R4830-B	29.49	0.41	1.03	0.43	1.43	8.45	2.36	0.10	Jurassic

Depth [m]	Sample	Mica/illite	I/S	Di-octahedral Smectite	Tri-octahedral Smectite	Kaolinite	Chlorite	Total	Clay Total	Period/Sub-Period
950	R0950-B	9.04	0.00	18.03	2.50	5.21	0.58	100.00	35.37	Tertiary
1050	R1050-B	10.01	5.34	18.50	3.08	9.86	0.87	100.00	47.65	Tertiary
1130	R1130-B	11.65	1.84	27.22	8.74	13.68	1.20	100.00	64.32	Tertiary
1250	R1250-B	2.20	2.85	10.83	4.22	3.48	0.55	100.00	24.14	Tertiary
1350	R1350-B	8.64	3.04	23.77	15.07	13.69	2.13	100.00	66.33	Tertiary
1450	R1450-B	10.85	0.00	29.36	14.04	14.02	1.25	100.00	69.51	Tertiary
1550	R1550-B	6.63	8.69	28.20	11.99	9.99	1.73	100.00	67.22	Tertiary
1650	R1650-B	6.09	6.24	31.87	13.09	11.37	1.74	100.00	70.39	Tertiary
1750	R1750-B	6.87	8.34	25.07	15.29	12.55	2.28	100.00	70.41	Tertiary
1850	R1850-B	3.57	6.06	32.81	13.78	9.86	1.54	100.00	67.62	Tertiary
1950	R1950-B	8.57	16.16	32.41	9.01	5.85	2.32	100.00	74.32	Tertiary
2450	R2450-B	13.73	5.83	16.29	8.67	7.28	5.05	100.00	56.85	Tertiary
2550	R2550-B	10.71	15.43	12.44	10.56	2.61	3.97	100.00	55.72	Tertiary
3060	R3060-B	17.80	10.02	7.43	4.03	10.55	4.91	100.00	54.73	Cretaceous
3140	R3140-B	14.27	17.16	2.58	3.99	7.41	4.03	100.00	49.44	Cretaceous
4300	R4300-B	11.37	24.99	6.94	3.77	7.95	4.20	100.00	59.22	Cretaceous
4330	R4330-B	11.34	28.69	4.46	6.23	10.48	6.96	100.00	68.16	Cretaceous
4632	R4632-B	6.07	29.46	0.78	1.98	14.46	0.80	100.00	53.56	Cretaceous
4650	R4650-B	8.37	26.48	1.87	1.08	13.76	0.63	100.00	52.19	Cretaceous
4707	R4707-B	2.96	0.00	2.19	0.00	2.77	0.30	100.00	8.21	Jurassic
4712	R4712-B	27.94	22.75	1.23	0.00	17.24	0.02	100.00	69.19	Jurassic
4771	R4771-B	21.33	19.58	2.28	0.00	10.72	0.66	100.00	54.57	Jurassic
4830	R4830-B	25.39	25.98	3.26	0.00	1.40	0.27	100.00	56.29	Jurassic

Table 4.4. Whole Rock Quantitative X-ray Diffraction analysis on samples from Magnus 211/12-2, using the full-pattern fitting method. The label I/S refers to the mixed layer phase illite/smectite.

Depth [m]	Sample	Quartz	Plagioclase	K-Feldspar	Calcite	Dolomite	Pyrite	Clinoptilolite	Halite	Period/Sub-Period
1449	M054-B	0.45	17.34	5.17	0.75	0.53	1.11	1.75	0.00	Tertiary
1532	M048-B	11.15	9.16	3.20	1.76	0.22	0.93	3.67	1.41	Tertiary
1567	M040-B	20.69	11.24	5.30	0.71	0.37	0.84	1.81	0.58	Tertiary
1580	M034-B	26.22	12.62	7.82	0.53	0.57	0.61	2.33	2.46	Tertiary
1610	M021-B	19.53	6.31	3.48	4.70	0.28	0.64	1.26	4.25	Tertiary
1700	M003-B	16.06	4.78	3.04	24.51	0.21	0.80	1.64	2.67	Tertiary
1802	M101-B	23.68	7.99	3.17	3.42	0.15	0.86	0.84	2.30	Cretaceous
2098	M082-B	34.06	9.86	3.76	0.20	0.17	0.31	0.87	3.10	Cretaceous
2399.5	M077-B	36.33	10.65	4.46	0.27	0.15	1.05	1.32	3.89	Cretaceous
2606	M073-B	29.12	5.68	2.44	2.10	0.10	0.46	0.91	4.80	Cretaceous
2709	M089-B	32.36	8.53	2.65	4.32	0.17	0.66	1.29	3.65	Cretaceous
2775.5	M069-B	30.08	5.79	2.48	2.89	0.07	0.73	0.95	5.06	Cretaceous
2880.5	M087-B	36.50	4.98	3.22	1.11	0.10	0.39	0.99	4.51	Cretaceous
3035	M190-B	26.64	6.43	1.14	8.21	0.11	1.05	1.17	4.61	Cretaceous
3220	M175-B	17.63	5.57	4.05	1.27	0.96	3.21	7.10	2.79	Cretaceous

Depth [m]	Sample	Mica/illite	I/S	Di-octahedral Smectite	Tri-octahedral Smectite	Kaolinite	Chlorite	Total	Clay Total	Period/Sub-Period
1449	M054-B	18.16	0.00	0.00	53.51	0.00	1.24	100.00	72.91	Tertiary
1532	M048-B	14.60	5.87	22.09	20.21	3.60	2.14	100.00	68.50	Tertiary
1567	M040-B	19.99	1.04	10.28	21.38	3.17	2.60	100.00	58.47	Tertiary
1580	M034-B	14.09	6.85	7.53	13.25	3.12	2.00	100.00	46.85	Tertiary
1610	M021-B	16.13	8.06	16.05	6.44	10.58	2.29	100.00	59.55	Tertiary
1700	M003-B	11.88	7.20	10.29	4.77	9.89	2.27	100.00	46.30	Tertiary
1802	M101-B	14.58	9.98	16.18	4.38	9.37	3.12	100.00	57.59	Cretaceous
2098	M082-B	19.98	0.00	11.53	2.75	10.01	3.41	100.00	47.68	Cretaceous
2399.5	M077-B	10.92	3.75	9.10	3.38	10.95	3.80	100.00	41.89	Cretaceous
2606	M073-B	16.12	10.24	8.92	3.13	12.01	3.96	100.00	54.38	Cretaceous
2709	M089-B	16.80	4.30	7.78	2.57	10.53	4.39	100.00	46.37	Cretaceous
2775.5	M069-B	13.67	12.48	6.60	4.34	11.14	3.73	100.00	51.95	Cretaceous
2880.5	M087-B	13.94	10.32	13.09	2.13	6.66	2.04	100.00	48.18	Cretaceous
3035	M190-B	14.39	12.81	4.44	3.76	11.22	4.02	100.00	50.64	Cretaceous
3220	M175-B	16.60	7.90	15.02	3.50	12.71	1.68	100.00	57.41	Cretaceous

The carbonate fraction in the whole rock mineralogy is generally low and shows no trend. Mixed-layer I/S shows a variable trend for both wells (Figure 4.15) with a general increase, this increase has the over print of diagenesis (e.g. Hower et al, 1976; Boles & Franks, 1979). The illite/mica (Figure 4.16) which is detrital in origin, is quite variable. However, the dominant control seems to be that of stratigraphy as there are no uniform trends from one well to the other, which is characteristic of diagenesis. Kaolinite (Figure 4.17) is persistent to the base of the wells and has a variable trend that is not in keeping with most diagenetic profiles that have kaolinite decreasing with increasing diagenesis. Equally, chlorite (Figure 4.18) is only present in a few percent so distinguishing a diagenetic trend

from the overprint of detrital input is not possible. Pyrite (Figure 4.19), an early diagenetic mineral, has a consistent trend with depth at only a few percent but increases rapidly into the Jurassic, where it constitutes 6-10% of the mineralogical make up. Clinoptilolite, a zeolite, is observable in all the samples (Figure 4.20), elevated levels are contemporaneous with low quartz and high di and tri-octahedral smectites, hinting at an igneous source either directly from Tertiary volcanism or from weathering of igneous rocks on the continental source area. K-feldspar exhibits a general decrease (Figure 4.21) with depth for both wells and is almost depleted by the Juassic in Rhum 3/29a4. Plagioclase (Figure 4.22) is variable with depth and disappears in the Jurassic. Plagioclase tends to be more common in sandstones than mudstones (Lee et al, 2003). The diagenesis of plagioclase generally follows that of K-feldspar and a source of Al for the illitization of smectite is generated (e.g. Hower et al, 1976) but additionally plagioclases have been demonstrated to be reprecipitated as Ca-enriched overgrowths (possibly zeolites) and clays (Karner & Schreiber, 1993). This possibly explains the presence of clinoptlilolite persisting to depth, well out of the Teriary volcanic zone.

The dataset presented is complex due to the changes in sediment input type and depositional environment over the period from the Jurassic to the Tertiary. The variable sediment input appears to be the dominant control but in parts diagenesis appears to play a role in the trends observed, however there are no clear diagenetic increases or decreases (compare Chapter 2).

The effects of Tertiary volcanism in both wells are demonstrated by a decrease in quartz and an increase in smectite and clinoptiliolite. The Cretaceous has the most constant trends and is the only section that shows diagenetic trends. The depth range is not enough to show complete diagenetic profiles. In contrast, the Jurassic represents a completely alternative environment with elevated pyrite levels and very low chlorite. If a diagenetic profile was complete chlorite should be as abundant as in the Cretaceous. As a consequence, differences in depositional environment and

associated sedimentary deposition are the dominant processes involved in the Northern North Sea.

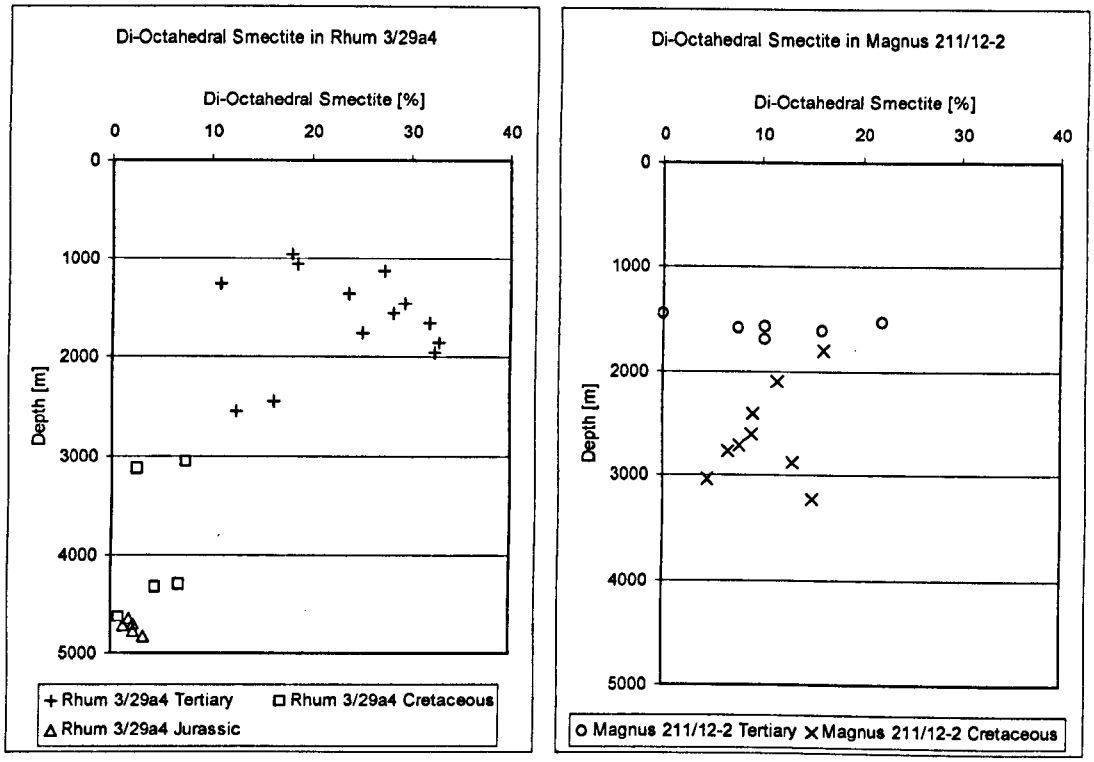

Figure 4.13. Whole Rock Quantitative X-ray Diffraction analysis trends for Di-Octahedral Smectite in Rhum 3/29a4 and Magnus 211/12-2.

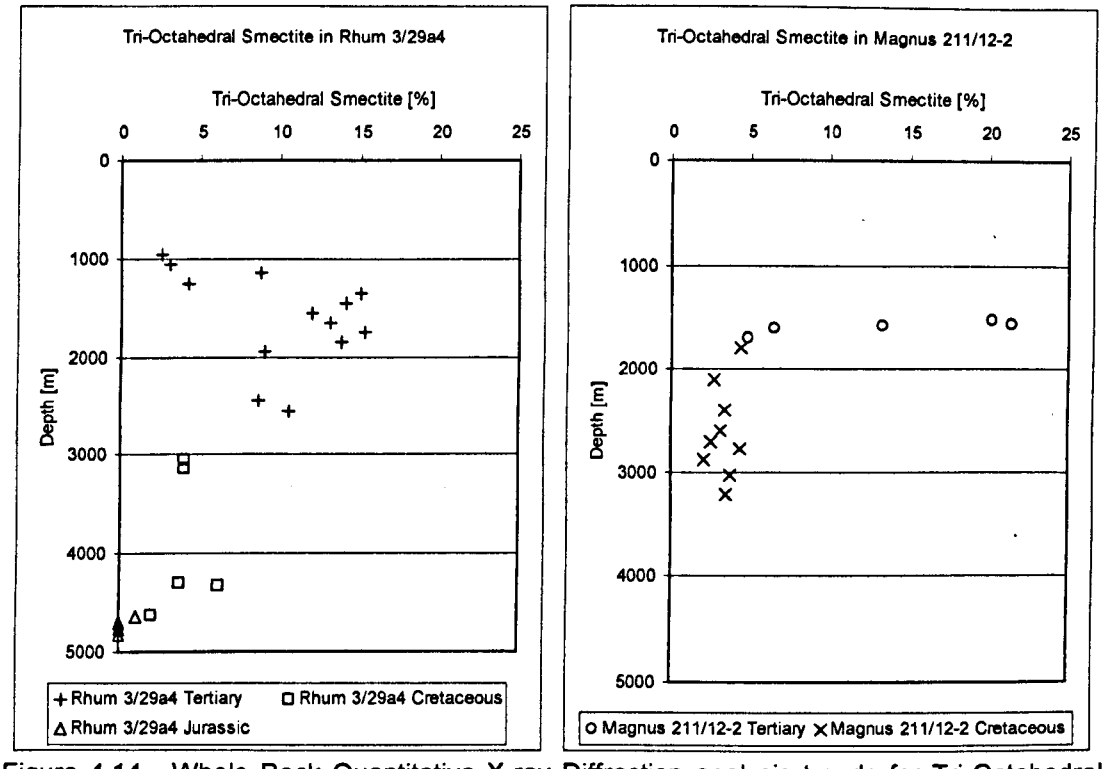

Figure 4.14. Whole Rock Quantitative X-ray Diffraction. analysis trends for Tri-Octahedral Smectite in Rhum 3/29a4 and Magnus 211/12-2.

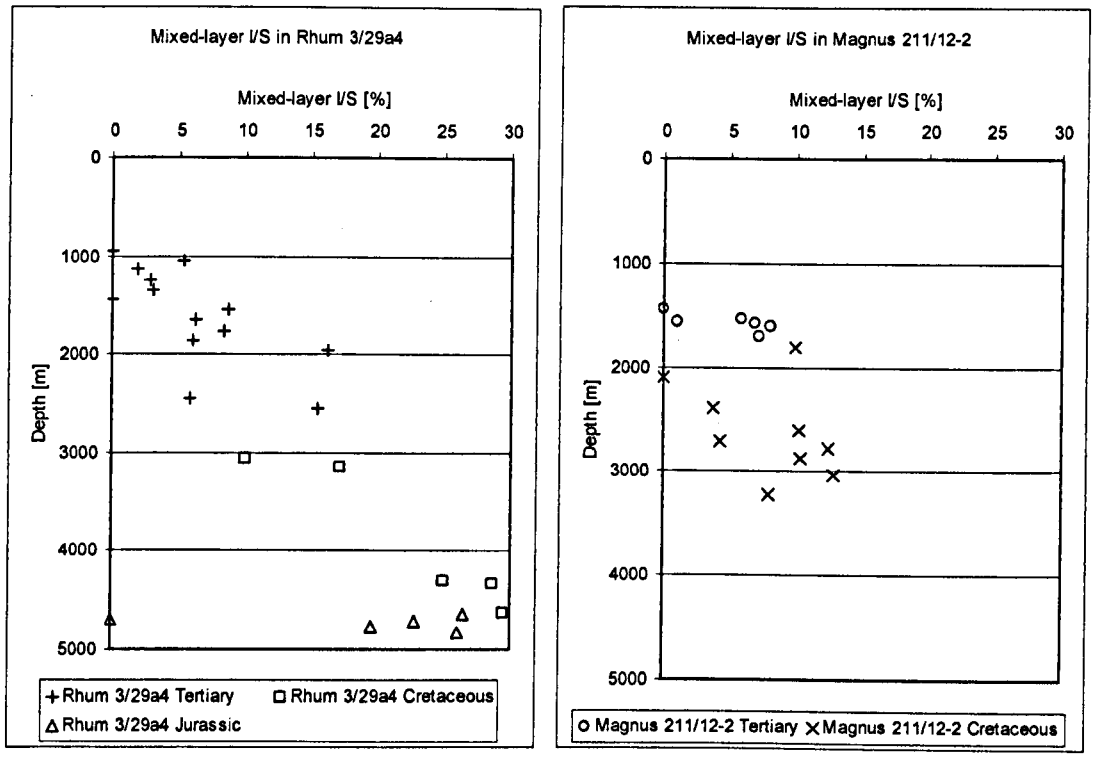

Figure 4.15. Whole Rock Quantitative X-ray Diffraction analysis trends for mixed-layer illite/smectite in Rhum 3/29a4 and Magnus 211/12-2.

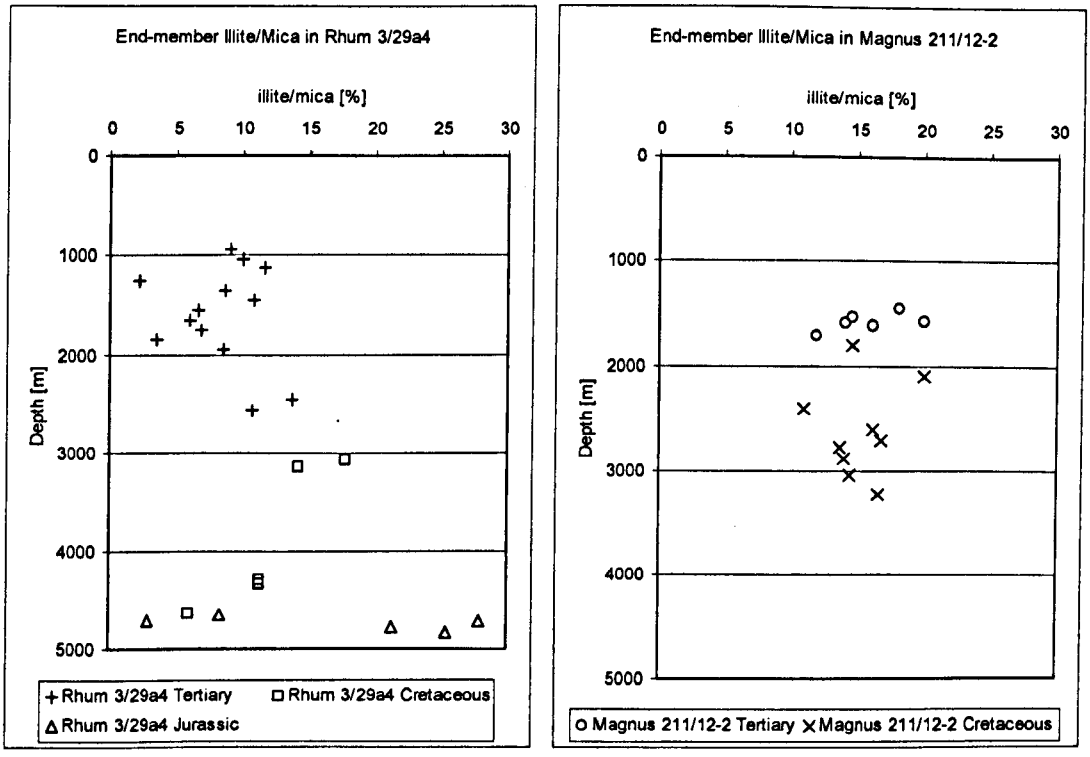

Figure 4.16. Whole Rock Quantitative X-ray Diffraction analysis trends for end-member illite in Rhum 3/29a4 and Magnus 211/12-2.

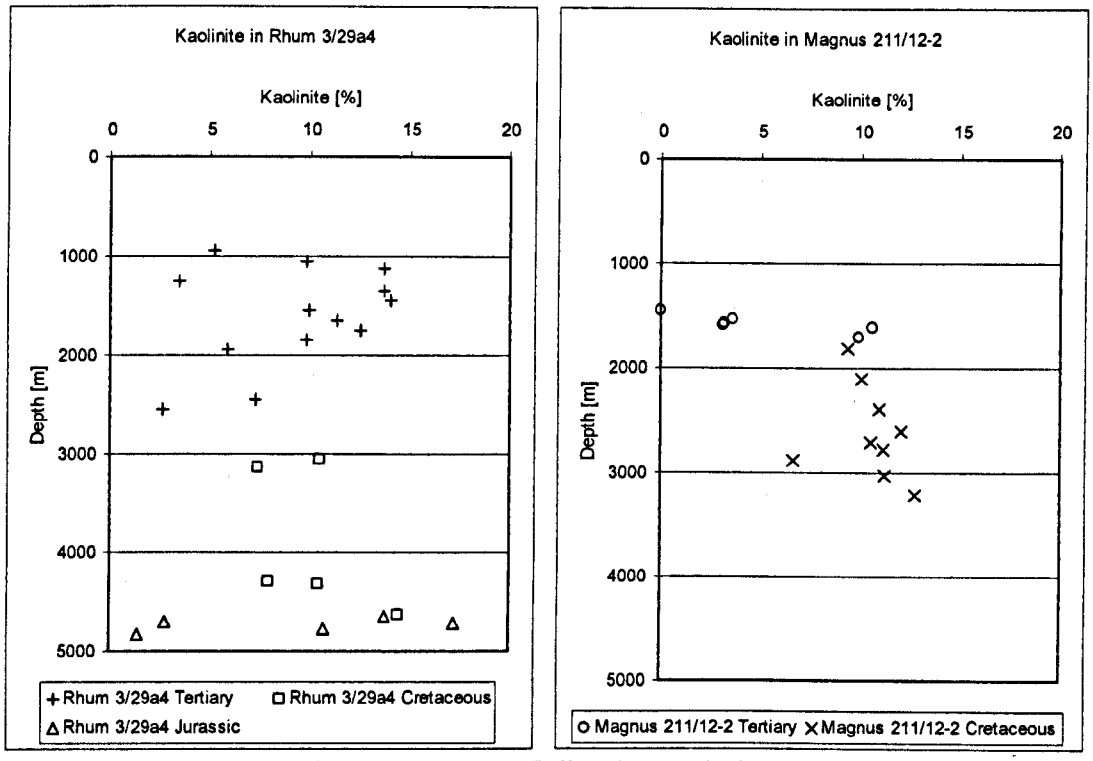

Figure 4.17. Whole Rock Quantitative X-ray Diffraction analysis trends for kaolinite in Rhum 3/29a4 and Magnus 211/12-2.

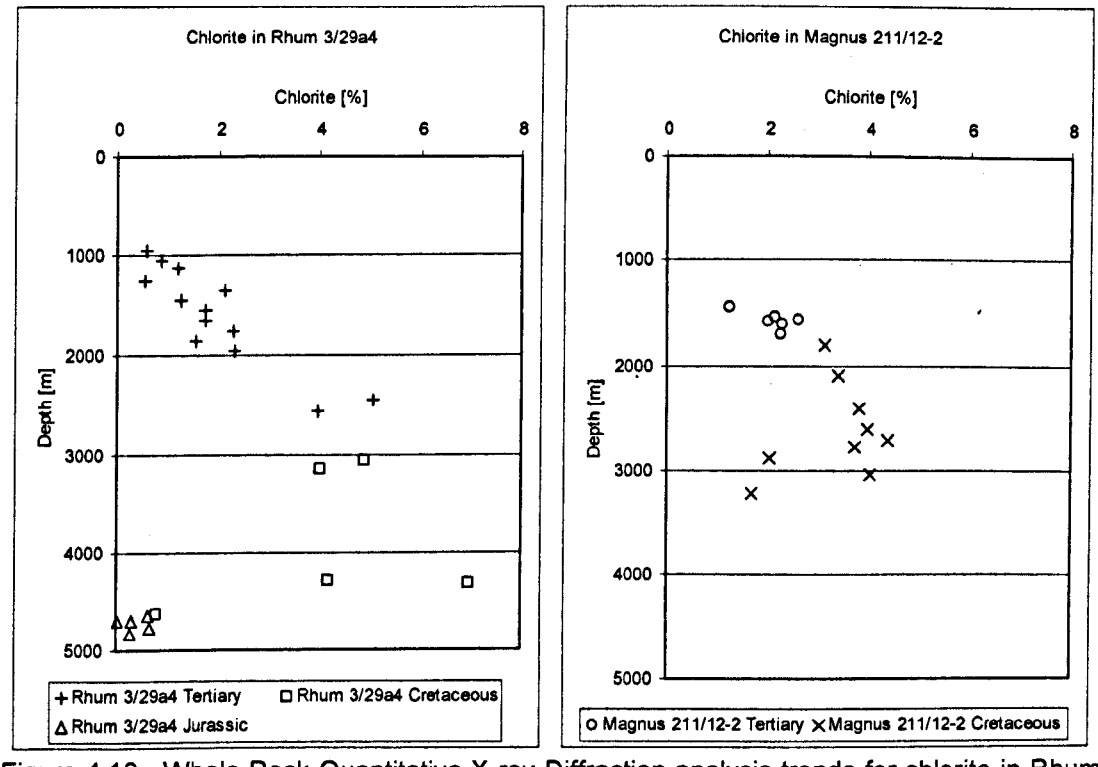

Figure 4.18. Whole Rock Quantitative X-ray Diffraction analysis trends for chlorite in Rhum 3/29a4 and Magnus 211/12-2.

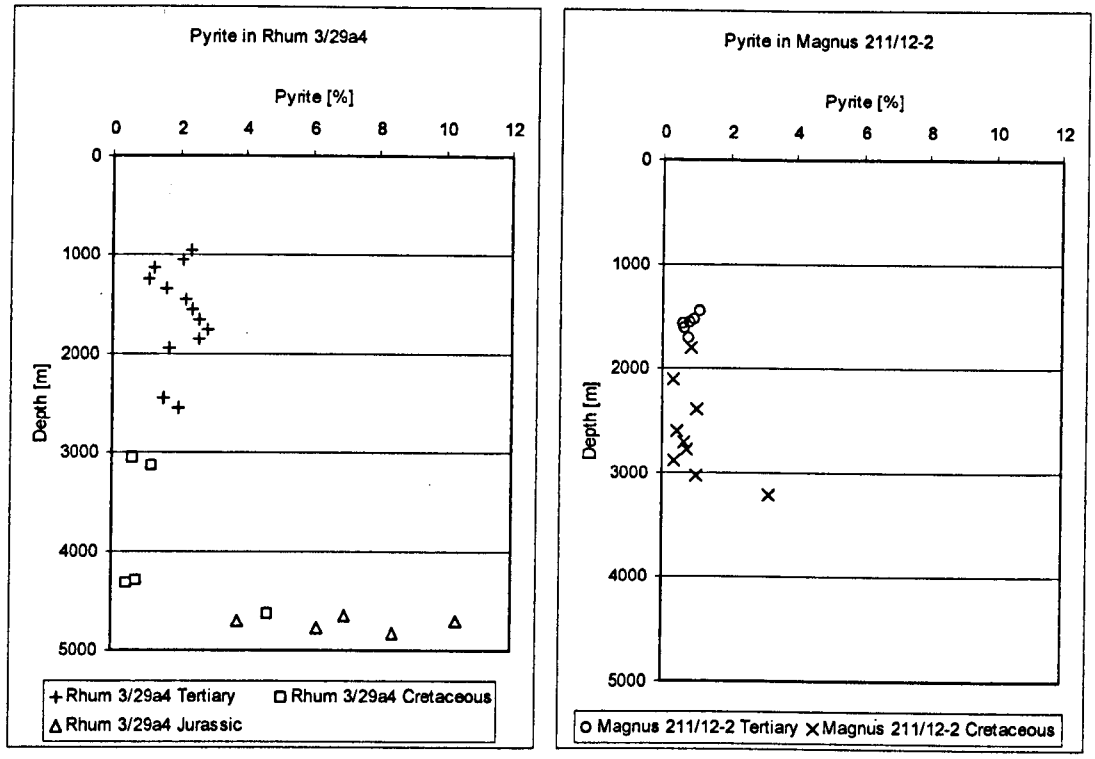

Figure 4.19. Whole Rock Quantitative X-ray Diffraction analysis trends for pyrite in Rhum 3/29a4 and Magnus 211/12-2.

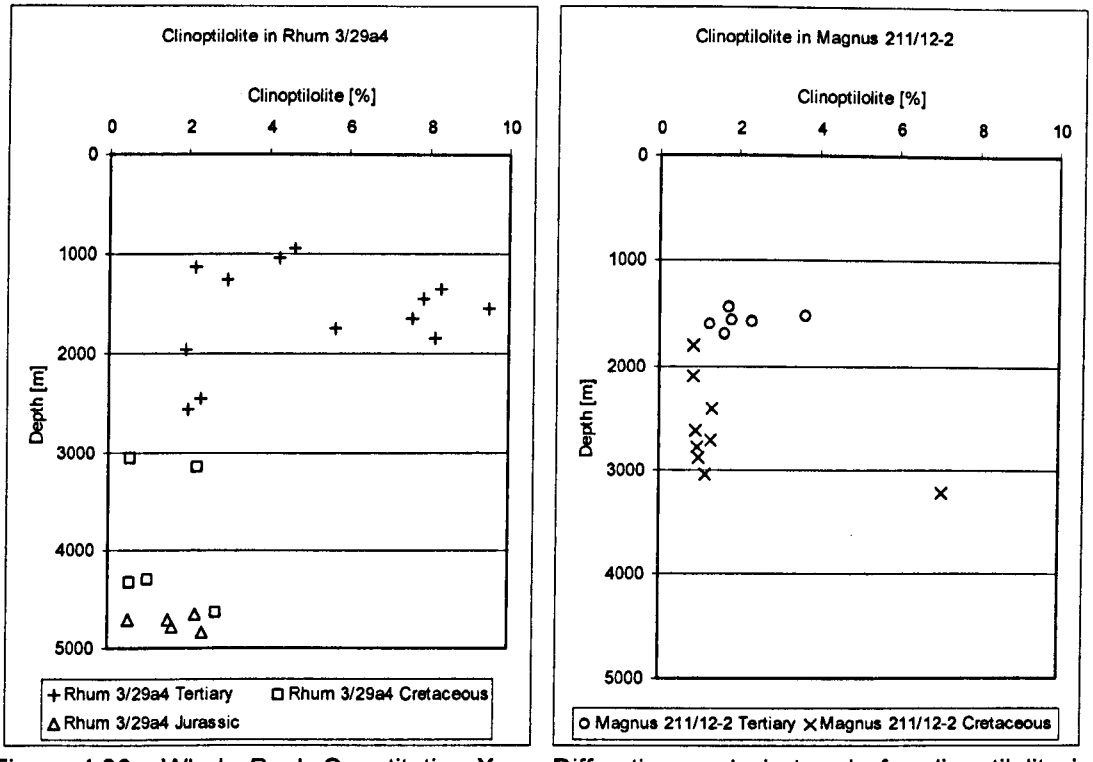

Figure 4.20. Whole Rock Quantitative X-ray Diffraction analysis trends for clinoptilolite in Rhum 3/29a4 and Magnus 211/12-2.

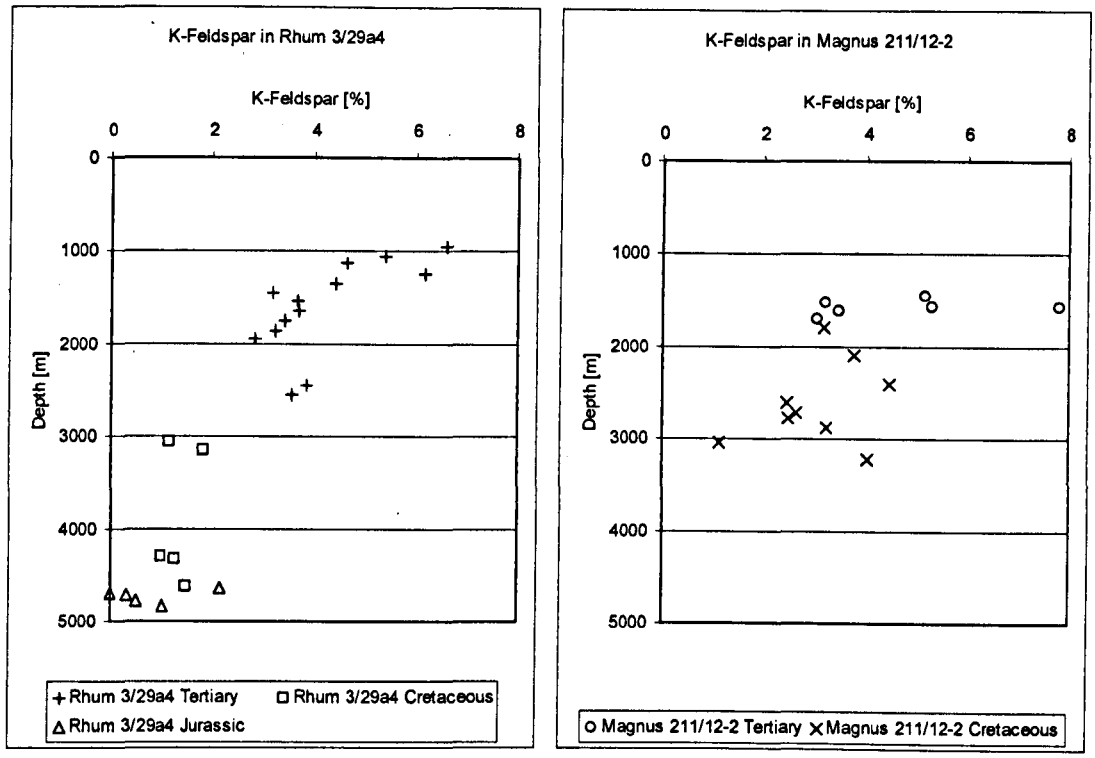

Figure 4.21. Whole Rock Quantitative X-ray Diffraction analysis trends for K-feldspar in Rhum 3/29a4 and Magnus 211/12-2.

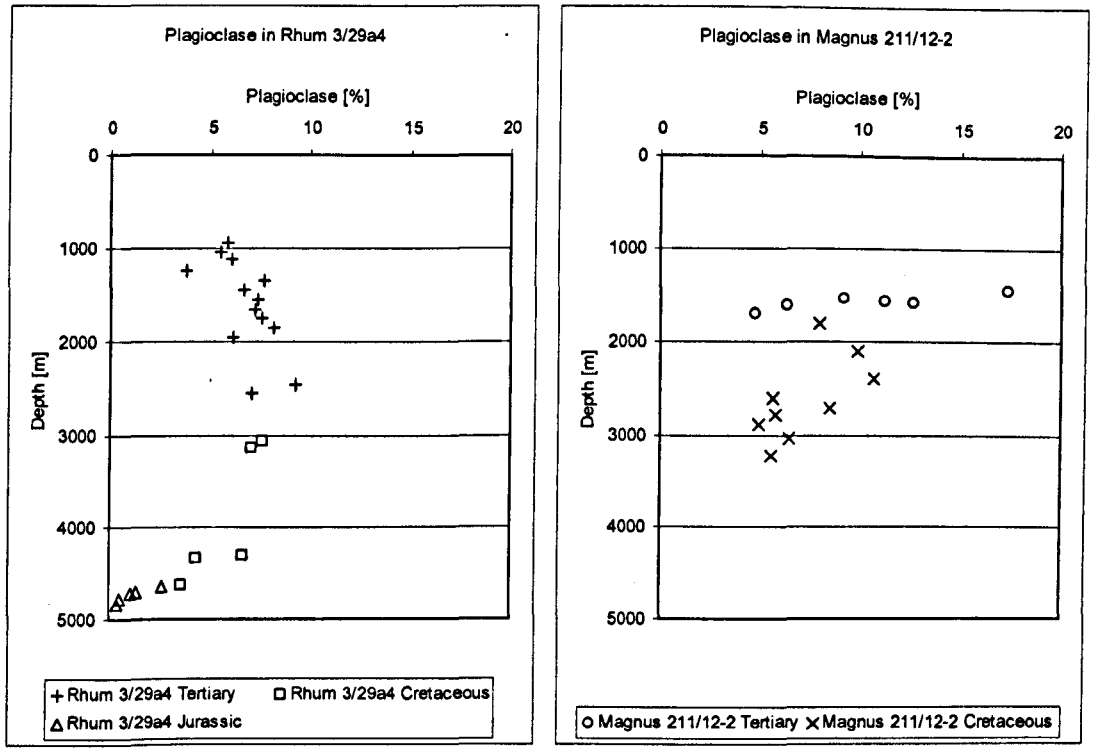

Figure 4.22. Whole Rock Quantitative X-ray Diffraction analysis trends for plagioclase in Rhum 3/29a4 and Magnus 211/12-2.

Table 4.5. Quantitative clay mineralogy in the <2μm clay size fraction for Rhum 3/29a4. Clino refers to the presence of Clinoptilolite and tri to the presence of tri-octahedral smectites. Exp. may be read as the percentage of smectite in illite/smectite.

Relative percentage of clay minerals in the <2μm clay size fraction								
Depth	XRD pattern name	Illite	Chlorite	Kaolin	Illite-smectite	*%Exp.	Comments	Age
1130	3-29A-4 1130	4	0	10	86	94	Tri	Tertiary
1190	3-29A-4 1190	5	0	12	83	89	Tri	Tertiary
1250	3-29A-4 1250	16	0	16	67	90	Fine-grained quartz	Tertiary
1350	3-29A-4 1350	4	0	15	81	94	clino, tri	Tertiary
1460	3-29A-4 1460	3	0	13	84	75	clino, tri	Tertiary
1550	3-29A-4 1550	2	0	10	88	89	clino, tri	Tertiary
1650	3-29A-4 1650	3	0	10	87	75	clino, tri	Tertiary
1750	3-29A-4 1750	5	0	24	71	84	clino, tri	Tertiary
1850	3-29A-4 1850	4	0	8	89	94	clino, tri	Tertiary
1950	3-29A-4 1950	4	1	5	91	66		Tertiary
1990	3-29A-4 1990	3	1	2	94	75		Tertiary
2050	3-29A-4 2050	5	3	4	88	60		Tertiary
2160	3-29A-4 2160	6	0	15	79	84	Tri	Tertiary
2250	3-29A-4 2250	8	1	5	87	75		Tertiary
2350	3-29A-4 2350	7	8	3	82	60		Tertiary
2450	3-29A-4 2450	7	6	4	83	49		Tertiary
2550	3-29A-4 2550	2	2	0	96	49		Tertiary
2740	3-29A-4 2740	19	8	6	66	49		Cretaceous
3050	3-29A-4 3050	16	10	6	68	45		Cretaceous
3500	3-29A-4 3500	17	9	10	64	45		Cretaceous
3980	3-29A-4 3980	0	0	0	0	45		Cretaceous
4120	3-29A-4 4120	17	10	15	58	49		Cretaceous
4300	3-29A-4 4300	12	4	9	75	49		Cretaceous
4470	3-29A-4 4470	7	5	5	83	49		Cretaceous
4650	3-29A-4 4650	14	2	20	64	35	Ordered	Jurassic

*%Exp = percentage expandable layers in mixed-layer illite-smectite

The mineralogy of clay minerals in the less than 2μm clay size fraction for Rhum 3/29a4 can be viewed in Tables 4.5 and Figures 4.23 to 4.27. The bulk of the clay fraction is mixed-layer illite-smectite with varying percentages of smectite, which decrease with depth and is diagenetic in origin as described by the classic Gulf of Mexico studies by Hower et al. (1976) and Boles and Franks (1979). Chlorite only appears below 1950m in the middle Tertiary and therefore must be diagenetic in origin and increases in abundance through the Cretaceous and then decline towards the Jurassic. The sample at 4650m is the only Jurassic sample measured and it only contains 2% chlorite. This is consistent with the measurements in the whole rock quantification presented above. Kaolinite generally decreases through the Tertiary and Cretaceous, the Jurassic sample has relative elevated levels in comparison to the Early Cretaceous samples. The sudden increase in illite in the down-hole trend coinsides with the boundary between the

Cretaceous and the Tertiary. The temperatures down the profile consist solely of corrected bottom hole temperature data, 104°C at 2927m, 130°C at 4405m, 150°C at 4710m and 151°C at 4865m.

Mineralogy of clay minerals in the less than 2μm clay size fraction for Magnus 211/12-2 may be viewed in Tables 4.6 and Figures 4.23 to 4.27. The bulk of the less than 2μm clay mineral fraction is composed of mixed layer illite-smectite, with decreasing percentages of smectite in the mixed layer phase as the diagenetic mineral reactions (Hower et al., 1976; Boles & Franks, 1979) in the basin evolve as a function of increased temperature and pressure. Kaolinite increases down the well, which is the reverse of the trend documented in chapter 2 and may be a function of sediment input change rather than solely a diagenetic change as there is a noticeable increase in the Cretaceous compared to the Tertiary. Likewise, the illite concentration increases at the same boundary point but the change is not as marked as that observed in Rhum 3/29a4. In contrast to Rhum 3/29a4 the chlorite in the less than 2μm fraction is present from the top of the sampled section and increases slightly with depth.

As with the whole rock mineralogy the effects of depositional environment and sediment supply can be seen in the less than 2μm clay size fraction of the clay minerals (Figures 4.23 to 4.27). The low chlorite in the base Cretaceous and Upper Jurassic and the high kaolinite concentrations diverge from published diagenetic trends (e.g. Hower et al, 1976; Boles & Franks, 1979) and suggest the overprint of changing sediment type through time. The decrease in the percentage of smectite in illite-smectite shows a rapid decrease in the Tertiary and a more constant decrease through the Cretaceous to a high termination value of ~35% S. The amount of K-feldspar is depleted by this point in the system.

Table 4.6. Results of the quantitative clay mineralogy in the <2μm clay size fraction for Magnus 211/12-2. Exp. May be read as the percentage of smectite in illite/smectite.

	Relative percentage of clay minerals in the <2mm clay size fraction							
depth	XRD pattern name	Illite	Chlorite	Kaolin	Illite-smectite	%Exp*	Comments	Age
1000	211-12-2-1000	9	3	7	81	75	Clinoptilolite	Tertiary
1100	211-12-2-1100	5	3	10	82	70	Clinoptilolite	Tertiary
1200	211-12-2-1200	4	4	8	84	75	Clinoptilolite	Tertiary
1300	211-12-2-1300	2	1	2	95	84	Clinoptilolite	Tertiary
1350	211-12-2-1350	3		2	95	84	Clinoptilolite	Tertiary
1413	211-12-2-1413	2	1	2	95	84		Tertiary
1449	211-12-2-1449				100	100	smectite is tri-octahedral	Tertiary
1475	211-12-2-1475	12	2	1	85	75		Tertiary
1525	211-12-2-1525	10	2	1	87	75		Tertiary
1572	211-12-2-1572	3		5	92	60	kaolin is kaolin/smectite?	Tertiary
1610	211-12-2-1610	9	5	9	77	66		Tertiary
1700	211-12-2-1700	10	6	7	77	66		Tertiary
1800	211-12-2-1800	10	5	12	73	60		Cretaceous
1907	211-12-2-1907	10	6	9	75	66		Cretaceous
1998	211-12-2-1998	11	5	12	72	66		Cretaceous
2100	211-12-2-2100	12	7	9	72	54		Cretaceous
2200	211-12-2-2200	10	6	7	77	60		Cretaceous
2300	211-12-2-2300	17	12	14	57	49		Cretaceous
2400	211-12-2-2400	18	9	15	58	54		Cretaceous
2490	211-12-2-2490	16	8	15	61	50		Cretaceous
2600	211-12-2-2600	19	10	12	59	49		Cretaceous
2710	211-12-2-2710	13	8	11	68	49		Cretaceous
2802	211-12-2-2802	12	7	10	71	49		Cretaceous
2876	211-12-2-2876	15	11	16	58	40		Cretaceous
2987	211-12-2-2987	11	8	13	68	40		Cretaceous
3080	211-12-2-3080	18	7	14	61	40		Cretaceous
	*%Exp = percentage expandable layers [smectite] in mixed-layer illite-smectite							

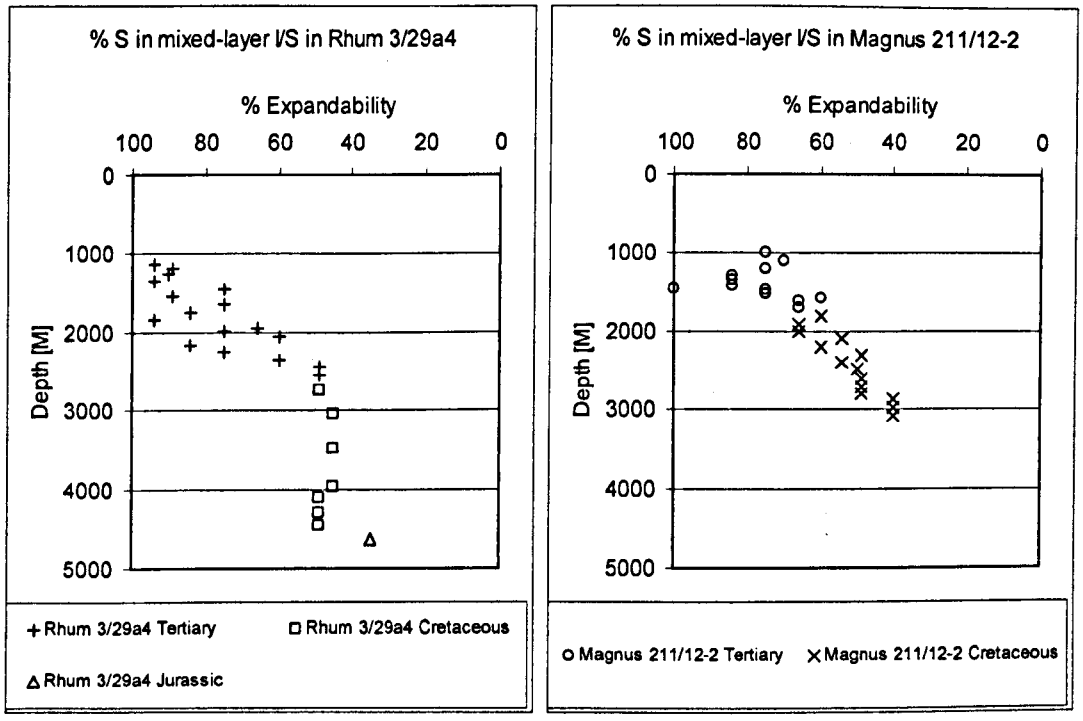

Figure 4.23. %smectite in mixed-layer illite/smectite from the quantitative clay mineralogy in the <2μm clay size fraction for Rhum 3/29a4 and Magnus 211/12-2.

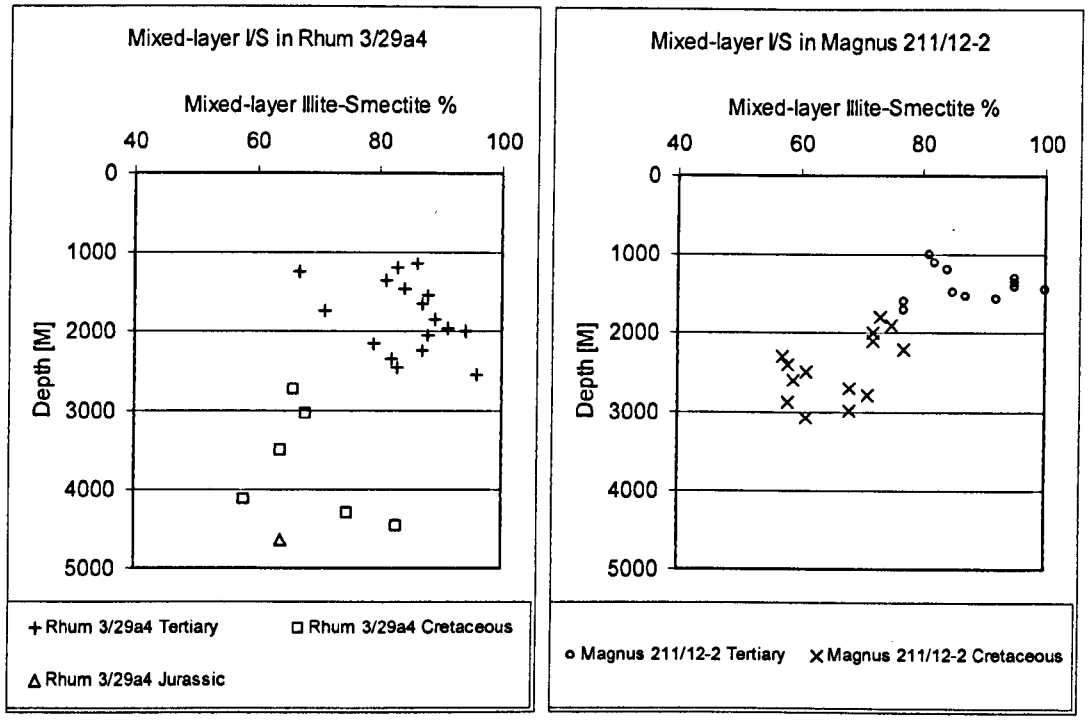

Figure 4.24. % of mixed-layer illite/smectite from the quantitative clay mineralogy in the <2μm clay size fraction for Rhum 3/29a4 and Magnus 211/12-2.

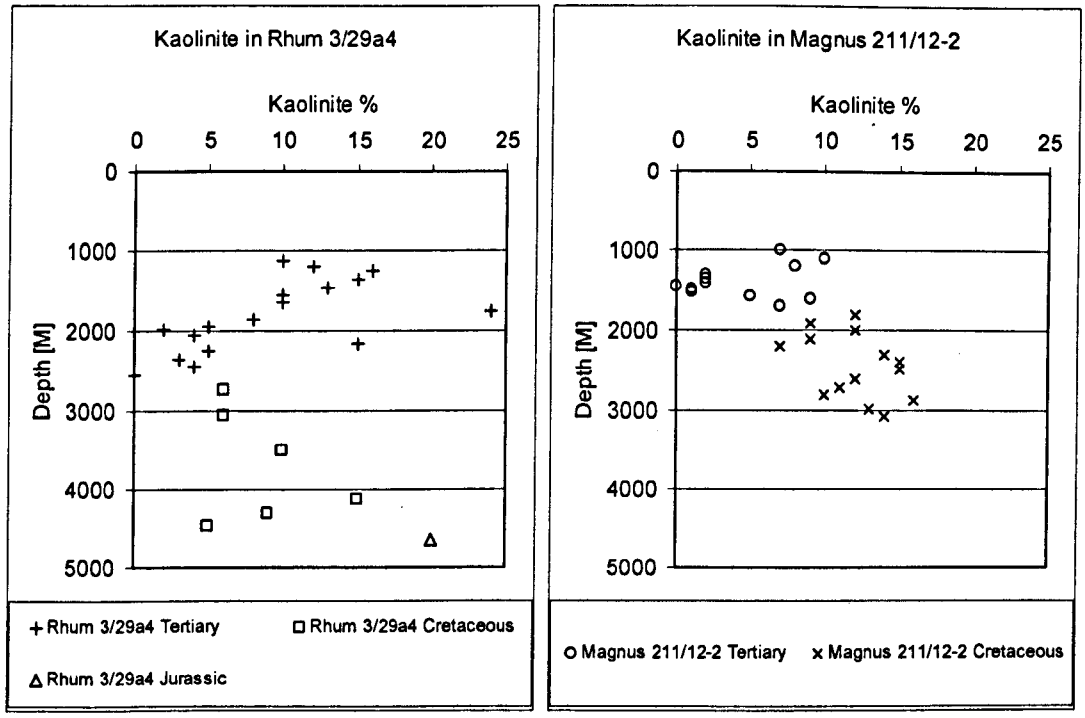

Figure 4.25. % kaolinite from the quantitative clay mineralogy in the <2μm clay size fraction for Rhum 3/29a4 and Magnus 211/12-2.

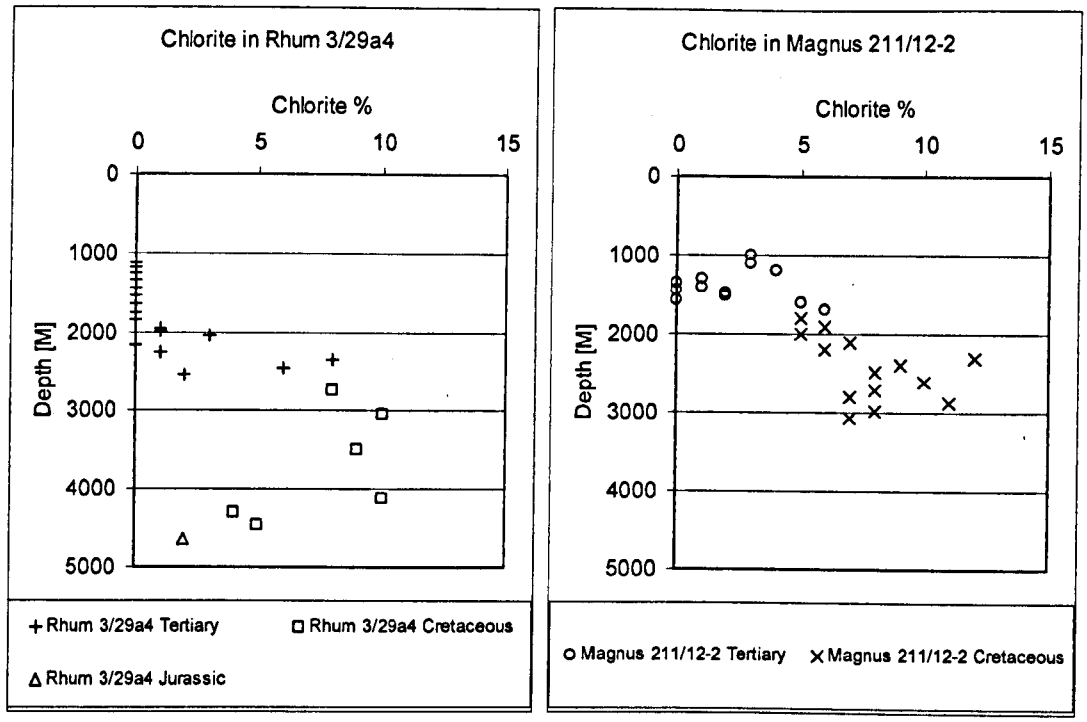

Figure 4.26. % chlorite from the quantitative clay mineralogy in the <2μm clay size fraction for Rhum 3/29a4 and Magnus 211/12-2.

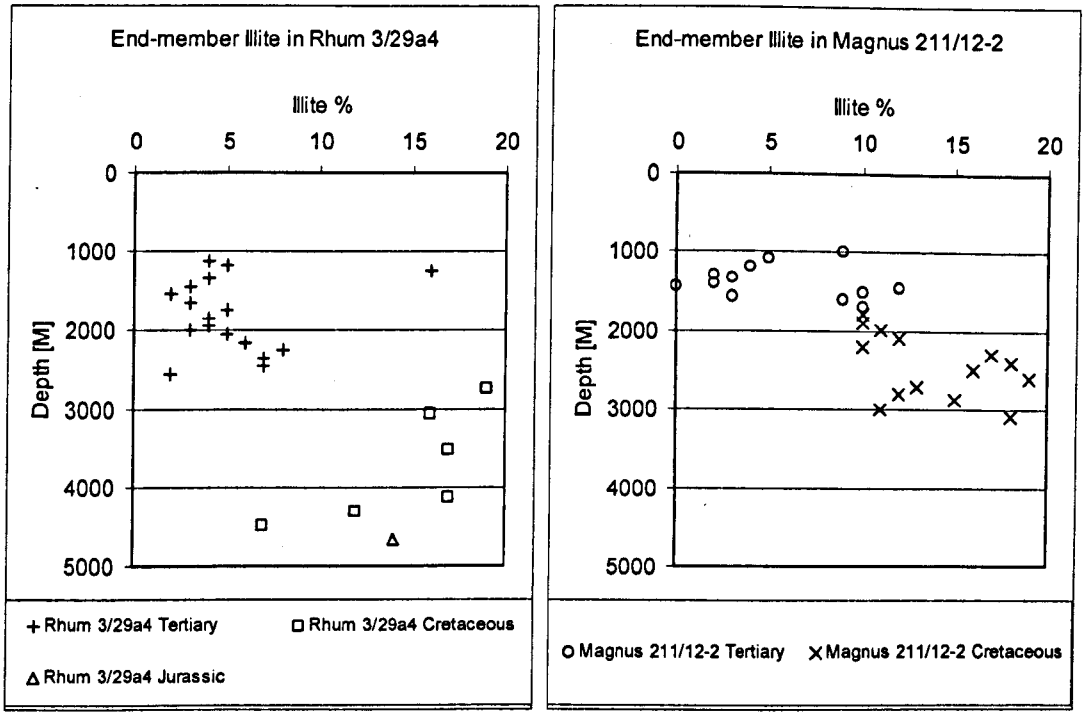

Figure 4.27. % end-member illite from the quantitative clay mineralogy in the <2μm clay size fraction for Rhum 3/29a4 and Magnus 211/12-2.

4.3.2: High Resolution X-ray Texture Goniometry (HRXTG):

4.3.2.1: Rhum 3/29a4:

The pole figures associated with HRXTG recorded for samples from Rhum 3/29a4 are shown in Figure 4.32. The maximum intensity (m.r.d.) contours for the I/S and C-K peaks along with the contour interval, the 2-theta positions for the measured peaks and associated Kα average d-spacings for Rhum 3/29a4, are presented in Table 4.7. The 2-theta positions for the I/S peak range from 3.34° 2-Θ to 4.05° 2-Θ, for the C-K peak 2-theta positions range from 5.52° 2-Θ to 5.95° 2-Θ. The associated d-spacings for these 2-theta positions calculated by using the average Kα radiation of Molybdenum, a weighted average (Brindley & Brown, 1980) and applying the Bragg Equation [1] are presented in Table 4.7.

$$2d\sin\theta = n\lambda \qquad [1]$$

where λ is the wavelength for Molybdenum (Kα = 0.710730). This value is a customary weighted average of $K\alpha_1$ and $K\alpha_2$, where $K\alpha_1$ is taken to have twice the weight of $K\alpha_2$ (Brindley and Brown, 1980).

As discussed previously, the intensity of the transmitted X-ray beam is not as great as typically recorded for the samples presented in Chapter 2. This also raises data quality issues. Figure 4.28 is an overlay of "2-theta scans" for samples from Rhum 3/29a4. Four samples of increasing depth are plotted, sample R1150 (Green line), sample R2550 (Blue line), sample R4707 (Brown line) and sample R4830 (Purple line) along with a run where no sample was introduced to the X-ray beam (Black line). The figure clearly shows the decreasing intensity recorded, especially so in the C-K peak region (d= 7Å). The deepest samples from the Jurassic have almost no peak height above the background (no sample), making peak identification and analysis problematic. What is apparent from the 2-theta scans (Figure 4.32) is the general scarcity of strong identifiable peaks in the d-7Å region. The d-10Å peak is also somewhat weak but is identifiable and measurable in most samples. These observations contrast strongly with the results presented in Chapter 2. As a consequence, the 'full scans' were taken at the peak

maximum in the d-7Å region, but the low intensity of the peak resulted in a large spread of 2-theta angles for the sample suite. The measurement at the d-10Å region was taken from a peak maximum where available. In the case of no clear peak being produced a second 2-theta scan was performed, if no peak was visible either no result was gathered or a cross reference with the previously gathered XRD data was made and a d-10Å position was chosen based on XRD mineralogy.

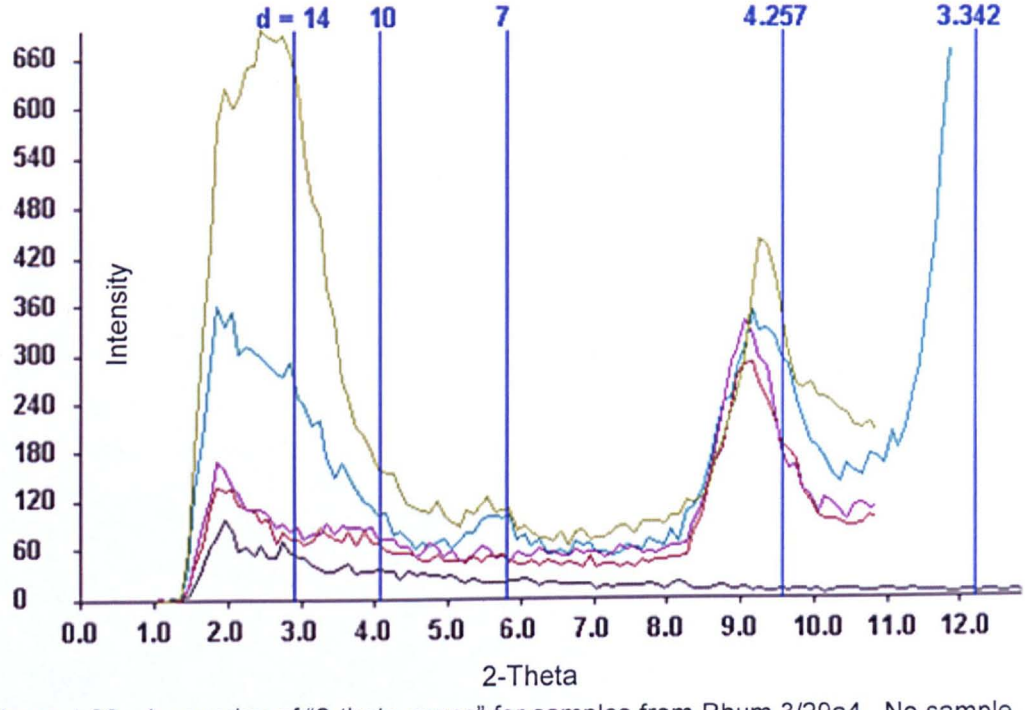

Figure 4.28. An overlay of "2-theta scans" for samples from Rhum 3/29a4. No sample (Black line), sample R1150 (Green line), sample R2550 (Blue line), sample R4707 (Brown line) and sample R4830 (Purple line).

Figure 4.29 shows fabric intensity as a function of depth. Three zones may be identified. From 1000m to 2600m there is a weak fabric produced, not more than ~2 m.r.d. and these fabric intensities are associated with a single pole or with multiple poles (Figure 4.32). They are all Tertiary samples Samples between 1050m and 2600m have wavy contour lines as plotted on the equal area lower hemisphere projections (Figure 4.32) for both mineral peaks. Also, where the fabric intensity is particularly low double or multiple peaks are visible (e.g R1850 and R1050). The Cretaceous samples measured between 3000m and 3140m show some variability. They have low

to moderate fabrics (~1.8 to ~3.80 m.r.d.). and this change in fabric is also co-incident with the changes in mineralogical characteristics presented above. The samples from the Jurassic (greater than 4700m) have a variable phyllosilicate preferred orientation that ranges from high to very high (Table 4.7). There are low intensities noted in several samples for their kaolinite + chlorite peak. These results qualitatively confirm the XRD observation of little chlorite in the Jurassic and are not a function of low d-7Å intensity. The samples in the Jurassic produced single poled projections, even when the fabric intensity was relatively low, the exception being sample R4830 where no C-K fabric was developed and this is evident from the pole figures (Figure 4.32).

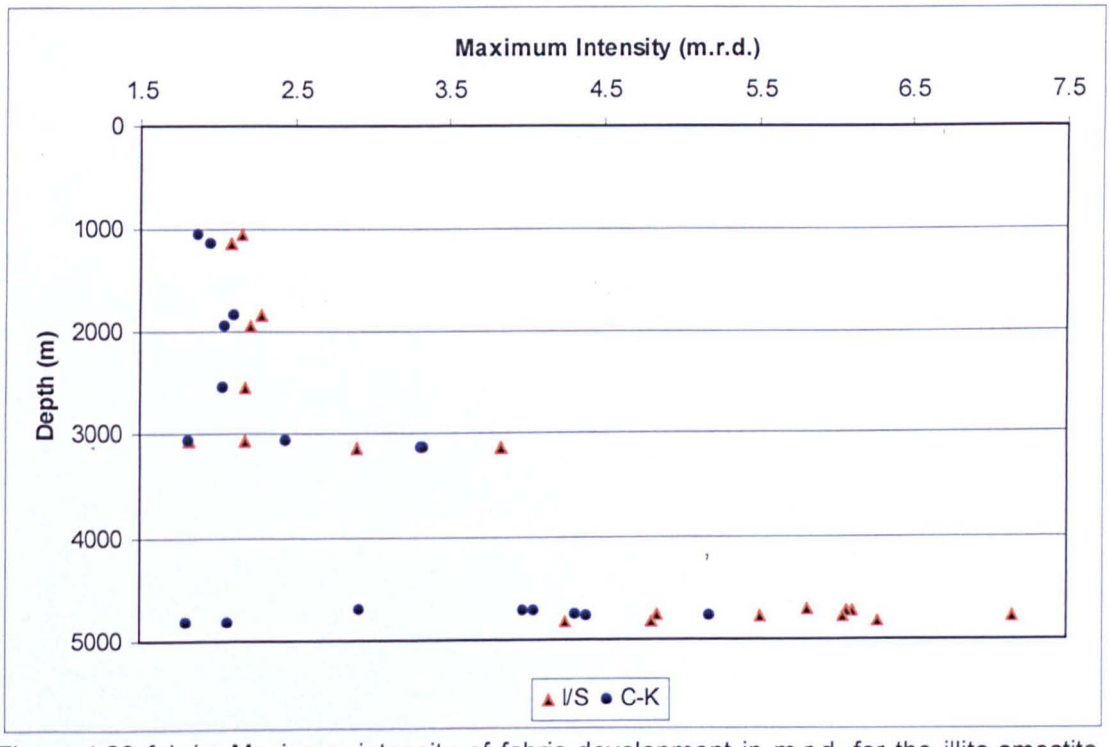

Figure 4.29 fabric: Maximum intensity of fabric development in m.r.d. for the illite-smectite and kaolinite-chlorite peaks with depth (m) for Rhum 3/29a4.

Table 4.7 The maximum intensity (m.r.d.) contours for the I/S and C-K peaks along with contour interval, the 2-theta positions for the measured peaks and associated Kα average d-spacings for Rhum 3/29a4, nd refers to not determined for this peak. X refers to a re-cut of the sample.

Sample ID	Depth (m)	Max. intensity mrd 'I-S'	Max. intensity mrd 'C-K'	Contour interval mrd	2-Theta 'I-S'	2-Theta 'C-K'	Kα ave. d-spacing 'I-S'	Kα ave. d spacing 'C-K'
R1050	1050	2.15	1.87	0.11	3.88	5.95	10.39	6.74
R1150	1150	2.08	1.95	0.11	3.83	5.55	10.50	7.21
RI850	1850	nd	2.11	0.11	nd	5.74	nd	7.04
R1850x	1850	2.28	nd	0.11	3.95	nd	10.17	nd
R1950	1950	2.21	2.05	0.11	3.92	5.64	10.23	7.07
R2550x	2550	2.18	2.04	0.11	4.05	5.64	9.94	7.11
R3060	3060	1.81	1.81	0.10	3.45	5.55	11.78	7.32
R3060x	3060	2.18	2.45	0.11	3.34	5.52	12.06	7.25
R3140	3140	2.9	3.32	0.21	3.54	5.64	11.39	7.11
R3140	3140	3.83	3.33	0.21	3.64	5.55	11.03	7.18
R4707	4707	5.82	2.92	0.55, 0.11	3.83	5.77	10.43	6.86
R4712	4712	6.11	4.06	0.55, 0.33	3.89	5.64	10.27	7.02
R4712x	4712	6.08	3.99	0.55, 0.33	3.92	5.75	10.19	6.89
R4759	4759	4.85	4.32	0.45, 0.33	3.73	5.74	10.80	6.98
R4771	4771	6.05	5.19	0.55, 0.45	3.76	5.64	10.18	7.07
R4771x	4771	5.52	4.40	0.45	3.88	5.56	10.34	7.17
R4771xx	4771	7.15	nd	0.55	3.75	5.55	10.70	7.18
R4830	4830	6.27	2.07	0.55, 0.11	3.95	5.52	10.06	7.13
R4830x	4830	4.26	1.80	0.33, 0.10	3.64	5.58	10.99	7.10
R4830xx	4830	4.82	nd	0.45	4.05	nd	9.86	nd

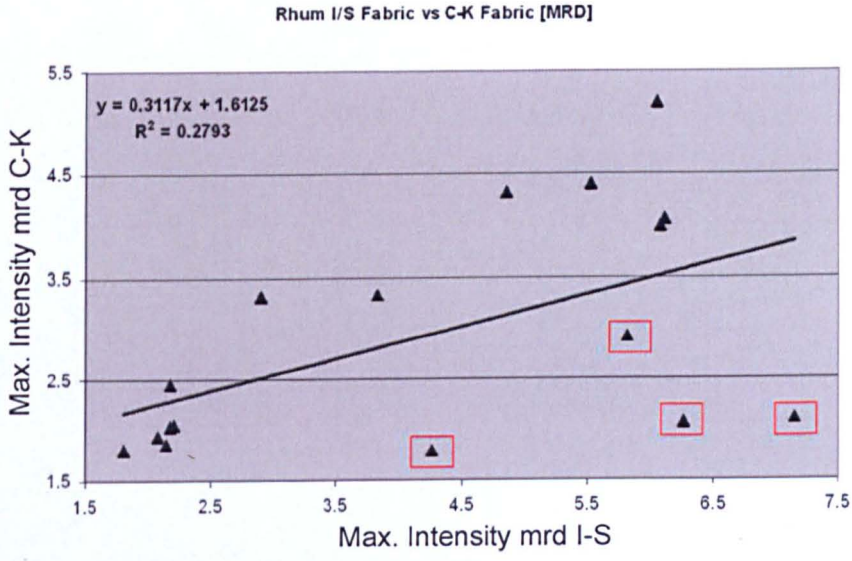

Figure 4.30. I/S against C-K maximum fabric intensity [m.r.d.] with a low correlation coefficient of 0.2793 for Rhum 3/29a4. The red squares indicate the samples removed for Figure 4.31.

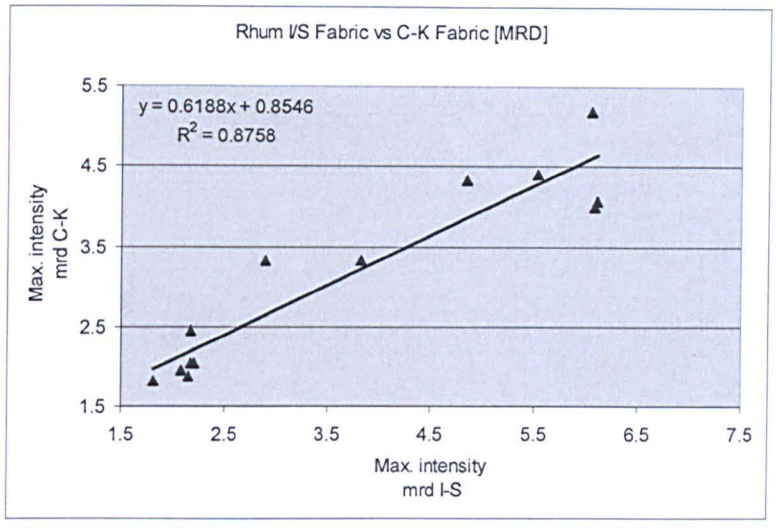

Figure 4.31. I/S against C-K maximum fabric intensity [m.r.d.] with a high correlation coefficient of 0.8758 for Rhum 3/29a4 after the anomalously low C-K fabric alignment in the Jurassic samples were removed.

Figure 4.30 compares the I/S and C-K fabric intensities (m.r.d.) for Rhum 3/29a4. A low correlation co-efficient (0.2793) was calculated for the correlation between I/S and C-K fabric intensity when all the data was analysed (Figure 4.30). When the samples with very low C-K fabrics and high I/S fabrics are removed, the criterion being that the difference between I/S and C-K fabric be less than 2.5 m.r.d. and/or no fabric was produced evidenced by the pole figures presented in Figure 4.32, the correlation coefficient changes from 0.2793 to 0.8758 (Figure 4.31). By removing the samples where no chlorite is present, the correlations between the I/S and C-K peaks for Rhum 3/29a4 approach the same correlations between peaks as is tabulated by Matenaar (2002) and Ho et al. (1999).

Figure 4.32: 2-theta scans and full pole figures for Rhum 3/29a4. Full pole figures are for the illite/smectite and kaolinite-chlorite peaks the fabric alignment in m.r.d. is stated below the pole figure.

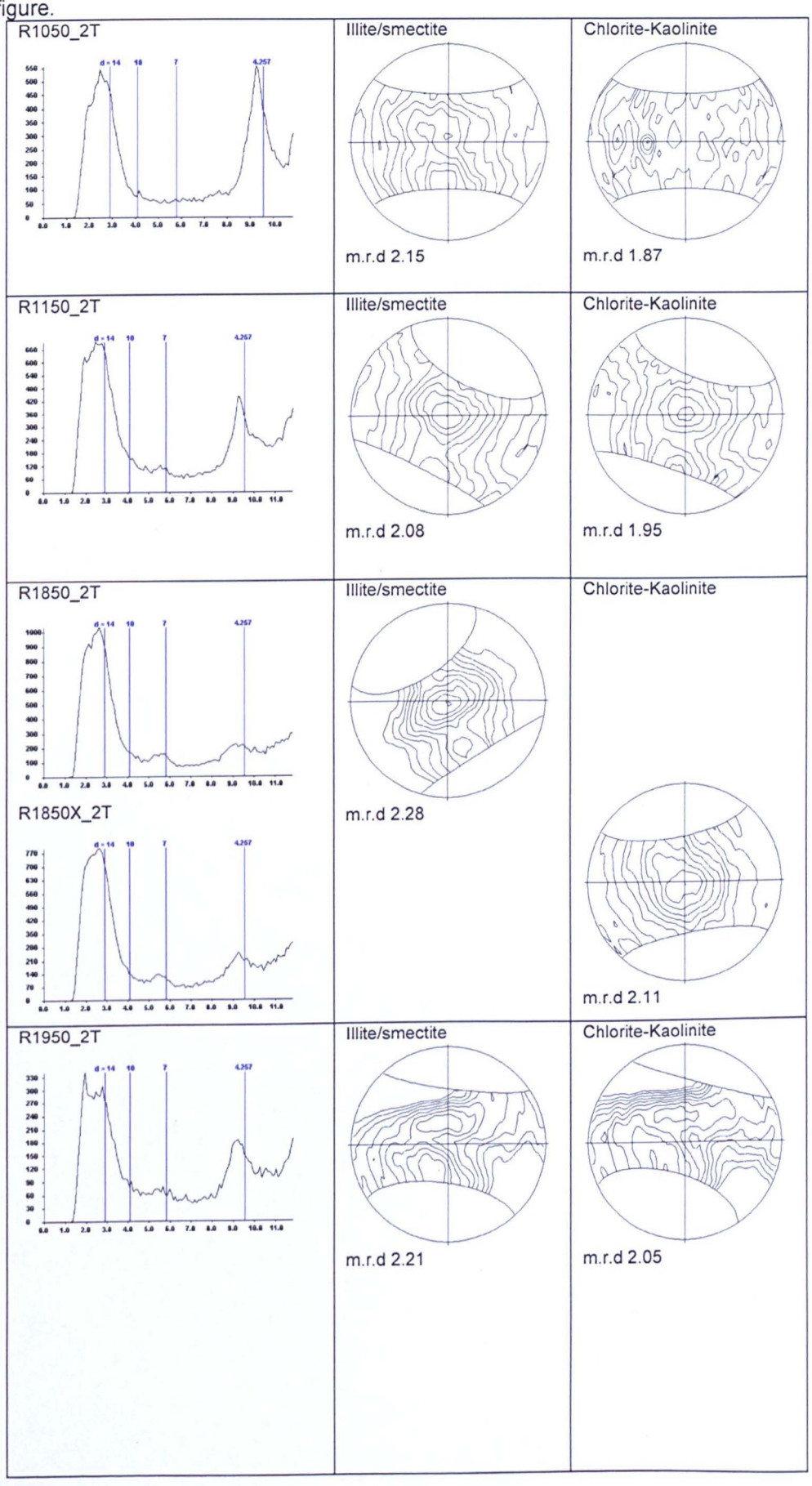

R2550_2T 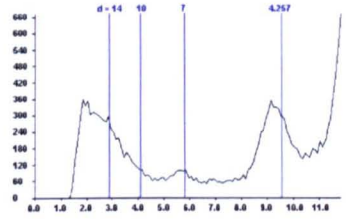 R2550X_2T 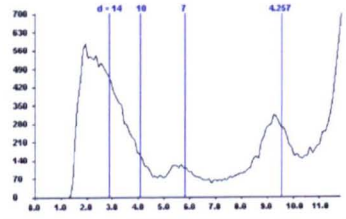	Illite/smectite 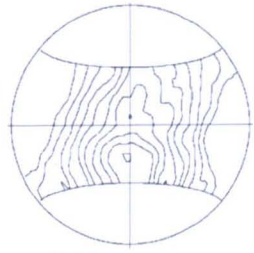 m.r.d 2.18	Chlorite-Kaolinite 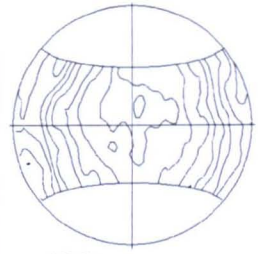 m.r.d 2.04
R3060_2T 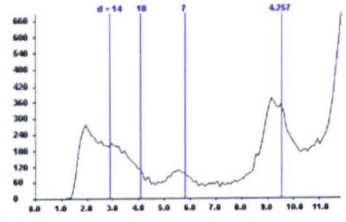	Illite/smectite 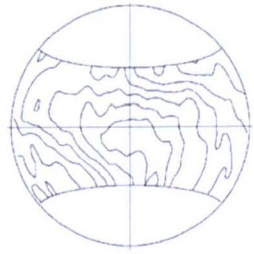 m.r.d 1.81	Chlorite-Kaolinite 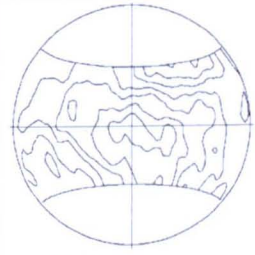 m.r.d 1.81
R3140_2T 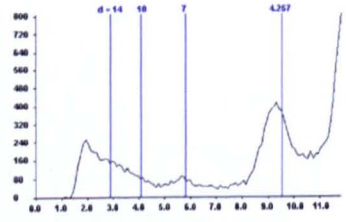 R3140X_2T	Illite/smectite 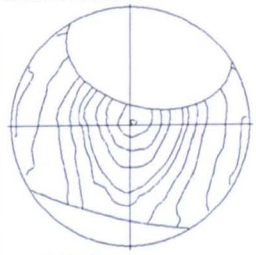 m.r.d 2.90	Chlorite-Kaolinite 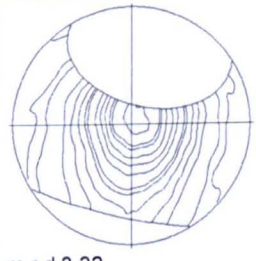 m.r.d 3.32
R4707_2T 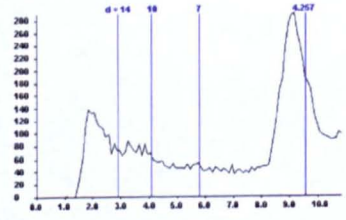	Illite/smectite 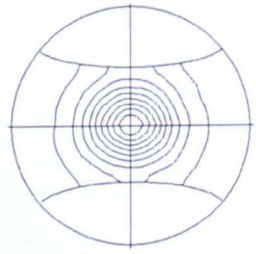 m.r.d 5.80	Chlorite-Kaolinite 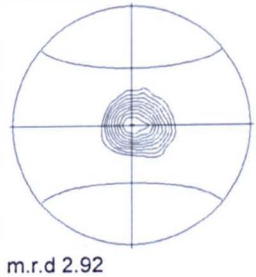 m.r.d 2.92

R4712_2T	Illite/smectite	Chlorite-Kaolinite
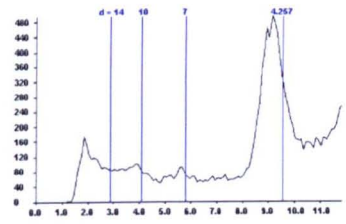	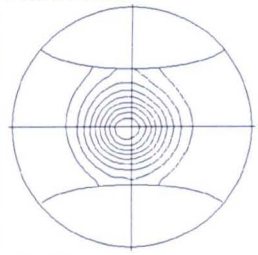	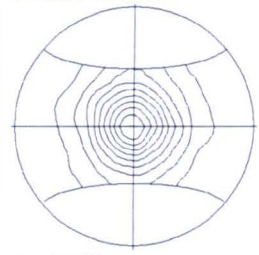
R4712X_2T	m.r.d 6.11	m.r.d 4.06
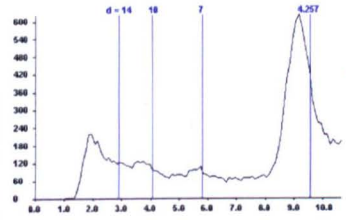	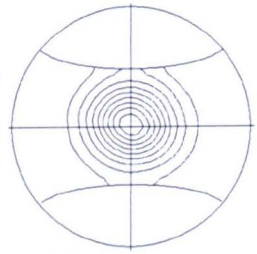	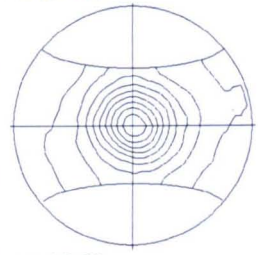
	m.r.d 6.08	m.r.d 3.99
R4759_2T	Illite/smectite	Chlorite-Kaolinite
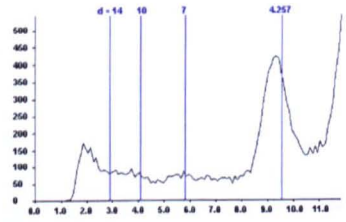	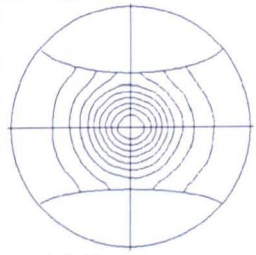	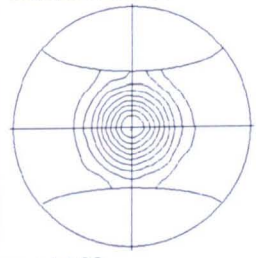
	m.r.d 4.85	m.r.d 4.32
R4771_2T	Illite/smectite	Chlorite-Kaolinite
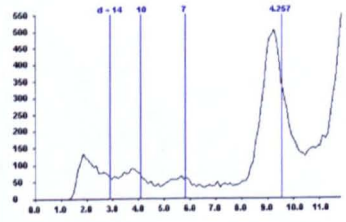	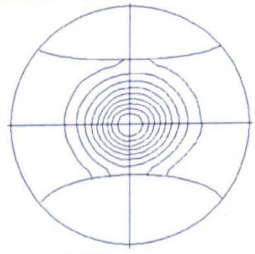	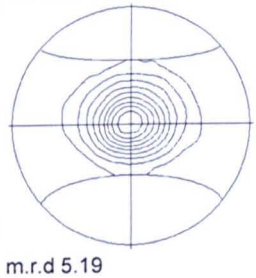
	m.r.d 6.05	m.r.d 5.19
R4771R_2T	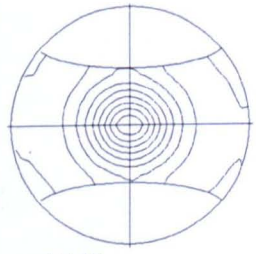	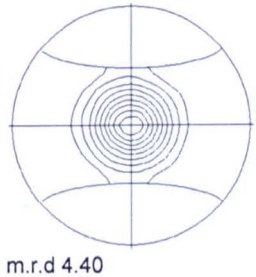
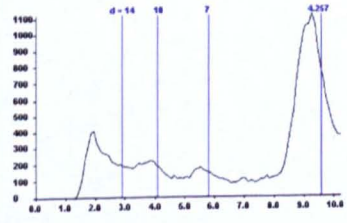	m.r.d 5.52	m.r.d 4.40

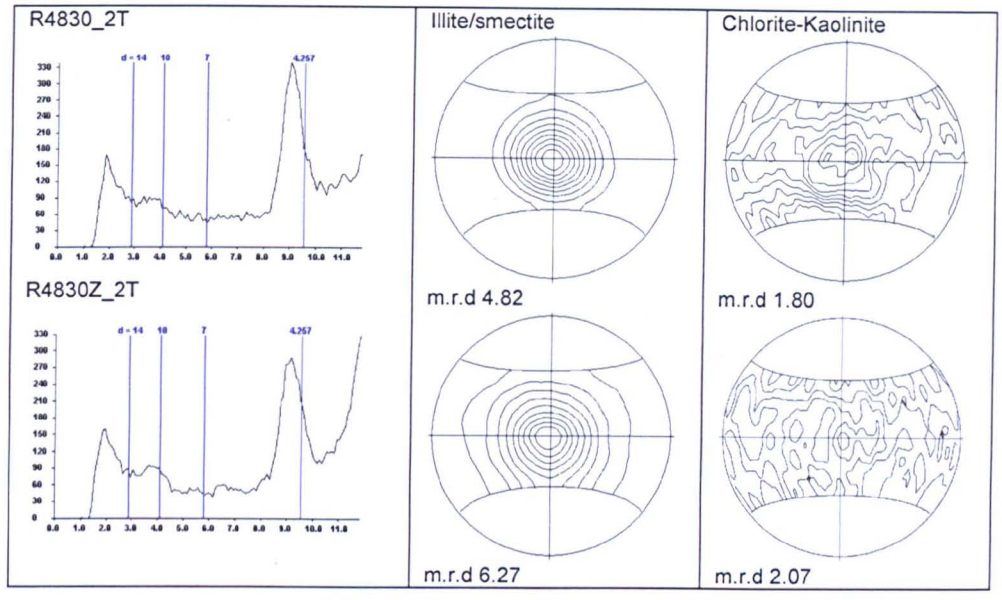

4.3.2.2: Magnus 211/12-2:

The pole figures plotted as equal area lower hemisphere projections for Magnus 211/12-2 are shown in Figure 4.35, with associated data in Table 4.8. As for Rhum, the intensity of diffracted X-rays was low, but there is no evidence that this has affected the pole figures and estimates of fabric intensity. The "2-theta scans" in Figure 4.35 shows the peak at a d-spacing of approximately 7Å to be more pronounced than in Rhum 3/29a4 and this is a reflection of the fact that QXRD reveals more chlorite and Kaolinite in these samples.

Phyllosilicate preferred orientation was taken at 2-theta angles that ranged between 3.17° 2-Θ and 4.05° 2-Θ for the I/S peak and between 5.54° 2-Θ and 5.83° 2-Θ for the C-K peak. The Kα d-spacings for these angles are in Table 4.8 and have been calculated in the same manner as for Rhum 3/29a4. Figure 4.33 is a plot of maximum intensity (m.r.d.) against depth for this well, it shows a range of fabric development from 1.92 m.r.d. (no fabric developed) to 3.81 m.r.d. (moderate fabric developed). There is a wide range of fabric development at a any given depth. The pole figures produced for this well (Figure 4.35) displays a mixture of wavy contour lines with weak maximum poles developed (e.g. sample M2399) to perfectly centred pole

figures with a clear 'bulls-eye' appearance. Fabric development is weak in both the shallow and deeper samples down to 3220m. The two peaks give comparable results for both I/S and C-K peaks and this visual observation was corroborated when a correlation co-efficient of 0.7024 was calculated when the I/S fabric intensity (m.r.d.) and the C/K fabric intensity (m.r.d.) were cross-plotted (Figure 4.34).

The reproducibility is within ~0.5 m.r.d. for each sample and reflects the fact that the technique measures on the scale of a square millimetre so the result is an average alignment of phyllosilicates over that area. The variability at a single depth is considerable in comparison to data from the Podhale Basin (Chapter 2) and reflects the changes in grain size distribution between samples.

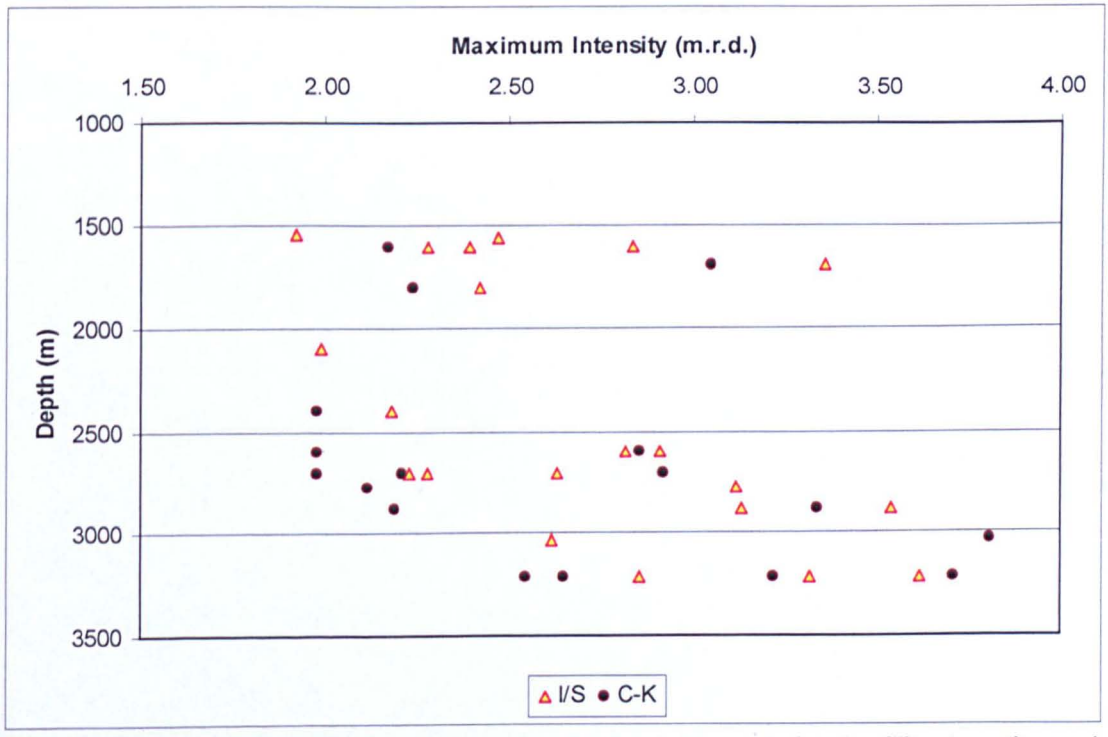

Figure 4.33: Maximum intensity of fabric development in m.r.d. for the illite-smectite and chlorite/kaolinite peaks with depth for Magnus 211/12-2.

Table 4.8. The maximum intensity (m.r.d.) contours for the I/S and C-K peaks along with contour interval, the 2-theta positions for the measured peaks and associated Kα average d-spacings for Magnus 211/12-2, nd refers to not determined for this peak. X refers to a re-analysis on the same same cut as the original, r refers to a re-cut of the sample.

Sample ID	Depth (m)	Max. intensity mrd 'I-S'	Max. intensity mrd 'C-K'	2-Theta 'I-S'	2-Theta 'C-K'	Kα ave. d spacing 'I-S'	Kα ave. d spacing 'C-K'
M1449	1449	nd	nd	nd	nd	nd	nd
M1532	1532	nd	nd	nd	nd	nd	nd
M1580	1550	1.92	nd	3.95	nd	10.25	nd
M1567	1567	2.47	nd	4.05	nd	10.01	nd
M1610	1610	2.39	2.17	3.92	5.58	10.29	7.21
M1610r	1610	2.28	nd	4.05	5.55	9.91	7.20
M1610x	1610	2.84	nd	4.14	5.74	9.72	6.98
M1700	1700	3.36	3.05	3.95	5.64	10.20	7.11
M1802	1802	2.42	2.24	4.05	5.77	10.04	7.04
M2098x	2098	1.99	nd	4.05	nd	10.04	Nd
M2399	2399	2.18	1.98	3.92	5.68	10.29	7.07
M2602	2602	2.91	2.86	3.89	5.77	10.45	7.04
M2602r	2602	nd	nd	nd	nd	nd	nd
M2602r	2602	2.82	2.92	3.89	5.68	11.45	8.15
M2706	2706	2.63	2.21	3.92	5.62	10.29	7.15
M2706x	2706	2.28	2.12	3.95	5.74	10.33	7.11
M2706x	2706	2.23	2.19	3.64	3.26	11.20	12.51
M2775	2775.5	3.12	3.34	3.95	5.55	10.22	7.23
M2880r	2880	3.54	3.81	3.86	5.80	11.48	7.96
M2880	2880.5	3.13	3.71	3.17	5.77	12.74	6.96
M2880r	2880.5	nd	nd	nd	nd	nd	nd
M3035	3035	2.62	2.65	3.94	5.70	10.30	7.11
M3220	3220	3.62	3.22	3.75	5.83	10.80	6.93
M3220ar	3220	3.32	2.55	3.86	5.54	10.48	7.29
M3220z	3220	2.86	nd	4.05	5.71	10.93	8.01

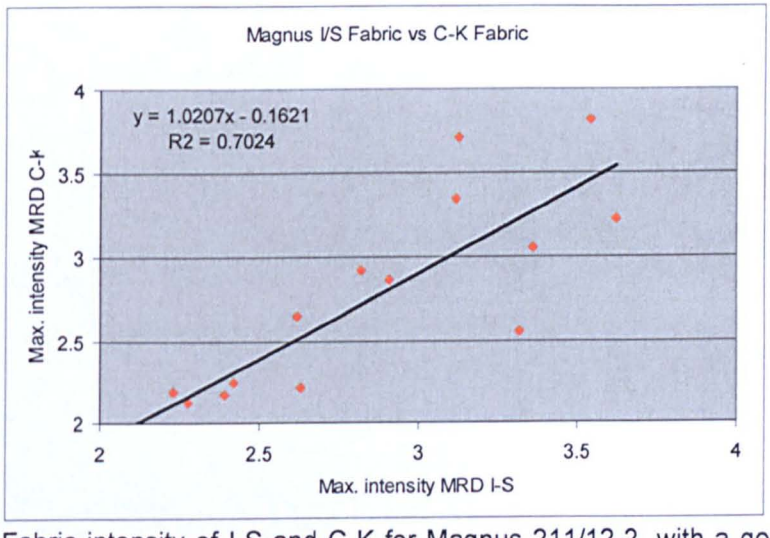

Figure 4.34. Fabric intensity of I-S and C-K for Magnus 211/12-2, with a good correlation coefficient between I/S and C-K fabric of 0.7024.

Figure 4.35. 2-theta scans and full pole figures for Magnus 211/12-2.Full pole figures are for the illite/smectite and kaolinite-chlorite peaks the fabric alignment in m.r.d. is stated below the pole figure.

M1449_2T 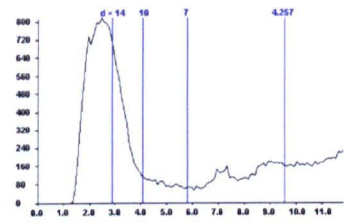 M1449X_2T 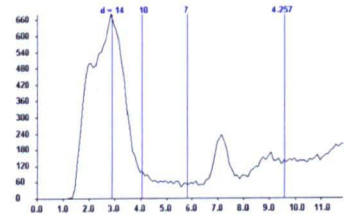	M1449 Illite/smectite	M1449 Chlorite-Kaolinite
M1532_2T 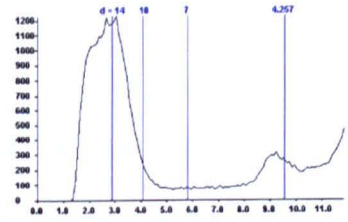 M1532X_2T 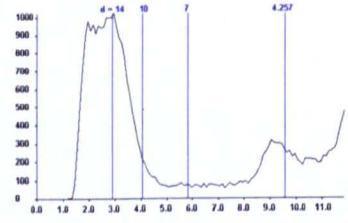	M1532 Illite/smectite	M1532 Chlorite-Kaolinite
M1567_2T 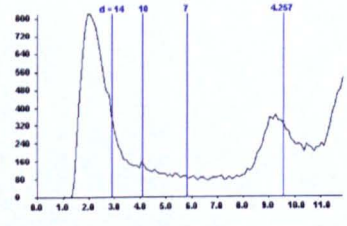	M1567 Illite/smectite 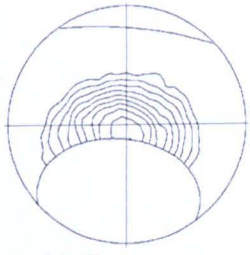 m.r.d 2.47	M1567 Chlorite-Kaolinite
M1580_2T 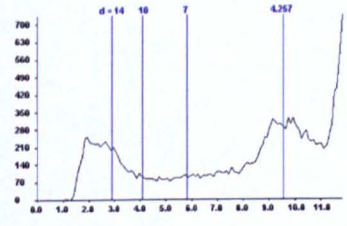	M1580 Illite/smectite 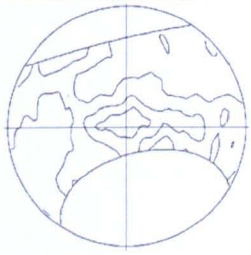 m.r.d 1.92	M1580 Chlorite-Kaolinite

M1610_2T 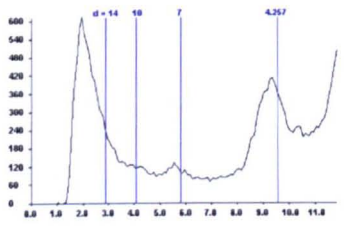	M1610 Illite/smectite 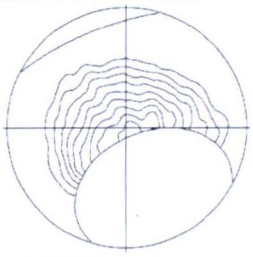	M1610 Chlorite-Kaolinite 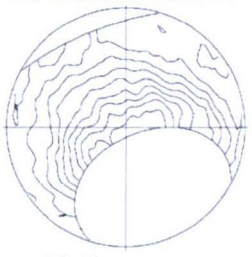
M1610X_2T 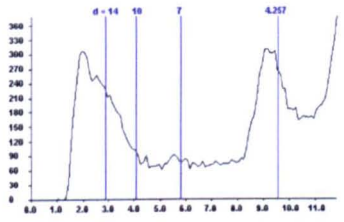	m.r.d 2.39 	m.r.d 2.17
	m.r.d 2.28	
M1700_2T 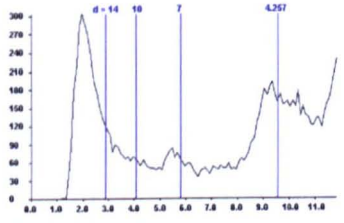	M1700 Illite/smectite 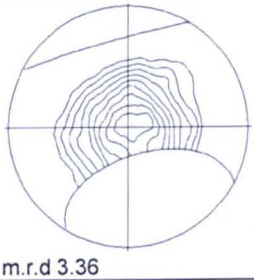	M1700 Chlorite-Kaolinite 
	m.r.d 3.36	m.r.d 3.05
M1802_2T 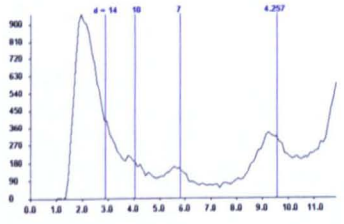	M1802 Illite/smectite 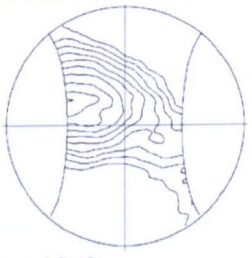	M1802 Chlorite-Kaolinite 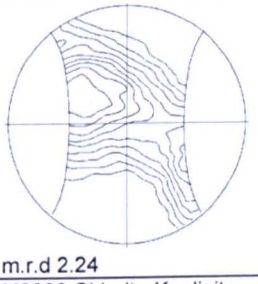
	m.r.d 2.42	m.r.d 2.24
M2098_2T 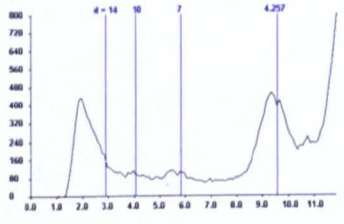	M2098 Illite/smectite	M2098 Chlorite-Kaolinite
M2098X_2T 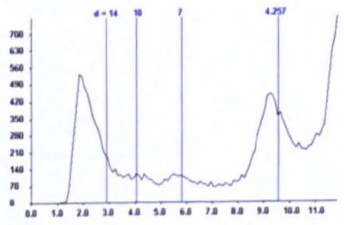		
	m.r.d 1.99	

M2399_2T 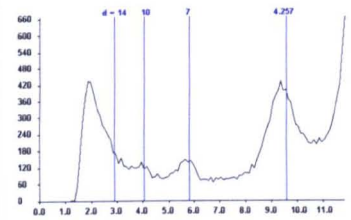	M2399 Illite/smectite 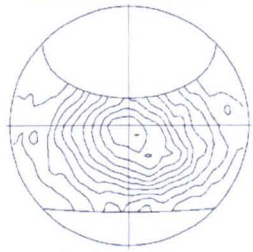 m.r.d 2.18	M2399 Chlorite-Kaolinite 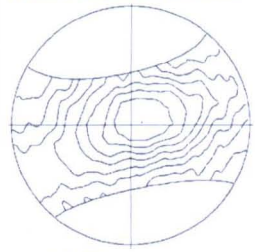 m.r.d 1.98
M2602_2T 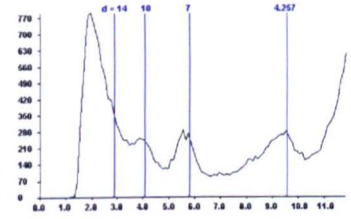	M2602 Illite/smectite 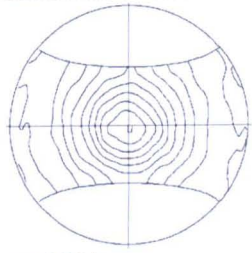 m.r.d 2.91	M2602 Chlorite-Kaolinite 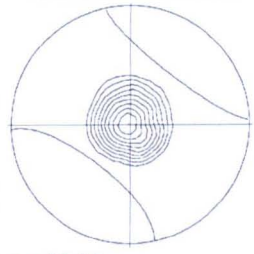 m.r.d 2.86
M2602X_2T 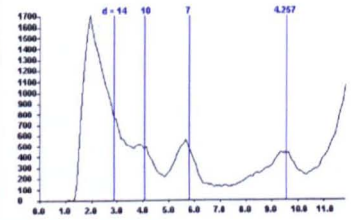	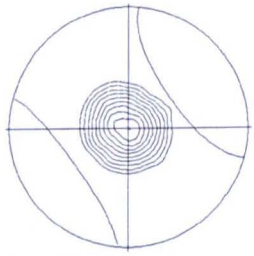 m.r.d 2.82	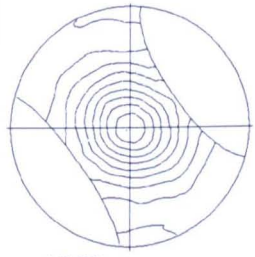 m.r.d 2.92
M2706_2T 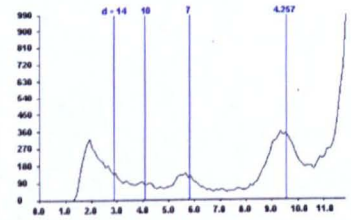	M2706 Illite/smectite 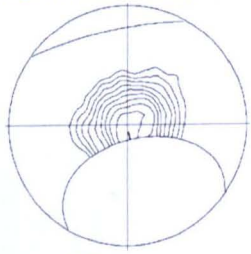 m.r.d 2.63	M2706 Chlorite-Kaolinite 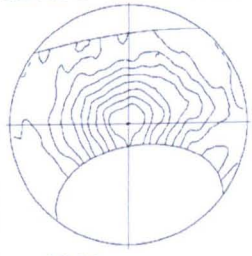 m.r.d 2.21
M2706X_2T 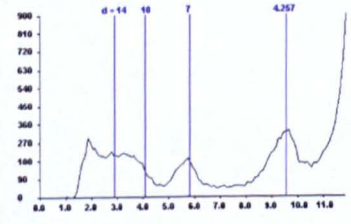	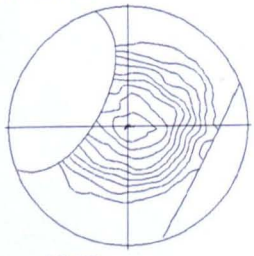 m.r.d 2.27	 m.r.d 2.12
M2775_2T 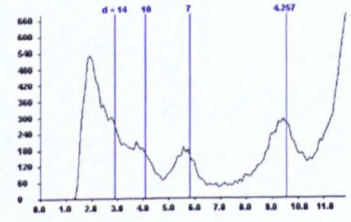	M2775 Illite/smectite 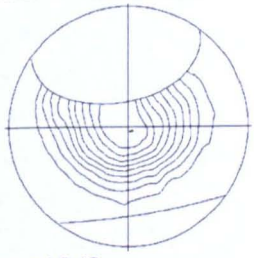 m.r.d 3.12	M2775 Chlorite-Kaolinite 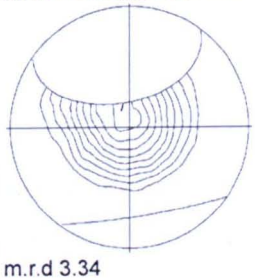 m.r.d 3.34

M2880_2T	M2880 Illite/smectite	M2880 Chlorite-Kaolinite
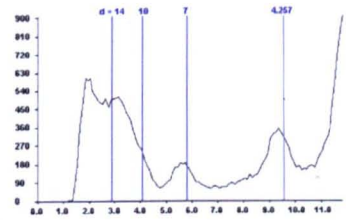		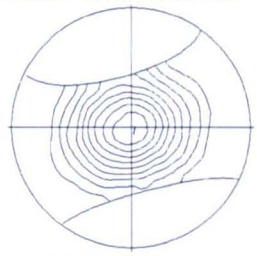
	m.r.d 3.13	m.r.d 3.71
M2880R_2T		
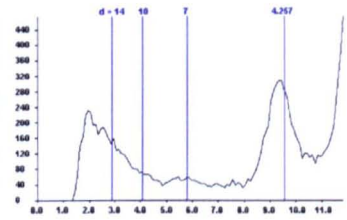	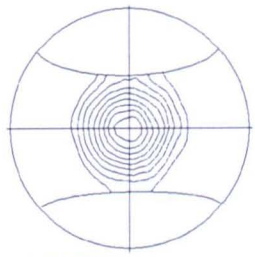	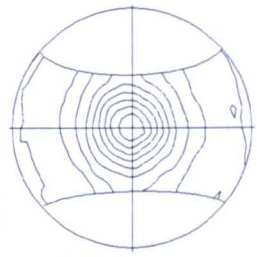
	m.r.d 3.54	m.r.d 3.81
M3035_2T_1	M3035 Illite/smectite	M3035 Chlorite-Kaolinite
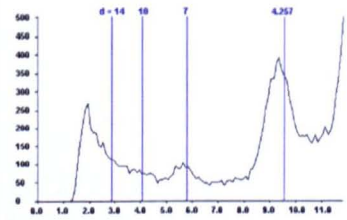		
M3035_2T_2		
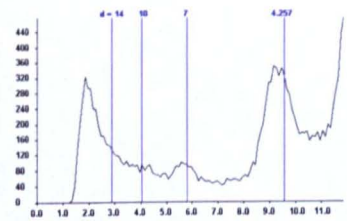		
	m.r.d 2.62	m.r.d 2.65
M3035x_2T		
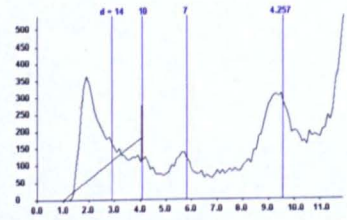		
M3220_2T	M3220 Illite/smectite	M3220 Chlorite-Kaolinite
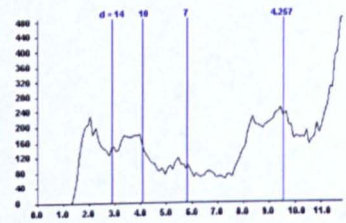	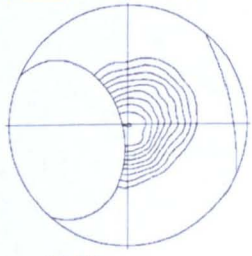	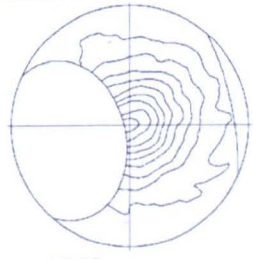
	m.r.d 3.62	m.r.d 3.22

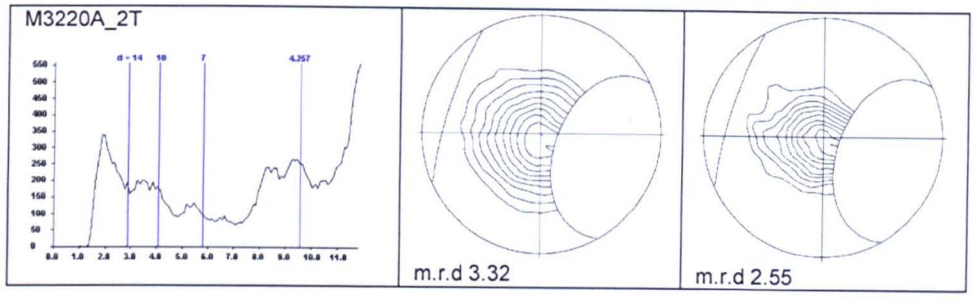

4.3.3: Backscattered Scanning Electron Microscopy (BSEM):

In describing the BSEM images collected in this study Rhum 3/29a4 and Magnus 211/12-2 will be dealt with, for the sake of brevity, at the same time as the observations and comments are directly applicable to both wells, even though they are discrete wells.

The scales used to capture images varied from 250x to 10000x magnification in order to assess the textural and mineralogical information on a variety of scales. The BSEM images presented here are unfortunately not the whole sequence, as 1-there was not enough material to sample the core material of the Jurassic and 2- the samples were prepared from exceptionally small pieces of cuttings material that did not produce good thin-sections for BSEM analysis. The thin-sections were often 'plucked and cratered' and in turn this caused the samples to charge under the electron beam even with the addition of carbon tape and silver paint to remove the electron charge.

Nevertheless, the collected images (Figures 4.36 to 4.45) reveal some interesting textures and relationships. Detrital phyllosilicate grains are predominantly ~3 to 20μm thick (width) packets of mica (may be referred to as illite) and chlorite (Figure 4.44). These initial packets are persistent to depths and appear diagenetically inert. The fine-grained detrital (at the surface/in the shallow samples) minerals predominantly illite/smectite are active in diagenetic reactions (e.g Hower et al. 1976) referred to as authigenic at depth and can be seen in all images as moderately sized

packets of illite-smectite and as isolated grains below the resolution of BSEM. Figure 4.45 shows a 2µm thick (width) illite/smectite grain (EDS traces consistent with I/S material, see Chapter 3) surrounded by other grains I/S grains of a variety of smaller scales. These grains are resolvable in this image to <0.1µm. The sample from Magnus 211/12-2 from 1802.5m (Figure 4.44) shows that the orientation of the detrital I/S has no visual preferred orientation.

The preferred orientation in the shallow samples (Figures 4.36, 4.37, 4.43, 4.44 & 4.45), down to ~2550m in Rhum 3/29a4 and ~2000m in Magnus 211/12-2, is poorly developed as measured by HRXTG, the BSEM confirms this visually. Sample R2550 shows little preferred orientation on any scale (Figures 4.36 & 4.37), likewise, Figures BSEM 4.43, 4.44 & 4.45 (Magnus 211/12-2, 1700m, 1802.5m, 1802.5m respectively) show no preferred fabric orientation. The deeper samples, from the Jurassic (R4712 and R4830, Figures 4.38, 4.39, 4.40, 4.41 & 4.42 respectively), show a much clearer visual preferred orientation. At low magnifications (Figures 4.38 & 4.41) it is hard to pick out preferred orientations of phyllosilicate grains as they are below the resolution of BSEM, so visual preferred orientations are defined by the sample 'splitting' or 'parting' along lines perpendicular to maximum effective stress as a function of either decompaction or drying but this is only visible in the deep samples where fabric as recorded by HRXTG is high. Higher magnifications (Figures 4.39 & 4.40) reveal that it is the alignment of phyllosilicates, seen in these figures, bending and wrapping around quartz grains, that give rise to a preferred fabric alignment.

Subrounded to subangular quartz grains typically ~5-30µm in diameter can be seen breaking up the alignment of platy phyllosilicate minerals (Figures 4.36, 4.37, 4.38, 4.39, 4.41 & 4.44). The effects of large quartz grains on preferred alignment is most stark in the samples where fabric is more greatly developed (e.g. Figures 4.38, 4.39 & 4.41). The size of the images is an important factor in the visual assessment of whether quartz has significantly disrupted fabric alignment. The size of the images in this study are between

200µm by 150µm to 12µm by 8µm, much smaller areas than are in fact measured by HRXTG, as this technique measures on the mm^2 scale. Therefore, although quartz can be seen to be disrupting fabric alignment, the technique measures on such a scale as to negate these localised disruptions.

Pyrite also disrupts fabric development where it is present in framboid form (Figures 4.38, 4.39 4.40, 4.41 & 4.42). QXRD reveals pyrite is not present in any significant quantities (more than 0.5%) until the Kimmeridge Clay Formation of the Jurassic where percentages rise to ~10%. At these percentages and in framboids form (as revealed by QXRD) fabric disruption by pyrite becomes significant.

As has already been discussed anoxia was present in the Jurassic giving rise to the pyrite seen in the BSEM images additionally conditions of low oxygen would have been prevalent in low energy conditions. Therefore the amount of coarse grained quartz input must have been low, Figure 4.38 (~17% quartz by XRD), have relatively few large (10µm+) quartz grains. This allows greater fabric development as there are less rounded or angular grains to break up platy phyllosilicate packing. This is somewhat offset by the presence of pyrite framboids for the reasons mentioned above. Depositional information from the Cretaceous and Tertiary is a harder to ascertain as there are so few micrographs from these samples. Although Figure 4.43 appears to show a lot of flocked material showing edge-to-face characteristics as described by O'Brien & Slatt (1990). Similar random orientations of smaller, less than 1µm, clay mineral grains can be seen in Figure 4.44.

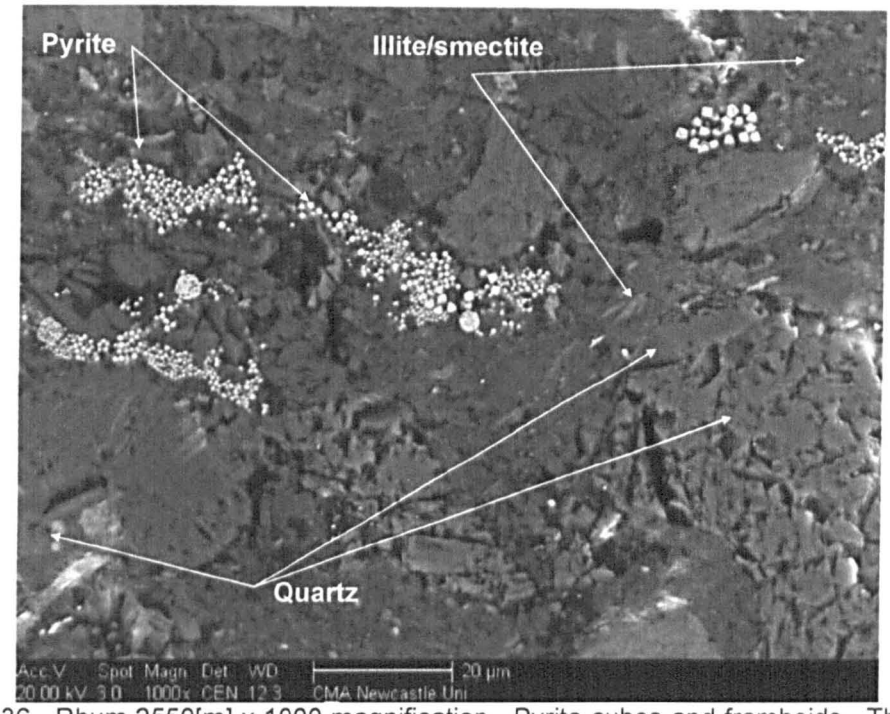

Figure 4.36. Rhum 2550[m] x 1000 magnification. Pyrite cubes and framboids. The quartz grain to the bottom right corner shows that the sample has been 'plucked' in preparation and the bright spot on this grain is due to charging.

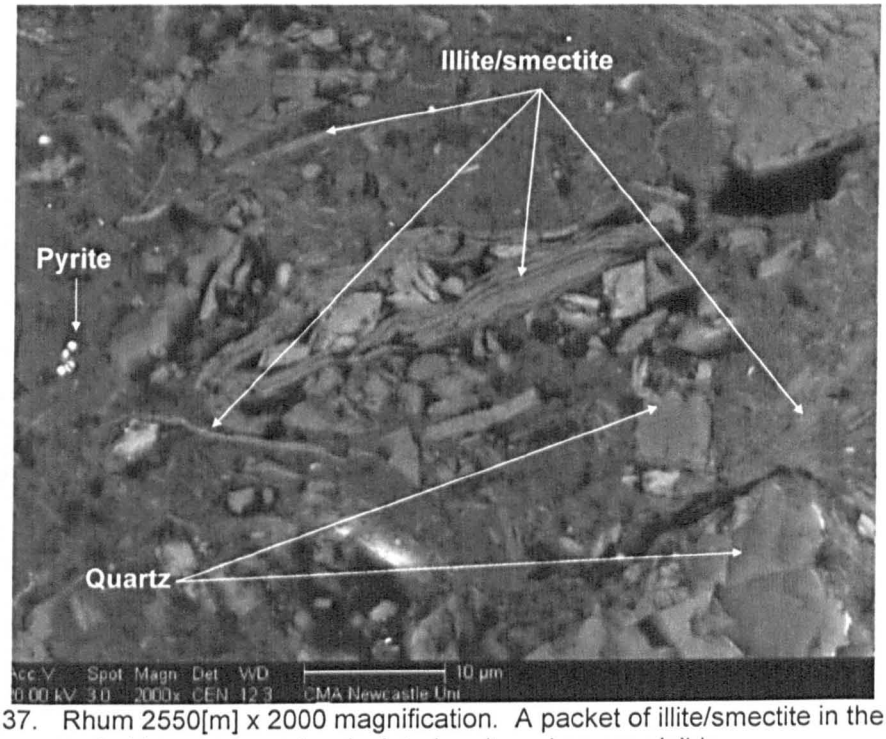

Figure 4.37. Rhum 2550[m] x 2000 magnification. A packet of illite/smectite in the centre of the shot surrounded by quartz grains, isolated pyrite cubes are visible.

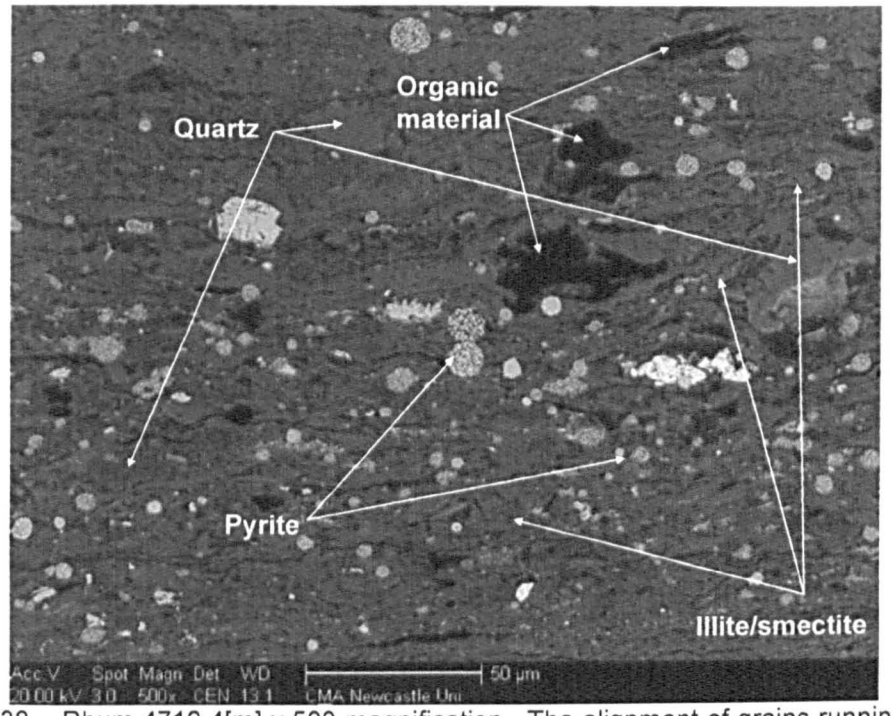

Figure 4.38. Rhum 4712.4[m] x 500 magnification. The alignment of grains running across the image, decompaction/drying has cleaved the sample along the general phyllosilicate preferred orientation. Pyrite framboids and quartz grains are breaking up the parallel alignment of platy phyllosilicates. The black areas are organic material.

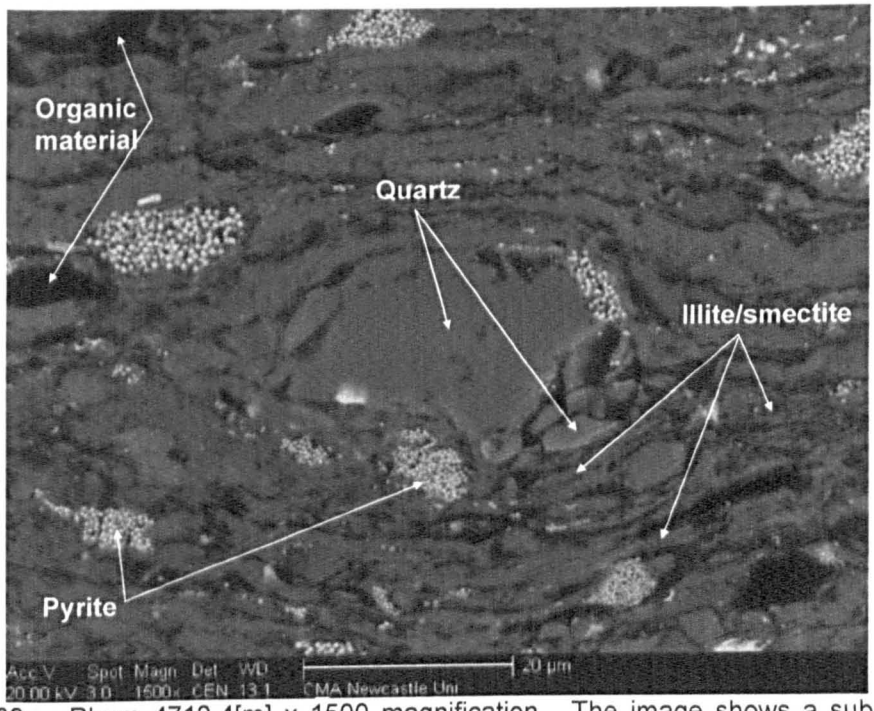

Figure 4.39. Rhum 4712.4[m] x 1500 magnification. The image shows a sub rounded quartz grain breaking up the alignment of phyllosilicate minerals, predominantly illite/smectite. There are also pockets of pyrite growth.

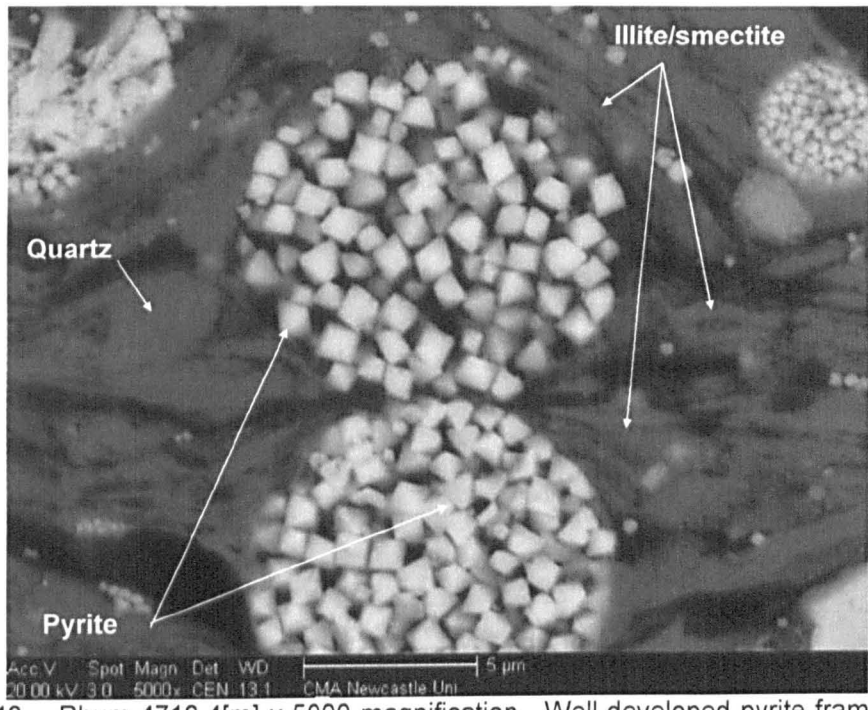

Figure 4.40. Rhum 4712.4[m] x 5000 magnification. Well developed pyrite framboids can be seen breaking up the alignment of phyllosilicate grains, which are forced to bend around them.

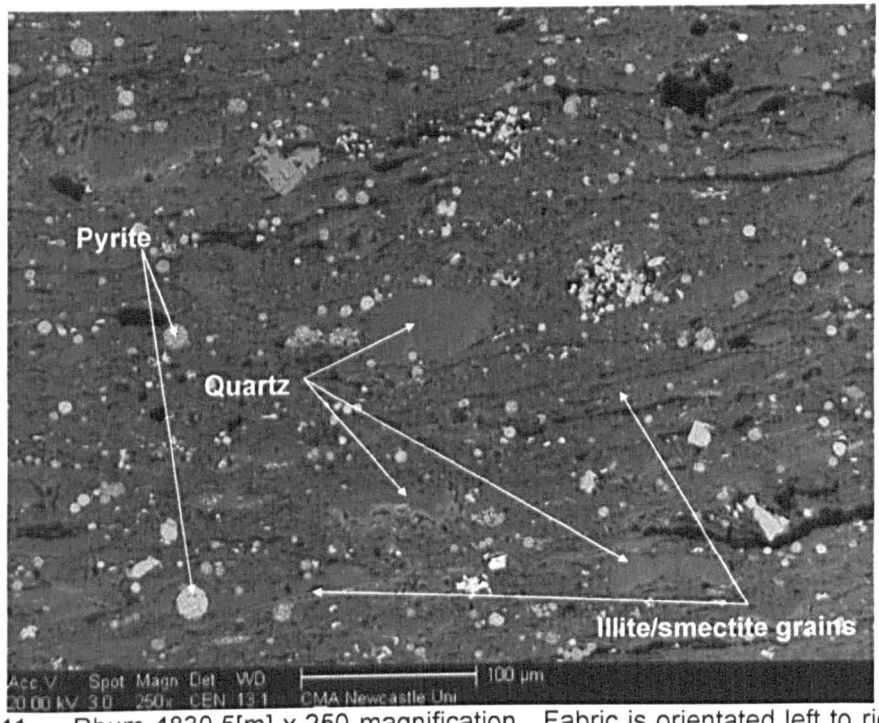

Figure 4.41. Rhum 4830.5[m] x 250 magnification. Fabric is orientated left to right in the image, quartz and pyrite can be seen breaking up this alignment and the sample has parted along the line of the fabric in response to decompaction/drying effect. The black areas on this image are organic material.

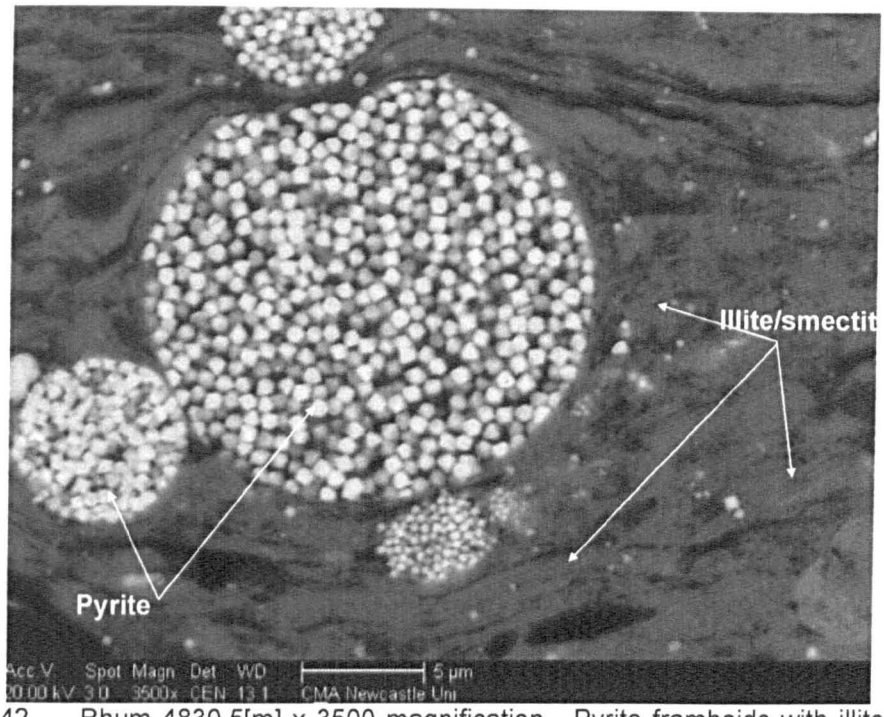

Figure 4.42. Rhum 4830.5[m] x 3500 magnification. Pyrite framboids with illite/smectite bending and wrapping around them.

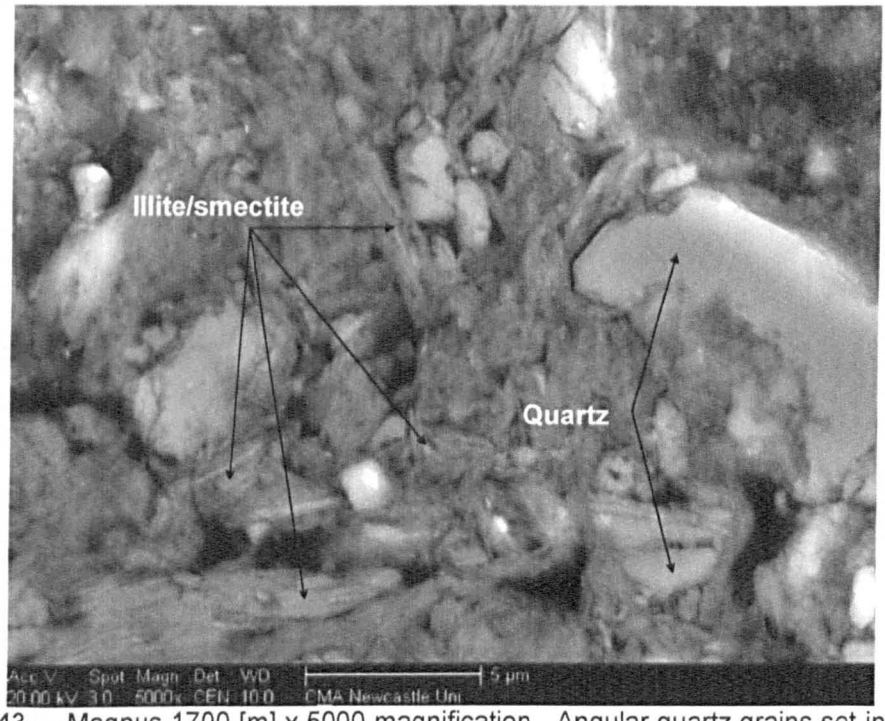

Figure 4.43. Magnus 1700 [m] x 5000 magnification. Angular quartz grains set in a matrix of phyllosilicate minerals, predominantly illite/smectite, whose orientation is quite random.

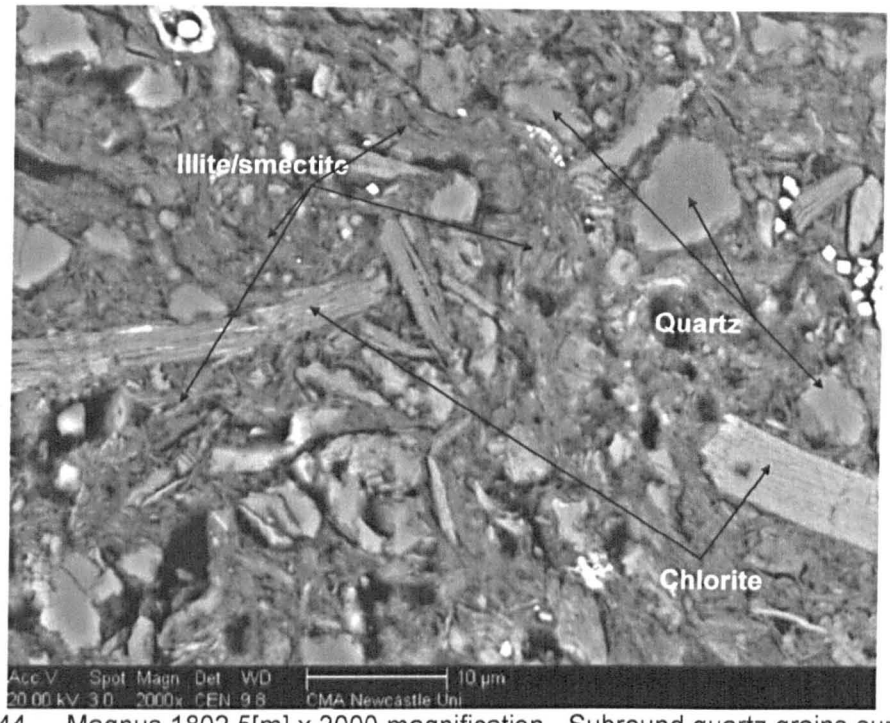

Figure 4.44. Magnus 1802.5[m] x 2000 magnification. Subround quartz grains surrounded by a variable matrix of phyllosilicate grains and groundmass below the resolution of the image. A large chlorite grain (arrowed) has undergone some replacement by pyrite and is probably detrital in origin. To the right of the quartz grain highlighted are small pyrite cubes. Areas of flocked illite/smectite are highlighted

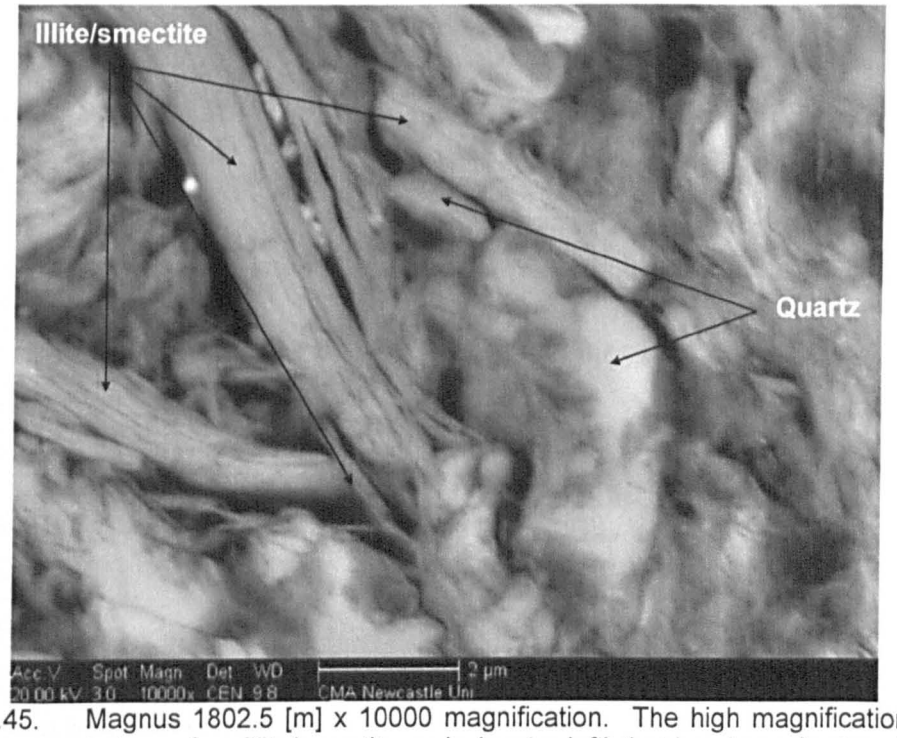

Figure 4.45. Magnus 1802.5 [m] x 10000 magnification. The high magnification image shows the morphology of an illite/smectite grain (centre left) that has been fractured. To its left are smaller packets of phyllosilicates.

4.3.4: Porosity:

4.3.4.1: Mercury Intrusion Porosimetry (MICP)

4.3.4.1.1: Rhum 3/29a4 MICP:

The absolute porosities for Rhum 3/29a4 range from 44% at the top of the section to as low as 14% at 3060m with the Lower Cretaceous at 22%. The results are in Table 4.9 and plotted against depth in Figure 4.46.

The grain density measurements using the small pycnometer method were not used in the analysis, rather a default grain density of 2.666 g/cm^3 was employed. The grain density determinations proved inaccurate as the results of the two quartz standards run at the same time as the sample analyses did not fall into the +/-0.02 g/cm^3 requirement of the method (Matenaar, 2002). Additionally, the fact that the samples have a high percentage of smectite means that the initial heating to 105°C prior to density measurement will have caused the loss of interlayer water from smectite (Colton-Bradley, 1987).

Table 4.9. Porosity percent and associated depth for Rhum 3/29a4, as measured by Mercury Intrusion Porosimetry.

Depth [m]	Porosity Percent
950	29
1050	35
1150	44
1250	42
1350	31
1650	28
1750	27
1850	30
1950	29
3060	14
3140	21
3550	22
4300	26
4330	22
4632	24
4650	22

The pore size distributions are in Figure 4.47. The pore size distributions may be divided into unimodal and bimodal distributions. There are three samples that show bimodal distributions, R1050, R1250 and R4330. These

results suggest that the sample is a mixture of mud and sand/silt sized material. The rest of the samples have a unimodal distribution that is variable between 3 and 30nm and the cumulative porosity trends are therefore quite similar in shape.

The porosities recorded at the base of the Cretaceous, 22%, 24% and 22% (Table 4.9), are somewhat higher than would be expected for samples buried to ~4500m. A value closer to 10% would be more realistic (Yang & Aplin, 1998) based on normal compaction trends. However, these sediments are highly overpressured (Illife, 2005, pers comms).

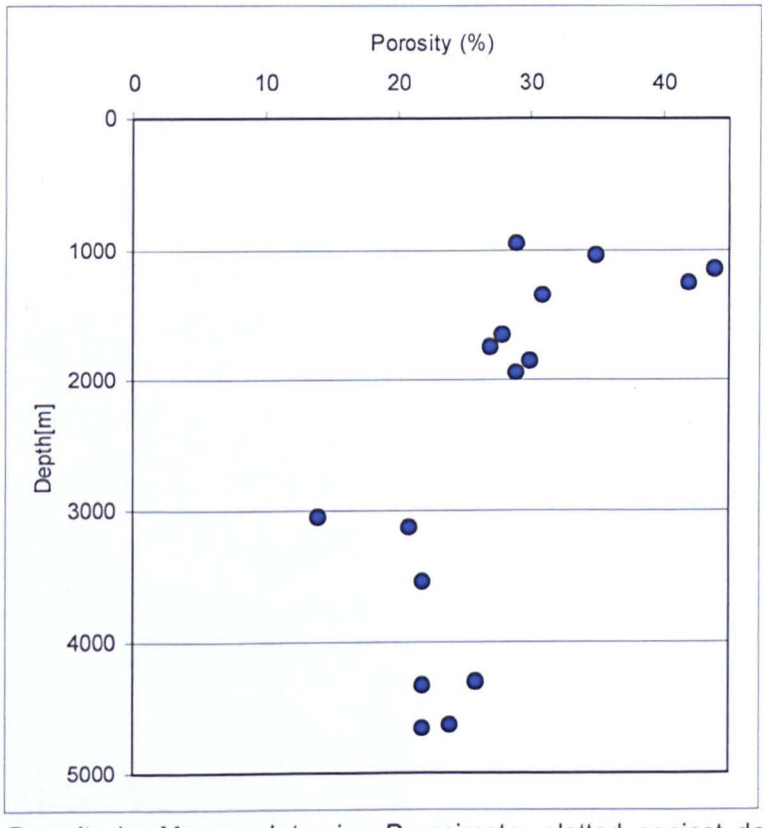

Figure 4.46. Porosity by Mercury Intrusion Porosimetry plotted against depth for Rhum 3/29a4.

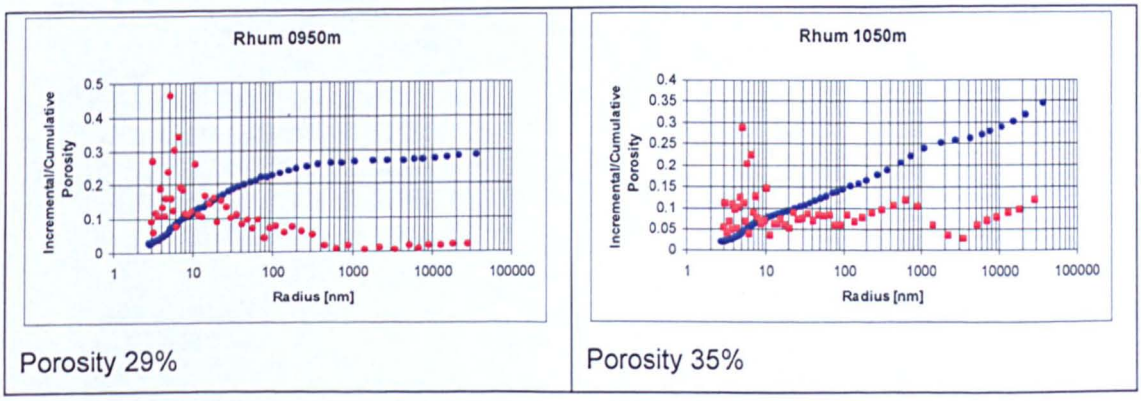

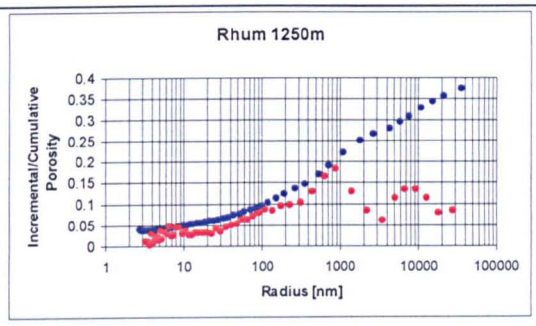

Porosity 42%

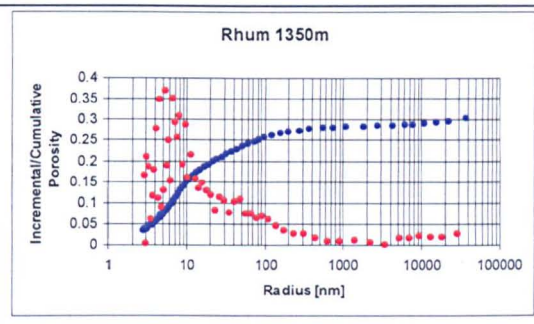

Porosity 31%

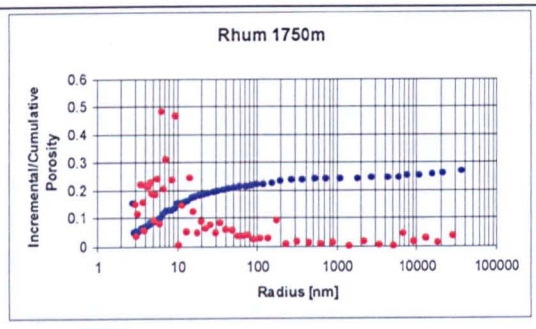

Porosity 27%

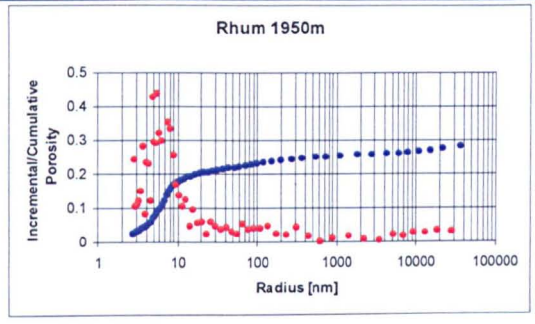

Porosity 29%

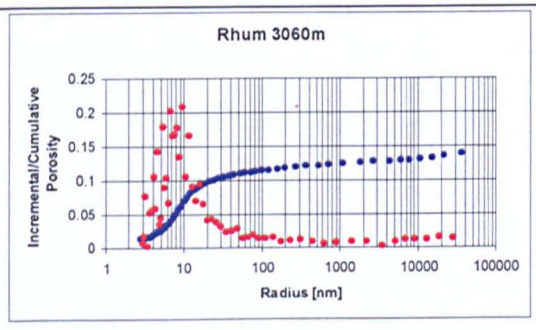

Porosity 14%

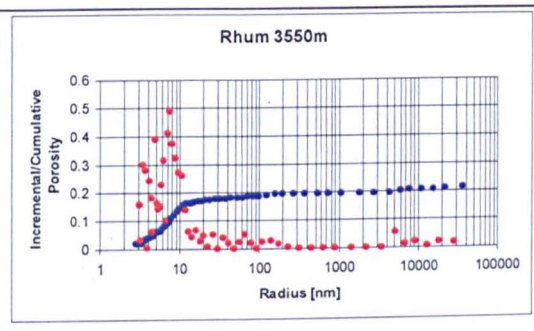

Porosity 22%

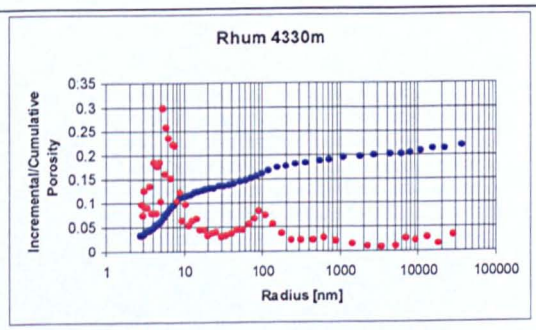

Porosity 22%

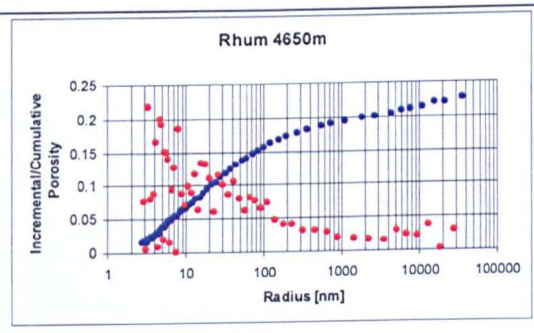

Porosity 22%

Figure 4.47: The red dots mark the pore throat sizes; the blue dots the cumulative porosity for four samples of varying depths from Rhum 3/29a4. Rhum 1050, 1250 and 4330 show a bimodal pore throat distribution.

4.3.4.1.2: Magnus 211/12-2 MICP:

Porosities for Magnus 211/12-2 range from 44% at 1449m to 20% at 2775.5m. The trend of porosity reduction with depth are plotted in Figure 4.48 and are in Table 4.10.

Depth [m]	Porosity Percent
1449	44
1532	38
1567	38
1580	44
1610	37
1700	29
1802.5	23
2098	22
2399.5	24
2602	20
2706	29
2775.5	20
2880.5	25

Table 4.10. Porosity percent and associated depth for Magnus 211/12-2, as measured by Mercury Intrusion Porosimetry.

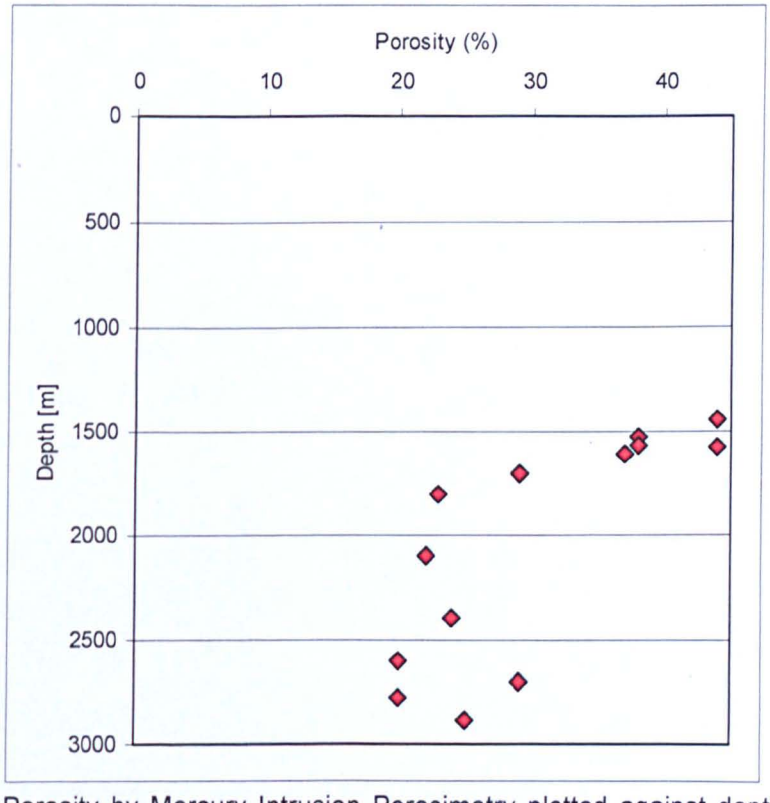

Figure 4.48. Porosity by Mercury Intrusion Porosimetry plotted against depth for Magnus 211/12-2.

Samples presented in Figure 4.49 are representative distributions for Magnus 211/12-2. Samples Magnus 101, 69 and 190 have a unimodal pore size distribution. Magnus 89 is bimodal and appears to have sand/silt material present based on the pore size distributions. The pore throat radii for the unimodal distributions range from 7 to 30nm.

The porosity measured by MICP for Magnus 211/12-2 is in keeping with a recent study on two adjacent wells, 211/13-1 and 211/13-3, by Worden et al. (2005) who recorded porosities of 35% at 1615m and 22% at 3316m. In this study 44% at 1449m is perhaps a little high given a normal compaction trend where porosity is ~30% at 1km, however, where high levels of smectite in illite/smectite exist 44% porosity in relatively shallow buried mudstones is not exceptional (e.g. Worden, 2004).

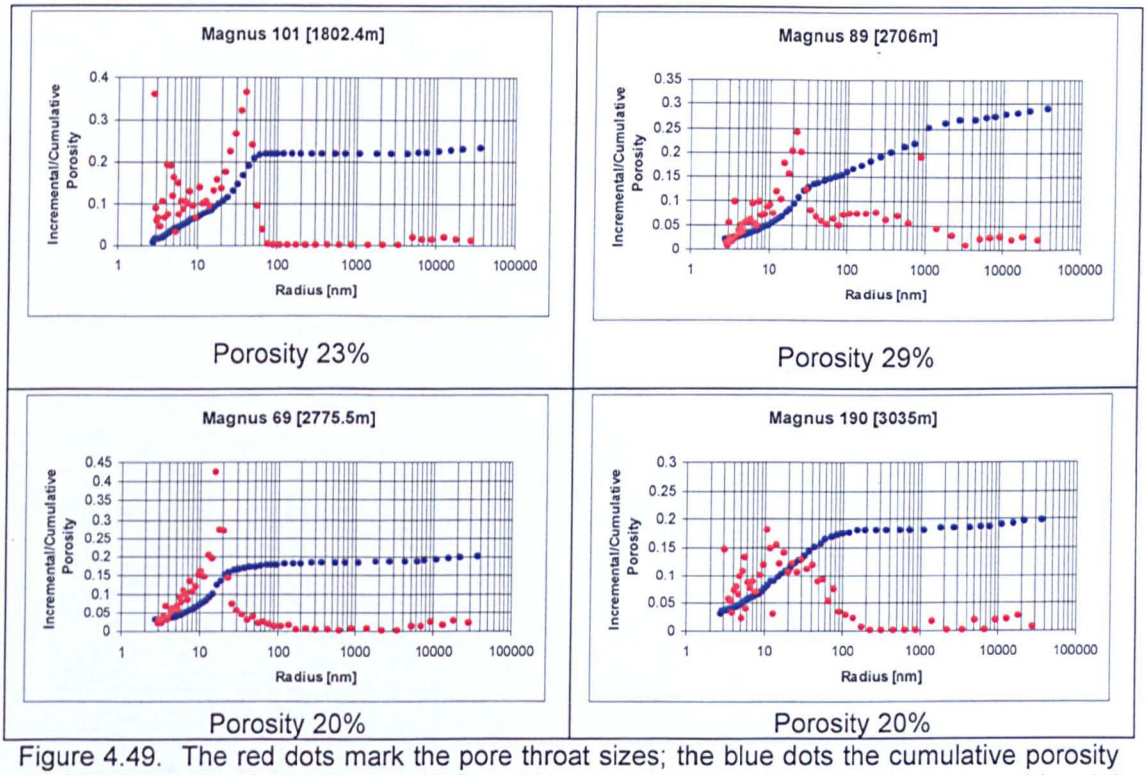

Figure 4.49. The red dots mark the pore throat sizes; the blue dots the cumulative porosity for four samples of varying depths from Magnus 211/12-2. Magnus 89 shows a bimodal pore throat distribution.

4.3.4.2: Porosity from the sonic log for Rhum 3/29a4:

The rationale for the addition of porosity data from the application of acoustic impedance is that no porosity measurements were taken for the samples

from the Jurassic. If an appreciation of porosity loss as a function of fabric alignment is to be looked at porosity values in the Jurassic have to be attained.

The Raiga-Clemenceau equation (1988)

$$\Phi = 1/C(\Delta t \log - \Delta tmatrix / \Delta tfluid - \Delta tmatrix)$$

Where Φ is porosity, Δt is the transit time from the sonic log, Δtmatrix is the transit time of the matrix and Δtfluid is the transit time of the pore fluid, was used to calculate the porosity from the sonic log for the entirety of the profile using a correction factor, *C*, of 1/1.60 (Figure 4.50). This was done as the equation by Wyllie (1956), which equates transit time to porosity, has been shown (Raymer et al., 1980) to give porosities that are too large for unconsolidated sediments. The Raiga-Clemenceau equation does not work for gas-filled sediments as this lowers sonic velocities (Hansen, 1996), but there is no evidence that the sediments in this study contain gas.

The porosities range from around 35% between 1000 and 2000m, then decrease to around 15%~20% between 2500 and 4500m. As the Jurassic strata, below 4650m, are encountered porosity decreases to less than 10%. There is good agreement at depths down to ~3500m with measured porosity by mercury intrusion, though the samples at the base of the Cretaceous are in less agreement.

Since the main aim of this section is to assess porosities in the Jurassic Figure 4.51 has been included. It shows the porosity in only the Jurassic samples below 4650m. The equation

$$\Phi = 1 - (66.8 / \Delta t \log)^{1/3.31}$$

used to calculate sonic porosities is from Okiongbo (2005) and is a relationship between shale porosity and transit times determined from shale cores using mercury porosimetry calibrated against transit times from sonic

logs recorded from strata that are only Jurassic in age, including three samples from Rhum 3/29a4. The porosities in the Jurassic calculated by this method are around 5%.

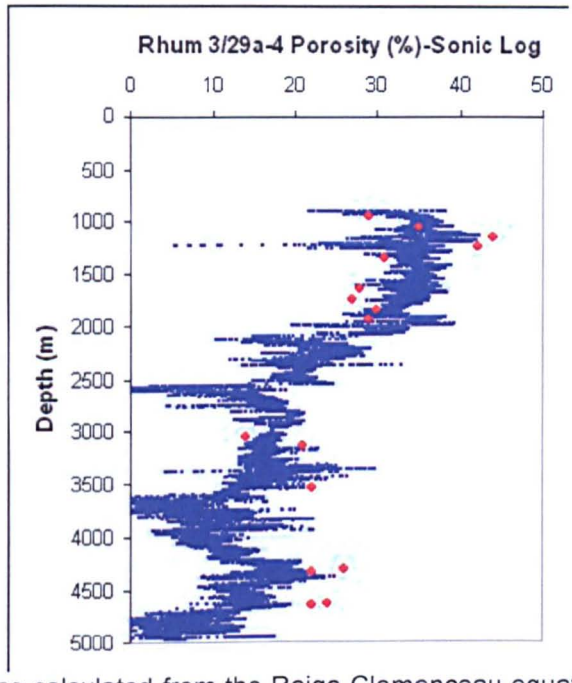

Figure 4.50. Porosity as calculated from the Raiga-Clemenceau equation from the sonic log data. The red dots are measured porosity by mercury intrusion.

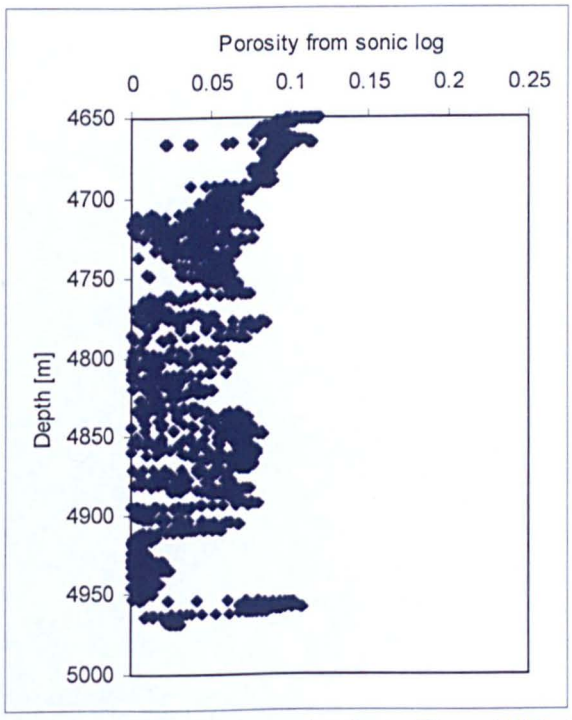

Figure 4.51. The porosity in the Jurassic samples from Rhum 3/29a4 using the equation of Okiongbo (2005).

4.4: Discussion:

The alignment of phyllosilicate grains in mudstones and siltstones is controlled by many different parameters. Grain size and effective stress have been demonstrated to be the dominant control on compaction (Matenaar, 2002) and therefore fabric alignment in the early stages of burial. Previous fabric studies related to diagenesis (e.g. Ho et al., 1999; Matenaar, 2002) have impressed the point that grain shape and the nature of depositional setting (e.g. Bennett et al., 1991) can have an effect on fabric development. The mineral reactions associated with diagenesis (e.g. Hower et al., 1976) have also been shown to effect fabric development (Ho et al., 1999; Worden et al., 2005).

This discussion concentrates on the nature of the fabric development in the Northern North Sea in the Rhum 3/29a4 and Magnus 211/12-2 wells in response to changes in physical and mineralogical conditions as a function of sediment supply, depositional environment, diagenesis and compaction by porosity loss.

4.4.1: Depositional Environments and the Associated Mineralogical Characteristics:

As has been discussed earlier the depositional environments in the Northern North Sea from the Jurassic to the late Tertiary were quite variable, with water depths and sediments sources changing, both in direction and content. Low energy anoxic environments dominated the Jurassic (Underhill 1998; Schwartz 1994) this is evident in samples from Rhum 3/29a4 where pyrite grains and framboids are present in significant quantities (QXRD and BSEM images). Matenaar (2002) has demonstrated that low sedimentation rates, in low energy environments promote better initial alignment of phyllosilicates, consequently, the high I/S fabric intensities may in part be interpreted as having been aided by fabric alignment conducible environments and original

depositional characteristics such as laminations may have been preserved as a direct result of anoxia halting bioburbation of the fresh sediment.

The mineralogical characteristics of the Jurassic are exemplified by the abundance of pyrite material (FeS_2) that is not seen anywhere else in the younger sections in any significant quantities. Also, QXRD reveals that chlorite percentages are very low; this could be as a result of different mineral pathways during diagenesis at depths up to ~4700m, or as a result of different source material entering the Jurassic system compared to the Cretaceous and Tertiary. Nevertheless, the low percentage of chlorite has had an effect on the quantification of fabric as maximum pole densities cannot e gathered in the absence of a phase.

Quartz percentages in the mudstones sampled is very variable between 17 and 85% and represents the fact that the material used in this study was extracted from siltstone/mudstone layers within the reservoir units and therefore has variable mudstone/siltstone/sandstone characteristics. Further, this suggests that even though anoxia was persistent in producing sulphur for pyrite formation there was some variability in sediment supply, consistent with a fluvio-deltaic setting in which depositional processes are complex and forced by flooding (storm action), tidal and current activities (Reading & Collinson, 1996).

The Cretaceous and Tertiary samples differ greatly from those of the Jurassic and have had a variety of depositional environments and sediment inputs. The Tertiary volcanism associated with the opening of the Atlantic (Ziegler, 1999) saw exceptional source materials introduced to the Northern North Sea Basin (Thyberg et al, 2000), whereas the Cretaceous was a time of carbonate production interspersed with siliciclastic mudstone deposition (Glennie, 1990). Clearly from the QXRD results anoxia was not as prevalent as in the Jurassic and the literature (e.g. Oakman & Partington 1998; Brewster & Dangerfield 1994) suggests that seas were deeper and more carbonate rich than the Jurassic. This led to entirely different depositional

environments which, due to the increased energy of the system, would have required clays to be deposited by flocculation (e.g. Chamley, 1989; Kranck, 1991) in estuary settings and by organo-mineralicc aggrages in the open ocean and probably different sediment source areas too resulting in little or no enhanced depositional aid to fabric development from the Late Jurassic onwards.

Mineralogically, the samples of the Cretaceous are the most consistent, in that they show constant trends with depth (Table 4.3 & 4.4) either increasing or decreasing as a function of the various diagenetic reactions at play. This hints at a relatively consistent sediment regime throughout the Cretaceous, or as consistent as one could hope for in a diagenetic study. At ~2000m thick this equates to a ~60°C temperature difference from the top of the section to the base (30°C/km geothermal gradient, see chapter 5 for details), which is insufficient to further explore these changes in relation to diagenesis.

The QXRD in this study shows that there are elevated levels of tri-octahedral smectites in the Tertiary and this implies that source areas and materials changed through time. The high levels of tri-octahedral smectites are co-incident with decreased levels of quartz and illite/mica suggesting some volcanic material input from the Tertiary opening of the Atlantic (Ziegler, 1999; Thyberg et al, 2000 and references therein) either from fallout from volcanic dust clouds with volcanic glass altering to smectite (e.g. Son et al, 2001) or through normal sedimentation regimes fed with sediment generated from the spreading centre to the west of what is today the Northern North Sea. This volcanic source is further evidenced by the presence of elevated levels of clinoptilolite, a zeolite, which commonly occurs as a devitrification product of volcanic glass shards in tuff and as vesicle fillings in basalts, andesites and rhyolites, with organic-acid dissolution of feldspars the most probable source of aluminium and cations for clinoptilolite formation (Huggert et al, 2005).

In any diagenetic study an appreciation of the starting materials must be held in mind. Sedimentation regimes have been demonstrated to have varied for the Northern North Sea from the Jurassic to the Late-Tertiary so phyllosilicate mineralogy at the time of deposition can be related to sediment provenance and facies (e.g. Weaver, 1989). This then leads to complications in interpreting diagenetic trends with depth and age, these complications then extend to the physical properties of the rocks and effects that variability in composition will have on fabric alignment.

4.4.2: Diagenetic Changes:

In assessing the fabric alignment of phyllosilicate minerals in mudstones, it is essential to have an understanding of the mineralogy of mudstones, since previous studies (Oertel & Curtis, 1972; Curtis et al, 1980; Ho et al, 1995; van der Pluijm et al, 1998; Jacob et al, 2000; Matenaar 2002; Aplin et al, 2003; Charpentier et al, 2003) have shown the significance of diagenesis on fabric development.

Most sedimentary basins exhibit the transition from smectite to mixed layered illite/smectite to illite (Perry & Hower, 1970; Hower et al, 1976; Boles & Franks, 1979; Pollastro, 1985; Ahn & Peacor, 1986; Bell, 1986; Land et al, 1987; Jiang et al, 1990; Eberl, 1993; Schegg & Leu, 1996; Nieto et al, 1996; Wang et al, 1996; Rask et al; 1997; Land et al, 1997; Lynch, 1997; Hover et al, 1999; Masuda et al, 2001; Son et al, 2001;). Essentially, smectite is converted to illite as in the equations listed below, with a source of potassium as a fuel for the reaction.

$$\text{Smectite} + Al^{3+} + K^{+} = \text{Illite} + Si^{4+} \text{ (Hower et al, 1976)}$$

Or

$$\text{Smectite} + K^{+} = \text{Illite} + \text{Chlorite} + \text{Quartz} + H^{+} \text{ (Boles and Franks, 1979)}$$

The difference between the equation postulated by Hower et al (1976) and by Boles and Franks (1979) is that Hower et al view the sedimentary system as a closed system with respect to potassium, whereas Boles and Franks see the reaction as essentially the "cannibalization" of smectite to form illite. The progression towards lower smectite percentages in the diagenetically formed mixed layer phase illite/smectite may be tracked through X-ray diffraction (Moore & Reynolds, 1997) on the separated clay fraction (<2μm) and the relative percentages point to the relative grade of diagenesis encountered.

Illitization of smectite is controlled by various parameters, temperature (e.g. Freed & Peacor, 1989), time (e.g. Środoń & Eberl, 1984; Velde, 1995), pressure (e.g. Środoń and Eberl, 1984; Buryakovsky et al, 1995), potassium availability (e.g. Hower et al, 1976; Moore and Reynolds, 1997) and the chemistry of pore fluids (e.g. Drief & Nieto, 2000). The stoichiometry has been examined for Gulf of Mexico by various workers (e.g. Land et al, 1987; Lynch, 1997; Land et al, 1997). The kinetics of the reaction is a study in itself and has been assessed by various authors (e.g. Vasseur & Velde, 1992; Huang et al, 1993; Hillier et al, 1995; Elliott & Matisoff, 1996; Elliott et al, 1999) with a unifying kinetic model still elusive.

The XRD analysis of the samples from the Northern North Sea for wells, Rhum 3/29a4 and Magnus 211/12-2 (presented previously), reveal that there is an increase in the percentage of illite in illite/smectite with increasing depth (Figures 4.23, 4.52 & 4.53). There are distinct differences in mineralogy between the Tertiary, Cretaceous and Jurassic, so discussing the profile as continuous reaction series is perhaps misleading. To compare the Jurassic with the Tertiary is not to compare like with like, the Jurassic is characterized by mineralogy consistent with an anoxic regime and the almost complete lack of chlorite seen in both the XRD and the 2-theta scans in HRXTG, either diagenetically produced or as initial detrital input. The Tertiary is swamped with volcanic alterating products such as clinoptilolite and di/tri-smectite from the alteration of volcanic glass (Son et al., 2001) associated with the opening

of the Atlantic (Ziegler, 1999). The illitization of smectite reaction has not run to the usual termination point by the base of the sections, which is usually at 80% of illite layers (e.g. Hower et al, 1970; Bell 1986; Rask et al, 1997) in the mixed layer phase illite/smectite. The Jurassic samples from Rhum 3/29a4 are hot enough (~150°C) to reach the termination of the reaction at greater than 80% illite layers (Weaver, 1989). The key to smectite in illite/smectite at 35% persisting to these temperatures appears to be related to K-feldspar dissolution, the key driver in the illitization of smectite (e.g. Boles & Franks, 1979; Hower et al., 1976). In Rhum 3/29a4, the illitization limiting factor appears to be K-feldspar availability, as in the deepest samples the amount of K-feldspar has decreased to almost zero from initial levels of more than 6%, this is consistent with other studies on potassium availability (e.g. Hower et al, 1976; Moore & Reynolds, 1997; references therein). Therefore, Rhum 3/29a4 may in fact represent a partially complete diagenetic pattern in each Period similar to those observed in the Gulf of Mexico (e.g. Burst, 1959; Hower et al., 1976) and the North Sea (Pearson et al., 1982) but be limited by potassium input to the basin at the time of sedimentation.

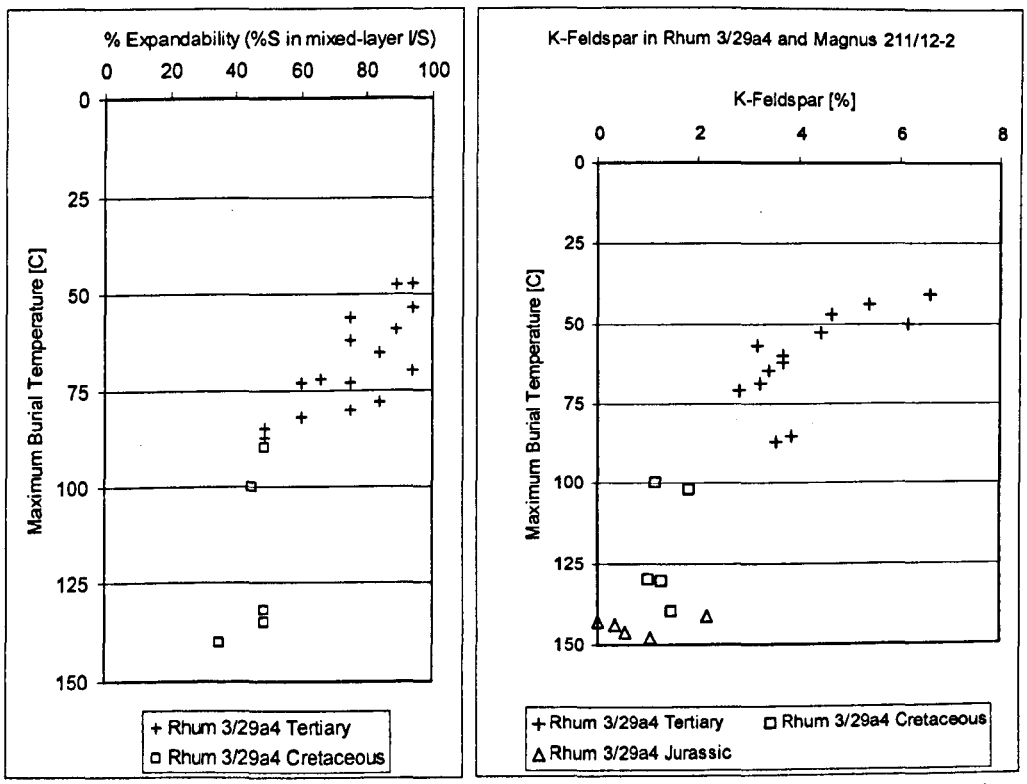

Figure 4.52. Illitization of smectite terminating at ~40%S layers in Rhum 3/29a4, left, and the depletion of K-feldspar to less than 1%, right. The temperature data come from modelling Rhum 3/29a4 in Genesis 4.8, see chapter 5 for details.

The deepest samples from Magnus 211/12-2 (110°C) have illite at 60% of layers. At the equivalent temperature in Rhum 3/29a4 illite comprises 55% of layers, the additional 40°C associated with the additional core depth for Rhum 3/29a4 only sees a further decrease in smectite of around 10%, so illite is comprising 65% of layers. Since the temperature in Magnus 211/12-2 is only 110°C and K-feldspar has not been completely depleted it appears that the reaction in this well has some way still to run. Consequently, Rhum 3/29a4 and Magnus 211/12-2 appear to represent incomplete illitization of smectite at their bases for differing reasons.

There are potentially other mineral reaction pathways at play in the basin, meaning that the 'classic' illitization of smectite (after Hower et al, 1976) is retarded. This latter point is worth exploring as there is evidence from studies by Merriman and Peacor (1998) and Merriman (2002) that tri-octahedral 2:1 smectites may form chlorites via the mixed layer phase corrensite, a mixed-layer chlorite-smectite (Figure 4.54).

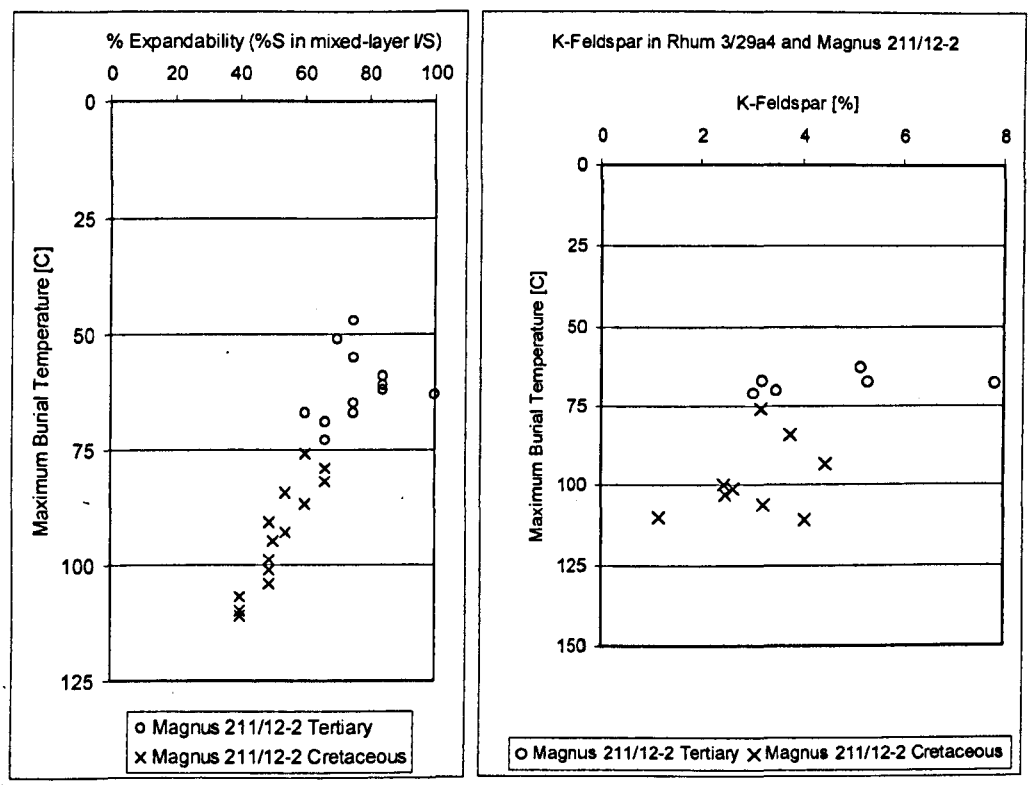

Figure 4.53. Illitization of smectite terminating at ~40%S layers in Magnus 211/12-2, left, and the incomplete depletion of K-feldspar, right. The temperature data come from modelling Magnus 211/12-2 in Genesis 4.8, see chapter 5 for details.

Cretaceous tri-octahedral smectite is not elevated in the same way that it is in the Tertiary. Therefore, Magnus 211/12-2 appears to simply be not buried deeply enough to attain the necessary temperatures in this part of the basin.

In addition to the illitization of smectite, as has been demonstrated in Figure 4.54 there are other diagenetic reactions happening in sedimentary basins to a greater or lesser extent. Boles and Franks (1979) have written their reaction, stated previously, to include the formation of chlorite from the illitization of smectite but equally, chlorite can form from kaolinite and smectite (Merriman 2002; Weaver, 1989) in response to burial diagenesis. There is no evidence that kaolinite is produced in diagenetic phyllosilicate reactions but it may form from the alteration of K-feldspar (Weaver, 1989), however, kaolinite may be persistent to high temperatures, 180°C+ (Dunoyer de Segonzac, 1970), so it may be inert in the system.

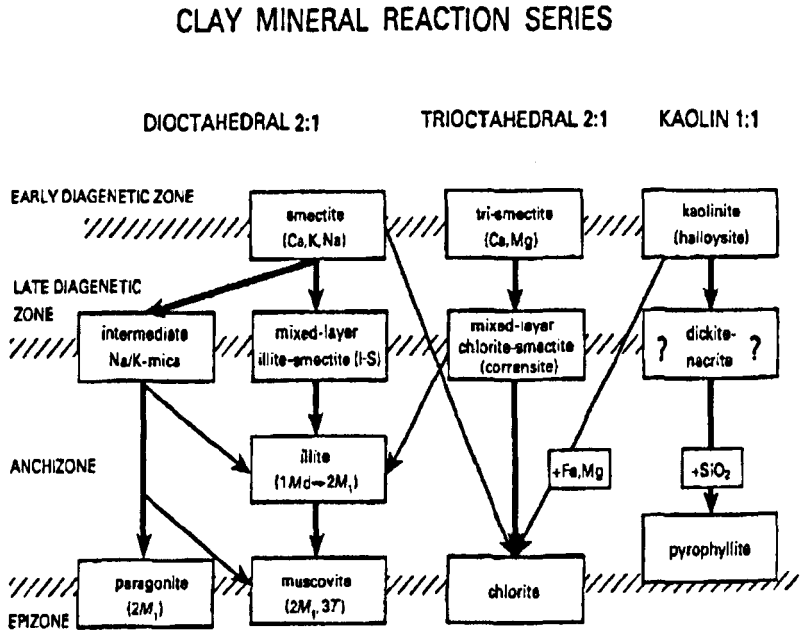

Figure 4.54. (After Merriman, 2002). The heavy arrows indicate main reaction progressions. The diagonal arrows indicate products contributed from one series to another. The approximate positions of reactants and products are shown in relation to metapelitic zones.

Time (Środoń & Eberl, 1984; Velde, 1995) is another limiting factor in the context of the kinetics (Velde & Vasseur, 1992; Huang et al, 1993; Hillier et al, 1995; Elliott & Matisoff, 1996; Elliott et al, 1999) of the illitization of

smectite. Recent sediments simply do not have the time to reach diagenetic maturity; sediments with rapid burial histories may also be likewise affected. Since the deepest samples in both wells are Jurassic in age time in this case is not going to be a relevant cause of incomplete illitization.

The results from the less than 2μm fraction shows that illite/smectite is less prevalent in the deeper samples and that the general trend is a decrease in both wells from around 90% in the Tertiary to around 60% of material in the Jurassic (Figure 4.55). This is accompanied by the fact that the free illite in the less than 2μm fraction (Figure 4.55) is increasing from around 2% to around 18%. Due to the particle size under consideration this may be viewed as a diagenetic effect and it may be interpreted that some percentage of illite in the deeper samples has formed at the expense of mixed-layer illite smectite. This observation is entirely in keeping with those of Pollastro (1985).

The imprint of diagenesis is not entirely clear. Kaolinite in most diagenetic sequences around the world that are related to the illitization of smectite show a decrease with depth (e.g. Środoń et al, in press; Boles & Franks, 1979, Hower et al, 1976). In Rhum 3/29a4 the trend has a decrease in the Tertiary followed by an increase in the Cretaceous. The Tertiary observation may be related to elevated levels of clinoptilolite and di/tri-octahedral smectite (e.g. Figures 4.13, 4.14, 4.20 & 4.57). Likewise in Magnus 211/12-2 the increase in kaolinite through the Tertiary and Cretaceous which again is inconsistent with accepted trends of diagenesis and appears linked once again to elevated di/tri-octahedral smectite concentrations.

Chlorite increases in both the Tertiary and Cretaceous in Magnus 211/12-2 as is predicted by the diagenetic reactions stated by Hower et al (1976) and Boles and Franks (1979), however, this is not accompanied by coincident kaolinite decrease. Chlorite increase in the Cretaceous of Rhum 3/29a4 may be related to the smectite to chlorite reaction pathway (Figures 4.54 & 4.58) postulated by Merriman (2002), since the change in the %I in I/S slows

considerably through the Cretaceous. Chlorite levels are particularly low in the Jurassic and Tertiary in Rhum 3/29a4 and points directly to the variation in sediment source as being the dominant control over that of diagenesis in assigning the mineralogical trends with depth. Separating the effects of diagenesis from sedimentary input variation is not possible in these wells.

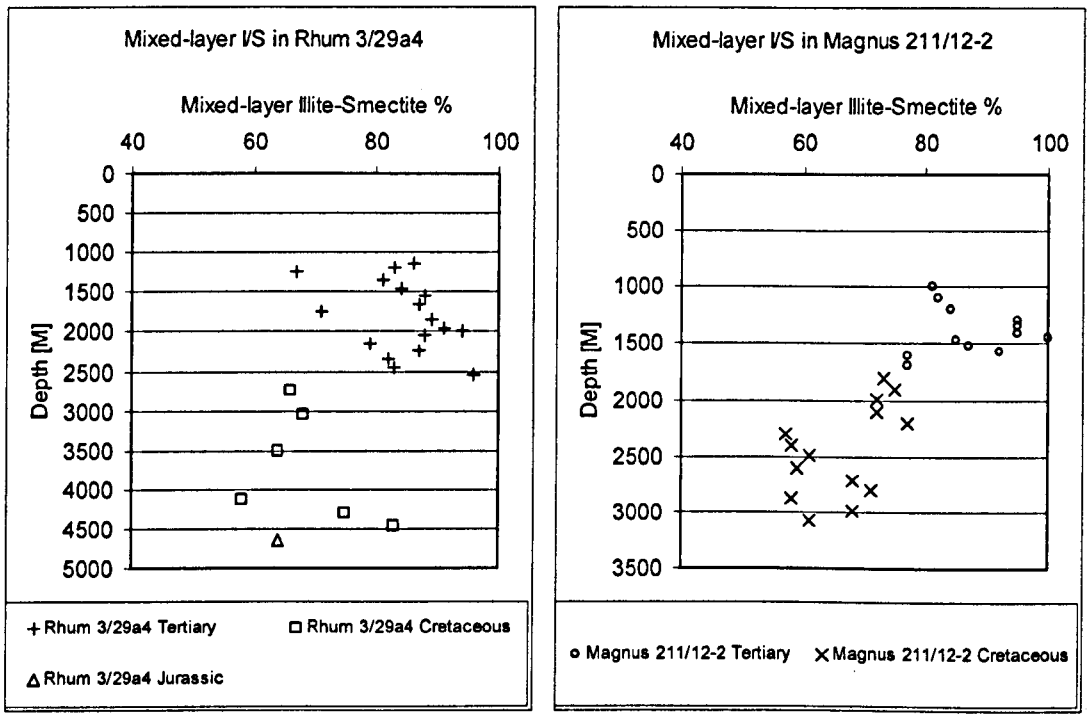

Figure 5.55. % mixed-layer illite-smectite in Rhum 3/29a4, left, and Magnus 211/12-2, right.

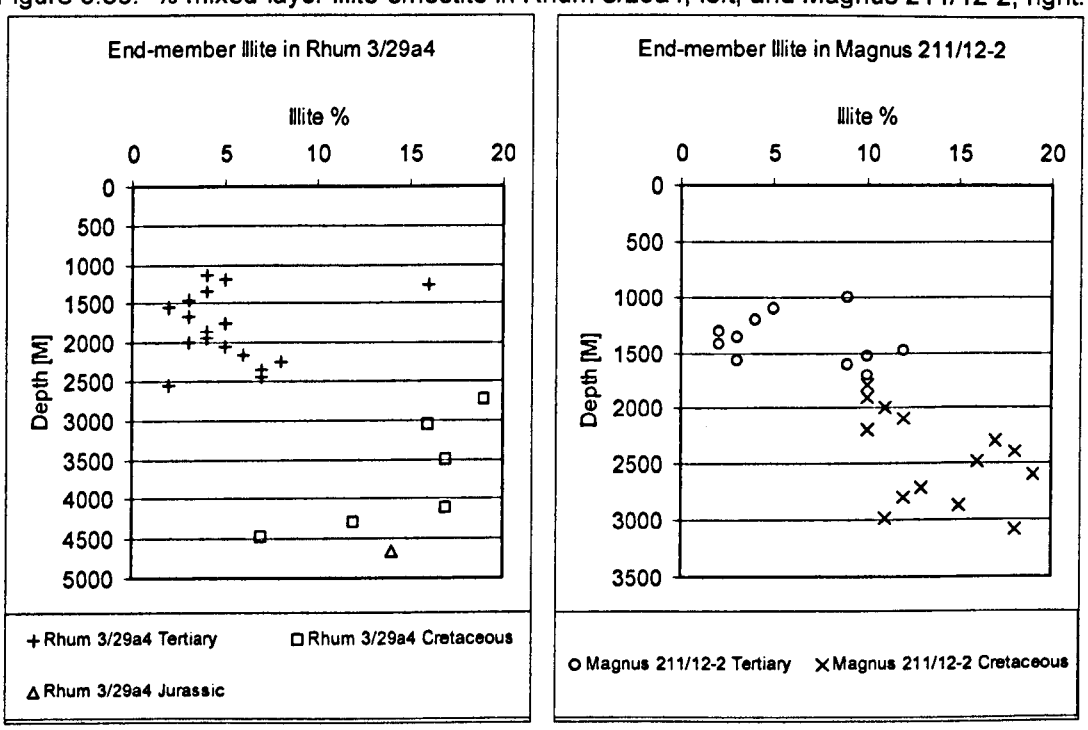

Figure 4.56. Free illite taken from the <2μm fraction by XRD with depth [m] for Rhum 3/29a4, left, and Magnus 211/12-2, right.

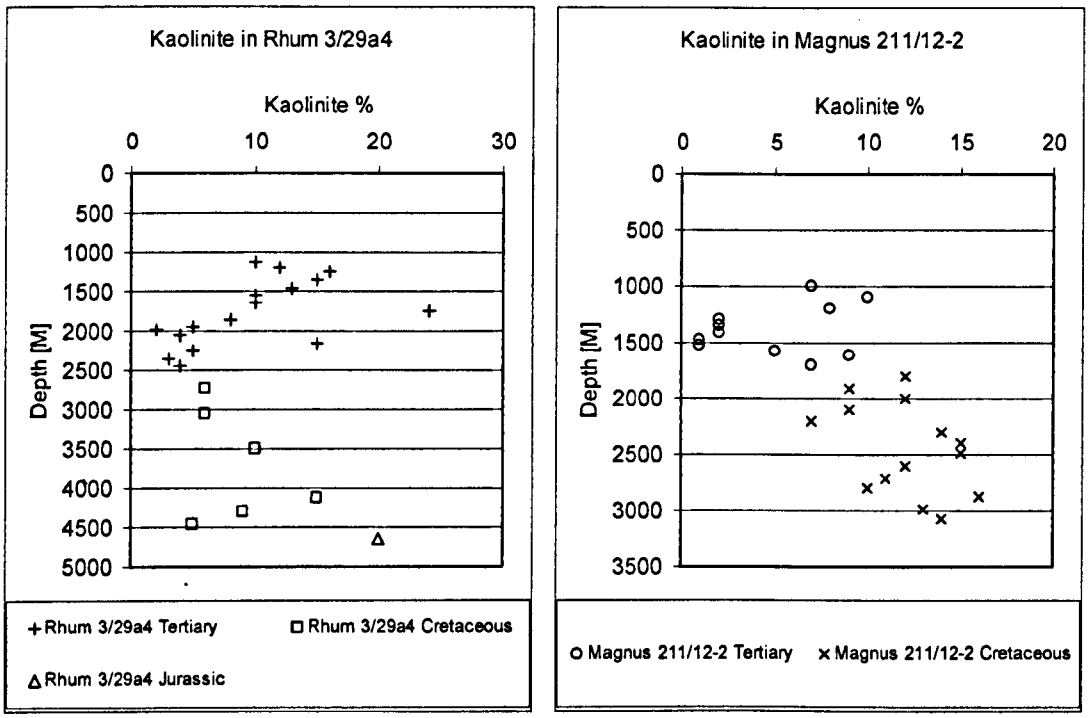

Figure 4.57. Chlorite in the <2µm fraction by XRD with depth [m] for Rhum 3/29a4, left, and Magnus 211/12-2, right.

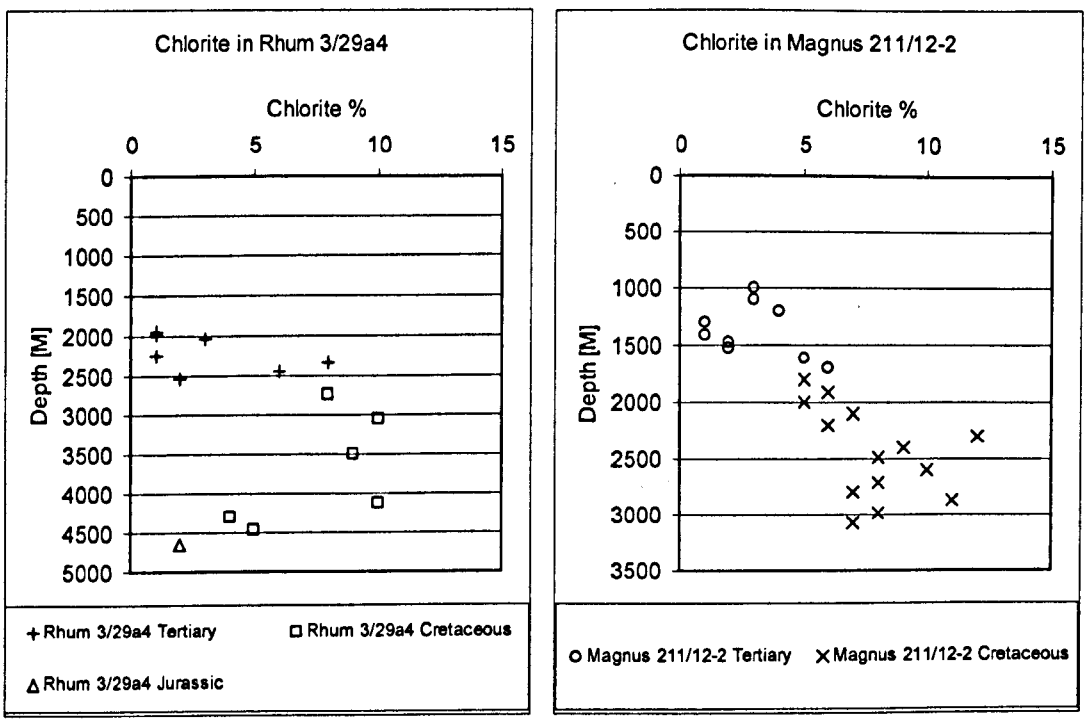

Figure 4.58. Chlorite in the <2µm fraction by XRD with depth [m] for Rhum 3/29a4, left, and Magnus 211/12-2, right.

4.4.3: Controls on fabric development:

There is a general link between grain size and depositional energy in sedimentary systems (e.g. Hjulstrøm 1935; Bouma, 1962). Essentially, the lower the energy of deposition, the smaller the grain size and this relationship has been recorded variously (e.g. Chamley, 1989; Aplin, 2000). The deposition of phyllosilicates and fine-grained muds in general is controlled by the energy of their environment. Studies (e.g. McCave, 1970; McCave, 1971; Schieber, 1998) have demonstrated that deposition of phyllosilicates is not limited to low-energy regimes, as flocculation of heavier silt or sand sized aggregates facilitates deposition where a single grain will remain in suspension (Chamley, 1989; Kranck, 1991). Flocculation can form many phyllosilicate microstructures that may be described as non-aligned with the resultant affect that there is no initial preferred orientation of platy phyllosilicates (e.g. Rieke & Chilingarian, 1974; O'Brien & Slatt, 1990; Bennett, et al, 1991). Additionally, initial preferred alignment may be further disrupted by bioburbation (e.g. Bennett, et al, 1991).

The Jurassic samples in this dataset may be candidates for depositionally enhanced fabric development, with anoxia retarding bioturbation activity in a generally low energy regime. It should be noted that by QXRD, the low energy environment has not preferentially selected phyllosilicates at the expense of quartz. Figure 4.59 reveal that the Jurassic sample from Rhum 3/29a4 at 4830m has less and finer quartz material than a Cretaceous sample at 2550m, with the deeper sample having a more aligned phyllosilicate matrix as a visual observation and quantified by HRXTG (Table 4.7).

In more energetic regimes such as those of the Cretaceous and Tertiary the deposition of fine-grained clay sized phyllosilicates would have been through flocculation. Flocculation then may result in initial non-alignment of phyllosilicates (e.g. O'Brien & Slatt, 1990; Bennett et al, 1991) at deposition, however how long clay flocs are retained first in bioburbation conditions and

second in burial conditions is debatable. Sintubtin (1994) has postulated that such structures were short lived, although this study has found flocculated material persistent to ~3000m (Figure 4.60) and Matenaar (2002) has poor preferred alignments in phyllosilicates down to ~5000m in the Gulf of Mexico.

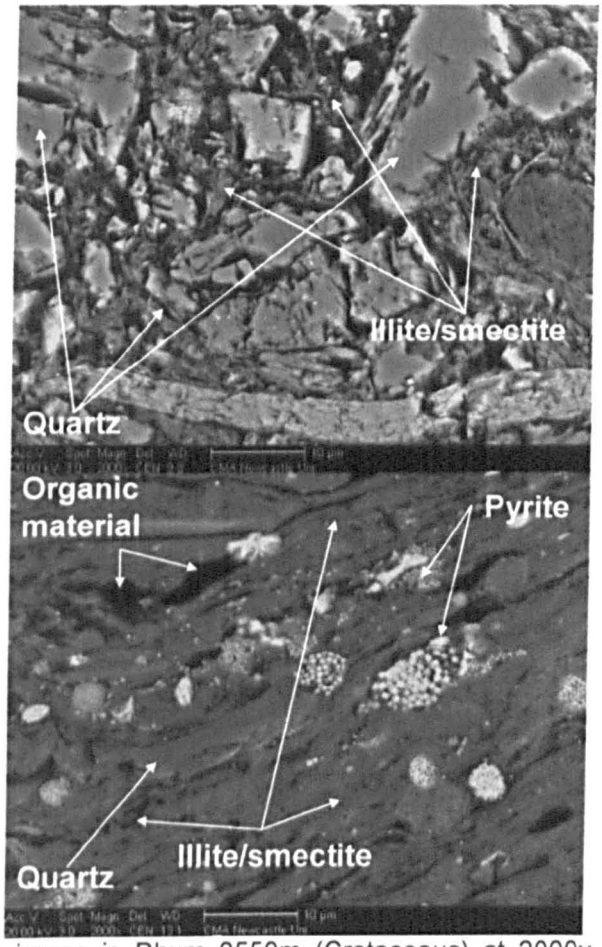

Figure 4.59. The top image is Rhum 2550m (Cretaceous) at 2000x magnification. The bottom image is Rhum 4830m (Jurassic) at 2000x magnification. The Jurassic sample from Rhum 3/29a4 has less and smaller quartz material than the sample from the Cretaceous at 2550m and the difference in grain size at the same magnification is obvious.

The BSEM images presented previously demonstrate that grain size and grain shape have a significant impact on fabric alignment. Quartz which can vary in shape from angular to well-rounded and in grain size from clay to silt size disrupts fabric development and various micrographs depict small platy phyllosilicates bending and wrapping around larger quartz grains. Ultimately, the potential for fabric alignment disruption is a function of size (Matenaar, 2002), abundance and whether the quartz material is in laminations, as isolated grains or the dominant component in a clast support matrix structure. Such laminations may be thick, thin, wavy or lenticular (O'Brien & Pietraszek-Mattner, 1998; O'Brien & Slatt, 1990) and their effect on fabric

measurements is dependent on them being significant on the 1mm^2 scale, the surface interaction area in HRXTG. The BSEM micrographs presented in this chapter show all of the above quartz structures and occurrences. Yet due to the low percentages of quartz present relative to total clay minerals the overall effect on preferred orientation of phyllosilicates by localised matrix supported quartz material is low. Pyrite and specifically pyrite framboids do not usually have a significant effect on fabric as they are not present in significant enough quantities to disrupt fabric. However, when their presence is as high as ~9% in the Jurassic of Rhum 3/29a4 it becomes a significant localised factor in the disruption of fabric. A couple of high magnification BSEM images presented earlier show that although the pyrite framboids appear to be quite porous they are extremely resistant to the effects of loading and maintain their rounded form at great depths causing phyllosilicates to bend and wrap around them, although their affect will be similar to quartz on the scale of HRXTG technique.

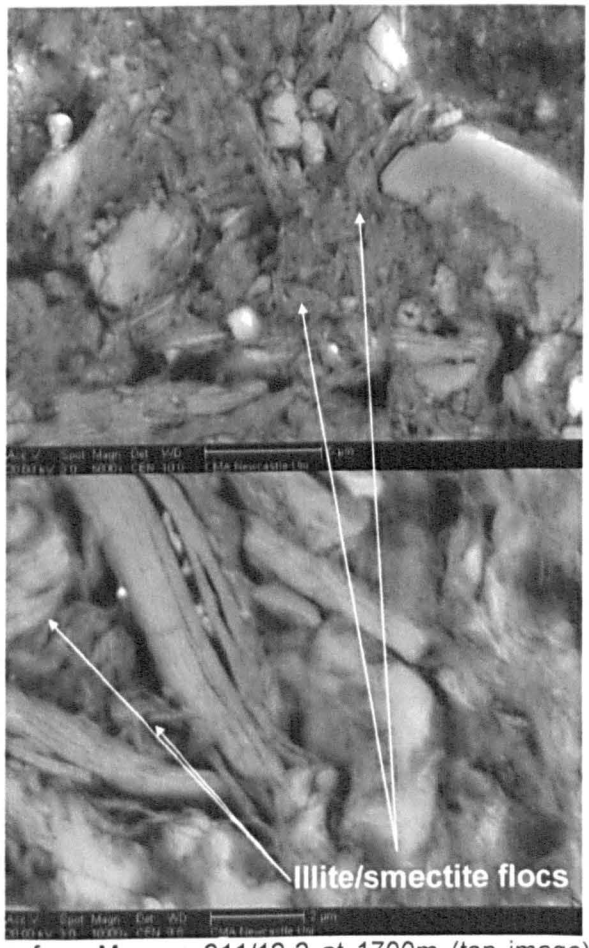

Figure 4.60. Samples from Magnus 211/12-2 at 1700m (top image) and 1802m (bottom image) at 5000x and 10000x magnification, respectively, showing the flocculation of illite/smectite particles persisting to present day burial depths.

The fact that there is a correlation between mineralogical change and fabric development with depth or at least increasing stress (e.g. Oertel & Curtis, 1972; Curtis et al, 1980; Ho et al, 1995; 1999; van der Pluijm et al, 1998; Jacob et al, 2000; Matenaar 2002; Aplin et al, 2003; Charpentier et al, 2003. Worden et al., 2005) suggests that there is a significant role for diagenetic mineral reactions in the development of preferred alignment of phyllosilicates. The samples from the Podhale Basin (Chapter 2) showed that in deep burial situations fabric development is linked to diagenesis. In this study where the samples are shallow buried and the effects of sediment loading are not as acute as in the Podhale Basin the effects of diagenetic reactions certainly in the Tertiary samples are less clear. As diagenesis proceeds through the Cretaceous samples the effects may be heightened, however the percentage of smectite in I/S is ~50% in both Rhum 3/29a4 and Magnus 211/12-2 so the distribution of layers is still randomly interstratified.

In this study, the effects of diagenesis in the formation of phyllosilicate preferred orientation are overshadowed by the effects of different sediment regimes through time. Consequently, the role of diagenesis in the preferred alignment of clay minerals in mudstones cannot be unravelled in this study. What can be noted is there is only a weak preferred alignment generated in the smectite-rich samples of both wells down to ~2500m. There is some evidence for incomplete illitization within the Cretaceous samples of Rhum 3/29a4 associated with a very small increase in preferred orientation alignment. A similar trend was noted by Worden et al (2005), however, the Cretaceous alone is not a thick enough (~2000m) or hot enough (~60°C temperature difference) sequence to fully observe the characteristics of illitization on preferred alignment. The Kimmeridge Clay Formation has generated extremely well aligned fabrics but discerning the imprint of depositional effects from those of diagenesis cannot be made.

4.4.4: Fabric and compaction trends:

With increasing loading porosity reduction will occur. Porosity decreases with increasing burial depth (e.g. Athy, 1930; Hedberg, 1936; Dzevanshir et al, 1986) and hence increasing effective stress and temperature needed to drive diagenetic mineral reactions. However, porosity reduction is a trade off between the rotation of grains (e.g. van der Pluijm et al, 1994), and grain size (e.g. Matenaar, 2002), grain shape (e.g. O'Brien and Slatt, 1990) and sorting effects (e.g. Weaver, 1989). Dissolution-recrystallisation reactions (e.g. Inoue et al, 1987; Moore & Reynolds, 1997) in mineral diagenesis and effective stress (e.g. Yang & Aplin, 2004) are also significant. Lithology and overpressuring will have a significant bearing on porosity reduction, with overpressuring holding pore structures open.

These caveats notwithstanding, there is a general relationship in this study between porosity reduction and fabric development. A weak fabric that is no greater than ~3 m.r.d. is developed with porosity at greater than 30% and these approximately correlate with Tertiary samples. An intermediate zone may be identified between 30% and 15% porosity and is characterised by variable preferred alignment that ranges from weak to moderate and correlates with the Cretaceous. A third zone with less than 15% porosity is associated with a strong to very strong preferred alignment of phyllosilicates and is entirely comprised of Jurassic samples (Figure 4.63).

High fabric and high porosity is not occurring in these samples, contrary to some observations made my Matenaar (2002). The results of this study are consistent with the depth-fabric-porosity study of Aplin et al (2003). The nature of the relationship between fabric and porosity in the Cretaceous samples of this study, 25% to 15% and 2.5 m.r.d. to 4.5 m.r.d., is similar to that described by Worden et al. (2005) for the Cretaceous of the Northern North Sea. Starting porosities of 44%, by MICP, at ~1000m are indicative of shallow buried sediments and are in line with porosity depth trends for the North Sea (Sclater & Christie, 1980) from sonic logs in normal pressure

systems. As a result the lack of preferred alignment of phyllosilicates in the Tertiary and Cretaceous as porosity is reduced must be as a result of depositional characteristics that are not conducive to aiding initial phyllosilicate alignment, these characteristics such as flocs of phyllosilicates have been seen in BSEM micrographs to be present even to ~3000m and porosities of ~20%.

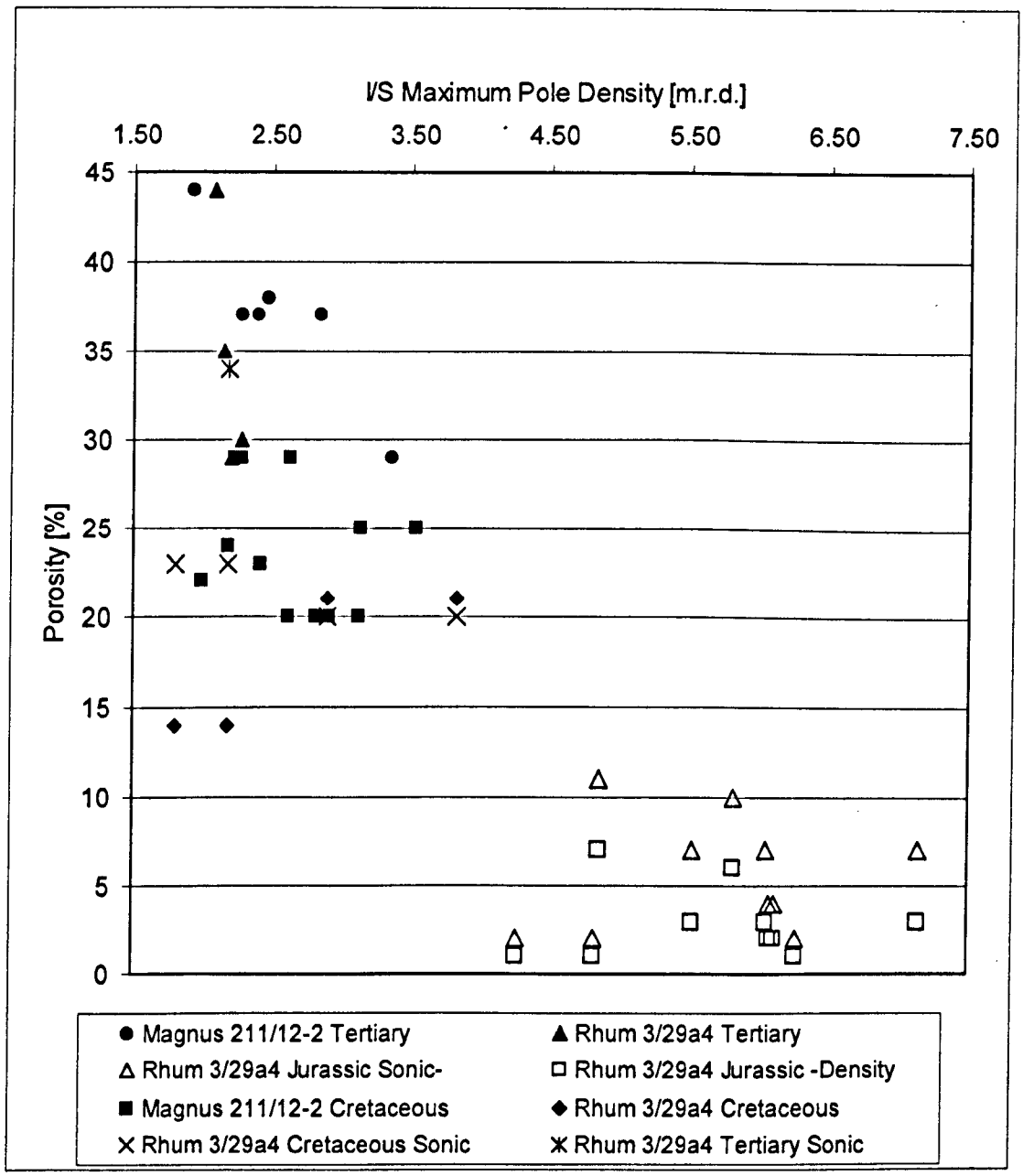

Figure 4.61. I/S Maximum Pole Density in m.r.d. plotted against percent porosity as recorded by Mercury Intrusion Porosimetry for Rhum 3/29a4 and Magnus 211/12-2 and the porosity from the Sonic Log (calculated using the Raiga-Clemenceau (1988) equation) and the Density Log (calculated using the equations derived by Okiongbo, 2005) for Rhum 3/29a4.

The Jurassic samples are very different in character to those of the Cretaceous and Tertiary in terms of their response to loading and porosity reduction. The depositional characteristics of the Jurassic samples have the biggest effect on their response to loading, as the potentially inherited preferred orientation of phyllosilicates and the relatively reduced size of the quartz material, relative to the Cretaceous and Tertiary, has aided the packing together of grains and therefore the porosity produced as a function of effective stress.

4.5: Conclusions:

This study has noted that there are significant differences in mineralogy between samples from the Tertiary, Cretaceous and Jurassic for both Magnus 211/12-2 and Rhum 3/29a4. The Tertiary is characterised by high smectite concentrations along with clinoptilolite and have been interpreted as alteration products of sediments related to the Tertiary Volcanism of the Northern Atlantic. The Cretaceous represents the least variable period in terms of mineralogy. The Jurassic shows signs of a much different depositional environment to the Tertiary and Cretaceous. Anoxia produced high pyrite concentrations that characterise samples from the Kimmeridge Clay Formation.

The diagenetic trends in Magnus 211/12-2 and Rhum 3/29a4 are unclear. The effects of variable sediment input are too strong to note changes related to diagenesis and the variable input has meant that one period to another cannot be treated as a continuous sequence. Notwithstanding, the illitization of smectite has terminated at ~40% of smectite layers in Rhum 3/29a4 and is co-incident with K-feldspar depletion. Diagenetic mineral reactions are incomplete in Magnus 211/12-2 as temperatures and burial depths are not high enough to facilitate complete reaction.

Fabric intensity has been shown to increase quantifiably with depth for both mineral peaks and in both wells and may be grouped into Tertiary, Cretaceous and Jurassic zones. The fabric intensity has increased from no fabric development to a clearly preferred orientation. Preferred phyllosilicate alignment is dependent on the nature of initial depositional mechanism highlighted by the difference between the Tertiary/Cretaceous and the Jurassic in this study. The development of fabric orientation is enhanced by loading (the vertical component of effective stress) and is the key to the preferred fabric intensities seen with depth in these wells. However, weak fabrics are persistent to 3km.

Overall these samples do not allow an appreciation of phyllosilicate preferred orientation development with diagenesis as there are too many uncertainties surrounding the nature of the diagenetic trends and the sources of sediment input. The study has highlighted the importance of a continuous sequence and the nature of the source material in a diagenetic study.

Chapter 5:
1-D Maturity modelling of two Northern North Sea wells and two wells from the Podhale Basin Southern Poland

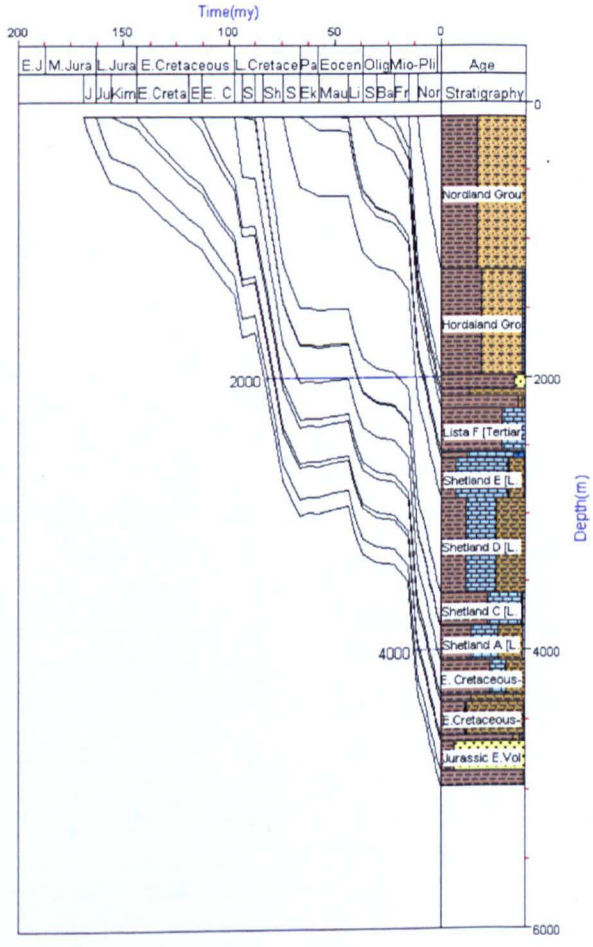

5.0: Introduction to the Modelling of Northern North Sea Wells and Podhale Basin:

This chapter deals with 1-D modelling of two wells from the Northern North Sea (Rhum 3/29a4 and Magnus 211/12-2) and the two wells from the Podhale basin (Chochołów PIG-1 and Bukowina Tatrzańska) that have been dealt with in a fabric reorientation and diagenetic context in chapters 2, 3 and 4. The modelling has been undertaken using the 1-D basin modelling software package, Genesis 4.8, formerly developed at ARCO Exploration and Production Technology and now handled by ZetaWare Inc (http://www.zetaware.com/).

Środoń et al (in press) have demonstrated that the Podhale Basin has been significantly uplifted and these results have been added to in Chapter 2. The maximum burial depth has been estimated based on the theoretical vitrinite reflectance data (after Rospondek & Marynowski, 2005; Marynowski, 2005 pers. Comms.). The geothermal gradient quoted by Środoń et al (in press) is based using on I/S as a palaeothermometer, since the illitization of smectite is dependent on the increase in temperature with burial and has been used, perhaps rather unsuccessfully, as a palaeothermometer (Pollastro, 1993 and references therein) as in the Gulf Coast Region where variable temperatures for either the onset or completion of illitization have been anticipated (Freed & Peacor, 1989). In addition chlorite has been postulated as a palaeothermometer (De Caritat et al., 1993; Walker, 1993) but has proved to be inaccurate (Jiang et al., 1994).

Consequently, this study models the Podhale Basin using Genesis 4.8 to test the validity of the burial and therefore maximum temperature estimates. Porosity and vitrinite reflectance data act as the main controls in the model and the sophisticated coupled mathematics in Genesis 4.8 allow the assessment of maximum burial depth and maximum burial temperature, required to integrate key fabric information (Chapter 6) gained through HRXTG with results published by Ho et al. (1999) and Matenaar (2002). In this chapter modelled vitrinite reflectance is used as a marker for maturity, as

it is the most widely used parameter to indicate maturity and is the primary calibration parameter for modelling temperature histories in basin analysis (Poelchau et al., 1997).

The context for this work is to solidify the relationships between the illitization of smectite and thermal maturity for two unrelated basins, as I/S change and vitrinite maturation are both controlled by kinetics. This work has principally been undertaken as plotting physical or chemical data as a function of depth leaves many unanswered questions, concerning the role of overpressure, burial rate, maximum burial depth and thermal gradient. Therefore, a modelled estimation of vitrinite reflectance is sought for each well that will give an estimate for maximum thermal maturity.

The aims of this chapter are to:

- Model in 1-D the porosity and vitrinite maturity characteristics of Rhum 3/29a4 and Magnus 211/12-2 and Chochołów PIG-1 and Bukowina PIG-1 thus assessing the complex interplay between lithology, sedimentation and burial history, erosion and heating rate.
- Gain a proxy for maturity, vitrinite reflectance (Ro), in the absence of true temperature data for each data point measured %I in I/S.
- Assess the burial histories and the maximum burial depths in the four wells analysed in this thesis so far.

The general topic of basin modelling includes 1-D, 2-D and 3-D simulations. 2-D and 3-D models combine thermal and fluid flow models and will not be dealt with in this work. 1-D models are better described as maturity models (Waples, 1998), in that they allow the prediction of when a source rock has reached hydrocarbon maturation. The inputs into the 1-D models do allow the prediction of overpressures in reservoirs (e.g. Darby et al., 1998) but only if flow is in 1-D, which it often is not. Additionally, 1-D models allow the easy visualisation of subsidence curves (e.g. Darby et al., 1998). In order to constrain the maturity and burial history of, most often, a reservoir or source

rock unit, some calibration of the model is required, typically by temperature data or by a temperature proxy or maturity indicator such as vitrinite reflectance (e.g. Archard et al., 1998; Schegg & Leu, 1998). The proper application of a maturity indicator can also give rise to an understanding of uplift and erosion that may have taken place in a basin and the analysis of both the subsidence curves and the maturity indicators gives semi-independent confirmation. When the model has been suitably calibrated with well control data (Hegre et al., 1998), a better understanding of the complex interplay between lithology, burial history and erosion can be gained, and maximum maturities can be assessed. Maturity can then be related to other diagenetic processes such as illitization and compaction.

5.1: Genesis 4.8:

Genesis 4.8 is a software package that reconstructs burial histories and calculates thermal histories in 1-D and is an efficient way to integrate geological, geochemical and geophysical data. It is of utmost importance to recognise that a model is just that; a model, and that it is accurate but may not be correct. All the variables and assumptions placed into the model must be retained with caveats in mind concerning data quality and the empirical or theoretic models within the model itself. The output results may be described as best estimates and the confidence in those estimates being correct is based on the confidence placed in the initial input data and the relative weight one must therefore place on one parameter over another. The key to effective modelling in general is to keep the model simple, yet true to geological reality; the user must use his or her geological understanding to constrain the model to reality.

5.1.1: Modelling Inputs:

A burial reconstruction includes a whole variety of parameters that are inherently linked (Figure 5.1) to give the final model output. In this section

the basic modelling approach is stated. Appendix 5.1 holds information with regard to the input parameters. Additionally, the assumptions and uncertainties in the model are stated in Appendix 5.2 as this chapter does not represent a critique of maturity modelling.

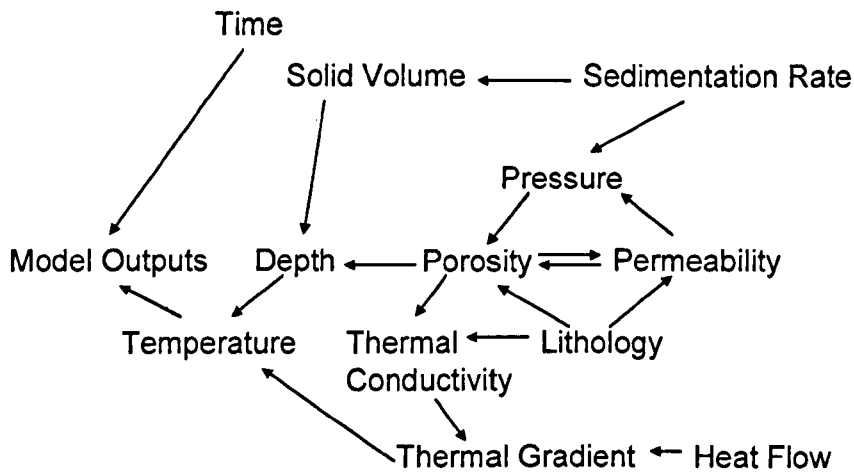

Figure 5.1. A burial history reconstruction that includes these parameters may reveal the net effect of their interaction. The following diagram shows the interdependencies of parameters that go into building a model.

Table 5.1. The inputs and/or calculated parameters in Genesis 4.8.

Density (Rock Grain),g/cm3	Hydrogen Index,mg/g TOC	Seal capacity (oil column),m
Density of Oil Expelled,g/cm3	Oil Expelled,mg/g rock	Seal capacity (gas column),m
Density of Oil Remaining,g/cm3	Oil Expelled (C15+),mg/g rock	Solid Hydrocarbon Reflectance,%
Density of Rock (Bulk),g/cm3	Oil Expelled (C6-C15),mg/g rock	Sterane A1,fraction
Density of Water,g/cm3	Oil Generated,mg/g rock	Sterane A3,fraction
Effective Stress,MPa	Oil Generated (C15+),mg/g rock	Sterane S1,fraction
Effective Stress (Maximum),MPa	Oil Generated (C6-C15),mg/g rock	Sub-Layer Thickness,meters
Expulsion Efficiency,%	Oil Generation Rate,mg/g rock/my	Subsidence (Tectonic),meters
Flow Velocity (Water),cm/my	Permeability (Average Vertical),md	Subsidence (Total),meters
Flux of Water (Cumulative),cm3	Porosity (Bulk),fraction	Subsiding Velocity (Matrix),m/my
Flux of Water (Vertical),cm3/my	Porosity of Each Lithology,fraction	Surface Temperature,C
Fractions of Each Lithology,fraction	Pressure (Capillary Entry),MPa	Temperature,C
Fractions of Each Kerogen Type,fraction	Pressure (Excess),MPa	Thermal Conductivity (Bulk),cal/cm2.s.C
Gas Expelled,mg/g rock	Pressure (Fluid),MPa	Thermal Gradient,C/m
Gas Expelled (C2-C5),mg/g rock	Pressure (Hydrostatic),MPa	Tmax,C
Gas Expelled (Methane),mg/g rock	Pressure (Total Overburden),MPa	TOC (Remaining),%
Gas Generated,mg/g TOC	Pressure Gradient,MPa/m	Transformation Ratio (HC),fraction
Gas Generated (C2-C5),mg/g rock	Production Index,fraction	Transformation Ratio (TG),fraction
Gas Generated (Methane),mg/g rock	Quartz cement,fraction	TSI,
Gas Generation Rate,mg/g rock/my	Rate of HC Expulsion,mg/g Rock	TTI (Waples Model),
Geothermal Gradient,C/100m	Ratio of Atomic H/C (LL Model),	User Biomarker A,fraction
GOR of Expelled Products,scf/bbl	Ratio of Atomic O/C (LL Model),	User Biomarker B,fraction
GOR of Residual Products,scf/bbl	Remaining Potential,mg/g TOC	Velocity (Acoustic),m/s
Heat Capacity (Bulk),cal/g C	Residual Coke Generated,mg/g TOC	Vitrinite Ro (ARCO),%
Heat Flow,cal/g.cm2.s	S1,mg/g Rock	Vitrinite Ro (LL Model),%
Hopane H1,fraction	S2,mg/g Rock	Vitrinite Ro (Waples Model),%
Hydraulic Potential,MPa	Saturation (HC),fraction	Vitrinite Ro (BP),%

In this study the manual inputs (i.e. the measured data) into Genesis 4.8 are lithology, age, vitrinite reflectance, temperature, surface temperature, pore pressure and porosity. These are by no means the only potential input parameters but are the ones available to this study. Genesis 4.8 calculates over 80 parameters (Table 5.1), which are derived from models and empirical

formulations within the model. The input parameters are those that may be obtained through production data and measurements made on core or cuttings material in the laboratory.

5.1.2: Setting up the modelled outputs:

The flow of work in the modelling process may be summed up in the following way;

1. Define the initial stratigraphy of the well in question based on the completion log
2. Define the initial lithological mix from the completion log.
3. Add in the measured data (e.g. porosity, vitrinite reflectance, temperature, pore pressure).
4. Refine the thermal properties of the model in order to match the calibrated data.
5. Refine the lithological mix based on the thermal properties of the model and the calibration data.
6. Set the fluid flow model and calibrate with porosity and pore pressure data.
7. Refine the lithological mix based on the changes made with the setting of the fluid flow model.
8. Refine the thermal model based on the changes from the above steps.
9. Check the final lithologies to make sure that they are geologically realistic.
10. Check all the modelled outputs to assess the final model situation and the overall adherence to the calibration data.

The settings for the thermal and fluid flow models are presented below, with more detail stated in Appendix 5.1 with uncertainties noted there. The thermal model is set to transient, fixed temperature at the base of the lithosphere. This implies that the base of lithosphere temperature is always 1330°C and that the effect of this temperature is of heat flow up into lower temperature regions. This flow is affected by the sediment pile and is

therefore not lasting or durable as fast sedimentation rates may cause temporarily lower heat flow in the sediments. Additionally, the lithosphere and crust are assumed to generate heat by Radiogenic Heat Production (RHP) and that the flow of this heat is advective.

As mentioned above the mantle lithosphere-aesthenosphere boundary is always taken to be 1330°C in Genesis 4.8 therefore thinner lithosphere thicknesses will result in higher total heat flow. A mantle thickness of 120km (Upper Crust 7km, Lower Crust 8km and Mantle Lid 105km) has been set based on the cross-section of the Rhum Field (Christiansson et al., 2000). Additionally, heat production in the lower crust and mantle lid has been turned to zero, under the assumption of no lithosphere stretching, these settings resulted from a process of iteration during the modelling on Rhum 3/29a4, Magnus 211/12-2, Chochołów PIG-1 and Bukowina Tatrzańska wells.

Surface temperature is a single input variable for the top of the section, and for marine deposition it will range between 0 and 10°C for the present day.

The fluid flow model is set to transient and the permeability model to the Dutta-Franklyn model, with the base of the well set to no flow predicted, a fracture gradient of 0.95 and an initial water density of 1.05g/cm^3. It should be emphasised that the settings used for burial history control are those used by BP as their defaults (Illife, 2005; Pers. Comms.).

For each lithology there is an equation relating porosity to effective stress in Genesis 4.8. Darcy's Law is then used to calculate fluid flow during burial from a porosity-permeability function and in turn is coupled to a calibration of void ratio and permeability (e.g. Dutta, 1987) and each lithology will have a different coefficient in the function. Finally, thermal conductivities will change with porosity loss so this then relates fluid flow to heat flow.

Where porosity is the key calibration data for fluid flow vitrinite reflectance is the key calibration data for the thermal side of the model. Consequently, the modelling method outlined in the work flow above resulted in an emphasis

being placed on the vitrinite reflectance data followed by temperature, in respect to the thermal model, with porosity being the main emphasis for calibration of the fluid flow model.

5.2: Modelled Results:

5.2.1: Rhum 3/29a4:

The lithological column presented in Figure 5.2 came about as a result of the initial input into Genesis 4.8 from the completion log as previously described but as the lithology presented in Table 5.2 attests the final lithology involved some minor changes to each lithological unit from the starting composition. The nature of these changes has to be seen in the context of the whole modelling with consideration of the temperature, pressure, porosity and vitrinite reflectance curves all taken into account.

Figure 5.2 and Table 5.2 shows that the Upper Tertiary samples have an even mix of shale and loose mud with other Tertiary horizons having a slightly more complex assemblage, as a reflection of lithology and therefore depositional environment. The base of the Tertiary sees the start of the carbonate-bearing sequences that dominate the Cretaceous, yet the fine-grained siliciclastic sequence is present throughout. The loose mud typical in the Tertiary has been replaced with tight mud as loading has decreased porosity and has squeezed out water. The fine-grained material in the Jurassic is predominantly shale however the reservoir units are naturally sandstone and dominate those horizons.

No significant hiatuses in deposition or unconformity events have been modelled into the sequence, as the completion log did not show any significant time gaps or loss of time intervals and the other modelling outputs (e.g. porosity and vitrinite reflectance) did not show 'dog-legs' or trend shifts, which would be indicative of an unconformity. This lithological output is, therefore, reasonable based on the completion log information (synthesised in chapter 4) and the modelling presented later.

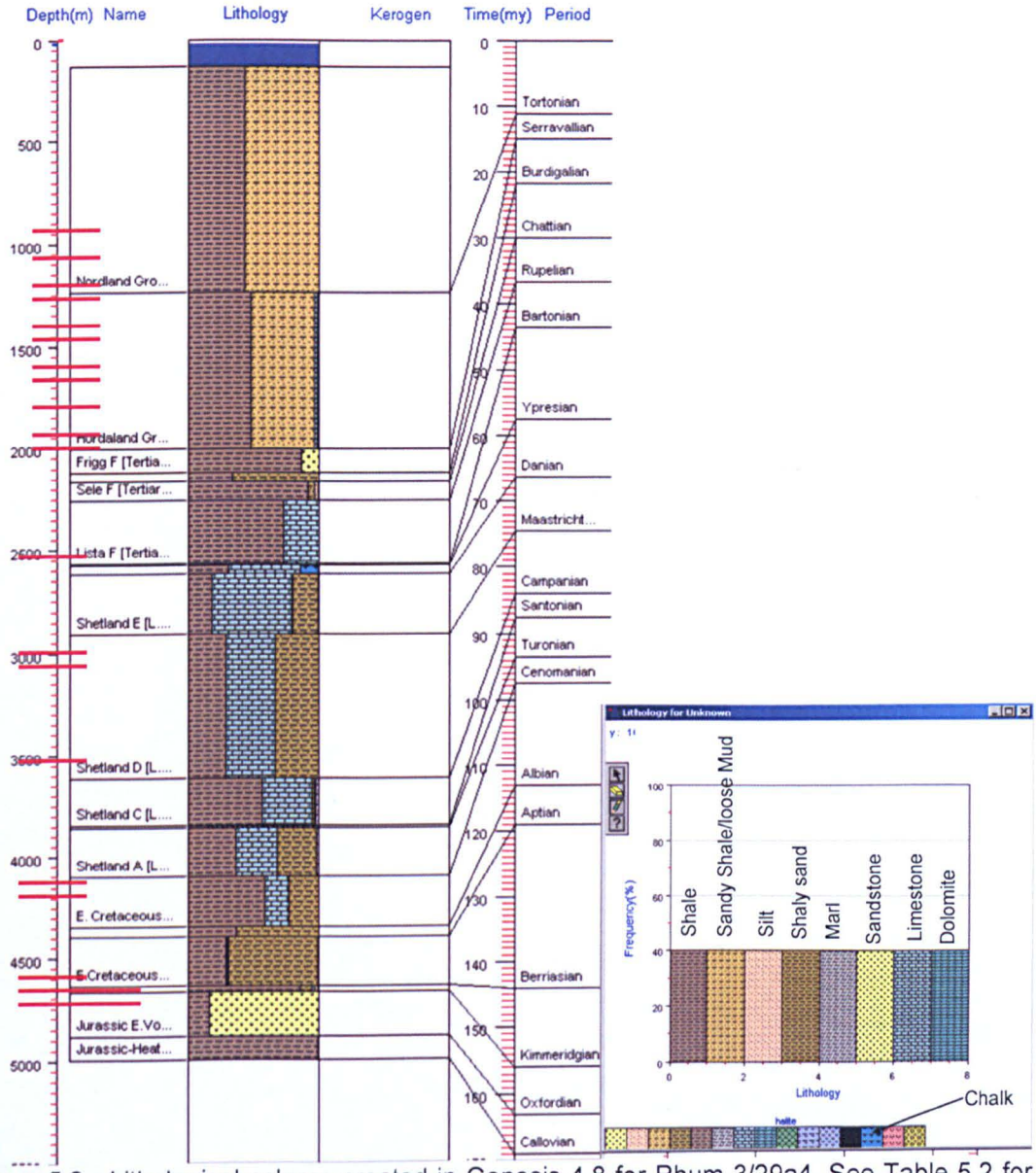

Figure 5.2. Lithological column created in Genesis 4.8 for Rhum 3/29a4. See Table 5.2 for lithological key.

Table 5.2. Formation name, top of formation, age and lithology percentage where; sh=shale, shs=loose mud, ls=limestone, ml=marl, ss=sandstone, ch=chalk, ssh=tight mud, do=dolomite, si=silt, for Rhum 3/29a4. See text for more information on how lithological mix was derived.

Formation Name	Top/ Thickness [m]	Ages [Ma]	Lithology and percentage of lithology type in each unit.
Nordland Group Tertiary	131.5	0	sh43,shs57
Hordaland Group Tertiary	1235	11.2	sh48,shs48,ls2,ml1,ss1
Frigg Formation [Tertiary-Hordaland Group Burdigalian (Early.Miocene)	2005	15.1	sh87,ss13
Balder Formation [Tertiary-Rogaland Group Chattian (Late Oligocene)	2119	21.8	sh34,ssh66
Sele Formation [Tertiary-Rogaland Group]Rupelian (Early.Oligocene)	2167	30	sh92,ssh5,si3,ml1
Lista Formation [Tertiary-Rogaland GroupBartonian (Late Eocene)	2259	36.6	sh73,ls27
Maureen Formation [Tertiary-Rogaland Group Ypresian (Early Eocene)	2569	43.6	sh90,ss10
Ekofisk Formation [Tertiary-Chalk Group]	2572	57.6	sh31,ls55,ch14
Shetland E Formation [L. Cretaceous]	2615	66.4	sh18,ls61,ml1,ssh19
Shetland D Formation [L. Cretaceous]	2909	74.5	sh29,ls37,ssh34,ml0,do0
Shetland C Formation [L. Cretaceous]	3611.5	84	sh57,ls37,ssh2,do1,ml2
Shetland B Formation [L. Cretaceous]	3844	87.5	sh16,ml84
Shetland A Formation [L.Cretaceous]	3853.5	93.5	sh37,ls32,ssh30,ml2,do0
Early Cretaceous-Rodby Formation	4095	97.5	sh59,ls19,ssh22
Early Cretaceous-Sola Formation	4342	113	sh37,ssh63
Early.Cretaceous-Valhall Formation	4392	119	sh29,ml1,ls1,ss0,ssh69
Kimmerage & Upper Main Reservoir Kimmeridgian Group (Lower Jurassic)	4633.5	144	sh86,ss0,ssh9,ml2,si3
Jurassic Early Volgian-Kimmeridgian-Oxfordian (Late Jurassic)	4667.5	156	sh17,ss83
Jurassic-Heather & Rattray Groups	4882.5	163	sh99,ss1,si0,ssh0
base	4996	169	

5.2.1.1: Burial History:

The burial history for Rhum 3/29a4 (Figure 5.3) is a relatively simple one. Steady burial in the Jurassic was followed by a period of rapid burial in the early Cretaceous. The middle and late Cretaceous saw slow but continued burial and the loss of some volume by compaction (Figure 5.3). The Tertiary saw 2000m of deposition in a short space of time that led to rapid burial of the sediment pile. Attributing exactly how much material was deposited lower down the section is notoriously difficult as compaction is a significant unknown in basin analysis (Giles et al., 1998). Compaction and therefore loss of rock volume as porosity decreases is built into Genesis 4.8. In addition to the simple burial plot (Figure 5.3) the model can be run to plot burial history as a function of either total subsidence (Figure 5.4) or more

usefully temperature. The temperature plot with burial history in Figure 5.4 demonstrates the rapid burial in the Tertiary as colder isotherms are pushed deeper (~700m and ~2200m). The temperature in this plot comes from the model calculating heating rates based on temperature data in the model from BHT/DST data or from equations in the model relating vitrinite reflectance to temperature and age. The time-temperature history shows maximum temperatures reached by each lithology. Due to the rapid burial in the Tertiary the Jurassic units now between ~120°C and ~160°C will not have been at these temperatures for more than ~10Ma, which is significant for the shape of the progress of illitization.

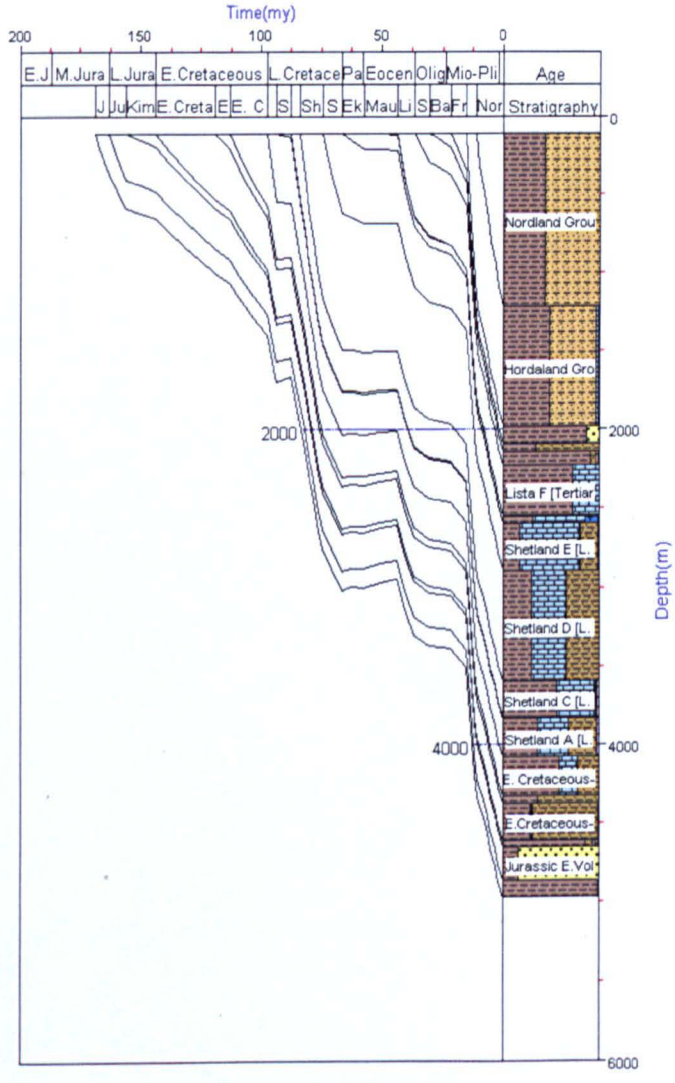

Figure 5.3. Burial history for Rhum 3/29a4.

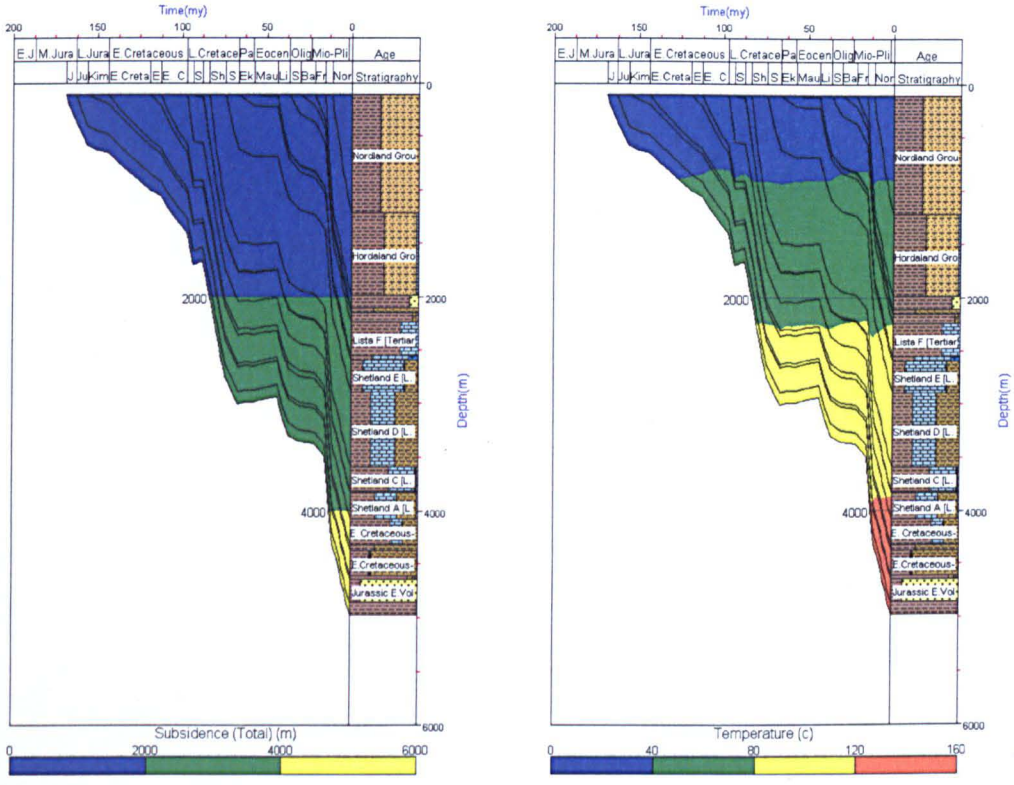

Figure 5.4. Burial history plot as a function of total subsidence for Rhum 3/29a4 (left), and the same burial history as a modelled temperature plot (right).

5.2.1.2: Vitrinite Reflectance:

The measured vitrinite reflectance, Ro, data for Rhum 3/29a4 was previously obtained by BP Exploration who have kindly offered it for this study. The trend in the measured data is plotted in Figure 5.5. The curves in the same figure are the default curves for Ro from ARCO, the LLNL model (Sweeney & Burnham, 1990) and BP Maximum and Minimum. The exact assumptions and the models used to generate the ARCO and BP Maximum and Minimum models are unknown to the user.

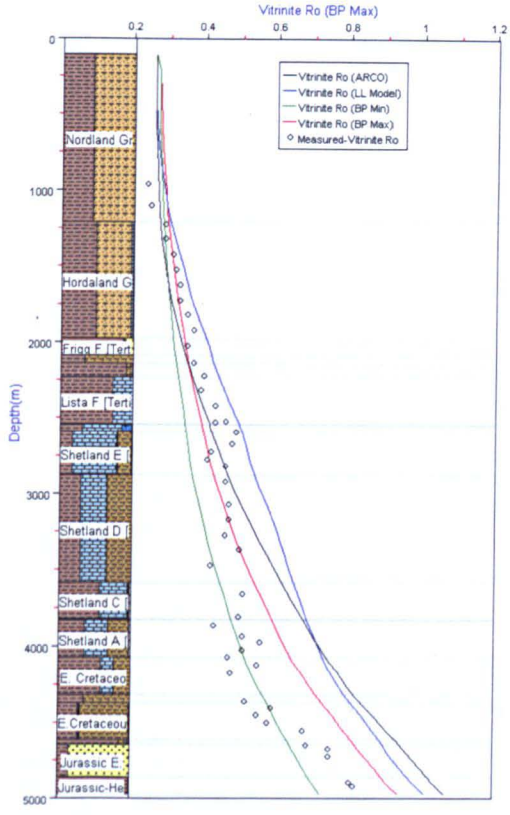

Figure 5.5. Measured Vitrinite Reflectance, Ro, data for Rhum 3/29a4 with modelled curves for Ro from ARCO, the LL model and BP maximum and minimum.

In this study the BP Maximum and Minimum vitrinite reflectance are the curves that estimate vitrinite reflectance the best for Rhum 3/29a4. The curves fit the data well at the top and base of the Ro profile. Fitting the data at the base of the section is the most important facet of vitrinite reflectance modelling as the upper sections of the curve will have little effect for changing the lithologies or thermal parameters because of the nature of the kinetics of vitrinite maturation, where time at maximum temperature is the critical factor. The fact that the curves fit the data at the top of the section simply proves that there has been no loss by erosion of significant amounts of sediment as vitrinite reflectance of surface material is taken to be ~0.25. The under-estimate of the Ro by the BP Maximum and Minimum curves in the middle of the section is probably a function of the quality of the vitrinite used in the analysis, which according to the technical report was low due to possible contamination issues in sampling. This latter scenario is based around the fact that the middle section was drilled with few casing points,

increasing the risk of the possibility of caving. There is a casing change right at the boundary between the Jurassic and Cretaceous and is marked by an increase in the quality of the vitrinite and the adherence of the data points to the BP curves. The samples from the Cretaceous therefore appear to be subject to cavings and mis-sampling.

5.2.1.3: Temperature:

The measured temperature data (Figure 5.6) in this study comes from a Bottom Hole Temperature (BHT) correction completed by Baker Hughes at the time of drilling. The inaccuracies of BHT use are highlighted in Appendix 5.1 but the necessary temperature corrections have been made at source and the results are as comprehensive as one could gain (Cawley, 2005; Pers. Comms.). The modelling has generated a good fit between the BHT and the modelled temperature.

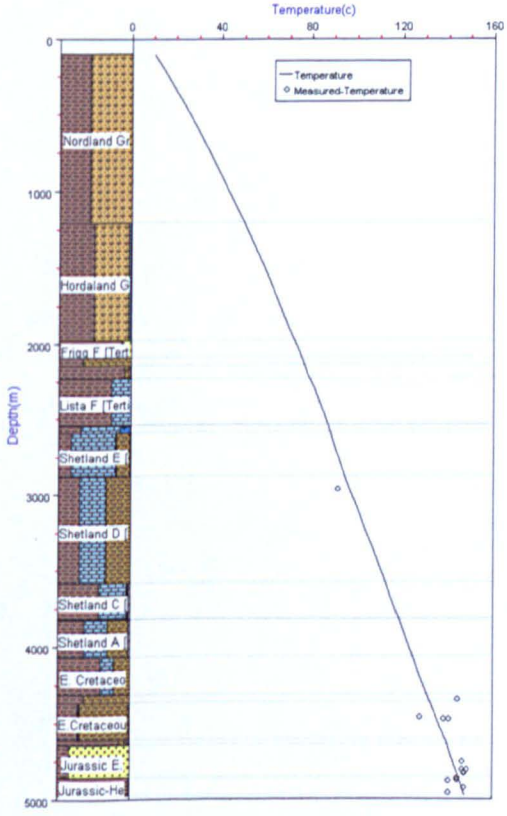

Figure 5.6. Measured and corrected Bottom-Hole-Temperature using 'time since circulation correction' modelled in Genesis 4.8 to produce the temperature curve plotted.

5.2.1.4: Pore Pressure:

The pressure data for this well comes from completion log tests done by the drilling team on the reservoir units in the Jurassic at the time the well was drilled. Figure 5.7 shows the modelled fluid pressure along with the lines for the hydrostatic and total overburden pressure. The well appears normally pressured in the Tertiary, until the Frigg Formation, and then significantly over pressured to the base of the well. Since there is very rapid Tertiary burial it is more than likely that overpressure has been caused by disequilibrium compaction. Since the well is thermally mature hydrocarbon generation in the reservoir units might be an additional cause of overpressure along with thermal expansion of fluids in the system.

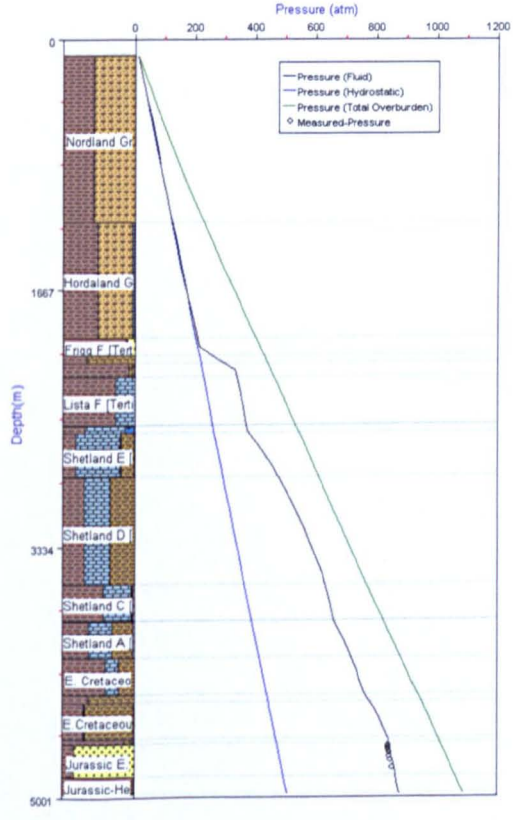

Figure 5.7. Modelled fluid pressure in Rhum 3/29a4, measured pressures in the reservoir units are from production completion log data. The overburden and hydrostatic lines are also plotted, the section below the Frigg Formation appear to be overpressured.

5.2.1.5: Porosity:

The measured porosity as recorded by Mercury Intrusion Porosimetry (see chapters 2 & 4 for the method) and the modelled bulk porosity are shown in Figure 5.8. The curve for bulk porosity shows the effect that overpressure has on the porosity trends. The measured results at the base of the Cretaceous and the modelled bulk porosity results appear to agree with one another and the fact that ~20% porosity has persisted to ~4500m suggests that the overpressure highlighted in the previous section is indeed real. If pore pressures were hydrostatic the porosities that could be expected at ~4000m would be ~10% (e.g. Dzevanshir et al., 1986), so overpressure has significantly held back compaction processes.

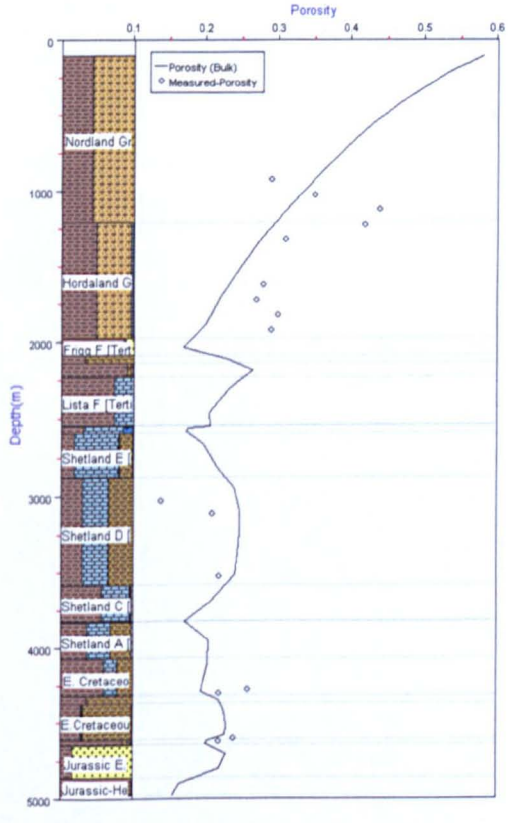

Figure 5.8. Measured porosity as recorded by Mercury Intrusion Porosimetry and the modelled bulk porosity.

The measured porosities in the Tertiary show a wide variation, probably reflecting the variability of individual samples. There is also a poor match in the measured porosities in the Shetland D formation where there is a

significantly lower porosity recorded by mercury injection porosimetry than the model would estimate. The bow-effect in the curve for estimated porosity in the same formation is due to the lithological mix in this unit. At a given effective stress carbonates have a higher porosity than shales and muds so the model has predicted elevated porosities in this unit.

5.2.1.6: Effective Stress:

The modelled effective stress increases to the base of the Tertiary and then does not significantly increase with depth. This suggests that the effects of stress are being negated due to increased pore pressures as a result of overpressure not allowing the lithologies to be compacted further. The fact that the fluid pressure increases beyond the hydrostatic and the decrease in porosity effectively start at the same depth shows that these two parameters are linked by equations in the model. Additionally, the effective stresses (Figure 5.9) calculated for Rhum 3/29a4 are the inverse of the porosity trend showing that effective stress is calculated from porosity in Genesis 4.8.

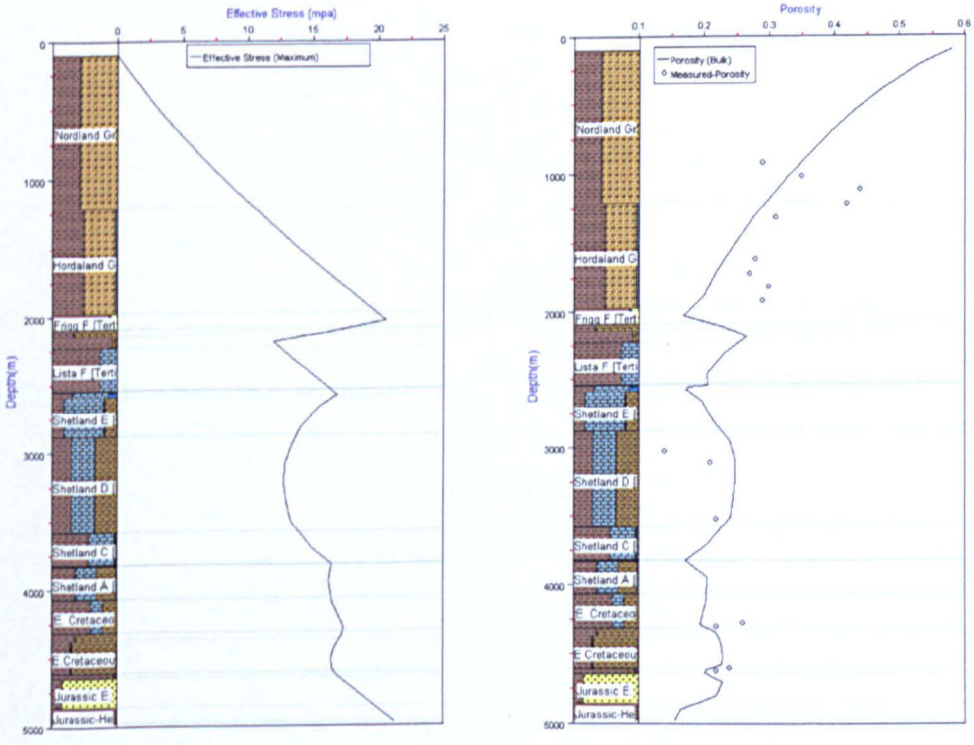

Figure 5.9. Modelled effective stress for Rhum 3/29a4 in MPa, left, and porosity, right, showing that the model has calculated effective stress from porosity as they are effectively inverses of one another.

5.2.2: Magnus 211/12-2:

As with Rhum 3/29a4 the thickness to the base of the lithosphere is taken to be fixed at 120km, with the thermal model as; transient and with a fixed temperature at the base of the lithosphere (1330°C). The significant difference between this model and that created for Rhum 3/29a4 is in thermal properties. The thickness to the base of the lithosphere has remained at 120km but the upper crust was set to 11km, the lower crust to 19km and the mantle lid to 90km. This is significantly different to the numbers entered for Rhum 3/29a4 but in the modelling process it proved the only geologically reasonable solution. The fluid flow model was set to transient and the Dutta-Franklyn permeability model was applied.

The lithological column presented in Figure 5.10 is based on the completion log for Magnus 211/12-2, as with Rhum 3/29a4 its exact lithology evolved as modelling was carried out. The exact percentages of each lithological type in each unit are presented in Table 5.3, along with the formation name taken from the completion log, the age and the tops information. The formation names have simply been assigned by period or epoch name rather than a classic formation name such as the Kimmeridge Clay Formation as this is what appears on the completion log for this well. The absolute ages are not as precise as for Rhum 3/29a4 as the information on the completion log is not as thorough.

The lithological column shows that silt becomes the most dominant lithology from the Jurassic to the Tertiary. Carbonates are present in the Cretaceous and in the Miocene, in similar age intervals to the lithological column for Rhum 3/29a4. The sandstone reservoir units in the Jurassic are picked out with a generally rather more complex unit lithology than higher up the section.

It should be noted that there are no unconformities in the model; however, it is clear from Figure 5.10 that there is little deposition between the Kimmeridgian and the Turonian. The completion log does not suggest

significant uplift and erosion giving an unconformity but the depositional style in the Jurassic as discussed in Chapter 4, was punctuated by frequent marine transgressions and forced regressions. It is, therefore, more than likely that hiatuses in deposition will have occurred, however, as already stated this is not as serious a consequence for modelling as the loss of strata at an unconformity.

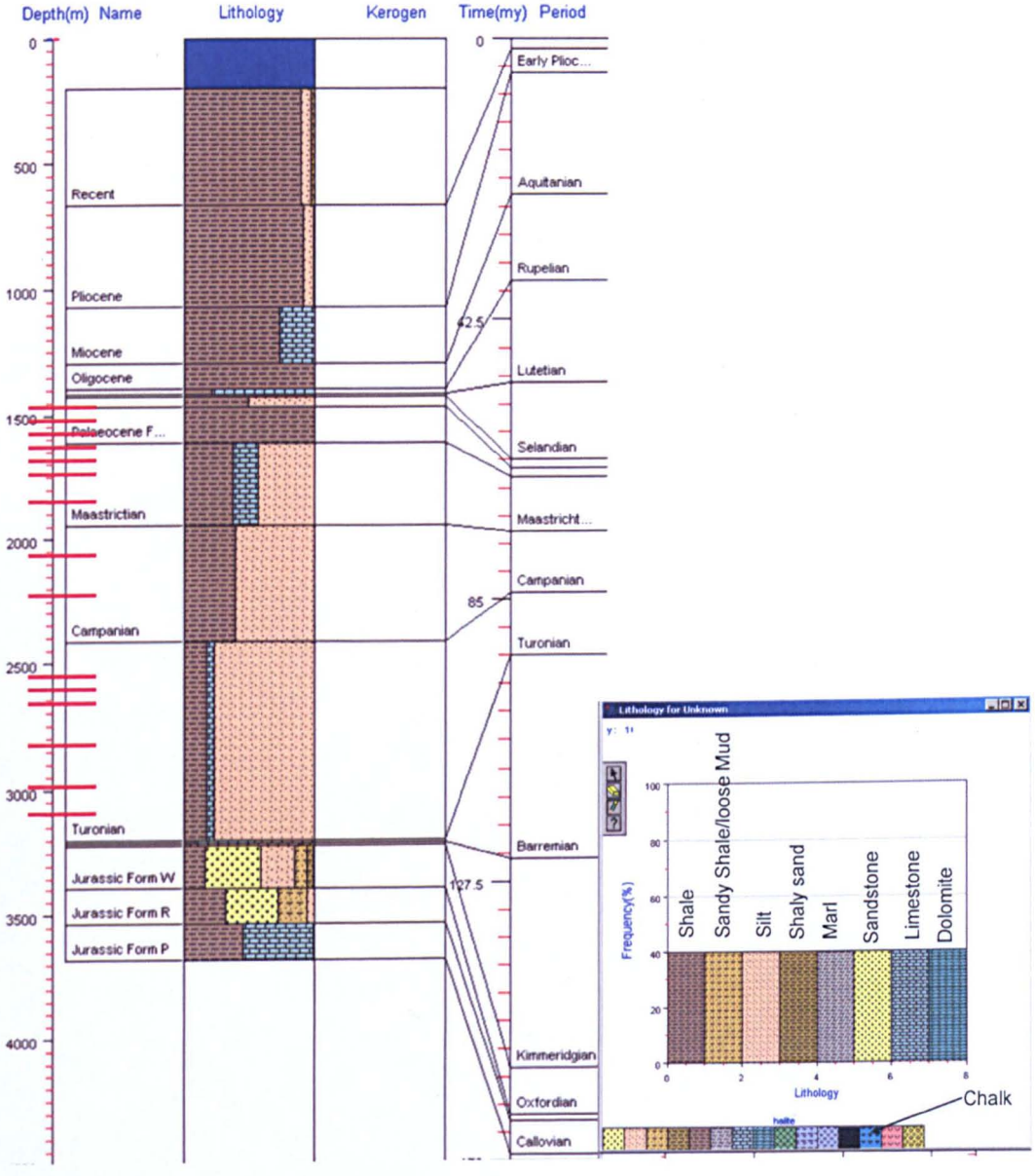

Figure 5.10. Lithological column created in Genesis 4.8 for Magnus 211/12-2, see Table 5.3 for lithology mix.

Table 5.3. The formation name, top of formation height, age and lithology percentage for Magnus 211/12-2 where; sh=shale, shs=loose mud, ls=limestone, ml=marl, ss=sandstone, ch=chalk, ssh=tight mud, do=dolomite, si=silt, as derived through modelling in Genesis 4.8

Formation Name	Top/thickness [m]	Ages [Ma]	Lithology and percentage of lithology type in each unit
Recent	200	0	sh90,si8,ssh2
Pliocene	666	1.6	sh92,si8
Miocene	1070	5.3	sh74,ls26
Oligocene	1297	23.7	sh100
Eocene	1397.5	36.6	sh21,ls79
Palaeocene Form VI	1414	52	sh100
Palaeocene Form IV	1429	63.6	sh49,si51
Palaeocene Form VI	1466	65	sh100
Maastrictian	1615	66.4	sh38,ls18,si43,ss0
Campanian	1943	74.5	sh40,si60
Turonian	2416.5	84	sh18,ls6,si77,ss0
Barremian-Aptian	3200	93.5	sh9,ls45,si46
Jurassic Form S	3208	124	sh5,si84,shs8,ssh3
Jurassic Form W	3222	156	sh16,ss43,si25,shs10,ssh6
Jurassic Form R	3391	163	sh32,ss41,shs23,si5
Jurassic Form P	3535	164	sh45,ls55
base	3683.5	169	

5.2.2.1: Burial History:

The burial history (Figure 5.11) is very similar to that for Rhum 3/29a4 (Figure 5.3). The profile is very simple with initial rapid burial in the Jurassic followed by a steadier and slower burial up to the Cretaceous where another period of rapid burial was followed by a much slower period. The Tertiary has a final period of rapid burial of around 1300m in less than 24Ma.

The relative simplicity of the burial history may reflect the fact that the completion log lacked some age information therefore the rapid burials at the start of a period or epoch may be slightly misleading and attributable to the lack of good age markers in the section. The maximum temperatures (Figure 5.12) in the Jurassic are between 100°C and 120°C based on heating rates but due to the rapid burial in the late Tertiary the time at maximum temperature will not be more than ~5Ma. The nature of the isotherms is indicative of the slow burial in the Cretaceous.

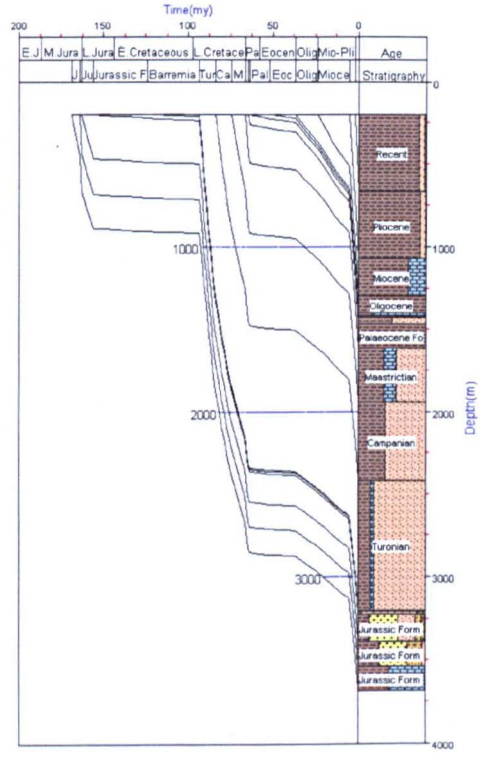

Figure 5.11. Burial history for Magnus 211/12-2.

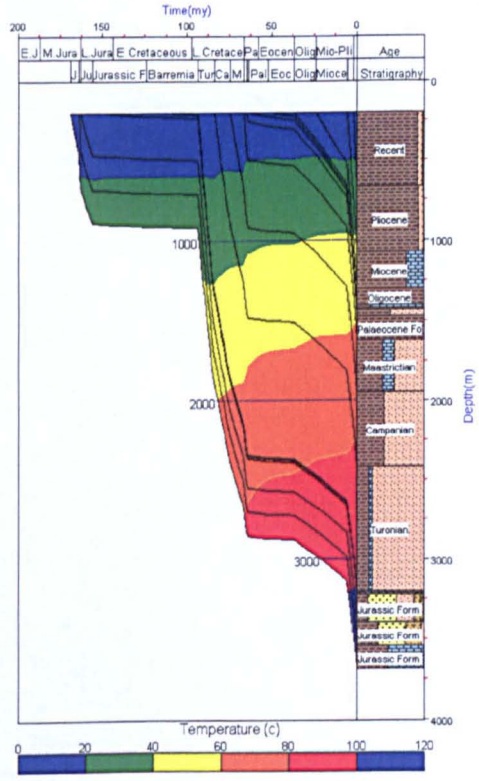

Figure 5.12. Time-temperature history for Magnus 211/12-2 as a function of depth[m].

5.2.2.2: Vitrinite reflectance:

No primary vitrinite reflectance data (Ro) was available for Magnus 211/12-2. Figure 5.13 is included to show the nature of the estimated vitrinite reflectance increase with burial depth. The BP average modelled vitrinite reflectance for each sample with a percent expandability is used later in this chapter.

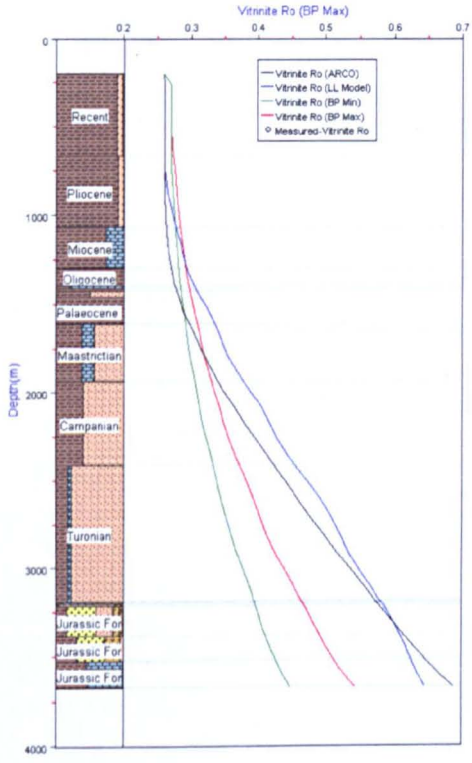

Figure 5.13. Estimated vitrinite reflectance curves modelled in Genesis 4.8 Magnus 211/12-2.

5.2.2.3: Temperature:

Corrected BHT data for Magnus 211/12 are taken from Okiongbo (2005). The modelled temperature has been fitted with these BHT data (Figure 5.14).

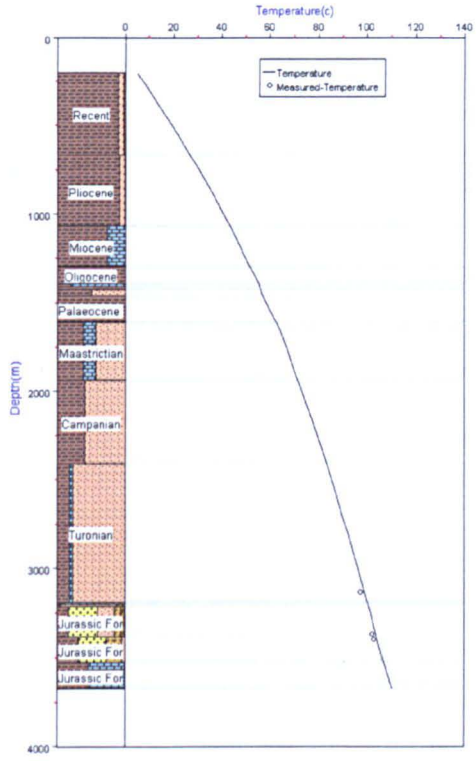

Figure 5.14. Measured BHT temperature data Magnus 211/12 and the modelled curve for Magnus 211/12-2.

5.2.2.4: Porosity:

The measured results in Figure 5.15 come from the mercury intrusion porosimetry measurements presented in chapter 4. The model has estimated a bulk porosity that is up to 5% less than the measured results. This is not surprising as there is no pressure data for Magnus 211/12-2 to in any way constrain the data as to whether there is any overpressure at play in the basin, which appears likely given that similar porosities were recorded by Worden et al. (2005) for adjacent wells in the same block. As was demonstrated with Rhum 3/29a4 there was significant overpressure in the Cretaceous and Jurassic formations and this may well be the case in Magnus 211/12-2 in the Cretaceous samples, however, as there is simply no pressure data this is merely speculation. The only way to achieve a better fit between the porosity data as measured by mercury intrusion porosimetry is to significantly change the silt and shale permeability, which is unrealistic.

The changes possible in terms of the thermal controls makes no significant difference to the estimated porosity trend, with only minute shifts in the curve for large changes in thermal properties.

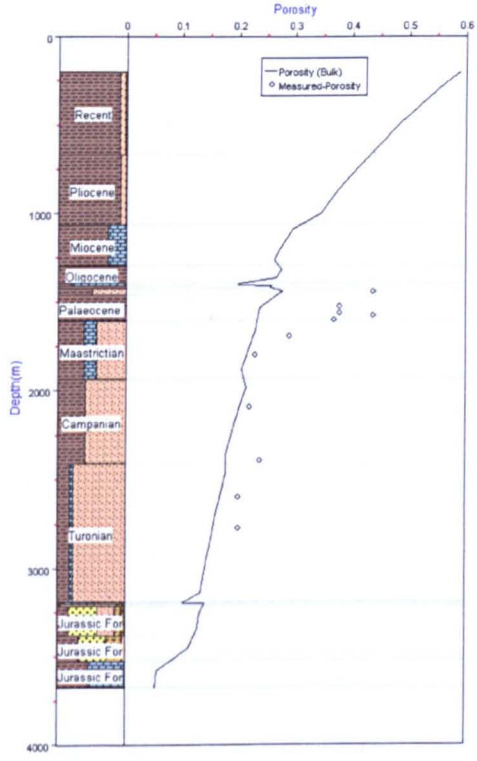

Figure 5.15. Modelled and measured porosity data (by mercury intrusion porosimetry) for Magnus 211/12-2.

5.2.3: Podhale Basin:

Given the obvious uplift in the Podhale Basin (Chapter 2) an assessment of maximum burial depth is required if I/S change and fabric intensity increase are to be correctly assessed. For the two wells from the Podhale Basin the aim is to model vitrinite reflectance so that maturity can be correlated with other measured parameters such as fabric orientation change and the %I in I/S.

The geological history of the Podhale Basin has been discussed by Środoń et al., (in press, summarised in Chapter 2) and in reconstructing a burial history and building a thermal model it presents the difficulty of having to join Chochołów PIG-1 and Bukowina Tatrzańska PIG-1 together into a virtual profile and factor in the significant unconformity present at the top of Chochołów PIG-1. Additionally, no completion log is available in this study so the lithological mixes are therefore quite simple and based on information furnished from the literature (Westwalewicz-Mogilska, 1986; Wieczorek, 1989; Wieczorek & Olszewska, 1999; Środoń et al., (in press)).

As with Rhum 3/29a4 and Magnus 211/12-2 the thickness to the base of the lithosphere is taken to be 120km, with the thermal model as transient, with a fixed temperature at the base of the lithosphere (1330°C). The fluid flow model is set to transient and the Dutta-Franklyn permeability model was applied. The distribution of the thickness between the upper crust, lower crust and mantle lid was set to upper crust (17km), lower crust (13km) and mantle lid (90km) for Chochołów PIG-1 and to upper crust (12km), lower crust (11km) and mantle lid (97km) for Bukowina Tatrzańska PIG-1. This reflects the increased sediment pile in Chochołów PIG-1 relative to Bukowina Tatrzańska PIG-1.

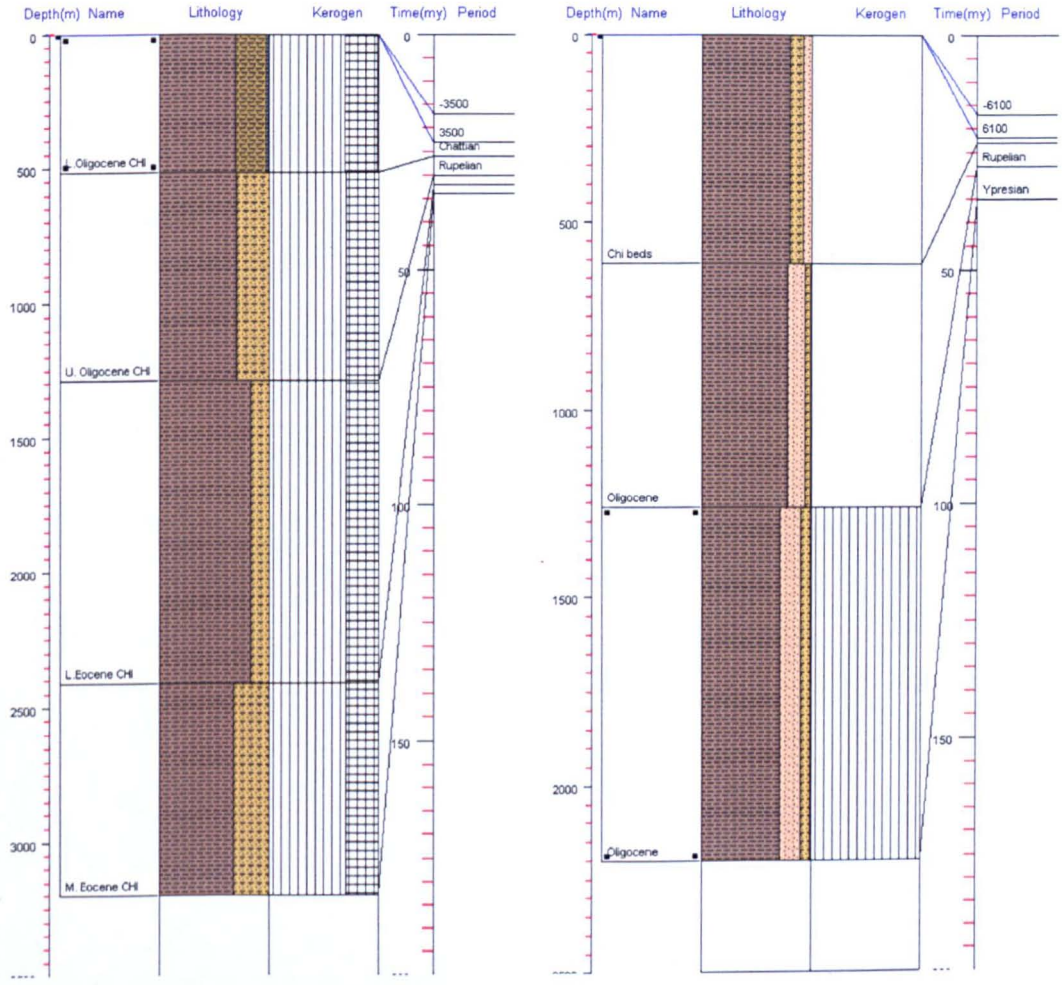

Figure 5.16. Lithological columns for Chochołów PIG-1, left, and Bukowina Tatrzańska PIG-1, right. The columns show the uplift discussed in chapter 2 and the very simplified lithology is after Środoń et al., (in press). The dark brown colour in the lithology mix is shale, the light brown is sandy shale and the pink is silt.

The lithological columns presented in Figure 5.16, for Chochołów PIG-1 and Bukowina Tatrzańska PIG-1, are very rough lithologies for the two wells in question as completion logs were not available in this study. The units are dominated by shale with the addition of silts and tight muds. It remains unclear when sedimentation ended (Garecka, 2005) and the division of the units within the basin have been divided informally (Środoń et al., in press).

The amount of erosion is based on the estimate presented in chapter 2 where the Ro data was used to estimate the amount of uplift in the Chochołów PIG-1 and Bukowina Tatrzańska PIG-1 wells. The best estimates were ~3500m in Chochołów PIG-1 and ~6100m in Bukowina Tatrzańska PIG-1 and these values have been used to define the maximum

burial depth of each well. The timing of the onset of uplift has been set at 17Ma (Środoń et al., in press).

5.2.3.1: Burial History:

Due to the simplicity of the lithological columns in Figure 5.16 the burial histories (Figure 5.17), are correspondingly simple. They show very rapid burial of the units after the deposition of the Oligocene aged units and simply plunge to their maximum burial depths. The uplift of these wells was equally swift. The exact timing of uplift is at 17Ma (Środoń et al., in press). The model predicts maximum burial temperatures at 120-160°C for Chochołów PIG-1 and 150-200°C for Bukowina Tatrzańska PIG-1, which are in line with those published by Środoń et al. (in press), based on their calculated palaeogeothermal gradient of 20-25°C/km, which is comparable to present day geothermal gradient (~21°C/km, after Cebulak et al., 2004).

The fast sedimentation rates in Bukowina Tatrzańska PIG-1 (~460m/Ma: 8300m of burial in 18Ma) and ~380m/Ma in Chochołów PIG-1 (6500m of burial in 17Ma) have caused temporarily lower heat flow in the sediment pile. Therefore, temperature as experienced by the sediment pile is not in equilibrium with sedimentation rate, hence the drawing down of cooler temperatures as the sediments are rapidly buried. As equally rapid uplift occurs, almost instantaneously warmer isotherms are pushed higher creating the asymmetric 'V' shape in the time-temperature history at the base of the two wells.

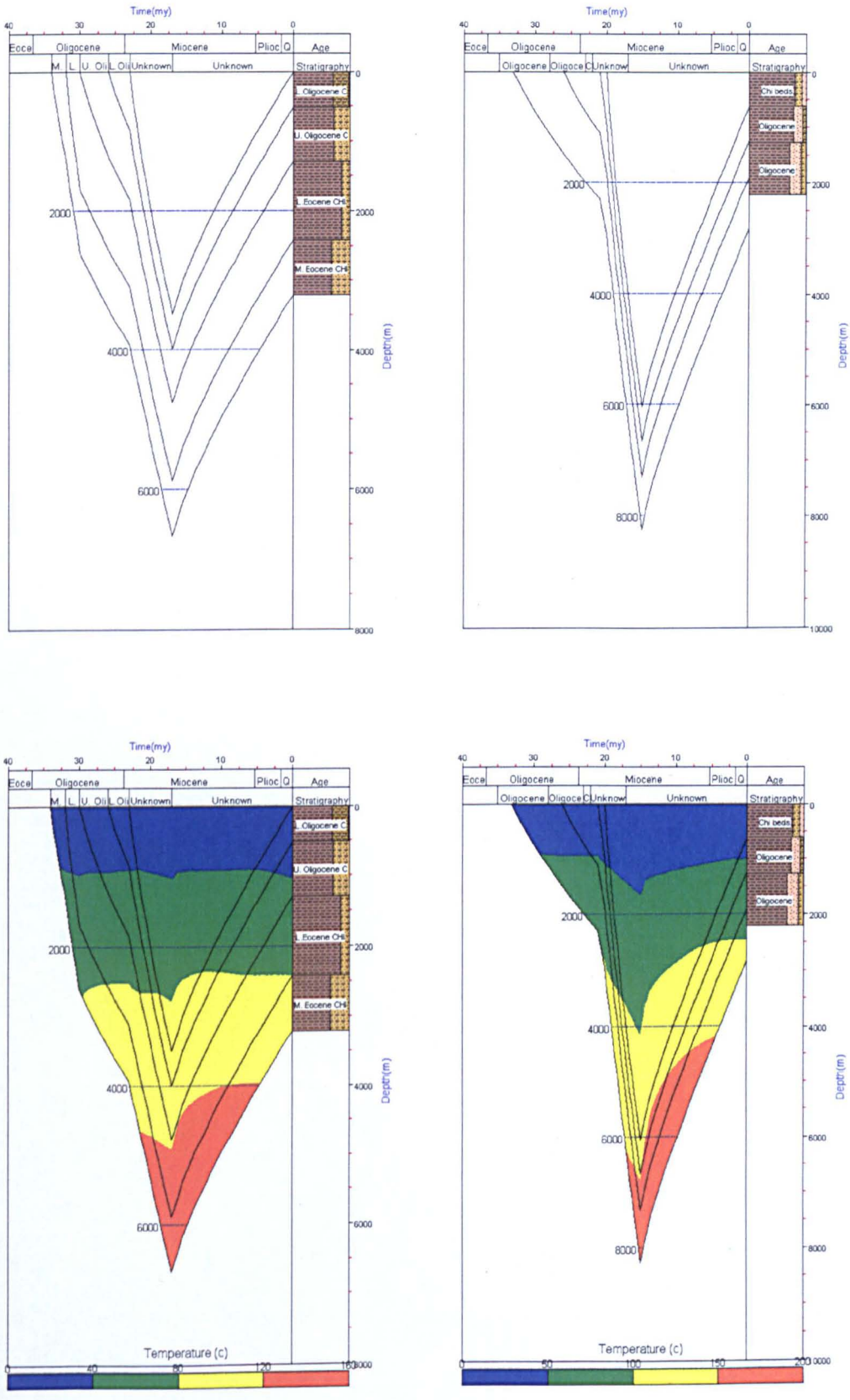

Figure 5.17. Burial histories for Chochołów PIG-1, left, and Bukowina Tatrzańska PIG-1, right. Lower plots show time-temperature histories.

5.2.3.2: Vitrinite Reflectance from MPI Index:

The vitrinite reflectance data presented here in Figure 5.18 is the theoretical vitrinite reflectance data presented in chapter 2 (after Respondek and Marynowski, 1999; Marynowski, 2005, pers. Comms.) calculated from the Methylphenanthrene Index (MPI, after Radke & Welte, 1981). The modelled Ro in Chochołów PIG-1 did not produce a really well defined match with the estimated curves produced in Genesis 4.8 for Chochołów PIG-1 as there is a lack of fitting at the top of the section compared to the base. In Bukowina Tatrzańska PIG-1 the fit between the measured data and the estimated curves is much more reasonable.

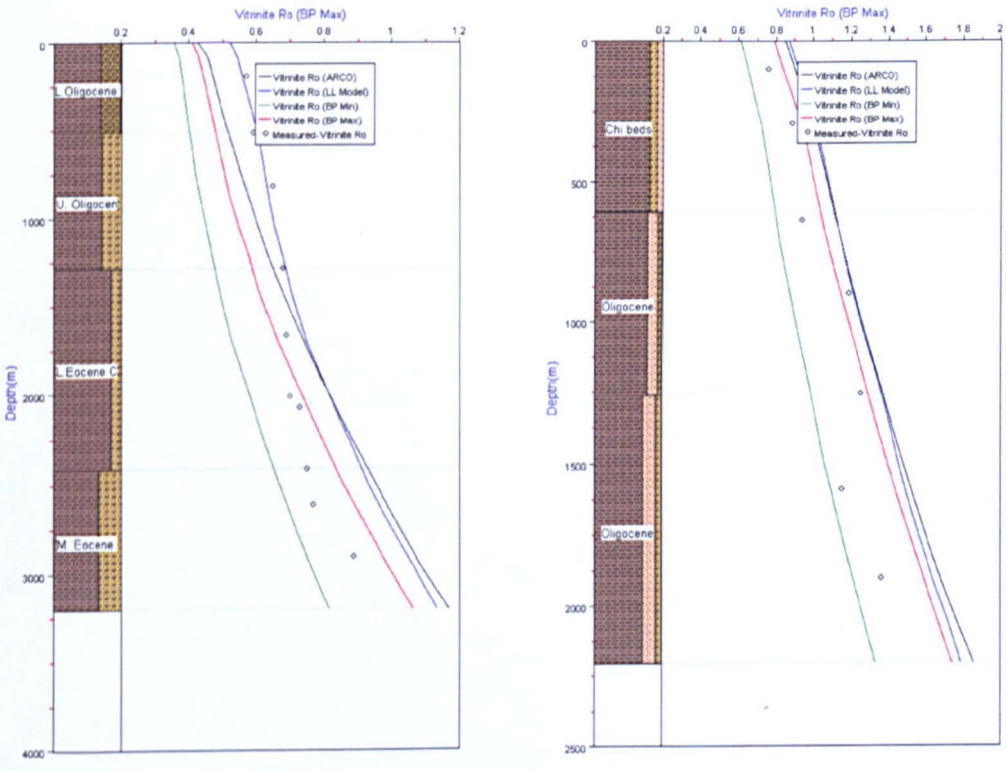

Figure 5.18. Measured vitrinite reflectance data using the MPI index from Chapter 2 and the modelled results in Genesis 4.8 for Chochołów PIG-1, left, and Bukowina Tatrzańska PIG-1, right.

In terms of which curve to use as a best estimate for modelled Ro, a case for any of the four could be made but for the sake of consistency the BP average Ro was used.

5.2.3.3: Porosity:

Chochołów PIG-1 and Bukowina Tatrzańska PIG-1 have porosities that were measured by mercury intrusion porosimetry (Chapter 2). These measured results are 1-2% higher than the modelled porosities (Figure 5.19). Measured porosities are those of deeply buried samples as the modelled and measured results are in close agreement. This suggests that the amounts of erosion from the two wells have been estimated correctly as the results are in the correct depth regime as predicted by the model.

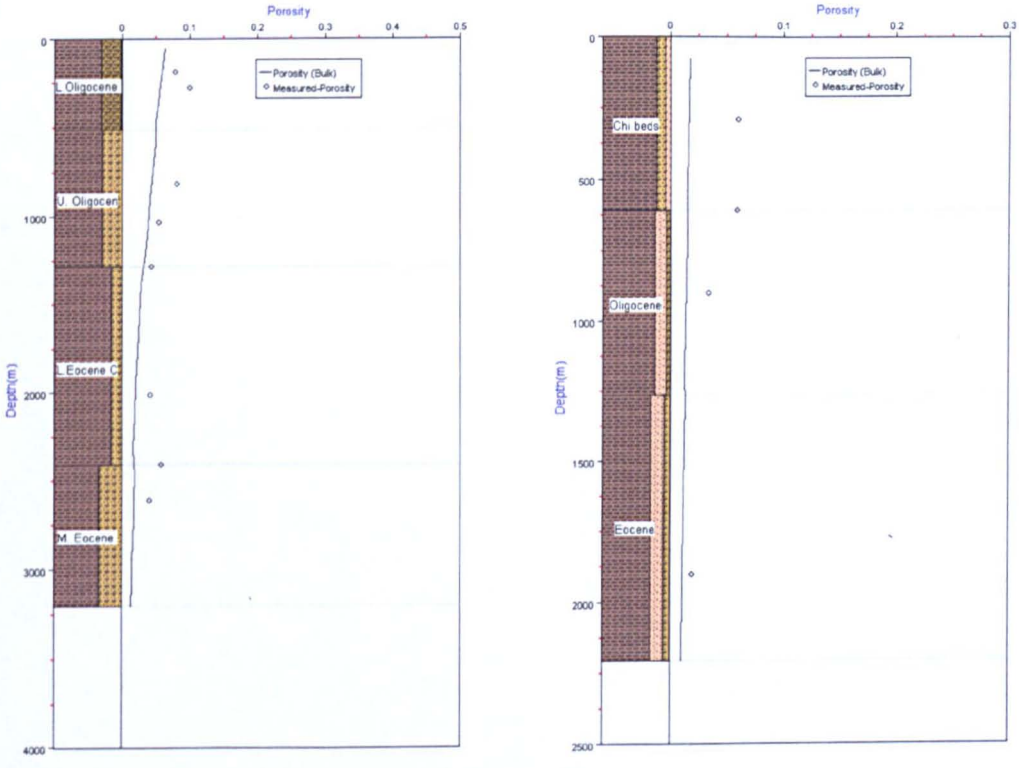

Figure 5.19. Modelled porosities for Chochołów PIG-1, left, and Bukowina Tatrzańska PIG-1, right, reflecting the difference in total burial depths encountered in these wells, the measured results are the porosity by mercury intrusion porosimetry.

5.2.4: Thermal Maturity from Vitrinite Reflectance:

The modelling has allowed an appreciation of the confidence that may be placed in the maturity data in this study. The measured vitrinite reflectance data for Rhum 3/29a4 produced a near perfect match with the estimated curves for BP maximum and minimum vitrinite reflectance. Further confidence in the thermal aspects of this model may be gained from the fact that temperature data from corrected BHT were matched by the estimated temperature curve and that overpressure was predicated where high porosities were measured in the Cretaceous.

Magnus 211/12-2 is more difficult to appreciate fully as the amount of well control data is not as complete as for Rhum 3/29a4. Nevertheless, Genesis 4.8 was able to generate a near perfect match between the measured BHT and the modelled estimates. The BHT data used in this study is open to the same sources of error as the vitrinite reflectance data. The modelled temperature curve intersects well with the measured data in the Cretaceous. Given the inaccuracies associated with BHT data (Hermanrud, 1990) vitrinite reflectance is the stronger maturity parameter but the fact that vitrinite reflectance and temperature were able to be resolved allowing them to be used as applicable outputs.

The Podhale Basin represents a different problem to the wells from the Northern North Sea as they have been significantly uplifted. The quality of the modelled vitrinite data (Rospondek & Marynowski, 2004; Marynowski, 2005 pers. comms) from the MPI index (after Radke & Welte, 1981) is high. The modelled results and the measured results for Chochołów PIG-1 have a slight mismatch at the top of the well but at the base they match and are consistent with a BP average vitrinite reflectance. In contrast the fit in Bukowina Tatrzańska PIG-1 is good between the measured and the modelled vitrinite reflectance, except for the middle of the section but this simply represents sample variation.

Figure 5.20 summarises the vitrinite reflectance characteristics of the four wells in question Magnus 211/12-2, Rhum 3/29a4, Bukowina Tatrzańska PIG-1 and Chochołów PIG-1, what is immediately apparent is that the two basins (Podhale and the Northern North Sea) have different thermal histories, but the wells within the basin have the same thermal characteristics. Bukowina Tatrzańska PIG-1 and Chochołów PIG-1 have significantly lower thermal gradients than Magnus 211/12-2 and Rhum 3/29a4 and probably reflects the difference in heat flow in oceanic and continental crustal settings. This lower thermal gradient will possibly have an effect on the rate of the conversion of smectite to illite as it is known that temperature is one of the driving forces behind illitization (e.g. Hillier et al., 1995; Huang et al., 1993; Velde & Vasseur, 1992; Pytte & Reynolds, 1989). This will therefore have an effect on fabric development, if illitization is accepted as being a significant fabric developer (e.g. Ho et al., 1999). These aspects will be covered in much greater depth in Chapter 6. Modelling the Podhale Basin has shown that the maximum burial depths postulated in Chapter 2 are valid based on porosity and vitrinite reflectance data.

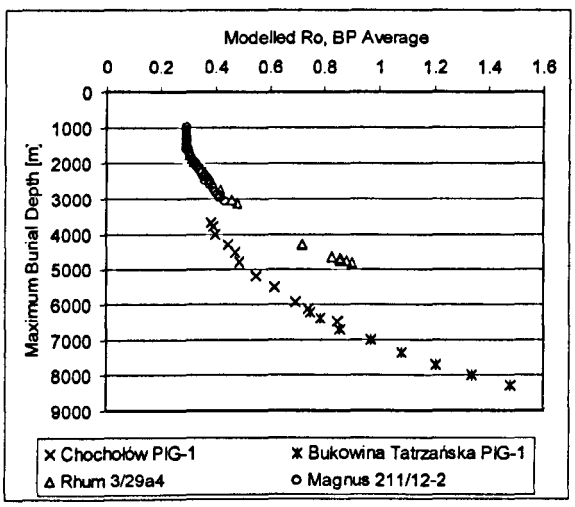

Figure 5.20. Estimated vitrinite reflectance against maximum modelled burial depth for Magnus 211/12-2, Rhum 3/29a4, Bukowina Tatrzańska PIG-1 and Chochołów PIG-1.

5.3: Discussion:

5.3.1: Compaction:

The estimated bulk porosities (Figure 5.21) demonstrates that the maximum burial depths estimated by modelling in this chapter and built upon those postulated by Środoń et al (in press) are broadly in the correct depth space (e.g. Athy, 1930; Hedberg, 1936; Sclater & Christie, 1980; Dzevanshir et al., 1986). There is a clear trend with increasing depth between Magnus 211/12-2, Chochołów and Bukowina Tatrzańska, that follows many of the published trends for shale porosity with depth (e.g. Athy, 1930; Hedberg, 1936, Dzevanshir et al., 1986). The modelling estimates that Magnus 211/12-2, Chochołów and Bukowina Tatrzańska are normally pressured and therefore follow normal compaction trends with depth. The high porosities in Rhum 3/29a4 have been demonstrated to be caused by significant overpressuring which should effect fabric alignment if mechanical processes alone drive re-orientation (e.g. Oertel & Curtis, 1972; Curtis et al., 1980; Sintubin, 1994; Jacob et al., 2000). When these estimated porosities are plotted with the measured porosities gained through mercury intrusion porosimetry there is a slight mismatch at depth in Chochołów and Bukowina Tatrzańska but this is only by a few percent and could represent an inaccurate maximum burial depth, simple sample heterogeneity or problems associated with injecting mercury into rocks with ~5% porosity. The fit of the measured data for Magnus 211/12-2 and Rhum 3/29a4 with the estimated porosities gained through modelling are much more in agreement. Where the modelling predicted open pores in Rhum 3/29a4 in response to overpressure the measured results record this more open porosity with values of ~20% porosity persisting to 4000m.

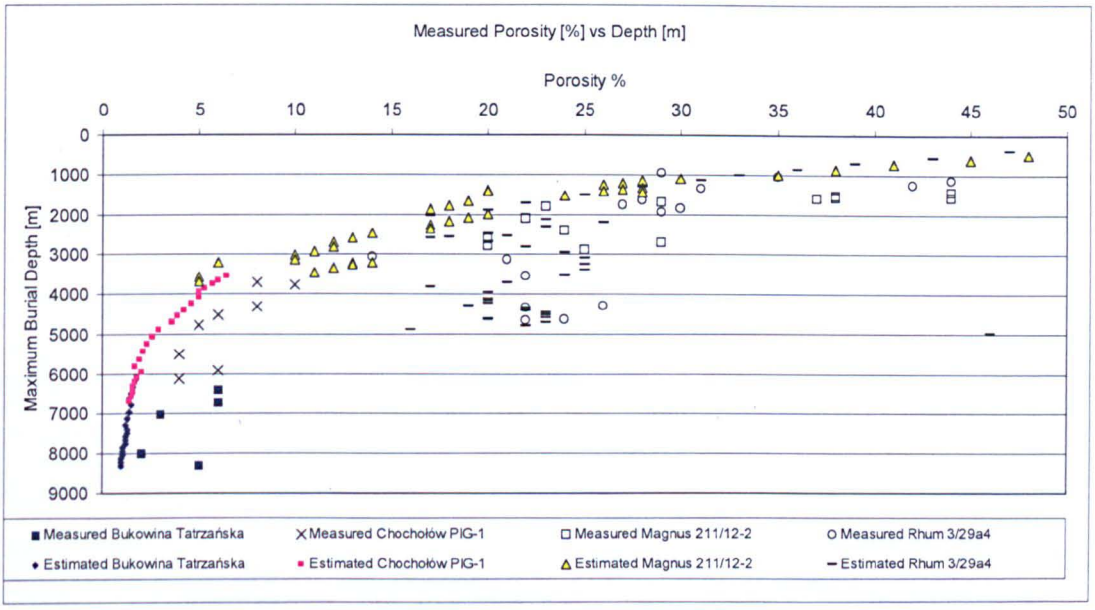

Figure 5.21. Estimated bulk porosity and measured porosity (by mercury intrusion porosimetry) against maximum modelled burial depth for Magnus 211/12-2, Rhum 3/29a4, Bukowina Tatrzańska and Chochołów.

5.3.2: Burial Histories and Erosion Estimates:

The burial histories presented previously for, Rhum 3/29a4 (Figure 5.3), Magnus 211/12-2 (Figure 5.11), Chochołów PIG-1 (Figure 5.17) and Bukowina Tatrzańska PIG-1 (Figure 5.17) show that the wells from the Northern North Sea have not experienced any significant uplift and erosion, whereas present day burial depths for the wells from the Podhale Basin do not represent maximum burial depths. Maximum burial depths have been estimated in Genesis 4.8 based on porosity and vitrinite reflectance data. Chapter 2 has demonstrated how the two wells from the Podhale Basin may be joined to create a virtual profile.

The timing of uplift in the Podhale Basin is based on the diagenetic ages,~17Ma (Środoń et al., in press), which accordingly maybe be interpreted as close to the ages of maximum palaeotemperatures (Clauer et al., 1997). Following the K-Ar age method of Clauer et al (1997), Środoń et al (in press) inferred maximum palaeotemperature ages to be 15.8Ma. This therefore describes a basin that underwent rapid burial and almost instantaneous uplift upon reaching maximum burial, with Chochołów PIG-1

experiencing uplift and erosion at ~230m/Ma and Bukowina Tatrzańska PIG-1 ~400m/Ma. Due to the age of the basin and the depth of burial the sedimentation rates were nearly comparable to these uplift results (Bukowina Tatrzańska PIG-1~ 460m/Ma and Chochołów PIG-1 ~380m/Ma) meaning a quite symmetrical burial history and basin profile.

5.3.3: Temperature Estimation and Palaeothermometry:

Estimating maximum temperature is necessary as studies by Ho et al. (1999) and Matenaar (2002) on the preferred alignment of phyllosilicates do not offer maturity data such as vitrinite reflectance.

The issue of maximum burial temperatures in the North North Sea is relatively easy to resolve. The corrected BHT data give a fairly reliable estimate of temperature at a given depth, given the caveats concerning BHT temperature corrections (Hermanrud et al., 1990; Hagen & Surdan, 1989). Additionally, there has been no uplift or erosion in the Rhum 3/29a4 and Magnus 211/12-2 sections (Figures, 5.3 & 5.11) analysed here. So, the BHT temperatures represent maximum burial temperatures and the model in Genesis 4.8 has resolved them against the other input parameters in the model.

The question of maximum temperature in Chochołów and Bukowina Tatrzańska is not so clear primarily due to the degree of uplift and erosion experienced by these wells and the Podhale Basin in general. The time-temperature histories produced by Genesis 4.8 was able to resolve the model for the maximum burial temperature histories in Chochołów and Bukowina Tatrzańska (Figure 5.17) with the present day geothermal gradient of 19°C to 23°C/km (Cebulak et al., 2004), and with the deduced maximum temperatures of 20°C to 25°C/km (Środoń et al., in press) based on I/S palaeothermometry. The use the illitization of smectite as a palaeothermometer is a study in itself, there are many proponents of the method (Hoffman & Hower, 1979; Pollastro, 1993; Środoń; 1995).

Constraining temperature to anywhere near the accuracy of even BHT has proved difficult (Weaver 1989), as there is a spread in the temperature position of the change from R0 to R1 ordering, 55% to 65% illite in I/S (Moore and Reynolds, 1997) that is the key marker for assigning temperature along with the reaction termination point.

In assigning a temperature to these changes in ordering and termination individual basins vary in the nature of the transition of smectite to illite, so much of the temperature estimates are based on the classic work of Hower et al (1976) in the Gulf of Mexico. The temperature character of other basins may be remarkably different; the Niger Delta (Velde et al., 1986) has a much lower temperature termination point and the Illinois Basin even lower, with a termination at 90% of illite layers in I/S but an inferred temperature of only 80°C (Moore, 1982).

The use of I/S as a palaeothermometer will only be applicable where the input is constant. This point is satisfied based on the mineralogical trends for the Podhale Basin presented in chapter 2, however, smectite to illite transition only occurs over a set temperature range. The Bukowina Tatrzańska PIG-1 well alone is of little use in I/S palaeothermometry as the %I in I/S does not change.

Applying a 21°C geothermal gradient to the Podhale basin continuous I/S profile using Chochołów PIG-1 and Bukowina Tatrzańska PIG-1 wells, gives a temperature change between R0 and R1 ordering in I/S, 55-65%illite at 5000m at 105°C and a vitrinite reflectance of 0.6Ro. This then follows that the maximum temperature at the termination of the illitization of smectite is 136.5°C, with the base of Bukowina Tatrzańska PIG-1 at 173.3°C. These latter results are at the top end of those published for the change in ordering (Weaver 1989), so must be considered with caution. In Figure 5.25 three zones of smectite illitization are noted. Zone Two where most of the I/S change occurs concurs with Zone Two noted by Eberl (1993). According to this study 60%S corresponded to 60°C and 20%S at 110°C. In the Northern North Sea 60%S is at ~2000m corresponding to 60°C (based on a

geothermal gradient of 30°C/km in Rhum 3/29a4), 20%S is not reached in the Northern North Sea due to a lack of K^+ availability to drive illite formation. In the Podhale Basin 60%S is at ~3700m (Figure 5.24) at a temperature of 78°C, 20%S has formed at 6500m, 136.5°C.

The above demonstrates partially the significant problems associated with the use of I/S as a temperature indicator and this is undoubtedly due to the complex kinetics of the conversion (e.g. Vasseur & Velde, 1992; Huang et al., 1993; Hillier et al., 1995; Elliott & Matisoff, 1996; Elliott et al., 1999) and the individual nature of basin sediment input, where the reaction activation energy will determine the shape and the depth of the reaction progress curve (Figure 5.22). Reaction progress is greater in older series which have a convex upward curve e.g. the Northern North Sea should there be enough K^+ to allow the reaction to run further. The Podhale Basin (if the high smectite portion of the curve were present) would be described as concave downwards. This suggests that the two basins have divergent kinetic drivers, with the Podhale Basin having a high activation energy requirement and would be temperature dependent, whereas the Northern North Sea has a low activation energy and is time dependent.

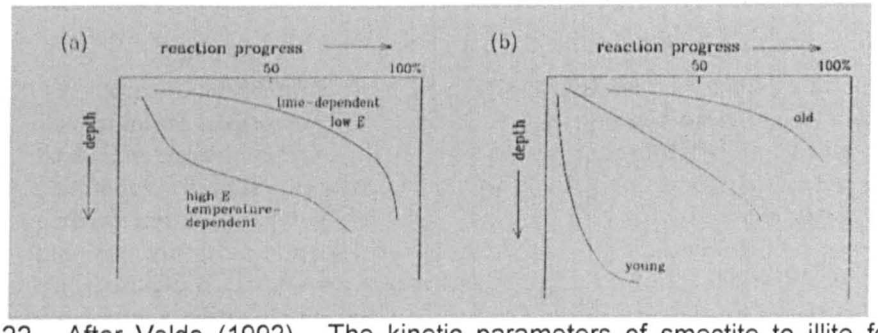

Figure 5.22. After Velde (1992). The kinetic parameters of smectite to illite formation. Reaction activation energy will determine the shape of the curve (a) and (b) the effect of relative age on reaction progression.

Therefore, in the absence of reliable temperature data, vitrinite reflectance or theoretical vitrinite reflectance (calculated from the methylphenantrene index) data is a better way of estimating maturity as the kinetics of vitrinite maturation are less complicated and better restrained (Sweeney & Burnham, 1990). Although inferring burial depth from vitrinite reflectance is not

possible as vitrinite maturity is a function of heating rate rather than depth alone.

5.3.4: Heating Rates:

Different types of sedimentary basins have different mechanisms of formation and therefore crustal settings which will effect the heating rates experienced by the basin fills and consequently the shape and depth of the smectite-illite reaction curve. Geothermal gradients range from 20-50°C/km with burial rates of between 20-400m/Ma, the product of the two is heating rate and that will normally lie between 1-10°C/Ma for most sedimentary basin settings (Gretner & Curtis, 1982).

Deposition and hence heating in Bukowina Tatrzańska PIG-1 began at ~35Ma, heating reached its maximum at 15.8Ma (Środoń et al., in press) equating to 19.2 Ma of heating. Maximum burial of Bukowina Tatrzańska PIG-1 is 8300m and applying the 21°C/km geothermal gradient of Cebulak et al., (2004) the well reached a maximum temperature of 173.3°C, a heating rate of 9.03°C/Ma. In Chochołów PIG-1 deposition began at 34Ma and reached maximum burial temperatures at 15.8Ma. Using the same geothermal gradient this equates to a maximum burial temperature of 136.5°C (6500m), a heating rate of 7.50°C/Ma. The Northern North Sea has experienced a much higher geothermal gradient but the basin has been forming since the Jurassic. Consequently, Rhum 3/29a4 has experienced 169Ma of heating and has reached a maximum temperature of 149°C, a heating rate of 0.90°C/Ma. At 3401m in Magnus 211/12 (164Ma of deposition) a temperature of 103°C occurs (based on a geothermal gradient of 30.3°C), consequently Magnus 211/12-2 has experienced a heating rate of 0.62°C/Ma.

These heating rates may be compared to those proposed by Hillier et al., (1995) for various basinal settings (Figure 5.23). The Podhale Basin heating rate is ~8°C/Ma with an Ro value of ~1 at 25% expandability this places the Podhale Basin in a continental rift setting. The Northern North Sea by

comparison has a much lower heating rate ~0.8°C/Ma and a vitrinite reflectance of ~0.3 at 70% expandability places this well in an old passive margin setting.

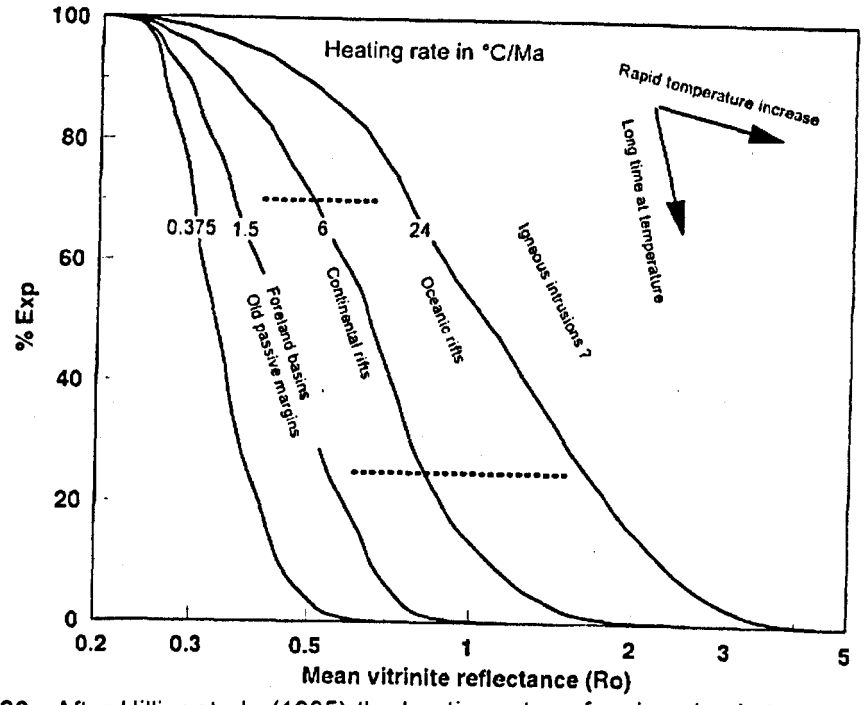

Figure 5.23. After Hillier et al., (1995) the heating rates of various basin types compared to %expandability and mean vitrinite reflectance.

5.3.5: Illitization of Smectite and Vitrinite Reflectance Relationships:

The thermal histories between wells from the Northern North Sea and the Podhale Basin are associated with different geothermal gradients ~30°C/km and ~21°C/km respectively. The trend in the percentage of illite in I/S (Figure 5.24) between the diagenetically immature samples in Magnus 211/12-2 and Rhum 3/29a4 and the more mature samples in Chochołów PIG-1 and Bukowina Tatrzańska PIG-1 is smooth, even with a 1.5km apparent offset between the basins. This offset is accounted for by the difference in thermal gradients between the two basins.

Figure 5.25 shows that there are three zones to the percentage expandability (%S in mixed-layer I/S) against estimated vitrinite reflectance for Magnus

211/12-2, Rhum 3/29a4, Bukowina Tatrzańska PIG-1 and Chochołów PIG-1. Zone one has a fixed vitrinite reflectance at around ~0.3Ro but a decrease in the percentage of smectite in I/S from 100% to 60%. This decrease in %S could reflect the natural variability of the input material to the sediment pile. Chapter 4 has noted the variable input material in the Tertiary of the Northern North Sea associated with North Atlantic volcanism. Variable input material is the most likely explanation as there is no apparent maturity increase for these rapidly buried Tertiary sediments.

Zone two shows a decrease in smectite in I/S from 60% to 20% of layers and an associated increase in Ro from ~0.3 to 0.8. Zone three has no decrease in smectite percent as the reaction has run to termination and is governed here by K^+ depletion as a source of K^+ is needed to form illite (Chapters 2 & 3). However, the organic maturity of the samples from the Podhale basin continues to increase.

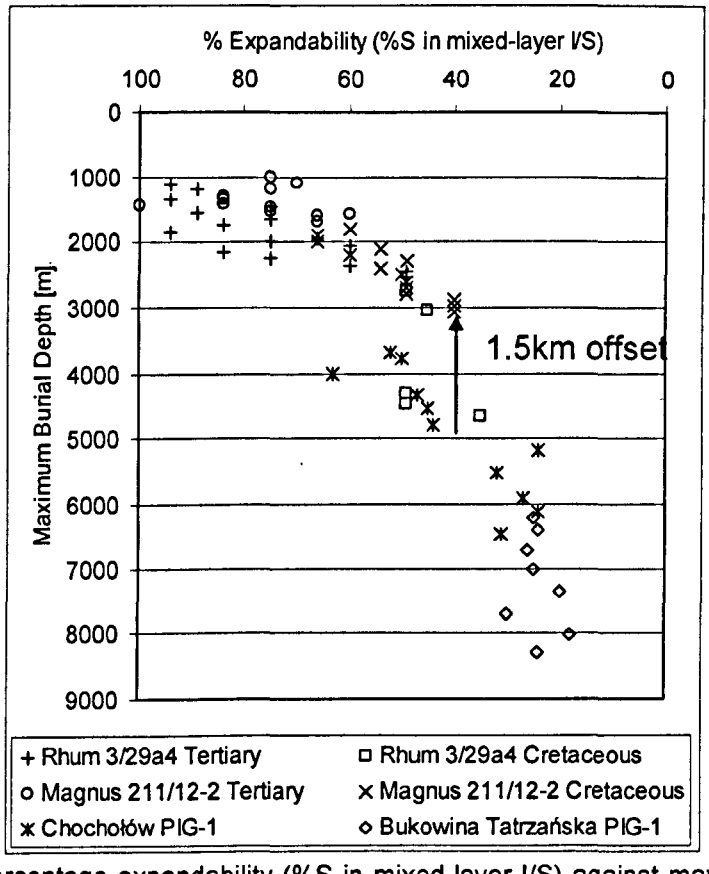

Figure 5.24. Percentage expandability (%S in mixed-layer I/S) against maximum modelled burial depth for Magnus 211/12-2, Rhum 3/29a4, Bukowina Tatrzańska and Chochołów. Showing the 1.5km offset between the northern North Sea and the Podhale Basin.

Additionally, when expandability is plotted as a function of maturity (Figure 5.25) rather than depth (Figure 5.24), the effects of the differences in geothermal gradient between the northern North Sea and the Podhale Basin are negated and the apparent 1.5km offset between the smectite to illite transition in the two basins is closed up and the reaction becomes a continuous profile.

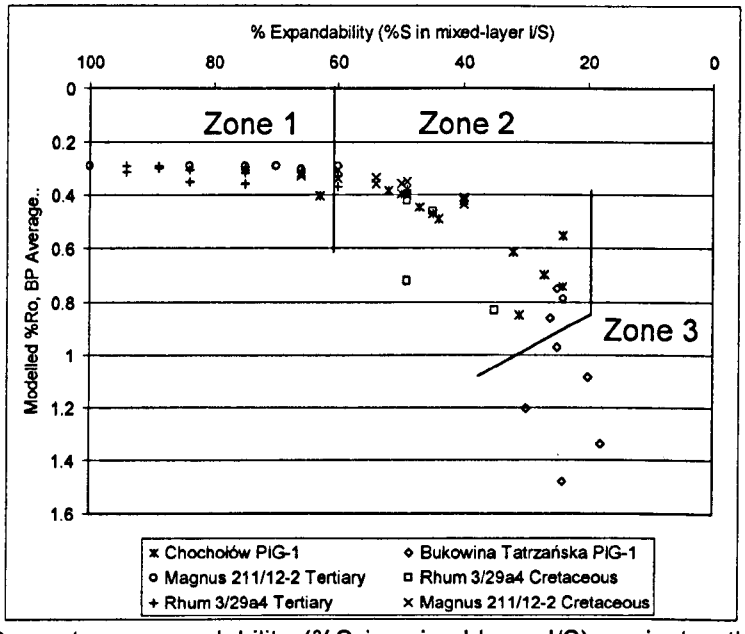

Figure 5.25. Percentage expandability (%S in mixed-layer I/S) against estimated vitrinite reflectance for Magnus 211/12-2, Rhum 3/29a4, Bukowina Tatrzańska and Chocholów.

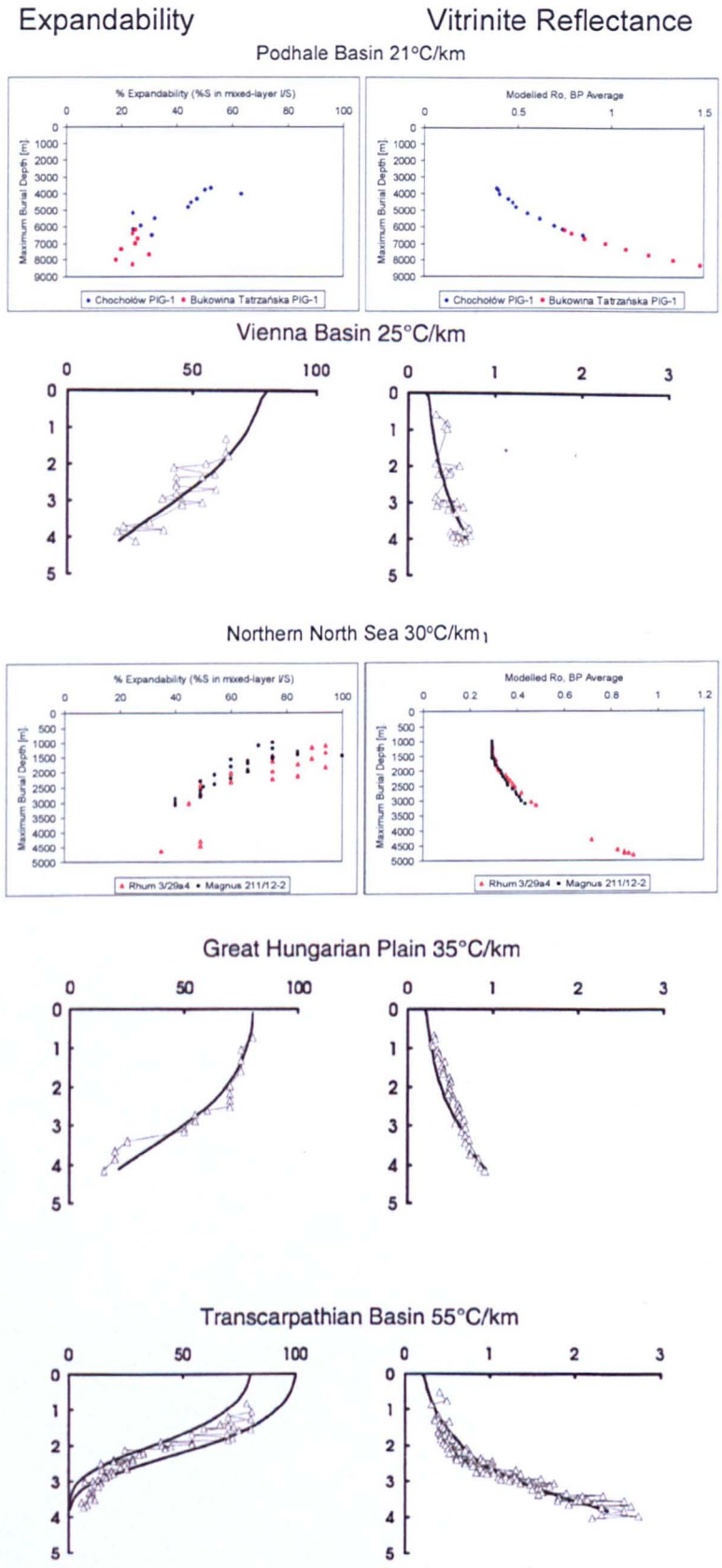

Figure 5.26. % Expandability and vitrinite reflectance with depth for the Northern North Sea, the Podhale Basin, (geothermal gradients 30°C/km and 21°C/km, respectively) compared to the Vienna Basin, The Great Hungarian Basin and the Transcarpathian Basin (geothermal gradients of 25°C/km, 35°C/km and 55°C/km, respectively, after Hillier et al., 1995).

The trends in % expandability with vitrinite reflectance in this study have once again highlighted the dependence of maturity and I/S change on temperature (e.g. Huang et al., 1993; Velde & Vasseur, 1992; Pytte & Reynolds, 1989). A change in geothermal gradient can have a significant effect on the shape of the I/S conversion trend as well as on vitrinite reflectance (Figure 5.26) (Hillier et al., 1995).

Following the convention of Hillier et al., (1995) when expandability is plotted against a log of vitrinite reflectance zone 2 as previously mentioned is highlighted and it is clear that this is the zone of most significant I/S conversion as a function of increasing maturity (Figure 5.27). The data from this study compare quite favourably with that of Hillier et al., (1995) (Figure 5.27).

As a consequence, a plot of expandability against vitrinite reflectance will effectively remove geothermal gradient as a factor as both the illitization of smectite and vitrinite reflectance are dependent on temperature to mature. Care should be taken in interpreting the I/S relationship in Magnus 211/12-2 and Rhum 3/29a4 as a continuous reaction series as Chapter 4 has highlighted the significant differences in sedimentary input for the Tertiary, Cretaceous and Jurassic.

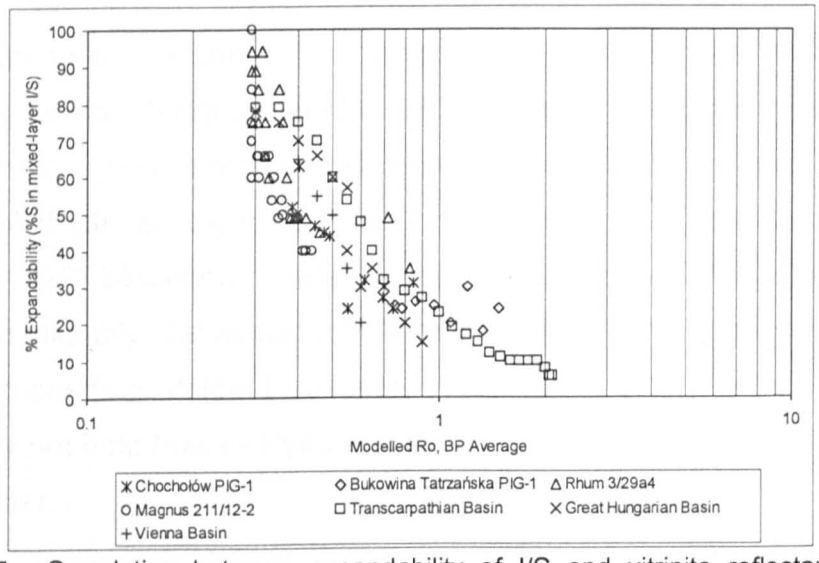

Figure 5.27. Correlation between expandability of I/S and vitrinite reflectance for the Northern North Sea, the Podhale Basin, the Great Hungerian Basin, the Vienna Basin and the Transcarpathian Basin (after Hillier et al., 1995). Vitrinite reflectance is plotted on a log scale.

A general assumption is that the progress of a chemical reaction is governed by kinetic constants. In first order kinetics [1]:

$$dS/dt = -kS \quad [1]$$

Where k is the rate constant, where in turn following the Arrhenius relationship [2]:

$$A\exp^{(-Ea/RT)} \quad [2]$$

(Aexp = frequency factor and exponential function, Ea = activation energy, R = universal gas constant, T in °K).

If these kinetics are true for the smectite to illite transition and the maturity of vitrinite, a relationship between the progress of the two reactions is to be expected (Figure 5.27). The reaction progress is dependent of several parameters, the time-temperature history, heating rate and most importantly maximum temperature.

Significant issues are presented by the data in this study with regard to smectite to illite kinetics. The Podhale Basin is not well constrained in terms of the time-temperature history. The heating rates have been shown to be significantly different between the Northern North Sea and the Podhale Basin. This will have an effect on the percentage expandability and mean vitrinite reflectance (Figure 5.27).

In smectite to illite kinetics, the difference in heating rates will result in differing activation energies (Velde, 1992). Previous smectite to illite kinetic models have predicated activation energies that are quite variable; 33kcal/mol (Pytte & Reynolds, 1989), 9kcal/mol and 17kcal/mol (Velde & Vasseur, 1992) 28kcal/mol (Huang et al., 1993) and 8kcal/mol (Hillier et al., 1995). Additionally, the assumption that smectite to illite kinetics follows first order reactions (e.g. Velde & Vasseur, 1992; Huang et al., 1993; Hillier et al., 1995) may not hold true as Pytte and Reynolds (1989) show that the kinetics is sixth order.

Consequently, unifying the kinetics beyond that which is already presented is not expedient as the dataset in this study does not present a clear geological

situation to undertake unifying kinetic modelling. However, the modelling has allowed an assessment of maximum burial temperature to be made.

5.4: Conclusions:

Maturity has been established for Magnus 211/12-2 and has been resolved for Rhum 3/29a4 and Bukowina Tatrzańska and Chochołów. The match in Rhum 3/29a4 between measured temperature, vitrinite reflectance, porosity and pore pressure and modelled outputs are robust. The match in the Podhale Basin is less constrained due to the availability of well control data. The method is robust based on the results from Rhum 3/29a4.

Modelling the Podhale Basin has successfully established maximum burial depths based on porosity and vitrinite reflectance. The base of Chochołów is at 6300m and the base of Bukowina Tatrzańska is at 8300m. Therefore, applying the present day geothermal gradient of the Podhale Basin yields a maximum burial temperature of ~130°C in Chochołów and ~170°C Bukowina Tatrzańska.

The relationship between I/S and depth has been shown to be a function of geothermal gradient. Using modelled vitrinite reflectance as a proxy for maximum temperature has shown that the I/S trend in the virtual well profile plotted for the Podhale Basin and the Northern North Sea has a continuous trend with three zones of I/S change noted. Unfortunately, the dataset does not afford a unifying kinetic model to be established for I/S change.

Chapter 6: Diagenetic Controls on the Phyllosilicate Fabric of Mudstones:

6.0: Discussion:

The preferred alignment of phyllosilicate minerals has been acquired for the Podhale Basin (Chapter 2) and for the Northern North Sea (Chapter 4) through the use of HRXTG. The results have shown a general increase in preferred alignment for both I/S material and kaolinite-chlorite with increasing burial depth. Mineralogy and the percentage of smectite in I/S through XRD measurement has also been discussed in these chapters. The relationship between time and temperature has been solidified in Chapter 5. Gaining modelled maximum temperature information for each sample where no temperature data existed allow the fabric data gathered here to be compared to that of previous studies (Ho et al., 1999; Matenaar, 2002), which relate preferred alignment change to diagenetic mineral reactions and mechanical compaction. This chapter offers an overall discussion of the data collected in this study and how it relates to the key studies of Ho et al. (1999) and Matenaar, (2002). The discussion focuses on I/S change, mechanical compaction and how these two factors influence the preferred alignment of phyllosilicate minerals.

6.1: Controls on the Illitization of Smectite:

The illitization of smectite has been used by many workers as the key marker of mineralogical maturity in a basin. Gulf Coast sediments have been the basis for numerous studies (e.g. Burst, 1959; Powers, 1967; Perry & Hower, 1970; Hower et al., 1976; Boles & Franks, 1979; Bell, 1986; Lynch, 1997; Rask et al., 1997). Other basins around the world; the Jurassic of South-eastern France (e.g. Artru & Gauthier, 1968), Carboniferous of Central Poland (e.g. Środoń & Eberl, 1984) and the Cainozoic and Mesozoic of the Rocky Mountains (e.g. Pollastro, 1985), as well as the North Sea Basin (e.g. Huggett, 1995; Thyne et al., 2001; Nadeau et al., 2002), the Swiss Molasses (e.g. Schegg & Leu, 1996; Wang et al., 1996) and various offshore Japan basins (e.g. Inoue et al., 1987; Son et al., 2001) have also described I/S change. Additionally, the illitization of smectite has previously been

demonstrated to play a role in the development of phyllosilicate preferred orientations (Ho et al., 1999; Matenaar, 2002; Worden et al., 2005).

Illitization of smectite is controlled by various parameters including temperature (e.g. Freed & Peacor, 1989), time (e.g. Środoń & Eberl, 1984; Velde, 1995), pressure (e.g. Środoń and Eberl, 1984; Buryakovsky et al., 1995), potassium availability (e.g. Hower et al., 1976; Moore and Reynolds, 1997) and the chemistry of pore fluids (e.g. Drief & Nieto, 2000). The reaction stoichiometry has been examined in Gulf of Mexico mudstones by various workers (e.g. Land et al., 1987; Lynch, 1997; Land et al., 1997), as have the kinetics of the reaction, which have been assessed by various authors (e.g. Vasseur & Velde, 1992; Huang et al., 1993; Hillier et al., 1995; Elliott & Matisoff, 1996; Elliott et al., 1999), with a unifying kinetic model still elusive.

Studies on the illitization of smectite describe an increase in the proportion of illite in mixed-layer (interstratified) illite/smectite (I/S) with increasing temperature. The classic work by Hower et al. (1976), on the Gulf Coast sediments, describes a solid-state reaction where:

$$\text{Smectite} + Al^{3+} + K^{+} = \text{illite} + Si^{4+}$$

Alternatively, Boles and Franks (1979) prefer a dissolution-precipitation reaction. This reaction is associated with the selective 'cannibalisation' of smectite layers to form illite and therefore describes significant volume loss, with the following reactants and products:

$$\text{Smectite} + K^{+} = \text{illite} + \text{chlorite} + \text{quartz} + H^{+}.$$

Intermediate reactions that represent a compromise between solid-state transformation and dissolution-precipitation have also been described (e.g. Ahn & Peacor, 1986; Inoue et al., 1987). The reaction of Hower et al. (1976)

implies that smectite transforms to illite directly by fixing K in interlayer sites with a penecontemporaneous substitution of Al for Si in the tetrahedral sheet. The source of the Al and K reactants is the local dissolution of K-feldspar and/or mica in a closed system. It has been observed (Hower et al., 1976) that it is the <0.1μm fraction that is active in diagenetic reactions with increasing depth and temperature, whereas the whole rock chemistry is constant.

The results from the two diagenetic studies presented in this thesis point to the importance of K-feldspar dissolution in the illitization of smectite. The percentage of smectite in illite smectite has reached 40% of layers in Magnus 211/12-2 at ~110°C. K-feldspar is not depleted so these sediments have the potential for further illitization (Figure 6.1). Rhum 3/29a4, on the other hand, has ~35% of smectite remaining in I/S with a temperature at its base of ~150°C and has almost completely depleted its supply of K-feldspar (Figure 6.2). The illitization of smectite in the Podhale Basin (Figure 6.3) is at 80% of layers and this termination is co-incident with K-feldspar deletion. These results suggest that the dissolution of K-feldspar is the key driver in the illitization of smectite in terms of the remaining expandability left at termination. This confirms the observation of Środoń and Eberl (1984) that the percentage of smectite in I/S at termination is a localised phenomena.

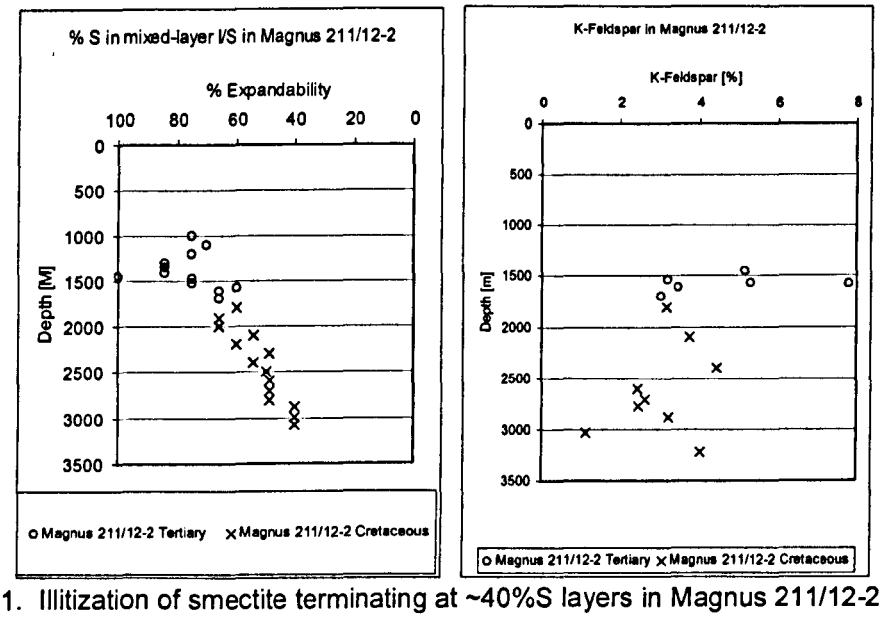

Figure 6.1. Illitization of smectite terminating at ~40%S layers in Magnus 211/12-2, left, and the incomplete depletion of K-feldspar, right.

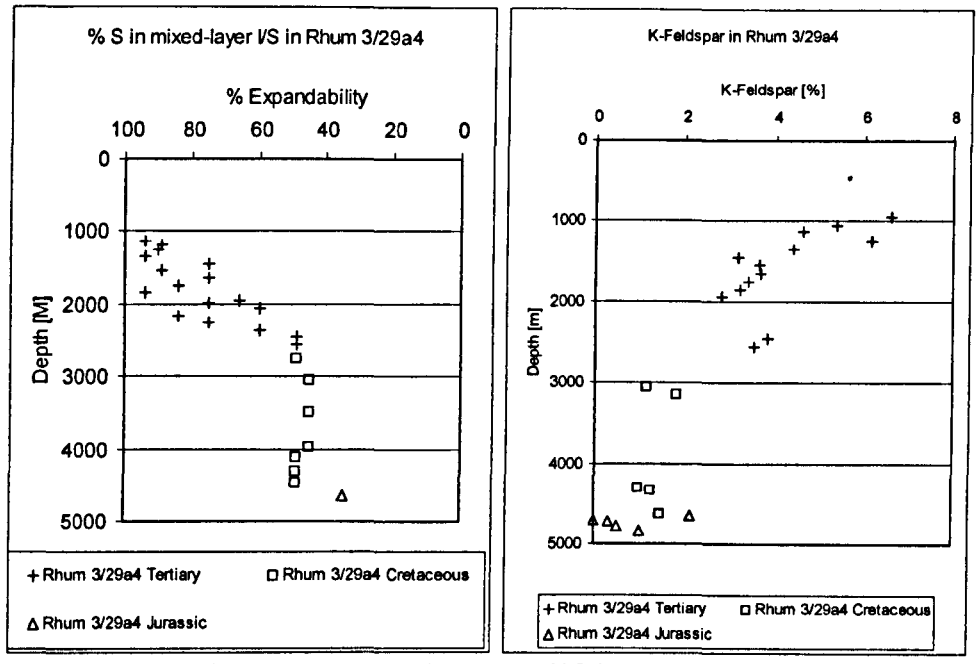

Figure 6.2. Illitization of smectite terminating at ~40%S layers in Rhum 3/29a4, left, and the depletion of K-feldspar to less than 1%, right.

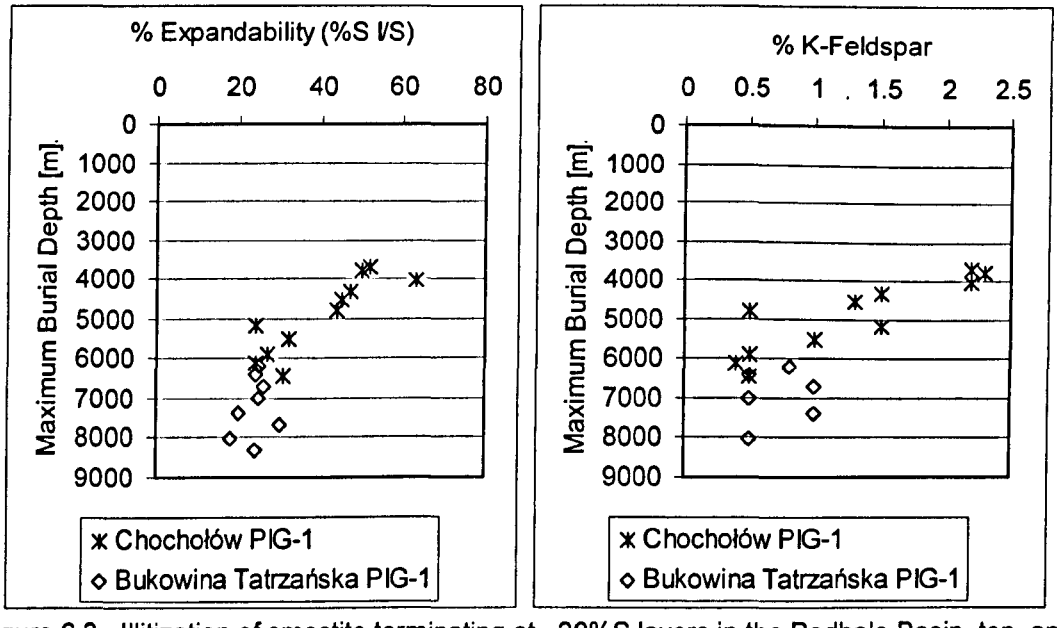

Figure 6.3. Illitization of smectite terminating at ~20%S layers in the Podhale Basin, top, and the depletion of K-feldspar to less than 0.5%, bottom.

The maturity modelling undertaken in Chapter 5 has allowed the formation of a continuous profile for the Podhale Basin and for the two wells from the Northern North Sea (Figure 6.4) with respect to the %S in I/S. The differences in geothermal gradients (Figure 6.5) between the two basins results in an offset of ~1.5km when %S is plotted with depth. Similarly, the two studies (Figure 6.4) from the Gulf of Mexico (Matenaar, 2002; Ho et al.,

1999) have significantly different geothermal gradients (Figure 6.4). Therefore, although attractive to use maximum burial depth, it is maximum burial temperature that represents a far better axis for plotting as it removes the differences in geothermal gradient (Figure 6.6). Additionally, in the absence of temperature data either yielded by BHT measurements or through modelling a proxy for temperature such as vitrinite reflectance or a theoretical vitrinite reflectance calculated from the MPI index (after Radke & Welte, 1981) may be used (Figure 6.7).

Figures 6.6 and 6.8 demonstrate that there are two trends in the %S versus temperature plots. The Podhale Basin and the Northern North Sea data show a continuous convex-up profile with illitization terminating at ~20%S layers (Velde, 1992), whereas the Gulf of Mexico (data from Ho et al., 1999 and Matenaar, 2002) terminates at less than ~20%S layers and shows a concave down reaction profile. The net result of combining all the data (Figure 6.6) are divergences of the two basin type at the top and the base of the profile but a common middle section coinciding with the onset of R0 to R1 ordering (Jadgozinski, 1949; Weaver, 1989 and references therein) in mixed-layer I/S. There is a decrease in %S from ~60% to ~20% of layers and this coincides with an increase in temperature from 75°C to 125°C.

The divergence of the convex up and concave down profiles at the top of the section is partly a function of variable sediment input as the %S in the detrital I/S is not uniform. The divergence at the base of the profile is a consequence of the availability of K-feldspar to drive the illitization of smectite beyond 80% of layers. Additionally, the shape of the reaction curve is controlled by the kinetics of I/S alteration (e.g. Vasseur & Velde, 1992; Huang et al., 1993; Hillier et al., 1995; Elliott & Matisoff, 1996; Elliott et al., 1999). The concave down reaction profile in the Gulf of Mexico samples (Figure 6.4 and after Ho et al., 1999; Matenaar, 2002) have a high activation energy in their kinetic transformation, which results in more rapid transformation at greater temperatures (Velde, 1992). Conversely, the wells from the Northern North Sea and the Podhale Basin (Figure 6.4) have low

activation energies and the reaction proceeds evenly at low temperatures but is continuous for many millions of years.

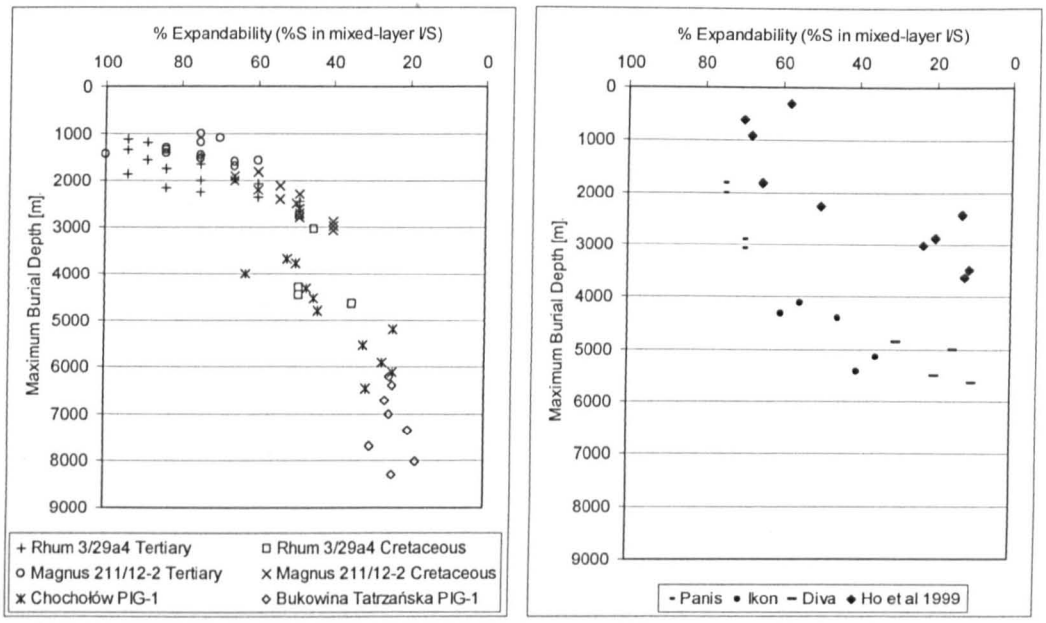

Figure 6.4. Illitization of smectite terminating at ~20%S layers in the virtual profile of the Podhale Basin and Northern North Sea well (Rhum 3/29a4 and Magnus 211/12-2), left, and the decrease in the %S in I/S for the Gulf of Mexico study of Ho et al. (1999) and Panis, Ikon and Diva (After Matenaar, 2002). Significant differences occur between wells due to differences in geothermal gradient. A ~1km offset occurs between the Podhale Basin and the wells from the Northern North Sea.

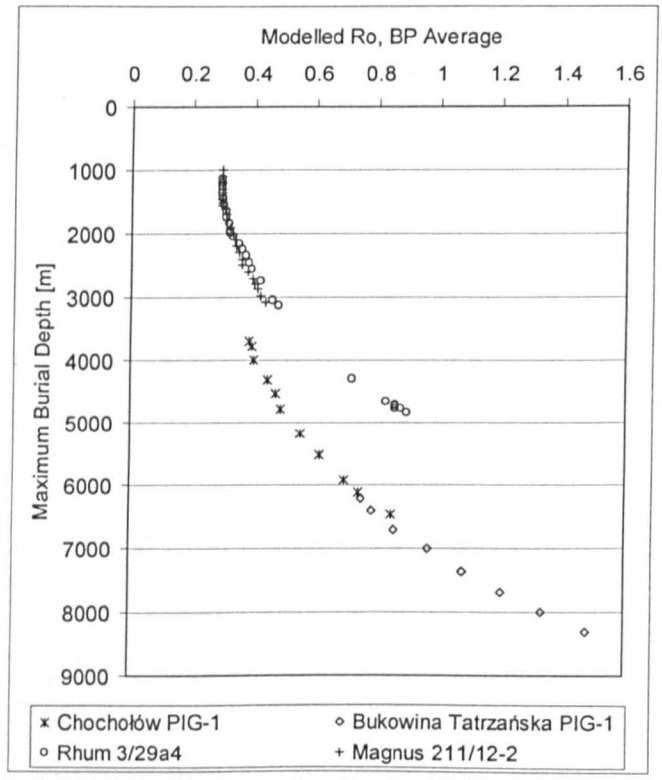

Figure 6.5. Modelled vitrinite reflectance for the Podhale Basin and Northern North Sea wells (Rhum 3/29a4 and Magnus 211/12-2). The break in the data point to different geothermal gradients.

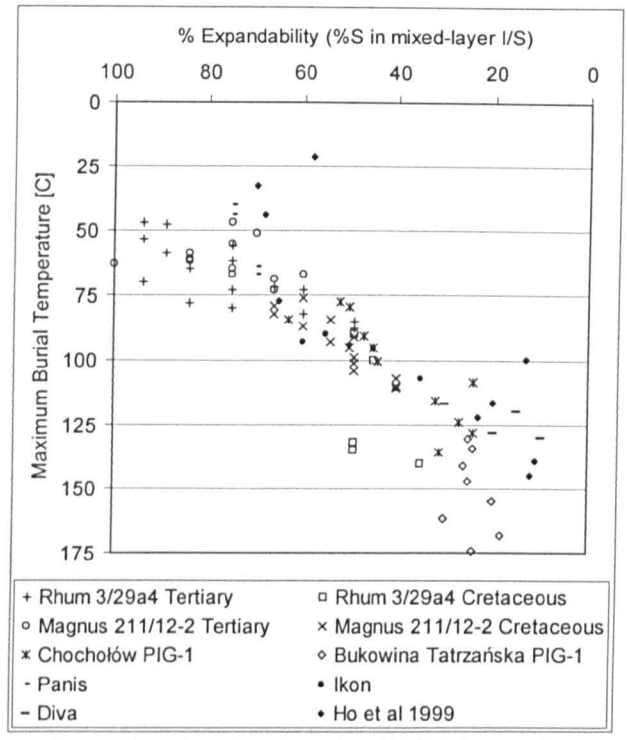

Figure 6.6. Illitization of smectite terminating at ~10%S layers in the virtual profile of the Podhale Basin, Northern North Sea well (Rhum 3/29a4 and Magnus 211/12-2) and the Gulf of Mexico study of Ho et al. (1999) and Panis, Ikon and Diva (After Matenaar, 2002). The significant offset noted in Figure 6.4 is removed in a plot of maximum burial temperature rather than depth. Temperature data for the Ho et al. (1999) study are based on a geothermal gradient of 37.5°C/km and a surface temperature of 10°C.

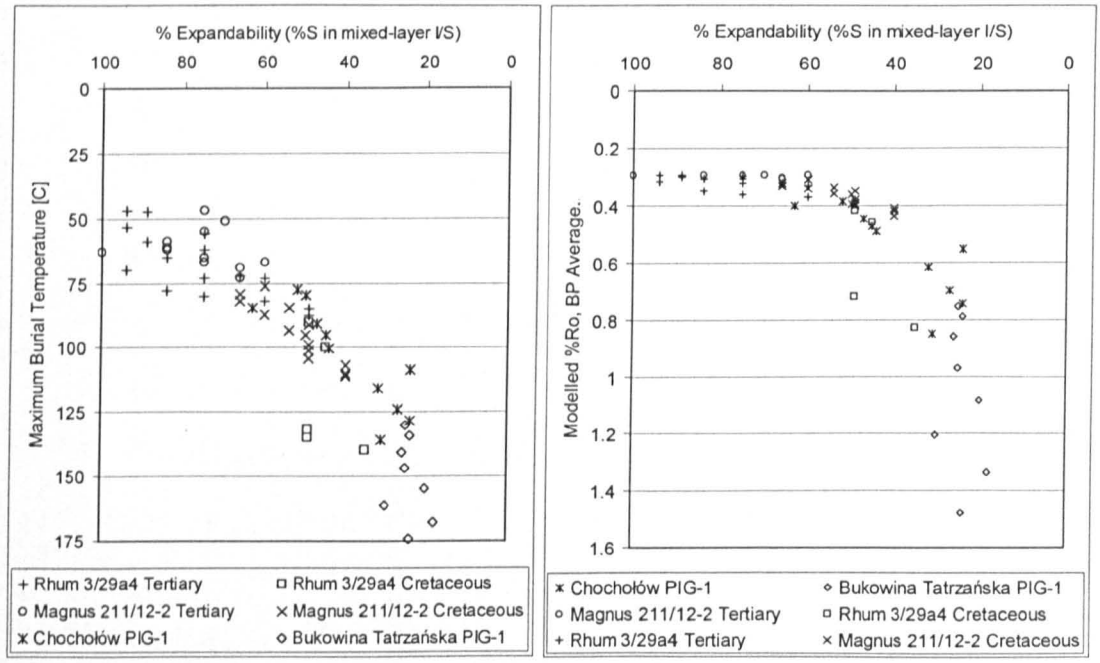

Figure 6.7. Illitization of smectite terminating at ~20%S layers in the virtual profile of the Podhale Basin and Northern North Sea well (Rhum 3/29a4 and Magnus 211/12-2) shows a continuous trend with temperature, left, and with a temperature proxy, vitrinite reflectance modelled in Genesis 4.8, right.

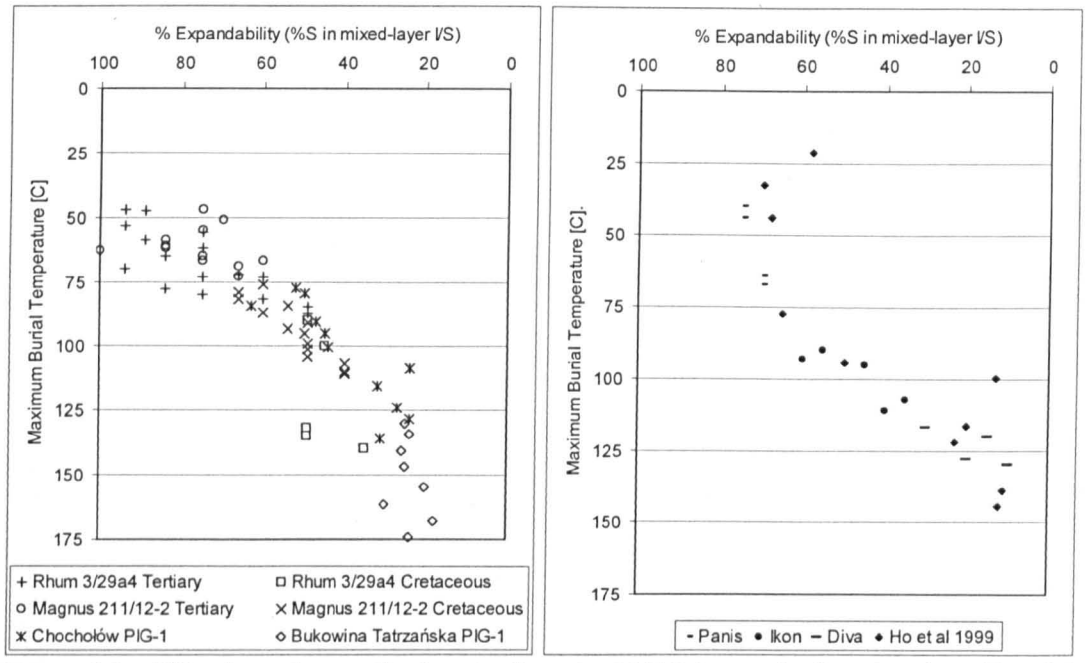

Figure 6.8. Illitization of smectite terminating at ~20%S layers in the virtual profile of the Podhale Basin and Northern North Sea well (Rhum 3/29a4 and Magnus 211/12-2) shows a convex up reaction profile, where as the Gulf of Mexico (data from Ho et al., 1999 and Matenaar, 2002) shows a concave down reaction profile.

6.2: Controls on the Enhancement of Phyllosilicate Preferred Orientation:

6.2.1: Mechanical Compaction:

Although the thermal histories between the basins are quite different the measured porosities (Figure 6.9) demonstrates that the maximum burial depths estimated by modelling in Chapter 5 and built upon those postulated by Środoń et al. (in press) are broadly in the correct depth space (e.g. Athy, 1930; Hedberg, 1936; Sclater & Christie, 1980). There is porosity reduction with increasing depth between Magnus 211/12-2, Chochołów PIG-1 and Bukowina Tatrzańska PIG-1, that follows many of the published trends for mudstone porosity with depth (e.g. Athy, 1930; Hedberg, 1936; Sclater & Christie, 1980; Dzevanshir et al., 1986; Giles et al., 1998). The 1-D maturity modelling carried out in Chapter 5 estimates that Magnus 211/12-2, Chochołów PIG-1 and Bukowina Tatrzańska PIG-1 are nearly normally

pressured and therefore follow normal compaction trends with depth. The high porosities at depth in Rhum 3/29a4 have been demonstrated to be caused by significant overpressuring which should effect fabric alignment if the purely mechanical processes in fabric re-orientation as assumed (e.g. Oertel & Curtis, 1972; Curtis et al., 1980; Sintubin, 1994; Jacob et al., 2000).

Additionally, the trend in porosity reduction in the Gulf of Mexico samples (Matenaar, 2002) follows a different trend to that of the Northern North Sea and the Podhale Basin (Figure 6.9). It has a more concave downwards trend whereas the other two basins are convex up. This same trend has been noted in the response of the illitization of smectite to increased depth and temperature (Figures 6.6 & 6.8).

If mechanical compaction is assumed to be the only driver of preferred phyllosilicate orientation change then the change in porosity demonstrated in Figure 6.9 results in a generally linear change in preferred orientation with maximum burial depth (Figure 6.10) for samples from the Northern North Sea and the Podhale Basin. When data from the studies of Matenaar (2002) and Ho et al (1999) are superimposed on the results from this study the relationship between sedimentary loading and preferred phyllosilicate orientation becomes more complex (Figure 6.10). Understandings of the sediment type and basin environment are important factors to be taken into account. Three types of phyllosilicate orientations may be observed in response to increasing depth: 1- a general trend; 2- a clay percentage effect trend; and 3- an overpressure/rapid burial trend. The results from this study show what may be described as a general trend in increased preferred phyllosilicate alignment with increasing maximum burial depth (Figure 6.10). It should be noted that these samples have ~50-55% total phyllosilicate material as quantified by XRD, whereas the samples described by Ho et al (1999) have very variable grain size distributions. The samples described as 'sandy' sit on the general trend as described by samples measured in this study, whereas the much finer-grained samples have increased preferred fabric alignments (~2 m.r.d.) for a given depth relative to the general trend.

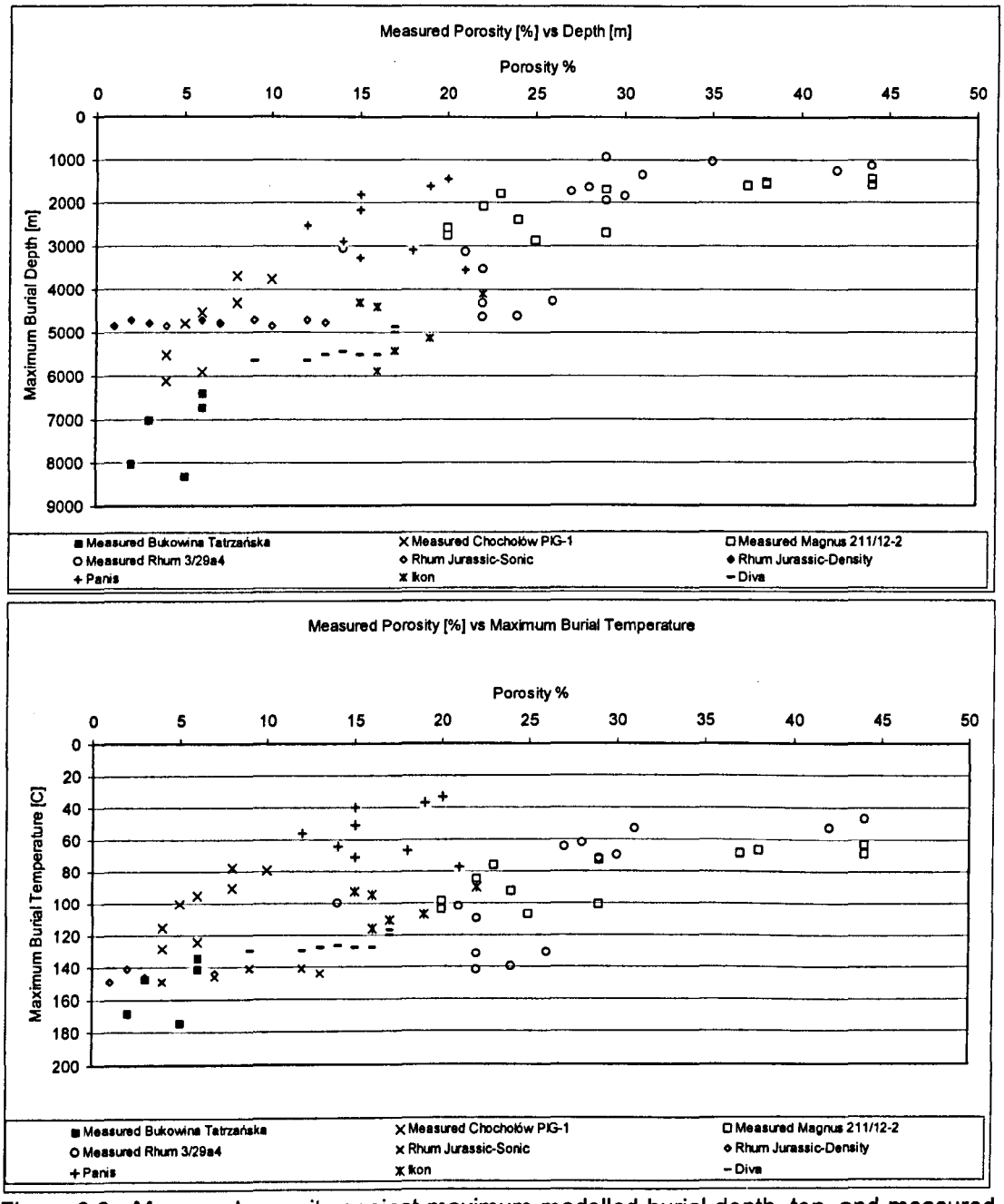

Figure 6.9. Measured porosity against maximum modelled burial depth, top, and measured porosity against maximum burial temperature, bottom, for Magnus 211/12-2, Rhum 3/29a4, Bukowina Tatrzańska PIG-1 and Chochołów PIG-1 and measured porosity for Panis, Ikon and Diva (After Matenaar, 2002).

Sample Chochołów-38 from the Podhale Basin that joins the samples from the Ho et al. (1999) study suggests that these samples have ~70% total phyllosilicate material with less than 20% quartz. Although, from the BSEM micrographs presented in this study from both the Podhale Basin and the Northern North Sea the role of quartz in disrupting fabric development appears to be offset by the amount of total phyllosilicate material, with the latter having the greater impact on fabric alignment. This observation follows

that of Matenaar (2002) who demonstrated that the granulometrical composition of the silt and clay fraction was more significant for primary phyllosilicate fabric than the overall grain size. The rapid burial noted in this study and by Matenaar (2002) may retard preferred orientation development to depths of around ~3 to ~5km, respectively, with these low fabric alignments observed in BSEM micrographs.

The three trends above highlight different physical burial processes. When phyllosilicate preferred alignment is expressed against porosity (Figure 6.11) it is remarkable how little change (less than 1 m.r.d. difference) there is in preferred phyllosilicate alignment between 45% and 15%. There is some spread in the data but this represents individual sample variability, however,30%of porosity is lost for only a ~0.5 m.r.d. increase in preferred orientation (from ~2 to ~2.5 m.r.d.). At 15% porosity and ~2.5 m.r.d. there is a key knick point in the trend. Porosity is reduced to almost zero and fabric alignment increases from ~2.5 m.r.d. to ~6.5 m.r.d. The implication is that in terms of porosity significant fabric alignment change is only associated with porosities that are less than ~15%. Additionally, this implies a small pore throat radius, with the development of preferred phyllosilicate fabrics only associated with pore throat radii of less than 10nm (Matenaar, 2002).

With an understanding of the depositional setting and burial depth/temperature in mind, the relationship between porosity and maximum pole density is compelling (Figure 6.11), especially below ~15% porosity, and allows some prediction of preferred alignment based on a measured porosity. At greater than 15% porosity it appears that the effective stress experienced by the mudstone horizons sampled are not high enough to facilitate the alignment of phyllosilicates, yet it is enough to significantly reduce porosity. This suggests that the flocculated clay material observed at ~3000m in the Northern North Sea and at ~5000m in the Gulf of Mexico (Matenaar, 2002) is held in its depositional arrangement. Prediction based on Figure 6.11 is not efficient in the case of surface or near surface sediments with a high preferred orientation and an open porosity. The deep sea clay noted by Matenaar (2002) with ~40% porosity and a preferred phyllosilicate alignment

of ~5.5 m.r.d. diverges from the predictions made based on Figure 6.11. Even in highly overpressured systems 40% porosity will not persist to depths beyond 1-2km (Illife, 2005, pers. comms), consequently with an understanding of the depositional setting and burial depth/temperature, predictions and interpretations based on Figure 6.11 can still be made.

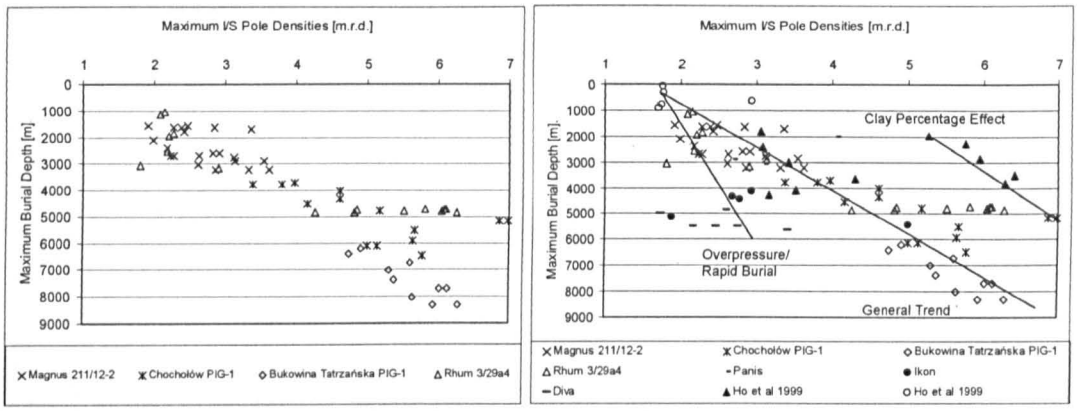

Figure 6.10. Fabric development (maximum pole density in M.R.D.) as measured by HRXTG against maximum burial depth for Magnus 211/12-2, Rhum 3/29a4, Bukowina Tatrzańska and Chochołów, left, and for Magnus 211/12-2, Rhum 3/29a4, Bukowina Tatrzańska and Chochołów, Gulf of Mexico wells Ikon Diva and Panis (after Matenaar 2002) and the Gulf of Mexico study by Ho et al. (1999), right.

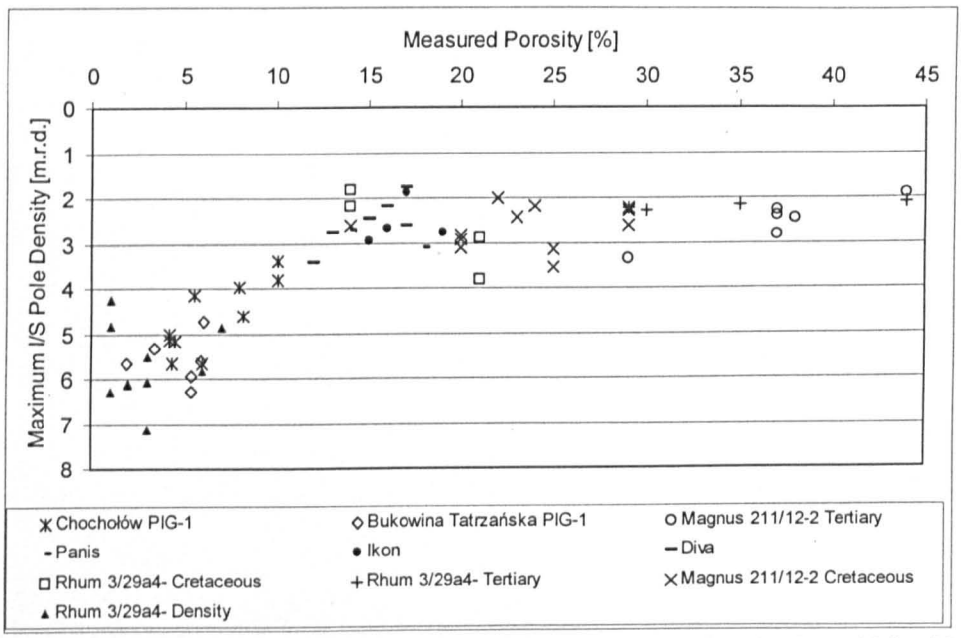

Figure 6.11. Measured porosity [%] against I/S maximum pole density [m.r.d.] for Magnus 211/12-2, Rhum 3/29a4, Bukowina Tatrzańska PIG-1, Chochołów PIG-1 and Gulf of Mexico wells Ikon Diva and Panis (after Matenaar 2002). Key preferred orientation change is at ~15% porosity.

The key implication of the data presented in Figure 6.11 is that depositional fabrics (flocculated clay material) assumed to be random (e.g. Sintubin, 1994, O'Brien & Slatt, 1990) with a typical phyllosilicate 'edge-to-face' morphology, except in the cases of depositionally aligned fabrics (e.g. Matenaar, 2002; Bennett et al, 1991), are more resistant to the effects of loading than have been previously suspected (Sintubin, 1994).

6.2.2: Smectite illitization:

In the samples from this study there is a general increase in phyllosilicate preferred orientation with increasing temperature (Figure 6.12), with the majority of the change occurring between 75°C and 125°C (Figure 6.13). Likewise, the phyllosilicate preferred orientation observed in the Gulf of Mexico samples (After Matenaar, 2002 and Ho et al., 1999) have a general increase. There is a greater spread of the data and this has been attributed to overpressure retarding preferred orientation development (Matenaar, 2002) and to grain size effects (Figure 6.13) decreasing the possibility of phyllosilicate alignment (Ho et al., 1999; Matenaar, 2002).

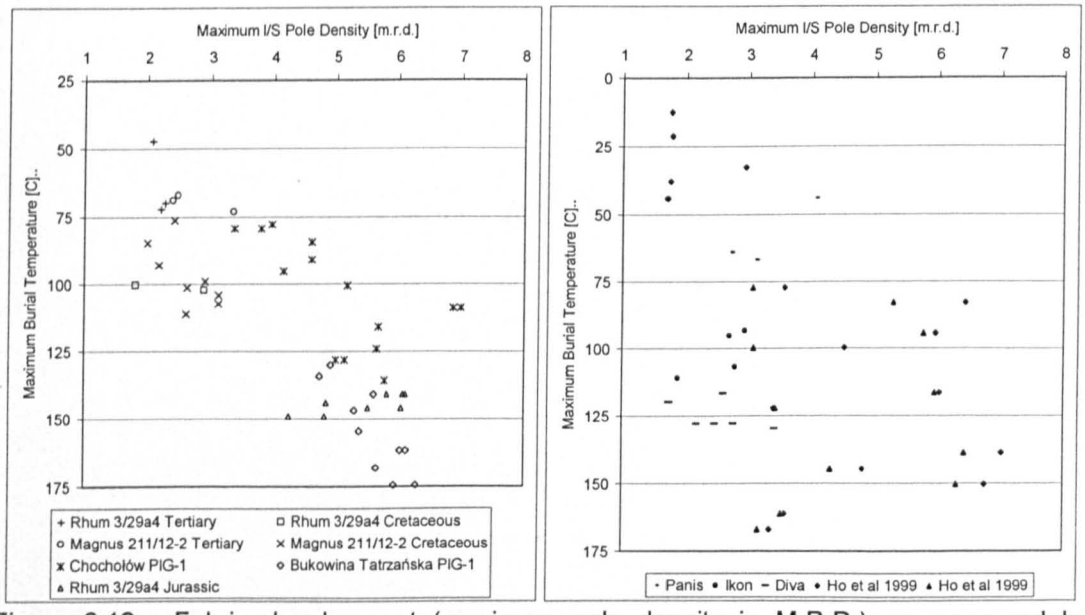

Figure 6.12. Fabric development (maximum pole density in M.R.D.) as measured by HRXTG against maximum burial temperature for Magnus 211/12-2, Rhum 3/29a4, Bukowina Tatrzańska and Chocholów,left, Gulf of Mexico wells Ikon Diva and Panis (after Matenaar 2002) and the Gulf of Mexico study by Ho et al. (1999), right. Large scatter of results at ~100°C reflects the various controls on fabric development at play in different basins.

This temperature window is coincident with the major change in I/S expandability (Figure 6.6). Phyllosilicate preferred orientation has been quantified to be low (less than ~2.5 m.r.d.) between 100% and 60% expandability (Figure 6.14) so that the majority of this fabric change occurs in the region of 60%S to 20%S in I/S. Expandability decrease is seen to terminate in the Podhale Basin samples at ~20%S, however fabric continues to increase, albeit at a much slower rate. Previously, in this thesis ATEM data have been presented that document crystallite change yet with no change in %S. Figure 6.14, therefore, documents 3 zones of preferred alignment increase. Zone 1 is affected by loading, a very large increase in vertical effective stress but no substantial fabric change is noted. Zone 2 sees less increase in the vertical component of effective stress than Zone 1 but much more increase in phyllosilicate alignment. Therefore, it is entirely influenced by I/S change. Zone 3 is affected by an increase in vertical component of effective stress that is similar to Zone 1 but is associated with only a modest increase in preferred alignment of phyllosilicates and is either a purely mechanical process in which the vertical component of effective stress drives continued alignment or is associated with mineralogical change in 'crystallite packets'.

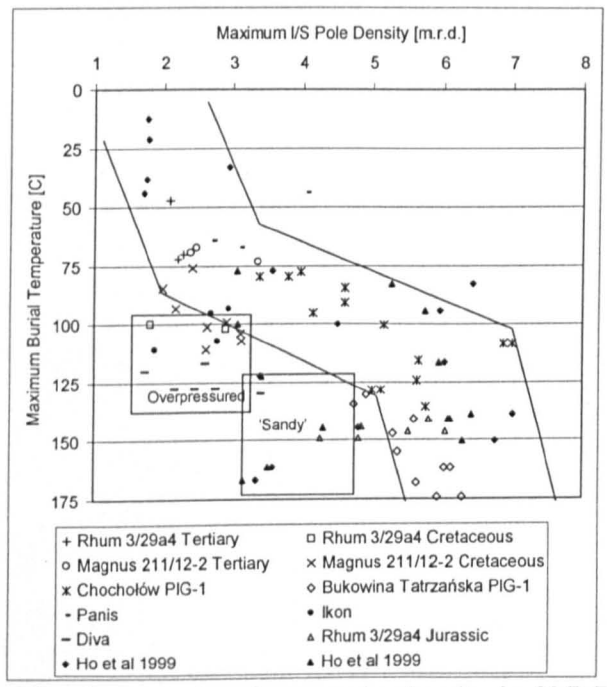

Figure 6.13. Fabric development (maximum pole density in M.R.D.) as measured by HRXTG against maximum burial temperature for Magnus 211/12-2, Rhum 3/29a4, Bukowina Tatrzańska and Chochołów, Gulf of Mexico wells Ikon Diva and Panis (after Matenaar 2002)

and the Gulf of Mexico study by Ho et al. (1999). Large scatter of results at ~100°C reflects the various controls on fabric development at play in different basins.

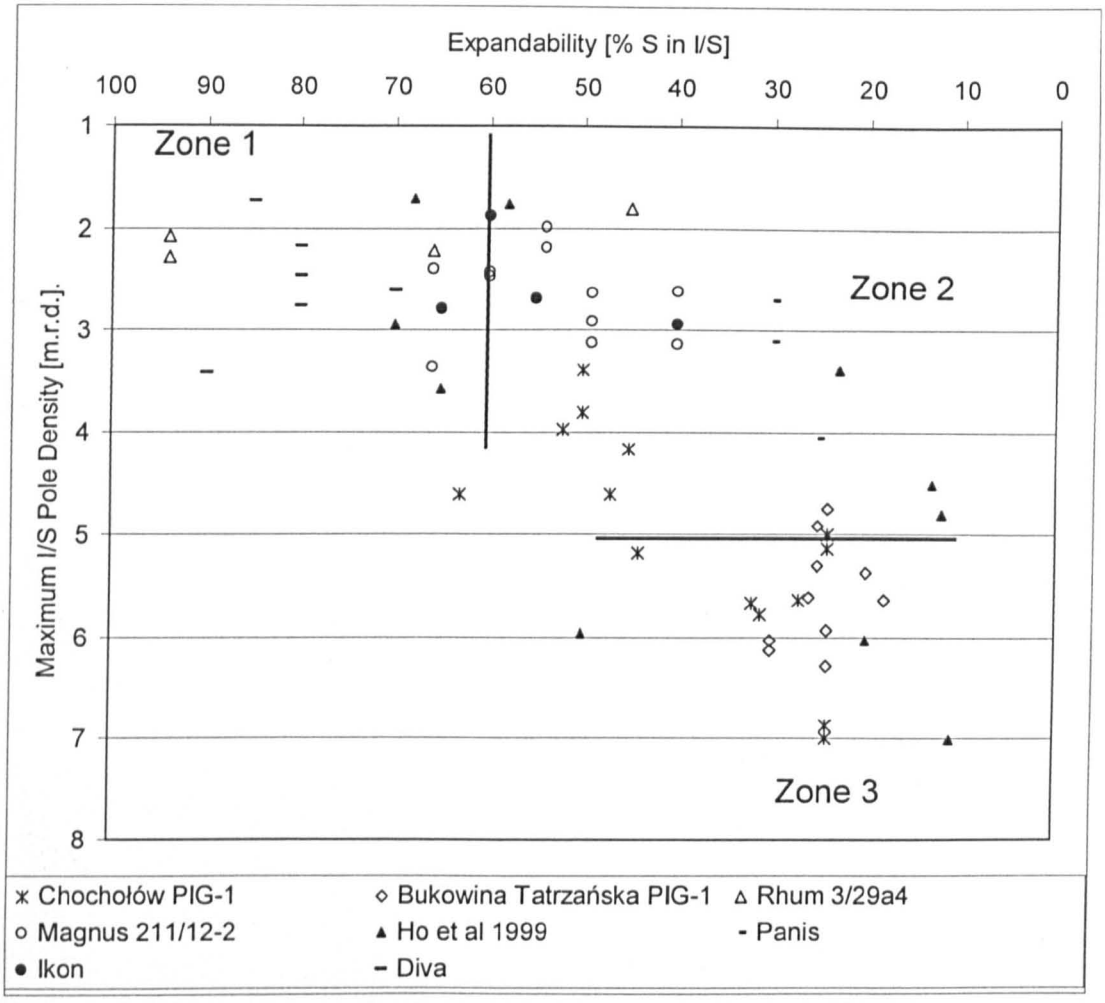

Figure 6.14. 3 zones of fabric development (maximum pole density in M.R.D.) as measured by HRXTG as a function of I/S change.

6.3: Diagenetic Controls on the Phyllosilicate Fabric of Mudstones:

The key results of this thesis are presented in Figure 6.16. The illitization of smectite is controlled by time, temperature and potassium availability. The change in ordering and the bulk of I/S change occurs between 75°C and 125°C, which is coincident with the bulk of phyllosilicate preferred orientation alignment.

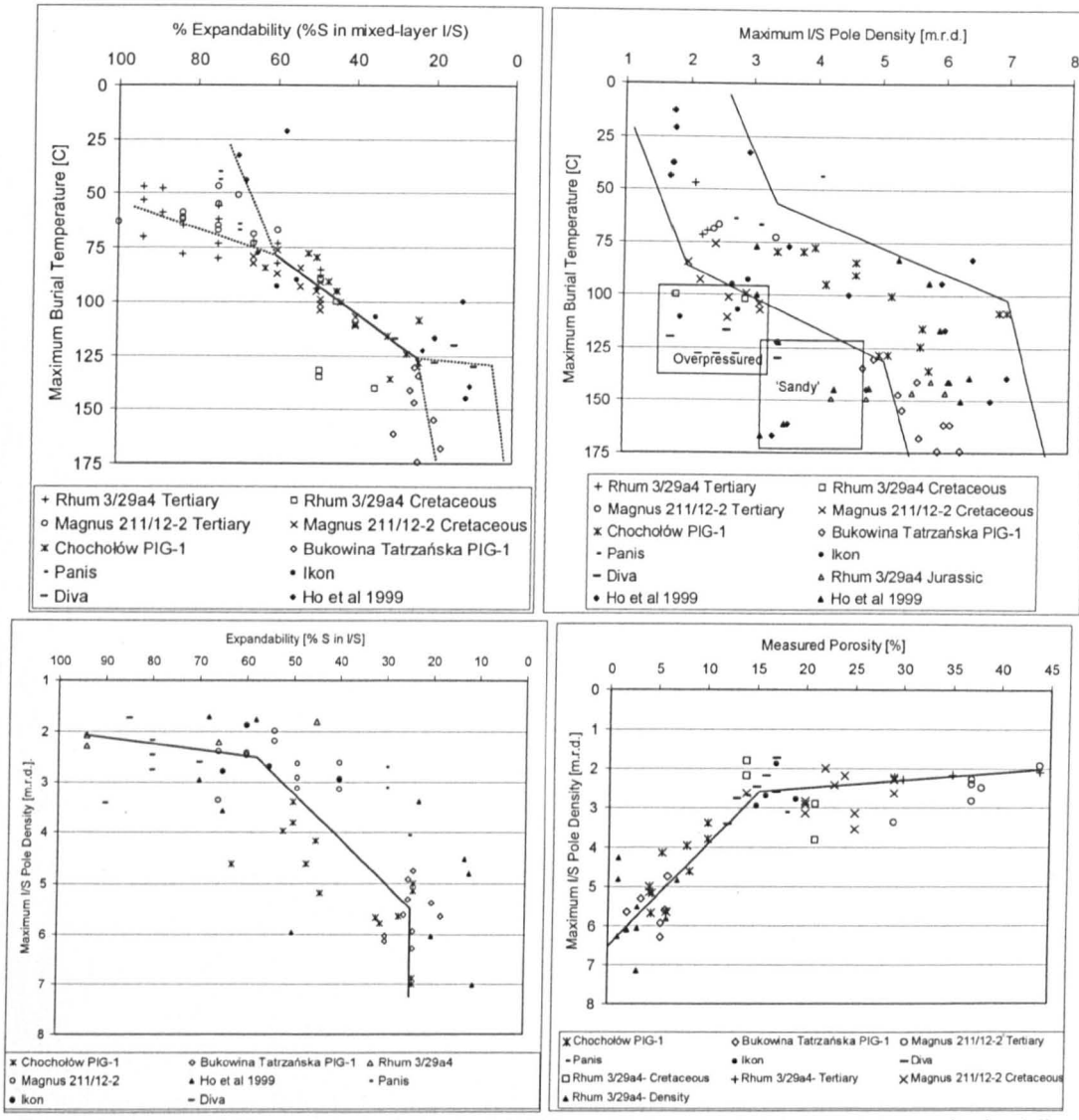

Figure 6.15. Top left, decrease in expandability with increasing temperature, dashed lines above 60%S show divergent paths in initiation of smectite to illite transformation, dashed lines below 20%S show divergent reaction paths in response to K-feldspar availability. Top right, maximum I/S pole density [m.r.d.] with maximum burial temperature [°C], overpressured samples (this study and Matenaar, 2002), 'sandy' samples (Ho et al., 1999) and inherited alignments (Matenaar, 2002) are marked, with the general fabric increase most marked between 75°C and 125°C. Bottom left, maximum I/S pole density [m.r.d.] with %S in I/S. Bottom right, the response of maximum I/S pole density [m.r.d.] increase to porosity decrease.

This I/S change and temperature interval is consistent with published temperature ranges in relation to I/S palaeothermometry (e.g. Hoffman & Hower, 1979; Pollastro, 1993; Środoń, 1995) and I/S transformation in general (e.g. Hower et al., 1976; Boles & Franks, 1979; Pearson et al., 1982; Środoń & Eberl, 1984). Additionally, I/S change is associated with the majority of phyllosilicate preferred alignment. Inherited alignment and grain size effects have significant influences over the range of maximum pole

densities encountered. However, the vertical component of effective stress is critical. I/S change and associated dissolution facilitates rotation of grains but it is loading that drives this change and gives increased phyllosilicate alignments. The two processes work together as loading alone appears insufficient to create wholesale fabric change whereas dissolution and mineral diagenesis without a loading regime has no power to effect orientation.

The above trends have a significant impact on which mechanism could be controlling I/S transition (discussed in Chapter 2). The MacEwan Crystallite Model (MacEwan et al., 1961) assumes a solid-state transformation with in situ change (I/S change by the reaction of Hower et al., 1976), whereas a Fundamental Particle Model (e.g. Nadeau et al., 1984a; 1984b; Nadeau, et al., 1985a; 1985b; Środoń et al., 1992; Dong & Peacor, 1996; Nadeau, 1998; Peacor, 1998) assumes direct precipitation after initial dissolution. This latter model may account for the rearrangement of phyllosilicate minerals seen to coincide with I/S transition (6.15). This dissolution-precipitation is not a wholesale change, rather Chapter 2 has suggested that perhaps only ~15% of the phyllosilicate minerals in the mudstone are reactive. Consequently, what is presented here is an idea of localised dissolution and re-precipitation around regions of grain defects or at the edge of grains that are in stress contact with other grains either quartz or other clay materials and the vertical component of effective stress forces neo-crystallites into a preferred orientation.

If dissolution-precipitation of neo-crystallites is a localised process, in which small areas of a grain diagenetically alter in response to the conditions they are under, which in turn is exploited by effective stress by rotation grains into an enhanced preferred alignment, it does not explain the coherency of a 'crystallite packet' as noted in the SADP collected as part of the ATEM analysis in this thesis. Larger packets producing more clearly identified single crystal patterns (Ahn & Peacor 1986; Li et al., 1997) and the single patterns in this study were predominantly associated with more diagenetically mature samples. Also, the nature of the smectite and illite interfaces in

interstratified 'crystallite packets' will have an effect on the SADP (Bell, 1986), as the boundary between smectite and illite layers might be layer terminating, which will change the crystal lattice planes under the scale of the electron beam and will produce what appears to be small amounts of turbostratic disorder. So as well as producing a phyllosilicate preferred orientation recorded by HRXTG, the mineralogical changes in smectite illitization have facilitated coherent crystallite patterns that have produced predominantly single crystal patterns.

The hypothesis of the control of reactive clay minerals over the clay particle realignment does not fully resolve why kaolinite and chlorite have the same amount of preferred orientation as I/S. The diagenetic evolution of kaolinite and chlorite in this work suggests that they are passive in reorientation into a preferred fabric and that they rely on diagenetic change to facilitate the initial reorientation and then allow vertical stress to govern their reorientation. The loss of kaolinite in diagenetic trends is associated with some volume loss (Giles et al., 1998). Chlorite is predominantly neo-formed so its alignment is a function of effective stress governing the orientation into which it may precipitate.

6.4: Conclusions:

The rationale for this study was to investigate the role of both mechanical compaction and diagenetic phyllosilicate mineral reactions on the phyllosilicate fabric of mudstones. The results have shown that:

- Smectite to illite changes occur predominantly in a temperature window between 75°C and 125°C. The relative ages of the basins studied have an effect on the shape of the reaction curves. K-feldspar dissolution is an important source of potassium to the system to form illite layers.
- Phyllosilicate preferred orientation is initially affected by random alignments or inherited preferred alignments that are a function of depositional environment.
- Grain size and phyllosilicate content affect the degree to which preferred alignments can be generated. In initially random alignments of phyllosilicate grains loading and porosity decrease to 15% do not significantly align grains. It is only with the onset of ordering changes in smectite illitization that enhanced alignments are observed.
- The role of vertical effective stress places the neo-formed phases into a preferred alignment but alone is not enough to form strong fabric alignments on initially random alignments of phyllosilicates.
- The results of the preferred alignment of phyllosilicates documented in this thesis points to the illitization of smectite being driven by a mechanism of dissolution-precipitation. ATEM data suggest some mineralogical change is continuing beyond I/S termination, that also has an effect on the nature of the SADP produced, and is aiding enhanced phyllosilicate alignment.

6.5: Future Work:

Work to date on the preferred orientation of phyllosilicate in mudstones has taken thus far has concentrated on trying to unravel the effects of mechanical compaction and diagenetic changes. Practical aspects to this work still remain in regard to petrophysical properties such as permeability and mechanical strength.

The most obvious future direction is to try to make a link between sonic velocity or seismic impedance and the alignment of phyllosilicates on the millimetre scale. This represents some significant upscaling issues; nevertheless the results of such research should not only help predict fluid flow in sedimentary basins but also locate clay mineral diagenesis in seismic or sonic surveys.

In direct relation to the samples from the Podhale Basin, a full scale TEM morphology study to produce lattice fringe images is extremely attractive for a study of the nature of crystallite packets in samples where the illitization of smectite has terminated. Such a study may be able to link crystallite size and mineral phase boundary conditions to the mechanism of phyllosilicate alignment and I/S change in samples that are already extremely well characterised.

Further the link between fabric change and mineral alignment in the diagenetic realm with those of the early stages of metamorphism has not received the full attention that they deserve. Work on cleavage development and the role of chlorite growth perpendicular to 'bedding' fabrics in lithologies with effectively 0% porosity offer an opportunity to study the mechanisms of phyllosilicate mineral growth and reorientation from diagenesis to zeolite and greenschist facies.

Preferred alignments of phyllosilicates will have effects on such properties as permeability and tortuosity of fluid flow through phyllosilicate dominated lithologies. Synthetically manufactured blocks of such material may be a

useful addition to clay barriers in nuclear waste repositories or in the clay barriers of refuse repositories.

7.0: References:

Ahn, J.H., Peacor, D.R. (1986a). Transmission and analytical electron microscopy of the smectite-to-illite transition. Clays and Clay Minerals, 34, 2, 165-179.

Ahn, J.H., Peacor, D.R. (1986b). Transmission and analytical electron microscope data for rectorite: implications for the origin and structure of "fundamental particles". Clays and Clay Minerals, 34, 2, 180-186.

Allen, P.A. and Allen, J.R. (1990). Basin Analysis principles and applications. Blackwell Science, London.

Allison, M.A., Nittrouer, C.A. (1998) Identifying accertionary mud shorefaces in the geologic record: insights from the modern Amazon dispersal system. In Schieber, J., Zimmerle, W., Sethi, P.S. (eds.) Shales and Mudstones I: Basin studies, Sedimentology, and Paleontology. E. Schweizerbart'sche Verlagsbuchhandlung Stuttgart, 147-161.

Altaner, S.P. (1989). Calculation of K diffusional rates in bentonite beds. Geochimica Cosmochimica Acta, 53: 923-931.

Altaner, S.P., and Ylagan, R.F. (1997). Comparison of structural models of mixed-layer illite/smectite and reaction mechanisms of smectite illitization. Clays and Clay Minerals, 45: 517-533.

Andrews, K., Dyson, D. and Keown, S. (1971). "Interpretation of electron diffraction patterns". Plenum New York.

Aplin, A.C., Yang. Y. And Hansen, S. (1995). Assessment of beta, the compression coefficient of mudstones and its relationship with detailed lithology. Marine and Petroleum Geology, 12 (8), 955-963.

Aplin, A.C., Fleet, A.J. and MacQuaker, J.H.S. (eds.) (1999). Muds and mudstones: physical and fluidflow properties. Geological Society, London, Special Publication. 158, 1-9.

Aplin, A.C. (2000). Mineralogy of modern marine sediments: A geochemical framework. In Vaughan, D.J. & Wogelius, R.A. (eds.) European Mineralogical Union Notes on Mineralogy: Volume 2 Environmental Mineralogy. Eotvos University Press, Budapest. 4, 125-172.

Aplin, A.C., Matenaar, I.F. and van der Pluijm, B. (2003). Influence of mechanical compaction and chemical diagenesis on the microfabric and fluid flow properties of Gulf of Mexico mudstones. Journal of Geochemical Exploration. 78-79. 449-451

Aplin, A.C. Matenaar, I. F., McCarty, D.K. and van der Pluijm B.A. (2005). Influence of Mechanical Compaction and Clay Mineral Diagenesis on the

Microfabric and Pore-Scale Properties of Deep Water Gulf of Mexico Mudstones. (In press).

Archard, G, Stafford, J, Bardwell, K, et al. (1998). A review of techniques used to determine geological and thermal history in the Southern North Sea,: in Duppenbecker, S.J. and Iliffe, J.E. (Eds) Basin Modelling: Practices and Progress, Geological Society, London, Special Publication, 141 pp 117-136.

Armagnac, C., Bucci, J., Kendall, C. G. and Lerche, I. (1989). Estimating the thickness of sediment removed at an unconformity using vitrinite reflectance data. Chapter 13 in: Naeser, N. D; McCulloh, T. H. ed. Thermal history of sedimentary basins—methods and case histories. Berlin,Springer-Verlag.

Artru, P.H., and Gauthier, J. (1968). Evolution géometrique et diagénétique d'une série miogeosynclinale (Lias inférieur à Berriasien) d'après du sondage de Valvignères (France sud-est). In: Bull. Centre Rech. Pau-SNPA, 2, pp. 101-116.

Athy, L.F. (1930.) Density, porosity, and compaction of sedimentary rocks. AAPG Bulletin, 14, 1-24.

Atwater, G.I. and Miller, E.E. (1965). The effect of decrease in porosity with depth on future development of oil and gas reserves in south Louisiana. AAPG Bulletin, 49, 334.

Bahr, D.B., Hutton, E.W.H., Syvitski, J.P., and Pratson, L. (2001). Exponential approximation to compacted sediment porosity profiles. Computers & Geosciences, 27(6): 691-700.

Baráth, I., Kováč, M., Soták J. and Lankreijer. A. (1997). Tertiray collision, metamorphism and basin forming processes in the eastern Slovakia (central Western Carpathians). In: Grecula, P., Hovorka, D. and Putiš, M. (Eds.): Geological Evolution of the Western Carpathians. Miner. Slovaca – monograph, 65-78.

Barker, C. (1996). Thermal Modelling of Petroleum Generation: Theory and Applications. Developments in Petroleum Science, 45, Elsevier Oxford.

Bathurst, R.G.C. (1975). Diagenesis on the Sea Floor. In Carbonate Sediments and their diagenesis. Developments in sedimentaology, 12, 361-413.

Beardsmore, G.R. and Cull, J.P (2001). Crustal Heat Flow; A guide to measurement and Modelling. Cambridge University Press, Cambridge, UK.

Bell, T.E. (1986). Microstructure in mixed-layer illite/smectite and its relationship to the reaction of smectite to illite. Clays and Clay Minerals, 34, No.2, 146-154.

Bennet, R.H., O'Brien, N.R., Hulbert, H. (1991). Determinants of Clay and Shale Microfabric Signatures: Processes and Mechanisms. In Bennett, R.H., Bryant, W.R., Hulbert, M.H. (eds.) Microstructure of Fine-Grained Sediments. Springer Verlag, 5-33.

Bish, D.L. (1994). Quantative X-ray diffraction analysis of soils. In: Quantative Methods in Soil Mineralogy [Ed. By Amonette, J.E. and Zelazny, L.W.], Soil Science Society of America, Madison. 295-308.

Bjørkum, P.A. (1996). How important is pressure in causing dissolution of quartz in sandstones? Journal of Sedimentary research, 66, 1, 147-154.

Bjørlykke, K. (1998). Clay mineral diagenesis in sedimentary basins-a key to the prediction of rock properties. Examples from the North Sea Basin. Clay minerals 33, 15-34.

Boles, J.R. and Franks, S.G. (1979). Clay diagenesis in Wilcox sandstones of southwest Texas: implications of smectite diagenesis on sandstone cementation. Journal of Sedimentary Petrology, 49, 55-70.

Bouma, A.H. (1962). Sedimentology of some flysch deposits. A graphic approach to facies interpretation. Elsevier Publ. Co., Amsterdam.

Bowles, F.A., Bryant, W.R., Wallin, C. (1969). Microstructure of unconsolidated and consolidated marine sediments. Journal of Sedimentary Petrology, 39, 4, 1546-1551.

Bowman, M.B.J. (1998). Cenozoic. In: Glennie, K.W. (Ed.) Petroleum Geology of the North Sea. Basic concepts and recent advances. 4th edition. Blackwell Science, London.

Brewster, B. and Butler, C. O. (1985). Compaction curves. AAPG Bulletin 69: 622-626.

Brewster, J. and Dangerfield, J.A. (1994). Chalk fields along the Lindenes Ridge, Eldfisk. Mar. Petr. Geol. 1, 239-278.

Brindley, G.W. and Brown, G. (1980). Crystal structures of clay minerals and their X-ray identification. Mineralogical Society Monograph No.5, London.

BRITISH STANDARDS 733. part 2 (1987). Pyknometers. Part 2. Methods for calibration and use of pyknometers. London: British Standard Institution.

Brown, A. (2005). Pers. Comms.

Brusewitz, A. M. (1986). Chemical and physical properties of Palaeozoic potassium bentonites from Kinnekulle, Sweden. Clays and Clay Minerals, 34, No.4, 442-454.

Burland, J. B. (1990). On the compressibility and shear strength of natural clays. Geotechnique, 40, No 3, 329-378.

Burst, J. F. (1959). Postdiagenetic clay mineral environmental relationships in the Gulf Coast Eocene. Clays and clay minerals, 6, 327-341.

Buryakovsky, L.A., Djevanshir, R.D. and Chilingar, G.V. (1995). Abnormally-high formation pressures in Azerbaijan and the South Caspian Basin (as related to smectite ↔ illite transformation during diagenesis and catagenesis). Journal of Petroleum Science and Engineering, 13, 203-218.

Cawley, S. (2005). Pers. Comms.

Cebulak, S., Kepinska, B., Marynowski, L. and Pajak, L. (2004). Wspolczesne I przeszle warunki termiczne badanego sektora podhalanskiego systemu geotermalnego. In: Kepinska, B. (Ed.) Badania warunkow termicznych podhalanskiego systmu geotermalnego przy zastosowaniu nowej metody oksyreaktywnej analizy termicznej (OTA) I metod mineralogicznych. Wydawnictwo IGSMiE PAN, Krakow, 80-87 (in Polish).

Chakravarti, I.M., Laha, R.G. and Roy J. (1967). Handbook of Methods of Applied Statistics, Volume I, John Wiley and Sons, pp. 392-394.

Chamley, H. (1989). Clay Sedimentology. Springer-Verlag Berlin Heidelberg.

Charpentier, D., Worden, R.H., Dillon, C.G. and Aplin, A.C. (2003). Fabric development and the smectite to illite transition in Gulf of Mexico mudstones: an image analysis approach. Journal of Geochemical Exploration, 78-79, 459-463.

Christiansson, P., Faleide, J.I., and Berge, A.M. (2000). Crustal structure in the northern North Sea: an integrated geophysical study. In Nøttvedt, A., Larsen, B.T., Olaussen, S., Tørudbakken, B., Skogseid, J., Gabrielsen, R.H., Brekke, H. & Ø. Birkeland, (eds.), Dynamics of the Norwegian Margin. Geological Society of London, Special Publication 167, 15-40

Clauer, N., Srodoň, J., Franců, J. and Šucha, V. (1997). K-Ar dating of illite fundamental particles separated from illite-smectite. Clay Minerals, 32, 181–196.

Cliff, G. and Lorimer, G.W. (1975). The quantitative analysis of thins specimens. Journal of Microscopy, 103, 203-207.

Colton-Bradley, V.A. (1987). Role of pressure in smectite dehydration-effects geopressure and smectite-to-illite alteration. AAPG Bull. 71, 11, 1414-1427.

Corrigan, J. (2003). Pers. Comms.

Craig, J.R. and Vaugan, D.J. (1981). Ore microscopy and ore petrography. John Wiley & Sons, New York

Curtis, C.D., Lipshie, S.R., Oertel, G. and Pearson, M.J. (1980). Clay orientation in some Upper Carboniferous mudrocks, its relationship to quartz content and some inferences about fissility, porosity and compactional history. Sedimentology, 27, 333-339.

Darby, D., Haszeldine, R. S. and Couples, G. D. (1998) Central North Sea overpressures: insights into fluid flow from one- and two-dimensional basin modelling: in Duppenbecker, S.J. and Iliffe, J.E. (Eds) Basin Modelling: Practices and Progress, Geological Society, London, Special Publication. 141 pp 95-107.

De Caritat, P., Hutcheon, I., Walshe, J.L., (1993): Chlorite geothermomerty: a review. Clays and Clay Minerals, 41, 2, 219-239.

de la Fuente, S., Cuadros, J., Fiore, S. and Linares, J. (2002). Electron Microscopy study of volcanic tuff alteration to illite-smectite under hydrothermal conditions. Clays and Clay Minerals; 48(3): 339 - 350.

Delage, P., Lefebvre, G. (1984). Study of a sensitive Champlain Clay and its evolution during consolidation. Canadian Geotechnical Journal, 21, 21-35.

Dewhurst, D.N., Aplin, A.C., Sarda, J.P., Yang, Y. (1998). Compaction-driven evolution of poroperm in natural mudstones: an experimental study. Journal of Geophysical Research, 103, 651-661.

Dewhurst, D.N., Aplin, A.C., Sarda, J.P. (1999). Influence of clay fraction on pore-scale properties and hydraulic conductivity of experimentally compacted mudstones. Journal of Geophysical Research, 104, No.B14, 29261-29274.

Dewhurst, D.N., Aplin, A.C., Yang, Y. (1999). Permeability and fluid flow in natural mudstones. In: Aplin, A.C., Fleet, A.J. and Macquaker, J.H.S. (eds.) Muds and Mudstones: Physical and Fluid Flow Properties. Geological Society, London, Special Publication, 158, 23-43.

Dong, H., and Peacor, D.R. (1996). TEM observations of coherent stacking relations in smectite, I/S and illite of shales: evidence for MacEwan crystallites and dominance of 2M1 polytypism. Clays and Clay Minerals, 44: 257-275.

Drief, A. and Nieto, F. (2000). Chemical composition of smectites formed in clastic sediments. Implications for the smectite-illite transformation. Clay Minerals 35 (4): 665-678.

DTI Oil and Gas website; http://www.og.dti.gov.uk/ (last accessed 12/12/05)

Dunoyer de Segonzac, (1970). The transformation of clay minerals during burial diagenesis and low-grade metamorphism. Sedimentology, 15, 281-346.

Dutta, N.C., (1987). Fluid flow in low permeable porous media: in Migration of hydrocarbons in sedimentary basins, B. Doligez (Ed.), Editions Technip, Paris, France; pp 567–595.

Dzevanshir, R.D., Buryakovsky, L.A., Chilingarian, G.V. (1986). Simple quantitative evaluation of porosity of argillaceous sediments at various depths of burial. Sedimentary Geology, 46, 169-175.

Eberl, D.D. (1993). Three Zones for illite formation during burial diagenesis and metamorphism. Clays and clay minerals, 41, no.1, 26-37.

Elliott, W.C., Aronson, J.L., Matisoff, G. and Gautier, D.L. (1991). Kinetics of the smectite to illite transformation in the Denver Basin: Clay mineral K-Ar data, and mathematical model results. The American Association of Petroleum Geologists Bulletin, 75, No.3, 436-462.

Elliott, W.C., Matisoff, G. (1996). Evaluation of kinetic models for the smectite to illite transformation. Clays and Clay Minerals, 44, 1, 77-87.

Elliott, W.C., Edenfield, A.M., Wampler, J.M., Matisoff, G. and Long, P.E. (1999). The kinetics of the smectite to illite transformation in the Cretaceous bentonites, Cerro Negro, New Mexico. Clays and clay minerals, 47, No.3, 286-296.

England, R.W., Butler, R.W.H. and Hutton, D.H.W. (1992). The role of Palaeocene magmatism in the Tertiary evolution of basins on the NW seaboard, 97-108. In Parker, J.R. (Ed.) Petroleum Geology of Northwest Europe. Proceedings of the 4th Conference, Volume 1.

Eslinger, E.V., Savin, S.M. and Yeh., H.-W. (1979). Oxygen ISOtope geothermometry of diagenetically altered shales. Soc. Econ. Paleo. Miner., Spec. Pub. 26, 113-124.

Fabricius, I.L. (2000). Interpretation of burial history and rebound from loading experiments and occurrence of microstylolites in mixed sediments of Carribean sites 999 and 1001. In Leckie, R.M., Sigurdsson, H., Acton, G.D., Draper, G. (eds.) Proceedings of the Ocean Drilling Program, Scientific Results, 165, 177-190.

Freed, R.L., Peacor, D.R. (1989). Variability in temperature of the smectite/illite reaction in Gulf Coast sediments. Clay Minerals, 24, 171-180.

Frey, M. (1970). The step from diagenesis to metamorphism in pelitic rocks during alpine orogenesis. Sedimentology, 15, 261-279.

Foscolos, A. E. and Kodama, H. (1974). Diagenesis of clay minerals from lower Cretaceous shales from northeastern British Columbia. Clays and Clay Minerals, 22, 319-335.

Galloway, W.E. (1974). Deposition and diagenetic alteration of sandstone in Northeast Pacific arc-related basins: Implications for graywacke genesis. Geological Society of America Bulletin, 85, 379-390.

Garecka, M. (2005). Calcareous nannoplankton from the Podhale Flysch (Oligocene-Miocene, Inner Carpathians, Poland). Studia Geologica Polonica, 124: 353-370.

Garrels, R.M. (1984). Montmorillonite/illite stability diagrams. Clays and Clay Minerals, 32, No.3, 161-166.

Giles, M.R., Indrelid, S.L., James, D.M.D. (1998). Compaction – the great unknown in basin modeling. In Dueppenbecker, S.J. & Iliffe, J.E. (eds.) Basin Modeling: Practice and Progress. Geological Society, London, Special Publication, 141, 15-43.

Glennie, K. W. (1998). Petroleum Geology of the North Se: Basic concepts and recent advances. Blackwell Science. London.

Goodhew, P.J. and Humphreys, F.J. (1988). Electron Microscopy and Analysis, 2nd Edition. Taylor and Francis, London.

Gretner, P.E., (1981). Pore pressure-fundamentals, general ramifications and implications for structural geology (rev.): American Association of Petroleum Geologists Continuing Education Course Note Series 4, 131 p.

Gretner, P.E. and Curtis, C. D. (1982). Role of temperature and time on organic metamorphism. Am. Assoc. Petrol. Geol. Bull. 66, 1124-1149.

Hansen, S. (1996a). A compaction trend for Cretaceous and Tertiary shales on the Norwegian Shelf based on sonic transit times. Petroleum Geosciences, 2, 159-166.

Hansen, S. (1996b). Quantification of net uplift and erosion on the Norwegian Shelf south of 66 N from sonic transit times of shale. Norsk Geologisk Tidsskrift, 76, 245-252.

Haq, B.U., Hardenbol, J. and Vail, P.R. (1988). Mesozoic and Cenozoic chronostratigraphy and cycles of sea-level change. In: Sea-level changes; an integrated approach (Ed. By Wilgus, C.K. et al) pp. 71-108. Soc. Econ. Paleont. Miner. Spec. Publ. 42.

Hedberg, H.D., (1936). Gravitational compaction of clays and shales. American Journal of Sciences, 31, 241-287.

Hegre JA, Pittion JL, Herbin JP, Lopatin NV, (1998). Geochemical modelling in an organic-rich source rock: the Bazhenov Formation: in Duppenbecker, S.J. and Iliffe, J.E. (Eds) Basin Modelling: Practices and Progress, Geological Society, London, Special Publication. 141, 137-155.

Hermanrud, C., Cao, S. and Lerche, I. (1990). Estimates of virgin rock temperature derived from BHT measurements: Bias and Error. Geophysics, 55(7), 924–31.

Hillier, S., Matyas, J., Matter, A. and Vasseur, G. (1995). Illite/smectite diagenesis and its variable correlation with vitrinite reflectance in the Pannonian Basin. Clays and Clay Minerals, 43, 2, 174-183.

Hillier, S. (1999). Use of an air-brush to spray dry samples for X-ray powder diffraction. Clay Minerals, 34, 127-135.

Hillier, S. (2002a). Accurate quantitative analysis of clay and other minerals in sandstones by XRD: comparison of a Rietveld and a reference intensity ratio method and the importance of sample preparation. Clay minerals, 35, 291-302.

Hillier, S (2002b). Spray drying for X-ray powder diffraction preparation. IUCR Commission on Powder Diffraction Newsletter No 27 June 2002. wwwiucr.org/iucr-top/comm/cpd/Newsletter/no27jul2002/index.html

Hillier, S. (2003). Quantitative analysis of clay and other minerals in sandstones by X-ray powder diffraction (XRPD). International Association of Sedimentology, Special Publication, 34, 213-251.

Hillier, S (2005). Pers. Comms.

Hinz, K., Eldholm, M., Block, M. and Skogseid, J. (1992). Evolution of North Atlantic volcanic continental margins, 901-914. In Parker, J.R. (Ed.) Petroleum Geology of Northwest Europe. Proceedings of the 4th Conference, Volume 2.

Hjulstrøm, F. (1955). Transportation of debris by moving water. In Trask, P.D. (ed.) Recent marine sediments. SEPM Spec. Publ., 4, 5-31.

Ho, N.C., Peacor, D.R., van der Pluijm, B.A. (1995). Reorientation of phyllosilicates in the mudstone-to-slate transition at Lehigh Gap, Pennsylvania. Journal of Structural Geology, 17, No.3, 345-356.

Ho, N.C., Peacor, D.R., van der Pluijm, B.A . (1996) Contrasting roles of detrital and authigenic phyllosilicates during slaty cleavage development. Journal of Structural Geology, 18, No.5, 615-623.

Ho, N.C. (1996). X-Ray Pole Figure Analysis. Software developed at the Geological Department, University of Michigan, USA.

Ho, N.C., Peacor, D.R., van der Pluijm, B.A. (1999). Preferred orientation of phyllosilicates in Gulf Coast mudstones and relation to the smectite-to-illite transition. Clays and Clay Minerals, 47, No.4, 495-504.

Ho, N.C., van der Pluijm, B.A., Peacor, D.R. (2001). Static recrystallisation and preferred orientation of phyllosilicates: Michigamme Formation, northern Michigan. Journal of Structural geology, 23, 887-893.

Hoffert, M.I. and Covey, C. (1992). Deriving global climate sensitivity from palaeoclimate reconstructions. Nature, 360, 573-576.

Hoffman, J. and Hower, J. (1979). Clay mineral assemblages as low grade metamorphic geothermometers: application to the trust faulted disturbed belt of Montana, U.S.A. In Schole, P.A., and Schluger, P.R., (eds). Society of Economic Paleontologists and Mineralogists, Special Publication, 26, 55-79.

Honty, M., Uhlik, P., Šucha, V., Čaplovičová, M., Franců, J., Clauer, N. and Biroň, A. (2004). Smectite-to-illite alteration in salt-bearing bentonites (the East Slovak Basin). Clays and Clay Minerals, 52 (5), 533-551.

Hover, V.C., Walter, L.M., Peacor, D.R. and Martini, A.M. (1999). Mg-smectite authigenesis in a marine evaporative environment, Salina Ometepec, Baja California. Clays and Clay Minerals, 47, No.3, 252-268.

Hower, J. and Mowatt, T.C. (1966). The mineralogy of illites and mixed-layer illite-montmorillonites. Amer. Miner., 51. 825-854.

Hower, J.; Eslinger, E.V.; Hower, M.E.; Perry, E.A. (1976). Mechanism of burial metamorphism of argillaceous sediment: 1. Mineralogical and chemical evidence. Geological Society of America Bulletin, 87, 725-737.

Huang, W.L., Longo, J.M. and Pevear, D.R. (1993). An experimentally derived kinetic model for smectite-to-illite conversion and its use as a geothermometer. Clays and clay minerals, 41, No.2, 162-177.

Huggett, J.M. (1995). Formation of authigenic illite in Palaeocene mudrocks from the central North Sea: A study by High Resolution Electron Microscopy. Clays and Clay Minerals, 43, No.6, 682-692.

Huggett, J.M. Gale A.S. and Wray, D.S. (2005). Diagenetic Clinoptilolite and Opal-CT from the Middle Eocene Wittering Formation, Isle of Wight, U.K. Journal of Sedimentary Research; v. 75; no. 4; p. 585-595.

Illife, J. (2005). Pers. Comms.

Inoue, A., Kohyama, N., Kitagawa, R., and Watanabe, T. (1987). Chemical and morphological evidence for the conversion of smectite to illite. Clays and Clay Minerals, 42: 276-287.

Inoue, A., Minato, H. and Utada, M. (1978). Mineralogical properties and occurrences of illite/montmorillonite mixed layer minerals formed from Miocene volcanic glassin Wago-Omono district. Clay Science, 5, 123-136.

International Centre for Diffraction Data, 1996.

Jacob, G., Kisch, H.J., van der Pluijm, B.A. (2000). The relationship of phyllosilicate orientation, X-ray diffraction intensity ratios, and c/b fissility ratios in metasedimentary rocks of the Helvetic zone of the Swiss Alps and the Caledonides of Jaemtland, central western Sweden. Journal of Structural Geology, 22, 245-258.

Jadgozinski, H. (1949). Eindimensionale Fehlordnung in Kristallen und ihr Einfluss auf die Röntgeninterferenzen. I. Berechnung des Fehlordnungsgrades aus den Röntgenintensitäten. Acta Crystallogr, 2: 201-207.

Jensen, R.P., and Doré, A.G., (1993). A recent shelf heating event-fact or fiction. In Doré, A.G., Augustson, JH; Hermann, C.; Steward,. DJ; Sylta, O. (Eds) Basin Modelling: Advances and Applications. Norsk Petroleums-Forening/NPF, Special Publication No. 3. 85-106.

Jiang, W.T., Peacor, D.R. and Merriman R,J. (1990). Transmission and analytical electron-microscopic study of mixed-layer illite smectite formed as an apparent replacement product of diagenetic illite. Clays and Clay Minerals 38 (5): 449-468.

Jiang, W.T., Peacor, D.R. and Buseck, P.R. (1994). Chlorite geothermometry? -contamination and apparent octahedral vacancies. Clays and Clay Minerals, 42, No.5, 593-605.

Karner, S.L. and Schreiber, B.C. (1993). Experimental simulation of plagioclase diagenesis atP-T conditions of 3.5 km burial depth Pure and Applied Geophysics Volume 141, Numbers 2-4, 221 – 247.

Katsube, T.J., Mudford, B.S., Best, M.E. (1991). Petrophysical characteristicsof shales from the Scotian shelf. Geophysics, 56, 1681-1689.

Kázmér, M., Dunkl, I., Frisch, W., Kuhlemann, J. and Ozsvárt, P. (2003). The Palaeogene forearc basin of the Eastern Alps and Western Carpathians: subduction erosion and basin evolution. Journal of the Geological Society, London, 160, 413-428.

Kim, J., Dong, H., Seabaugh, J., Newell, S.W. and Eberl, D.D. (2004). Role of microbles in the smectite-to-illite reaction. Science 303, 830-832.

Kisch, H.J. (1983). Mineralogy and petrology of burial diagenesis (burial metamorphism) and incipient metamorphism in clastic rocks. In Larsen, G., Chlingar, G.V. (eds.) Developments in Sedimentology 25B: Diagenesis in Sediments and Sedimentary Rocks II, Elsevier, 289-493.

Klimentidis, R.E. and MacKinnon, I.D.R. (1986) High-resolution imaging of ordered mixed-layer clays. Clays and Clay Minerals, 34, No.2, 155-164.

Klimentidis, R.E. and MacKinnon, I.D.R. (1986) High-resolution imaging of ordered mixed-layer clays. Clays and Clay Minerals, 34, No.2, 155-164.

Knipe, R.J. (1981). The interaction of deformation and metamorphism in slates. In: Lister, G.S., Behr, H.J., Weber, K. & Zwart, H.J. (Eds) The Effect of Deformation on Rocks. Tectonophysics, 78, 249-272.

Kotarba, M. And Środoń, J. (2003) Pers. comms.

Kranck, K (1991). Interparticle grain size relationships resulting from flocculation. In In Bennett, R.H., Bryant, W.R., Hulbert, M.H. (eds.) Microstructure of Fine-Grained Sediments. Springer Verlag, 125-130.

Kranck, K., Smith, P.C. and Milligan, T.G. (1996a). Grain-size characteristics of fine-grained unflocculated sediments. 1. "One-round" distributions. Sedimentology, 43, 589-596.

Kranck, K., Smith, P.C. and Milligan, T.G. (1996b). Grain-size characteristics of fine-grained unflocculated sediments. 1. "Multi-round" distributions. Sedimentology, 43, 597-606.

Lachenbruch, A.H., and Brewer, M.C. (1959). Dissipation of the temperature effect of drilling a well in Arctic Alaska: U..S. Geological Survey Bulletin 1083-C, p. 73-109

Land, L.S., Milliken, K.L. and McBride, E.F. (1987). Diagenetic evolution of Cenozoic sandstones, Gulf of Mexico sedimentary basin. Sedimentary Geology, 50, 195-225.

Land, L.S., Mack, L.E., Milliken, K.L. and Lynch, F.L. (1997). Burial diagenesis of argillaceous sediment, south Texas Gulf of Mexico sedimentary basin: a re-examination. GSA Bulletin, 109, No.1, 2-15.

Lanson, B., Beaufort, D., Berger, G., Bauer, A., Cassagnabere, A. and Meunier, A. (2002). Authigenic kaolin and illitic minerals during burial diagenesis of sandstones: a review. Clay Minerals. 37, 1-22.

Lee, M. R., Thompson, P., Poeml, P. and Parsons, I. (2003). Peristeritic plagioclase in North Sea hydrocarbon reservoir rocks: Implications for diagenesis, provenance and stratigraphic correlation. American Mineralogist, Volume 88, pages 866–875.

Lerche, I. (1993). Theoretical aspects of problems in basin modelling. In Doré, A.G., Augustson, JH; Hermann, C.; Steward,. DJ; Sylta, O. (Eds) Basin Modelling: Advances and Applications. Norsk Petroleums-Forening/NPF, Special Publication No. 3. 35-66.

Li, G., Peacor, D.R., Coombs, D.S. (1997). Transformation of smectite to illite in bentonite and associated sediments from Kaka Point, New Zealand: contrast in rate and mechanism. Clays and Clay Minerals, 45, No.1, 54-67.

Lynch, F.L. (1997) Frio shale mineralogy and stoichiometry of the smectite-to-illite reaction: the most important reaction in clatic sedimentary diagenesis. Clays and Clay Minerals, 45, No.6, 618-631.

MacEwan, D.M.C., Ruiz, A.R. and Brown, G. (1961). Interstratified Clay Minerals. In: G. Brown (Editor), The X-ray identification and Crystal Structures of Clay Minerals. Miner. Soc. London, 393-445.

Macquaker, J.H.S., Curtis, C.D. & Coleman, M.L. (1997). The role of iron in mudstone diagenesis: Comparison of Kimmeridge clay formation mudstones from onshore and offshore (UKCS) localities. Journal of Sedimentary Research, 67 (5): 871-878 Part A.

Magara, K. (1978). Compaction and Fluid Migration: Practical Petroleum Geology (Developments in Petroleum Science no 9. Elsevier. Amsterdam.

Maltman, A.J. (1981). Primary bedding-parallel fabrics in structural geology. Journal of the Geology Society London, 138, 475-483.

Márton, E., Mastella, L. and Tokarski, A.K. (1999). Large Counterclockwise Rotation of the Inner West Carpathian Paleogene Flysch _ Evidence from Paleomagnetic Investigations of the Podhale Flysch (Poland). Phys. Chem. Earth (A), 24, 645-649.

Marynowski, L. (2005). Pers. Comms.

Masuda, H., Peacor, D.R. and Dong, H. (2001). Transmission electron microscopy study of conversion of smectite to illite in mudstones of the Nankai Trough: contrast with coeval bentonites. Clays and Clay Minerals, 49, No.2, 109-118.

Matenaar, I.F. (2002). Compaction and microfabric rearrangement of fine-grained siliciclastic sediments. Unpublished, PhD thesis. University of Newcastle-Upon-Tyne.

McCarty, D. K. and Reynolds, R. C. (1995). Rotationally disordered illite/smectite in Palaeozoic K-bentonites. Clays and Clay Minerals, 43, 271-284.

McCave, I.N. (1970). Deposition of fine-grained sediment from tidal currents. Journal of Geophysical Research, 75, 4151-4159.

McCave, I.N. (1971). Wave effectiveness at the seabed and its relationship to bedforms and deposition of mud. Journal of Sedimentary Petrology, 41, 89-96.

Merriman, R.J., Roberts, B., Peacor, D.R. (1990). A transmission electron microscope study of white mica crystallite size distribution in a mudstone to slate transitional sequence, North Wales, UK. Contrib. Mineral. Petrol., 106, 27-40.

Merriman, R.J., Roberst, B., Peacor, D.R. and Hirons, S.R. (1995) Strain-related differences in the crystal growth of white mica and chlorite: a TEM and XRD study of the development of metapelitic microfabrics in the Southern Uplands thrust terrane, Scotland. Journal of Metamorphic Geology, 13, 559-576.

Merriman, R.J. and Peacor, D.R. (1998). Very low-grade metapelites: mineralogy, microfabrics and measuring reaction progress. In: Frey, M. and Robinson, D. (Eds.) Low-Grade Metamorphism. Blackwell Science. UK.

Merriman, R.J. (2002). Contrasting clay mineral assemblages in British Lower Palaeozoic slate belts: the influence of geotectonic setting. Clay minerals, 37, 207-219.

Moore, D.M., Reynolds, R.C. Jr. (1997). X-ray diffraction and the identification and analysis of clay minerals 2nd Edition. Oxford University Press, Oxford, New York.

Moore J. (2005). Integration of the sedimentological and petrophysical properties of mudstone samples. Unpublished PhD Thesis. University of Newcastle-Upon-Tyne.

Mumme, W.G., Tsambourakis, G., Madsen, I.C. and Hill, R.J. (1996). Improved petrological modal analyses from X-ray powder diffraction data by use of the Rietveld method 1. Selected sedimentary rocks. Journal of Sedimentary Research, 66, 132-138.

Nadeau, P.H., Tait, J.M., McHardy, W.J. and Wilson, M.J. (1984a). Interstratified XRD characteristics of physical mixtures of elementary clay particles. Clay Minerals. 19, 923-925.

Nadeau, P.H., Wilson, M.J., McHardy, W.J. and Tait, J.M. (1984b). Interstratified clay as fundamental particles. Science, 225, 923-925.

Nadeau, P.H. (1985). The physical dimensions of fundamental clay particles. Clay Minerals, 20, 499-514.

Nadeau, P.H., Wilson, M.J., McHardy, W.J. and Tait, J.M. (1985). The nature of some illitic clays from bentonites and sandstones: Implications for the conversion of smectite to illite during diagenesis. Mineral. Mag. 49, 393-400.

Nadeau, P.H. and Bain, D.C. (1986). Composition of some smectites and diagenetic illitic clays and implications for their origin. Clays and Clay Minerals, 34, No.4, 455-464.

Nadeau, P.H. (1998). Fundamental Particles and the advancement of geoscience: response to "implications of TEM data for the concept of fundamental particles". The Canadian Mineralogist, 36, 1409-1414.

Nadeau, P.H., Peacor, D.R., Yan, J. and Hillier, S. (2002). I-S precipitation in pore space as the cause of geopressuring in Mesozoic mudstones, Egersund Basin, Norwegian continental shelf. American Mineralogist. 87, 1580-1589.

Neuzil C.E. (1994). How permeable are clays and shales? Water Resources Research, 22, 2007-2020.

Nieto, F., Ortega-Huertas, M., Peacor, D.R. and Arostegui, J. (1996). Evolution of illite/smectite from early diagenesis through incipient metamorphism in sediments of the Basque-Cantabrian Basin. Clays and clay minerals, 44, 304-323.

Oakman, C.D. and Partington, M.A. (1998). Cretaceous. In: Glennie, K.W. (Ed.) Petroleum Geology of the North Sea. Basic concepts and recent advances. 4th edition. Blackwell Science, London.

O'Brien, N.R. (1970). The fabric of shale – an electron microscope study. Sedimentology, 15, 229-246.

O'Brien, N.R. (1987). The effects of bioturbation on the fabric of shale. Journal of Sedimentary Petrology, 57, 449-455.

O'Brien, N.R., Slatt, R.M. (1990). Argillaceous Rock Atlas, Springer-Verlag, New York.

O'Brien, N.R., Pietraszek-Mattner, S. (1998). Origin of the fabric of laminated fine-grained glaciomarine deposits. Journal of Sedimentary Research, 68, 5, 832-840.

Oertel, G. (1970). Deformation of a slaty, lapillar tuff in the Lake District, England. GSA Bulletin, 81, 1173-1188.

Oertel,, G., Curtis, C.D. (1972). Clay-ironstone concretion preserving fabrics due to progressive compaction. GSA Bulletin, 83, 2597-2606.

Oertel, G. (1983). The relationship of strain and preferred orientation of phyllosilicate grains in rocks – a review. Tectonophysics, 100, 413-447.

Oertel, G., Engelder, T., Evans, K. (1989). A comparison of the strain of crinoid columnals with that of their enclosing silty and shaly matrix on the Appalachian Plateau, New York. Journal of Structural Geology, 11, No.8, 975-993.

Okiongbo, K. S., (2005). Volumetrics of Petroleum Generation and Compaction of the Kimmeridge Clay Formation. Unpublished PhD Thesis. University of Newcastle-Upon-Tyne.

Olsen, H. W. (1962). Hydraulic flow through saturated clays. Clays and Clay Minerals, 9, 131-162.

Olszewska, B. W. and Wieczorek. J. (1998). The Palaeogene of the Podhale Basin (Polish Inner Carpathians) – micropalaeontological perspective. Przeglad Geologiczny, 46, 721-728.

Page, R.H., Wenk, H.R. (1979). Phyllosilicate alteration of plagioclase studied by transmission electron microscopy. Geology, 7, 393-397.

Peacor, D.R. (1998). Implications of TEM data for the concept of fundamental particles. The Canadian Mineralogist, 36, 1397-1408.

Pearson, M.J., Watkins, D. & Small, J.S. (1982). Clay diagenesis and organic maturation in northern North Sea sediments. Proceedings of the International Clay Conference, Bologna and Pavia, 665-675.

Pearson, F.J. (1999). What is the porosity of a mudrock? In: Aplin, A.C., Fleet, A.J. and Macquaker, J.H.S. (eds.) Muds and Mudstones: Physical and Fluid Flow Properties. Geological Society, London, Special Publication, 158, 9-21.

Perry, E. and Hower, J. (1970). Burial diagenesis in Gulf Coast pelitic sediments. Clays and Clay Minerals, 18, 165-177.

Poelchau, H.S., Baker, D.R., Hantschel, T., Horsfield, B. and Wygrala, B. (1997). Basin simulation and the design of the conceptual basin model. Pp. 5–70 in: Petroleum and Basin Evolution (D.H. Welte, B. Horsfield and D.R. Baker, editors). Springer, Berlin, Heidelberg, New York.

Pollastro, R.M. (1985). Mineralogical and morphological evidence for the formation of illite at the expense of illite/smectite. Clays and Clay Minerals, 33: 265-274.

Pollastro, R. M. (1993). Considerations and applications of the illite/smectite geothermometer in hydrocarbon-bearing rocks of Miocene to Mississippian age: Clays and Clay Minerals, v. 41, p. 119-133.

Potter, P.E., Matnard, J.B., and Pryor, W.A. (1980). Sedimentology of Shale. Springer Verlag, New York.

Powers, M. C. (1967). Fluid-release mechanisms in compacting marine mudrocks and their importance in oil exploration. American Association of Petroleum Geologists, Bulletin, 51, 1240-1254.

Pytte, A. and Reynolds, R.C., Jr. (1989). The kinetics of the smectite ti illite reaction in contact metamorphic shales. In: The thermal history of Sedimentary Basins: Methods and Case Histories, Naeser, N.D. and McCulloch, T.H. (Eds.) Springer-Verlag, New York, 133-140.

Radke, M. and Welte, D.H. (1981). The Methylphenanthrene Index (MPI): A Maturity Parameter based on Aromatic Hydrocarbons. In Bjøroy M. (Ed.): Advances in Organic Geochemistry 1981. 504-512.

Raiga-Clemenceau, L., Martin, J. P., and Nicoletis, S. (1988). The concept of acoustic formation factor for more accurate porosity determination from sonic transit time data. The Log Analysist, 29, 54-59.

Ramseyer, K. and Boles, J.R. (1986). Mixed-layer illite/smectite minerals in Tertiary sandstones and shales, San Joaquin Basin, California. Clays and Clay Minerals, 34, No.2, 115-124.

Rask, J.H., Bryndzia, L.T., Braunsdorff, N.R. and Murray, T.E. (1997). Smectite illitization in Pliocene-age Gulf of Mexico mudstones. Clays and Clay Minerals, 45, No.1, 99-109.

Raymer, L. L., Hunt, E. R., Gordner, J. S. (1980). An improved sonic transit time to porosity transformation. Society of Professional Well Log Analysts-21st annual logging symposium, 1-13.

Reading, H. G., & Collinson, J. D. (1996). Clastic coasts. In (Ed. Reading, H. G.) Sedimentary Environments: Processes, Facies and Stratigraphy. Blackwell Science. London

Rieke, H.H.; Chilingarian, G.V. (1974). Compaction of argillaceous sediments. Developments in Sedimentology 16, Elsevier.

Rock, G. J. (2003). The iron geochemistry of mudstones and metapelites. Unpubl. PhD Thesis University of Newcastle-Upon-Tyne.

Rospondek, M. and Marynowski, L. (2004). Phenyl-Polyaromatic compounds and terphenyls in the Polish Carpathian sedimentary rocks. Mineralogical Society of Poland – Special Papers. Volume 24. 341-344

Roux, B., Sanyal, S.K., and Brown, S.L., (1980). An improved approach to estimating true reservoir temperature from transient temperature data, SPE-8888: Society of Petroleum Engineers, California Regional Meeting preprint, 8 p.

Schegg, R. and Leu, W. (1996). Clay mineral diagenesis and thermal history of the Thonex Well, Western Swiss Molasse Basin. Clays and Clay Minerals, 44, No.5, 693-705.

Schegg, R., and Leu, W., (1998). Analysis of erosion events and paleogeothermal gradients in the North Alpine Foreland Basin of Switzerland,: in Duppenbecker, S.J. and Iliffe, J.E. (Eds) Basin Modelling: Practices and Progress, Geological Society, London, Special Publication. 141 pp 137-155.

Scheidegger, A. E. (1974). The physics of flow through porous media. 3rd edition. University of Toronto Press.

Schieber, J. (1998). Deposition of mudstones and shales: overview, problems and challenges. In Schieber, J., Zimmerle, W., Sethi, P.S. (eds.) Shales and Mudstones I: Basin studies, Sedimentology, and Paleontology. E. Schweizerbart'sche Verlagsbuchhandlung Stuttgart, 131-146.

Schieber, J., Zimmerle, W. (1998). The history and promise of shale research. In Schieber, J., Zimmerle, W., Sethi, P.S. (eds.) Shales and Mudstones I: Basin studies, Sedimentology, and Paleontology. E. Schweizerbart'sche Verlagsbuchhandlung Stuttgart, 1-10.

Schlömer, S. and Krooss, B.M. (1997). Experimental characterisation of the hydrocarbon sealing efficiency of cap rocks. Marine and Petroleum Geology, 14, 565-580.

Schmitz, U. (1994). Die Britishe und Norwegische Nordsee. In: Kilke, H. (Ed.) Regionale Erdöl- und Erdgas- geolgie der Erde. Gebrűder Borntraeger, Berlin.

Scholle, P.A., Tirsgaard, H., & Clausen, L. (2006). Predictive Modeling and Timing of Porosity-Preserving Events in Maastrichtian-Danian Chalk Reservoirs of the North Sea. The Deep Frontier: Advances in Reservoir Quality Prediction (AAPG) AAPG Annual Convention, April 9-12.

Schweitzer, P.N., (1993). Modern average global sea-surface temperature. US Geological Survey Digital Data Series, CD-ROM.

Sclater, J.G., Christie, P.A.F. (1980). Continental stretching: an explanation of the post-mid-cretaceous subsidence of the Central North Sea basin. Journal of Geophysical Research, 85, B7, 3711-3739.

Severin, K.P. (2004). Energy dispersive spectrometry of common rock forming minerals. Springer. Kluwer Academic Publish. Amsterdam.

Sintubin, M. (1994). Clay fabrics in relation to the burial history of shales. Sedimentology, 41, 1161-1169.

Skempton, A. W. (1970). The consolidation of clays by gravitational compaction. Q. J. geol. Lond., 125, 373-411.

Snyder, R.L. and Bish, D.L. (1989). Quantative analysis: In: Modern Powder Diffraction, Reviews in Mineralogy Vol. 20 [Eds; Bish, D.L. and Post, J.E.] Mineralogy Society of America, Washington, DC.101-144.

Son, B. K., Yoshimura, T. and Fukasawa, H. (2001). Diagenesis of dioctahedral and trioctahedral smectites from alternating beds in Miocene to Pleistocene rocks of the Niigata Basin, Japan. Clays and clay minerals, 49, 333-346.

Sorby, H.C. (1853). On the origin of slaty cleavage, Edinb. New Philos. J., 10, 136.

Sorby, H.C. (1856). On the theory of slaty cleavage, Phil. Mag., 12, 127.

Spangler, W. M. L., and Jenne, R. L. (1990). Dataset TD-9641 (U.S. Monthly Normals of Temperature and Precipitation). In "World Monthly Surface Station Climatology and Associated Datasets" (1994 ed.). World Weather Disc Associates, Seattle.

Środoń, J. (1975). Mixed-layer smectire/illites in the bentonites and tonsteins of the upper Silesian coal basin. Polska Akademia Nauk. Komisja Nauk Mineralogicznych. Prace Mineralogiczne 49. Krokow.

Środoń, J., and Eberl, D.D. (1984). Illite. In: Micas, Reviews in Mineralogy (Ed S.W. Bailey), 13, pp. 495-544. Mineralogical Society of America, Washington, D.C.

Środoń, J., Morgan, D.J., Eslinger, E.V., Eberl, D.D. and Karlinger, M. R. (1986). Chemistry of illite/smectite and end-member illite. Clays and Clay Minerals, 34, No.4, 368-378.

Środoń, J., Elsass, F., McHardy, W.J. and Morgan, D.J. (1992). Chemistry of illite-smectite inferred from TEM measurements of fundamental particles. Clay Minerals. 27, 137-158.

Środoń, J. (1995). Reconstruction of maximum palaeotemperatures at present erosional surface of the Upper Silesia Basin, based on the composition of illite/smectite in shales. Studia Geologica Polonica, 108, 9-20.

Środoń, J. (2003). Pers. Comms.

Środoń, J., Kotarba, M., Biroń, A., Such, P., Clauer, N. and Wójtowicz, A. (In press). Diagenetic history of the Podhale-Orava Basin and the underlying Tatra sedimentary structural unit (Western Carpathians): Evidence from XRD and K-Ar of illite-smectite. Clay Minerals.

Suggate, R.P. (1998). Relationships between depth of burial, vitrinite reflectance and geothermal gradient. Journal of Petroleum Geology, 21, 5-32.

Swarbrick, R.E., Osborne, M.J., Grunberger, D., Yardley, G.S., MacLeod, G., Aplin, A.C., Larter, S.R., Knight, I., Auld, H.A. (2000). Integrated study of the Judy Field (Block 30/7a) – an overpressured Central North Sea oil/gas field. Marine and Petroleum Geology, 17, 993-1010.

Sweeney, J.J. & Burnham, A.K. (1990). "Applications of a Simple Model of Vitrinite Reflectance Based on Chemical Kinetics," AAPG Bulletin 74, 1559-1570

Tari, G., Báldi, T. and Báldi-Beke, M. (1993). Paleaogene retroarc flexural basin beneath the Neogene Pannonian Basin: a geodynamic model. Tectonophysics, 226: 455.

Teichmüller, M. (1970). Bestimmung des Inkohlungsgrades von kohligen Einschlussen in Sedimenten des Oberrheingrabens: ein Hilfsmittel bei der Klärung geothermischer Fragen. In: Graben Problems. Illies, J.H. and Müller, S. (Eds) Upper Mantle Sci. Proj. Sci. Rept., 27, 124-142.

Terzaghi, K. (1921). Die physikalischen Grundlagen des technisch-geologischen Gutachtens. Zeitschrift des Österreichischen Ingeneurs und Architekten Verein, September Issue, Table V.

Thyberg, B.I., Jordt, H., Bjørlykke, K. and Faleide, J.I. (2000). Relationship between sequence stratigraphy, mineralogy and geochemistry in Cenozoic sediments of the northern North Sea. In Nøttvedt, A., et al (Eds.) Dynamics of the Norwegian margin. Geological Society, London, Special Publication, 167, 245-272.

Thyne, G., Boudreau, B.P., Ramm, M. & Midtbø, R.E. (2001). Simulation of Potassium feldspar dissolution and illitization in the Statfjord Formation, North Sea. AAPG Bulletin, 85, No.4, 621-635.

Tomita, K., Yamane, H. and Kawano, M. (1993). Synthesis of smectite from volcanic glass at low temperatures. Clays and Clay Minerals. 41, no.6. 655-661.

Underhill, J.R. (1998). Jurassic. In: Glennie, K.W. (Ed.) Petroleum Geology of the North Sea. Basic concepts and recent advances. 4th edition. Blackwell Science, London.

Ungerer, P., Burrus, J., Doligez, B. Chenet, P. Y. and Bessis, F. (1990). Basin Evaluation by Integrated Two Dimensional Modeling of Heat Transfer, Fluid Flow, Hydrocarbon Generation, and Migration : AAPG Bulletin, v. 74, p.309.

van der Pluijm B. A., Lee J. H., Peacor D. R. (1988). Analytical electron microscopy and the problem of potassium diffusion. Clay and Clay Minerals, 36, 498 504.

van der Pluijm, B.A., Ho, N. & Peacor, D.R. (1994). High-resolution X-ray texture goniometry. Journal of Structural Geology, 16, 1029-1032.

van der Pluijm, B.A., Ho, N. & Peacor, D.R. and Meeriman, R.J. (1998). Contradictions of slate formation resolved? Nature, 392, 348.

Van der Pluijm, B. A., (2005). Pers. Comms.

Vasseur, G., Djeranmaigrei, I., Grunberger, D., Rousset, G., Tessier, D., and Velde, B. (1995). Evolution of structural and physical parameters of clays during experiemental compaction. Marine and Petroleum Geology, 12 (8), 941-954.

Velde, B., Suzuki, T. and Nicot, E. (1986). Pressure-Temperature-Composition of illite/smectite mixed-layer minerals: Niger delta mudstones and other examples. Clays and Clay Minerals, 34, 435–441

Velde, B. (1992). Introduction to clay minerals: chemistry, origins, uses and environmental significance. Chapman & Hall. London

Velde, B. and Vasseur, G. (1992). Estimation of the diagenetic smectite to illite transformation in time-temperature space. American Mineralogist, 77, 967-976.

Velde, B. (1995). Use of the smectite to illite conversion model: effects of order of magnitude. Bull. Centres Rech. Explor.-Prod. Elf Aqutaine, 19, 1, 235-242.

Vik, E. & Hermanrud, C. (1993). Transient thermal effects of rapid subsidence in the Haltenbanken area. In Doré, A.G., Augustson, JH; Hermann, C.; Steward,. DJ; Sylta, O. (Eds) Basin Modelling: Advances and Applications. Norsk Petroleums-Forening/NPF, Special Publication No. 3. 107-118.

Walker, J. R., (1993). Chlorite polytype geothermometry, Clays and Clay Minerals, 41, 260-267.

Wang, H., Frey, M. and Stern, W.B. (1996). Diagenesis and metamorphism of clay minerals in the Helvetic Alps of Eastern Switzerland. Clays and Clay Minerals, 44, No.1, 96-112.

Waples, D.W., (1998). Basin modelling: how well have we done? In: Düppenbecker, S.J. and Iliffe, J.E. (eds) Basin Modelling: Practices and Progress, Geologic Society London, Special Publications, 141, 1-14.

Weaver, C.E. (1989). Clays, Muds and Shales. Elsevier. Oxford.

Wenk, H.R. (1985). Measurement of pole figures. In Wenk, H.R. (ed.) Preferred orientation in deformed metals and rocks: An introduction to modern texture analysis. Academic Press, INC., 11-48.

Westwalewicz-Magilska, E. (1986). Nowe spojrzenie na genezę osadów fliszu podhalańskiego. Przeglad Geologiczny 12, 690-698 (in Polish).

Whittaker, E. T. and Robinson, G. (1967). "Normal Frequency Distribution." In The Calculus of Observations: A Treatise on Numerical Mathematics, 4th ed. New York: Dover, pp. 164-208.

Wieczorek, J. (1989). Model Hecho dla fliszu podhalańskiego? Przeglad Geologiczny., 37 419-423.

Wieczorek, J. and Olszewska, B. (1999). Mesozoic basement of the Podhale Basin (Western Carpathians, Poland). Geologica Carpathica, 50, 84-86.

Worden, R.H., Ruffell, A.H., and Cornford, C. (2000). Surface temperature, sequence stratigraphy and deep burial diagenesis. Clay Minerals, 35, 13-23.

Worden, R.H., Charpentier, D., Aplin, A.C. and Fisher, Q.J (2004). Structural Diagenesis: Fundamental Advances and New Applications from a Holistic View of Mechanical and Chemical Processes Mineralogical and Microstructural Variations During Mudstone Diagenesis: Gulf of Mexico and North Sea. February 8-11, 2004 — Austin, Texas.

Worden, R.H., Charpentier, D., Fisher, Q.J. and Aplin, A.C. (2005). Fabric development and the smectite to illite transition in Upper Cretaceous mudstones from the North Sea: an image analysis approach. In:Shaw, R.P. (ed.), Understanding the Micro to Macro Behaviour of Rock-Fluid Systems. Geological Society, London, Special Publications,
249, 103-114

Wyllie, M. R. J., Gregory, A. R., and Gardner, G . H. F. (1956). Elastic wave velocities in heterogeneous and porous media. Geophysics, 21, 41-70.

Yang, Y. and Aplin, A.C. (1997). A method for the disaggregation of mudstones. Sedimentology, 44, 559-562

Yang, Y., Aplin, A.C. (1998). Influence of lithology and compaction an the pore size distribution and modeled permeability of some mudstones from the Norwegian margin In: Marine and Petroleum Geology, 15, 163-175.

Yang, Y.L. and Aplin, A.C., (2004). Definition and practical application of mudstone porosity-effective stress relationships. Petroleum Geoscience, 12, 153-162.

Zetaware INC. http://www.zetaware.com/support/ First accessed 09/09/05

Ziegler, P.A. (1999). Evolution of the Artic-North Atlantic and the Western Tethys—A visual presentation of a series of palaeogeographic-palaeotectonic maps. Search and Discovery Article #30002.

8.0: Appendices:

Appendix 2.1. Chochołów PIG-1 2-theta, and the pole figures for the measured peaks, illite-smectite and kaolinite/chlorite along with their measured m.r.d. values. Depth values are in Actual Burial Depth, (ABD) and Proposed Maximum Burial Depth (MBD).

Chi-04_2-theta

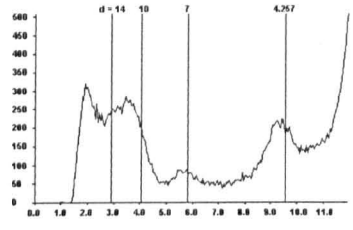

(ABD) 193[m] (MBD) 3693[m]

Chi-04 illite/smectite

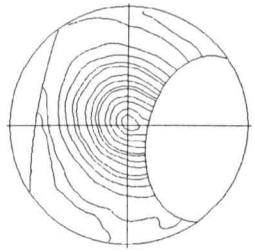

m.r.d. 3.97

Chi-04 chlorite-kaolinite

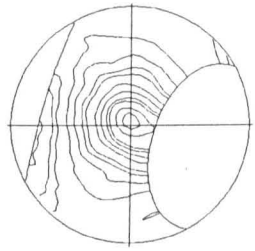

m.r.d. 3.63

Chi-06_2-theta

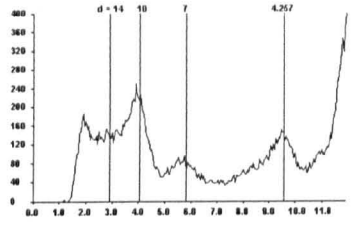

(ABD) 280[m] (MBD) 3780[m]

Chi-06 illite/smectite

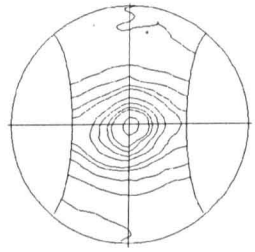

m.r.d. 3.38

Chi-06 chlorite-kaolinite

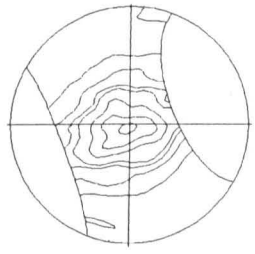

m.r.d. 2.84

Chi-06_2-theta

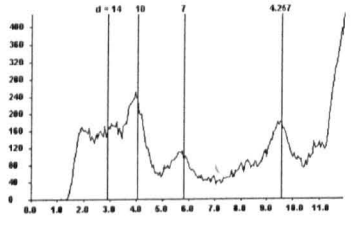

(ABD) 280[m] (MBD) 3780[m]

Chi-06 illite/smectite

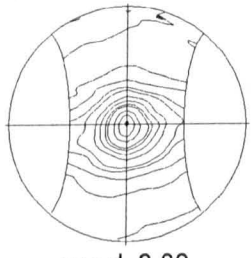

m.r.d. 3.80

Chi-06 chlorite-kaolinite

m.r.d. 2.98

Chi-12_2-theta

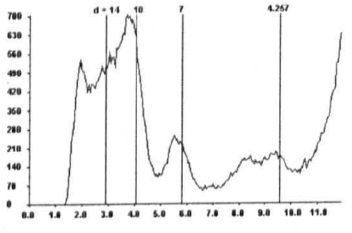

(ABD) 513[m] (MBD) 4013[m]

Chi-12 illite/smectite

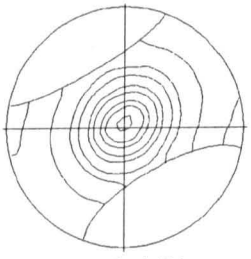

m.r.d. 4.61

Chi-12 chlorite-kaolinite

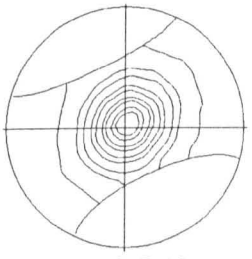

m.r.d. 5.43

Chi-20_2-theta

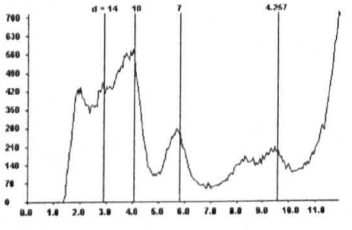

(ABD) 820[m] (MBD) 4320[m]

Chi-20 illite/smectite

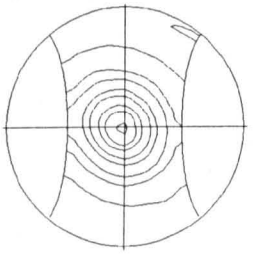

m.r.d. 4.61

Chi-20 chlorite-kaolinite

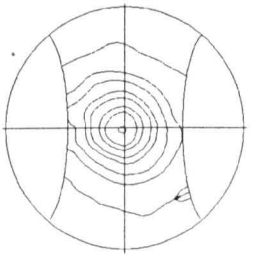

m.r.d. 4.55

Chi-23_2-theta

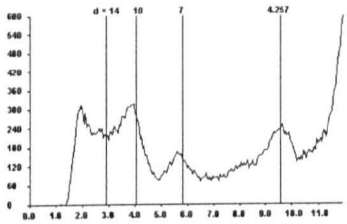

(ABD) 1031[m] (MBD) 4531[m]

Chi-23 illite/smectite

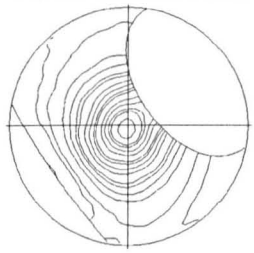

m.r.d. 4.16

Chi-23 chlorite-kaolinite

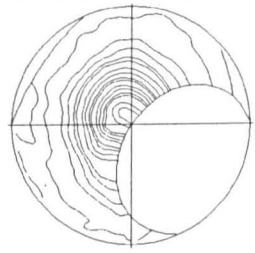

m.r.d. 4.72

Chi-28_2-theta

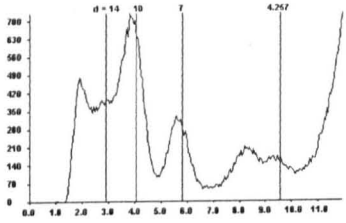

(ABD) 1283[m] (MBD) 4783[m]

Chi-28 illite/smectite

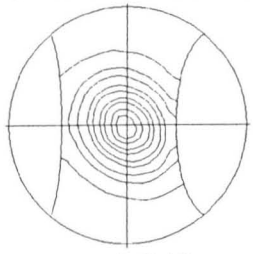

m.r.d. 5.18

Chi-28 chlorite-kaolinite

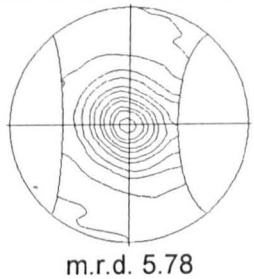

m.r.d. 5.78

Chi-38_2-theta

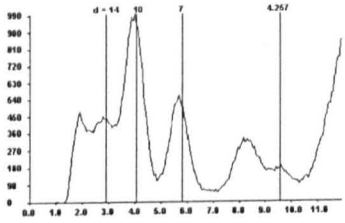

(BHD) 1671[m] (MBD) 5171[m]

Chi-38 illite/smectite

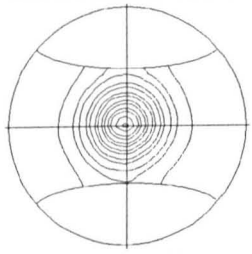

m.r.d. 6.99

Chi-38 chlorite-kaolinite

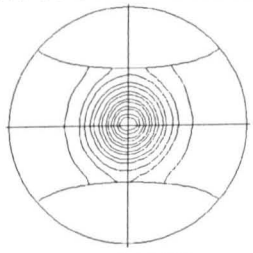

m.r.d. 7.36

Chi-38_2-theta

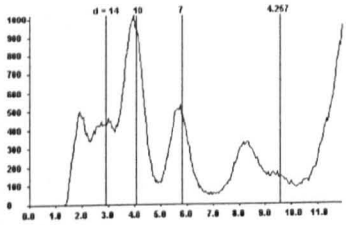

(ABD) 1671[m] (MBD) 5171[m]

Chi-38 illite/smectite

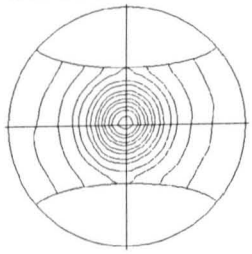

m.r.d. 6.87

Chi-38 chlorite-kaolinite

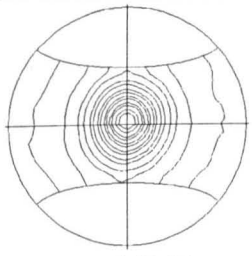

m.r.d. 7.44

Chi-44_2-theta

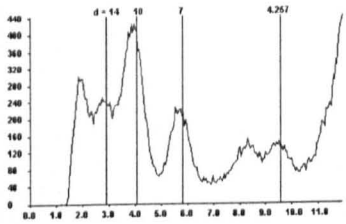

(ABD) 2011[m] (MBD) 5511[m]

Chi-44 illite/smectite

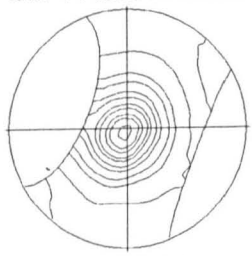

m.r.d. 5.67

Chi-44 chlorite-kaolinite

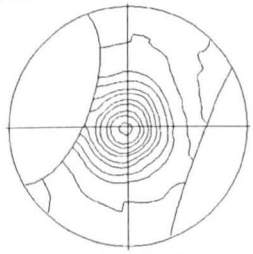

m.r.d. 5.68

Chi-56_2-theta

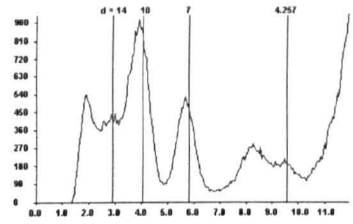

(ABD) 2410[m] (MBD) 5910[m]

Chi-56 illite/smectite

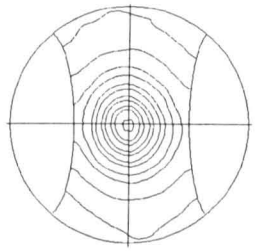

m.r.d. 5.65

Chi-56 chlorite-kaolinite

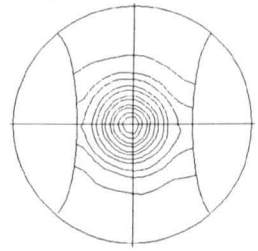

m.r.d. 6.29

Chi-60_2-theta

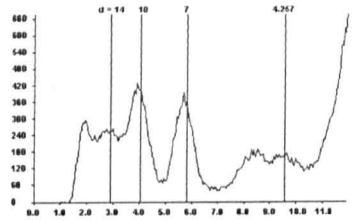

(ABD) 2611[m] (MBD) 6111[m]

Chi-60 illite/smectite

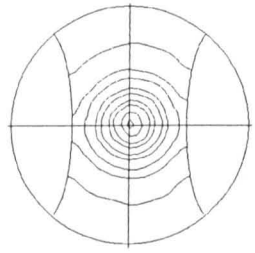

m.r.d. 5.00

Chi-60 chlorite-kaolinite

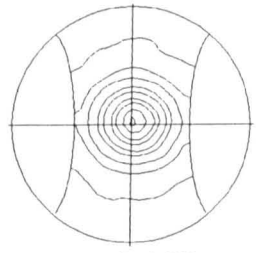

m.r.d. 4.96

Chi-60_2-theta

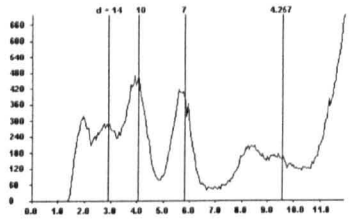

(ABD) 2611[m] (MBD) 6111[m]

Chi-60 illite/smectite

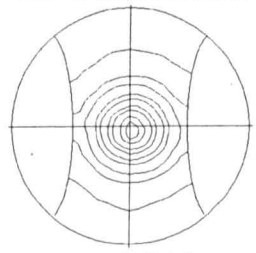

m.r.d. 5.14

Chi-60 chlorite-kaolinite

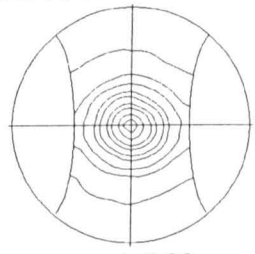

m.r.d. 5.20

Chi-66_2-theta

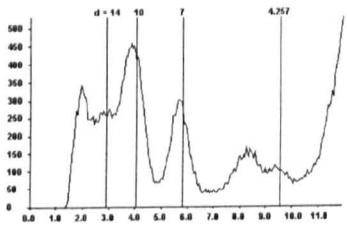

(ABD) 2967[m] (MBD) 6467[m]

Chi-66 illite/smectite

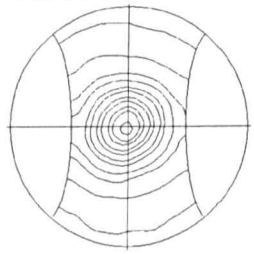

m.r.d. 5.78

Chi-66 chlorite-kaolinite

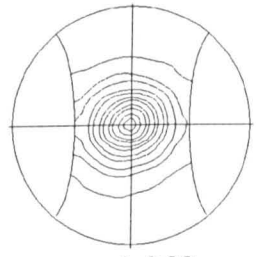

m.r.d. 6.23

Appendix 2.1 continured. Bukowina Tatrzańska PIG-1 2-theta, and the pole figues for the measured peaks, illite-smectite and kaolinite/chlorite along with their measured m.r.d. values, Actual Burial Depth (ABD) and Proposed Maximum Burial Depths (MBD).

BkT01_2-theta

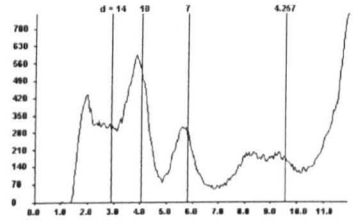

(ABD) 102[m] (MBD) 6208[m]

BkT01 illite/smectite

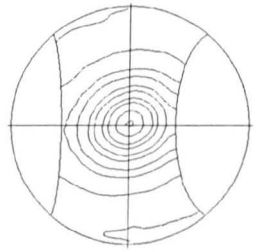

m.r.d. 4.92

BkT01 chlorite-kaolinite

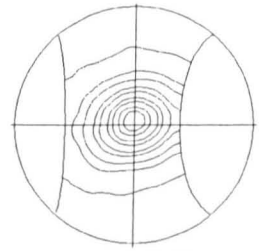

m.r.d. 5.27

BkT06_2-theta

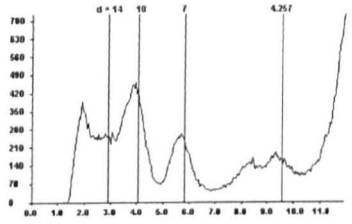

(ABD) 293[m] (MBD) 6399[m]

BkT06 illite/smectite

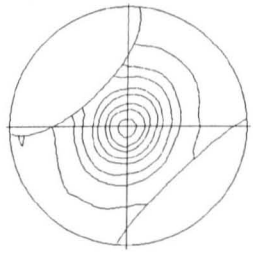

m.r.d. 4.75

BkT06 chlorite-kaolinite

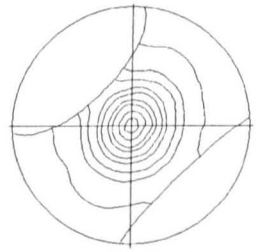

m.r.d. 5.12

BkT12_2-theta

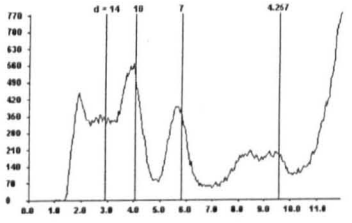

(ABD) 610[m] (MBD) 6716[m]

BkT12 illite/smectite

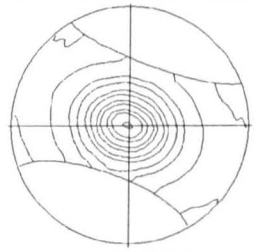

m.r.d. 5.61

BkT12 chlorite-kaolinite

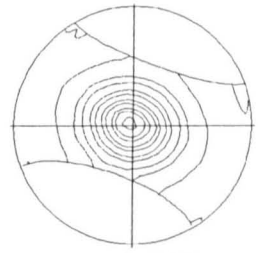

m.r.d. 5.66

BkT17_2-theta

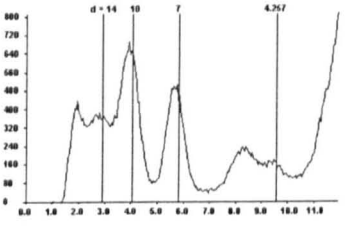

(ABD) 902[m] (MBD) 7008[m]

BkT17 illite/smectite

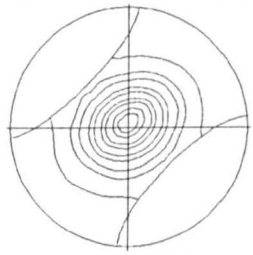

m.r.d. 5.31

BkT17 chlorite-kaolinite

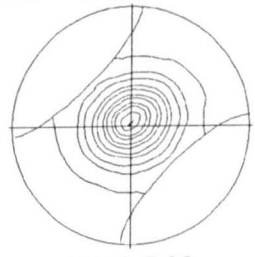

m.r.d. 5.93

BkT23_2-theta

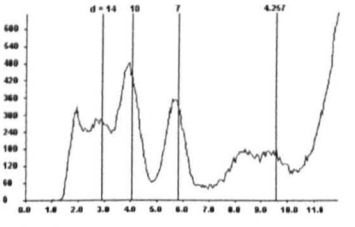

(ABD)1261[m] (MBD) 7367[m]

BkT23 illite/smectite

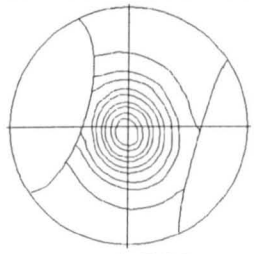

m.r.d. 5.38

BkT23 chlorite-kaolinite

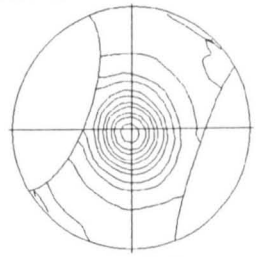

m.r.d. 5.82

BkT28_2-theta

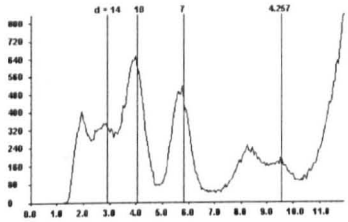

(ABD)1594[m] (MBD) 7700[m]

BkT28 illite/smectite

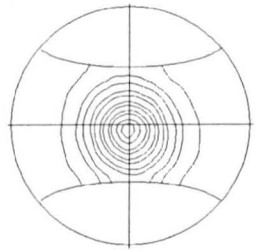

m.r.d. 6.13

BkT28 chlorite-kaolinite

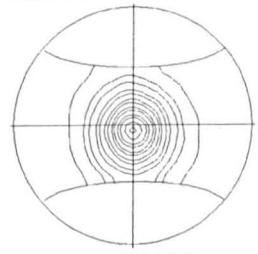

m.r.d. 7.00

BkT28_2-theta

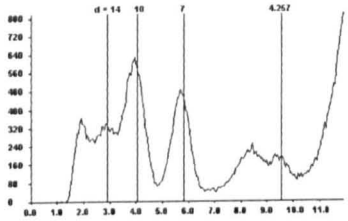

(ABD) 1594[m] (MBD) 7700[m]

BkT28 illite/smectite

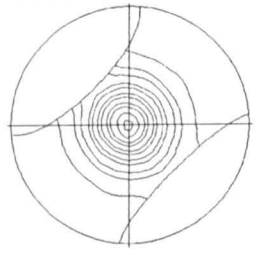

m.r.d. 6.03

BkT28 chlorite-kaolinite

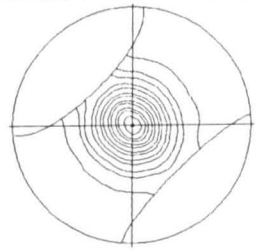

m.r.d. 6.96

BkT35_2-theta

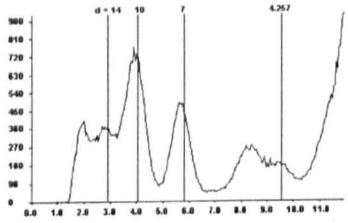

(ABD) 1904[m] (MBD) 8010[m]

BkT35 illite/smectite

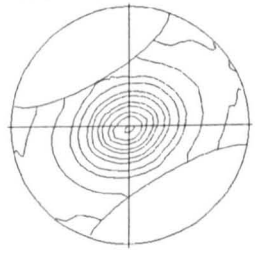

m.r.d. 5.65

BkT35 chlorite-kaolinite

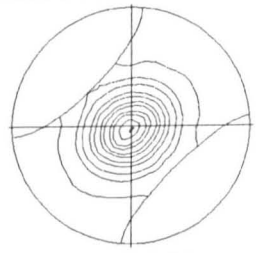

m.r.d. 5.93

BkT41_2-theta

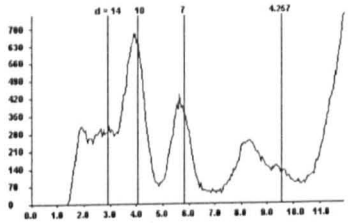

(ABD)2200[m] (MBD) 8306[m]

BkT41 illite/smectite

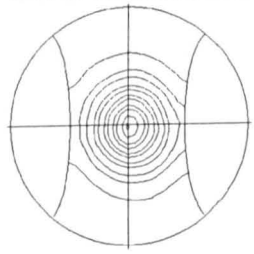

m.r.d. 5.94

BkT41 chlorite-kaolinite

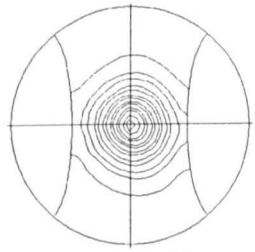

m.r.d. 7.18

BkT41_2-theta

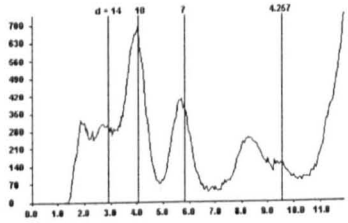

(ABD)2200[m] (MBD) 8306[m]

BkT41 illite/smectite

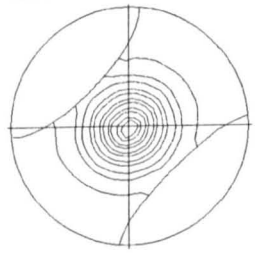

m.r.d. 6.29

BkT41 chlorite-kaolinite

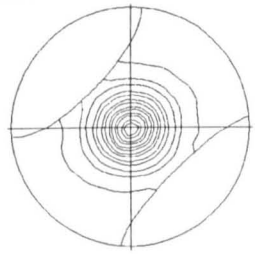

m.r.d. 7.32

Appendix 3.1: Structural Formulae for the illite and smectite standards as measured by SEM-EDS.

Illite standard

(Al	Fe	Mg	Ti)	Octahedral. Total	(Si	Al)	O10(OH)2	Ca	K
1.48	0.24	0.22	0.02	1.96	3.76	0.24		0.008	0.54
1.48	0.26	0.23	0.02	1.99	3.75	0.25		0.009	0.48
1.44	0.24	0.18	0.05	1.91	3.79	0.21		0.000	0.61
1.43	0.24	0.22	0.05	1.93	3.77	0.23		0.000	0.59
1.64	0.19	0.17	0.01	2.01	3.69	0.31		0.000	0.44
1.42	0.30	0.20	0.02	1.93	3.70	0.30		0.016	0.65
1.52	0.21	0.19	0.02	1.95	3.78	0.22		0.000	0.55
1.12	0.31	0.14	0.28	1.85	3.73	0.27		0.009	0.58
1.53	0.20	0.21	0.01	1.96	3.76	0.24		0.000	0.57
1.47	0.24	0.20	0.02	1.93	3.81	0.19		0.000	0.56
1.50	0.21	0.18	0.03	1.92	3.76	0.24		0.000	0.64
1.67	0.12	0.12	0.02	1.93	3.53	0.47		0.000	0.78
1.46	0.25	0.18	0.03	1.92	3.76	0.24		0.014	0.62
1.44	0.27	0.17	0.02	1.90	3.87	0.13		0.001	0.58
1.46	0.24	0.23	0.03	1.96	3.75	0.25		0.000	0.57
1.44	0.24	0.16	0.01	1.85	3.99	0.01		0.001	0.58
1.42	0.29	0.21	0.02	1.94	3.74	0.26		0.000	0.64
0.92	0.42	0.12	0.42	1.89	3.48	0.52		0.004	0.55
1.52	0.14	0.15	0.05	1.86	3.71	0.29		0.000	0.80
1.48	0.25	0.20	0.01	1.94	3.79	0.21		0.000	0.58
1.46	0.26	0.20	0.01	1.93	3.76	0.24		0.007	0.63
1.35	0.33	0.18	0.04	1.90	3.74	0.26		0.003	0.70
1.48	0.22	0.21	0.03	1.94	3.79	0.21		0.003	0.56
1.49	0.16	0.19	0.03	1.88	3.87	0.13		0.000	0.66
1.46	0.28	0.22	0.02	1.98	3.70	0.30		0.006	0.53
1.53	0.21	0.20	0.01	1.94	3.81	0.19		0.003	0.56
1.51	0.21	0.23	0.03	1.98	3.70	0.30		0.000	0.55
1.56	0.20	0.20	0.02	1.99	3.66	0.34		0.000	0.56
1.54	0.18	0.21	0.03	1.95	3.82	0.18		0.004	0.49
1.40	0.27	0.16	0.04	1.86	3.77	0.23		0.000	0.76
1.46	0.22	0.17	0.03	1.88	3.91	0.09		0.004	0.58
1.51	0.21	0.21	0.04	1.97	3.70	0.30		0.008	0.54
1.59	0.16	0.23	0.01	1.98	3.79	0.21		0.000	0.47
1.45	0.25	0.16	0.03	1.89	3.89	0.11		0.000	0.57
1.53	0.20	0.20	0.03	1.97	3.67	0.33		0.002	0.61
1.49	0.30	0.16	0.04	1.99	3.69	0.31		0.001	0.47
1.57	0.16	0.15	0.01	1.89	3.94	0.06		0.000	0.52
1.47	0.25	0.20	0.02	1.93	3.75	0.25		0.007	0.61
1.51	0.22	0.18	0.01	1.92	3.88	0.12		0.000	0.54
1.47	0.22	0.19	0.02	1.90	3.88	0.12		0.000	0.60
1.49	0.20	0.19	0.02	1.91	3.89	0.11		0.001	0.54
1.25	0.20	0.18	0.25	1.89	3.73	0.27		0.001	0.53
1.50	0.20	0.21	0.02	1.93	3.95	0.05		0.003	0.46
1.47	0.24	0.19	0.02	1.91	3.88	0.12		0.000	0.55
1.39	0.26	0.26	0.11	2.02	3.65	0.35		0.003	0.44
1.44	0.26	0.24	0.02	1.97	3.51	0.49		0.000	0.79
1.46	0.22	0.21	0.03	1.91	3.87	0.13		0.002	0.56
1.51	0.21	0.18	0.02	1.92	3.87	0.13		0.003	0.53

1.28	0.28	0.20	0.17	1.93	3.73	0.27	0.000	0.50
1.47	0.22	0.20	0.03	1.92	3.80	0.20	0.015	0.59
1.45	0.26	0.21	0.02	1.94	3.76	0.24	0.009	0.60
1.48	0.24	0.21	0.01	1.95	3.72	0.28	0.002	0.63
1.48	0.22	0.20	0.03	1.93	3.76	0.24	0.009	0.59
1.40	0.26	0.22	0.06	1.95	3.73	0.27	0.003	0.59
1.48	0.22	0.20	0.03	1.93	3.85	0.15	0.009	0.52
1.48	0.25	0.23	0.02	1.98	3.70	0.30	0.001	0.57
1.47	0.22	0.20	0.02	1.92	3.73	0.27	0.078	0.55
1.43	0.24	0.19	0.03	1.90	3.89	0.11	0.006	0.56

Smectite Standard

(Al	Fe	Mg	Ti)	Octahedral Total	(Si	Al)	O10(OH)2	Ca	K
1.52	0.23	0.36	0.00	2.12	3.94	0.06		0.027	0.01
1.59	0.21	0.31	0.01	2.12	3.89	0.11		0.023	0.01
1.60	0.20	0.32	0.00	2.11	3.91	0.09		0.029	0.00
1.60	0.19	0.32	0.01	2.12	3.91	0.09		0.019	0.00
1.58	0.20	0.30	0.01	2.09	3.93	0.07		0.040	0.01
1.62	0.19	0.29	0.00	2.10	3.93	0.07		0.030	0.00
1.59	0.03	0.04	0.03	1.69	4.15	-0.15		0.018	0.76
1.57	0.20	0.30	0.00	2.07	4.00	0.00		0.035	0.01
1.62	0.19	0.33	0.00	2.14	3.88	0.12		0.016	0.01
1.55	0.23	0.35	0.01	2.14	3.86	0.14		0.020	0.01
1.64	0.16	0.32	0.01	2.12	3.92	0.08		0.012	0.00
1.61	0.19	0.30	0.00	2.10	3.92	0.08		0.031	0.00
1.32	0.33	0.39	0.06	2.10	3.84	0.16		0.044	0.09
1.64	0.20	0.27	0.00	2.11	3.91	0.09		0.018	0.00
1.62	0.19	0.30	0.00	2.11	3.91	0.09		0.021	0.00
1.59	0.19	0.29	0.01	2.09	3.95	0.05		0.024	0.02
1.60	0.20	0.29	0.01	2.11	3.91	0.09		0.026	0.01
1.60	0.21	0.30	0.01	2.12	3.90	0.10		0.018	0.00
1.58	0.20	0.32	0.01	2.12	3.90	0.10		0.026	0.00
1.55	0.20	0.39	0.00	2.15	3.89	0.11		0.026	0.01
1.60	0.20	0.30	0.01	2.11	3.90	0.10		0.025	0.01
1.60	0.20	0.26	0.01	2.08	3.92	0.08		0.028	0.03
1.57	0.21	0.34	0.01	2.13	3.86	0.14		0.037	0.01
1.61	0.20	0.32	0.00	2.12	3.91	0.09		0.019	0.00
1.60	0.21	0.30	0.01	2.12	3.91	0.09		0.019	0.00
1.61	0.20	0.27	0.01	2.09	3.96	0.04		0.019	0.01
1.63	0.20	0.25	0.01	2.09	3.93	0.07		0.026	0.01
1.60	0.20	0.29	0.01	2.10	3.91	0.09		0.020	0.02
1.63	0.20	0.25	0.01	2.08	3.93	0.07		0.026	0.01
1.63	0.22	0.23	0.01	2.09	3.92	0.08		0.018	0.00
1.64	0.20	0.23	0.01	2.08	3.93	0.07		0.021	0.01
1.61	0.19	0.31	0.01	2.12	3.91	0.09		0.018	0.01
1.60	0.20	0.31	0.01	2.11	3.91	0.09		0.020	0.01
1.63	0.21	0.26	0.01	2.10	3.90	0.10		0.019	0.01
1.60	0.20	0.29	0.00	2.10	3.94	0.06		0.023	0.01
1.58	0.20	0.33	0.00	2.11	3.96	0.04		0.014	0.01
1.61	0.19	0.30	0.00	2.11	3.92	0.08		0.020	0.00
1.61	0.21	0.30	0.00	2.12	3.90	0.10		0.018	0.01
1.60	0.19	0.34	0.00	2.13	3.90	0.10		0.018	0.00
1.56	0.20	0.36	0.01	2.13	3.91	0.09		0.028	0.01
1.63	0.21	0.19	0.01	2.03	3.96	0.04		0.068	0.00
1.64	0.19	0.18	0.01	2.03	3.96	0.04		0.063	0.01
1.63	0.22	0.17	0.01	2.03	3.93	0.07		0.071	0.01
1.66	0.19	0.18	0.00	2.04	3.94	0.06		0.064	0.00
1.65	0.19	0.18	0.01	2.02	3.95	0.05		0.072	0.00
1.64	0.20	0.19	0.01	2.03	3.93	0.07		0.073	0.00
1.65	0.20	0.20	0.00	2.04	3.92	0.08		0.072	0.00
1.64	0.21	0.18	0.00	2.03	3.93	0.07		0.072	0.00
1.63	0.23	0.18	0.01	2.04	3.90	0.10		0.074	0.00
1.66	0.20	0.19	0.01	2.05	3.93	0.07		0.045	0.01
1.63	0.22	0.19	0.00	2.04	3.91	0.09		0.070	0.00
1.63	0.22	0.18	0.01	2.04	3.92	0.08		0.074	0.00

1.63	0.21	0.19	0.01	2.04	3.93	0.07	0.062	0.00
1.62	0.21	0.19	0.01	2.03	3.96	0.04	0.068	0.00
1.65	0.21	0.18	0.01	2.04	3.92	0.08	0.059	0.00
1.65	0.20	0.18	0.00	2.03	3.95	0.05	0.062	0.01
1.65	0.21	0.19	0.01	2.05	3.94	0.06	0.040	0.01
1.61	0.23	0.21	0.00	2.06	3.94	0.06	0.045	0.00
1.63	0.21	0.19	0.01	2.04	3.94	0.06	0.058	0.01
1.64	0.22	0.18	0.01	2.05	3.92	0.08	0.051	0.00
1.59	0.24	0.20	0.00	2.04	3.99	0.01	0.046	0.00
1.57	0.26	0.21	0.01	2.05	3.96	0.04	0.047	0.01
1.58	0.21	0.20	0.00	2.01	4.02	-0.02	0.030	0.10
1.59	0.23	0.22	0.01	2.05	3.98	0.02	0.047	0.00
1.58	0.23	0.22	0.01	2.04	3.99	0.01	0.040	0.01
1.62	0.20	0.22	0.00	2.04	4.02	-0.02	0.037	0.00
1.58	0.21	0.22	0.01	2.02	4.06	-0.06	0.050	0.00
1.61	0.19	0.22	0.01	2.04	4.04	-0.04	0.026	0.01
1.59	0.22	0.21	0.01	2.03	4.04	-0.04	0.033	0.00
1.59	0.22	0.22	0.00	2.03	4.05	-0.05	0.034	0.01
1.58	0.23	0.22	0.00	2.03	4.02	-0.02	0.043	0.00
1.58	0.23	0.22	0.00	2.04	4.01	-0.01	0.039	0.01
1.56	0.26	0.22	0.01	2.04	4.01	-0.01	0.033	0.00
1.58	0.23	0.21	0.01	2.03	4.04	-0.04	0.033	0.00
1.57	0.25	0.22	0.00	2.04	4.03	-0.03	0.031	0.01
1.56	0.26	0.20	0.01	2.03	4.01	-0.01	0.033	0.00
1.58	0.23	0.22	0.01	2.04	3.99	0.01	0.055	0.01
1.59	0.20	0.20	0.00	1.99	4.13	-0.13	0.049	0.01
1.61	0.19	0.15	0.00	1.95	4.19	-0.19	0.044	0.02
1.62	0.19	0.21	0.01	2.03	4.04	-0.04	0.031	0.01
1.57	0.24	0.22	0.01	2.04	4.02	-0.02	0.028	0.01
1.58	0.24	0.21	0.00	2.03	4.00	0.00	0.052	0.01
1.59	0.21	0.20	0.01	2.01	4.08	-0.08	0.033	0.02
1.59	0.22	0.22	0.01	2.04	4.01	-0.01	0.031	0.01
1.62	0.21	0.20	0.01	2.04	4.01	-0.01	0.035	0.00
1.60	0.21	0.22	0.01	2.03	4.04	-0.04	0.032	0.01
1.58	0.20	0.21	0.04	2.03	4.02	-0.02	0.036	0.01
1.60	0.17	0.20	0.00	1.97	4.20	-0.20	0.032	0.01
1.62	0.22	0.20	0.00	2.04	4.00	0.00	0.030	0.01
1.60	0.23	0.22	0.00	2.05	3.99	0.01	0.028	0.01
1.58	0.26	0.20	0.01	2.04	3.99	0.01	0.028	0.01
1.54	0.31	0.18	0.01	2.04	3.97	0.03	0.034	0.01
1.63	0.19	0.23	0.01	2.05	4.00	0.00	0.021	0.01
1.60	0.24	0.20	0.01	2.05	3.99	0.01	0.026	0.01
1.57	0.26	0.20	0.01	2.04	4.00	0.00	0.036	0.01
1.56	0.21	0.22	0.03	2.02	3.97	0.03	0.075	0.02
1.61	0.22	0.22	0.01	2.05	3.99	0.01	0.024	0.01
1.60	0.21	0.23	0.01	2.05	4.00	0.00	0.034	0.01
1.59	0.23	0.22	0.01	2.05	4.00	0.00	0.029	0.01

Appendix 3.2: Structural Chochołów-06 and Bukowina Tatrzańska-41as measured by SEM-EDS.

Chochołów-06

(Al	Fe	Mg	Ti)	Octahedral Total	(Si	Al)	O10(OH)2	Ca	K
0.91	0.30	0.33	0.03	1.57	2.97	1.03		1.037	0.54
1.49	0.12	0.17	0.12	1.90	3.22	0.78		0.177	0.76
1.22	0.50	0.36	0.02	2.09	3.48	0.52		0.057	0.47
0.32	1.22	0.98	0.01	2.53	2.70	1.30		0.265	0.16
0.83	0.18	0.89	0.01	1.92	3.16	0.84		0.795	0.38
1.40	0.20	0.22	0.02	1.84	3.64	0.36		0.310	0.43
0.92	0.29	0.25	0.04	1.51	3.07	0.93		1.084	0.45
1.49	0.22	0.20	0.02	1.93	3.26	0.74		0.143	0.84
0.82	0.64	0.46	0.10	2.03	3.26	0.74		0.259	0.50
1.19	0.22	0.39	0.01	1.80	3.39	0.61		0.555	0.48
0.92	0.51	0.39	0.04	1.86	3.36	0.64		0.462	0.48
0.45	0.61	1.74	0.01	2.81	2.63	1.37		0.286	0.11
1.43	0.30	0.33	0.04	2.09	3.34	0.66		0.034	0.62
1.35	0.24	0.15	0.11	1.85	3.16	0.84		0.273	0.78
1.79	0.03	-0.02	0.02	1.82	4.46	-0.46		0.022	0.01
1.25	0.24	0.21	0.04	1.74	4.01	-0.01		0.232	0.49
1.19	0.41	0.41	0.02	2.04	3.67	0.33		0.143	0.32
1.10	0.25	0.39	0.03	1.77	3.40	0.60		0.597	0.46
1.37	0.26	0.33	0.02	1.98	3.54	0.46		0.197	0.43
1.36	0.26	0.27	0.02	1.91	3.70	0.30		0.199	0.43
1.09	0.38	0.27	0.04	1.78	3.43	0.57		0.457	0.53
1.23	0.24	0.28	0.04	1.78	3.43	0.57		0.406	0.65
1.19	0.47	0.50	0.04	2.20	3.23	0.77		0.110	0.42
0.81	0.34	0.26	0.02	1.42	3.24	0.76		1.180	0.39
0.77	0.51	0.43	0.08	1.79	3.19	0.81		0.635	0.53
1.89	0.06	0.05	0.02	2.02	3.28	0.72		0.026	0.62
1.54	0.12	0.13	0.02	1.81	3.19	0.81		0.418	0.64
1.29	0.33	0.35	0.02	1.99	3.44	0.56		0.106	0.69
1.40	0.23	0.23	0.02	1.88	4.05	-0.05		0.101	0.32
1.03	0.54	0.21	0.03	1.81	3.52	0.48		0.421	0.39
0.86	0.33	0.39	0.03	1.60	3.22	0.78		0.961	0.43
1.38	0.24	0.18	0.06	1.86	4.05	-0.05		0.062	0.35
1.93	0.06	0.03	0.02	2.03	3.19	0.81		0.002	0.72
1.88	0.08	0.04	0.02	2.02	3.14	0.86		0.014	0.80
1.48	0.23	0.17	0.02	1.90	3.37	0.63		0.227	0.62
1.18	0.26	0.29	0.04	1.77	3.37	0.63		0.562	0.44
1.15	0.39	0.28	0.01	1.83	3.64	0.36		0.353	0.43
1.90	0.07	0.03	0.02	2.01	3.10	0.90		0.010	0.85
1.07	0.27	0.36	0.04	1.73	3.45	0.55		0.650	0.37
1.33	0.34	0.25	0.03	1.94	3.30	0.70		0.212	0.67
0.99	0.23	0.21	0.04	1.47	3.67	0.33		0.866	0.35
1.81	0.10	0.08	0.00	2.00	3.23	0.77		0.021	0.82
0.02	1.57	1.59	0.01	3.18	2.00	2.00		0.016	0.02
1.19	0.53	0.26	0.04	2.02	3.41	0.59		0.164	0.44
1.32	0.33	0.33	0.02	2.00	3.38	0.62		0.206	0.51
1.16	0.49	0.27	0.03	1.95	3.48	0.52		0.246	0.41
1.09	0.38	0.33	0.02	1.82	3.40	0.60		0.524	0.39
1.36	0.29	0.27	0.02	1.94	3.58	0.42		0.140	0.58
1.43	0.26	0.22	0.03	1.94	3.92	0.08		0.033	0.38
-0.57	0.20	0.16	0.04	-0.18	2.15	1.85		4.033	0.42
1.63	0.17	0.13	0.03	1.95	3.23	0.77		0.021	0.98
1.13	0.26	0.25	0.11	1.76	3.66	0.34		0.420	0.37
1.64	0.14	0.12	0.02	1.92	4.01	-0.01		0.055	0.22
1.39	0.32	0.11	0.04	1.86	3.79	0.21		0.036	0.62
1.59	0.20	0.13	0.01	1.93	3.77	0.23		0.120	0.34
1.24	0.23	0.40	0.07	1.95	3.56	0.44		0.269	0.39
1.24	0.24	0.18	0.02	1.67	3.43	0.57		0.602	0.50
1.40	0.22	0.27	0.03	1.92	3.43	0.57		0.209	0.64
1.52	0.19	0.23	0.02	1.97	3.52	0.48		0.060	0.66

0.64	0.23	0.18	0.06	1.10	2.80	1.20	1.738	0.55
1.17	0.25	0.30	0.02	1.74	3.35	0.65	0.641	0.44
1.27	0.25	0.45	0.01	1.98	3.41	0.59	0.300	0.48
1.32	0.30	0.24	0.03	1.88	3.73	0.27	0.155	0.52
0.55	1.01	0.77	0.02	2.35	2.92	1.08	0.263	0.27
1.36	0.30	0.21	0.02	1.89	3.84	0.16	0.160	0.34
-0.25	0.24	1.43	0.02	1.43	2.20	1.80	2.273	0.36
1.45	0.24	0.29	0.02	2.00	3.65	0.35	0.109	0.41
1.31	0.35	0.25	0.02	1.93	3.59	0.41	0.159	0.54
0.81	0.26	0.28	0.03	1.38	3.16	0.84	1.280	0.40
0.85	0.27	0.56	0.02	1.70	3.36	0.64	0.836	0.40
1.40	0.27	0.29	0.03	1.98	3.73	0.27	0.099	0.39
1.09	0.27	0.26	0.02	1.64	3.51	0.49	0.702	0.39
1.18	0.30	0.21	0.06	1.75	4.06	-0.06	0.244	0.35
1.13	0.25	0.29	0.01	1.68	3.17	0.83	0.762	0.55
1.14	0.35	0.18	0.17	1.84	3.44	0.56	0.156	0.74
1.02	0.27	0.38	0.04	1.71	4.01	-0.01	0.426	0.36
1.03	0.32	0.32	0.08	1.75	3.54	0.46	0.548	0.36
0.82	0.21	0.80	0.02	1.84	2.74	1.26	0.939	0.62
1.17	0.30	0.10	0.08	1.64	3.11	0.89	0.441	1.11
1.08	0.27	0.27	0.23	1.85	3.36	0.64	0.336	0.46
1.53	0.17	0.22	0.02	1.94	3.47	0.53	0.127	0.67
1.12	0.34	0.23	0.02	1.71	3.56	0.44	0.490	0.54
0.74	0.99	0.51	0.01	2.25	2.96	1.04	0.252	0.30
1.13	0.38	0.25	0.07	1.82	3.51	0.49	0.317	0.57
0.65	1.25	0.70	0.01	2.60	2.65	1.35	0.023	0.18
1.51	0.22	0.25	0.02	2.00	3.69	0.31	0.019	0.49
0.57	1.19	0.61	0.01	2.39	2.76	1.24	0.166	0.35
1.07	0.22	0.19	0.01	1.49	4.20	-0.20	0.655	0.18
0.67	0.25	0.36	0.04	1.32	3.08	0.92	1.437	0.41
1.12	0.37	0.47	0.03	1.99	3.29	0.71	0.333	0.52
1.39	0.22	0.28	0.02	1.91	3.76	0.24	0.161	0.45
1.01	0.41	0.34	0.15	1.91	3.73	0.27	0.215	0.31
0.99	0.26	0.28	0.01	1.54	3.49	0.51	0.913	0.35
1.30	0.35	0.37	0.02	2.03	3.47	0.53	0.150	0.48
0.70	0.29	0.36	0.04	1.38	3.18	0.82	1.320	0.35
0.33	0.86	1.20	0.07	2.46	2.90	1.10	0.015	0.82
0.86	0.23	0.39	0.05	1.52	3.14	0.86	1.111	0.40
1.50	0.14	0.19	0.01	1.84	3.43	0.57	0.241	0.74
1.31	0.29	0.35	0.02	1.96	3.63	0.37	0.182	0.47
1.47	0.31	0.21	0.03	2.02	3.45	0.55	0.063	0.55
1.25	0.47	0.32	0.02	2.05	3.15	0.85	0.105	0.80
1.12	0.46	0.27	0.05	1.89	3.46	0.54	0.233	0.62
1.39	0.22	0.27	0.02	1.90	3.88	0.12	0.144	0.38
0.32	0.19	0.24	0.23	0.98	2.81	1.19	1.965	0.34
1.48	0.09	0.11	0.02	1.70	3.99	0.01	0.305	0.39
1.27	0.15	0.36	0.01	1.80	2.99	1.01	0.606	0.75
1.38	0.31	0.35	0.02	2.07	3.71	0.29	0.028	0.37
1.20	0.50	0.45	0.02	2.18	3.39	0.61	0.038	0.42
0.23	0.20	0.16	0.02	0.62	3.20	0.80	2.338	0.40
0.81	0.24	0.37	0.02	1.43	3.38	0.62	1.154	0.39
1.64	0.15	0.23	0.01	2.02	3.41	0.59	0.036	0.66
1.13	0.17	0.35	0.06	1.70	4.16	-0.16	0.313	0.40
1.72	0.09	0.14	0.06	2.00	3.21	0.79	0.011	0.84
1.65	0.11	0.11	0.02	1.89	3.72	0.28	0.021	0.66
1.20	0.42	0.43	0.01	2.06	3.56	0.44	0.152	0.36
1.18	0.18	0.44	0.01	1.81	3.14	0.86	0.667	0.54
1.63	0.28	0.20	0.05	2.16	3.11	0.89	0.009	0.54
1.55	0.13	0.09	0.29	2.05	3.07	0.93	0.045	0.48
1.68	0.19	0.13	0.06	2.07	3.17	0.83	0.001	0.70
1.93	0.08	0.04	0.01	2.06	3.41	0.59	0.007	0.42
1.66	0.08	0.03	0.01	1.78	4.00	0.00	0.003	0.66
1.63	0.12	0.05	0.01	1.82	4.15	-0.15	0.003	0.45
1.84	0.04	0.04	0.01	1.92	3.78	0.22	0.002	0.47
1.76	0.05	0.05	0.02	1.88	3.92	0.08	0.005	0.45
1.66	0.18	0.06	0.01	1.91	3.64	0.36	-0.004	0.68

0.96	0.73	0.44	0.00	2.14	3.91	0.09	0.010	0.10
1.11	0.91	0.47	0.01	2.50	2.64	1.36	0.005	0.31
1.78	0.04	0.02	0.01	1.85	3.95	0.05	0.003	0.51
1.77	0.04	0.05	0.01	1.88	3.88	0.12	0.001	0.52
2.00	0.07	0.02	0.01	2.10	3.24	0.76	0.002	0.46
1.52	0.32	0.13	0.04	2.01	3.31	0.69	0.011	0.71
1.38	0.45	0.25	0.20	2.26	2.91	1.09	0.008	0.33
1.27	0.29	0.25	0.02	1.82	3.25	0.75	0.119	1.27
1.45	0.21	0.27	0.01	1.94	3.39	0.61	0.064	0.91
1.48	0.27	0.18	0.02	1.96	3.46	0.54	0.008	0.79
1.51	0.01	0.01	0.01	1.53	4.24	-0.24	0.002	1.16
1.31	0.36	0.25	0.00	1.92	4.38	-0.38	0.016	0.05
1.62	0.20	0.16	0.02	2.00	3.44	0.56	0.007	0.70
-0.33	0.14	0.16	1.93	1.90	2.10	1.90	0.004	0.41
1.87	0.02	-0.06	0.01	1.83	4.29	-0.29	0.047	0.06
1.84	0.06	-0.02	0.00	1.89	3.96	0.04	0.034	0.29
1.81	0.03	-0.04	0.00	1.80	4.29	-0.29	0.051	0.18
1.85	0.02	-0.06	0.01	1.81	4.39	-0.39	0.044	0.03
1.86	0.01	-0.08	0.00	1.80	4.33	-0.33	0.084	0.03
1.82	0.04	-0.06	0.01	1.81	4.38	-0.38	0.052	0.03
1.83	0.02	-0.05	0.00	1.80	4.36	-0.36	0.081	0.01
0.33	0.10	0.16	1.35	1.95	2.44	1.56	0.017	0.50
1.44	0.01	0.00	0.00	1.46	4.13	-0.13	0.001	1.50
1.78	0.09	0.12	0.02	2.01	3.34	0.66	0.003	0.72
1.25	0.35	0.48	0.09	2.18	3.43	0.57	0.025	0.39
1.42	0.19	0.32	0.01	1.94	3.87	0.13	0.041	0.53
0.94	0.34	0.60	0.03	1.91	3.23	0.77	0.632	0.35
1.43	0.22	0.24	0.04	1.93	3.96	0.04	0.022	0.41
-0.03	2.08	0.83	0.01	2.88	2.13	1.87	0.012	0.03
1.44	0.14	0.26	0.01	1.85	3.33	0.67	0.361	0.65
1.53	0.20	0.16	0.01	1.90	3.83	0.17	0.170	0.29
0.93	0.83	0.57	0.02	2.36	3.18	0.82	0.007	0.30
1.05	0.43	0.29	0.26	2.03	3.42	0.58	0.026	0.47
1.63	0.05	0.03	0.01	1.73	4.08	-0.08	0.124	0.50
0.18	1.83	0.96	0.00	2.97	2.00	2.00	0.016	0.01
1.60	0.24	0.09	0.05	1.98	3.16	0.84	-0.001	0.94
1.69	0.19	0.11	0.03	2.01	3.19	0.81	-0.003	0.84
1.37	0.33	0.09	0.03	1.82	3.24	0.76	0.149	1.08
1.26	0.22	0.26	0.03	1.77	3.39	0.61	0.449	0.62
0.89	0.65	0.57	0.08	2.19	3.09	0.91	0.288	0.26
0.54	0.23	0.22	0.02	1.01	3.50	0.50	1.709	0.26
1.32	0.28	0.28	0.08	1.96	3.13	0.87	0.125	0.93
-0.03	0.84	0.54	0.03	1.38	2.40	1.60	1.898	0.19
0.83	0.67	0.71	0.06	2.27	3.27	0.73	0.075	0.43
0.27	1.08	1.20	0.07	2.62	2.71	1.29	0.017	0.52
1.00	0.22	0.15	0.04	1.41	3.90	0.10	0.830	0.31
1.72	0.02	-0.05	0.00	1.69	4.08	-0.08	0.384	0.02
1.71	0.11	0.16	0.04	2.01	3.46	0.54	-0.022	0.68

Bukowina Tatrzańska-41

(Al	Fe	Mg	Ti)	Octahedral Total	(Si	Al)	O10(OH)2	Ca	K
1.23	0.56	0.35	0.03	2.17	3.31	0.69		0.008	0.48
1.51	0.15	0.13	0.03	1.82	3.87	0.13		0.131	0.50
1.60	0.12	0.24	0.05	2.01	3.33	0.67		0.121	0.58
1.26	0.21	0.24	0.12	1.83	3.34	0.66		0.357	0.57
1.79	0.09	0.05	0.04	1.96	3.22	0.78		0.048	0.81
1.60	0.16	0.10	0.02	1.89	3.96	0.04		0.074	0.32
1.56	0.18	0.20	0.01	1.95	3.64	0.36		0.101	0.49
1.36	0.21	0.25	0.02	1.83	3.56	0.44		0.344	0.49
1.39	0.21	0.57	0.02	2.19	3.21	0.79		0.158	0.46
1.15	0.46	0.49	0.01	2.12	3.50	0.50		0.136	0.35
1.52	0.21	0.22	0.02	1.98	3.96	0.04		0.034	0.23
1.58	0.16	0.26	0.02	2.01	3.61	0.39		0.057	0.49
1.27	0.27	0.25	0.09	1.88	3.50	0.50		0.246	0.54
1.45	0.24	0.29	0.02	2.00	3.52	0.48		0.022	0.69
0.87	0.21	0.30	0.02	1.40	3.14	0.86		1.235	0.47
1.38	0.21	0.36	0.01	1.95	3.81	0.19		0.116	0.44
0.47	0.21	0.17	0.04	0.89	3.23	0.77		1.935	0.35
1.52	0.17	0.23	0.03	1.95	3.56	0.44		0.140	0.50
1.52	0.11	0.15	0.04	1.82	3.83	0.17		0.155	0.51
1.28	0.29	0.10	0.07	1.74	3.83	0.17		0.101	0.78
1.71	0.07	0.02	0.01	1.81	3.94	0.06		0.177	0.29
1.29	0.36	0.32	0.03	2.00	3.63	0.37		0.107	0.46
1.57	0.14	0.18	0.02	1.91	3.88	0.12		0.068	0.40
1.55	0.24	0.24	0.02	2.04	3.56	0.44		0.030	0.47
0.85	0.75	0.79	0.02	2.41	2.97	1.03		0.161	0.24
0.68	0.46	0.48	0.04	1.66	3.10	0.90		1.025	0.32
1.45	0.24	0.22	0.02	1.93	4.04	-0.04		0.015	0.33
0.36	0.13	0.14	0.02	0.65	2.76	1.24		2.501	0.43
1.47	0.29	0.21	0.01	1.98	3.51	0.49		0.015	0.70
1.33	0.37	0.36	0.01	2.08	3.40	0.60		0.087	0.54
1.13	0.25	0.21	0.03	1.63	3.36	0.64		0.533	0.87
0.86	0.56	0.53	0.04	1.99	3.08	0.92		0.541	0.37
0.94	0.52	0.41	0.02	1.88	3.18	0.82		0.588	0.39
1.37	0.20	0.25	0.05	1.88	3.63	0.37		0.210	0.50
1.26	0.11	0.13	0.02	1.52	3.86	0.14		0.655	0.37
1.28	0.09	0.14	0.01	1.52	3.15	0.85		0.956	0.50
0.76	1.07	0.50	0.02	2.35	2.80	1.20		0.084	0.46
1.33	0.33	0.36	0.01	2.03	3.56	0.44		0.135	0.43
-0.02	0.21	0.25	0.05	0.49	2.67	1.33		2.831	0.40
0.43	0.22	0.25	0.03	0.92	2.73	1.27		2.127	0.46
1.54	0.17	0.21	0.04	1.97	3.47	0.53		0.088	0.63
-0.26	0.16	0.21	0.03	0.14	2.45	1.55		3.488	0.34
1.57	0.16	0.19	0.02	1.94	3.36	0.64		0.161	0.67
1.42	0.17	0.18	0.02	1.80	3.92	0.08		0.210	0.43
1.04	0.43	0.44	0.06	1.97	3.58	0.42		0.299	0.29
1.30	0.33	0.26	0.01	1.90	3.85	0.15		0.165	0.38
1.69	0.13	0.13	0.02	1.97	3.41	0.59		0.032	0.72
1.49	0.36	0.26	0.02	2.13	3.17	0.83		0.033	0.61
1.25	0.49	0.40	0.02	2.16	3.32	0.68		0.090	0.39
0.99	0.22	0.20	0.00	1.41	3.04	0.96		1.258	0.41
1.56	0.26	0.26	0.03	2.12	3.21	0.79		0.020	0.61
1.55	0.09	0.15	0.02	1.82	3.55	0.45		0.282	0.55
1.57	0.15	0.16	0.03	1.91	3.46	0.54		0.144	0.64
1.61	0.11	0.18	0.01	1.91	3.98	0.02		0.017	0.42
1.85	0.07	0.06	0.01	2.00	3.74	0.26		0.058	0.22
1.12	0.42	0.52	0.01	2.08	3.09	0.91		0.323	0.54
1.47	0.25	0.26	0.03	2.01	3.46	0.54		0.039	0.66
1.58	0.19	0.17	0.03	1.96	3.52	0.48		0.028	0.67
1.66	0.11	0.09	0.03	1.89	3.82	0.18		0.041	0.48
1.77	0.09	0.03	0.01	1.90	3.85	0.15		0.005	0.46
1.41	0.15	0.14	0.04	1.74	3.40	0.60		0.452	0.59
1.51	0.13	0.25	0.03	1.92	3.53	0.47		0.167	0.59
0.58	0.08	0.12	0.02	0.80	3.66	0.34		1.888	0.26

1.02	0.46	0.67	0.02	2.18	3.20	0.80	0.318	0.28
1.12	0.35	0.12	0.07	1.66	3.12	0.88	0.481	1.00
1.36	0.31	0.35	0.02	2.03	3.06	0.94	0.286	0.62
1.36	0.25	0.23	0.02	1.86	3.62	0.38	0.207	0.59
1.52	0.17	0.28	0.03	1.99	3.46	0.54	0.082	0.64
1.30	0.24	0.34	0.08	1.96	3.35	0.65	0.286	0.45
0.72	0.75	0.68	0.01	2.17	3.03	0.97	0.477	0.18
1.29	0.21	0.33	0.02	1.86	3.27	0.73	0.457	0.54
1.20	0.13	0.20	0.03	1.57	3.73	0.27	0.697	0.34
1.47	0.22	0.27	0.02	1.97	3.74	0.26	0.107	0.39
1.53	0.17	0.16	0.02	1.88	3.91	0.09	0.064	0.46
1.57	0.14	0.18	0.02	1.90	3.67	0.33	0.091	0.59
1.30	0.28	0.34	0.05	1.98	3.44	0.56	0.202	0.52
1.17	0.14	0.19	0.02	1.52	3.39	0.61	0.802	0.61
1.52	0.10	0.20	0.01	1.83	4.04	-0.04	0.118	0.41
1.37	0.15	0.25	0.18	1.95	3.44	0.56	0.109	0.55
0.59	0.58	0.79	0.02	1.97	2.89	1.11	0.828	0.32
1.45	0.22	0.33	0.03	2.03	3.32	0.68	0.210	0.48
1.25	0.41	0.59	0.01	2.26	3.40	0.60	0.032	0.34
1.13	0.41	0.56	0.01	2.10	3.38	0.62	0.288	0.28
1.30	0.28	0.33	0.02	1.93	3.53	0.47	0.233	0.52
0.13	0.39	1.03	0.01	1.56	3.11	0.89	1.488	0.24
1.61	0.11	0.14	0.01	1.88	4.01	-0.01	0.035	0.42
0.60	0.24	0.67	0.06	1.57	2.95	1.05	1.236	0.49
1.32	0.24	0.37	0.04	1.97	3.44	0.56	0.260	0.45
1.10	0.55	0.56	0.05	2.26	3.33	0.67	0.050	0.29
1.43	0.19	0.19	0.03	1.84	3.50	0.50	0.279	0.56
1.48	0.12	0.20	0.01	1.81	3.86	0.14	0.251	0.39

Appendix 3.3: Selected Area Diffraction Patterns for Chochołów-06, Chochołów-28, Chochołów-60, Bukowina Tatrzańska-06 and Bukowina Tatrzańska-41.

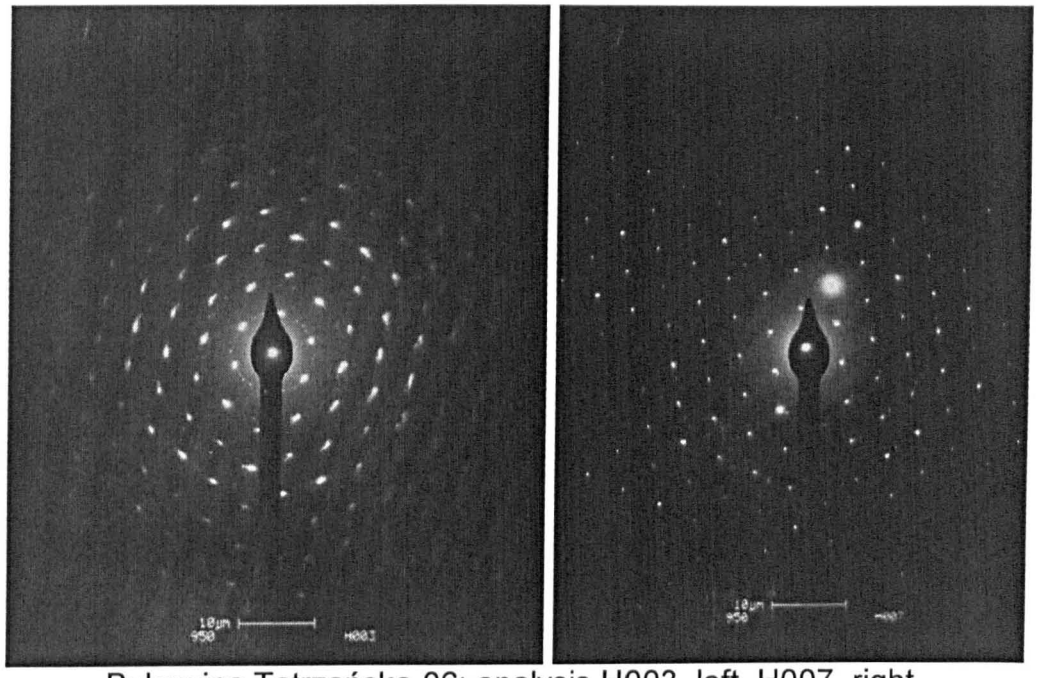

Bukowina Tatrzańska-06: analysis H003, left, H007, right.

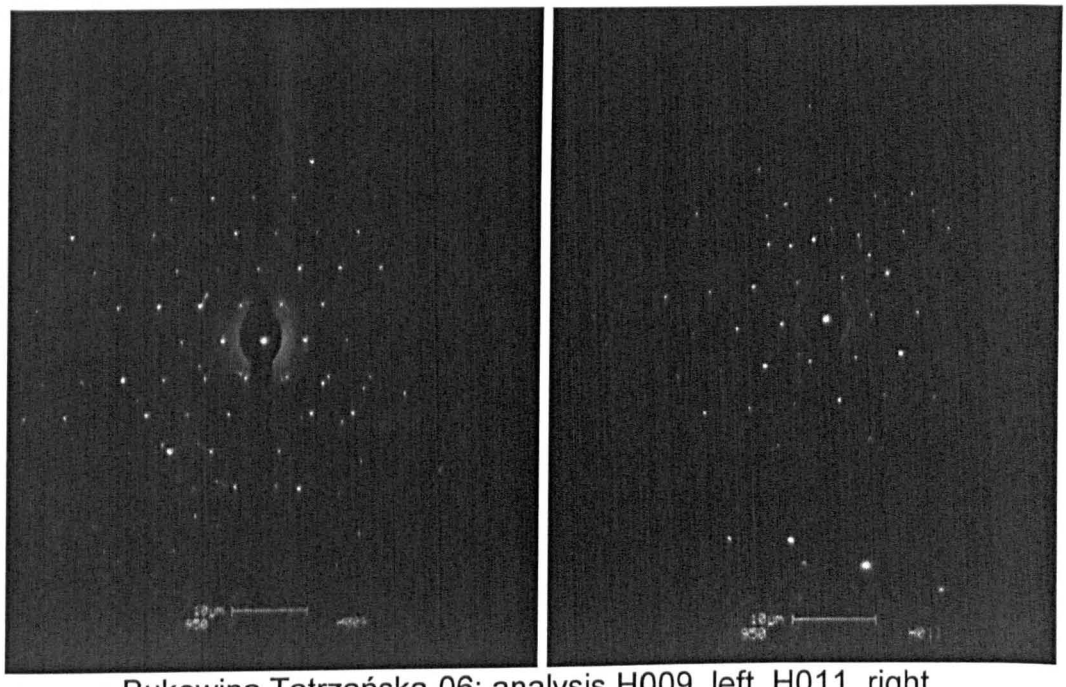

Bukowina Tatrzańska-06: analysis H009, left, H011, right.

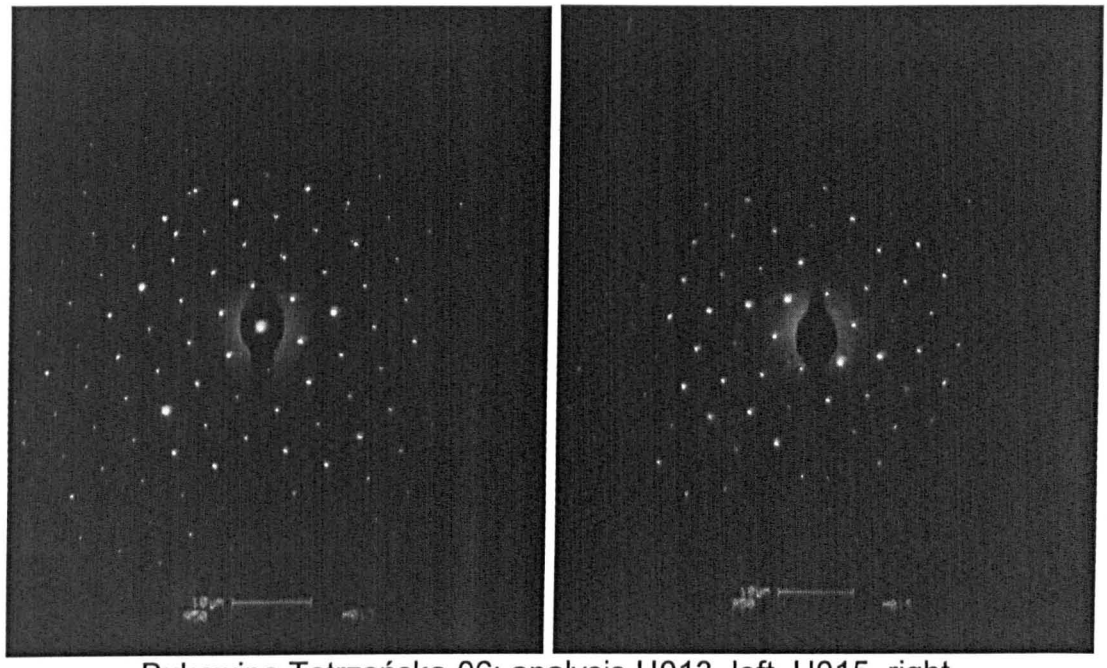

Bukowina Tatrzańska-06: analysis H013, left, H015, right.

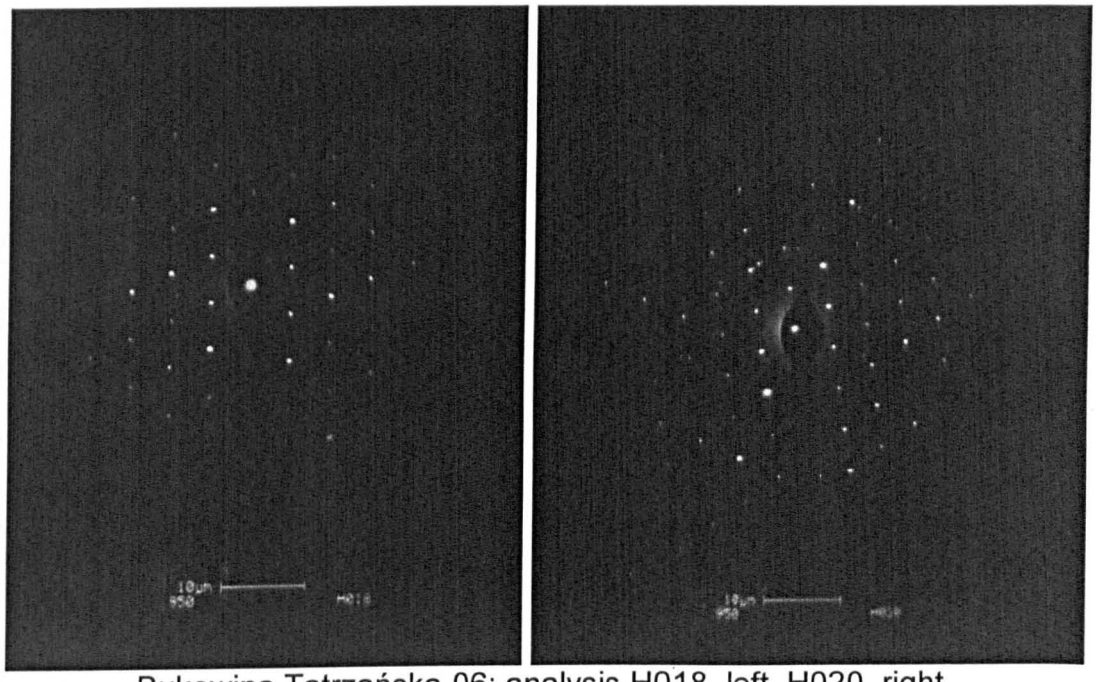

Bukowina Tatrzańska-06: analysis H018, left, H020, right.

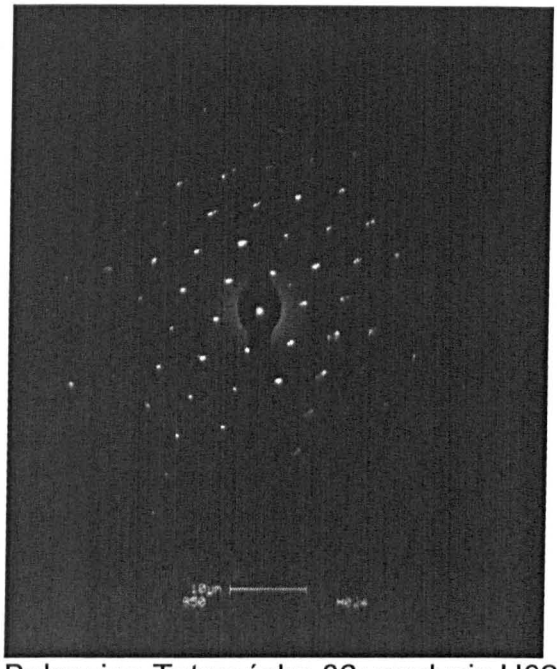

Bukowina Tatrzańska-06: analysis H024

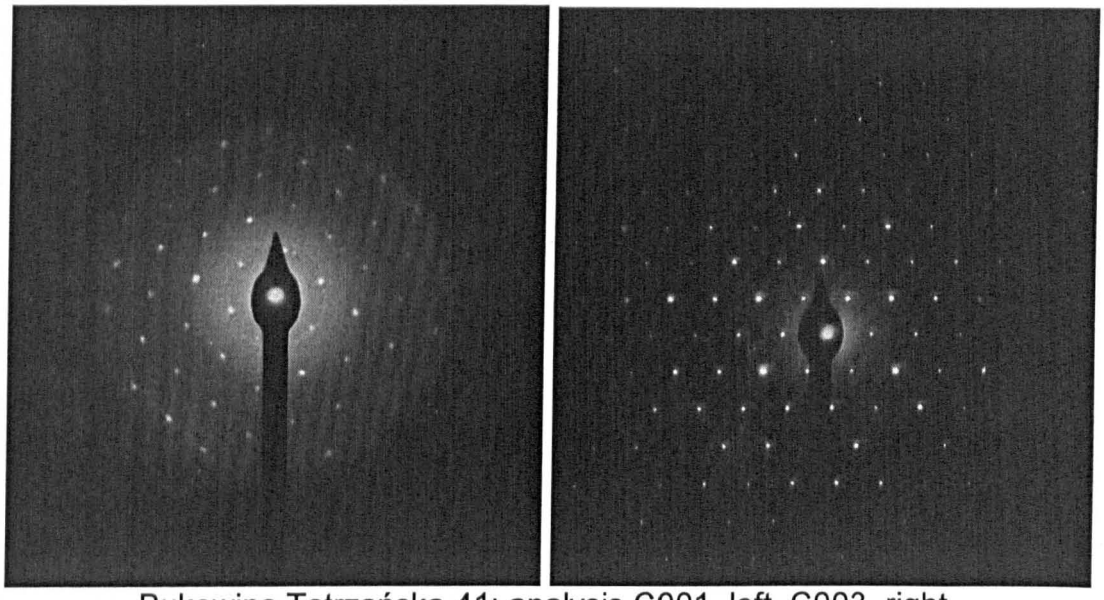

Bukowina Tatrzańska-41: analysis C001, left, C003, right.

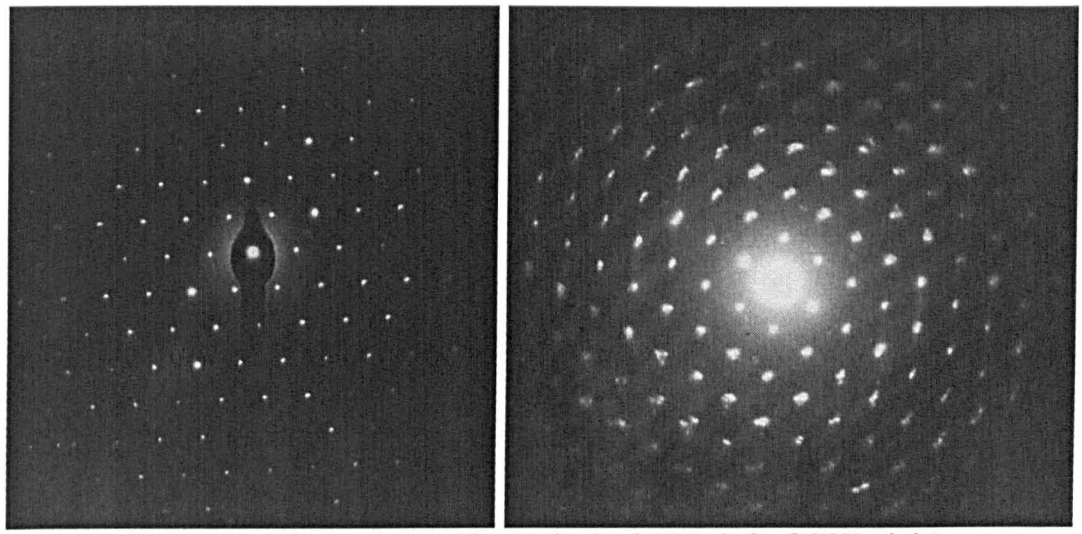

Bukowina Tatrzańska-41: analysis C005, left, C007, right.

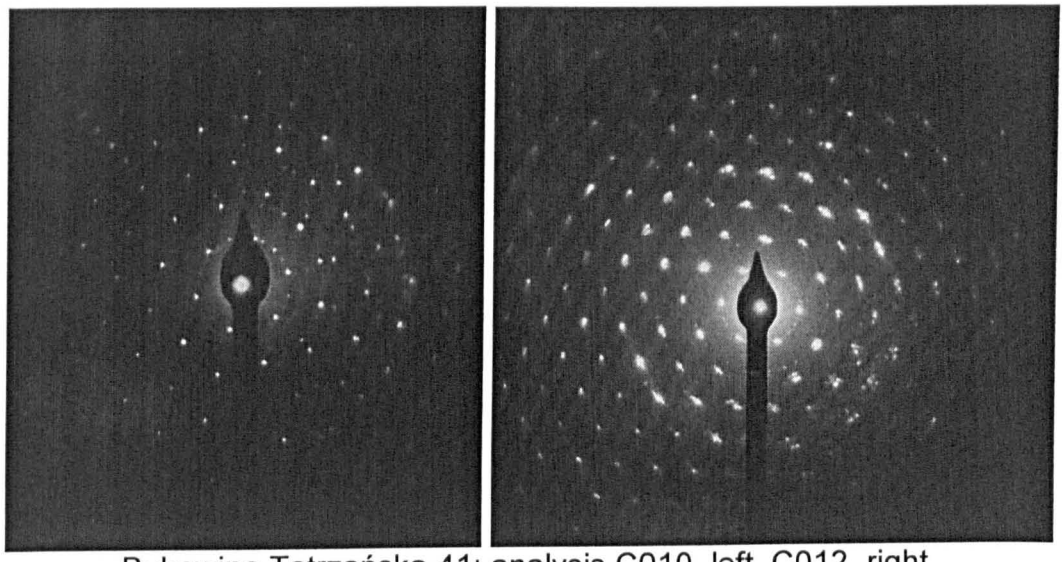

Bukowina Tatrzańska-41: analysis C010, left, C012, right.

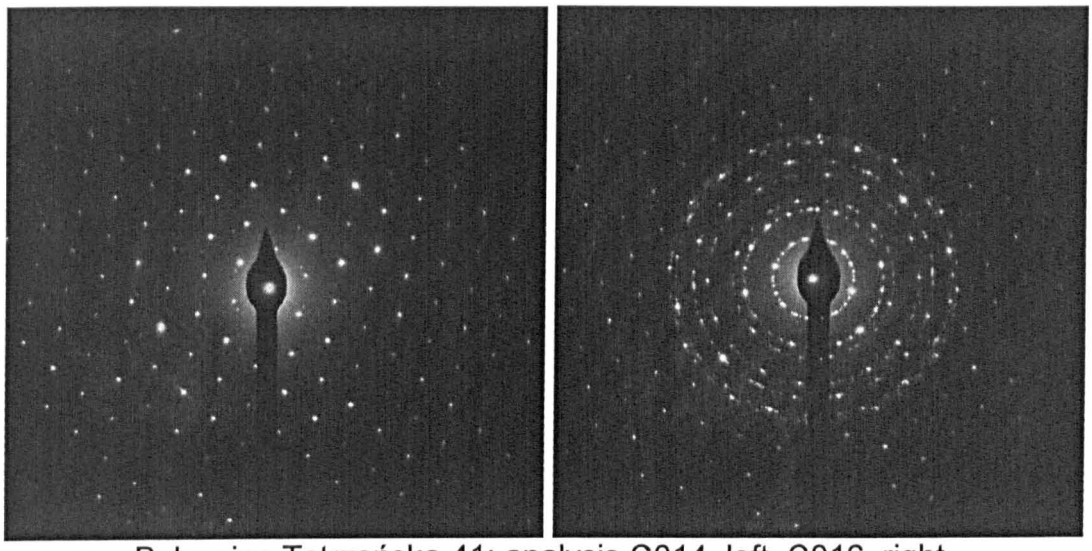

Bukowina Tatrzańska-41: analysis C014, left, C016, right.

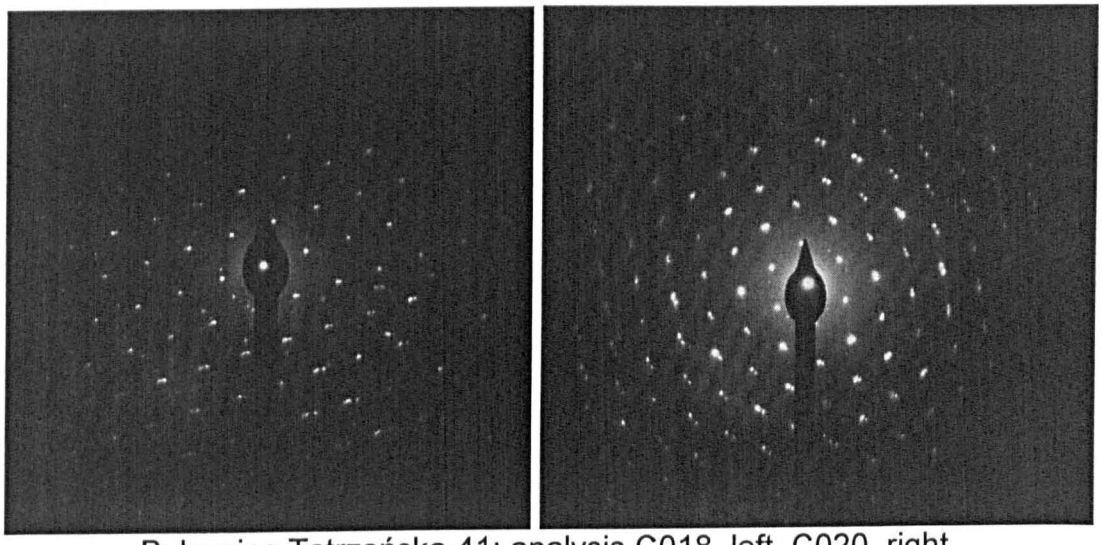

Bukowina Tatrzańska-41: analysis C018, left, C020, right.

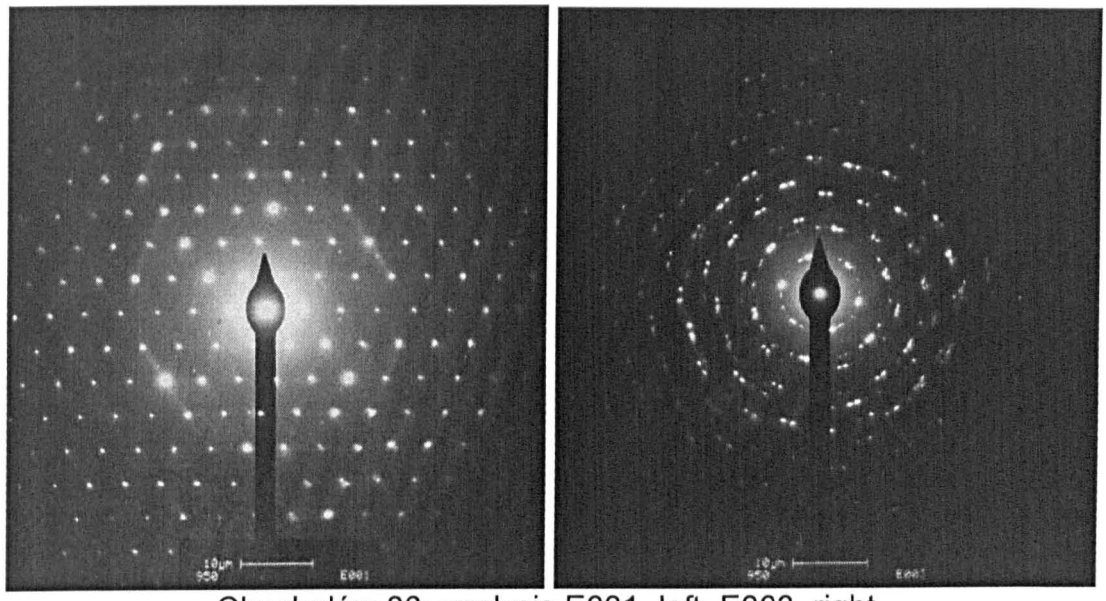

Chochołów-06: analysis E001, left, E003, right.

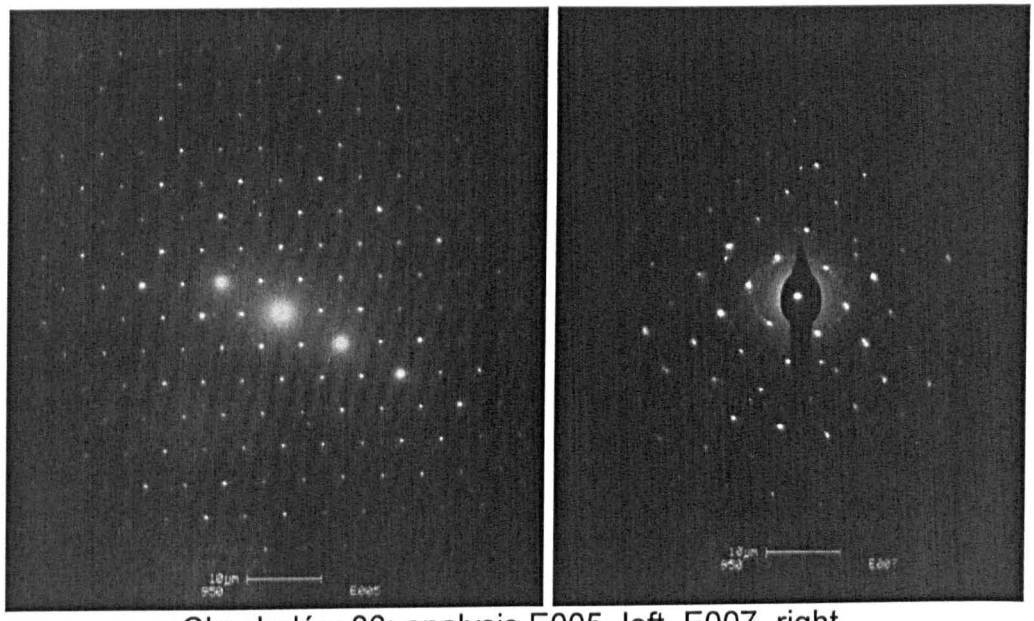

Chochołów-06: analysis E005, left, E007, right.

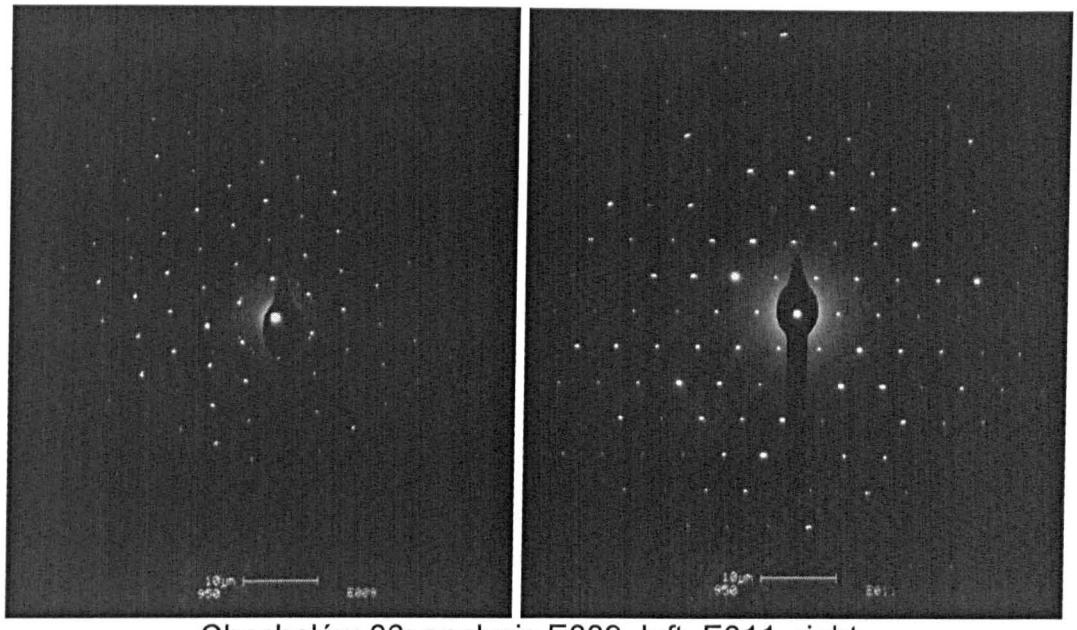

Chochołów-06: analysis E009, left, E011, right.

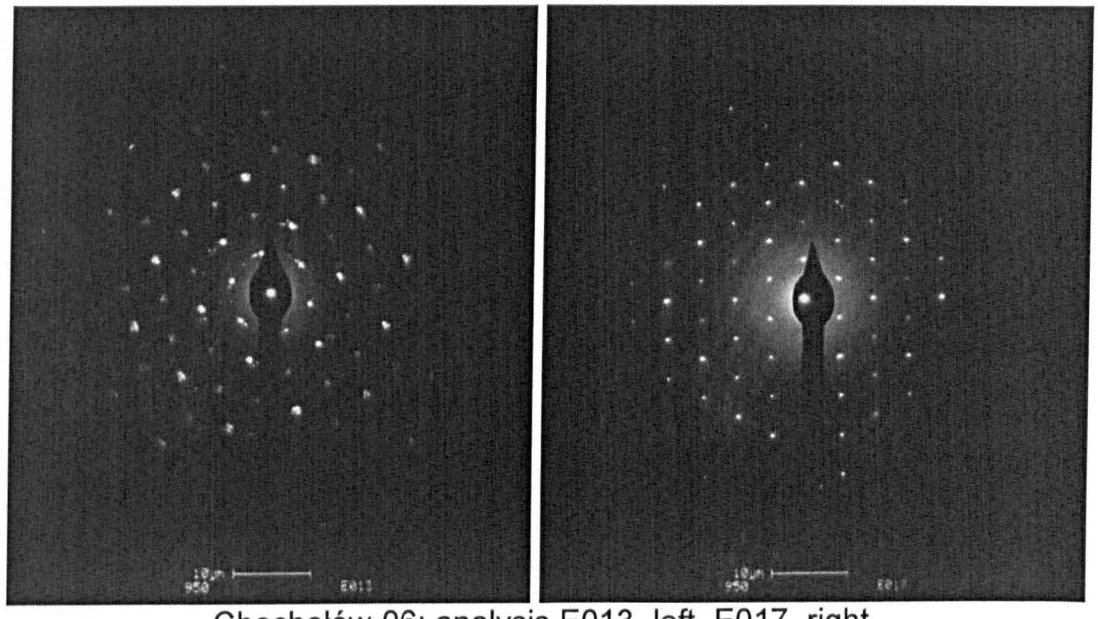

Chochołów-06: analysis E013, left, E017, right.

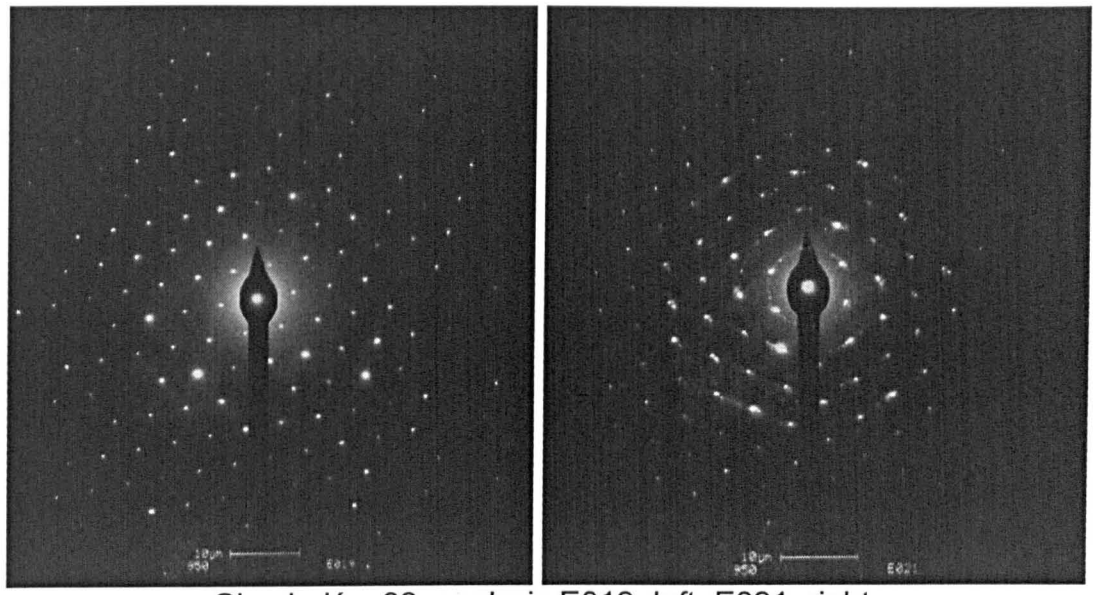

Chochołów-06: analysis E019, left, E021, right.

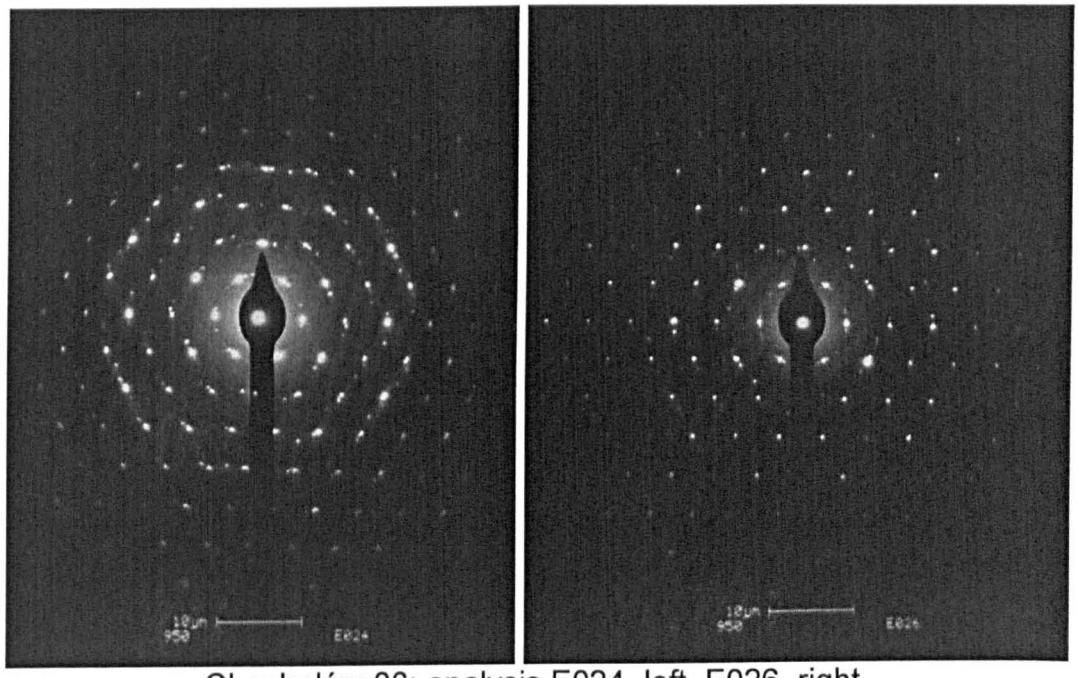

Chochołów-06: analysis E024, left, E026, right.

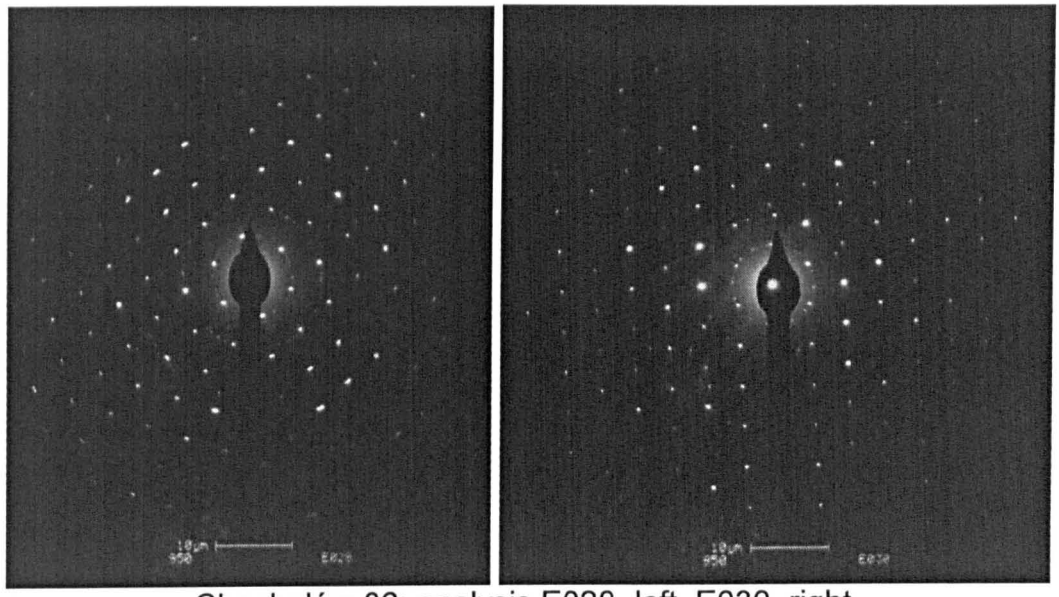

Chochołów-06: analysis E028, left, E030, right.

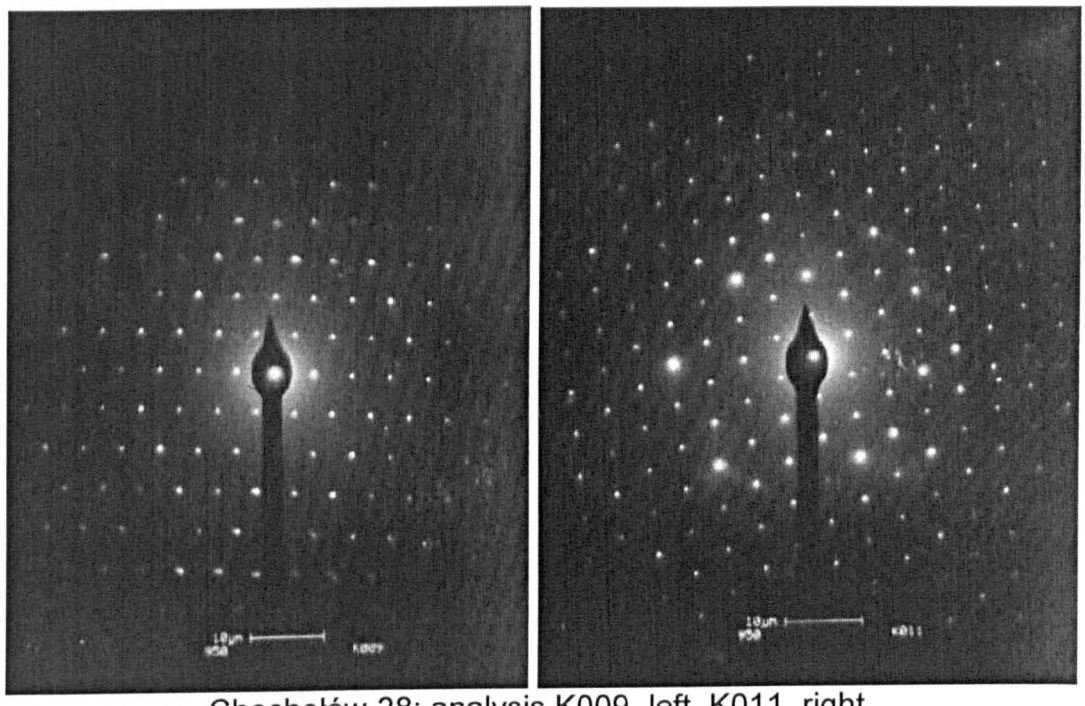

Chochołów-28: analysis K009, left, K011, right.

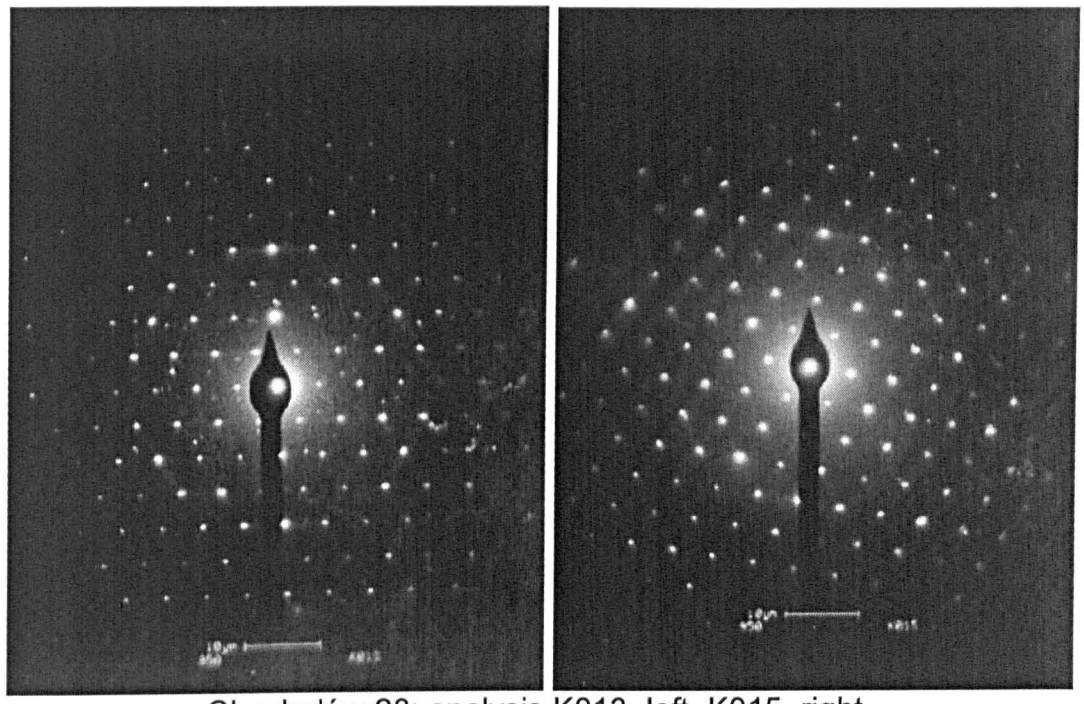

Chochołów-28: analysis K013, left, K015, right.

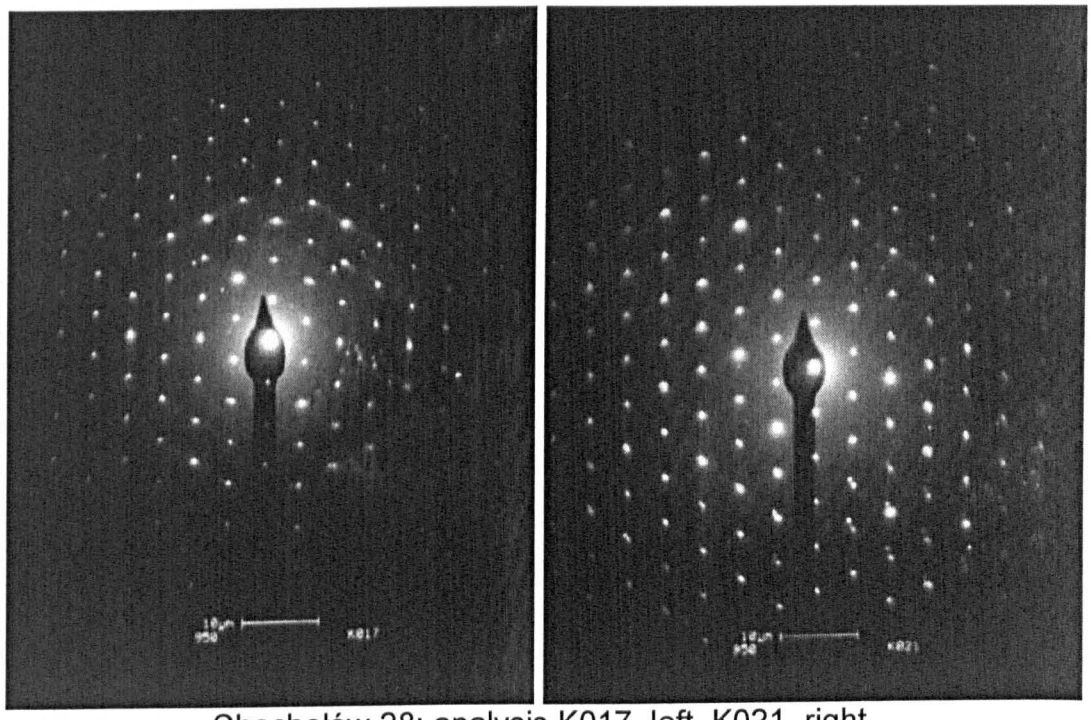

Chochołów-28: analysis K017, left, K021, right.

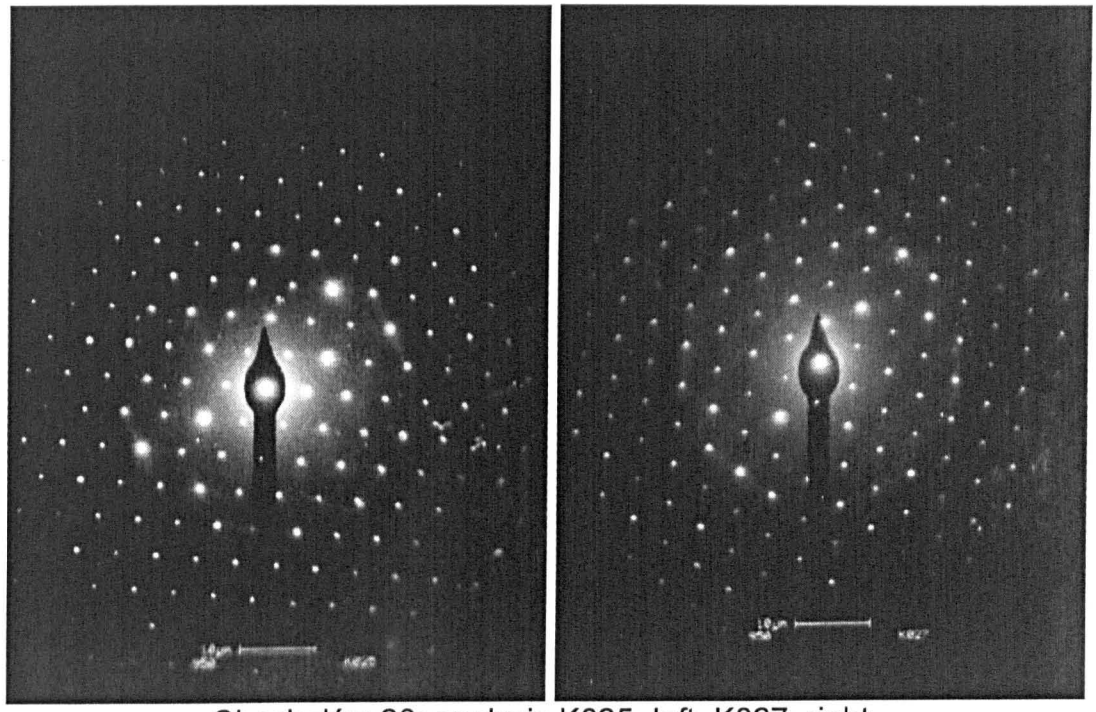

Chochołów-28: analysis K025, left, K027, right.

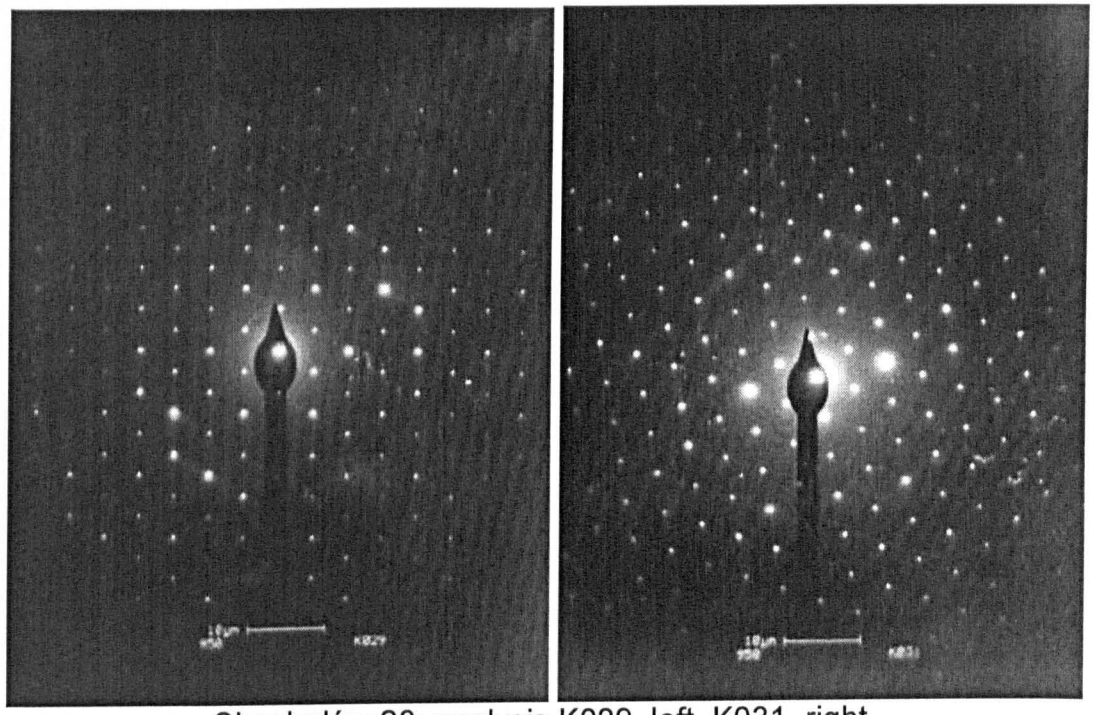

Chochołów-28: analysis K029, left, K031, right.

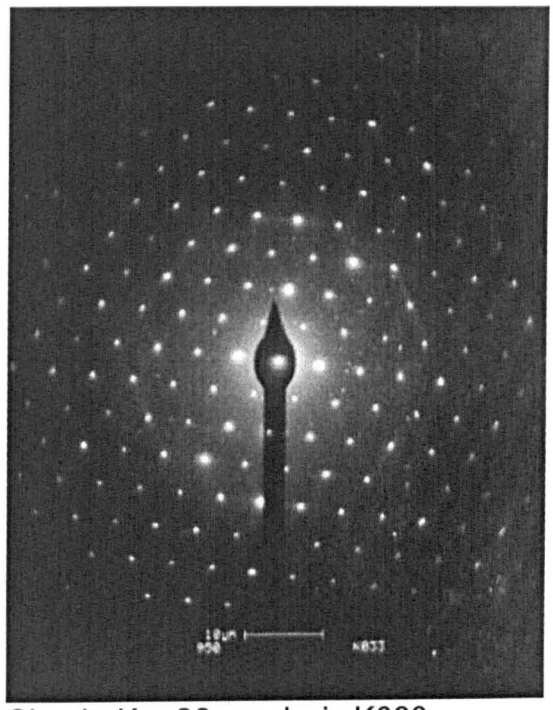

Chochołów-28: analysis K033

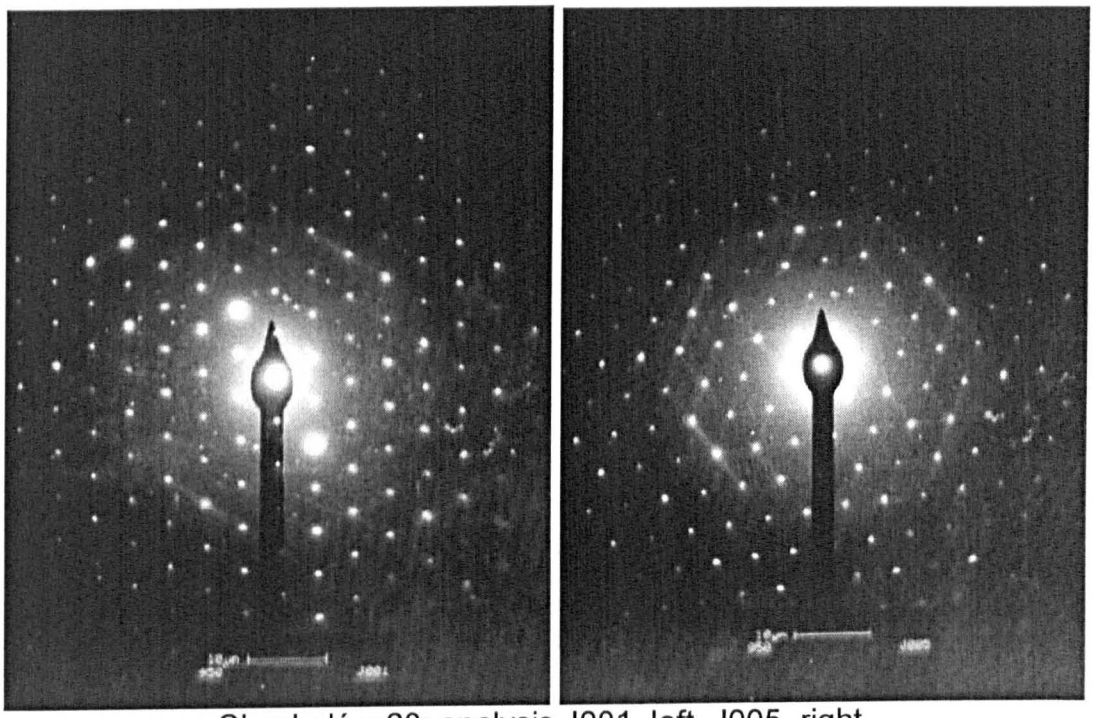

Chochołów-60: analysis J001, left, J005, right.

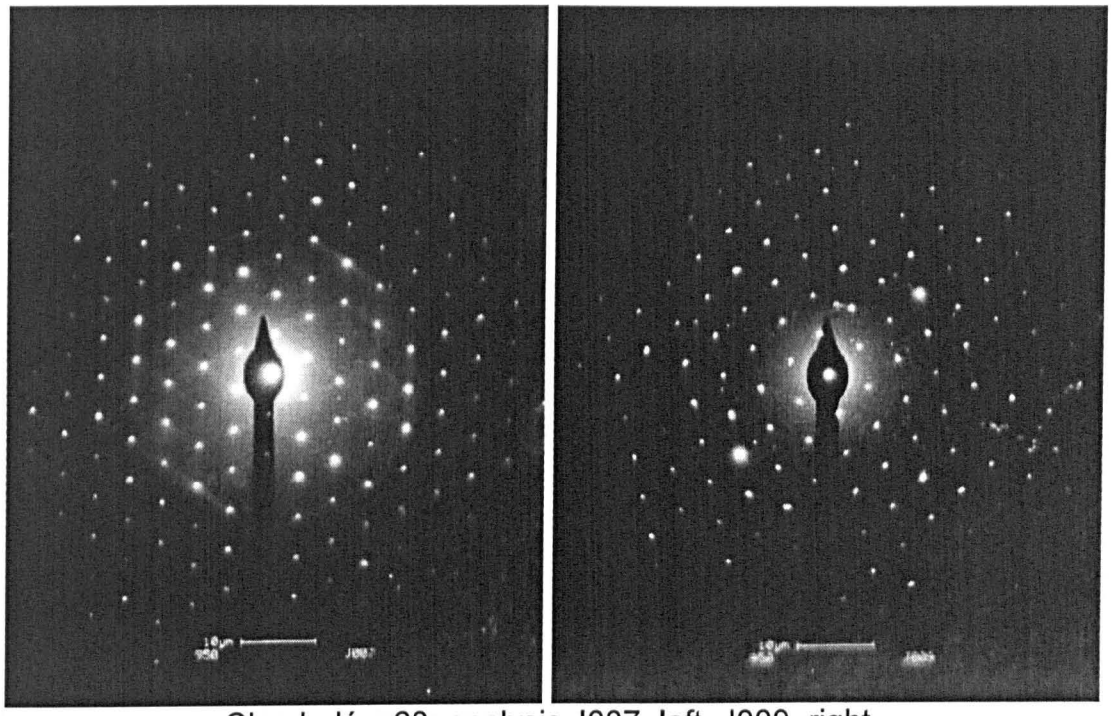

Chochołów-60: analysis J007, left, J009, right.

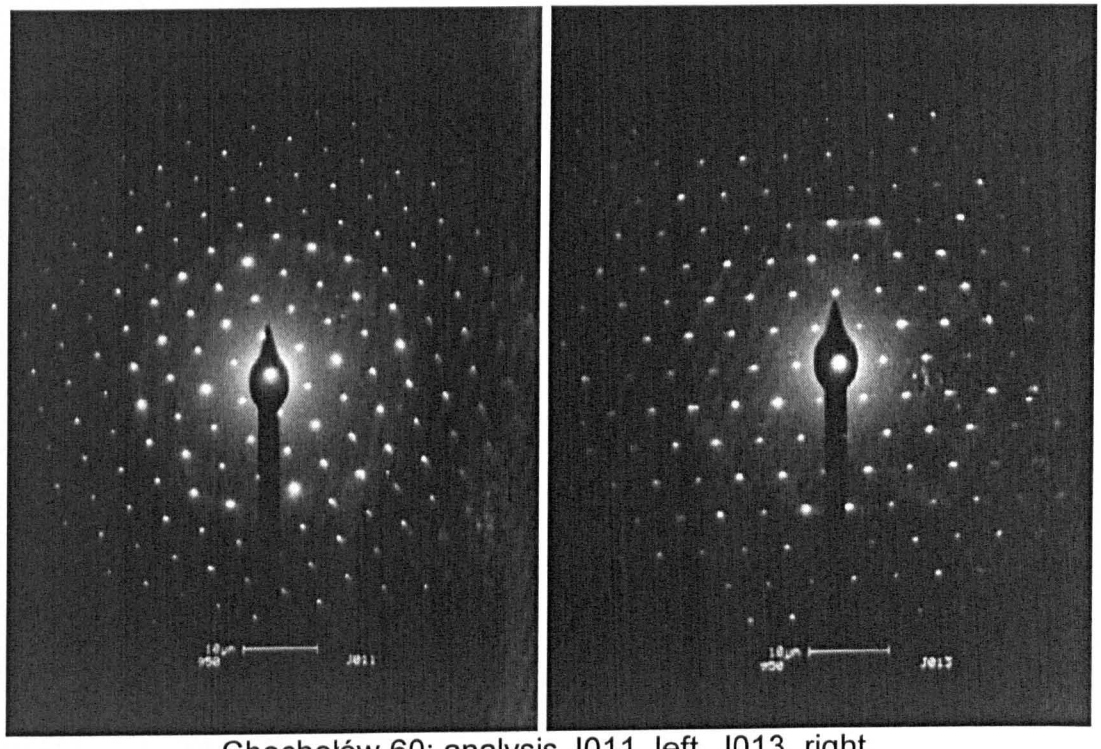

Chochołów-60: analysis J011, left, J013, right.

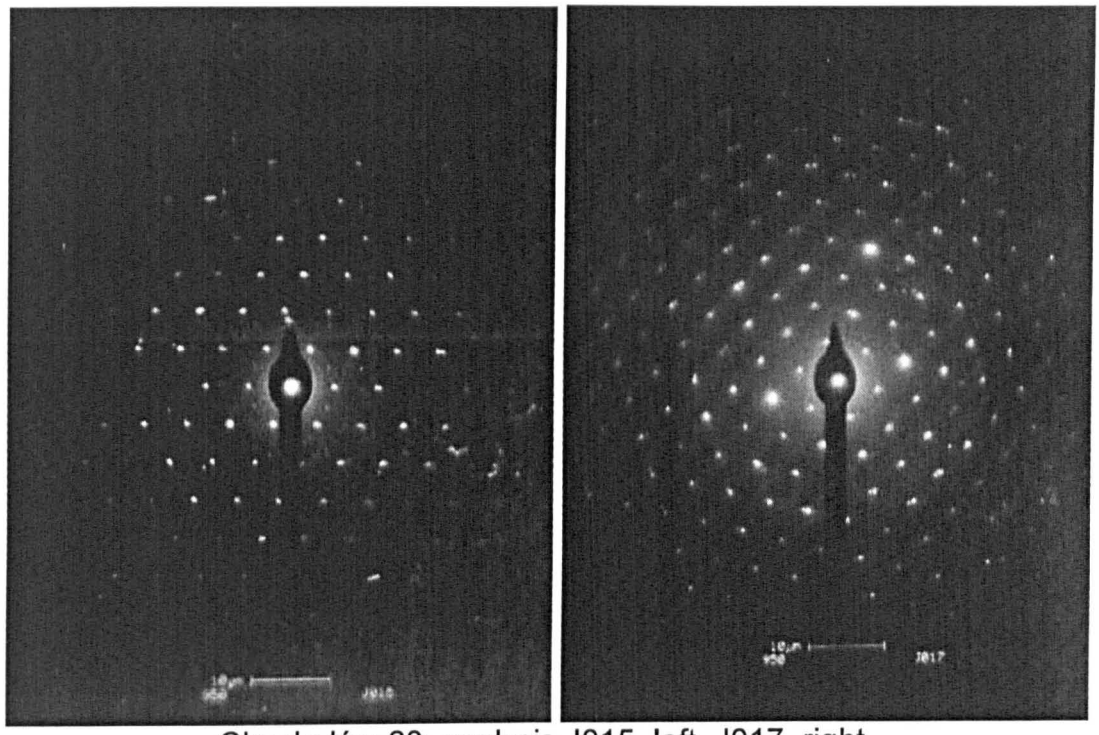

Chochołów-60: analysis J015, left, J017, right.

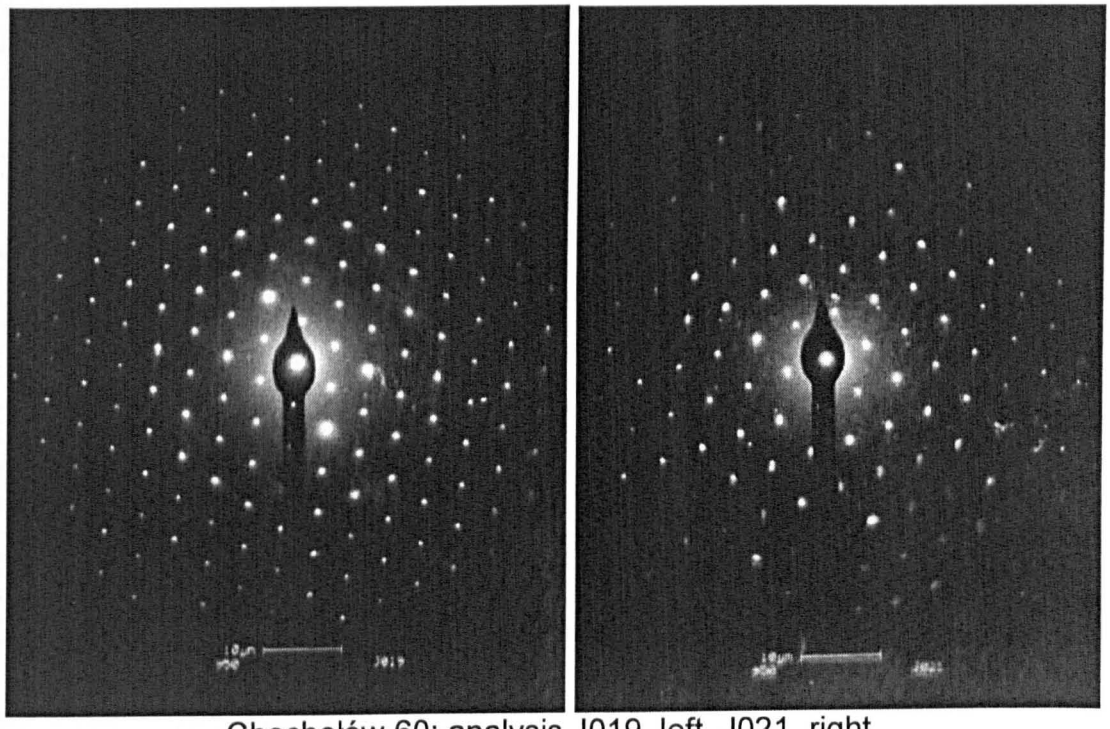

Chochołów-60: analysis J019, left, J021, right.

Appendix 4.1: Rhum 3/29a4 and Magnus 211/12-2 QXRD traces.

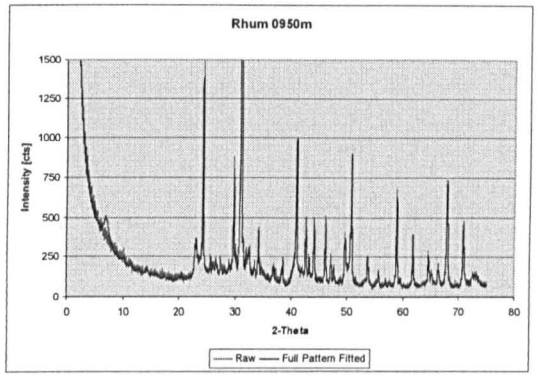

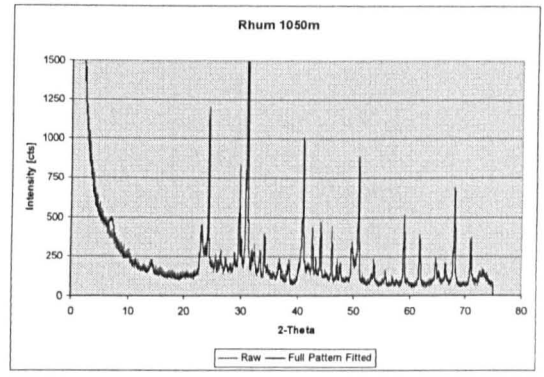

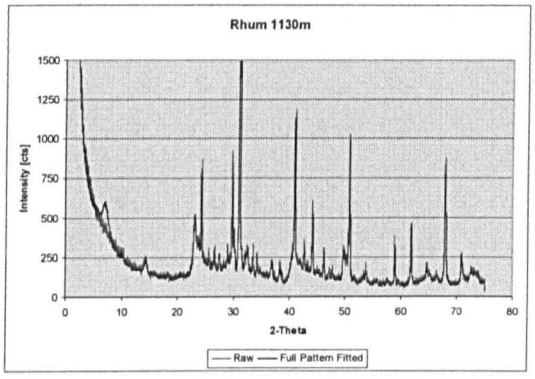

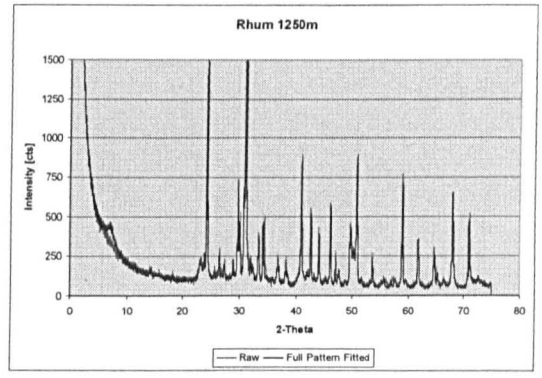

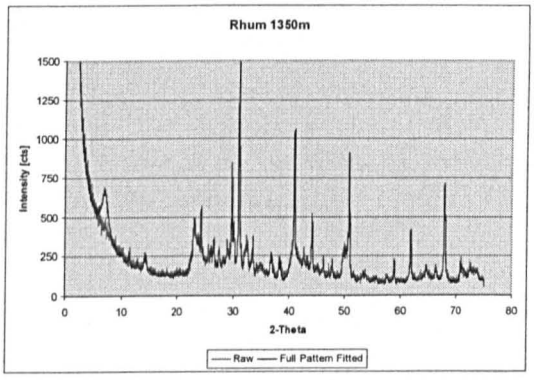

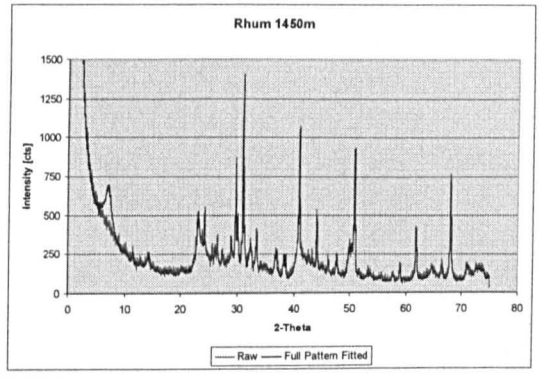

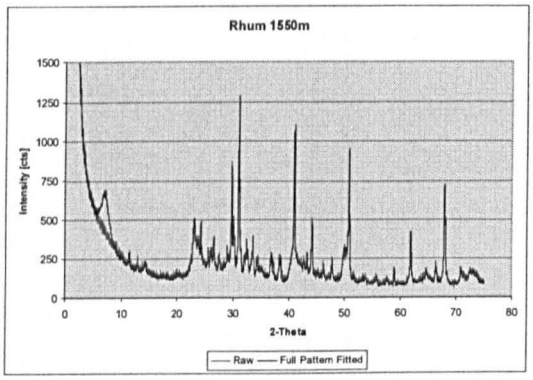

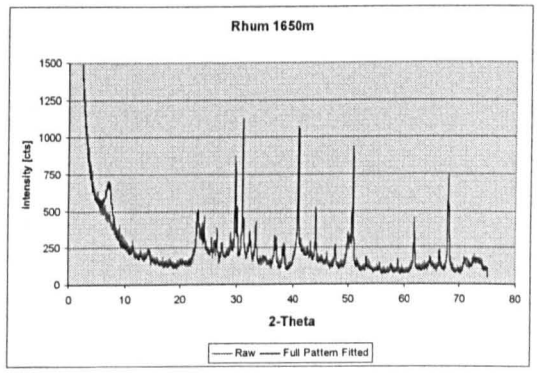

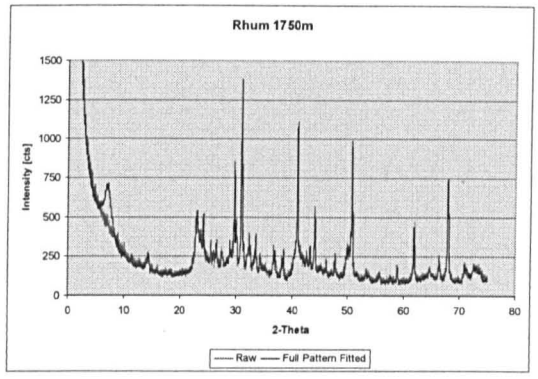
Rhum 1750m
Intensity [cts]
2-Theta
Raw
Full Pattern Fitted

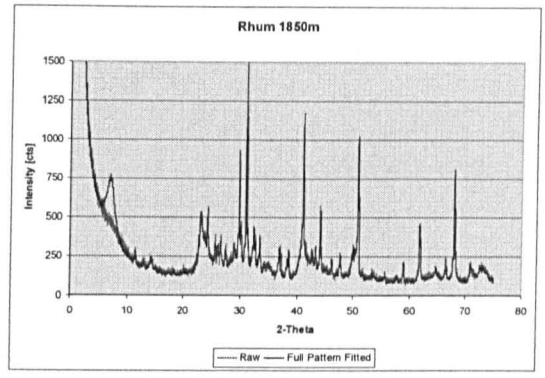
Rhum 1850m
Intensity [cts]
2-Theta
Raw
Full Pattern Fitted

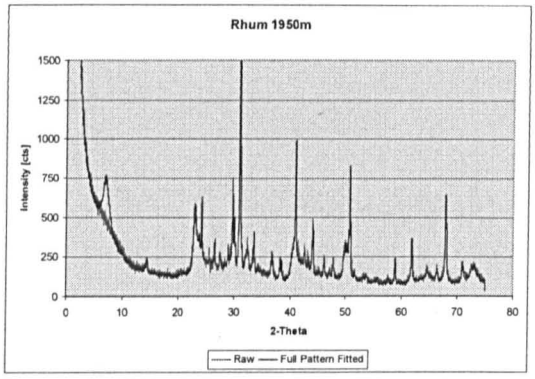
Rhum 1950m
Intensity [cts]
2-Theta
Raw
Full Pattern Fitted

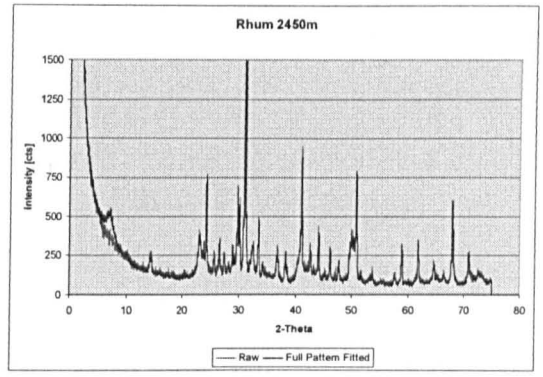
Rhum 2450m
Intensity [cts]
2-Theta
Raw
Full Pattern Fitted

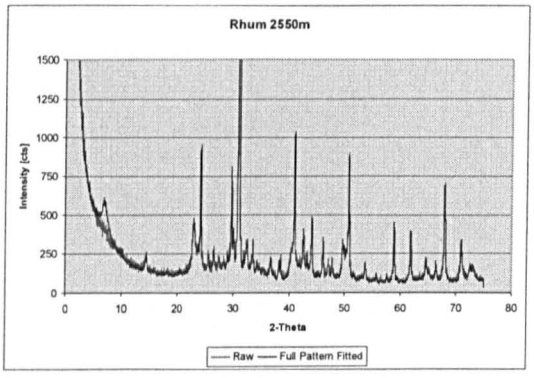
Rhum 2550m
Intensity [cts]
2-Theta
Raw
Full Pattern Fitted

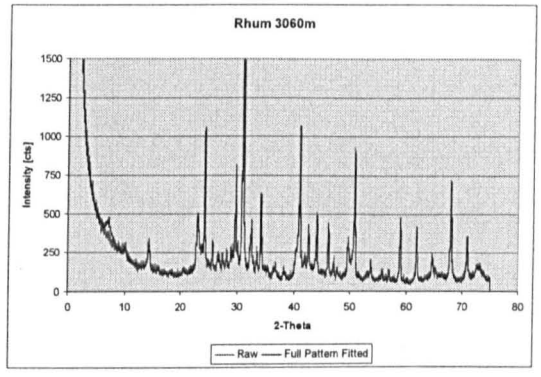
Rhum 3060m
Intensity [cts]
2-Theta
Raw
Full Pattern Fitted

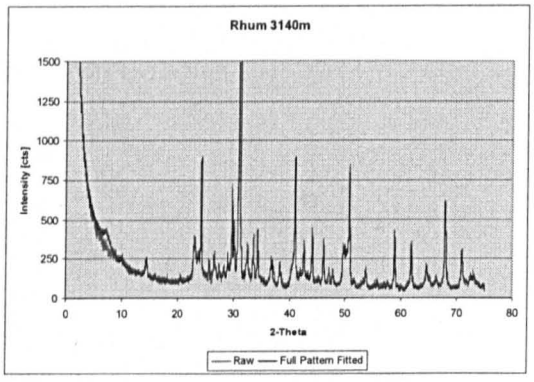
Rhum 3140m
Intensity [cts]
2-Theta
Raw
Full Pattern Fitted

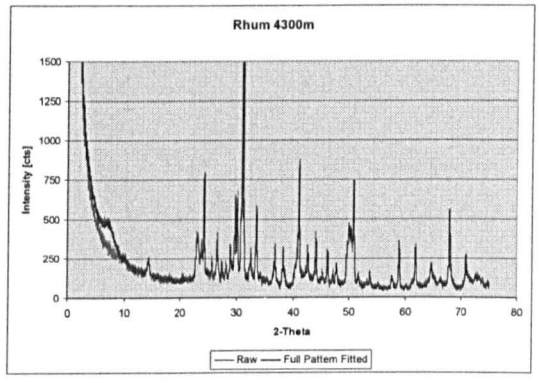
Rhum 4300m
Intensity [cts]
2-Theta
Raw
Full Pattern Fitted

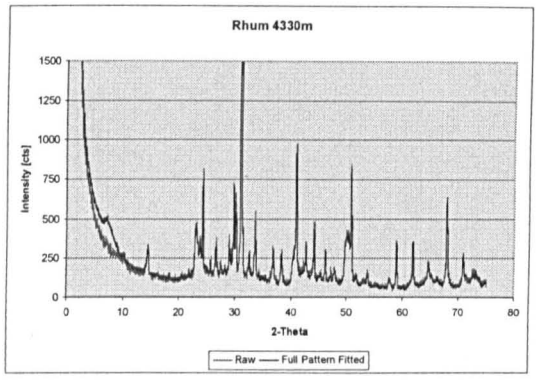
Rhum 4330m
Intensity [cts]
2-Theta
Raw
Full Pattern Fitted

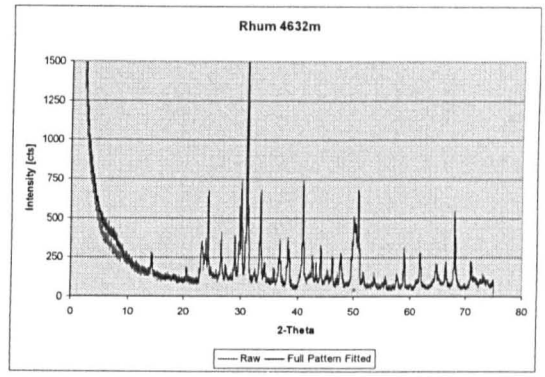
Rhum 4632m
Intensity [cts]
2-Theta
Raw
Full Pattern Fitted

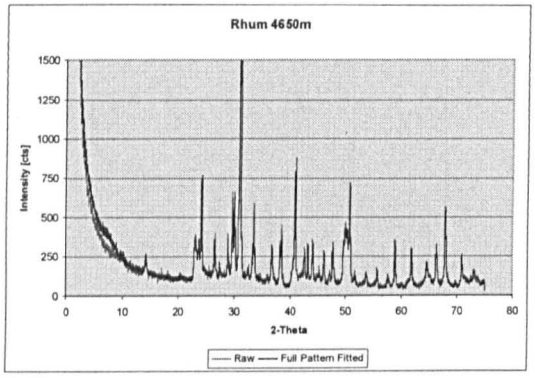
Rhum 4650m
Intensity [cts]
2-Theta
Raw
Full Pattern Fitted

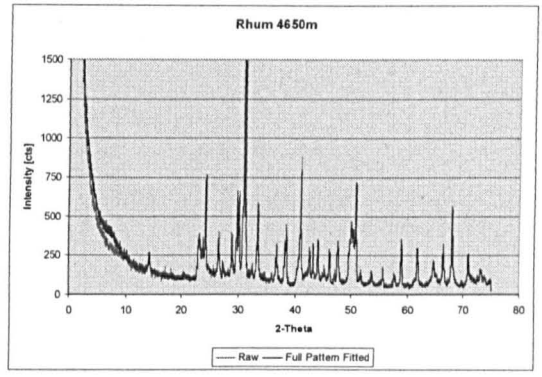
Rhum 4650m
Intensity [cts]
2-Theta
Raw
Full Pattern Fitted

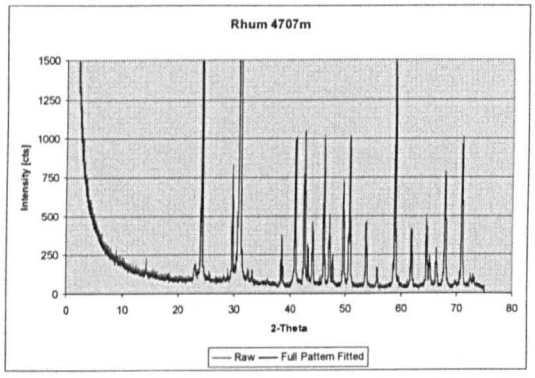
Rhum 4707m
Intensity [cts]
2-Theta
Raw
Full Pattern Fitted

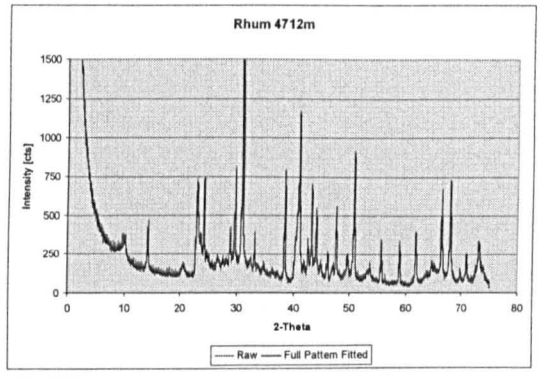
Rhum 4712m
Intensity [cts]
2-Theta
Raw
Full Pattern Fitted

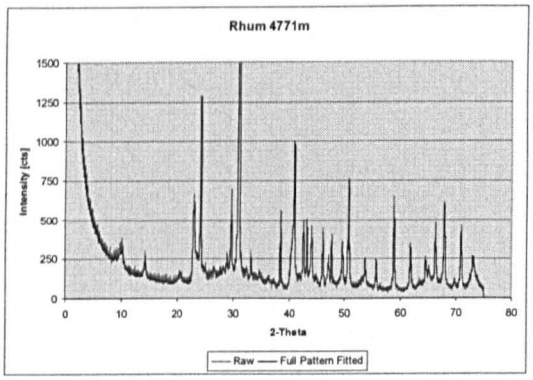
Rhum 4771m
Intensity [cts]
2-Theta
Raw
Full Pattern Fitted

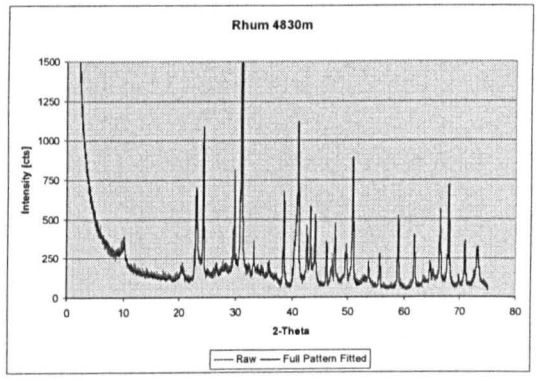
Rhum 4830m
Intensity [cts]
2-Theta
Raw
Full Pattern Fitted

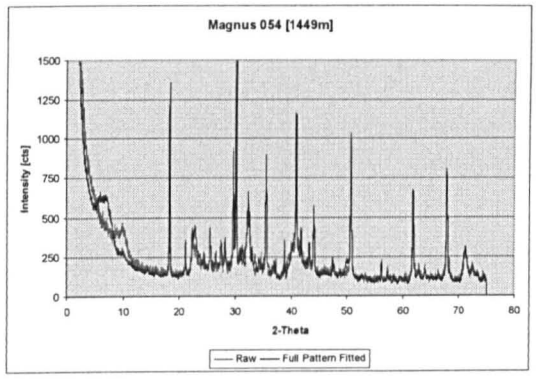
Magnus 054 [1449m]
Intensity [cts]
2-Theta
Raw
Full Pattern Fitted

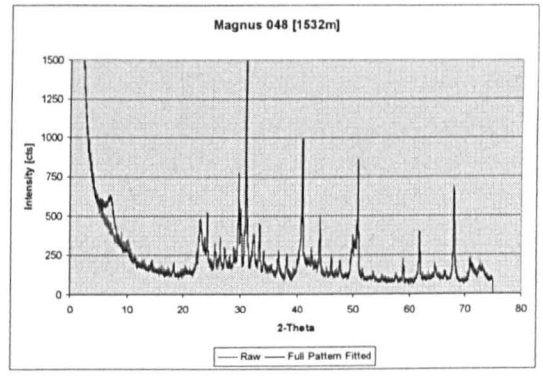
Magnus 048 [1532m]
Intensity [cts]
2-Theta
Raw
Full Pattern Fitted

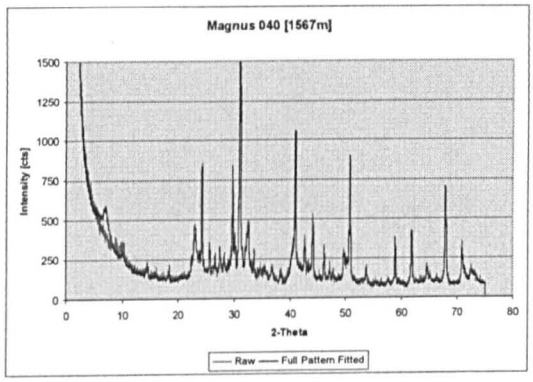
Magnus 040 [1567m]
Intensity [cts]
2-Theta
Raw
Full Pattern Fitted

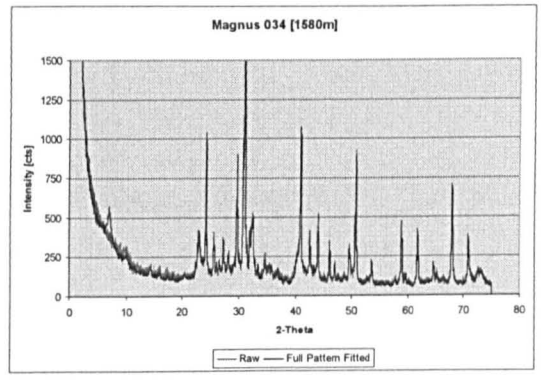
Magnus 034 [1580m]
Intensity [cts]
2-Theta
Raw
Full Pattern Fitted

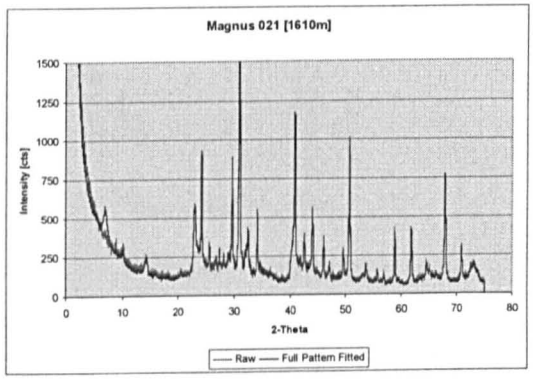
Magnus 021 [1610m]
Intensity [cts]
2-Theta
Raw
Full Pattern Fitted

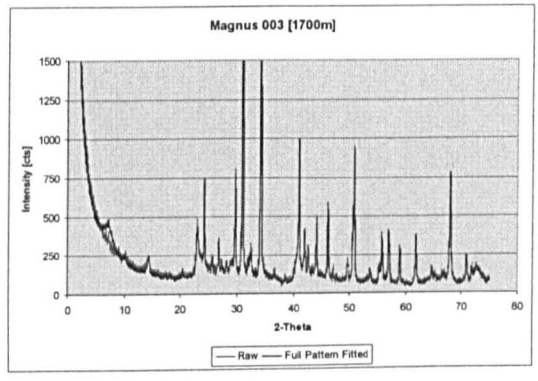
Magnus 003 [1700m]
Intensity [cts]
2-Theta
Raw
Full Pattern Fitted

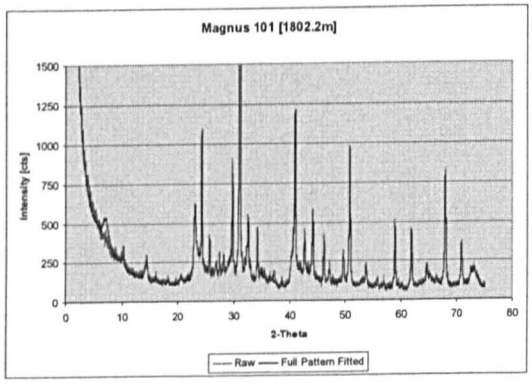
Magnus 101 [1802.2m]
Intensity [cts]
2-Theta
Raw
Full Pattern Fitted

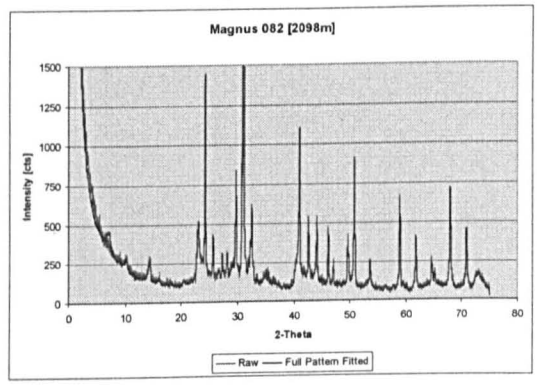
Magnus 082 [2098m]
Intensity [cts]
2-Theta
Raw
Full Pattern Fitted

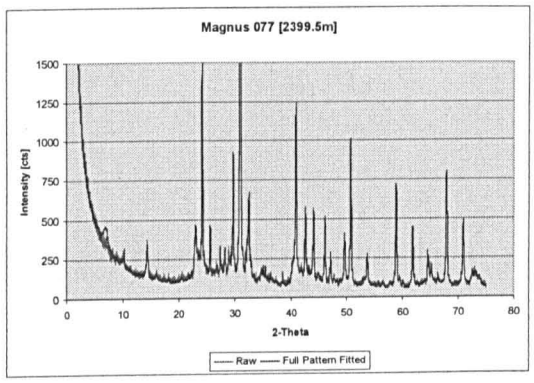
Magnus 077 [2399.5m]
Intensity [cts]
2-Theta
Raw
Full Pattern Fitted

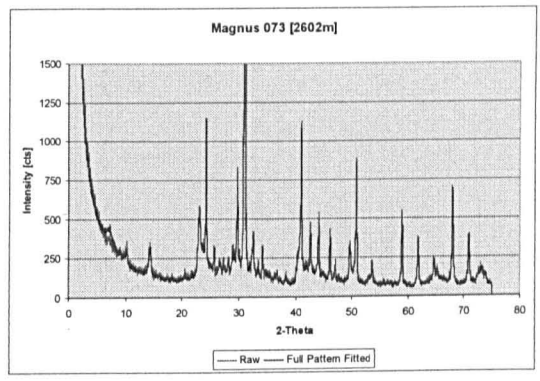
Magnus 073 [2602m]
Intensity [cts]
2-Theta
Raw
Full Pattern Fitted

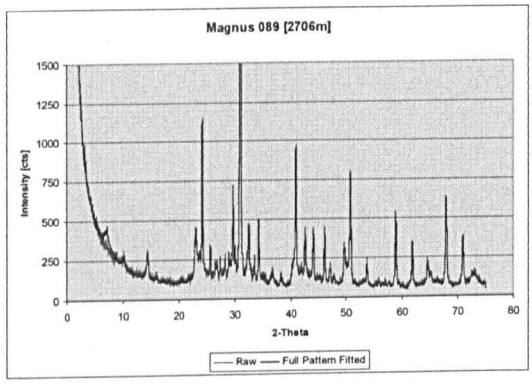
Magnus 089 [2706m]
Intensity [cts]
2-Theta
Raw
Full Pattern Fitted

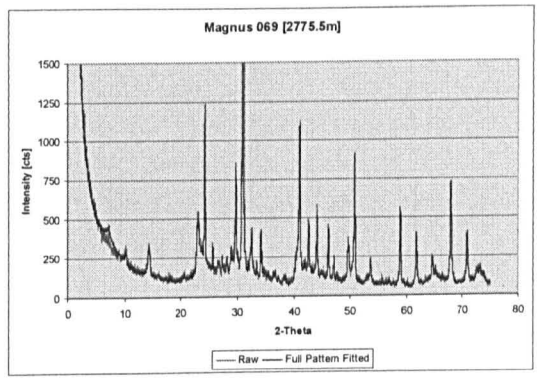
Magnus 069 [2775.5m]
Intensity [cts]
2-Theta
Raw
Full Pattern Fitted

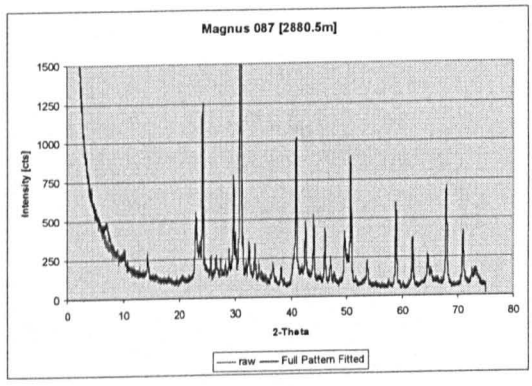
Magnus 087 [2880.5m]
Intensity [cts]
2-Theta
raw
Full Pattern Fitted

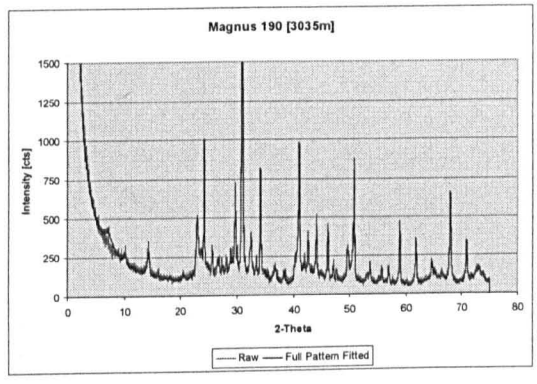
Magnus 190 [3035m]
Intensity [cts]
2-Theta
Raw
Full Pattern Fitted

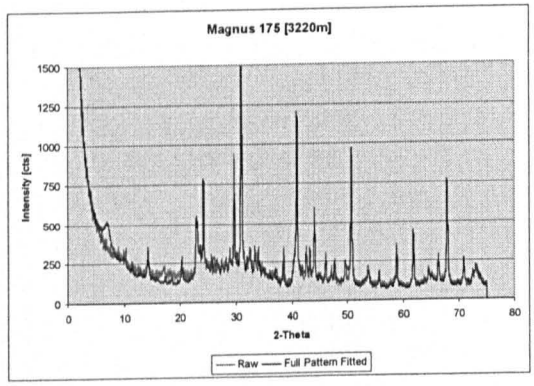
Magnus 175 [3220m]
Intensity [cts]
2-Theta
Raw
Full Pattern Fitted

Appendix 5.1:

5.1.1: Lithology:

Lithology in this study comes from the synthesis of the information gathered from the completion logs of the wells in question. This is based on an assessment of the sonic, gamma ray and resistivity logs produced by downhole measurement at or close to the time of drilling and the lithology key and lithological descriptions by the mudlogger/well site geologist that furnish the completion log. The Genesis program allows the input (Figures 5.1x & 5.2x) of 15 different lithologies; sandstone, silt, shalysand, sandyshale, shale, marl, limestone, dolomite, halite, gypsum, anhydrite, coal, chalk, igneous and conglomerate, in varying percentages designated by the user from an appreciation of the completion log. The initial lithological mix of the chosen lithological units is done by first defining the stratigraphy of the well in question and then making an assessment of the lithological mix of each unit and whether it would be more appropriate to further divide the stratigraphy once the lithological mix has been assessed.

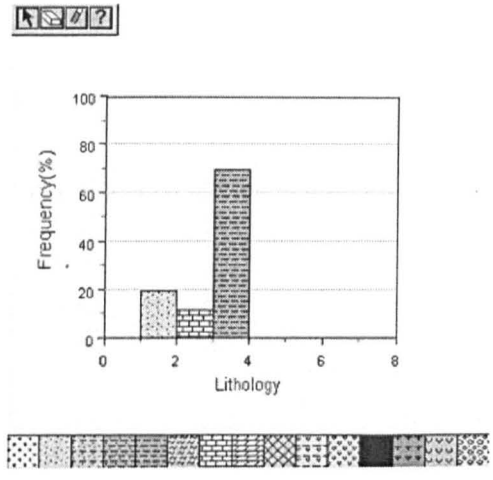

Figure 5.1x. The 15 input lithologies in Genesis 4.8, with three user defined lithologies (silt, 20%, limestone, 10% and shale, 70%) for a chosen unit.

In the hypothetical example in Figures 5.1x & 5.2x the chosen layer is 300m thick and has a lithological mix of silt, (20%), limestone, (10%), and shale, (70%), these being present as thinner units within the overall unit. However, it is not necessary to divide this lithological unit into smaller single lithology units as the unique mixing model in Genesis 4.8 preserves the properties of

end member lithologies and does not model the unit as the average or weighted average of the three incorporated lithology types (ZetaWare, 2005). The way Genesis 4.8 calculates the properties of these unique mixes is through coupled mathematics as some of the properties are interdependent. In the first construction of the model this lithology must be viewed as a first iteration and will change subtly as the model is refined as more parameters, such as temperature, pressure, vitrinite reflectance are added to the model.

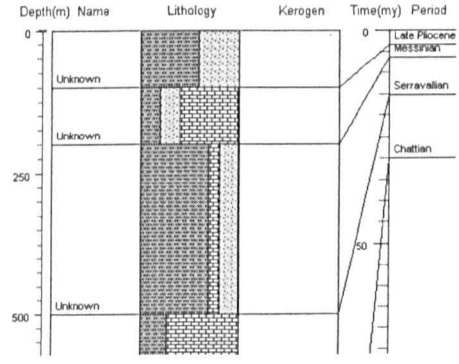

Figure 5.2x. The input lithologies in Figure 5.2 are between 200 and 500m in this hypothetical section.

5.1.2: Age:

The age input parameter in this study was simply that which is read off of the completion log; in general it is defined from the stratigraphy and the occurrence of marker beds. Absolute ages are not as important the chronostratigraphic stage or lithostratigraphic group.

An understanding of the stratigraphy is essential as hiatuses in deposition and erosional unconformities can be entered into the model. Unconformities may be highlighted in the stratigraphy or through the early stages of modelling where dog-legs in, for example, the porosity or vitrinite reflectance trend with depth may be evident and describe the erosional loss of sediment. The way Genesis 4.8 views an unconformity is as essentially equal time of deposition and equal time of erosion at some fixed rate taken to be the rate

of accumulation prior to deposition (see Lerche, 1993 for a discussion of this method).

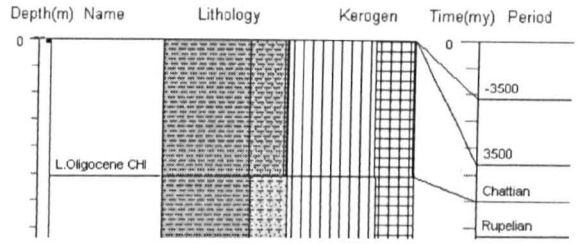

Figure 5.3x. A 3500m unconformity modelled into Chocholow PIG-1.

Figure 5.3x shows the 3500m unconformity at the top of the Chocholow PIG-1 well from the Podhale Basin in southern Poland. Here, the model assumes that the time from the top of the Chattian to the end of the erosional event was equally divided between sediment accumulation and sediment erosion.

5.1.3: Vitrinite Reflectance; Porosity:

Vitrinite Reflectance (Ro), is a secondary analysis and may be imported into Genesis 4.8 as a text file, in the same way that porosity data (in this study from mercury intrusion porosimetry) may be imported. This data helps to calibrate the model to measured results and does not solely rely on the theory or empirical formulations in the model (see the next section for more on compaction within the model).

5.1.4: Surface Temperature:

Measurements of temperature at depth are of limited value if the thermal profile cannot be extrapolated back to the surface. Surface temperature is a single input variable for the top of the section, and for marine deposition it will range between 0 and 10°C for the present day. The importance of surface temperature on deep burial diagenesis has been described by Worden et al (2000). Present day mean annual surface temperature can be approximated

reasonably well as a function of latitude both for land surface data (Spangler & Jenne, 1980) and sea surface temperature (Schweitzer, 1993). Palaeoclimate reconstructions (e.g. Hoffert and Covey, 1992) have ably demonstrated that mean global temperatures have fluctuated through time relative to the present. As a consequence the effects of surface temperature will be a function of latitude and relative sea level as it has been demonstrated that 3rd order sea level changes can have a significant effect on the temperature profile of a basin (Worden et al., 2000). Additionally, if deposition of the strata in question occurred in deep water, a bottom water temperature estimate is needed to model subsurface temperatures and this will be variable depending on water depth and latitude.

5.1.5: Downhole Temperature:

Temperature data is often based on bottom hole temperature (BHT) data and is notoriously unreliable (Hermanrud et al., 1990). BHT data should only be used as a last resort given the large uncertainties associated with correcting these data (Corrigan, 2003). More reliable types of temperature data (i.e., temperature measurements from electronic pressure/temperature gauges used on modern DST/PT equipment from permeable intervals, production log temperature measurements from shut-in production wells) should be sought to constrain the subsurface thermal regime whenever possible (Jensen & Doré, 1993). In the absence of the above data a Horner correction (Lachenbruch & Brewer, 1959), or an empirical correction using time since circulation correction (e.g. Roux et al, 1982) should be used to convert raw BHT (Hermanrud et al., 1990; Vik & Hermanrud 1993). In this study all BHT data presented has been corrected using time since circulation method.

5.1.6: Pore Pressure:

The pore pressure data is sourced from the well test data usually at the foot of the completion log or as a sundry appendix to the log.

5.2. Appendix:

5.2.1: Modelling assumptions and uncertainties:

With maturity modelling in Genesis 4.8 there are a series of models built into the modelling software whose sources and base assumptions are not available to the user. This lack sight into the model results from the simple fact that the models and assumption are numerous and in using Genesis 4.8 to model burial histories and so on, there is simply not time to go into every aspect of the model itself, the empirical determinations and process modelling, and create a critique. However, some of the assumptions in the model will be commented upon.

Heat input into the system comes from two primary sources, that which is generated in the aesthenosphere and that which is generated in the lithosphere and in the crust. The temperature at the lithosphere-asethenosphere boundary is taken to be a fixed temperature of 1330°C, and the thickness of this boundary and for the purposes of this modelling study in Genesis 4.8 is taken to be 120km.

Heat is generated in one region and flows to another, as heat flows form higher temperature regions to lower temperature regions. This implies that any temperature difference will cause heat to flow and the temperature of any lithology is proportional to the heat it retains. There are three factors that control terrestrial heat generation.

- The thickness of lithosphere. Since at the base it is always 1330°C, thinner lithosphere results in higher total heat flow to cooler regions of the lithosphere (i.e. up into the sediment pile).
- The Radiogenic Heat Production (RHP) and thickness of the lithosphere, mostly from granites, may account for up to 50% of heat flow in crustal sediments. Thin crusts will produce little heat by RHP.

- The RHP from sediments, is a relatively small contribution but may become significant when the sediment column is significant.

Genesis 4.8 calculates temperature from given heat flow and thermal conductivity information. Thermal conductivity is given for each different lithology and is a function of porosity. Heat flow may be calculated from present day temperature measurements and the known conductivities of each lithology present in a system.

The definitions and units of measurement are:

- Thermal gradient (G) — Rate of change of temperature with depth °C/100m, °C/km or °F/ft .
- Thermal conductivity (K) — power per length · degree. W/m·K or cal/cm/sec.
- Heat flow (Q) — Rate of heat transfer, expressed as or power per unit area. mW/m^2 or HFU ($cal/cm^2/sec$).
- Radiogenic heat production (RHP) — source of heat in sediments or basement, mW/m^3
- Basic formula — Heat flow Q = K·G.

Thermal conductivity of rocks and fluids vary from 20 to 400 mW/m^2 or 0.5-9.6 $cal/cm^2/sec$ (Barker, 1996) for a given heat flow, shales, having a low conductivity, will result in higher thermal gradients. Higher porosity also means lower bulk conductivity because fluids have much lower thermal conductivities than the rock matrix. Each lithology in a basin fill has a different thermal conductivity which has been defined by Gretener (1981) and these are implicit in Genesis 4.8. In addition, transient effects at the base of the lithosphere and fast sedimentation rates may cause temporarily lower heat flow in sediments and thermal conductivity will increase with decreasing porosity for all lithologies.

5.2.2: Compaction in the burial model:

If a burial history in Genesis 4.8 were not to incorporate compaction, the burial history diagram would have burial paths that would be parallel and would therefore assume that porosity would remain unchanged through time. This is clearly not the case and additional factors need to be addressed such as;

- Compaction during burial means unit thickness changes (e.g. Giles et al., 1998; Brewster & Butler, 1985) and is based on increased effective stress with depth, where effective stress results from subtracting pore pressure from overburden stress. .
- Empirically, porosity is largely a function of depth (e.g. Athey, 1930; Bahr et al., 2001; Yang & Aplin, 1998). But mineral diagenesis must be factored in.
- Overburden pressure is never going to be homogenous in terms of lithology or porosity therefore the amount of compaction a unit receives is a function of its lithology and porosity.
- The weight of overburden is partly borne by pore fluids and compaction cannot occur if fluid cannot escape and it is well known that overpressured rocks have anomalous porosities (e.g. Scholle et al., 2006).

The above all create a significant problem for the model to solve because parameters such as porosity, effective stress, and permeability are interdependent and the model cannot solve them sequentially. Therefore the model requires mathematical coupling and the simultaneous solution of systems of equations. How these all interact are unseen by the user and must be held in mind that they are happening in the software as the model is executed.

It should be noted that the equations in the model are unseen but the assumptions behind porosity loss with depth are governed by lithology type.

A change in lithology in the model will result in an increase or decrease in predicted/estimated porosity based on the parameters in Genesis 4.8 for each of the 15 lithology types it handles and the relative proportion of those in stratigraphical unit (how the model handles mixed lithology has been previously mentioned). The model solves for porosity under normal compaction (hydrostatic conditions) as well as in overpressure situations as the depth-porosity relationship for each lithology is know through empirical measurement either by physical determination or by wire-line techniques. As a result the porosity-effective stress relationship may be derived (e.g. after Magara, 1978, Yang & Aplin, 1998) and the empirical relationship between porosity and effective stress for each lithology can be calibrated against known examples (e.g. after Ungerer et al., 1990).

The simultaneous solution of systems of equations in Genesis 4.8 using coupled mathematics and the interdependent nature of these equations would follow something like this; effective stress is coupled to void ratio. For each lithology there will therefore be an equation relating porosity to effective stress. Darcy's Law is then used to calculate fluid flow during burial from a porosity-permeability function and in turn is coupled to a calibration of void ratio and permeability (e.g. Dutta 1987) and each lithology will have a different coefficient in the function. Finally, thermal conductivities will change with porosity loss so this then relates fluid flow to heat flow.

5.2.3: Pressure:

The common causes of overpressure in a basin are;

- Compaction disequilibrium
- Uplift and erosion
- Hydrocarbon generation
- Heating (thermal expansion of fluid)
- Tectonic compression

The model can incorporate overpressure prediction but it requires at least porosity data as a cross-check to the prediction, as overpressure will give anomalously high porosity results relative to depths and normal pressure systems. The key to modelling overpressure is the porosity-effective stress relationship in Genesis 4.8, as it is calibrated to porosity by the various lithological mixes possible and thus to permeability allowing overpressure prediction. The equations for fluid pressure will create a curve plotted against depth that will change as a function of lithology, burial depth and rate of burial. Additionally, velocity data is often used to calibrate overpressure, although it is not available to this study.

5.2.4: Vitrinite Reflectance:

The study of sedimentary organic matter metamorphism from kerogens to hydrocarbons has been increasingly exploited. The key attraction of vitrinite reflectance in this context is its sensitivity to temperature ranges that largely correspond to those of hydrocarbon generation (i.e. 60 to 120°C) (e.g.Armagnac et al., 1989) and the temperatures at which illite-smectite ordering changes (Weaver, 1989). This means that, with a suitable calibration, vitrinite reflectance can be used as an indicator of maturity in hydrocarbon source rocks and mudstones in general. Generally, the onset of oil generation is correlated with a reflectance of 0.5-0.6% and the termination of oil generation with reflectance of 0.85-1.1%. Genesis 4.8 uses four equations to derive Ro curves as a function of increasing thermal maturity, the Lawrence Livermore National Laboratory (LLNL) model (e.g. Sweeney & Burnham 1990) and the ARCO model, plus two BP models referred to as BP maximum and BP minimum (no references for the exact equations). All four models are essentially kinetic models that model the increase in Ro with increasing temperature in subtly different ways.

Where porosity is the key calibration data for fluid flow vitrinite reflectance is the key calibration data for the thermal side of the model.

As mentioned above the mantle lithosphere-aesthenosphere boundary is always taken to be 1330°C in Genesis 4.8 therefore thinner lithosphere thicknesses will result in higher total heat flow. Figures 5.4x, 5.5x & 5.6x show the thermal settings used in this study, where a default crust and mantle thickness of 120km has been set based on the cross-section of the Rhum area published in the Millennium Atlas. Additionally, heat production in the lower crust and mantle lid (Figure 5.6x) has been turned to zero, under the assumption of no lithosphere stretching, these settings resulted from a process of iteration during the modelling on Rhum 3/29a4 and Magnus 211/12-2 wells.

Figure 5.4x shows the thermal controls used in this study. The thermal model is set to transient, fixed temperature at the base of the lithosphere. This implies that the base of lithosphere temperature is always 1330°C and that the effect of this temperature is of heat flow up into lower temperature regions. However this flow is affected by the sediment pile and is therefore not lasting or durable as fast sedimentation rates may cause temporarily lower heat flow in the sediments. Additionally, the lithosphere and crust are assumed to generate heat by RHP and that the flow of this heat is advective.

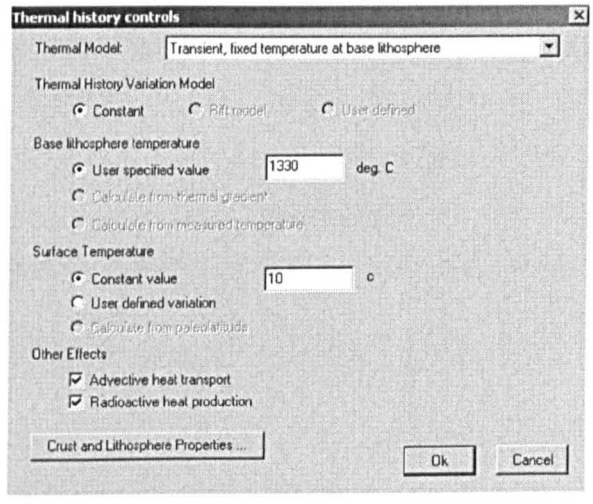

Figure 5.4x. Thermal controls set in Genesis 4.8 for this study, 1330°C base of lithosphere temperature, a constant surface value temperature, under conditions of a transient thermal model with the fixed temperature of 1330°C at the base of the lithosphere. Additionally, RHP is assumed to occur with advective heat transport.

The fixed conditions at the crust-mantle boundary will have a key effect on how heat flow will operate in the basin. If the base of the lithosphere is a constant temperature boundary, then thicker crust will result in lower thermal gradients and heat flows in the basin. Alternatively, if the base of the crust is a constant heat flow boundary, with a constant flow of heat from the aesthenosphere, then crustal thickness has little effect on the thermal gradient beyond that of heat production (Beardsmore & Cull, 2001).

The effects of other thermal models will change the model significantly, Genesis 4.8 allows a further 4 models to be selected (Figure 5.5x). These changes allow the position of heat production to be moved from the lithosphere-aesthenosphere boundary up to the base of the sediment pile. This may be applicable in basins intruded by dykes and sills. Alternatively, the flow properties can be changed. A steady state heat flow model may be appropriate for sediments close to a spreading centre.

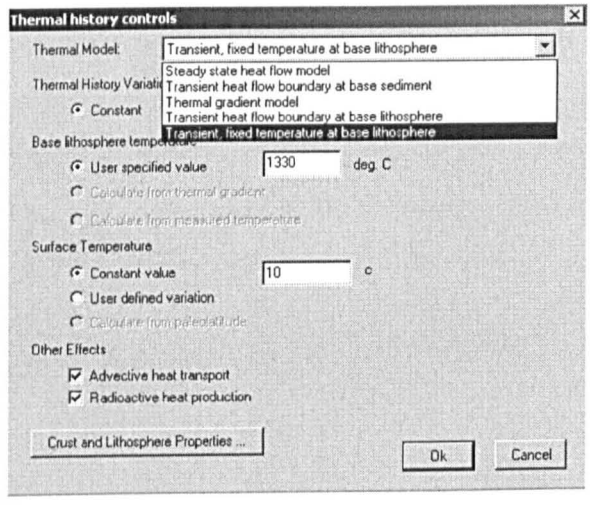

Figure 5.5x. The other possible thermal controls set in Genesis 4.8.

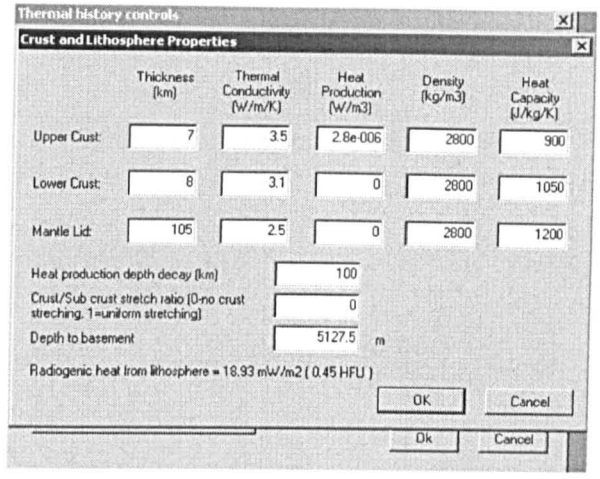

Figure 5.6x. The crust and lithosphere properties set in Genesis 4.8 for Rhum 3/29a4 and Magnus 211/12-2, where a default crust and mantle thickness of 120km has been set and heat production in the lower crust and mantle lid has been turned to zero, under the assumption of no lithosphere stretching, these settings resulted from the iterative nature of the modelling on these two wells.

As well as the thermal models used in this study being open to variation the burial history controls may also be set in Genesis 4.8 (Figure 5.8). The fluid flow model is set to transient and the permeability model to the Dutta-Franklyn model, with the base of the well set to no flow predicted, a fracture gradient of 0.95 and an initial water density of 1.05g/cm^3. It should be emphasised that the settings used for burial history control are those used by BP as their defaults (Illife, 2005; Pers. Comms.). A transient fluid flow model is used as a steady state fluid flow model will assume a constant durable flow, whereas a transient model takes into account that flow might not be steady or durable. The selection of the Dutta-Franklyn permeability model over the Koseny-Carman model is quite arbitrary, but in choosing the Dutta-Franklyn model a choice regarding the calibration of the Dutta-Franklyn model is made as it will apply a different empirical relationship between permeability and void ratio for the various lithologies the model solves for.

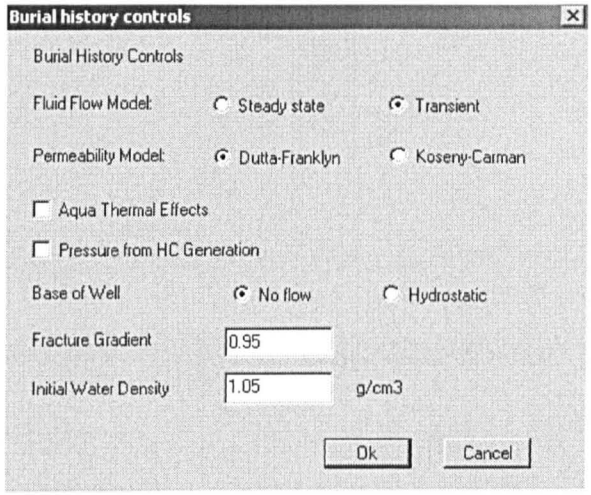

Figure 5.7x. The Burial History Controls, with the default settings selected for this study.